

IMPACT FACTOR  
**11.082**

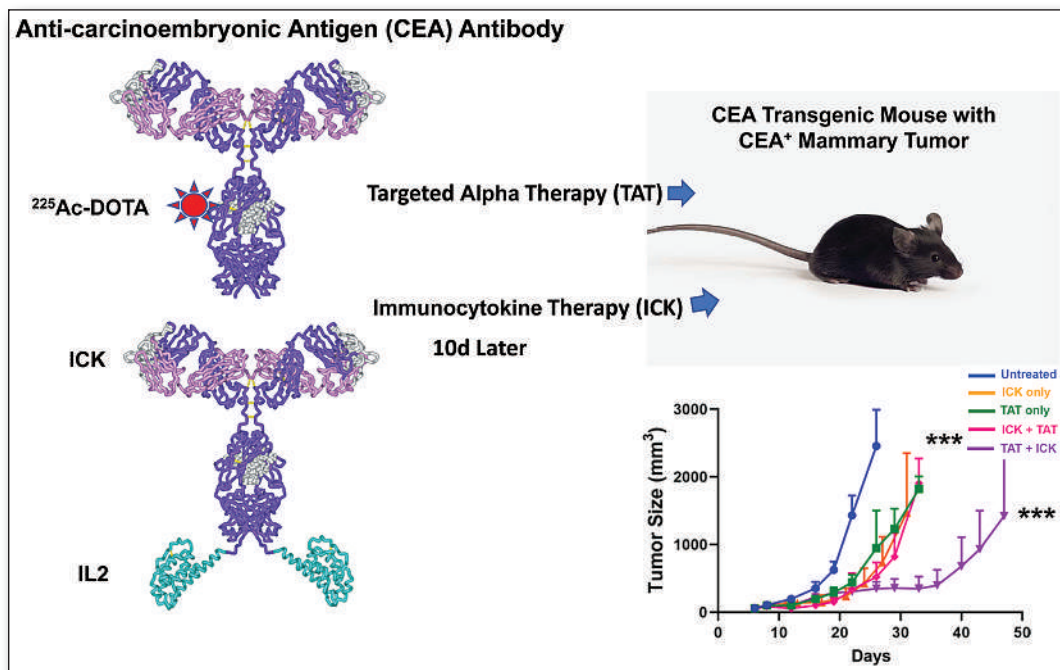
#1 NUCLEAR MEDICINE,  
MOLECULAR IMAGING  
AND MOLECULAR  
RADIOTHERAPY JOURNAL

# JNM

The Journal of Nuclear Medicine

## FEATURED ARTICLE

Improved Tumor Responses with Sequential Targeted  $\alpha$ -Particles Followed by Interleukin 2 Immunocytokine Therapies in Treatment of CEA-Positive Breast and Colon Tumors in CEA Transgenic Mice. Megan Minnix et al. See page 1859.



Cardiac amyloidosis prevalence: bone scintigraphy in >10,000 patients offers new insights. Christian Nitsche et al. See page 1906.

# A novel investigational PSMA-targeting technology for prostate cancer imaging

In recent years, radiopharmaceutical innovations have greatly improved our ability to detect and localize prostate cancer. Until recently, conventional imaging, including bone scan, computed tomography (CT), and magnetic resonance imaging (MRI), has been the standard of care in prostate cancer imaging. These conventional imaging modalities have limitations, including diagnostic performance at low prostate-specific antigen (PSA) levels.<sup>1,2</sup> Technological advances have led to the research and development of more sensitive imaging agents and modalities.<sup>1,3</sup> Specifically, positron emission tomography (PET) radiopharmaceuticals are increasingly being used to target prostate-specific membrane antigen (PSMA), and a growing body of scientific evidence supports their favorable imaging performance.<sup>1</sup> *Blue Earth Diagnostics is exploring a new investigational PSMA targeting technology with unique potential.*<sup>4-6</sup>

## PSMA as a target

PSMA is an obvious target for PET imaging in prostate cancer. It is a well characterized type II transmembrane protein with folate hydrolase activity. Present in normal prostatic tissue, PSMA is upregulated in the majority of primary and metastatic prostate cancer lesions.<sup>7-9</sup>

Several characteristics make PSMA an ideal target for molecular imaging, including:

- High expression on prostate cancer cells<sup>10</sup>
- Limited expression on benign prostate tissue and extraprostatic tissue<sup>10</sup>
- Well-characterized binding site that can be targeted by small-molecule ligands<sup>10</sup>

- Internalization of bound agents, allowing for concentration within tumor cells<sup>10</sup>
- PSMA expression can be correlated with Gleason grade and has been shown to be enhanced in metastatic and castrate-resistant prostate cancer<sup>9,10</sup>

PSMA imaging agents are designed to bind to the extracellular domain of PSMA to then be internalized by prostate cancer cells via endocytosis. When labeled with a  $\beta^+$  emitting radioisotope, these agents can detect extracellular expression of PSMA with PET imaging.<sup>9-11</sup> PSMA-targeting radiopharmaceuticals are characterized by rapid clearance from the blood and nontarget tissue, which can result in low background activity.<sup>9</sup>

## Radioisotope selection and labeling

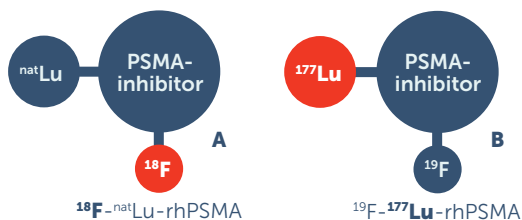
Currently available PSMA agents are either labeled with gallium-68 (<sup>68</sup>Ga) or fluorine-18 (<sup>18</sup>F), 2  $\beta^+$  emitting radioisotopes. In recent years, <sup>18</sup>F has been recognized to have certain advantages over <sup>68</sup>Ga.<sup>9</sup>

While <sup>68</sup>Ga can be produced with either a cyclotron or generator, production capacity via generator is limited to 2 to 4 patient doses daily. <sup>68</sup>Ga also has a relatively short half-life of 68 minutes, limiting its transportation

to centers.<sup>9</sup> <sup>18</sup>F has an 110-minute half-life and may be produced in large batches via a cyclotron, which allows for centralized production and subsequent broad distribution to imaging facilities (see Table 1).<sup>12,13</sup>

Blue Earth Diagnostics is at the forefront in the investigation of prostate cancer imaging, with worldwide exclusive licenses to radiohybrid PSMA (rhPSMA) technology.

**Figure 1. Example of a radiohybrid structure**



Adapted from Wurzer A et al. *J Nucl Med*. 2020.<sup>6</sup>

The rhPSMA design features 2 radionuclide acceptor sites that can be labeled with  $\alpha$  or  $\beta$  emitting radionuclides (Figure 1). Figure 1A depicts the rhPSMA molecule for potential diagnostic use, where one acceptor site is labeled with a radioactive imaging isotope, and the other site with a nonradioactive isotope. Figure 1B depicts the molecule for potential therapeutic use, where one acceptor site is labeled with a radioactive therapeutic isotope and the other site with a nonradioactive isotope.<sup>6</sup>

Review the phase 3 clinical studies for rhPSMA technology<sup>4,5</sup>:

- Learn more about the LIGHTHOUSE study in men with newly diagnosed prostate cancer at [clinicaltrials.gov/ct2/show/NCT04186819](https://clinicaltrials.gov/ct2/show/NCT04186819)
- Learn more about the SPOTLIGHT study in men with suspected prostate cancer recurrence at [clinicaltrials.gov/ct2/show/NCT04186845](https://clinicaltrials.gov/ct2/show/NCT04186845)

## Blue Earth Diagnostics is committed to breaking new ground

Blue Earth Diagnostics is an established leader in the development of novel PET imaging agents to inform clinical management decisions with the goal of positively impacting overall outcomes for patients with prostate cancer.

Our goals are to:

- Develop cutting-edge technology
- Build innovative solutions
- Enhance access to radiopharmaceuticals and provide customer and practice support

Register at [prostatecancer-blueearthdx.com](https://prostatecancer-blueearthdx.com) for the latest company news and developments.

Sponsored by Blue Earth Diagnostics, Inc.

### Radiohybrid PSMA technology is investigational and not approved by the US Food and Drug Administration (FDA).

**References:** 1. Jadvar H, Calais J, Fanti S, et al. *J Nucl Med*. 2022;63(1):59-68. doi:10.2967/jnumed.121.263262 2. Expert Panel on Urologic Imaging; Froemming AT, Verma S, Eberhardt SC, et al. *J Am Coll Radiol*. 2018;15(5S):S132-S149. doi:10.1016/j.jacr.2018.03.019 3. Crawford ED, Koo PJ, Shore N, et al. *J Urol*. 2019;201(4):682-692. doi:10.1016/j.juro.2018.05.164 4. Blue Earth Diagnostics. March 17, 2022. Accessed July 27, 2022. <https://clinicaltrials.gov/ct2/show/NCT04186819> 5. Blue Earth Diagnostics. March 17, 2022. Accessed July 27, 2022. <https://clinicaltrials.gov/ct2/show/NCT04186845> 6. Wurzer A, Di Carlo D, Schmidt A, et al. *J Nucl Med*. 2020;61(5):735-742. doi:10.2967/jnumed.119.234922 7. Sarkar S, Das S. *Biomed Eng Comput Biol*. 2016;7(suppl 1):1-15. doi:10.4137/BECB.S34255 8. Hofman MS, Hicks RJ, Maurer T, Eiber M. *Radiographics*. 2018;38(1):200-217. doi:10.1148/rg.2018170108 9. Piron S, Verhoeven J, Vanhove C, De Vos F. *Nucl Med Biol*. 2022;106-107:29-51. doi:10.1016/j.nucmedbio.2021.12.005 10. Donin NM, Reiter RE. *J Nucl Med*. 2018;59(2):177-182. doi:10.2967/jnumed.117.191874 11. Tolvanen T, Kalliokoski K, Malaspina S, et al. *J Nucl Med*. 2021;62(5):679-684. doi:10.2967/jnumed.120.252114 12. Jacobson O, Kiesewetter DO, Chen X. *Bioconjug Chem*. 2015;26(1):1-18. doi:10.1021/bc500475e 13. Gorin MA, Pomper MG, Rowe SP. *BJU Int*. 2016;117(5):715-716. doi:10.1111/bju.13435 14. Conti M, Eriksson L. *EJNMMI Phys*. 2016;3(1):8. doi:10.1186/s40658-016-0144-5



©2022 Blue Earth Diagnostics, Inc. All rights reserved. MLR22-P003A 08/22

In addition,  $^{18}\text{F}$  has an energy profile that may contribute to a more favorable spatial resolution, which may enable  $^{18}\text{F}$  to better detect lesions that are small and near each other compared with  $^{68}\text{Ga}$  (see Table 1).<sup>9,12-14</sup>

**Table 1. Radioisotope features<sup>9,12-14</sup>**

	$^{18}\text{F}$	$^{68}\text{Ga}$
Half-life	110 minutes	68 minutes
Positron decay ratio	97%	89%
Maximum positron energy	0.635 MeV	1.899 MeV
Mean positron range	0.6 mm	3.5 mm
Production method	Cyclotron	Generator or cyclotron

# MAKE YOUR PLANS FOR

# San Francisco

Register today to attend the **2023 SNMMI Mid-Winter and ACNM Annual Meeting**—January 26-28 in San Francisco, CA. As an attendee, you will have access to the full educational program—including a dedicated brain imaging track—industry-led satellite symposia, robust exhibit hall, and more. Sessions include:

- ✔ Acute Rapid Onset Dementing Disorders
- ✔ Artificial Intelligence in Nuclear Cardiology
- ✔ Brain Imaging Read with the Experts – Basics
- ✔ PSMA RPT: Clinical Trials and Practice
- ✔ Basics of Quantitative SPECT and PET
- ✔ New Diseases and Challenges of How We Use NM in Dementia
- ✔ Hybrid PET/CT Cardiac Imaging: Opportunities and Challenges
- ✔ How to Keep Out of Trouble in Clinical Nuclear Medicine: The Legal Issues
- ✔ New Radiotracers Read with Experts: FES, Dotatate, PyL
- ✔ Pediatric Imaging and Therapy

**EARLY BIRD REGISTRATION DEADLINE:**

**DECEMBER 15, 2022**

**[www.snmmi.org/MWM2023](http://www.snmmi.org/MWM2023)**

JANUARY 26-28  
**2023**



2023 *Mid-Winter Meeting*

**ACNM**  
ANNUAL MEETING



## SNMMI NEWSLINE

- 13N** 2022 SNMMI Highlights Lecture: Oncology and Therapy, Part 1  
Heiko Schöder
- 19N** SNMMI Leadership Update: SNMMI Adopts New Strategic Plan  
Munir Ghesani
- 21N** Newsbriefs
- 22N** From the Literature

## DISCUSSIONS WITH LEADERS

- 1783** Leading in Urology and Pioneering in Social Media Outreach: A Conversation Among Declan Murphy, Ken Herrmann, and Michael Hofman  
Declan Murphy, Ken Herrmann, and Michael Hofman

## THE STATE OF THE ART

- 1786** Fibroblast Activation Protein Inhibitor Imaging in Nonmalignant Diseases: A New Perspective for Molecular Imaging  
Christian Schmidkonz, Torsten Kuwert, Armin Atzinger, Michael Cordes, Georg Schett, Andreas Ramming, and Theresa Götz

## CONTINUING EDUCATION

- 1793** From Concept to Regulatory Drug Approval: Lessons for Theranostics  
Marlon Perera and Michael J. Morris

## FOCUS ON MOLECULAR IMAGING

- 1802** Nanoparticle Diagnostics and Theranostics in the Clinic  
Roger M. Pallares, Felix M. Mottaghy, Volkmar Schulz, Fabian Kiessling, and Twan Lammers

## THERANOSTICS

### Clinical

- 1809** Validation of <sup>18</sup>F-rhPSMA-7 and <sup>18</sup>F-rhPSMA-7.3 PET Imaging Results with Histopathology from Salvage Surgery in Patients with Biochemical Recurrence of Prostate Cancer  
Markus Kroenke, Lilit Schweiger, Thomas Horn, Bernhard Haller, Kristina Schwamborn, Alexander Wurzer, Tobias Maurer, Hans-Jürgen Wester, Matthias Eiber, and Isabel Rauscher
- 1815** Using <sup>68</sup>Ga-PSMA-11 PET/CT for Therapy Response Assessment in Patients with Metastatic Castration-Resistant Prostate Cancer: Application of EAU/EANM Recommendations in Clinical Practice  
Chloé S. Denis, François Cousin, Bram De Laere, Roland Hustinx, Brieuc R. Sautois, and Nadia Withofs

- 1822** <sup>68</sup>Ga-PSMA-11 PET/MRI in Patients with Newly Diagnosed Intermediate- or High-Risk Prostate Adenocarcinoma: PET Findings Correlate with Outcomes After Definitive Treatment

Farshad Moradi, Heying Duan, Hong Song, Guido A. Davidzon, Benjamin I. Chung, Alan E. C. Thong, Andreas M. Loening, Pejman Ghanouni, Geoffrey Sonn, and Andrei Iagaru

- 1829** Correlation of <sup>68</sup>Ga-RM2 PET with Postsurgery Histopathology Findings in Patients with Newly Diagnosed Intermediate- or High-Risk Prostate Cancer

Heying Duan, Lucia Baratto, Richard E. Fan, Simon John Christoph Soerensen, Tie Liang, Benjamin Inbeh Chung, Alan Eih Chih Thong, Harcharan Gill, Christian Kunder, Tanya Stoyanova, et al.

- 1836** ■ **SPECIAL CONTRIBUTION.** Joint EANM, SNMMI, and IAEA Enabling Guide: How to Set up a Theranostics Center

Ken Herrmann, Luca Giovannella, Andrea Santos, Jonathan Gear, Pinar Ozgen Kiratli, Jens Kurth, Ana M. Denis-Bacelar, Roland Hustinx, Marianne Patt, Richard L. Wahl, et al.

- 1844** Repetitive Early <sup>68</sup>Ga-FAPI PET Acquisition Comparing <sup>68</sup>Ga-FAPI-02, <sup>68</sup>Ga-FAPI-46, and <sup>68</sup>Ga-FAPI-74: Methodologic and Diagnostic Implications for Malignant, Inflammatory/Reactive, and Degenerative Lesions

Frederik M. Glatting, Jorge Hoppner, Dawn P. Liew, Antonia van Genabith, Anna-Maria Spektor, Levin Steinbach, Alexander Hubert, Clemens Kratochwil, Frederik L. Giesel, Katharina Dendl, et al.

### Basic

- 1852** A Dimeric FAP-Targeting Small-Molecule Radioconjugate with High and Prolonged Tumor Uptake

Andrea Galbiati, Aureliano Zana, Matilde Bocci, Jacopo Millul, Abdullah Elsayed, Jacqueline Mock, Dario Neri, and Samuele Cazzamalli

- 1859** ■ **FEATURED ARTICLE OF THE MONTH.** Improved Tumor Responses with Sequential Targeted  $\alpha$ -Particles Followed by Interleukin 2 Immunocytokine Therapies in Treatment of CEA-Positive Breast and Colon Tumors in CEA Transgenic Mice

Megan Minnix, Maciej Kujawski, Erasmus Poku, Paul J. Yazaki, Jeffrey Y. Wong, and John E. Shively

## ONCOLOGY

### Clinical

- 1865** <sup>18</sup>F-DOPA PET/CT at the Forefront of Initial or Presurgical Evaluation of Small-Intestine Neuroendocrine Tumors  
Eric Ouvrard, Louis De Mestier, Caroline Boursier, Boumediene Lachachi, Nicolas Sahakian, Elodie Chevalier, Nidaa Mikail, Josefina Carullo, Aurélie Bando-Delaunay, Thomas Walter, et al.
- 1871** First-in-Humans PET Imaging of Tissue Factor in Patients with Primary and Metastatic Cancers Using <sup>18</sup>F-labeled Active-Site Inhibited Factor VII (<sup>18</sup>F-ASIS): Potential as Companion Diagnostic  
Mathias Loft, Camilla Christensen, Malene M. Clausen, Esben A. Carlsen, Carsten P. Hansen, Niels Kroman, Seppo W. Langer, Claus Høgdall, Jacob Madsen, Nic Gillings, et al.

## 1880 <sup>89</sup>Zr-Labeled High-Density Lipoprotein Nanoparticle PET Imaging Reveals Tumor Uptake in Patients with Esophageal Cancer

Kang H. Zheng, Jeffrey Kroon, Jasper Schoormans, Oliver Gurney-Champion, Sybren L. Meijer, Suzanne S. Gisbertz, Maarten C.C.M. Hulshof, Danielle J. Vugts, Guus A.M.S. van Dongen, Bram F. Coolen, et al.

## 1887 ■ BRIEF COMMUNICATION. <sup>18</sup>F-FDG PET/CT Staging of Head and Neck Cancer: Interobserver Agreement and Accuracy—Results from Multicenter ACRIN 6685 Clinical Trial

Rathan M. Subramaniam, Fenghai M. Duan, Justin Romanoff, Jian Qin Yu, Twyla Bartel, Farrokh Dehdashti, Charles M. Intenzo, Lilja Solnes, JoRean Sicks, Brendan C. Stack Jr, et al.

## 1891 Safety and Efficacy of <sup>166</sup>Ho Radioembolization in Hepatocellular Carcinoma: The HEPAR Primary Study

Margot T.M. Reinders, Karel J. van Erpecum, Maarten L.J. Smits, Arthur J.A.T. Braat, Joep de Bruijne, Rutger Bruijnen, Dave Sprengers, Robert A. de Man, Erik Vegt, Jan N.M. IJzermans, et al.

## 1899 Noninvasive Assessment of Acute Graft-Versus-Host Disease of the Gastrointestinal Tract After Allogeneic Hemopoietic Stem Cell Transplantation Using <sup>18</sup>F-FDG PET

Martin H. Cherk, Robert Khor, Thomas W. Barber, Kenneth S.K. Yap, Sushrut Patil, Patricia Walker, Sharon Avery, Stuart Roberts, William Kemp, Alan Pham, et al.

## CARDIOVASCULAR

### Clinical

## 1906 ■ FEATURED CLINICAL INVESTIGATION ARTICLE. Prevalence and Outcomes of Cardiac Amyloidosis in All-Comer Referrals for Bone Scintigraphy

Christian Nitsche, Katharina Mascherbauer, Raffaella Calabretta, Matthias Koschutnik, Carolina Dona, Varius Dannenberg, Felix Hofer, Kseniya Halavina, Andreas A. Kammerlander, Tatjana Traub-Weidinger, et al.

## NEUROLOGY

### Basic

## 1912 Evaluation of (*rac*)-, (*R*)-, and (*S*)-<sup>18</sup>F-OF-NB1 for Imaging GluN2B Subunit-Containing *N*-Methyl-D-Aspartate Receptors in Nonhuman Primates

Hazem Ahmed, Ming-Qiang Zheng, Kelly Smart, Hanyi Fang, Li Zhang, Paul R. Emery, Hong Gao, Jim Ropchan, Ahmed Haider, Gilles Tamagnan, et al.

### Translational

## 1919 First-in-Human Evaluation of <sup>18</sup>F-PF-06445974, a PET Radioligand That Preferentially Labels Phosphodiesterase-4B

Yuichi Wakabayashi, Per Stenkrona, Ryosuke Arakawa, Xuefeng Yan, Maia G. Van Buskirk, Madeline D. Jenkins, Jose A. Montero Santamaria, Kevin P. Maresca, Akihiro Takano, Jieih-San Liow, et al.

## AI/ADVANCED IMAGE ANALYSIS

### Clinical

## 1925 <sup>18</sup>F-FDG PET Maximum-Intensity Projections and Artificial Intelligence: A Win-Win Combination to Easily Measure Prognostic Biomarkers in DLBCL Patients

Kibrom B. Girum, Louis Rebaud, Anne-Ségolène Cottureau, Michel Meignan, Jérôme Clerc, Laetitia Vercellino, Olivier Casasnovas, Franck Morschhauser, Catherine Thieblemont, and Irène Buvat

## 1933 Distinction of Lymphoma from Sarcoidosis on <sup>18</sup>F-FDG PET/CT: Evaluation of Radiomics-Feature-Guided Machine Learning Versus Human Reader Performance

Pierre Lovinfosse, Marta Ferreira, Nadia Withofs, Alexandre Jadoul, Céline Derwael, Anne-Noelle Frix, Julien Guiot, Claire Bernard, Anh Nguyet Diep, Anne-Françoise Donneau, et al.

## 1941 Fully Automated, Semantic Segmentation of Whole-Body <sup>18</sup>F-FDG PET/CT Images Based on Data-Centric Artificial Intelligence

Lalith Kumar Shiyam Sundar, Josef Yu, Otto Muzik, Oana C. Kulterer, Barbara Fueger, Daria Kifjak, Thomas Nakuz, Hyung Min Shin, Annika Katharina Sima, Daniela Kitzmantl, et al.

## ENDOCRINOLOGY

### Translational

## 1949 Development of Fluorinated NP-59: A Revival of Cholesterol Use Imaging with PET

Allen F. Brooks, Wade P. Winton, Jenelle Stauff, Janna Arteaga, Bradford Henderson, Jeremy Niedbala, Peter J.H. Scott, and Benjamin L. Viglianti

## GASTROENTEROLOGY

### Basic

## 1956 Staging Liver Fibrosis by Fibroblast Activation Protein Inhibitor PET in a Human-Sized Swine Model

Ali Pirasteh, Sarvesh Periyasamy, Jennifer Jean Meudt, Yongjun Liu, Laura M. Lee, Kyle M. Schachtschneider, Lawrence B. Schook, Ron C. Gaba, Lu Mao, Adnan Said, et al.

## ILLUSTRATED POST

## 1962 A Long Axial Field of View Enables PET/CT in Toddler Without Sedation

Michala Reichkender, Flemming L. Andersen, Lise Borgwardt, Ulrikka Nygaard, Elisabeth Albrecht-Beste, Kim F. Andersen, Anna Ljunggren, Nynne Abrahamsen, Annika Loft, Liselotte Højgaard, et al.

## DEPARTMENTS

### 10A Recruitment

### 12A This Month in JNM

The Official Publication of **SNMMI**

## Publications Committee

TODD E. PETERSON, PhD, FSNMMI  
*Chair*

CAROLYN J. ANDERSON, PhD, FSNMMI

PAIGE B. BENNETT, MD

JOYITA DUTTA, PhD

MICHAEL M. GRAHAM, PhD, MD, FACR,  
FSNMMI

HOSSEIN JADVAR, MD, PhD, FACNM,  
FSNMMI

STEVEN M. LARSON, MD, FACNM

HEINRICH R. SCHELBERT, MD, PhD, FSNMMI

HEIKO SCHÖDER, MD, MBA, FSNMMI

DAVID M. SCHUSTER, MD

JESSICA WILLIAMS, CNMT, RT(N),  
FSNMMI-TS

HARVEY A. ZIESSMAN, MD, FSNMMI

## *Ex officio*

JOHANNES CZERNIN, MD, FSNMMI

MUNIR GHESANI, MD, FACNM, FACR

ARNOLD M. STRASHUN, MD, FSNMMI

KATHY S. THOMAS, MHA, CNMT,

PET, FSNMMI-TS

HENRY F. VANBROCKLIN, PhD, FSNMMI

## Associate Director of Communications

SUSAN ALEXANDER

## Senior Copyeditor

SUSAN NATH

## Senior Publications & Marketing Service Manager

STEVEN KLEIN

## Editorial Production Manager

PAULETTE MCGEE

## Editorial Project Manager

MARK SUMIMOTO

## Director of Communications

REBECCA MAXEY

## CEO

VIRGINIA PAPPAS

**MISSION STATEMENT:** *The Journal of Nuclear Medicine* advances the knowledge and practice of molecular imaging and therapy and nuclear medicine to improve patient care through publication of original basic science and clinical research.

*JNM* (ISSN 0161-5505 [print]; ISSN 2159-662X [online]) is published monthly by SNMMI, 1850 Samuel Morse Drive, Reston, VA 20190-5316. Periodicals postage is paid at Herndon, VA, and additional mailing offices. Postmaster, send address changes to *The Journal of Nuclear Medicine*, 1850 Samuel Morse Drive, Reston, VA 20190-5316. The costs of publication of all nonsolicited articles in *JNM* were defrayed in part by the payment of page charges. Therefore, and solely to indicate this fact, these articles are hereby designated "advertisements" in accordance with 18 USC section 1734.

**DISCLOSURE OF COMMERCIAL INTEREST:** Johannes Czernin, MD, editor-in-chief of *The Journal of Nuclear Medicine*, has indicated that he is a founder of Sofie Biosciences and holds equity in the company and in intellectual property invented by him, patented by the University of California, and licensed to Sofie Biosciences. He is also a founder and board member of Trethera Therapeutics and holds equity in the company and in intellectual property invented by him, patented by the University of California, and licensed to Triangle. He also serves on the medical advisory board of Actinium Pharmaceuticals and on the scientific advisory boards of POINT Biopharma, RayzeBio, and Jubilant Pharma and is a consultant for Amgen. No other potential conflicts of interest were reported. Manuscripts submitted to *JNM* with potential conflicts are handled by a guest editor.

**EDITORIAL COMMUNICATIONS** should be sent to: Editor-in-Chief, Johannes Czernin, MD, *JNM* Office, SNMMI, 1850 Samuel Morse Drive, Reston, VA 20190-5316. Phone: (703) 326-1185; Fax: (703) 708-9018. To submit a manuscript, go to <https://submit-jnm.snmjournals.org>.

**BUSINESS COMMUNICATIONS** concerning permission requests should be sent to the publisher, SNMMI, 1850 Samuel Morse Drive, Reston, VA 20190-5316; (703) 708-9000; home page address: [jnm.snmjournals.org](http://jnm.snmjournals.org). Subscription requests and address changes should be sent to Membership Department, SNMMI at the address above. Notify the Society of change of address and telephone number at least 30 days before date of issue by sending both the old and new addresses. Claims for copies lost in the mail are allowed within 90 days of the date of issue. Claims are not allowed for issues lost as a result of insufficient notice of change of address. For information on advertising, contact Team SNMMI (Kevin Dunn, Rich Devanna, and Charlie Meitner; (201) 767-4170; fax: (201) 767-8065; [TeamSNMMI@cunnasso.com](mailto:TeamSNMMI@cunnasso.com)). Advertisements are subject to editorial approval and are restricted to products or services pertinent to nuclear medicine. Closing date is the first of the month preceding the date of issue.

**INDIVIDUAL SUBSCRIPTION RATES** for the 2022 calendar year are \$603 within the United States and Canada; \$648 elsewhere. Make checks payable to the SNMMI. CPC IPM Sales Agreement No. 1415158. Sales of individual back copies from 1999 through the current issue are available for \$60 at <http://www.snmml.org/subscribe> ([subscriptions@snmml.org](mailto:subscriptions@snmml.org); fax: (703) 667-5134). Individual articles are available for sale online at <http://jnm.snmjournals.org>.

COPYRIGHT © 2022 by the Society of Nuclear Medicine and Molecular Imaging. All rights reserved. No part of this work may be reproduced or translated without permission from the copyright owner. Individuals with inquiries regarding permission requests, please visit <http://jnm.snmjournals.org/site/misc/permission.xhtml>. Because the copyright on articles published in *The Journal of Nuclear Medicine* is held by the Society, each author of accepted manuscripts must sign a statement transferring copyright (available for downloading at <http://jnm.snmjournals.org/site/misc/fora.xhtml>). See Information for Authors for further explanation (available for downloading at <http://www.snmjournals.org/site/misc/fora.xhtml>).

The ideas and opinions expressed in *JNM* do not necessarily reflect those of the SNMMI or the Editors of *JNM* unless so stated. Publication of an advertisement or other product mentioned in *JNM* should not be construed as an endorsement of the product or the manufacturer's claims. Readers are encouraged to contact the manufacturer with any questions about the features or limitations of the products mentioned. The SNMMI does not assume any responsibility for any injury or damage to persons or property arising from or related to any use of the material contained in this journal. The reader is advised to check the appropriate medical literature and the product information currently provided by the manufacturer of each drug to be administered to verify the dosage, the method and duration of administration, and contraindications.



# Accuracy When It Matters

Illuccix has the sensitivity and specificity to allow for confidence in guiding clinical decision making<sup>1</sup>

Sensitivity and specificity data were provided from two prospective, open label studies designed to assess <sup>68</sup>Ga-PSMA-11 PET sensitivity, and specificity. See risk for misdiagnosis and radiation risks in the Important Safety Information.



References: <sup>1</sup>Illuccix (kit for preparation of gallium Ga 68 gozetotide injection) prescribing information.

Illuccix® is a trademark of Telix Pharmaceuticals (US) Inc.  
© 2022 Telix Pharmaceuticals (US) Inc.  
All rights reserved.  
US-ILL-2200087 10/2022

## Introducing Illuccix® in your practice

Speak with a live representative to get all your questions answered and prep work completed ahead of time so you receive reimbursement upon delivery of your first dose of Illuccix®. Schedule your one-on-one onboarding appointment by:

- Calling 1-(844) 45-TELIX (1-844-455-8638)
- Going to <https://illucixhcp.com/booking>

This service is available Monday through Friday 8:00 AM to 8:00 PM ET.

### INDICATIONS AND USAGE

Illuccix®, after radiolabeling with Ga 68, is a radioactive diagnostic agent indicated for positron emission tomography (PET) of prostate-specific membrane antigen (PSMA) positive lesions in men with prostate cancer:

- with suspected metastasis who are candidates for initial definitive therapy
- with suspected recurrence based on elevated serum prostate-specific antigen (PSA) level

## IMPORTANT SAFETY INFORMATION

### WARNINGS AND PRECAUTIONS

#### Risk for Misdiagnosis

Image interpretation errors can occur with gallium Ga 68 gozetotide PET. A negative image does not rule out the presence of prostate cancer and a positive image does not confirm the presence of prostate cancer. The performance of gallium Ga 68 gozetotide for imaging of biochemically recurrent prostate cancer seems to be affected by serum PSA levels and by site of disease. The performance of gallium Ga 68 gozetotide for imaging of metastatic pelvic lymph nodes prior to initial definitive therapy seems to be affected by Gleason score. Gallium Ga 68 gozetotide uptake is not specific for prostate cancer and may occur with other types of cancer as well as non-malignant processes such as Paget's disease, fibrous dysplasia, and osteophytosis. Clinical correlation, which may include histopathological evaluation of the suspected prostate cancer site, is recommended.

#### Radiation Risks

Gallium Ga 68 gozetotide contributes to a patient's overall long-term cumulative radiation exposure. Long-term cumulative radiation exposure is associated with an increased risk for cancer. Ensure safe handling to minimize radiation exposure to the patient and health care workers. Advise patients to hydrate before and after administration and to void frequently after administration.

### ADVERSE REACTIONS

The safety of gallium Ga 68 gozetotide was evaluated in 960 patients, each receiving one dose of gallium Ga 68 gozetotide. The average injected activity was  $188.7 \pm 40.7$  MBq ( $5.1 \pm 1.1$  mCi). No serious adverse reactions were attributed to gallium Ga 68 gozetotide. The most commonly reported adverse reactions were nausea, diarrhea, and dizziness, occurring at a rate of < 1%.

### DRUG INTERACTIONS

#### Androgen deprivation therapy and other therapies targeting the androgen pathway

Androgen deprivation therapy (ADT) and other therapies targeting the androgen pathway, such as androgen receptor antagonists, can result in changes in uptake of gallium Ga 68 gozetotide in prostate cancer. The effect of these therapies on performance of gallium Ga 68 gozetotide PET has not been established.

You are encouraged to report suspected adverse reactions of prescription drugs to the FDA.

**Please note this information is not comprehensive.**

**Please see brief summary of the full prescribing information on the next page, or visit [illucixhcp.com](https://illucixhcp.com) for full prescribing information.**

## Illuccix (kit for the preparation of gallium Ga 68 gozetotide Injection)

**BRIEF SUMMARY: Consult the full prescribing information for complete product information**

### WARNINGS AND PRECAUTIONS

#### Risk for Misdiagnosis

Image interpretation errors can occur with gallium Ga 68 gozetotide PET. A negative image does not rule out the presence of prostate cancer and a positive image does not confirm the presence of prostate cancer. The performance of gallium Ga 68 gozetotide for imaging of biochemically recurrent prostate cancer seems to be affected by serum PSA levels and by site of disease [see Clinical Studies (14)]. The performance of gallium Ga 68 gozetotide for imaging of metastatic pelvic lymph nodes prior to initial definitive therapy seems to be affected by Gleason score [see Clinical Studies (14)]. Gallium Ga 68 gozetotide uptake is not specific for prostate cancer and may occur with other types of cancer as well as non-malignant processes such as Paget's disease, fibrous dysplasia, and osteophytosis. Clinical correlation, which may include histopathological evaluation of the suspected prostate cancer site, is recommended.

#### Radiation Risks

Gallium Ga 68 gozetotide contributes to a patient's overall long-term cumulative radiation exposure. Long-term cumulative radiation exposure is associated with an increased risk for cancer. Ensure safe handling to minimize radiation exposure to the patient and health care workers. Advise patients to hydrate before and after administration and to void frequently after administration [see Dosage and Administration (2.1, 2.3)].

### ADVERSE REACTIONS

#### Clinical Trials Experience

Because clinical trials are conducted under widely varying conditions, adverse reaction rates observed in the clinical trials of a drug cannot be directly compared to rates in the clinical trials of another drug and may not reflect the rates observed in practice. The safety of ILLUCCIX has been established based on studies of another formulation of gallium Ga 68 gozetotide in patients with prostate cancer [see Clinical Studies (14)]. Below is a display of the adverse reactions in these studies. The safety of gallium Ga 68 gozetotide was evaluated in 960 patients, each receiving one dose of gallium Ga 68 gozetotide. The average injected activity was  $188.7 \pm 40.7$  MBq ( $5.1 \pm 1.1$  mCi). No serious adverse reactions were attributed to gallium Ga 68 gozetotide. The most commonly reported adverse reactions were nausea, diarrhea, and dizziness, occurring at a rate of < 1%.

### DRUG INTERACTIONS

Androgen deprivation therapy and other therapies targeting the androgen pathway Androgen deprivation therapy (ADT) and other therapies targeting the androgen pathway, such as androgen receptor antagonists, can result in changes in uptake of gallium Ga 68 gozetotide in prostate cancer. The effect of these therapies on performance of gallium Ga 68 gozetotide PET has not been established.

### USE IN SPECIFIC POPULATIONS

#### **Pregnancy**

##### Risk Summary

ILLUCCIX is not indicated for use in females. There are no available data with gallium Ga 68 gozetotide injection use in pregnant women to evaluate for a drug-associated risk of major birth defects, miscarriage, or adverse maternal or fetal outcomes. All radiopharmaceuticals, including ILLUCCIX, have the potential to cause fetal harm depending on the fetal stage of development and the magnitude of the radiation dose. Animal reproduction studies have not been conducted with gallium Ga 68 gozetotide.

#### **Lactation**

##### Risk Summary

ILLUCCIX is not indicated for use in females. There are no data on the presence of gallium Ga 68 gozetotide in human milk, the effect on the breastfed infant, or the effect on milk production.

#### **Pediatric Use**

The safety and effectiveness of gallium Ga 68 gozetotide in pediatric patients have not been established.

#### **Geriatric Use**

The efficacy of gallium Ga 68 gozetotide PET in geriatric patients with prostate cancer is based on data from two prospective studies [see Clinical Studies (14)]. Most patients in these trials were 65 years of age or older (72%). The efficacy and safety profiles of gallium Ga 68 gozetotide appear similar in younger adult and geriatric patients with prostate cancer, although the number of younger adult patients in the trials was not large enough to allow definitive comparison.

<sup>1</sup> Illuccix Prescribing Information.



**EDITOR-IN-CHIEF**

**Johannes Czernin, MD**  
University of California at Los Angeles  
Los Angeles, California

**IMMEDIATE PAST EDITOR**

**Dominique Delbeke, MD, PhD**  
Vanderbilt University Medical Center  
Nashville, Tennessee

**NEWSLINE EDITOR**

**Harvey A. Ziessman, MD**  
Takoma Park, Maryland

**ASSOCIATE EDITORS, CONTINUING EDUCATION**

**Hossein Jadvar, MD, PhD, MPH, MBA, FACNM, FSNMMI**

University of Southern California  
Los Angeles, California

**Lale Kostakoglu, MD, MPH**  
University of Virginia Health System  
Charlottesville, Virginia

**ASSOCIATE EDITORS**

**Ramsey Derek Badawi, PhD**

UC Davis Medical Center  
Sacramento, California

**Henryk Barthel, MD, PhD**

Leipzig University  
Leipzig, Germany

**Frank M. Bengel, MD**

Hannover Medical School  
Hannover, Germany

**Lisa Bodei, PhD**

Memorial Sloan Kettering Cancer Center  
New York, New York

**Irene Buvat, PhD**

Université Paris Sud  
Orsay, France

**Jérémie Calais, MD**

University of California at Los Angeles  
Los Angeles, California

**Marcelo F. Di Carli, MD**

Brigham and Women's Hospital  
Boston, Massachusetts

**Alexander E. Drzewga, MD**

University Hospital of Cologne  
Cologne, Germany

**Jan Grimm, MD, PhD**

Memorial Sloan Kettering Cancer Center  
New York, New York

**Ken Herrmann, MD, MBA**

Universitätsklinikum Essen  
Essen, Germany

**Thomas A. Hope, MD**

University of California, San Francisco  
San Francisco, California

**Jason S. Lewis, PhD**

Memorial Sloan Kettering Cancer Center  
New York, New York

**David A. Mankoff, MD, PhD**

University of Pennsylvania  
Philadelphia, Pennsylvania

**Heiko Schöder, MD**

Memorial Sloan Kettering Cancer Center  
New York, New York

**Wolfgang Weber, MD**

Technical University of Munich  
München, Germany

**SERIES EDITOR, FOCUS ON MI**

**Carolyn J. Anderson, PhD**

University of Missouri  
Columbia, Missouri

**SERIES EDITOR, HOT TOPICS**

**Heinrich R. Schelbert, MD, PhD**

University of California at Los Angeles  
Los Angeles, California

**CONSULTING EDITORS**

**Nancy Knight, PhD**

University of Maryland School of Medicine  
Baltimore, Maryland

**Barry A. Siegel, MD**

Mallinckrodt Institute of Radiology  
St. Louis, Missouri

**Arnold M. Strashun, MD**

SUNY Downstate Medical Center  
Scarsdale, New York

**H. William Strauss, MD**

Memorial Sloan Kettering Cancer Center  
New York, New York

**ASSOCIATE EDITORS (INTERNATIONAL)**

**Gerald Antoch, MD**

Düsseldorf, Germany

**Richard P. Baum, MD, PhD**

Bad Berka, Germany

**Ambros J. Beer, MD**

Ulm, Germany

**François Bénard, MD, FRCPC**

Vancouver, Canada

**Thomas Beyer, PhD**

Vienna, Austria

**Andreas K. Buck, MD, PhD**

Würzburg, Germany

**Ignasi Carrió, MD**

Barcelona, Spain

**June-Key Chung, MD**

Seoul, Korea

**Stefano Fanti, MD**

Bologna, Italy

**Markus Hacker, MD**

Wien, Austria

**Rodney J. Hicks, MD, FRACP**

Melbourne, Australia

**Michael S. Hofman, MBBS, FRACP**

Melbourne, Australia

**Ora Israel, MD**

Haifa, Israel

**Andreas Kjaer, MD, PhD, DMSc**

Copenhagen, Denmark

**Adriaan A. Lammertsma, PhD**

Amsterdam, The Netherlands

**Michael Lassman, PhD**

Würzburg, Germany

**Helmut R. Mäcke, PhD**

Freiburg, Germany

**Wim J.G. Oyen, MD, PhD**

Milan, Italy

**John O. Prior, MD, PhD**

Lausanne, Switzerland

**Osman Ratib, MD, PhD**

Geneva, Switzerland

**Mike Sathekge, MBChB, MMed, PhD**

Pretoria, South Africa

**Markus Schwaiger, MD**

München, Germany

**Andrew M. Scott, MD**

Heidelberg, Australia

**Nagara Tamaki, MD, PhD**

Kyoto, Japan

**Jia-He Tian, PhD**

Beijing, China

**Mei Tian, MD, PhD**

Hangzhou, China

**EDITORIAL CONSULTANTS**

**Martin S. Allen-Auerbach, MD**

Los Angeles, California

**Magnus Dahlbom, PhD**

Los Angeles, California

**Andrew Quon, MD**

Los Angeles, California

**Christiaan Schiepers, MD, PhD**

Los Angeles, California

**Daniel H. Silverman, MD, PhD**

Los Angeles, California

**Roger Slavik, PhD**

Winterthur, Switzerland

**EDITORIAL BOARD**

**Diane S. Abou, PhD**

St. Louis, Missouri

**Valentina Ambrosini, MD, PhD**

Bologna, Italy

**Norbert Avril, MD**

Cleveland, Ohio

**Shadfar Bahri**

Los Angeles, California

**Jacques Barbet, PhD**

Saint-Herbalin, France

**Bradley Jay Beattie, PhD**

New York, New York

**Matthias Richard Benz, MD**

Los Angeles, California

**Elie Besserer-Offroy, PhD, FACS**

Los Angeles, California

**Pradeep Bhambhvani, MD**

Birmingham, Alabama

**Angelika Bischof-Delaloye, MD**

Lausanne, Switzerland

**Christina Bluemel, MD**

Würzburg, Germany

**Ronald Boellaard, PhD**

Groningen, The Netherlands

**Nicolaas Bohnen, MD**

Ann Arbor, Michigan

**Wesley E. Bolch, PhD**

Gainesville, Florida

**Elias H. Botvinick, MD**

San Francisco, California

**Winfried Brenner, MD, PhD**

Berlin, Germany

**Richard C. Brunken, MD**

Cleveland, Ohio

**Ralph Buchert, PhD**

Hamburg, Germany

**Alfred Buck, MD**

Menzingen, Switzerland

**Denis B. Buxton, PhD**

Bethesda, Maryland

**Weibo Cai, PhD**

Madison, Wisconsin

**Federico Caobelli, MD**

Basel, Switzerland

**Giuseppe Carlucci, PhD**

Los Angeles, California

**Richard E. Carson, PhD**

New Haven, Connecticut

**Paolo Castellucci, MD**

Bologna, Italy

**Francesco Ceci, MD, PhD**

Turin, Italy

**Juliano J. Cerri**

Curitiba, Brazil

**Delphine Chen, MD**

Seattle, Washington

**Xiaoyuan Chen, PhD**

Singapore

**Simon R. Cherry**

Davis, California

**Arturo Chiti, MD**

Rozzano, Italy

**Peter M. Clark, PhD**

Los Angeles, California

**Christian Cohade, MD**

Montreal, Canada

**Ekaterina (Kate) Dadachova, PhD**

Saskatoon, Canada

**Issa J. Dahabreh, MD**

Boston, Massachusetts

**Heike Elisabeth Daldrop-Link, MD, PhD**

Stanford, California

**Farrokh Dehdashti, MD**

St. Louis, Missouri

**Robert C. Delgado-Bolton, MD, PhD**

Logroño, Spain

**Thorsten Derlin, MD**

Hannover, Germany

**Elisabeth G.E. de Vries, PhD**

Groningen, The Netherlands

**David W. Dick, PhD**

Iowa City, Iowa

**Vasken Dilsizian, MD**

Baltimore, Maryland

**Sharmila Dorbala, MBBS**

Lexington, Massachusetts

**Jacob Dubroff, MD, PhD**

Philadelphia, Pennsylvania

**Janet F. Eary, MD**

Bethesda, Maryland

**W. Barry Edwards, PhD**

Columbia, Missouri

**Matthias Eiber, MD**

Munich, Germany

**David Eidelberg, MD**

Manhasset, New York

**Georges El Fakhri, PhD**

Boston, Massachusetts

**Peter J. Ell, MD**

London, United Kingdom

**EDITORIAL BOARD, continued**

**Keigo Endo, MD**  
Nantan, Japan

**Einat Even-Sapir, MD, PhD**  
Tel Aviv, Israel

**Frederic H. Fahey, DSc**  
Boston, Massachusetts

**Melpomeni Fani, PhD, MSc**  
Basel, Switzerland

**Andrea Farolfi, MD**  
Bologna, Italy

**Wolfgang Peter Fendler, MD**  
Essen, Germany

**James W. Fletcher, MD**  
Indianapolis, Indiana

**Amy M. Fowler, MD, PhD**  
Madison, Wisconsin

**Kirk A. Frey, MD, PhD**  
Ann Arbor, Michigan

**Andrei Gafita**  
Los Angeles, California

**Victor H. Gerbaudo, PhD, MSHCA**  
Boston, Massachusetts

**Frederik L. Giesel, MD, PhD, MBA**  
Düsseldorf, Germany

**Serge Goldman, MD, PhD**  
Brussels, Belgium

**Stanley J. Goldsmith, MD**  
New York, New York

**Martin Gotthardt, MD, PhD**  
Nijmegen, The Netherlands

**Michael Graham, MD, PhD**  
Iowa City, Iowa

**David Groheux, MD, PhD**  
Paris, France

**Uwe A. Haberkorn, MD**  
Heidelberg, Germany

**Mathieu Hatt, PhD, HDR**  
Brest, France

**Wolf-Dieter Heiss, MD**  
Cologne, Germany

**Karl Herholz, MD**  
Manchester, United Kingdom

**Thomas F. Heston, MD**  
Las Vegas, Nevada

**John M. Hoffman, MD**  
Salt Lake City, Utah

**Carl K. Hoh, MD**  
San Diego, California

**Jason P. Holland, DPhil**  
Zurich, Switzerland

**Roland Hustinx, MD, PhD**  
Liege, Belgium

**Andrei H. Iagaru, MD**  
Stanford, California

**Masanori Ichise, MD**  
Chiba, Japan

**Heather A. Jacene, MD**  
Boston, Massachusetts

**Francois Jamar, MD, PhD**  
Brussels, Belgium

**Jae Min Jeong, PhD**  
Seoul, Korea

**John A. Katzenellenbogen, PhD**  
Urbana, Illinois

**Kimberly A. Kelly, PhD**  
Charlottesville, Virginia

**Laura M. Kenny, MD, PhD**  
London, United Kingdom

**Fabian Kiessling, MD**  
Aachen, Germany

**E. Edmund Kim, MD, MS**  
Orange, California

**Francoise Kraeber-Bodéré, MD, PhD**  
Nantes, France

**Clemens Kratochwil, MD**  
Heidelberg, Germany

**Kenneth A. Krohn, PhD**  
Portland, Oregon

**Brenda F. Kurland, PhD**  
Pittsburgh, Pennsylvania

**Constantin Lapa, MD**  
Augsburg, Germany

**Suzanne E. Lapi, PhD**  
Birmingham, Alabama

**Steven M. Larson, MD**  
New York, New York

**Dong Soo Lee, MD, PhD**  
Seoul, Korea

**Jeffrey Leyton, PhD**  
Sherbrooke, Canada

**Hannah M. Linden, MD**  
Seattle, Washington

**Martin A. Lodge, PhD**  
Baltimore, Maryland

**Katharina Lückeroth, PhD**  
Los Angeles, California

**Susanne Lütje, MD, PhD**  
Bonn, Germany

**Umar Mahmood, MD, PhD**  
Boston, Massachusetts

**H. Charles Manning, PhD**  
Nashville, Tennessee

**Giuliano Mariani, MD**  
Pisa, Italy

**Chester A. Mathis, PhD**  
Pittsburgh, Pennsylvania

**Alan H. Maurer, MD**  
Philadelphia, Pennsylvania

**Jonathan McConathy, MD, PhD**  
Birmingham, Alabama

**Alexander J.B. McEwan, MD**  
Edmonton, Canada

**Yusuf Menda, MD**  
Iowa City, Iowa

**Philipp T. Meyer, MD, PhD**  
Freiburg, Germany

**Matthias Miederer, MD**  
Mainz, Germany

**Erik Mittra, MD, PhD**  
Portland, Oregon

**Christine E. Mona, PhD**  
Los Angeles, California

**Dae Hyuk Moon, MD**  
Seoul, Korea

**Jennifer Murphy, PhD**  
Los Angeles, California

**Helen Nadel, MD, FRCPC**  
Stanford, California

**Matthias Nahrendorf, MD, PhD**  
Boston, Massachusetts

**Yuji Nakamoto, MD, PhD**  
Kyoto, Japan

**David A. Nathanson, PhD**  
Los Angeles, California

**Nghi C. Nguyen, MD, PhD**  
Dallas, Texas

**Sridhar Nimmagadda, PhD**  
Baltimore, Maryland

**Egbert U. Nitzsche, MD**  
Aarau, Switzerland

**Medhat M. Osman, MD, PhD**  
Saint Louis, Missouri

**Christopher J. Palestro, MD**  
New Hyde Park, New York

**Miguel Hernandez Pampaloni, MD, PhD**  
San Francisco, California

**Neeta Pandit-Taskar, MD**  
New York, New York

**Ashwin Singh Parihar, MBBS, MD**  
Saint Louis, Missouri

**Michael E. Phelps, PhD**  
Los Angeles, California

**Gerold Porenta, MD, PhD**  
Vienna, Austria

**Sophie Poty, PhD**  
Montpellier, France

**Edwin (Chuck) Pratt, PhD, MS Eng**  
New York, New York

**Daniel A. Pryma, MD**  
Philadelphia, Pennsylvania

**Valery Radchenko, PhD**  
Vancouver, Canada

**Caius G. Radu, MD**  
Los Angeles, California

**Isabel Rauscher, MD**  
Munich, Germany

**Nick S. Reed, MBBS**  
Glasgow, United Kingdom

**Mark Rijpkema, PhD**  
Nijmegen, The Netherlands

**Steven P. Rowe, MD, PhD**  
Baltimore, Maryland

**Mehran Sadeghi, MD**  
West Haven, Connecticut

**Orazio Schillaci, MD**  
Rome, Italy

**Charles Ross Schmidlein, PhD**  
New York, New York

**David M. Schuster, MD**  
Atlanta, Georgia

**Travis Shaffer, PhD**  
Stanford, California

**Sai Kiran Sharma, PhD**  
New York, New York

**Anthony F. Shields, MD, PhD**  
Detroit, Michigan

**Barry L. Shulkin, MD, MBA**  
Memphis, Tennessee

**Yu Shyr, PhD**  
Nashville, Tennessee

**Albert J. Sinusas, MD**  
New Haven, Connecticut

**Riener H.J.A. Slart, MD, PhD**  
Groningen, The Netherlands

**Piotr Slomka, PhD, FACC**  
Los Angeles, California

**Simon John Christoph Soerensen, MD**  
Stanford, California

**Ida Sonni, MD**  
Los Angeles, California

**Michael G. Stabin, PhD**  
Richland, Washington

**Lisa J. States, MD**  
Philadelphia, Pennsylvania

**Sven-Erik Strand, PhD**  
Lund, Sweden

**Rathan M. Subramaniam, MD, PhD, MPH**  
Dunedin, New Zealand

**John Sunderland, PhD**  
Iowa City, Iowa

**Suleman Surti, PhD**  
Philadelphia, Pennsylvania

**Julie Sutcliffe, PhD**  
Sacramento, California

**David Taieb, MD, PhD**  
Marseille, France

**Laura H. Tang, MD, PhD**  
New York, New York

**Ukihide Tateishi, MD, PhD**  
Tokyo, Japan

**James T. Thackeray, PhD**  
Hannover, Germany

**Mathew L. Thakur, PhD**  
Philadelphia, Pennsylvania

**Alexander Thiel, MD**  
Montreal, Canada

**Daniel L.J. Thorek, PhD**  
St. Louis, Missouri

**David W. Townsend, PhD**  
Singapore

**Timothy Turkington, PhD**  
Durham, North Carolina

**Gary A. Ulaner, MD, PhD**  
Irvine, California

**David Ulmert, MD, PhD**  
Los Angeles, California

**Christopher H. van Dyck, MD**  
New Haven, Connecticut

**Douglas Van Nostrand, MD**  
Washington, District of Columbia

**Patrick Veit-Haibach, MD**  
Toronto, Canada

**Nerissa Viola-Villegas, PhD**  
Detroit, Michigan

**John R. Votaw, PhD**  
Atlanta, Georgia

**Richard L. Wahl, MD**  
St. Louis, Missouri

**Anne Marie Wallace, MD**  
La Jolla, California

**Martin A. Walter, MD**  
Geneva, Switzerland

**Rudolf A. Werner, MD**  
Wuerzburg, Germany

**Andreas G. Wibmer, MD**  
New York, New York

**Anna M. Wu, PhD**  
Duarte, California

**Randy Yeh, MD**  
New York, New York

**Hyewon (Helen) Youn, PhD**  
Seoul, Korea

**Pat B. Zanzonico, PhD**  
New York, New York

**Brian M. Zeglis, PhD**  
New York, New York

**Robert Zeiser, MD**  
Freiburg, Germany

**Hong Zhang, MD, PhD**  
Hangzhou, China

**Hongming Zhuang, MD, PhD**  
Philadelphia, Pennsylvania

**Sibylle I. Ziegler, PhD**  
Munich, Germany

**ASSISTANT TO THE EDITOR**

**Joshua N. Wachtel**  
Los Angeles, California

# MISSOURI S&T

## Kummer Professor of Nuclear Engineering and Radiation Science

### Job Description

The Kummer Professor of NERS will possess the skills, knowledge and experience to:

- Drive strategic and operational efforts to grow life science related nuclear science/technology research and leverage existing capabilities in the research area.
- Drive strategic and operational efforts to establish the Department as a nationally recognized leader in medical application of nuclear science.
- Work with talented students and faculty in a multidisciplinary framework to promote growth in the research of life sciences applications of nuclear science with particular interest in medical application.

### Minimum Qualifications

An earned doctoral degree in a STEM field from an accredited university.

### Preferred Qualifications

- Credentials commensurate with appointment as a tenured full professor. Candidates outside academia may present other credentials in lieu of traditional university scholarly output.
- Extensive research and/or career experience in a life sciences application of Nuclear Engineering and/or Radiation Science related area.

We invite nominations and applications for the position of the Kummer Endowed Professor with emphasis on bio-applications of nuclear engineering, radiation science and radiology. This is a growth area to address expanding nuclear science application in life sciences, with particular interest in medical science. Missouri S&T has existing synergistic research areas and activities in nuclear medicine and imaging. The hire for this position will sustain both internal and external collaborations and leverage existing capabilities including our 200-kW nuclear reactor, aimed at oncology applications, high energy dosimetry or biological impact. The faculty will also help drive the expansion of nuclear medicine and health physics path in nuclear engineering at S&T. The faculty will maintain collaborative work with Hospitals and Medical Schools. The MURR facility at Columbia, MO is available to the faculty for research collaboration.

The Kummer Institute for Student Success, Research and Economic Development was established in October 2020 through a gift of \$300 million from June and Fred Kummer. The Institute is transforming Missouri S&T by cultivating leadership and technological innovation and fostering expansion of academic- industry partnerships to directly address emerging needs of industry.

**The Nuclear Engineering and Radiation Science** undergraduate program is one of only 35 nuclear engineering degree programs in the nation. The educational mission is to offer students career-focused opportunities in nuclear engineering, energy and nonproliferation, and radiation science and medical applications. Our research mission is to become nationally recognized leaders in micro reactor development, medical imaging and radiotherapy and/or radiodiagnostic applications, and materials in advanced nuclear systems. The department is home to seven tenured/tenure-track faculty, four jointly appointed faculty, 116 undergraduate students, and 24 graduate students. The department operates a 200 kW MTR-type reactor used for research and student operator training.

Founded in 1870 as the Missouri School of Mines and Metallurgy, Missouri University of Science and Technology is one of the top technological institutions in the nation and among the first technological institutions established west of the Mississippi River. Located about 100 miles southwest of St. Louis in the multicultural community of Rolla, Missouri, S&T is an accessible, safe, and friendly campus surrounded by Ozarks scenery. Missouri S&T has undertaken a number of initiatives to improve campus life and the work/life balance of its faculty and staff (see <http://hr.mst.edu>). Missouri S&T seeks to meet the needs of dual-career couples. ([Dual Career Partner Assistance Program](#))

Candidates should electronically submit their application (pdf or Word format) consisting of a 1) cover letter, 2) curriculum vitae, 3) research statement, 4) teaching statement, 5) diversity statement, and 6) list of four references to Missouri S&T's Human Resources Office at: <http://hr.mst.edu/careers/academic-employment> using Reference #00083444. Applications will be reviewed as they are received until the position is filled. Deadline for priority consideration is Thursday, December 15, 2022. For more information, please contact the Search Committee Chair, Hu Yang, at 573-341-4854, or [huyang@mst.edu](mailto:huyang@mst.edu).

Missouri University of Science & Technology is fully committed to achieving the goal of a diverse and inclusive academic community of faculty, staff and students. We seek individuals who are committed to this goal and our core campus values of integrity, inclusion, sustainability, creativity, partnerships and lifelong success. The University of Missouri is an Equal Opportunity/Access/Affirmative Action/Pro Disabled & Veteran Employer.

**Discussions with leaders:** Ken Herrmann, MD, MBA, and Michael Hofman, MBBS, FRACP, talk with Declan Murphy, FRACS, FRCS, about his career in genitourinary oncology and widely influential outreach activities in social media. . . . . **Page 1783**

**FAPI PET/CT in nonmalignant diseases:** Schmidkonz and colleagues offer a comprehensive review of fibroblast-activation protein inhibitor imaging in nonmalignant diseases to clarify current and potential roles of this class of molecules in nuclear medicine. . . . . **Page 1786**

**FDA approval for theranostic agents:** Perera and Morris present an educational overview of regulatory approval for novel radiopharmaceutical agents, including the importance of trial design for agents targeting prostate cancer and regulatory experience with  $^{223}\text{Ra}$  and  $^{177}\text{Lu}$ -PSMA-617. . . . **Page 1793**

**Nanoparticle diagnostics and theranostics:** Pallares and colleagues provide an overview of nanoparticle-based imaging agents in the clinic and discuss preclinical progress and translational avenues for use in diagnostic and theranostic applications. . . . . **Page 1802**

**Histopathologic validation of  $^{18}\text{F}$ -rhPSMA PET:** Kroenke and colleagues investigate the accuracy and predictive value of 2 PSMA-targeting radiopharmaceuticals in assessment of lymph node metastases as validated by histopathology. . . . . **Page 1809**

**PSMA PET/CT for therapy assessment:** Denis and colleagues use recent European recommendations to compare response assessment to a novel hormonal agent for metastatic castration-resistant prostate cancer between PSMA PET/CT and conventional imaging. . . . . **Page 1815**

**Initial  $^{68}\text{Ga}$ -PSMA-11 PET and outcomes:** Moradi and colleagues examine the prognostic value of  $^{68}\text{Ga}$ -PSMA-11 uptake in the primary lesion and presence of metastatic disease on PET in newly diagnosed prostate cancer before initial therapy. . . . . **Page 1822**

**$^{68}\text{Ga}$ -RM2 PET in primary prostate cancer:** Duan and colleagues compare preoperative  $^{68}\text{Ga}$ -RM2 PET, targeting gastrin-releasing peptide receptors, with postsurgery histopathology in patients with newly diagnosed intermediate- or high-risk prostate cancer. . . . . **Page 1829**

**Setting up a theranostics center:** Herrmann and members of a joint European Association of Nuclear Medicine, SNMMI, and International Atomic Energy Agency advisory group provide an enabling guide for radiopharmaceutical stakeholders interested in establishing dedicated theranostics centers. . . . . **Page 1836**

**Repetitive  $^{68}\text{Ga}$ -FAPI PET acquisition:** Glattig and colleagues report on the diagnostic value of repetitive early PET imaging with  $^{68}\text{Ga}$ -FAPI-02,  $^{68}\text{Ga}$ -FAPI-46, and  $^{68}\text{Ga}$ -FAPI-74 for malignant, inflammatory/reactive, and degenerative lesions and describe implications for future  $^{68}\text{Ga}$ -FAPI imaging. . . . . **Page 1844**

**FAP ligand with prolonged tumor uptake:** Galbiati and colleagues detail the development and in vivo characterization of BiOncoFAP, a new dimeric fibroblast-activation protein-binding motif with extended tumor residence time and favorable tumor-to-organ ratios. . . . . **Page 1852**

**$\alpha$ -Particle and immunocytokine therapy:** Minix and colleagues investigate tumor reduction and survival outcomes with low-dose targeted  $\alpha$ -therapy followed by a 4-dose immunocytokine regimen in mouse breast and colon cancer tumor models. . . . . **Page 1859**

**PET/CT for SiNET staging:** Ouvrard and colleagues compare the respective values of  $^{68}\text{Ga}$ -DOTATOC and  $^{18}\text{F}$ -DOPA PET/CT for initial staging or presurgical work-up of patients with small-intestine neuroendocrine tumors. . . . . **Page 1865**

**First-in-humans tissue factor PET:** Loft and colleagues report on PET imaging with an  $^{18}\text{F}$ -radiolabeled active-site inhibited version of the tissue factor natural ligand coagulation factor VII and describe its potential as a diagnostic companion for tissue-factor-targeted therapies. . . . . **Page 1871**

**HDL PET and esophageal cancer:** Zheng and colleagues use a multimodal imaging approach to assess tumor uptake of exogenously administered,  $^{89}\text{Zr}$ -labeled high-density lipoprotein nanoparticles in patients with esophageal cancer. . . . **Page 1880**

**PET/CT and head and neck cancer staging:** Subramaniam and colleagues look at multicenter interobserver agreement and accuracy in  $^{18}\text{F}$ -FDG PET/CT imaging for staging of clinical N0 neck in head and neck cancer. . . . . **Page 1887**

**$^{166}\text{Ho}$  radioembolization in HCC:** Reinders and colleagues establish the toxicity profile of  $^{166}\text{Ho}$  radioembolization in patients with measurable, liver-dominant hepatocellular carcinoma and no or very limited curative treatment options. . . . . **Page 1891**

**PET and GI graft-vs.-host disease:** Cherk and colleagues explore the diagnostic utility of  $^{18}\text{F}$ -FDG PET/CT in noninvasive assessment of patients with clinically suspected acute graft-versus-host disease of the gastrointestinal tract associated with allogeneic hemopoietic stem cell transplantation. . . . . **Page 1899**

**Cardiac amyloidosis in bone scan referrals:** Nitsche and colleagues assess cardiac amyloidosis prevalence and outcomes in a large population referred for  $^{99\text{m}}\text{Tc}$ -DPD bone scintigraphy over a decade-long period. . . . . **Page 1906**

**PET imaging of GluN2B-NMDA:** Ahmed and colleagues report on in vivo characterization of  $^{18}\text{F}$ -OF-NB1 derivatives in nonhuman primates and comment on the potential for imaging of glutamate receptor subtype 2B-containing *N*-methyl-D-aspartate receptors in several neuropathologies. . . . . **Page 1912**

**Evaluation of  $^{18}\text{F}$ -PF-06445974:** Wakabayashi and colleagues investigate the properties of the newly developed phosphodiesterase-4-selective radioligand  $^{18}\text{F}$ -PF-06445974 in the brains of rodents, monkeys, and humans. . . . **Page 1919**

**PET MIP prognostic biomarkers in DLBCL:** Girum and colleagues explore whether total metabolic tumor volume and tumor dissemination can be replaced by artificial intelligence-generated surrogate features from maximum-intensity projections of whole-body  $^{18}\text{F}$ -FDG PET in diffuse large B-cell lymphoma. . . . . **Page 1925**

**Machine learning in sarcoidosis and lymphoma:** Lovinfosse and colleagues describe development and validation of radiomics signatures to differentiate sarcoidosis from Hodgkin lymphoma and diffuse large B-cell lymphoma. . . . . **Page 1933**

**PET/CT multiorgan segmentation:** Shiyam Sundar and colleagues introduce multiple-organ objective segmentation software that generates subject-specific, multiorgan segmentation using data-centric artificial intelligence principles to facilitate high-throughput systemic investigations via whole-body PET imaging. . . . . **Page 1941**

**Development of fluorinated NP-59:** Brooks and colleagues prepare and evaluate an  $^{18}\text{F}$  analog of the  $^{131}\text{I}$  scintiscanning/SPECT agent NP-59 to serve as a PET agent for functional imaging of the adrenal glands based on cholesterol use. . . . . **Page 1949**

**$^{68}\text{Ga}$ -FAPI PET for staging liver fibrosis:** Pirasteh and colleagues research the utility of PET in staging liver fibrosis by correlating liver uptake of  $^{68}\text{Ga}$ -labeled fibroblast-activation protein inhibitor with histology in a human-sized swine model. . . . . **Page 1956**

**Pediatric PET without sedation:** Reichkendler and colleagues report on fast and flexible long-axial-field-of-view  $^{18}\text{F}$ -FDG PET/CT acquisition in an unanesthetized 17-mo old with suspected incomplete Kawasaki disease. . . . . **Page 1962**

# 2022 SNMMI Highlights Lecture: Oncology and Therapy, Part 1

Heiko Schöder, MD, MBA, Memorial Sloan Kettering Cancer Center and Weill Cornell Medical College, New York, NY

*From the Newsline Editor: The Highlights Lecture, presented at the closing session of each SNMMI Annual Meeting, was originated and presented for more than 30 years by Henry N. Wagner, Jr., MD. Beginning in 2010, the duties of summarizing selected significant presentations at the meeting were divided annually among 4 distinguished nuclear and molecular medicine subject matter experts. Each year Newsline publishes these lectures and selected images. The 2022 Highlights Lectures were delivered on June 14 at the SNMMI Annual Meeting in Vancouver, Canada. In this issue we feature the first part of the lecture by Heiko Schöder, MD, MBA, Chief of the Molecular Imaging and Therapy Service in the Department of Radiology at Memorial Sloan Kettering Cancer Center and professor of radiology at Weill Cornell Medical College (both in New York, NY), who spoke on oncology and therapy topics at the meeting. Note that in the following presentation summary, numerals in brackets represent abstract numbers as published in The Journal of Nuclear Medicine (2022;63[suppl 2]).*

It is a pleasure to present the highlights in oncology and therapy from the SNMMI Annual Meeting, and I thank the organizers for reinviting me. More than 400 abstracts were considered in preparing this lecture, and, needless to say, only a few could be included in the limited presentation time. I want to thank all the researchers who provided me with slides.

## Trends

At the 2022 SNMMI Annual Meeting we saw a new trend in geographic origins of oncology abstracts, with almost half coming from Asia and Australia (48%) and smaller contributions from the United States (25%), Europe (18%), Canada (5%), Africa (2%), and South America (1.5%). Major representation from countries in this category came from China (105 abstracts), the United States (103), Italy (39), India (39), and Germany (29). Quantity is not always or necessarily quality; the majority of the highest rated abstracts came from North America (42%), followed by Asia/Australia (35%), and Europe (23%). In contrast to last year, when the subject-matter distribution was about 80% diagnostic and 20% therapeutic, this year we saw 76% diagnostic- and 24% therapeutic-related abstracts. This may indicate a general trend, part of the growing interest in nuclear medicine therapies that will be reflected in this lecture.

It is always interesting to look at general trends in subject matter. In terms of keywords in titles of oncologic and therapeutic presentations at this meeting, FDG was still dominant (105 abstracts). However, it was followed closely by prostate-specific membrane antigen (PSMA) (101), with fibroblast-activation protein inhibitor (FAPI) rapidly rising (29). (This trend is also reflected in the published literature). Top radiolabels represented

in abstract titles included  $^{18}\text{F}$  (121),  $^{68}\text{Ga}$  (78),  $^{177}\text{Lu}$  (37), and  $^{225}\text{Ac}$  (11).

## Clinical Diagnostics FAPI Imaging

We will begin with the youngest and newest kid on the block, FAPI, and then review notable PSMA and FDG presentations. A large number of studies focused on FAPI, many of which were conducted in smaller patient samples. In general, these studies reported that FAPI has 1 or more advantages over FDG for disease detection and, in some instances, for staging. The studies provided evidence of FAPI benefit in differentiated thyroid cancer, gastrointestinal (GI) malignancies, breast cancer, hepatocellular carcinoma, and others. The theme is basically the same: FAPI provides very interesting data, but what we clearly need are more and larger prospective studies looking systematically at its utility in these diseases.

I have chosen only 1 of these FAPI abstracts to highlight here as an example. Chen et al. from the First Affiliated Hospital of Xiamen University (China) reported on “Comparison of  $^{68}\text{Ga}$ -FAPI and  $^{18}\text{F}$ -FDG uptake in patients with gastric signet-ring cell carcinoma: A multicenter retrospective study” [2370]. As you know, this disease is difficult to image with  $^{18}\text{F}$ -FDG PET. Figure 1 highlights the higher uptake intensity and greater tumor-to-background ratios of the  $^{68}\text{Ga}$ -FAPI agent. When compared with  $^{18}\text{F}$ -FDG in 34 patients (16 men, 18 women; median age, 51 y [range, 25–85 y]), the FAPI agent had higher detection rates in primary tumors (73% vs 18%), local recurrence (100% vs 29%), nodal metastases (77% vs 23%), and distant metastases (93% vs 39%). (Both modalities missed 6 smaller [(0.3–1.1-cm) primary tumors.] More interesting, perhaps, is the fact that there were no lesion sites in which FDG provided an advantage over FAPI. In the majority of lesions FAPI provided more information. The authors concluded that their data suggest that “ $^{68}\text{Ga}$ -FAPI PET has the potential to replace  $^{18}\text{F}$ -FDG PET in the diagnosis of patients with gastric signet-ring cell carcinoma.”

Other notable studies on FAPI PET/CT were presented by: Fu et al. from the First Affiliated Hospital of Xiamen University (China), who reported on “ $^{68}\text{Ga}$ -FAPI PET/CT in metastatic differentiated thyroid cancer detection: Comparison with  $^{18}\text{F}$ -FDG PET/CT” [2361]; Ballal et al. from the All India Institute of Medical Sciences (New Delhi) and the TRIGA Research Reactor/Johannes Gutenberg Universität Mainz (Germany), who reported on “Head-to-head comparison of  $^{68}\text{Ga}$ -DOTA.SA.FAPi versus  $^{18}\text{F}$ -FDG PET/CT in



Heiko Schöder, MD, MBA

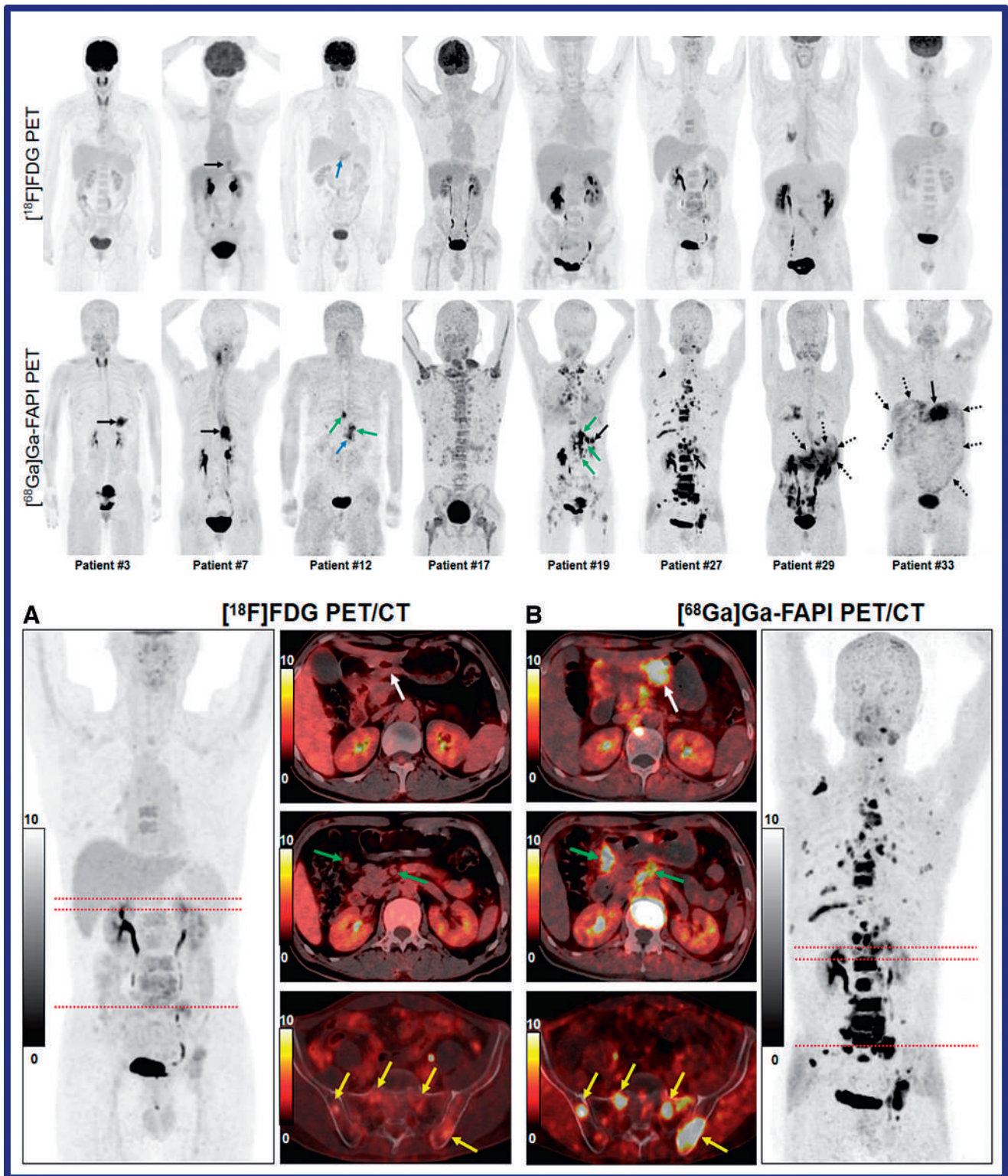


**FIGURE 1.** Comparison of  $^{68}\text{Ga}$ -FAPI and  $^{18}\text{F}$ -FDG PET/CT in gastric signet-ring cell carcinoma. Top: Example patients imaged with  $^{18}\text{F}$ -FDG (top row) and  $^{68}\text{Ga}$ -FAPI (bottom row) PET/CT. Bottom: Comparative imaging in a single patient with  $^{18}\text{F}$ -FDG (left) and  $^{68}\text{Ga}$ -FAPI (right) PET/CT.  $^{68}\text{Ga}$ -FAPI imaging resulted in higher detection rates in primary tumors (73% vs 18%), local recurrence (100% vs 29%), nodal metastases (77% vs 23%), and distant metastases (93% vs 39%).

radioiodine refractory differentiated thyroid cancer patients” [2371]; Li et al. from Peking Union Medical College Hospital and the Chinese Academy of Medical Sciences (Beijing,

China), who reported on “ $^{68}\text{Ga}$ -FAPI-04 and  $^{18}\text{F}$ -FDG PET/CT for identifying primary and metastatic lesions in patients with gastrointestinal cancer: A comparative study”

[2369]; Novruzov et al. from the Azerbaijan National Centre of Oncology (Baku, Azerbaijan), who reported on “Head-to-head comparison of  $^{68}\text{Ga}$ -FAPI-46 PET/CT and  $^{18}\text{F}$ -FDG PET/CT in breast carcinoma staging: A clinical trial update from Azerbaijan” [2372]; Wu et al. from Peking Union Medical College Hospital and the Chinese Academy of Medical Sciences (both in Beijing, China), who reported on “ $^{68}\text{Ga}$ -FAPI and  $^{18}\text{F}$ -FDG PET/CT in evaluation of primary and metastatic lesions in late-stage hepatocellular carcinoma” [2373]; and Pang et al. from the First Affiliated Hospital of Xiamen University/Xiamen University (China), who reported that “ $^{68}\text{Ga}$ -FAPI PET/CT improves tumor detection and staging in patients with pancreatic cancer and comparison with  $^{18}\text{F}$ -FDG PET/CT” [2374].

### Prostate Cancer

Prostate cancer remains a challenging problem worldwide. It is the dominant malignancy in the male population in 112 countries: all of North and South America, Australia, and much of Africa and Europe. *The Lancet* Commission on Prostate Cancer, introduced in 2021 (James et al., *The Lancet*. 2021;397[10288]:1865–1866), cites “genomic tools and imaging, particularly PSMA PET/CT” as “likely to be increasingly important in treatment decisions in the future.” The commission will assess these and other diagnostic and treatment developments to determine “what is likely to constitute the best approach in different health care settings [including in lower middle-income countries] and make policy and clinical practice recommendations.”

At this meeting, as in the peer-reviewed literature, some studies on PSMA agents in prostate cancer are exciting and others, although possibly less exciting, are essential for regulatory approval and for conduct of clinical trials. Kuo et al. from the University of Arizona (Tucson), Invicro (Needham, MA), Medstar Georgetown University Hospital (Washington, DC), Warren Alpert Medical School of Brown University (Providence, RI), and McMaster University (Hamilton, Canada), on behalf of the SPOTLIGHT Study Group, reported on “Inter- and intrareader reproducibility of  $^{18}\text{F}$ -rhPSMA-7.3 PET image interpretation in patients with suspected prostate cancer recurrence: Results from a phase 3, prospective, multicenter study (SPOTLIGHT)” [2539]. Their data indicated a high degree of inter- and intrareader agreement across 3 blinded readers given the same set of scans after completing the same training. Interreader agreement was >75% overall and greatest for the pelvic lymph node region, with 87% concordance. Intrareader agreement was >85% overall. Although reproducibility was lower for the prostate/prostate bed than other regions, the substantial reproducibility in regions outside the prostate fossa is of clinical importance because of the potential to influence treatment selection. These types of studies are important for creation and validation of the large clinical trial data needed to obtain regulatory approval and reimbursement for PSMA agents and other novel radiopharmaceuticals and techniques.

Olivier et al. from the Centre Hospitalier Universitaire Nancy (France), the Centre Léon Bérard (Lyon, France),

Centre Jean Perrin (Clermont-Ferrand, France), Hôpital Européen Georges-Pompidou (Paris, France), and ABX Advanced Biochemical Compounds (Radeberg, Germany) reported on a “Phase III study of  $^{18}\text{F}$ -PSMA-1007 versus  $^{18}\text{F}$ -fluorocholine PET to compare the detection rate of prostate cancer lesions in patients with biochemical recurrence after previous definitive treatment for localized prostate cancer” [2537]. This study contributed to the regulatory approval of PSMA-1007 in France. We all know instinctively that PSMA is a better imaging agent than others we have had available in prostate cancer, but it is important to have the hard data for regulatory approval. The design of this multicenter study is interesting. Patients ( $n = 190$ ) in an intent-to-treat population with suspected prostate cancer recurrence underwent both choline and PSMA imaging in a random order. Blinded readers used a 3-point qualitative scale (no recurrence, undetermined, recurrence) to report findings. In 172 patients, PET imaging resulted in a more accurate diagnosis as determined by an independent panel of experts and additional data. Of these more accurate diagnoses, 72% were attributed to  $^{18}\text{F}$ -PSMA-1007, 5% to  $^{18}\text{F}$ -fluorocholine, and 23% to the 2 tracers equally.  $^{18}\text{F}$ -PSMA-1007 PET/CT identified disease relapse in more patients than did  $^{18}\text{F}$ -fluorocholine PET/CT, especially at low prostate-specific serum antigen levels.

In developing clinical trials to assess and validate PSMA imaging, it will be important to move beyond counting and measuring each individual lesion to the increasing application of artificial intelligence (AI) tools that facilitate lesion identification, tracking, activity measurement, and even assessment of volume change over time. Calais et al. from the University of California Los Angeles, Technical University of Munich (Germany), Stanford University (CA), EXINI Diagnostics AB (Lund, Sweden), Lund University (Sweden), Veterans Affairs Greater Los Angeles (CA), and Memorial Sloan Kettering Cancer Center (New York, NY) reported on a “Prospectively planned and independent validation of aPROMISE in a phase III CONDOR study for rapid lesion detection and standardized quantitative evaluation for  $^{18}\text{F}$ -DCFPyL (PSMA) imaging in prostate cancer” [2496]. The aPROMISE tool performs both AI-based CT segmentation of bone and soft tissue and hotspot detection/segmentation to yield total PSMA  $\text{SUV}_{\text{mean}}$ , total PSMA tumor volume, and a total PSMA score (Fig. 2). The AI tool required relatively little observer interaction and was comparable or superior in accuracy to manual assessment. The time needed to score an  $^{18}\text{F}$ -DCFPyL scan using aPROMISE in a patient with metastatic disease was dramatically shorter (median, 1.4 min) than manual reading time in the original CONDOR study (~15 min). The authors concluded that the AI-based total PSMA score “warrants future clinical investigation to define its clinical context of use as an imaging biomarker.”

Many studies and guidelines have been published highlighting the importance of PET imaging for radiation treatment planning in lung, cervix, and other cancers. It comes as no surprise that PSMA can also contribute to radiation treatment planning in prostate cancer. In salvage radiotherapy, radiation

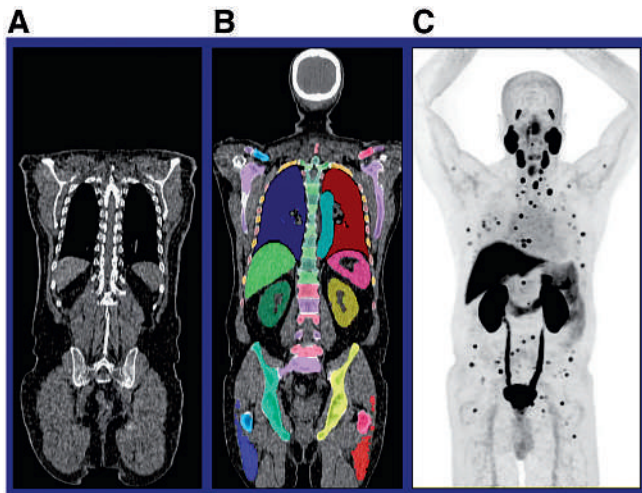


**FIGURE 2.** aPROMISE for rapid lesion detection and standardized quantitative evaluation for  $^{18}\text{F}$ -DCFPyL (PSMA) imaging in prostate cancer. In this example  $^{18}\text{F}$ -DCFPyL image (A), the aPROMISE tool performed both AI-based CT segmentation of bone and soft tissue (B) and hot spot detection/segmentation (C) to yield total PSMA  $\text{SUV}_{\text{mean}}$ , total PSMA tumor volume, and a total PSMA score. The time needed to score an  $^{18}\text{F}$ -DCFPyL scan using aPROMISE in metastatic disease was dramatically shorter (median, 1.4 min) than average manual reading time (~15 min).

oncologists currently use contouring guidelines based on expert consensus (e.g., those from RTOG) to determine the volume to be irradiated, without reference to information from patterns of recurrence seen on advanced imaging such as PSMA PET. Can PSMA PET imaging contribute to refining planning treatment volumes? Sonni et al. from the University of California Los Angeles, the University of Miami Miller School of Medicine (FL), and the VA Greater Los Angeles Healthcare System (CA) looked at “PSMA PET mapping of postoperative local recurrence and impact on prostate fossa contouring guidelines for salvage radiation therapy” [2538]. This study analyzed the typical patterns of prostate fossa recurrence after radical prostatectomy using  $^{68}\text{Ga}$ -PSMA-11 PET/CT and evaluated the location of recurrences as compared to RTOG clinical target volume (CTV) definitions. In 127 patients, the authors found that PSMA-positive prostate fossa recurrences were fully covered by the CTV in 68 (54%) patients, partially covered in 43 (34%), and fully outside the CTV in 16 (13%). Recurrences were in close proximity to the rectal wall in 9% and bladder wall in 3% of all patients. The heatmaps in the example in Figure 3 clearly show that the standard volume (green), would not have included disease as shown on the PSMA PET.

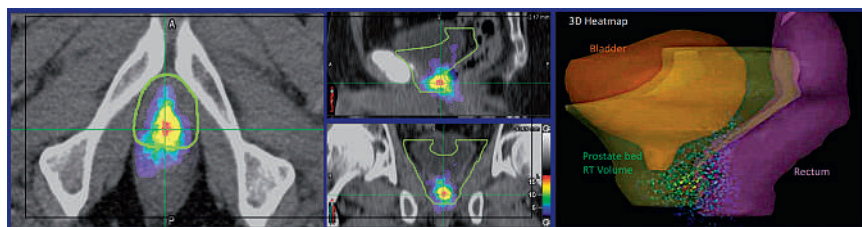


**FIGURE 3.** PSMA PET mapping of postoperative local recurrence compared with planning based on prostate fossa contouring guidelines for salvage radiation therapy. Patient example with: (left and middle) 2D heatmap of prostate bed recurrence on  $^{68}\text{Ga}$ -PSMA-11 PET/CT and RTOG-based clinical treatment volume (CTV; green outline); (right) 3D heatmap of prostate bed recurrence on  $^{68}\text{Ga}$ -PSMA-11 PET/CT and RTOG-based CTV, showing proximity to rectal and bladder walls. The authors concluded that PSMA PET-based data should inform the update of commonly used prostate bed contouring guidelines.

The authors concluded that PSMA PET-based data should inform the update of commonly used prostate bed contouring guidelines and that new contouring guidelines should consider reducing coverage at the anterior and superior borders (near pubic bone) and extending coverage at the posterior, posterolateral, and inferior borders.

Duan et al. from Stanford University (CA) recently published data on a  $^{68}\text{Ga}$ -labeled bombesin antagonist ( $^{68}\text{Ga}$ -RM2) targeting gastrin-releasing peptide receptors (GRPRs), which are overexpressed in prostate cancer (*J Nucl Med.* 2022; May 12 ahead of print). Their results showed high agreement between  $^{68}\text{Ga}$ -PSMA-11 and  $^{68}\text{Ga}$ -RM2 imaging in patients with newly diagnosed intermediate- or high-risk prostate cancer. Against this background we heard a presentation at this meeting that found somewhat different results (perhaps related to patient selection). Tang et al. from Xiangya Hospital/Central South University (Changsha City, China) reported on “Comparison of  $^{68}\text{Ga}$ -GRPR PET/CT with  $^{68}\text{Ga}$ -PSMA PET/CT in initial diagnosing of prostate cancer using histopathology: Results from 207 participants” [2540]. Overall,  $^{68}\text{Ga}$ -PSMA PET/CT performed better than  $^{68}\text{Ga}$ -GRPR PET/CT. Although  $^{68}\text{Ga}$ -GRPR PET/CT showed higher sensitivity in imaging low-risk disease, uptake in benign prostatic hyperplasia and early clinically insignificant prostate cancer was greater. The authors concluded that  $^{68}\text{Ga}$ -GRPR PET/CT “may not be a direct competitor or have a complementary role” to that of PSMA PET/CT in fully characterizing prostate cancer at different stages. They added that the fact that  $^{68}\text{Ga}$ -GRPR uptake was not specific for prostate cancer may suggest that GRPR may not be an imaging target for initial diagnosis. This raises a number of questions about the role of GRPR in prostate cancer diagnosis and indicates that we need more data.

### Other Cancers

Carlsen et al. from the Rigshospitalet/Copenhagen University (Copenhagen, Denmark) reported on a “Prospective phase II trial of prognostication by  $^{68}\text{Ga}$ -NODAGA-E [c(RGDyK)]<sub>2</sub> PET/CT for integrin  $\alpha_v\beta_3$  imaging in patients with neuroendocrine neoplasms (NENs)” [2209]. The authors used this novel tracer in PET/CT imaging in 97 patients with NENs of all grades (78% low-grade, 22% high-grade disease), and tumor  $\text{SUV}_{\text{max}}$  for each patient was evaluated as a predictor of progression-free and overall survival at follow-up of at least 1 y (median, 32 mo). During follow-up, 62 patients (64%) experienced progressive disease and 26

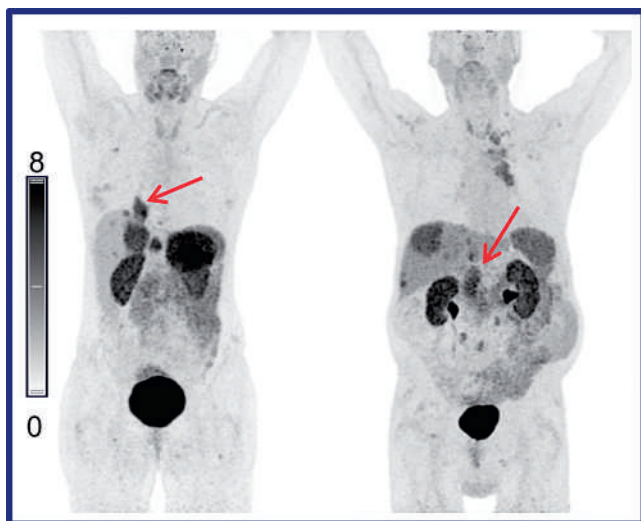


**FIGURE 4.** Prognostic utility of  $^{68}\text{Ga}$ -NODAGA-E[c(RGDyK)]<sub>2</sub> PET/CT integrin  $\alpha_v\beta_3$  imaging in patients with neuroendocrine neoplasms (NENs). Example imaging in patients with a metastatic lung NEN (left) and a metastatic pancreatic NEN (right). Higher tracer uptake was significantly correlated with worse prognosis.

(27%) died. The intensity of  $^{68}\text{Ga}$ -NODAGA-E[c(RGDyK)]<sub>2</sub> uptake increased from grade 1 to grade 2 and was positive in almost all grade 3 patients (Fig. 4). Higher uptake correlated with worse prognosis. The suggestion is not that this tracer will replace DOTATATE but that it provides interesting additional prognostic information and so could serve as a companion diagnostic for treatments targeting  $\alpha_v\beta_3$ .

Ulaner et al. from the Hoag Family Cancer Institute (Irvine, CA) and the University of Southern California (Los Angeles) reported on “A prospective clinical trial of  $^{18}\text{F}$ -fluorestradiol ( $^{18}\text{F}$ -FES) PET/CT compared to standard-of-care imaging in patients with newly diagnosed and suspected recurrent breast cancer” [2590].  $^{18}\text{F}$ -FES is an estrogen receptor–targeting PET tracer approved by the FDA as an adjunct to biopsy in patients with recurrent or metastatic breast cancer. Particular utility is expected in patients with lobular breast cancer and those with heterogeneous metastatic disease (to determine the extent of estrogen receptor–positive disease). The authors of this study plan to enroll a total of 120 patients

in 2 cohorts: 1 with locally advanced stage 2B–3C cancer and 1 with treated breast cancer and suspected recurrence. Patients undergo both  $^{18}\text{F}$ -FES PET/CT and standard-of-care imaging (either CT/bone scan or  $^{18}\text{F}$ -FDG PET/CT). Preliminary results reported at the SNMMI meeting on the first 39 patients enrolled suggest that  $^{18}\text{F}$ -FES PET/CT detects more unsuspected distant metastases at initial staging and also at the time of suspected recurrence and may outperform current imaging methods for detection of clinically significant and treatment-altering disease in patients in both study cohorts. These cohorts represent novel patient populations that could benefit from  $^{18}\text{F}$ -FES PET/CT. Figure 5 shows comparative  $^{18}\text{F}$ -FDG PET/CT and  $^{18}\text{F}$ -FES PET/CT imaging in a 59-y-old woman with previously treated invasive lobular breast cancer and elevated tumor markers. Benign granulomatous inflammation produced false-positive findings for lung recurrence on  $^{18}\text{F}$ -FDG PET/CT, but these lesions were not  $^{18}\text{F}$ -FES avid. However, many  $^{18}\text{F}$ -FES–avid nodal, GI, osseous, and peritoneal metastases were missed on  $^{18}\text{F}$ -FDG imaging. Tissue sampling of a peritoneal lesion demonstrated recurrent lobular breast cancer.

One of the main applications for  $^{18}\text{F}$ -FDG PET has been and remains lymphoma, in which the tracer is used for staging, restaging, response assessment, and (more than in any other disease) for the conduct of clinical trials. In these trials, we are increasingly interested in looking at more than just the number of lesions and visual criteria by applying radiomics principles to extract more information. Eertink et al. from Amsterdam University Medical Centers (The Netherlands), Erasmus Medical Centre (Rotterdam, The Netherlands), the Universitätsklinikum Essen (Germany), the University of Duisburg-Essen/University Hospital Essen (Germany), Universitätsklinikum Leipzig (Germany), Kings College (London, UK), Guy’s and St. Thomas Hospital (London, UK), Istituto Imaging Della Svizzera Italiana/Ente Ospedaliero Cantonale, Semmelweis University (Budapest, Germany), and VU University Medical Center (Amsterdam, The Netherlands), on behalf of the PETRA Consortium, reported that “ $^{18}\text{F}$ -FDG PET radiomics features result in more accurate prediction of outcome for diffuse large B-cell lymphoma (DLBCL) patients than currently used International Prognostic Index (IPI) score” [2490]. This group has done remarkable work in collecting and analyzing these and

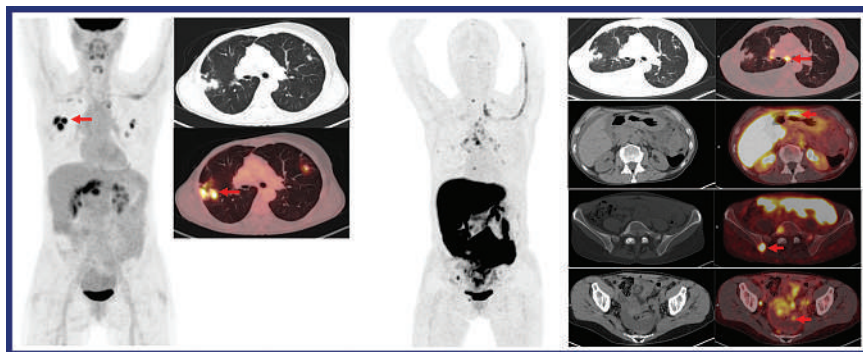


**FIGURE 5.**  $^{18}\text{F}$ -fluorestradiol ( $^{18}\text{F}$ -FES) PET/CT vs standard-of-care imaging in newly diagnosed and suspected recurrent breast cancer. Comparative  $^{18}\text{F}$ -FDG PET/CT (left) and  $^{18}\text{F}$ -FES PET/CT (right) imaging in a 59-y-old woman with previously treated invasive lobular breast cancer and elevated tumor markers. Benign granulomatous inflammation produced false-positive findings for lung recurrence (arrows) on  $^{18}\text{F}$ -FDG PET/CT; these lesions were not  $^{18}\text{F}$ -FES avid. However, many  $^{18}\text{F}$ -FES–avid nodal, gastrointestinal, osseous, and peritoneal metastases (arrows) were missed on  $^{18}\text{F}$ -FDG imaging. Tissue sampling of a peritoneal lesion demonstrated recurrent lobular breast cancer.

similar data and have already published a number of articles in this area. In their presentation at the SNMMI meeting, the authors reported on a study designed to externally validate the radiomics model developed in the HOVON-84 trial, using datasets from other DLBCL studies within the PETRA database, and to identify an optimal model to predict outcomes in that database by combining radiomics features and clinical parameters. They identified several criteria validated as providing prognostic information and applied these as model in other clinical trials including a total of 1,090 patients. The new PETRA model, combining quantitative radiomics features extracted from baseline  $^{18}\text{F}$ -FDG PET/CT scans with components of the IPI score, significantly improved identification of patients at risk of relapse when treated with standard first-line treatment regimens compared with the IPI score alone. It is clear that these and other radiomics models will contribute to the use of multiple datapoints beyond SUV that will be crucial in the conduct of future clinical trials, particularly those drawing on multiple studies and very large patient populations.

We are often told that we are either not doing enough or are doing too much  $^{18}\text{F}$ -FDG PET imaging. It is important that we address such criticisms with data on usage, utility, and compliance with validated guidelines. Sterbis et al. from the University of Colorado Medical Center (Aurora, CO) and the Edward Hines Jr. VA Hospital (Hines, IL) reported on “Lack of adherence to

guideline-based imaging prior to adjuvant radiation in patients with non-small cell lung cancer (NSCLC)” [2596]. The authors used National Cancer Institute Surveillance, Epidemiology, and End Results program data (which should be taken with a grain of salt) in patients with NSCLC who had received adjuvant radiation therapy and undergone imaging with CT angiography or CT and/or PET with or without CT. They looked at adherence to National Comprehensive Cancer Network guidelines for imaging in this setting prior to adjuvant radiation therapy, which recommend that “PET/CT should be obtained preferably within 4 wk before treatment,” ideally in the treatment position. In this study, only 56.3% of patients had preradiation imaging with PET. Predictors of decreased PET/CT usage included stage III or IV disease, initial treatment with chemotherapy or chemoradiation, black or other/unknown ethnicity, initial diagnosis with CT or CT angiography alone, and/or neuroendocrine or squamous cell biology. Both inferior overall survival and inferior cancer-specific survival were associated with decreased preradiation PET/CT usage. It is a challenge and an area of great concern that this modern and timely imaging technology is not widely enough available or routinely and equitably offered across all populations.

*Dr. Schöder's lecture will be continued in the next issue of The Journal of Nuclear Medicine and will cover clinical radionuclide therapy and experimental studies.*

## SNMMI Adopts New Strategic Plan

*Munir Ghesani, MD, SNMMI President*

For more than 50 years, SNMMI has successfully educated professionals, policymakers, and the general public about nuclear medicine and molecular imaging. Advances in the field have signaled an expansion of the profession and its ability to contribute to improved health outcomes, necessitating that SNMMI leaders examine the society's long-range future. This past spring the SNMMI leadership did just that, participating in a 1½-day strategic planning session.

To inform the strategic planning session, an environmental assessment was conducted to engage as many voices as possible. The assessment included one-on-one interviews, an external environmental scan, and a survey of 383 members from a wide cross-section of the organization. Board members reviewed and prioritized SNMMI's strategic opportunities and discussed membership expectations. They also addressed, discussed, and refined SNMMI's mission and vision statements and identified strategic objectives and initiatives.

With the completion of the strategic planning process, I am pleased to share SNMMI's new vision and mission statements:

- **Vision:** SNMMI is the leading global organization transforming the science and practice of diagnostic and therapeutic nuclear medicine.
- **Mission:** Empowering our members to transform the science and practice of precision nuclear medicine for diagnosis and therapy to advance patient care.

To support the society's vision and mission statement, 9 new strategic goals—with corresponding objectives and tactics—have been identified.

**Goal 1: Expand integration of best practices in all aspects of nuclear medicine to optimize patient care and access.** To achieve this goal, SNMMI will work toward greater inclusion of nuclear medicine in the guidelines of the National Comprehensive Cancer Network, increase the number of designated Therapy Centers of Excellence, and incorporate best practices in all aspects of nuclear imaging and therapy.

**Goal 2: Attract and engage a diverse, multidisciplinary, and global membership by offering opportunities, services, and resources that anticipate and fulfill members' needs.** Objectives include reimagining the SNMMI membership structure, improving member benefits and services, improving membership communication, and increasing the society's brand awareness. The society will also build a forward-thinking leadership and career development program and improve the diversity and inclusiveness of SNMMI volunteer opportunities.

**Goal 3: Ensure high-quality, focused, needs-based education for all segments of the profession that is easily accessible and documentable to increase utilization.** This goal will be achieved by increasing utilization of educational resources for both members and nonmembers.

**Goal 4: Accelerate discovery, research, and translation in nuclear medicine and molecular imaging through funding, education, and support for professionals.** SNMMI will work to increase research funding and its infrastructure for research, as well as education, training, and mentorship for research personnel. The society will lead multicenter clinical trials through the SNMMI Clinical Trials Network and Therapy Clinical Trials Network and enhance research on artificial intelligence, machine learning, and deep learning, among other objectives.

**Goal 5: Ensure that patients and the medical community recognize the value of nuclear medicine, molecular imaging, and radionuclide therapy.** This goal will be achieved by educating patients, referring physicians, and other medical societies about radiopharmaceutical therapies. SNMMI will also expand outreach at the regional, local, and institutional levels; increase awareness among health care administrators; and promote media coverage of nuclear medicine and molecular imaging.

**Goal 6: Sustain and grow a diverse and qualified workforce that is prepared for current and future diagnostic and therapeutic nuclear medicine needs to provide equitable care.** SNMMI will analyze and assess workforce needs, showcase the field as a thriving career path, and foster the growth, value, and diversity of early career nuclear medicine and molecular imaging professionals. SNMMI will also ensure that nuclear medicine and molecular imaging programs have the necessary informational resources to be successful.

**Goal 7: Position SNMMI to address the rapidly changing needs of the profession and members.** SNMMI will review its organizational structure and core membership offerings, as well as those of outside organizations. The society will develop a sustainable organizational model considering SNMMI membership priorities, staffing, and fiscal health.

**Goal 8: Engage stakeholders to develop, promote, implement, and sustain policies to ensure equitable patient access to appropriate nuclear medicine procedures.** Objectives for this goal include working closely with the Centers for Medicare & Medicaid Services, legislators, and



Munir Ghesani, MD

private payers to advocate on reimbursement and patient access issues and educating stakeholders about changes to relevant public policy requirements. SNMMI will leverage coalitions to advocate for issues of mutual interest and focus on state level advocacy, in addition to other objectives.

**Goal 9: Ensure that the Annual Meeting remains relevant by continuously reimagining the meeting in ways that meet the changing needs of the nuclear medicine**

**and molecular imaging community.** This goal will be achieved by creating a 3-year plan to reimagine the meeting, creating meaningful networking opportunities, and introducing innovative programming.

We look forward to working with members from all areas of the field on this new strategic plan. Together we can transform the science and practice of diagnostic and therapeutic nuclear medicine.

## SNMMI and Lobular Breast Cancer Alliance Research Grant

The SNMMI Mars Shot Fund and the Lobular Breast Cancer Alliance announced on October 3 that applications are being accepted for the new and jointly sponsored \$100,000 Invasive Lobular Carcinoma (ILC) Research Grant. This initiative, a first-time collaboration between the 2 organizations, aims to fund a research project focused on advancing ILC breast cancer imaging and treatments to improve patient outcomes.

To be selected, research projects must focus on ILC and molecular imaging or therapy for lobular breast cancer. Priority projects may have molecular imaging as the primary focus of the proposed research, or, alternatively, researchers may investigate methods that integrate other imaging and/or molecular science with radionuclide methods, including hybrid imaging techniques such as PET/CT, SPECT/CT, and PET/MR imaging. Patient advocates will be included as voting members in the application review process.

Applications are due by December 15. Additional information on application and proposal submission is available at: [https://www.snmmi.org/AboutSNMMI/Content.aspx?ItemNumber=41839&utm\\_source=Email&utm\\_medium=Informz&utm\\_campaign=Email%20Outreach&\\_zs=iOqn91&\\_zl=qKhr6](https://www.snmmi.org/AboutSNMMI/Content.aspx?ItemNumber=41839&utm_source=Email&utm_medium=Informz&utm_campaign=Email%20Outreach&_zs=iOqn91&_zl=qKhr6).

*SNMMI*

## DOE Breaks Ground for Stable Isotope Production and Research Center

The U.S. Department of Energy (DOE), in coordination with Oak Ridge National Laboratory (ORNL; TN), on October 24 held a groundbreaking event on the ORNL campus for the Stable Isotope Production and Research Center (SIPRC), which will expand the nation's capability to enrich stable isotopes for medical, industrial, and research applications. DOE also announced \$75 million

to support the SIPRC with funding provided through the Inflation Reduction Act, which in FY 2022 delivered \$1.55 billion to the Office of Science to accelerate national laboratory infrastructure projects.

SIPRC will provide DOE with multiple production systems that can enrich a wide range of stable isotopes. The facility includes space to add additional systems and expand the building footprint in the future as demand increases. SIPRC will be part of the DOE Isotope Program, which produces and sells isotopes that are in short supply or otherwise unavailable. The research conducted at SIPRC supports the Program's innovative work to develop advanced manufacturing techniques and novel isotope separations to build out a safe and reliable domestic supply chain.

The facility is scheduled for completion in 2025 and will be housed in the same space as the Enriched Stable Isotope Prototype Plant. SIPRC will establish a domestic full-production cascade for enriched stable isotopes. It will also reduce the nation's reliance on foreign sources of enriched stable isotopes by facilitating new capabilities to produce useful quantities of priority stable isotopes. This will address the void left when operation of the Oak Ridge calutrons ceased in 1998.

*U.S. Department of Energy*

## NIH to Investigate Function of Every Human Gene

The National Institutes of Health on September 27 announced the launch of a program intended to better understand the function of every human gene and to generate a catalog of the molecular and cellular consequences of inactivating each gene. The Molecular Phenotypes of Null Alleles in Cells (MorPhiC) program, managed by the National Human Genome Research Institute (NHGRI), aims to systematically investigate the function of each gene through multiple phases that will each build on the work of the previous.

The program will be funded initially for 5 y for a total of \$42.5 million.

Phase 1 of the program will focus on 1,000 protein-coding genes and serve as a pilot phase, with 3 goals: exploring multiple methods of inactivating (knocking out) gene function, developing molecular and cellular systems that model multiple human tissues and developmental stages, and developing molecular and cellular approaches to cataloging gene function that other researchers can reproduce.

"The function of thousands of genes is still a mystery, and they likely serve vital biological roles," said Colin Fletcher, PhD, NHGRI program director in the Division of Genome Sciences. "Understanding fundamental biology can help us figure out why certain diseases occur and how we can develop drugs to target and treat those diseases."

More than 6,000 of the estimated 19,000 protein-coding genes have not been well studied. Among those that have been studied, only small subsets of their functions are well characterized. All data over the course of the project will be made available to the broader research community. If Phase 1 is successful, NIH will activate a second phase to characterize a larger set of human genes.

"MorPhiC is meant to add another layer of functional information between the gene knockout at the DNA level and the organism-level effects. We want to catalog the effects of knocking out each gene within cells and—together with information from other studies—use that to understand how genes function to produce an organism," said Adam Felsenfeld, PhD, NHGRI program director in the Division of Genome Sciences. Recipients of funding for phase 1 of the MorPhiC program include researchers at Northwestern University Feinberg School of Medicine (Chicago, IL), the University of California San Francisco, Sloan Kettering Institute for Cancer Research (New York, NY), Jackson Laboratory (Farmington, CT), and the University of Miami (FL).

*National Institutes of Health*

Each month the editor of *Newsline* selects articles on diagnostic, therapeutic, research, and practice issues from a range of international publications. Most selections come from outside the standard canon of nuclear medicine and radiology journals. These briefs are offered as a window on the broad arena of medical and scientific endeavor in which nuclear medicine now plays an essential role. The lines between diagnosis and therapy are sometimes blurred, as radiolabels are increasingly used as adjuncts to therapy and/or as active agents in therapeutic regimens, and these shifting lines are reflected in the briefs presented here. We include a small section on noteworthy reviews of the literature.

### **<sup>68</sup>Ga-DOTATATE PET/CT in Sarcoidosis**

Lee et al. from the Hospital of the University of Pennsylvania (Philadelphia) and the Brigham and Women's Hospital/Harvard Medical School (Boston, MA) reported on October 20 ahead of print in the *Journal of Nuclear Cardiology* on the potential clinical utility of <sup>68</sup>Ga-DOTATATE PET/CT compared with that of <sup>18</sup>F-FDG PET/CT for diagnosis and response assessment in cardiac sarcoidosis. The study included 11 patients who underwent imaging with both tracers, and the 2 studies were interpreted independently before comparison. The researchers found that patient-level concordance between studies with the 2 tracers was 91%, with 10 patients having multifocal DOTATATE uptake indicating active cardiac sarcoidosis and 1 with diffuse DOTATATE uptake. Segment-level agreement between the 2 types of studies was 77.1%. The SUV<sub>max</sub>-to-blood pool ratio was lower with <sup>68</sup>Ga-DOTATATE PET/CT (3.2 ± 0.6) than with <sup>18</sup>F-FDG (4.9 ± 1.5). Eight patients also underwent follow-up <sup>68</sup>Ga-DOTATATE PET/CT, which showed 1 case of complete response and 1 of partial response, compared with 3 complete and 1 partial response on follow-up <sup>18</sup>F-FDG PET/CT. The authors summarized

their findings that “compared to <sup>18</sup>F-FDG PET/CT, <sup>68</sup>Ga-DOTATATE PET/CT can identify active cardiac sarcoidosis with high patient-level concordance but with moderate segment-level concordance, low signal-to-background ratio, and underestimation of treatment response.”

*Journal of Nuclear Cardiology*

### **Predictive and Prognostic Imaging Biomarkers in the TheraP Trial**

The TheraP Trial Investigators and the Australian and New Zealand Urogenital and Prostate Cancer Trials Group published on October 14 ahead of print in *Lancet Oncology* an analysis from their landmark trial, focusing on <sup>68</sup>Ga-prostate-specific membrane antigen (PSMA)-11 PET and <sup>18</sup>F-FDG PET parameters as predictive and prognostic biomarkers in patients receiving <sup>177</sup>Lu-PSMA-617 or cabazitaxel for metastatic castration-resistant prostate cancer. After reviewing the overall protocol and criteria for the TheraP study, a multicenter, open-label, randomized phase 2 trial with 200 participants (99 treated with the PSMA agent and 101 with cabazitaxel), the authors evaluated an SUV<sub>mean</sub> of ≥10 on <sup>68</sup>Ga-PSMA-11 PET as a predictive biomarker of response. A metabolic tumor volume of ≥200 mL on <sup>18</sup>F-FDG PET was tested as a prognostic biomarker. Over a median follow-up of 18.4 mo, 35 of the men assigned to <sup>177</sup>Lu-PSMA-617 and 30 assigned to cabazitaxel therapy had high PSMA uptake (SUV<sub>mean</sub> ≥ 10). The odds of prostate-specific antigen (PSA) response to the PSMA agent were significantly higher for those with SUV<sub>mean</sub> ≥ 10 than those with SUV<sub>mean</sub> < 10. The PSA response rate in patients with SUV<sub>mean</sub> ≥ 10 was 91% for <sup>177</sup>Lu-PSMA-617 and 47% for cabazitaxel treatment. Corresponding response rates in patients with SUV<sub>mean</sub> < 10 were 52% and 32%. High metabolic tumor volumes (≥200 mL) on <sup>18</sup>F-FDG PET were seen in 30% of patients assigned to

<sup>177</sup>Lu-PSMA-617 treatment and 30% of those assigned to cabazitaxel. The authors concluded that “in men with metastatic castration-resistant prostate cancer, PSMA PET SUV<sub>mean</sub> was predictive of higher likelihood of favorable response to <sup>177</sup>Lu-PSMA-617 than cabazitaxel, which provided guidance for optimal <sup>177</sup>Lu-PSMA-617 use.” High <sup>18</sup>F-FDG PET metabolic tumor volumes were associated with lower responses, regardless of randomly assigned treatment, an indication that additional research may define the need for treatment intensification.

*Lancet Oncology*

### **PET/CT and Prognosis in RT of Rhabdomyosarcoma**

Cheriyalinal Parambil et al. from Tata Memorial Hospital/Homi Bhabha National Institute (Mumbai, India) reported on October 14 ahead of print in the *Journal of Pediatric Hematology/Oncology* on a study of the prognostic significance of persistent <sup>18</sup>F-FDG avidity on PET in residual masses after definitive radiation treatment in pediatric rhabdomyosarcoma. The retrospective study included 63 children with group III ( $n = 55$ ) and group IV ( $n = 8$ ) rhabdomyosarcoma who underwent PET/CT imaging at 3 mo after radiation for local control. Residual masses were visualized in 10 patients (15.9%), and anatomic residual disease was visualized in 24 (38.1%), with no <sup>18</sup>F-FDG-avid areas in 29 (46.0%). Over a median follow-up of 38 mo, 3-y event-free survival for children with <sup>18</sup>F-FDG-avid residual masses was 40.0% compared with 71.9% for those who had no such masses. Three-year overall survival of patients with <sup>18</sup>F-FDG-avid residual masses was 50.8% compared with 77.0% for the remaining patients. These results were sustained on multivariate analysis. The authors concluded that “persistent metabolic activity in residual disease postchemoradiotherapy in rhabdomyosarcoma may portend a poorer prognosis with an increased risk of relapse.” They added that “this subset of high-risk patients needs to be identified, and further trials are warranted

to develop strategies to improve their outcomes.”

*Journal of Pediatric Hematology/  
Oncology*

### **<sup>11</sup>C-Choline PET/CT in Primary Hyperparathyroidism**

In a study published on October 10 ahead of print in *Surgery*, Saha et al. from the Mayo Clinic (Rochester, MN) reported on <sup>11</sup>C-choline PET/CT in evaluation of primary hyperparathyroidism, with a focus on utility when conventional imaging techniques fail to provide accurate preoperative localization. The study included 43 patients in whom multiple standard imaging modalities had failed to localize disease and who underwent limited-coverage neck-and-chest <sup>11</sup>C-choline PET/CT. Thirty-three patients had positive findings on <sup>11</sup>C-choline PET/CT. Of the 25 patients who proceeded to surgery, 18 were reoperations. Twenty of the 25 patients achieved an operative cure. <sup>11</sup>C-choline PET/CT was found to have a sensitivity of 64% and positive predictive value of 72%, with 5 false-positive findings (lymph nodes, normal parathyroid, and a recurrent laryngeal nerve neuroma). These results were compared with those from standard imaging modalities, including ultrasound, <sup>123</sup>I-sestamibi, and 4D CT. The authors concluded that <sup>11</sup>C-choline PET/CT “is a useful adjunct for parathyroid localization in a complex population of patients who have failed standard localization techniques, including ultrasound, <sup>123</sup>I-sestamibi, 4D CT, and/or prior operations.” They added that although <sup>11</sup>C-choline PET/CT may not be needed routinely, “it may aid in preoperative localization in the reoperative setting.”

*Surgery*

### **Clinical Experience with Implementation of 2015 ATA Guidelines**

Wu et al. from the University of Calgary/University of Calgary Cumming School of Medicine (Canada) reported on October 13 ahead of print in *Thyroid* on the clinical outcomes of the implementation of the 2015 American Thyroid

Association (ATA) guidelines for management of thyroid nodules and differentiated thyroid cancer (DTC) using the modified ATA recurrence risk (RR) stratification system. A total of 479 patients with DTC were assigned a modified ATA RR (253 [53%] low-, 129 [27%] intermediate-, and 97 [20%] high-RR) and American Joint Committee on Cancer 8th-edition stage. These and the ATA recommendations guided surgical management, radioiodine treatment, and adjuvant therapies. Responses to treatment were evaluated at 2 y after surgery, which included 227 (47%) total thyroidectomies plus radioiodine, 178 (37%) total thyroidectomies only, and 74 (16%) lobectomies. The 2-y responses to treatment were excellent for 66 (89%) patients undergoing lobectomy, 149 (84%) with total thyroidectomy only, and 121 (53%) with total thyroidectomy plus radioiodine treatment. Of patients stratified at low-RR, 216 (85%) had excellent responses to treatment, 32 (13%) had indeterminate treatment responses, 4 (2%) had biochemical incomplete responses, and 1 had a structural incomplete response to treatment. Of patients stratified at intermediate-RR, 83 (64%) saw excellent, 30 (23%) saw indeterminate, 7 (6%) saw biochemical incomplete, and 9 (7%) saw structural incomplete treatment responses. With the worst study outcomes, patients in the high-RR saw 37 (38%) excellent responses, 18 (19%) indeterminate, 10 (10%) biochemical incomplete, and 32 (33%) structural incomplete responses to treatments. The authors concluded that the “2015 ATA RR stratification system is useful for predicting disease status at 2-y posttreatment in patients with DTC” and “may reduce thyroid cancer overtreatment by including lobectomy as a definitive treatment option for low-risk thyroid cancers and selective use of radioiodine for intermediate- and high-risk patients.”

*Thyroid*

### **Cardiovascular Complications and Long COVID**

In an article published on September 23 in *Frontiers in Cardiovascular Medicine* (2022;9:968584), Murata et al. from

Nihon University School of Medicine (Tokyo, Japan) reported on a study using multimodality imaging to investigate the prevalence of cardiovascular disorders, particularly in patients with cardiovascular “long COVID.” The study drew patients from a total of 584 individuals admitted to the hospital with COVID-19 between January 2020 and September 2021. At clinical assessment over a median follow-up of 163 d, 52 (9%) patients with complaints of chest pain, dyspnea, or palpitations were suspected to have cardiovascular long COVID and were enrolled in the study. Patients underwent electrocardiography, chest X-ray imaging, and echocardiography, as well as cardiac MR and SPECT/CT imaging depending on initial findings. Cardiovascular disorders were present in 27%; of these, 15% had myocardial injury, 8% had pulmonary embolisms, and 4% both. Patients with cardiovascular disorders had significantly higher incidences of severe COVID conditions (36% vs 8%) and in-hospital cardiac events (71% vs. 24%) than those who did not. A severe COVID condition and in-hospital severe condition proved to be independent risk factors for cardiovascular disorders in cardiovascular long COVID patients. No patients died during the study period, and no adverse events were reported. The authors cited other investigators’ observations that long COVID itself is unlikely to result in organic cardiovascular disease, and, when it does, is likely to be quite mild. Despite the fact that patients with long COVID and cardiovascular complications tended to have longer-lasting symptoms of long COVID, the prognosis did not seem to be worse. They concluded that “early detection of cardiovascular problems in cardiology for symptomatic long COVID patients may inform patients of the duration of symptoms and allow symptoms to be shortened through appropriate therapeutic intervention.”

*Frontiers in Cardiovascular  
Medicine*

### **PSMA PET/CT and Dose-Escalated Salvage RT in PCa**

Tamihardja et al. from the University of Würzburg (Germany) reported on

October 10 in *Cancers (Basel)* (2022; 14[19]:4956) on a study of oncologic outcomes with prostate-specific membrane antigen (PSMA) PET/CT-guided salvage radiotherapy for localized macroscopic prostate cancer recurrence. The study included 367 men who received such radiation treatment after radical prostatectomy. Of these, 111 patients were staged by either  $^{68}\text{Ga}$ -PSMA-I&T or  $^{18}\text{F}$ -PSMA-1007 before radiation. A total of 59 (53.2%) of these patients were treated for PSMA PET-positive macroscopic prostatic fossa recurrence. Over a median follow-up of 38.2 mo, the 3-y biochemical progression-free survival rate was 89.1% and the 3-y metastasis-free survival rate reached 96.2%. The cumulative 3-y late grade 3 genitourinary toxicity rate was 3.4%, with no late grade 3 toxicities reported. The authors concluded that “PSMA PET/CT-guided dose-escalated salvage radiotherapy with a simultaneous integrated boost to the local recurrence achieved encouragingly high rates of 3-y biochemical progression-free survival, metastasis-free survival, and overall survival,” with effective disease control and low toxicity rates.

*Cancers (Basel)*

### Choroid Plexus Imaging in Presymptomatic MS

In an article published on October 13 in *Neurology, Neuroimmunology, and Neuroinflammation* (2022;9[6]:e200026), Ricigliano et al. from the Sorbonne Université; Paris Brain Institute, ICM, CNRS, Inserm; St Antoine Hospital; Pitié-Salpêtrière Hospital; Hôpital Fondation Adolphe de Rothschild; Université Paris-Saclay, CEA, CNRS, Inserm; and Service Hospitalier Frédéric Joliot, Orsay (all in Paris, France) reported on a study assessing whether imaging characteristics of the choroid plexus are detectable at the earliest stages of multiple sclerosis (MS), before clinical symptom onset. The retrospective study included 27 individuals with presymptomatic MS, 97 with clinically definite MS (CDMS), and 53

healthy controls, all of whom underwent cross-sectional 3T-MR imaging. A subset of 22 CDMS individuals, 19 healthy controls, and 1 individual with presymptomatic MS (imaged 8 mo before conversion to CDMS) also underwent translocator protein (TSPO)  $^{18}\text{F}$ -DPA-714 PET imaging. Choroid plexus  $^{18}\text{F}$ -DPA-714 uptake was calculated as the average SUV. Compared with healthy controls, individuals with presymptomatic MS had 32% larger choroid plexuses, similar to those with MS. Baseline PET imaging in the presymptomatic case who later developed MS showed 33% greater choroid plexus inflammation than in healthy controls. Postmortem studies in the choroid plexus of this individual identified a population of CD163<sup>+</sup> mononuclear phagocytes expressing TSPO in MS, possibly contributing to the increased  $^{18}\text{F}$ -DPA-714 uptake. The authors concluded that “by identifying an imaging signature in choroid plexuses already in presymptomatic MS, our work supports their role from the early phases of disease development and encourages further investigations on the involvement of choroid plexus immune infiltration and blood-cerebrospinal fluid barrier dysfunction in disease onset.”

*Neurology, Neuroimmunology, and Neuroinflammation*

### Reviews

Review articles provide an important way to stay up to date on the latest topics and approaches through valuable summaries of pertinent literature. The Newsline editor recommends several general reviews accessioned into the PubMed database in September and October. Linguanti et al. from the University of Florence and the IRCCS-Humanitas Research Hospital (Rozzano; both in Italy) reported in the September 27 issue of *Cancers (Basel)* (2022;14[19]:4700) on “Metabolic imaging in B-cell lymphoma during CAR-T cell therapy.” In the October 17 issue of the *Medical Journal of Australia* (2022;217[8]:424–433), Williams et al. from the Royal Melbourne Hospital,

Peter MacCallum Center Centre, Monash University, Cabrini Institute/Cabrini Health (all in Melbourne, Australia), Singapore General Hospital, and University College London (UK) presented “Modern paradigms for prostate cancer detection and management.” An overview of “Positron emission tomography in autoimmune encephalitis: Clinical implications and future directions” was provided by Li et al. from Beijing Tiantan Hospital/Capital Medical University and the China National Clinical Research Center for Neurological Diseases (both in Beijing, China) on October 19 ahead of print in *Acta Neurologica Scandinavica*. Hawkey et al. from Duke University School of Medicine (Durham, NC) and Tulane Cancer Center (New Orleans, LA) published an assessment of “The value of phenotypic precision medicine in prostate cancer” on October 6 ahead of print in the *Oncologist*. “Novel tracers for molecular imaging of interstitial lung disease: A state of the art review” was offered online ahead of print in the September 21 issue of *Autoimmunity Reviews* by Broens et al. from the Vrije Universiteit Amsterdam (The Netherlands). The October issue of *Surgical Oncology Clinics of North America* published several reviews of state-of-the-art imaging techniques, including Szidonya et al. from the Oregon Health and Science University (Portland), Semmelweis University (Budapest, Hungary), University of Iowa Hospitals and Clinics (Iowa City), and University of Colorado School of Medicine (Aurora) with “Molecular and anatomic imaging of neuroendocrine tumors (2022;31[4]:649–671); Graves et al. from the University of California Davis (Sacramento), the University of California, San Francisco, and New York University Langone Health (NY) with “Innovations in parathyroid localization imaging (2022;31[4]:631–647); and Goodman et al. from the University of California, San Francisco, with “Molecular imaging for estrogen receptor-positive breast cancer: Clinical applications of whole body and dedicated breast positron emission tomography” (2022;31[4]: 569–579).

# Leading in Urology and Pioneering in Social Media Outreach

## A Conversation Among Declan Murphy, Ken Herrmann, and Michael Hofman

Declan Murphy<sup>1,2</sup>, Ken Herrmann<sup>3</sup>, and Michael Hofman<sup>2</sup>

<sup>1</sup>University of Melbourne, Melbourne, Victoria, Australia; <sup>2</sup>Peter MacCallum Cancer Centre, Melbourne, Victoria, Australia; and

<sup>3</sup>Universitätsklinikum Essen, Essen, Germany

**K**en Herrmann, MD, MBA, a professor of nuclear medicine at the Universitätsklinikum Essen (Germany), and Michael Hofman, MBBS, FRACP, director of the Prostate Cancer Theranostics and Imaging Centre of Excellence at the Peter MacCallum Cancer Centre (Melbourne, Australia), talked with Declan Murphy, FRACS, FRCS, about his career in genitourinary (GU) oncology. Dr. Murphy is a consultant urologist, the director of robotic surgery, and the director of GU oncology at the Peter MacCallum Cancer Centre and a professorial fellow at the University of Melbourne. He is an internationally recognized subject matter expert in GU oncology, with a focus on prostate cancer, including prostate-specific membrane antigen (PSMA) imaging and theranostics. He has been chief investigator on numerous large-scale competitive GU oncology grants and leads an active team of clinical researchers at Peter MacCallum.

After completing specialist urology training at Guy's and St. Thomas' Hospital (London, U.K.), Dr. Murphy spent a year in Melbourne as a fellow in laparoscopic and robotic urology under the supervision of Tony Costello. He returned to Melbourne in 2010 to take up his current positions. In 2020 he was named Australia's top researcher in urology, based on publications and citations in top journals in the field. He is a member of the invitation-only Advanced Prostate Cancer Consensus Conference and of the exclusive Association of Academic European Urologists. He holds senior editorial positions at the *BJU International*, *European Urology*, *Nature Reviews Urology*, and *Prostate Cancer & Prostatic Diseases* and is on the board of reviewers for many other journals.

Dr. Murphy is active on social media, with a large Twitter following and a busy YouTube channel. He blogs regularly for several websites and hosts the popular *GU Cast* podcast, focusing on GU oncology topics.

**Dr. Herrmann:** Welcome, Dr. Murphy. Everyone knows you as the driving force of the GU program at the Peter MacCallum Cancer Centre. Please tell us how you came to be there.

**Dr. Murphy:** I grew up and completed my medical and surgical training in the beautiful west of Ireland, followed by urology training at Guy's and St. Thomas' in England and a GU oncology fellowship at the Royal Melbourne Hospital and Peter MacCallum Cancer Centre in Melbourne. We said goodbye to Melbourne and returned to the U.K. in 2007. However, we returned to Australia in 2010, when Peter MacCallum invited me to contribute to building a new cancer center and lead the GU oncology team.

**Dr. Hofman:** Our paths almost crossed when I did a nuclear medicine fellowship at Guy's and St Thomas'. When did you realize the importance of nuclear medicine in urology? While exposed to the PET Center at St Thomas' or when you arrived in Australia?

**Dr. Murphy:** While at Guy's Hospital, in Urology up until 2009, we used bone scans but not PET, despite increasing interest in <sup>18</sup>F-FDG PET around the world. In addition, choline PET was unrealistic for many centers. After moving to Peter MacCallum in 2010, the GU community showed little interest in PET imaging. While we did have a choline PET program running at Peter Mac, there were logistic and technical problems resulting from scanning availability, and the clinical utility was limited. Therefore, our multidisciplinary tumor team had no involvement with nuclear medicine up until the arrival of PSMA PET/CT in 2014.

**Dr. Hofman:** Tell us how your interest was sparked.

**Dr. Murphy:** I'll never forget it. I ran into Rodney Hicks (MD, FRACP) and Dr. Hofman at lunch, and they told me about PSMA PET imaging. I hadn't heard of it, but they said it was going to be sensational. I initially ignored this, but then I saw the imaging of the first patient scanned at Peter MacCallum in mid-2014—and it was indeed sensational. We still show that first case, as you could see the prostate tumor, lymph nodes, and bone metastases all in one scan, with a stunning tumor-to-background ratio. Sometimes in oncology a stunning image can be just as dramatic as a significant *P* value. That image is where our enthusiasm started. Then you and your nuclear medicine colleagues, especially your colleagues in Germany, began to produce the data. We haven't looked back since.

**Dr. Herrmann:** You were one of the first urologists in Australia to see the value of PSMA PET/CT. Despite concerns about stage migration and possible downsides of new technologies, you and your team embraced it. Why?

**Dr. Murphy:** The stage migration issue does get overexpressed. It comes back to the design of the proPSMA study, with the primary endpoint being accuracy (Fig. 1). Accuracy was very attractive for this novel imaging technology, because we knew there were problems with conventional technologies for staging prostate cancer. Bone scans have false-positives and -negatives, and CT scans often miss lymph node involvement. We were making decisions based on poor-quality information; if better-quality information is available, that should not be described as stage migration. It should be described as improved accuracy.



Declan Murphy, FRACS, FRCS



**FIGURE 1.** Dr. Declan Murphy (left) and Dr. Michael Hofman (right) accepting the 2021 Australian Clinical Trials Alliance (ACTA) Trial of the Year Award for the ProPSMA study.

**Dr. Herrmann:** That is an excellent point. When you look at PSMA PET/CT, how early can we implement it? For example, is there potential for replacing multiparametric MRI for detection of prostate cancer?

**Dr. Murphy:** In the 2014–2017 era, multiparametric MRI was used for early detection, after an elevated prostate-specific antigen (PSA) level and before biopsy. Now we use it routinely for all patients, with any suspicion of prostate cancer guiding the need for biopsy. But we know there are limitations for MRI, and patients

presented at the European Association of Urology (EAU) this summer, showed very encouraging results documenting excellent tolerability and safety, and we look forward to publishing the final data in early 2023.

**Dr. Herrmann:** Urology is an important partner in driving the acceptance of theranostics in Europe. How do you see this in the United States and globally?

**Dr. Murphy:** Prostate cancer multidisciplinary meetings need to include the nuclear medicine team, to benefit our patients. A message for the readership of *The Journal of Nuclear Medicine* is that urology and nuclear medicine can partner really well. Everyone should advance partnerships that they have with their colleagues, optimally selecting patients for FDA-approved therapies and research studies. I'm very optimistic that we'll see more successful partnerships around the world as these technologies become more available.

**Dr. Herrmann:** On a society level, EAU and the European Association of Nuclear Medicine (EANM) do a great job partnering. How do you see this on a global level?

**Dr. Murphy:** This is indeed really important. EAU and EANM established a productive relationship over many years, including joint section meetings and many joint publications. This could or should be the template toward which we aspire. But we really need to turbocharge these advances, because that's what's required (especially for patient care) on a global level.

**Dr. Herrmann:** In addition to your outstanding scientific track record, you are also famous for your social media activities, including the GU podcast, your Twitter activities, your YouTube presence, and, of course, outstanding movielike talks. Tell us how you embraced social media and what nuclear medicine can learn from you?

---

"If you're not embedded with these clinical teams, there's a high risk that the technology that you learned in your fellowship will be gone by the wayside 5 years later."

---

with normal or equivocal MRIs but with concerning features (such as young age or high PSA density) may need biopsies as well. I don't think PSMA PET will replace MRI, but there is a subset of patients with normal or equivocal MRI results in whom PSMA PET/CT can add value, and we are evaluating this in a further randomized study.

**Dr. Hofman:** Not only did you embrace PSMA PET/CT early for diagnosis, but you also embraced it for therapy—designing and participating in the first prospective study of lutetium PSMA that led directly to the TheraP trial and now investigating lutetium PSMA as a first-line therapy in the UpFrontPSMA and LuTectomy trials. What do you think of the use of lutetium PSMA early, either before surgery or instead of surgery?

**Dr. Murphy:** It is very important to have scientific rigor in evaluating these exciting new technologies. Successful randomized trials in patients with advanced disease have demonstrated the utility of lutetium PSMA, which is now FDA-approved and included in guidelines. We also need to use prospective studies to evaluate early metastatic and high-risk localized prostate cancer. That's my first message.

We recently operated on the final patient (number 20) in our LuTectomy trial, in which patients received lutetium PSMA before radical prostatectomy. The initial data from the first 10 patients,

**Dr. Murphy:** I joined Twitter in 2011. This was triggered by an article describing how an academic hematologist found Twitter to be quite useful for looking at newly released papers and opinions. So I just made a Twitter profile, typed in "prostate cancer," and started following a few of my friends who were leaders in the field. All of a sudden, my phone was lighting up with these great papers, just-published opinions, and images. I became very active and was soon appointed as associate editor for social media for the *British Journal of Urology*. We developed a strong social media strategy using Twitter, YouTube, and blogging to disseminate information outward—but also engaging with clinicians and researchers inward. To me, it is surprising that 10 years later Twitter remains the most important tool for clinicians and researchers who want to keep up to date with content and also have some fun engaging with their colleagues and friends around the world. Especially for an imaging-based specialty like nuclear medicine, it's a great opportunity to share interesting images and tell tales.

**Dr. Herrmann:** My cointerviewer, Dr. Hofman, is also a social media giant. He will follow up with more detailed social media questions.

**Dr. Hofman:** You recently transitioned away from Twitter toward podcasting and YouTube TV. What led you to this transition, and how do you see this new form of knowledge dissemination playing out?

**Dr. Murphy:** Spotify made a large investment in podcasting in about 2019, and Apple Music put a huge investment into podcasts. This caught my attention. At around that time, mirroring technology in cars was beginning to take off, so that podcasts could be played while driving. The world was transitioning to on-demand for everything. These technologic and behavioral changes resulted in a tremendous boom in the market for on-demand podcasting. I wanted to use my time biking to work to listen to urology-related topics, but there was not much out there. We decided to set up a podcast just for ourselves, our local community, to discuss hot topics that we talked about on Twitter. In early 2020 we bought some technology and spent a couple of months trying to figure out how to set up a podcast. Then suddenly the pandemic hit, and we posted our very first podcast at the end of March 2020, when Melbourne was in complete lockdown. The EAU meeting had been canceled, along with the presentation by Dr. Hofman on the proPSMA study to coincide with publication in *The Lancet*, so we made the proPSMA study the topic of our first podcast. Now 2.5 years later we are approaching 100 episodes and many tens of thousands of downloads. I am convinced that the pandemic facilitated the acceleration of our podcasting program.

Today, my colleague Renu Eapen (a real talent) and I talk about anything to do with GU oncology. We absolutely love talking about nuclear medicine, and therefore, we have had lots of interactions with PSMA experts from around the world. About a year ago we expanded into YouTube, because that was growing in the podcasting world. I read an article saying that YouTube gave different value for visual bites and that you could grow, not split, your podcasting audience by going into YouTube. I also quite like video technology, and now it's like a TV production.

**Dr. Hofman:** *You recently talked about obsolescence in surgical training. I wonder what advice you would give a young doctor thinking about nuclear medicine training?*

**Dr. Murphy:** The title of the talk was "Avoiding Obsolescence as a Cancer Surgeon." I was just about to turn 50 when I was tasked to give this talk challenging my own relevance and future job security. My first message was that lifelong learning is essential. Looking back to my training as a young surgeon, we did basic surgery, including radical mastectomy and axillary lymph node clearance, with techniques that would never be used in patients today. No matter what you're doing out there today (and certainly in surgical training), it's important to understand that by the time you reach midcareer, there's a high chance that all these things are going to be obsolete. Therefore, of course, lifelong learning has to be essential not only to remain relevant but to do the best for our patients.

Nuclear medicine is a naturally evolving specialty, where new ligands and new imaging technologies such as total-body PET will

always be creating new opportunities for your imaging capabilities. What the theranostics revolution in prostate cancer has shown us is that the most important thing for nuclear medicine practitioners, especially those who do theranostics, is to embed yourselves with clinical teams, whether these are in oncology or in functional imaging. If you're not embedded with these clinical teams, there's a high risk that the technology that you learned in your fellowship will be gone by the wayside 5 years later. If you work embedded in clinical teams, then you are much more likely to evolve and to help develop the best research questions for your patients.

**Dr. Herrmann:** *Success of institutional programs often boils down to individuals. How do you transfer your enthusiasm, your energy, and your visionary thinking to the next generation of clinicians?*

**Dr. Murphy:** In surgery, we have traditionally had problems with too many men. One of our favorite missions is to attract fantastic, smart young women to urology. In part, this is because we need to change the structure of our workforce to be more representative. But also, to be brutally honest, it's a competitive world out there and we have all these wonderful young women doctors coming through. Unless we are attractive to them as a specialty, we will lose the smartest people. They will go to other areas in medicine where they feel more valued or more looked after. So, making sure we have a diverse workplace is important. The best workforce is diverse, and that sometimes takes a lot of strategy, leadership, and planning. In surgery, certain specialties (and urology is one of them) have far too many men. We have to actually go out of our way to ask: How are we going to change that? How are we going to change our scientific meetings to make them more sex-balanced? How are we going to change our training programs or the way we offer flexible training to young women? That is one of the points in my "Avoiding Obsolescence"—how to include young women in our specialty and make sure we are attracting the best people. We also need to think about other people who are not as well represented as they could be and reach out, widening participation.

**Dr. Herrmann:** *What 3 wishes do you have from or for nuclear medicine for the future?*

**Dr. Murphy:** Wish number 1 is around imaging technology. Can you please accelerate total-body PET/CT into clinical practice all around the world? Because I think this will be a game changer for prostate cancer. Wish number 2: please keep developing radio-guided surgery opportunities in prostate cancer. This offers great promise, but we're not there yet. Number 3: we are at only the start of the theranostics revolution in GU oncology. I encourage you to be ambitious and change the world for all our GU oncology patients.

**Dr. Herrmann:** *Dr. Murphy, Dr. Hofman, thank you very much for your time.*

# Fibroblast Activation Protein Inhibitor Imaging in Nonmalignant Diseases: A New Perspective for Molecular Imaging

Christian Schmidkonz<sup>1,2</sup>, Torsten Kuwert<sup>1</sup>, Armin Atzinger<sup>1</sup>, Michael Cordes<sup>1</sup>, Georg Schett<sup>3</sup>, Andreas Ramming<sup>3</sup>, and Theresa Götz<sup>2</sup>

<sup>1</sup>Department of Nuclear Medicine, Friedrich–Alexander University Erlangen–Nürnberg and University Hospital Erlangen, Erlangen, Germany; <sup>2</sup>Institute for Medical Engineering, Technical University of Applied Sciences Amberg–Weiden, Weiden, Germany; and <sup>3</sup>Rheumatology and Immunology, Department of Internal Medicine 3, Friedrich–Alexander University Erlangen–Nürnberg and University Hospital Erlangen, Erlangen, Germany

Fibroblast activation protein- $\alpha$  (FAP- $\alpha$ ) is a type II transmembrane glycoprotein that is overexpressed in activated fibroblasts such as those in the stroma of tumors or in the fibrotic processes accompanying various benign diseases. The recent development and clinical implementation of radiolabeled quinolone-based tracers suitable for PET that act as FAP inhibitors (FAPIs) have opened a new perspective in molecular imaging. Although multiple studies have investigated the use of FAPI imaging in cancer, evidence concerning its use in nonmalignant diseases is still scarce. Herein, we provide a comprehensive review of FAPI imaging in nonmalignant diseases to clarify the current and potential role of this class of molecules in nuclear medicine.

**Key Words:** fibroblast activation protein; inflammatory diseases; PET; molecular imaging; fibrosis

**J Nucl Med 2022; 63:1786–1792**  
DOI: 10.2967/jnumed.122.264205

**F**ibroblast activation protein- $\alpha$  (FAP- $\alpha$ ) is a type II transmembrane glycoprotein that is overexpressed in cancer-associated fibroblasts. These cells play a crucial role in the development of the tumor microenvironment, which is involved in tumor growth, migration, and progression (1,2). FAP- $\alpha$  is present on the cell membrane of activated fibroblasts in approximately 90% of epithelial neoplasms, whereas resting fibroblasts and most other cell types have little to no FAP expression. Therefore, the development of radiolabeled quinolone-based tracers suitable for PET that act as FAP inhibitors (FAPIs) was a major breakthrough in nuclear medicine (3–7). Direct comparisons between FAPIs and the dominant PET tracer in oncology in the last 40 years, <sup>18</sup>F-FDG, raise hopes for more sensitive and specific molecular imaging techniques that might also guide the way for novel therapeutic treatment options (8,9).

However, fibroblast activation is not confined only to tumors but also occurs in immune-mediated diseases. Indeed, inflammation is directly linked to mesenchymal stromal activation, which leads to tissue damage. Activated FAP-positive fibroblasts play a major role in

this process and can acquire heterogeneous activation states. Catabolic FAP-positive extracellular matrix-degrading phenotypes of fibroblasts are associated with, for example, cartilage destruction and bone erosions, as seen in rheumatoid arthritis (10). On the other hand, mesenchymal stromal activation can also result in their differentiation into FAP-positive extracellular matrix-producing fibroblasts positive for purine-rich box1, which is the dominant phenotype in fibrotic diseases. Fibrotic diseases such as systemic sclerosis (SSc) and IgG4-related disease (IgG4-RD) are characterized by fibroblast activation and an excessive accumulation of extracellular matrix, which disrupts the physiologic tissue architecture and often leads to severe dysfunction of the affected organs. Fibrotic tissue responses across different diseases have been estimated to account for up to 45% of deaths in high-income countries and cause a socioeconomic burden of tens of billions of U.S. dollars per year (11). Because of the elevated clinical and economic relevance of these disease groups, a noninvasive imaging approach toward accurately detecting and quantifying mesenchymal tissue responses would be desirable (6). However, assessment of the molecular dynamics of mesenchymal stromal activation and fibrosis remains challenging (12). In this review, we provide an overview of the use of FAPI PET/CT in nonmalignant diseases.

## FAPI IMAGING IN IgG4-RD

Despite being inflammatory, immune-mediated diseases are associated with substantial activation of tissue-resident fibroblasts, resulting in fibrosis and organ damage. IgG4-RD is a paradigm of the inflammation-versus-fibrosis dichotomy: it is characterized by both autoimmune inflammation and tumefactive tissue fibrosis, with a predilection for the pancreas, salivary glands, kidney, aorta, and other organs (13). Although antiinflammatory drugs can reduce inflammatory activity in IgG4-RD, they have only a limited effect on the fibrotic disease component (14). During the disease course, there is a progression from a proliferative phenotype that is characterized by dense inflammatory lymphoplasmocytic infiltrates to a fibrotic phenotype with sparse cellular infiltrates but a greater degree of fibrosis (15).

In a cross-sectional clinical study, 27 patients with histologically confirmed IgG4-RD underwent both <sup>18</sup>F-FDG PET/CT and <sup>68</sup>Ga-FAPI-04 PET/CT, as well as MRI and histopathologic assessment (12). In a longitudinal approach, <sup>18</sup>F-FDG PET/CT and <sup>68</sup>Ga-FAPI-04 PET/CT data were evaluated before and after immunosuppressive treatment and were correlated with MRI and clinical data. Dual-tracer imaging revealed 3 distinct phenotypes of disease: proliferative, mixed,

Received Aug. 12, 2022; revision accepted Sep. 13, 2022.

For correspondence or reprints, contact Christian Schmidkonz (christian.schmidkonz@uk-erlangen.de).

Published online Sep. 15, 2022.

COPYRIGHT © 2022 by the Society of Nuclear Medicine and Molecular Imaging.

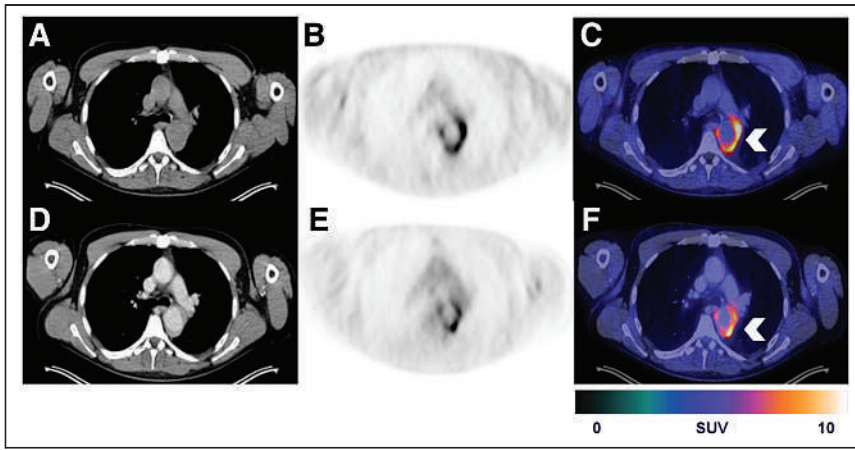


**FIGURE 1.**  $^{68}\text{Ga}$ -FAPI-04 PET/CT (A–C) and  $^{18}\text{F}$ -FDG PET/CT (D–F) images of man with histologically confirmed IgG4-RD. Tissue mass surrounding thoracic aorta exhibits increased  $^{68}\text{Ga}$ -FAPI-04 and increased  $^{18}\text{F}$ -FDG accumulation (arrowheads), typical of mixed phenotype.

and fibrotic (Fig. 1). The proliferative phenotype was characterized by intense lymphocyte infiltration, whereas fibroblasts were abundant in the fibrotic phenotype. Although the  $^{18}\text{F}$ -FDG signal was positive in the inflammatory and mixed phenotypes, the fibrotic phenotype remained negative on  $^{18}\text{F}$ -FDG PET/CT but positive on  $^{68}\text{Ga}$ -FAPI-04 PET/CT (Fig. 2). Follow-up imaging revealed that antiinflammatory treatment of IgG4 manifestations significantly reduced  $^{18}\text{F}$ -FDG PET uptake in more than 90% of inflammatory lesions. In contrast, fibrotic lesions demonstrated only a partial reduction in uptake after antiinflammatory treatment. Furthermore, more than 50% of active  $^{68}\text{Ga}$ -FAPI-04 lesions were persistently detectable after 6 mo of antiinflammatory treatment. Interestingly, persistent fibrotic activity resulted in constant or further progression of the fibrotic lesion mass whereas lesions with a significant reduction in  $^{68}\text{Ga}$ -FAPI-04 uptake decreased in size. These findings suggest that  $^{18}\text{F}$ -FDG–negative IgG4-RD manifestations should not be misinterpreted as functionally inactive and that patients with  $^{68}\text{Ga}$ -FAPI-04–positive lesions may require different forms of treatment because therapies that focus on proliferative disease features such as glucocorticoids may be sufficient to stop fibrosis.

Because of the development of specific treatments tackling fibrotic responses, such as pirfenidone or inhibitors of the transcription factor purine-rich box1,  $^{68}\text{Ga}$ -FAPI-04 PET/CT might be an ideal tool to detect shifts from inflammatory to fibrotic disease and for evaluation of the treatment response in IgG4-RD (16). Luo et al. evaluated the use of  $^{18}\text{F}$ -FDG PET/CT and  $^{68}\text{Ga}$ -FAPI-04 PET/CT in 26 patients in a prospective cohort study (17). They compared the rates of PET/CT positivity for the involved organs and the respective uptake values of IgG4-RD lesions. Although  $^{68}\text{Ga}$ -FAPI-04 PET/CT was

visually positive for detecting involvement of IgG4-RD in all patients,  $^{18}\text{F}$ -FDG PET/CT results were positive in 24 patients (92%). In the 136 involved organs,  $^{68}\text{Ga}$ -FAPI-04 PET/CT additionally detected 18 involved organs (13%) in 13 patients (50%), compared with  $^{18}\text{F}$ -FDG PET/CT. All  $^{18}\text{F}$ -FDG–avid lymph node involvement was missed by  $^{68}\text{Ga}$ -FAPI-04 PET/CT. This is most likely explained by the missing storiform fibrosis pattern typical of IgG4-RD. Visual comparison of the uptake and extension of the involved organs revealed higher uptake and a more pronounced disease extension in the pancreas, bile duct/liver, and salivary glands for  $^{68}\text{Ga}$ -FAPI-04 PET/CT than for  $^{18}\text{F}$ -FDG PET/CT. A similar pattern was observed for the quantitative comparison of  $\text{SUV}_{\text{max}}$ , which demonstrated significantly higher values for  $^{68}\text{Ga}$ -FAPI-04 PET/CT than for  $^{18}\text{F}$ -FDG PET/CT. The authors concluded that  $^{68}\text{Ga}$ -FAPI-04 PET/CT might be a promising tool for the assessment of IgG4-RD.

CT than for  $^{18}\text{F}$ -FDG PET/CT. The authors concluded that  $^{68}\text{Ga}$ -FAPI-04 PET/CT might be a promising tool for the assessment of IgG4-RD.

#### FAPI IMAGING IN PULMONARY FIBROSIS (PF)

PF, as an example of mesenchymal stroma activation, can arise as an idiopathic disorder or in the context of autoimmune diseases such as SSc. SSc is a prototypical fibrotic disease that shows PF development in 84% of patients and is their leading cause of death (18,19). Currently, the progression of PF in SSc is judged by measuring the accrual of lung damage represented by fibrosis on CT and the functional decline in forced vital capacity. This approach requires long-term follow-up to detect changes and does not directly assess the activity of tissue remodeling at the time of assessment. Furthermore, it often does not predict the course of PF in individual patients and does not enable appropriate risk stratification. In a single-center pilot study, Bergmann et al. tested the hypothesis that quantification of fibroblast activation by  $^{68}\text{Ga}$ -FAPI-04 PET/CT can be correlated with PF activity and disease progression in patients with SSc (20). The authors recruited 21 patients who had SSc-associated PF confirmed by high-resolution CT (HRCT) and who fulfilled the classification criteria of the American College of Rheumatology and the European League Against Rheumatism. Another 21 patients without SSc or PF, who were examined for other clinical reasons, were enrolled as controls. All patients underwent  $^{68}\text{Ga}$ -FAPI-04 PET/CT and standard-of-care procedures, including HRCT and pulmonary function tests at baseline. The patients were followed for 6 mo with HRCT and pulmonary function tests for a comparison with the baseline  $^{68}\text{Ga}$ -FAPI-04 PET/CT results and for prediction of PF progression. A subset of patients treated with the antifibrotic drug nintedanib underwent follow-up at between 6 and 10 mo, with use of  $^{68}\text{Ga}$ -FAPI-04 PET/CT to determine the changes in PF over time. The authors found that  $^{68}\text{Ga}$ -FAPI-04 accumulated in fibrotic areas of the lungs in patients with SSc-associated PF, whereas there was no significant uptake in the control group (Fig. 3).  $^{68}\text{Ga}$ -FAPI-04 uptake was significantly higher in patients with extensive disease, with previous progression of PF, or with higher clinical activity scores than those with limited disease, previously stable interstitial lung disease, or low clinical activity scores. Increased  $^{68}\text{Ga}$ -FAPI-04 uptake at baseline was associated with progression of PF independently of the

#### NOTEWORTHY

- FAPI imaging has a potential role in nonmalignant diseases.
- FAPI PET/CT is the only available imaging modality that can directly assess the dynamics of PF.
- FAPI PET/CT can differentiate inflammatory from fibrotic disease.
- An early FAPI signal in acute myocardial infarction is a predictor of adverse left ventricular remodeling.

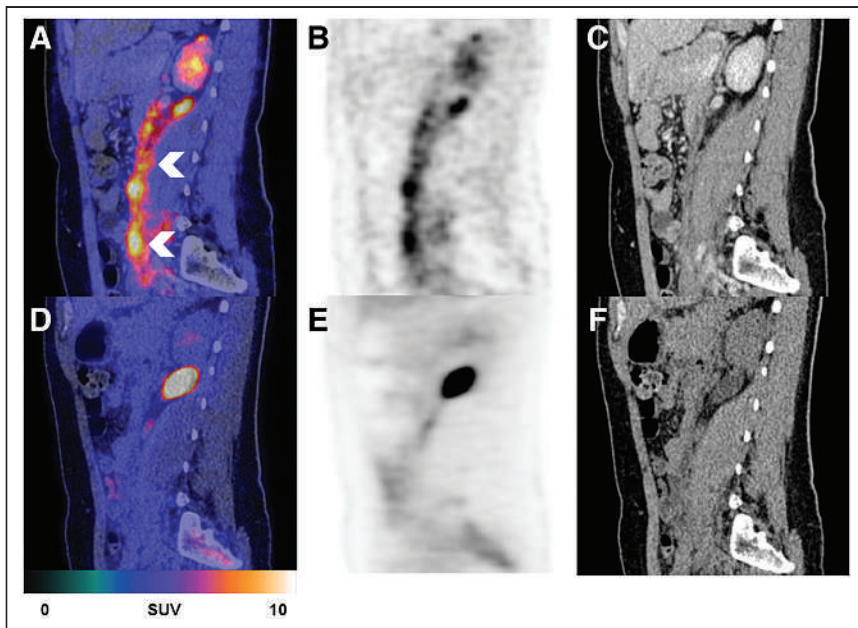


**FIGURE 2.**  $^{68}\text{Ga}$ -FAPI-04 PET/CT (A–C) and  $^{18}\text{F}$ -FDG PET/CT (D–F) images of woman with histologically confirmed IgG4-RD presenting with  $^{68}\text{Ga}$ -FAPI-04-positive retroperitoneal mass (arrowheads) that demonstrates no significant  $^{18}\text{F}$ -FDG uptake, typical of fibrotic phenotype.

extent of the involvement on HRCT and the forced vital capacity at baseline. Furthermore, the authors provided initial evidence that changes in  $^{68}\text{Ga}$ -FAPI-04 scores over time might correlate with changes after treatment with nintedanib, the first approved fibroblast-targeting antifibrotic drug. They concluded that, in contrast to other techniques such as pulmonary function tests, which measure the cumulative result of tissue damage,  $^{68}\text{Ga}$ -FAPI-04 PET/CT is the only available imaging modality that can directly assess the dynamics of PF. Further studies are warranted to clarify whether  $^{68}\text{Ga}$ -FAPI-04 PET/CT might improve the risk assessment of patients with SSc-associated PF and allow earlier, more accurate treatment and dynamic monitoring of the molecular response to fibroblast-targeting therapies.

Röhrich et al. evaluated the static and dynamic imaging properties of  $^{68}\text{Ga}$ -FAPI-46 PET/CT in 15 patients with fibrotic interstitial lung disease (fILD) and suspected lung cancer (21). Static PET/CT scans and dynamic scans were performed on 12 patients and an additional 3 patients, respectively. SUV measurements of

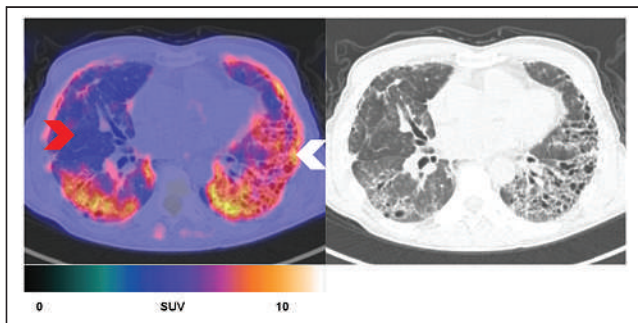


**FIGURE 3.**  $^{68}\text{Ga}$ -FAPI-04 PET/CT images of man with SSc-associated PF.  $^{68}\text{Ga}$ -FAPI-04 uptake is increased in fibrotic lung areas (white arrowhead), whereas there is no significant  $^{68}\text{Ga}$ -FAPI-04 accumulation in healthy nonfibrotic lung tissue (red arrowhead).

55 morphologically typical fibrotic lesions on CT and 3 lung cancer lesions yielded a considerably elevated uptake at each of the static imaging time points. The  $\text{SUV}_{\text{max}}$  and  $\text{SUV}_{\text{mean}}$  of fILD and the lung cancer lesions decreased over time, with a more pronounced decrease in fILD than in lung cancer lesions. Because of the decreasing background activity over time, the fILD manifestations demonstrated relatively stable target-to-background ratios, whereas the target-to-background ratios of the lung cancer manifestations tended to increase during the sequential PET examinations. These findings highlight the potential use of quantitative PET imaging at sequential time points to differentiate between malignant and fibrotic lesions. Röhrich et al. also evaluated the use of dynamic PET acquisitions. Although fILD lesions showed an early peak in tracer accumulation with a slowly decreasing signal intensity over time, lung cancer manifestations presented an increasing time-activity curve with a delayed peak and gradual washout. In contrast to the current imaging standard (HRCT, which is not capable of determining disease activity),  $^{18}\text{F}$ -FDG PET/CT is of limited use for the assessment of antifibrotic drugs (22). Röhrich et al. evaluated FAP expression using immunohistochemistry in both human fILD biopsies and whole-lung sections of Nedd4-22/2 mice, serving as a gold standard. FAP-positive areas were localized to the transition zone between healthy lung tissue and fibrotic areas in human fILD sections. In Nedd4-22/2 mice, healthy lung parenchyma demonstrated only low FAP expression, but fibrotic lesions exhibited FAP upregulation. These impressive results suggest a promising role for FAPI imaging in fibrotic lung diseases for evaluating disease activity and the response to antifibrotic treatment.

#### FAPI IMAGING IN CARDIOVASCULAR DISEASES

In cardiac disease, myocardial fibrosis contributes to the development and progression of heart failure. Myocardial fibroblast activation is essential for repair and regeneration after myocardial damage, such as from myocardial infarction or progressive heart failure. Several studies have described the molecular pathways leading to the activation of quiescent fibroblasts, which have emerged as attractive targets to support cardiac repair and prevent loss of function (23,24). Heart failure related to the development of fibrosis is among the most common adverse effects of modern cancer therapy, which includes radiotherapy, conventional chemotherapy, immunotherapy, and targeted therapy (25,26). In a retrospective study, Siebermair et al. analyzed the datasets of 32 patients who underwent  $^{68}\text{Ga}$ -FAPI-04 PET/CT for cancer staging (27). All examinations were analyzed visually and quantitatively with respect to cardiac uptake. Quantitative measurements were correlated with clinical covariates, including previous anticancer treatment, age, left ventricular ejection fraction (LVEF), coronary artery disease, and cardiovascular risk factors. Of the 32 patients, 6 (18.8%) demonstrated visually increased uptake clearly above the background level, and on quantitative analysis, this uptake was also significantly higher than in remote myocardium. No significant differences with respect to cancer entity and

applied chemotherapy and immunotherapy were observed. In contrast, a significant correlation of coronary artery disease, age, and LVEF with uptake could be demonstrated. The authors concluded that the measurement of myocardial fibroblast activation using  $^{68}\text{Ga}$ -FAPI-04 PET/CT might be useful for risk stratification regarding the early detection or progression of coronary artery disease and left ventricular remodeling.

In a larger cohort of 229 patients, Heckmann et al. retrospectively analyzed the correlation between myocardial uptake, cardiovascular risk factors, and metabolic disease in patients with metastatic cancer (28). The modeling cohort comprised 185 patients—and the confirmatory cohort 44 patients—who were analyzed by application of the American Heart Association 17-segment model of the left ventricle. Multivariate regression models revealed a significant correlation among left ventricular uptake, hypothyroidism, a body mass index above  $25 \text{ kg/m}^2$ , previous radiation to the chest, previous intake of platinum derivatives, and a history of diabetes mellitus. Interestingly, although a single cardiovascular risk factor led to a relatively mild increase in signal intensity, patients with multiple risk factors exhibited a more pronounced increase. FAPI uptake was most noticeable in patients with arterial hypertension and metabolic diseases, characterized by diabetes mellitus and obesity. These findings are also supported by animal data from diabetes mellitus models and transaortic constriction, which promote cardiac hypertrophy and excessive cardiac fibrosis (29,30). On the basis of their findings, Heckmann et al. concluded that high  $^{68}\text{Ga}$ -FAPI signal intensities are linked to cardiovascular risk factors, specifically arterial hypertension, diabetes mellitus, and obesity. They suggest further studies to systematically compare  $^{68}\text{Ga}$ -FAPI PET/CT scans with other cardiac imaging modalities and possibly gene expression profiles to pave the way to clinical practice.

In acute myocardial infarction, an immediate organized inflammatory immune reaction triggers the activation of fibroblasts (31,32). Activated myofibroblasts migrate to injured tissue and contribute to fibrotic scar formation, which preserves the wall architecture and prevents mechanical complications such as ventricular wall rupture. However, excessive fibrosis development is suggested to cause a progressive decline in ventricular systolic function, potentially leading to the development of chronic heart failure (33). Current imaging modalities such as MRI assess these structural changes primarily at a disease stage at which the damage has already occurred (34). Therefore, the assessment of local fibroblast activation suggesting structural remodeling after ischemia might be a promising approach to risk stratification. In a proof-of-concept study, Kessler et al. examined the pattern of  $^{68}\text{Ga}$ -FAPI-46 uptake in the myocardium of patients after acute myocardial infarction to investigate its association with the affected coronary artery and to correlate the  $^{68}\text{Ga}$ -FAPI-46 signal with biomarkers of myocardial damage, including parameters of left ventricular function (35). Ten patients who had undergone  $^{68}\text{Ga}$ -FAPI-46 PET/CT after percutaneous coronary intervention for risk stratification after acute myocardial infarction were retrospectively analyzed. Uptake patterns in polar maps and axial images were assessed according to the 17-segment model of the American Heart Association. To assess the level of agreement between the localized uptake and the myocardial areas supplied by the culprit vessel, a visual grading scale was established. Furthermore, myocardial uptake was quantified and the myocardial volume of FAPI accumulation was determined and correlated with biomarkers of myocardial damage, including left ventricular function. On visual interpretation, PET/CT demonstrated moderate-to-intense myocardial uptake in all 10 patients. The affected myocardium showed a partial or complete match between uptake and the confirmed culprit lesion by coronary angiography in 44% and

56% of patients, respectively. Quantitative evaluation revealed a strong correlation between the myocardial volume of  $^{68}\text{Ga}$ -FAPI-46 accumulation and the peak creatine kinase level but an inverse correlation between the myocardial volume of  $^{68}\text{Ga}$ -FAPI-46 accumulation and left ventricular function. On the basis of these results, the authors concluded that the PET-derived volume of myocardial fibroblast activation can truly reflect the extent of myocardial injury after acute myocardial infarction. In contrast to the signal derived from cardiac MRI (CMR), which usually persists for months to years after local damage, predominantly reflecting fibrotic remodeling,  $^{68}\text{Ga}$ -FAPI-46 PET/CT offers a functional modality to assess local damage with consecutive repair mechanisms within days of the ischemic event.

In a retrospective single-center study, Diekmann et al. tested the hypothesis that  $^{68}\text{Ga}$ -FAPI-46 PET/CT reflects a myocardial signal early after acute myocardial infarction that is distinct from CMR-derived tissue characteristics and predicts later development of ventricular dysfunction (36). Their analysis included 35 patients who had undergone clinical resting myocardial perfusion SPECT,  $^{68}\text{Ga}$ -FAPI-46 PET/CT, and CMR within 11 d after reperfusion therapy for acute myocardial infarction. Although the infarct size was determined from SPECT by comparison to a reference database, quantitative analysis of left ventricular tracer accumulation determined the extent of FAP upregulation. On the basis of late gadolinium enhancement derived from CMR, they found that the area of myocardial FAP upregulation was significantly larger than that of the SPECT perfusion defect or the infarct area. Interestingly, late gadolinium enhancement was detected in only 56% of FAP-positive segments, whereas an elevated T1 and T2 signal was visible in 74% and 68% of tracer-positive segments, respectively. Myocardial FAP volume correlated only weakly with simultaneously measured LVEF at baseline, whereas there was a significant inverse correlation with LVEF obtained at later follow-up. Altogether, the results of Diekmann et al. suggest that the area of elevated FAP signal extends beyond the injured infarct region and involves regions without prolonged T1 and T2 relaxation, which are CMR markers of interstitial fibrosis, infiltration, or edema. On the basis of their findings, the cell-based signal of fibroblast activation is distinct from CMR-derived interstitial characteristics and may be complementary. Early FAP signal was associated with a subsequent impairment of LVEF, suggesting that it might be a predictor of adverse left ventricular remodeling.

In a prospective study, Xie et al. explored the correlation of  $^{18}\text{F}$ -NOTA-FAPI PET/CT with CMR parameters in patients with ST-segment elevation myocardial infarction who underwent successful primary percutaneous coronary intervention (37). They further investigated the value of  $^{18}\text{F}$ -NOTA-FAPI imaging in predicting cardiac functional recovery, as well as the correlation of  $^{18}\text{F}$ -NOTA-FAPI activity with circulating FAP and inflammatory biomarkers. They prospectively recruited 14 patients with first-time ST-segment elevation myocardial infarction after primary percutaneous coronary intervention and 14 sex-matched healthy controls who had completed  $^{18}\text{F}$ -NOTA-FAPI PET/CT and blood sample collection. All patients underwent  $^{18}\text{F}$ -NOTA-FAPI PET/CT and CMR, whereas 10 patients underwent additional follow-up CMR. Myocardial  $^{18}\text{F}$ -NOTA-FAPI tracer accumulation was evaluated quantitatively for extent and intensity and correlated with myocardial injury biomarkers derived from CMR. Although no visible uptake was detected in healthy controls, localized but inhomogeneous myocardial  $^{18}\text{F}$ -NOTA-FAPI uptake was observed in all patients with ST-segment elevation myocardial infarction; this uptake was greater than in the edematous and infarcted myocardium. Myocardial  $^{18}\text{F}$ -NOTA-FAPI activity was

significantly associated with the myocardial biomarkers T2-weighted imaging, late gadolinium enhancement, and extracellular volume, at both per-patient and per-segment levels, but not with circulating FAP or inflammatory biomarkers. Furthermore, an inverse correlation was observed with the follow-up LVEF. To summarize these results,  $^{18}\text{F}$ -NOTA-FAPI imaging is feasible for assessing myocardial damage and has prognostic value for cardiac recovery after myocardial infarction. Further larger studies are warranted to evaluate the potential role of  $^{18}\text{F}$ -NOTA-FAPI PET/CT for the assessment of myocardial remodeling after myocardial infarction and to analyze fibroblast-targeted antifibrotic therapies.

Wu et al. retrospectively analyzed the use of  $^{68}\text{Ga}$ -FAPI-04 PET/CT for the in vivo imaging of FAP expression in human arterial walls (38). Their study included 41 patients who underwent  $^{68}\text{Ga}$ -FAPI-04 PET/CT either for suspected hepatic lesions or for IgG4-RD. Correlations were calculated of the uptake of  $^{68}\text{Ga}$ -FAPI-04 in large arterial walls with the degree of calcification derived from CT and cardiovascular risk factors. Focal arterial  $^{68}\text{Ga}$ -FAPI-04 uptake was detected in 1,177 arterial segments in all 41 patients. Analysis of all segments revealed a significant correlation between the extent of calcification and the intensity of uptake. Noncalcified arterial segments had significantly higher uptake than mildly calcified segments, whereas severely calcified segments exhibited the lowest uptake. Patients in the high-risk group, who had at least 4 cardiovascular risk factors, demonstrated significantly higher  $^{68}\text{Ga}$ -FAPI-04 uptake than the low-risk group. Xie et al. concluded that  $^{68}\text{Ga}$ -FAPI-04 PET/CT might have potential for imaging fibroblast activation in the arterial wall and thus might provide new insights into the pathologic mechanisms of arteriosclerosis.

Kupusovic et al. conducted a proof-of-concept study to assess  $^{68}\text{Ga}$ -FAPI uptake in the pulmonary vein region of the left atrium after pulmonary vein isolation with cryoballoon ablation and radiofrequency ablation as a surrogate for thermal damage (39). Twelve patients who had undergone  $^{68}\text{Ga}$ -FAPI PET after pulmonary vein isolation were included and compared with 5 patients without cardiac comorbidities who underwent  $^{68}\text{Ga}$ -FAPI PET for tumor staging. In 10 of the 12 patients, significant  $^{68}\text{Ga}$ -FAPI uptake was detected, whereas no uptake was observed in 2 patients or in any control patients. All postcryoballoon ablation patients had intense uptake, whereas in the radiofrequency ablation group, 2 patients had intense uptake, 1 patient had moderate uptake, and 2 patients had no uptake at all. Quantitative evaluation revealed significantly higher uptake in cryoballoon ablation patients than in radiofrequency ablation patients, suggesting that the cryoballoon ablation procedure causes a more pronounced fibroblast activation after tissue injury than does radiofrequency ablation. Future studies are warranted to assess whether this modality can contribute to a better understanding of the mechanisms of atrial fibrillation recurrence after pulmonary vein isolation.

Chen et al. explored the association of cardiac fibroblast activation with clinical and CMR parameters in patients with chronic thromboembolic pulmonary hypertension (CTEPH) (40). Thirteen CTEPH patients were prospectively enrolled and underwent  $^{68}\text{Ga}$ -FAPI-04 PET/CT, right heart catheterization, and echocardiography; 11 of these patients additionally underwent CMR. Another 13 subjects without any cardiac morbidities comprised a control group to establish the reference range of cardiac  $^{68}\text{Ga}$ -FAPI-04 uptake. Although there was no suspected cardiac  $^{68}\text{Ga}$ -FAPI-04 uptake in the control group, 10 CTEPH patients (77%) showed increased inhomogeneous  $^{68}\text{Ga}$ -FAPI-04 uptake in the right ventricle (RV), localized mainly in the free wall. Notably, increased

$^{68}\text{Ga}$ -FAPI-04 uptake was also observed in the right atrium of 11 CTEPH patients but was significantly lower than in the RV. A significant correlation between the RV  $^{68}\text{Ga}$ -FAPI-04 accumulation and the thickness of the RV wall was observed, whereas an inverse correlation was demonstrated with the RV fraction area change and the tricuspid annular plane systolic excursion (TAPSE) as indices of RV function. No significant correlation was found between PET and CMR parameters. On the basis of the correlation of both RV fraction area change and TAPSE with the increased  $^{68}\text{Ga}$ -FAPI-04 accumulation, the authors suggested that FAP activation reflects longitudinal and transversal contraction of the overloaded RV in CTEPH. This might be of further importance because change in RV fraction area and TAPSE are related to survival in pulmonary hypertension (41,42). Thus,  $^{68}\text{Ga}$ -FAPI-04 imaging may have the potential to be an effective means for assessing the outcome of CTEPH patients. The authors demonstrated that increased fibroblast activation reflects thickening of the RV wall and decreased RV contractile function. FAPI imaging might therefore be a promising approach toward assessing RV fibrosis in CTEPH patients and monitoring future tailored antifibrotic treatments.

Gu et al. prospectively enrolled 16 patients with pulmonary artery hypertension to investigate the feasibility of  $^{68}\text{Ga}$ -FAPI-04 PET/CT for assessing RV fibrotic remodeling and the relationship of  $^{68}\text{Ga}$ -FAPI-04 uptake with parameters of pulmonary hemodynamics and cardiac function (43). All patients underwent right heart catheterization and echocardiography for the assessment of pulmonary hemodynamics and cardiac function. Myocardial  $^{68}\text{Ga}$ -FAPI-04 uptake was assessed visually and quantitatively as  $\text{SUV}_{\text{max}}$ . Of the 16 patients, 12 (75%) exhibited heterogeneous signal in the RV free wall and insertion point. Patients with a TAPSE of less than 17 mm, who were considered the impaired RV function group, had significantly higher uptake than those with a TAPSE of 17 mm or more in both the RV free wall and the insertion point, indicating that RV uptake of  $^{68}\text{Ga}$ -FAPI-04 is associated with RV dysfunction. Furthermore, there was a significant positive correlation between cardiac  $^{68}\text{Ga}$ -FAPI-04 uptake and total pulmonary resistance and the level of N-terminal pro-B-type natriuretic peptide. Gu et al. concluded that  $^{68}\text{Ga}$ -FAPI-04 PET/CT is feasible for directly visualizing fibrotic remodeling of the RV in patients with pulmonary artery hypertension.

#### **FAPI IMAGING IN BENIGN LESIONS ENCOUNTERED IN ONCOLOGIC IMAGING**

Qin et al. retrospectively reviewed 129 PET/CT or  $^{68}\text{Ga}$ -DOTA-FAPI-04 PET/MRI scans to identify foci of elevated uptake in the bones and joints (44). All lesions were categorized as malignant or benign disease. Elevated uptake of  $^{68}\text{Ga}$ -DOTA-FAPI-04 in or around the bone or joint was found in 82 patients (63.6%). In total, 295 lesions were identified, including 94 malignant lesions (31.9%) and 201 benign lesions (68.1%). Although the malignant lesions were all classified as metastases, the benign lesions comprised osteofibrous dysplasia, degenerative bone disease, periodontitis, arthritis, and other inflammatory or trauma-related abnormalities. Quantitative analysis revealed significantly higher  $^{68}\text{Ga}$ -DOTA-FAPI-04 uptake in bone metastases than in benign lesions, although there was some overlap between the 2 entities. Differences in  $\text{SUV}_{\text{max}}$  among subgroups of benign diseases were statistically significant, with much higher uptake in periodontitis. In a subgroup of 29 patients who underwent both

$^{18}\text{F}$ -FDG and  $^{68}\text{Ga}$ -DOTA-FAPI-04 PET, significantly more lesions with higher uptake were identified by  $^{68}\text{Ga}$ -DOTA-FAPI-04 imaging. On the basis of these findings, the authors concluded that abnormal osseous  $^{68}\text{Ga}$ -DOTA-FAPI-04 uptake should be carefully assessed in patients with malignant tumors to avoid misdiagnosis due to overlap of uptake between benign and malignant bone lesions. Furthermore,  $^{68}\text{Ga}$ -DOTA-FAPI-04 PET also has the potential to locate and evaluate the extent of both malignant tumors and benign diseases in bones and joints.

Zheng et al. retrospectively reviewed 182 patients with various suspected cancers who underwent  $^{68}\text{Ga}$ -FAPI-04 PET/CT to characterize benign lesions showing increased  $^{68}\text{Ga}$ -FAPI-04 tracer accumulation (45). They detected 185 primary tumors and 360 benign lesions with uptake, including inflammatory processes, exostoses, hemorrhoids, fractures, and hepatic fibrosis. Lesions were diagnosed as benign on the basis of imaging findings, clinical information, or histologic biopsy. Quantitative analysis revealed a significantly higher  $\text{SUV}_{\text{max}}$  for malignant lesions than for benign lesions, but with a significant overlap between them. The authors concluded that some benign lesions can easily be diagnosed by a combination of CT findings, location, and clinical data but that some lesions still may be confused with malignant lesions or need further clarification.

### FAPI IMAGING IN RHEUMATOID ARTHRITIS

In a preclinical evaluation and pilot clinical study, Ge et al. evaluated the novel tracer  $^{18}\text{F}$ -AIF-NOTA-FAPI-04 for PET imaging of rheumatoid arthritis (46). In the inflamed joints of patients with rheumatoid arthritis, fibroblast-like synoviocytes are key effector cells that exacerbate the inflammatory destruction of adjacent articular cartilage and bone by producing matrix metalloproteinase enzymes and proinflammatory cytokines. FAP is highly expressed in rheumatoid arthritis-derived fibroblast-like synoviocytes and is a specific marker for disease activity. Ge et al. performed this pilot study to image activated fibroblast-like synoviocytes in vitro, in arthritic joints of mice with collagen-induced arthritis, and in 2 patients with rheumatoid arthritis. They found that the binding of  $^{18}\text{F}$ -AIF-NOTA-FAPI-04 increased significantly in activated fibroblast-like synoviocytes compared with controls. Compared with  $^{18}\text{F}$ -FDG imaging,  $^{18}\text{F}$ -AIF-NOTA-FAPI-04 showed high uptake in inflamed joints in the early stage of arthritis, and this uptake correlated positively with arthritis scores. Furthermore,  $^{18}\text{F}$ -AIF-NOTA-FAPI-04 PET/CT in 2 patients with rheumatoid arthritis revealed nonphysiologically high uptake in the synovium of arthritic joints. The authors concluded that  $^{18}\text{F}$ -AIF-NOTA-FAPI-04 is a promising radiotracer for imaging of rheumatoid arthritis and might potentially complement current noninvasive diagnostic parameters.

### FAPI IMAGING IN RENAL FIBROSIS

Kidney fibrosis leads to a progressive reduction in kidney function, ultimately resulting in kidney failure. To date, all diagnostic tools to detect kidney fibrosis have been invasive, requiring kidney biopsies with subsequent histologic validation. In a retrospective study, Conen et al. analyzed the PET data of 81 patients who received  $^{68}\text{Ga}$ -FAPI-04,  $^{68}\text{Ga}$ -FAPI-46,  $^{68}\text{Ga}$ -PSMA, or  $^{68}\text{Ga}$ -DOTATOC (47). Kidney function parameters were correlated with the  $\text{SUV}_{\text{max}}$  and  $\text{SUV}_{\text{mean}}$  of the renal parenchyma. The authors found a negative correlation between glomerular filtration rate and  $^{68}\text{Ga}$ -FAPI uptake for both  $\text{SUV}_{\text{max}}$  and  $\text{SUV}_{\text{mean}}$ , which was not the case for  $^{68}\text{Ga}$ -DOTATOC and  $^{68}\text{Ga}$ -PSMA. Conen et al. concluded that this correlation suggests

a specific binding of  $^{68}\text{Ga}$ -FAPI rather than a potential unspecific retention in the renal parenchyma, underlining the potential value of  $^{68}\text{Ga}$ -FAPI for the noninvasive quantitative evaluation of kidney fibrosis.

Zhou et al. evaluated the use of  $^{68}\text{Ga}$ -FAPI-04 PET/CT in 13 patients with histologically confirmed renal fibrosis (48). All patients underwent renal puncture before undergoing  $^{68}\text{Ga}$ -FAPI-04 PET/CT. The  $^{68}\text{Ga}$ -FAPI-04 examinations found that 12 of the 13 patients had increased uptake. Furthermore,  $\text{SUV}_{\text{max}}$  and target-to-background ratios correlated with the pathology of kidney tissue. The authors concluded that  $^{68}\text{Ga}$ -FAPI-04 PET/CT is a valuable tool to diagnose renal fibrosis without a biopsy.

### CONCLUSION

The development of FAPIs suitable for PET/CT has opened a new chapter in molecular imaging. Besides their successful use in oncologic diseases, several studies presented in this review suggest a potential role for FAPI imaging in immune-mediated inflammatory and fibrotic diseases, as well as cardiovascular diseases, and for distinguishing between benign and malignant lesions. However, current data rely predominantly on retrospective analyses, and evidence is still scarce for many possible indications. Well-defined patient cohorts and, ideally, prospective randomized trials are needed to include FAPI imaging in guidelines and to fully exploit the potential of this novel imaging technique.

### DISCLOSURE

No potential conflict of interest relevant to this article was reported.

### REFERENCES

1. Loktev A, Lindner T, Mier W, et al. A tumor-imaging method targeting cancer-associated fibroblasts. *J Nucl Med*. 2018;59:1423–1429.
2. Balkwill FR, Capasso M, Hagemann T. The tumor microenvironment at a glance. *J Cell Sci*. 2012;125:5591–5596.
3. Lindner T, Loktev A, Altmann A, et al. Development of quinoline-based theranostic ligands for the targeting of fibroblast activation protein. *J Nucl Med*. 2018;59:1415–1422.
4. Kratochwil C, Flechsig P, Lindner T, et al.  $^{68}\text{Ga}$ -FAPI PET/CT: tracer uptake in 28 different kinds of cancer. *J Nucl Med*. 2019;60:801–805.
5. Sollini M, Kirienco M, Gelardi F, Fiz F, Gozzi N, Chiti A. State-of-the-art of FAPI-PET imaging: a systematic review and meta-analysis. *Eur J Nucl Med Mol Imaging*. 2021;48:4396–4414.
6. Kuwert T, Schmidkonz C, Prante O, Schett G, Ramming A. FAPI-PET opens a new window for understanding of immune-mediated inflammatory diseases. *J Nucl Med*. 2022;63:1136–1137.
7. Schmidkonz C. Perspective on fibroblast activation protein-specific PET/CT in fibrotic interstitial lung diseases: imaging fibrosis—a new paradigm for molecular imaging? *J Nucl Med*. 2022;63:125–126.
8. Calais J. FAP: the next billion dollar nuclear theranostics target? *J Nucl Med*. 2020;61:163–165.
9. Ferdinandus J, Costa PF, Kessler L, et al. Initial clinical experience with  $^{90}\text{Y}$ -FAPI-46 radioligand therapy for advanced-stage solid tumors: a case series of 9 patients. *J Nucl Med*. 2022;63:727–734.
10. Croft AP, Campos J, Jansen K, et al. Distinct fibroblast subsets drive inflammation and damage in arthritis. *Nature*. 2019;570:246–251.
11. Gurtner GC, Werner S, Barrandon Y, Longaker MT. Wound repair and regeneration. *Nature*. 2008;453:314–321.
12. Schmidkonz C, Rauber S, Atzinger A, et al. Disentangling inflammatory from fibrotic disease activity by fibroblast activation protein imaging. *Ann Rheum Dis*. 2020;79:1485–1491.
13. Stone JH, Zen Y, Deshpande V. IgG4-related disease. *N Engl J Med*. 2012;366:539–551.

14. Della-Torre E, Feeney E, Deshpande V, et al. B-cell depletion attenuates serological biomarkers of fibrosis and myofibroblast activation in IgG4-related disease. *Ann Rheum Dis*. 2015;74:2236–2243.
15. Zhang W, Stone J. Management of IgG4-related disease. *Lancet Rheumatol*. 2019;1:E55–E65.
16. Wohlfahrt T, Rauber S, Uebe S, et al. PU.1 controls fibroblast polarization and tissue fibrosis. *Nature*. 2019;566:344–349.
17. Luo Y, Pan Q, Yang H, Peng L, Zhang W, Li F. Fibroblast activation protein–targeted PET/CT with <sup>68</sup>Ga-FAPI for imaging IgG4-related disease: comparison to <sup>18</sup>F-FDG PET/CT. *J Nucl Med*. 2021;62:266–271.
18. Distler O, Assassi S, Cottin V, et al. Predictors of progression in systemic sclerosis patients with interstitial lung disease. *Eur Respir J*. 2020;55:1902026.
19. Tyndall AJ, Bannert B, Vonk M, et al. Causes and risk factors for death in systemic sclerosis: a study from the EULAR Scleroderma Trials and Research (EUSTAR) Database. *Ann Rheum Dis*. 2010;69:1809–1815.
20. Bergmann C, Distler JH, Treutlein C, et al. <sup>68</sup>Ga-FAPI-04 PET-CT for molecular assessment of fibroblast activation and risk evaluation in systemic sclerosis-associated interstitial lung disease: a single-centre, pilot study. *Lancet Rheumatol*. 2021;3:e185–e194.
21. Röhrich M, Leitz D, Glatting FM, et al. Fibroblast activation protein–specific PET/CT imaging in fibrotic interstitial lung diseases and lung cancer: a translational exploratory study. *J Nucl Med*. 2022;63:127–133.
22. Bondue B, Castiaux A, Van Simaey G, et al. Absence of early metabolic response assessed by <sup>18</sup>F-FDG PET/CT after initiation of antifibrotic drugs in IPF patients. *Respir Res*. 2019;20:10.
23. Travers JG, Kamal FA, Robbins J, Yutzey KE, Blaxall BC. Cardiac fibrosis: the fibroblast awakens. *Circ Res*. 2016;118:1021–1040.
24. Aghajanian H, Kimura T, Rurik JG, et al. Targeting cardiac fibrosis with engineered T cells. *Nature*. 2019;573:430–433.
25. Haslbauer JD, Lindner S, Valbuena-Lopez S, et al. CMR imaging biosignature of cardiac involvement due to cancer-related treatment by T1 and T2 mapping. *Int J Cardiol*. 2019;275:179–186.
26. Totzeck M, Schuler M, Stuschke M, Heusch G, Rassaf T. Cardio-oncology: strategies for management of cancer-therapy related cardiovascular disease. *Int J Cardiol*. 2019;280:163–175.
27. Siebermair J, Köhler M, Kupusovic J, et al. Cardiac fibroblast activation detected by Ga-68 FAPI PET imaging as a potential novel biomarker of cardiac injury/remodeling. *J Nucl Cardiol*. 2021;28:812–821.
28. Heckmann MB, Reinhardt F, Finke D, et al. Relationship between cardiac fibroblast activation protein activity by positron emission tomography and cardiovascular disease. *Circ Cardiovasc Imaging*. 2020;13:e010628.
29. Cavalera M, Wang J, Frangogiannis NG. Obesity, metabolic dysfunction, and cardiac fibrosis: pathophysiological pathways, molecular mechanisms, and therapeutic opportunities. *Transl Res*. 2014;164:323–335.
30. Müller OJ, Heckmann MB, Ding L, et al. Comprehensive plasma and tissue profiling reveals systemic metabolic alterations in cardiac hypertrophy and failure. *Cardiovasc Res*. 2019;115:1296–1305.
31. Prabhu SD, Frangogiannis NG. The biological basis for cardiac repair after myocardial infarction: from inflammation to fibrosis. *Circ Res*. 2016;119:91–112.
32. Lafuse WP, Wozniak DJ, Rajaram MV. Role of cardiac macrophages on cardiac inflammation, fibrosis and tissue repair. *Cells*. 2020;10:51.
33. Sutton MGSJ, Sharpe N. Left ventricular remodeling after myocardial infarction: pathophysiology and therapy. *Circulation*. 2000;101:2981–2988.
34. Öm S, Manhenke C, Anand IS, et al. Effect of left ventricular scar size, location, and transmural on left ventricular remodeling with healed myocardial infarction. *Am J Cardiol*. 2007;99:1109–1114.
35. Kessler L, Kupusovic J, Ferdinandus J, et al. Visualization of fibroblast activation after myocardial infarction using <sup>68</sup>Ga-FAPI PET. *Clin Nucl Med*. 2021;46:807–813.
36. Diekmann J, Koenig T, Thackeray JT, et al. Cardiac fibroblast activation in patients early after acute myocardial infarction: integration with magnetic resonance tissue characterization and subsequent functional outcome. *J Nucl Med*. 2022;63:1415–1423.
37. Xie B, Wang J, Xi X-Y, et al. Fibroblast activation protein imaging in reperfused ST-elevation myocardial infarction: comparison with cardiac magnetic resonance imaging. *Eur J Nucl Med Mol Imaging*. 2022;49:2786–2797.
38. Wu M, Ning J, Li J, et al. Feasibility of in vivo imaging of fibroblast activation protein in human arterial walls. *J Nucl Med*. 2022;63:948–951.
39. Kupusovic J, Kessler L, Nekolla SG, et al. Visualization of thermal damage using <sup>68</sup>Ga-FAPI-PET/CT after pulmonary vein isolation. *Eur J Nucl Med Mol Imaging*. 2022;49:1553–1559.
40. Chen B-X, Xing H-Q, Gong J-N, et al. Imaging of cardiac fibroblast activation in patients with chronic thromboembolic pulmonary hypertension. *Eur J Nucl Med Mol Imaging*. 2022;49:1211–1222.
41. Mauritz G-J, Kind T, Marcus JT, et al. Progressive changes in right ventricular geometric shortening and long-term survival in pulmonary arterial hypertension. *Chest*. 2012;141:935–943.
42. Forfia PR, Fisher MR, Mathai SC, et al. Tricuspid annular displacement predicts survival in pulmonary hypertension. *Am J Respir Crit Care Med*. 2006;174:1034–1041.
43. Gu Y, Han K, Zhang Z, et al. <sup>68</sup>Ga-FAPI PET/CT for molecular assessment of fibroblast activation in right heart in pulmonary arterial hypertension: a single-centre, pilot study. *J Nucl Cardiol*. March 23, 2022 [Epub ahead of print].
44. Qin C, Song Y, Liu X, et al. Increased uptake of <sup>68</sup>Ga-DOTA-FAPI-04 in bones and joints: metastases and beyond. *Eur J Nucl Med Mol Imaging*. 2022;49:709–720.
45. Zheng S, Lin R, Chen S, et al. Characterization of the benign lesions with increased <sup>68</sup>Ga-FAPI-04 uptake in PET/CT. *Ann Nucl Med*. 2021;35:1312–1320.
46. Ge L, Fu Z, Wei Y, et al. Preclinical evaluation and pilot clinical study of <sup>18</sup>F-AIF-NOTA-FAPI-04 for PET imaging of rheumatoid arthritis. *Eur J Nucl Med Mol Imaging*. 2022;49:4025–4036.
47. Conen P, Pennetta F, Dendl K, et al. <sup>68</sup>Ga-FAPI uptake correlates with the state of chronic kidney disease. *Eur J Nucl Med Mol Imaging*. 2022;49:3365–3372.
48. Zhou Y, Yang X, Liu H, et al. Value of Ga-FAPI-04 imaging in the diagnosis of renal fibrosis. *Eur J Nucl Med Mol Imaging*. 2021;48:3493–3501.

# From Concept to Regulatory Drug Approval: Lessons for Theranostics

Marlon Perera<sup>1</sup> and Michael J. Morris<sup>2</sup>

<sup>1</sup>*Urology Service, Department of Surgery, Memorial Sloan Kettering Cancer Center, New York, New York; and* <sup>2</sup>*Genitourinary Oncology Service, Department of Medicine, Memorial Sloan Kettering Cancer Center, New York, New York*

**Learning Objectives:** On successful completion of this activity, participants should be able to (1) describe an overview of the FDA approval process, including data required for FDA application; (2) consider the difficulties and hurdles of FDA approval for therapies relating to prostate cancer and radiopharmaceuticals; and (3) recognize that despite these difficulties, recent FDA approval of radiopharmaceuticals in prostate cancer has occurred, specifically for <sup>223</sup>Ra and <sup>177</sup>Lu-PSMA-617.

**Financial Disclosure:** Dr. Morris is a consultant paid less than \$5,000 for the National Comprehensive Cancer Network and an investigator for accelerator applications for Johnson & Johnson and Novartis. This work was supported by the Sidney Kimmel Center for Prostate and Urologic Cancers at MSK and an NIH/NCI Cancer Center support grant to Memorial Sloan Kettering Cancer Center (P30 CA008748). Dr. Perera is sponsored by the Australian–American Fulbright Commission administered through a 2021–2022 Fulbright Future Scholarship funded by the Kinghorn Foundation. The authors of this article have indicated no other relevant relationships that could be perceived as a real or apparent conflict of interest.

**CME Credit:** SNMMI is accredited by the Accreditation Council for Continuing Medical Education (ACCME) to sponsor continuing education for physicians. SNMMI designates each *JNM* continuing education article for a maximum of 2.0 AMA PRA Category 1 Credits. Physicians should claim only credit commensurate with the extent of their participation in the activity. For CE credit, SAM, and other credit types, participants can access this activity through the SNMMI website (<http://www.snmmilearningcenter.org>) through December 2025.

Radiopharmaceutical therapy is an emerging treatment modality that has demonstrated increasing importance as a significant component in the treatment of cancer. Prostate cancer (PCa) remains one of the commonest solid-organ tumors and is associated with significant societal burdens. Despite significant disease heterogeneity, PCa remains an ideal candidate for radiopharmaceutical therapy because of the prolonged disease course, metastatic disease tropism, and sensitivity to radiation therapy. To date, advanced PCa remains one of the most successful arenas for the development and approval of radiopharmaceutical agents. In this review, we aim to summarize the complex processes required to obtain regulatory approval for a novel agent and highlight the limitations and hurdles specific to the approval of radiopharmaceutical agents. In advanced PCa, we outline the importance of a framework for trial design with respect to defining disease state and acceptable outcome measures—as recommended by the Prostate Cancer Clinical Trials Working Group (PCWG). Finally, using the principles mandated by the Food and Drug Administration approval process and the framework provided by the PCWG, we outline experience with the successful approval of the radiopharmaceutical agents <sup>223</sup>Ra and <sup>177</sup>Lu-PSMA-617.

**Key Words:** theranostics; PSMA; FDA; drug approval; radium, lutetium

**J Nucl Med 2022; 63:1793–1801**

DOI: 10.2967/jnumed.121.263301

**B**roadly speaking, radiopharmaceutical therapy is defined by delivery of radioactive agents to tumor-associated targets (1). Radiopharmaceutical agents comprise both a targeting ligand and a

radioactive payload. The targeting ligand facilitates delivery of the therapeutic radionuclide to the tumor microenvironment or directly to the tumor cells. The payload in radiopharmaceuticals is a radioactive nuclide, primarily either  $\alpha$ - or  $\beta$ -emitting. Exceptions to this simplistic structural overview of radiopharmaceuticals exist, such as <sup>131</sup>I and <sup>223</sup>Ra, for which the chemical properties of the compound act to both target and emit therapeutic radiation.

Cellular injury occurs as a result of emitted  $\alpha$ - or  $\beta$ -particles via radiation-induced DNA damage (2).  $\beta$ -particle emitters, such as <sup>177</sup>Lu, <sup>90</sup>Y, and <sup>131</sup>I, provide short-range emissions (0.5 to >10 mm) and produce significant cellular injury to nearby cells (3).  $\alpha$ -particle emitters, such as <sup>212</sup>Bi and <sup>223</sup>Ra, produce emissions that travel shorter distances than  $\beta$ -emitters but provide more energy deposition per unit length, resulting in an increased potency and thus frequently causing irreparable DNA damage (4). Unlike traditional radiotherapy approaches, radiopharmaceuticals are typically delivered systemically, which allows the potential for radioactivity exposure to disseminated metastatic disease (1). Further, the ability to target tumor-associated matter allows the radioactivity to be exposed with increasing specificity, preserving physiologic tissue. These tissues targeted by radiopharmaceuticals are typically either malignant cells or cells within the tumor microenvironment, such as osteoclasts and osteoblasts in <sup>223</sup>Ra (5). Some radiopharmaceutical agents may accumulate or concentrate in physiologic regions, such as the renal cortex or salivary glands (6); specific morbidity may occur in these organs as a result of radioactivity exposure.

The role of radiopharmaceuticals in oncology is rapidly expanding. A dramatic increase in the number of radiopharmaceuticals approved by the U.S. Food and Drug Administration (FDA) has occurred since 2009, due in part to the release of clear guidelines for FDA approval of radiopharmaceuticals (7). The positive public perception and popularity of radiopharmaceuticals may be attributed to positive trial outcomes that demonstrated improvements in the way patients feel, function, and survive. Additionally, the availability of companion diagnostic imaging with radiopharmaceuticals and visualization and estimation of radiopharmaceutical

Received Jun. 17, 2022; revision accepted Nov. 3, 2022.  
For correspondence or reprints, contact Michael J. Morris ([morrism@mskcc.org](mailto:morris@mskcc.org)).  
COPYRIGHT © 2022 by the Society of Nuclear Medicine and Molecular Imaging.

biodistribution and response provides an attractive feature for patients and clinicians (8). For example, companion imaging for  $^{223}\text{Ra}$ -dichloride is  $^{99\text{Tc}}$ -bisphosphonate bone scanning, and for  $^{177}\text{Lu}$ -PSMA-617, companion imaging is  $^{68}\text{Ga}$ -PSMA-11 or  $^{18}\text{F}$ -PSMA-DCFPyl PET. From a financial perspective, large pharmaceutical firms are increasingly investing in such technologies (9). Market projections for prostate cancer (PCa) therapies suggest that annual sales of prostate-specific membrane antigen (PSMA)-targeted radiopharmaceuticals could exceed \$1.1 billion (10).

Bringing any drug to market requires time, strategy, financial resources, data, and adherence to regulatory guidance. It is an intrinsically complex process, and most drugs in clinical trials will not achieve this goal. In this review, we highlight PCa as a case study in bringing radiopharmaceuticals to FDA approval. PCa is among the common malignancies in the developed world and is responsible for considerable public burden in contemporary clinical practice. PCa has a widely heterogeneous disease course, with a proportion of patients progressing to advanced, disseminated disease. Patients are generally elderly, with diverse comorbidities and medical risks. The disease is bone-tropic, and anticancer responses are therefore difficult to assess as endpoints in early clinical trials. Despite these challenges, significant advances in therapeutic strategies that leverage the biology of the disease, and clinically qualifying interim endpoints in clinical trials, have resulted in new tools exerting long-term disease control even in the metastatic state. These treatments for metastatic disease include chemotherapy (11,12) and therapies that target the androgen receptor (13) and DNA repair (14). These principles, in addition to the radiosensitivity of PCa, make PCa an ideal disease to assess radiopharmaceutical therapy. Recently 2 radiopharmaceuticals have been approved for PCa, making it one of the most successful arenas for developing radiopharmaceuticals.

Given that the role of these agents is projected to expand, it is imperative that clinicians and investigators, particularly those involved in nuclear medicine, are aware of the pathways and hurdles required to obtain FDA approval for novel radiopharmaceuticals. The current review aims to provide an educational overview of the process for acquiring FDA approval for a novel radiopharmaceutical for PCa. We highlight the potential barriers and pitfalls to this process and outline several cases of successful approval of agents for advanced PCa.

## OVERVIEW OF THE FDA APPROVAL PROCESS

In the United States, regulation of the development, production, and sale of novel pharmaceuticals and devices, including radiopharmaceuticals, is governed by the FDA. After the federal Food, Drug, and Cosmetics Act of 1938 (15), all drugs in the United States required approval for safety by the FDA. Multiple subsequent iterations in 1962 and 1976 broadened the regulation to include devices; further, approval required demonstration of efficacy in addition to safety (16). Over the past decades, the approval process has become increasingly complex; presently, the FDA approval process is among the most comprehensive and stringent regulatory processes worldwide (Fig. 1). Although such complex processes ensure public safety, the current timeline from initial conception of molecular agents to regulatory approval by the FDA may take up to 10–15 y and cost up to billions of dollars (17).

### IND Application

Although the conceptualization and preclinical phases of pharmaceutical agents are not covered in the scope of this review, these

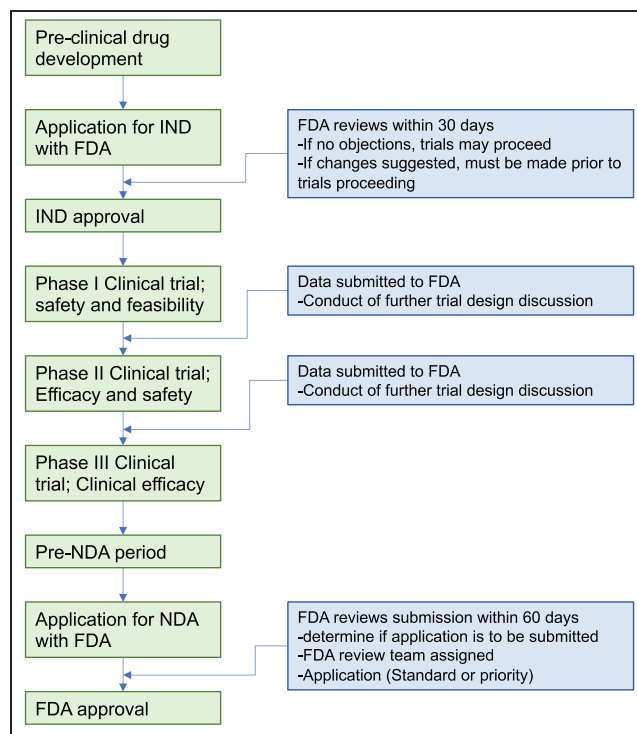


FIGURE 1. Overview of FDA process for new drug approval (19).

stages are fundamental in the progression to clinical-stage trials and subsequent FDA approval. When the intended agent is ready to progress to human clinical trials, initial contact with the FDA should be sought. At this time, the drug's sponsor applies for a commercial investigational-new-drug (IND) application with the FDA. IND applications to the FDA require disclosure of available preclinical data and human data, manufacturing information, and the protocols of the intended studies (18). The preclinical and human data relevant for the IND application may include pharmacologic profile, toxicity, and efficacy data for the respective disease process. Manufacturing information may include composition profile, manufacturer methodology and controls, and compound stability.

### Clinical Trials

As part of IND approval, ideally an early-stage trial design is submitted, with the objective of achieving the specific goals required for FDA approval—demonstration of safety and efficacy. Defining efficacy is imperative, as FDA applications will be rejected because of “a lack of substantial evidence that the drug will have the effect it purports or is represented to have” (15). Broadly speaking, efficacy may be established if the drug or device provides a positive and clinically meaningful effect on how an individual feels, functions, or survives (19). Feel and function may be measured by patient-reported outcomes, clinically reported outcomes, observer-reported outcomes, performance outcomes, or biomarker data. Data relevant to these questions are acquired by methodically designed and conducted phase I, II, and III trials. After each trial is completed, data are submitted to the FDA before subsequent trial phases proceed.

Phase I trials are typically low-volume studies on healthy individuals, aimed to evaluate treatment safety, acceptable dosing strategies, and adverse effects (20). However, completion of phase I trials in the realm of radiopharmaceuticals is not mandatory, and a

phase II dose might be advanced despite the absence of a formal phase I study (21). For example, <sup>177</sup>Lu-PSMA-617 did not complete formal phase I trials before progressing to phase II trials. This was possible because of the publication of safety and tolerability in the form of retrospective series from international centers where regulations for novel radiopharmaceuticals are less restrictive (22).

Phase II trials are moderate-sized trials on individuals with the target disease and aim to determine efficacy and provide additional safety data. Phase III trials are large trials to discern treatment efficacy, monitor adverse effects, and compare with current treatment regimens. Historically, 2 adequate and well-controlled clinical studies that are designed “to distinguish the effect of a drug from the other influences, such as spontaneous change, placebo effect or biased observation” are required for FDA approval (23). However, the FDA Modernization Act in 1997 provided flexibility so that based on relevant science, data from a single well-controlled clinical investigation and confirmatory evidence are sufficient to establish efficacy.

#### **New-Drug Application (NDA)**

After completion of the phase III trials, an NDA may be submitted to the FDA. The NDA application requires all data pertaining to the drug, including manufacturing, quality control, chemical properties (formula, pharmacokinetics), indications, and data obtained from the phase I, II, and III clinical trials. Expedited reviews may be requested at an early point in the regulatory process and include “fast track,” “breakthrough therapy,” or “accelerated approval” (24).

#### **ISSUES WITH DEVELOPMENT OF RADIOPHARMACEUTICALS**

Despite the well-defined FDA approval process via IND and NDA applications, several specific challenges exist in fostering the progression of novel radiopharmaceuticals (25). Logistically, development of radiopharmaceuticals is complex because of the broad, multidisciplinary approach required to recruit and treat patients. Specifically, the target population of patients intended for treatment with radiopharmaceuticals is those with disseminated disease, often managed by medical oncologists. However, radiopharmaceuticals and other radioactive therapies are typically administered and managed by clinicians in the nuclear medicine and radiology fields.

Radiopharmaceutical use can be more complex than systemic therapies such as immunotherapy or cytotoxic chemotherapeutic agents. Within the United States, the Nuclear Regulatory Commission maintains stringent training and education requirements for physicians to be authorized users of radiopharmaceuticals for medical purposes. The formulation location of the radiopharmaceutical compound must be considered, keeping in mind that many agents will have a limited half-life that requires timely administration. Such formulation, dispensing, and disposal of radiopharmaceuticals require specific expertise by radiochemists or radiopharmacists, of whom there is a recognized shortage (26). Radiation safety before, during, and after treatment must be considered, as well as the availability of qualified personnel to ensure staff, patient, and caregiver safety. Associated set-up costs for radiopharmaceuticals and associated imaging are considerable (27).

Finally, as with all novel treatments, production of scientific data is critical in development and eventual clinical application. Development of such agents requires motivated investigators because of the regulatory and logistic barriers and the significant periods from benchtop preclinical research to clinical trials. In some regions of

the world, there may be limited regulatory oversight of drugs, and the resulting ease of clinical access for new treatments provides no impetus to perform clinical trials and contribute data to the medical literature.

#### **ISSUES WITH DRUG APPROVALS IN PCa**

PCa treatment options have expanded, with increasing complexity in various stages of PCa. Given the variety of therapeutic approaches and lengths of treatment, the risk a patient faces at a certain time point varies widely. For example, in metastatic PCa, patients are typically treated with a combination of androgen deprivation therapy, androgen receptor inhibitors, or cytotoxic chemotherapy (docetaxel) (11). Accordingly, a patient’s risk may vary on the basis of prior therapies or non-disease-related factors, such as risk of death from competing causes. For example, after extended periods of androgen deprivation therapy with or without androgen receptor inhibitors or chemotherapy, PCa progression in the setting of continued castration denotes castration-resistant PCa (CRPC) (28). Contextualizing the various disease settings of metastatic PCa is critical in exploring the role of various novel radiopharmaceuticals under investigation or development.

Development of novel radiopharmaceuticals in PCa poses specific issues relevant to the FDA approval process. For several reasons, there are barriers for novel agents proposing to improve survival outcomes in PCa. PCa is a heterogeneous disease that may compromise survival in some patients but demonstrate a more indolent course in others. Further, PCa patients are an older population, typically with comorbidities that may compete with PCa. Additionally, the propensity for bone metastatic deposits is problematic, given the difficulty in determining treatment response based on RECIST or other standard response criteria. PCa also lacks a biomarker that is accepted by the FDA as an indicator of clinical benefit. Neither prostate-specific membrane antigen (PSMA) nor any other serum biomarker has been shown to be a surrogate for clinical benefit; neither of these is recognized by regulatory agencies as being clinically qualified as an endpoint for drug approval (29,30). Finally, long PCa survival times and the lack of an accepted intermediate endpoint lead to trial designs requiring prolonged periods of follow-up (29).

To assist in providing consensus and meeting these clinical trial design challenges, the Prostate Cancer Clinical Trials Working Group (PCWG) initially issued recommendations to standardize outcomes in metastatic PCa trials. The PCWG provides a framework to organize clinical trial design by prior treatments, disease distribution and extent, risk of death from PCa or competing causes, and primary outcome measures. The first iteration of these recommendations, PCWG1, was published in 1999 and outlined recommendations for phase II clinical trials on CRPC (31). Two subsequent iterations have been published to broaden the recommendations for clinical trials in PCa: PCWG2 in 2008 (29) and PCWG3 in 2016 (32). PCWG2 and PCWG3 furnished a framework for regulatory drug approval that outlined the clinical course of PCa in a series of clinical states. They also provided recommendations on standardized eligibility criteria, assessment intervals, and endpoints for clinical trials.

Given the prolonged nature of overall survival and the lack of measurable disease in bone, PCWG2 and PCWG3 noted the need for an intermediate-progression endpoint, rather than a treatment-response surrogate endpoint. Accordingly, radiographic progression-free survival (rPFS) was identified in PCWG2 and PCWG3

as a potential surrogate for overall survival. Clear, objective definitions for rPFS were proposed in PCWG2, denoted by the “2 + 2” rule: at least 2 new lesions on the first posttreatment scan with at least 2 additional lesions on the next scan. After the flare period, progression was defined as 2 new lesions relative to the first post-treatment scan, confirmed on a subsequent scan. Use of the 2 + 2 rule is beneficial as it does not require specialized software, it is generalizable, it is not time-consuming, and only 2 lesions are required to be counted. Additionally, this definition compensates for posttreatment flare that may be observed in bone scintigraphy (33). rPFS was subsequently credentialed in several trials, including the COUGAR-302 and PREVAIL trials (13). rPFS was shown to be closely associated with overall survival, with an estimated correlation coefficient of 0.72 (13,34).

#### **PATHWAYS TO APPROVAL FOR <sup>223</sup>RA-DICHLORIDE AND <sup>177</sup>LU-PSMA-617**

Despite the barriers to FDA approval of radiopharmaceuticals, there have been several recent success stories. Early radiopharmaceutical approval was successfully obtained for palliation of painful bone metastases via <sup>89</sup>Sr-chloride (35) and <sup>153</sup>Sm-ethylenediamine tetra(methylene phosphonic acid) (36). Unlike these older bone-seeking radiopharmaceuticals that were tested in studies designed to demonstrate relief of pain, the more recent radiopharmaceuticals <sup>223</sup>Ra and <sup>177</sup>Lu-PSMA617 achieved FDA approval in advanced PCa on the basis of prolonging overall survival. As outlined below, approval of these agents was achieved by adherence to the principles outlined in the PCWG framework and compliance with FDA regulatory requirements.

#### **<sup>223</sup>Ra**

<sup>223</sup>Ra is an  $\alpha$ -emitting radionuclide, and the radiopharmaceutical <sup>223</sup>Ra-dichloride is used to treat skeletal metastases and is in commercial use under the trade name Xofigo (Bayer). PCa bone metastases are characterized by dysregulated bone metabolism, are mediated by tumor-associated growth factors, and result in an abundance of new disorganized bone formation (37). <sup>223</sup>Ra is an earth alkali metal that is substituted for calcium in hydroxyapatite within areas of osteoblast-mediated new bone formation (38). Accordingly, for PCa, <sup>223</sup>Ra targets the bone microenvironment rather than metastatic tumor cells themselves. The resulting local  $\alpha$ -emission causes DNA double-strand breaks in adjacent tumor cells and in osteoblasts and osteoclasts (39). This mode of targeting and cell injury is advantageous because the treatment effect is directed to a metastatic disease compartment rather than cell-by-cell.

<sup>223</sup>Ra-dichloride was among the first radiopharmaceuticals achieving FDA approval in May 2013 for advanced PCa on the basis of prolonging overall survival (40). Data used to support the IND and NDA applications originated from early phase I and II trials. Phase I trials assessed 15 patients with PCa and bone metastases who received increasing doses of <sup>223</sup>Ra-dichloride, starting at 46 kBq/kg and then increasing to 93, 163, 213, and 250 kBq/kg (41). With this, safety and tolerability were demonstrated, although dose-limiting toxicity and maximal tolerated dose were not formally identified. Encouragingly, most patients reported pain palliation by 8 wk; on the basis of these promising results, subsequent trials proceeded. Phase II trials on patients with CRPC and bone metastases demonstrated acceptable safety and tolerability (42). Nilsson et al. (42) enrolled 64 patients to receive either <sup>223</sup>Ra-dichloride (50 kBq/kg every 4 wk) or placebo, with a primary endpoint of total alkaline

phosphatase and time to skeleton-related events. This trial reported a significant response to alkaline phosphatase ( $-65.6\%$  vs.  $9.3\%$ ,  $P < 0.0001$ ) and delayed skeleton-related events (hazard ratio [HR], 1.75; 95% CI, 0.96–3.19;  $P = 0.065$ ) in the <sup>223</sup>Ra-dichloride group. A difference in overall survival was also reported in the <sup>223</sup>Ra-dichloride group (HR, 2.12; 95% CI, 1.13–3.98;  $P = 0.020$ ).

Efficacy was further demonstrated in the subsequent phase III ALSYMPCA trial (43), which recruited 922 metastatic PCa patients with 2 or more bone metastases on skeletal scintigraphy and no evidence of visceral metastases. Patients were randomized 2:1 to receive the standard of care either with or without <sup>223</sup>Ra-dichloride (at a dose of 50 kBq/kg of body weight). The primary endpoint was overall survival, powered to detect an HR of 0.76 for the risk of death in the <sup>223</sup>Ra group. At a preplanned interim analysis, the trial reached its primary endpoint, with patients who received <sup>223</sup>Ra-dichloride demonstrating an improved overall survival (14.0 vs. 11.2 mo in the placebo arm; HR, 0.699;  $P = 0.002$ ). Secondary outcomes were observed, including a reduction in alkaline phosphatase ( $P < 0.001$ ), a delayed time to an increase in alkaline phosphatase (6.4 vs. 3.8 mo; HR, 0.17;  $P < 0.001$ ), and a delayed time to an increase in prostate-specific antigen (PSA) (3.6 vs. 3.4 mo; HR, 0.64;  $P < 0.001$ ) in the <sup>223</sup>Ra-dichloride group. Patients in the <sup>223</sup>Ra-dichloride group also demonstrated a prolonged time to the first symptomatic skeletal event (15.6 vs. 9.8 mo; HR, 0.66;  $P < 0.001$ ). However, no imaging-based outcome measures were used in the ALSYMPCA design. After the interim analysis, the trial was stopped early and FDA approval was granted after a priority review due to unmet medical need and successful achievement of the primary endpoints (44). Despite the success of the ALSYMPCA trial, trial design limitations existed. The absence of radiologic outcomes or monitoring during the trial resulted in a paucity of data highlighting metastatic bone disease during treatment with <sup>223</sup>Ra. Moreover, the trial design did not allow for collation of data on asymptomatic pathologic fractures.

A postapproval modification to the use of <sup>223</sup>Ra-dichloride was released by the European Medicines Agency, based on the results of the ERA 223 trial (45). ERA 223 randomized 806 patients to abiraterone acetate (1,000 mg daily) plus prednisolone with or without <sup>223</sup>Ra-dichloride (55 kBq/kg once every 4 wk) versus placebo. Eligible men had chemotherapy-naïve CRPC with bone metastases, and the primary endpoint was symptomatic skeletal event-free survival. The study was unmasked prematurely after more fractures and deaths were noted in the <sup>223</sup>Ra group; patients died on average 2.6 mo earlier than in the placebo group and demonstrated a higher rate of fractures (29% vs. 11%). Accordingly, the European Medicines Agency recommended that <sup>223</sup>Ra be restricted to patients who had 2 previous treatments for PCa and that <sup>223</sup>Ra not be used with abiraterone acetate plus prednisolone (46). A comparable trial called the PEACE III trial, aimed to assess an alternative novel antiandrogen, enzalutamide, with and without <sup>223</sup>Ra, was performed (47). Given the outcomes of the ERA 223 trial, the PEACE III trial mandated the use of bone-modifying agents such as denosumab or zoledronic acid, which resulted in reduced fracture rates (47).

#### **<sup>177</sup>Lu-PSMA-617**

More recently, <sup>177</sup>Lu PSMA-617 (Pluvicto, Novartis) achieved FDA approval after a priority review for metastatic CRPC (48). <sup>177</sup>Lu-PSMA-617 is a  $\beta$ -particle emitter, targeting PSMA-positive cells and the associated tumor microenvironment (49). PSMA is a transmembrane protein of intense interest for PCa, initially

discovered 25 y ago (49). Physiologically, the function of PSMA is related to the hydrolysis of C-terminal residues of small peptides in the extracellular space, and PSMA is implicated in folate metabolism. PSMA represents an ideal target in PCa, given that PSMA expression increases 1,000-fold in malignant cells with increasing dysplasia (50). In the setting of diagnostics, PSMA PET imaging with <sup>68</sup>Ga or <sup>18</sup>F has shown utility in accurate localization (51,52).

In the setting of radiopharmaceuticals, early feasibility and tolerability data for <sup>177</sup>Lu-PSMA-617 were produced in a retrospective German multicenter review (22). This retrospective review examined 145 patients with metastatic CRPC who were treated off clinical trials in a compassionate-use program and had PSMA expression on PSMA PET, excluding patients who experienced progression under second-line antiandrogens or chemotherapy. <sup>177</sup>Lu-PSMA-617 was administered every 8–12 wk, up to 4 cycles. A PSA response of more than 50% was observed in 45% of patients after the first <sup>177</sup>Lu-PSMA-617 cycle and 57% after a second cycle. Overall, <sup>177</sup>Lu-PSMA-617 demonstrated acceptable toxicity, with 12% of patients experiencing grade 3–4 hematotoxicity.

Initial phase II data were produced in the LuPSMA trial based in Australia (53). This single-arm trial recruited 30 men with progressive CRPC after prior treatment with taxane-based chemotherapy and second-generation antiandrogen therapy. Patients underwent pretreatment PSMA PET screening to confirm high PSMA expression. Up to 4 cycles of <sup>177</sup>Lu-PSMA-617 were administered at 6-wk intervals, with doses varying from 6 to 8.5 GBq based on tumor burden. The primary endpoint of a PSA decline of more than 50% was achieved in 17 of 30 patients. A coprimary endpoint was

imaging response (on conventional imaging or PSMA PET), for which 40% of patients had nonprogressive disease. This group subsequently published TheraP, an open-label randomized, phase II trial comparing <sup>177</sup>Lu-PSMA-617 with cabazitaxel (54). TheraP enrolled 200 men with metastatic CRPC and PSMA PET–positive disease, who were previously treated with docetaxel and had progressive PSA based on the PCWG3 criteria. Patients were randomized 1:1 to receive either cabazitaxel (20 mg/m<sup>2</sup> every 3 wk for a maximum of 10 cycles) or <sup>177</sup>Lu-PSMA-617 (8.5 GBq, decreasing by 0.5 GBq per cycle, every 6 wk for a maximum of 6 cycles). The primary endpoint for TheraP was PSA response rate (PSA reduction of ≥50% from baseline), and secondary endpoints included progression-free survival, which was denoted by either PSA progression or rPFS as defined by the PCWG3. The <sup>177</sup>Lu-PSMA-617 group had a greater PSA response (66% vs. 37%, *P* < 0.0001), delayed radiographic progression (HR, 0.64; 95% CI, 0.46–0.86; *P* = 0.0070), and PSA progression (HR, 0.60; 95% CI, 0.44–0.83; *P* = 0.0017). The toxicity of <sup>177</sup>Lu-PSMA-617 was acceptable when compared with the cabazitaxel control group. More recently, phase II data assessing <sup>177</sup>Lu-PSMA-617 within the United States confirmed the previous findings of tolerability and therapeutic dosing schedules (55,56).

VISION, an international phase III prospective, randomized, open-label trial, reported results in late 2021 (57). The VISION trial design was derived from the design of ALSYMPCA with respect to the control and treatment groups (similarities defined in Table 1). In total, 831 men with metastatic CRPC and previous chemotherapy exposure were randomized 2:1 to receive a protocol-defined standard-of-care treatment with or without <sup>177</sup>Lu-PSMA-617. Eligible

**TABLE 1**  
Comparison of <sup>223</sup>Ra and <sup>177</sup>Lu-PSMA-617 Phase III Trial Designs

Type of review	ALSYMPCA (43)	VISION (57)
Therapeutic agent	<sup>223</sup> Ra	<sup>177</sup> Lu-PSMA-617
Patient eligibility	Progressive CRPC; 2 or more bone metastases based on bone scintigraphy with no visceral metastases; previous docetaxel or docetaxel-ineligible	Progressive metastatic CRPC; PSMA-positive disease, based on PSMA-PET; 1 or more androgen receptor inhibitors; previous taxane chemotherapy (1 or 2 agents)
Treatment arm	<sup>223</sup> Ra (50 kBq/kg), up to 6 doses every 4 wk	<sup>177</sup> Lu-PSMA-617 (7.4 GBq), up to 4 cycles every 6 wk
Control arm	Standard of care: for example, antiandrogens, excluding concurrent use of chemotherapy, EBRT, systemic radionuclides	Standard of care: for example, antiandrogens, excluding concurrent use of chemotherapy, EBRT, systemic radionuclides, immunotherapy
Primary endpoints	Overall survival	Overall survival; rPFS
Secondary endpoints	Total ALP (time to increase, total ALP response); time to PSA increase; time to first symptomatic skeletal event (first use of EBRT for skeletal symptoms or new symptomatic pathologic fracture, spinal cord compression or tumor-related orthopedic intervention)	Objective response and disease control (RECIST); time to first symptomatic skeletal event (first use of EBRT for skeletal symptoms or new symptomatic pathologic fracture, spinal cord compression or tumor-related orthopedic intervention)
FDA-approved indications	CRPC with symptomatic bone metastases and no visceral metastases	PSMA-positive metastatic CRPC, previous treatment with androgen receptor pathway inhibition and taxane-based chemotherapy

ALP = alkaline phosphatase; EBRT = external-beam radiotherapy.

patients had to have demonstrated PSMA-positive metastatic disease and no PSMA-negative lesions based on  $^{68}\text{Ga}$ -PSMA-11 PET. The liberal standard-of-care inclusion criteria allowed patients to have access to concurrent treatments, excluding cytotoxic chemotherapy, systemic radioisotopes (e.g.,  $^{223}\text{Ra}$ ), immunotherapy and investigational drugs. These exclusions regarding concurrent therapy existed given the lack of safety data on combining  $^{177}\text{Lu}$ -PSMA-617 with these agents. The VISION trial had alternate primary endpoints, meaning the trial would be positive if either or both endpoints were reached. These endpoints were rPFS (as defined by PCWG3) and overall survival. The VISION trial met both of its primary endpoints, prolonging rPFS (8.7 vs. 3.4 mo; HR, 0.40; 95% CI, 0.29–0.57;  $P < 0.001$ ) and overall survival (15.3 vs 11.3 mo; HR, 0.62; 95% CI, 0.52–0.74;  $P < 0.001$ ). Unlike the ALSYMPCA trial, the VISION trial included radiographic outcome measures, including objective response and disease control according to RECIST; 9.2% of patients achieved a complete response in the  $^{177}\text{Lu}$ -PSMA-617 group, compared with 0% in the control group. The VISION trial also met other secondary endpoints, including delay to first symptomatic skeletal event (11.5 vs. 6.8 mo; HR, 0.50; 95% CI, 0.40–0.62;  $P < 0.001$ ) in the  $^{177}\text{Lu}$ -PSMA-617 group.

After achievement of the primary outcome measures of the VISION trial, an NDA priority review was submitted to the FDA, and approval was confirmed in April 2022 (48). Given the inclusion of PSMA PET in the trial protocol, the FDA approval stipulated that  $^{177}\text{Lu}$ -PSMA-617 eligibility was contingent on PSMA-positive expression on PSMA-11 PET-based imaging (48).

#### FUTURE OF RADIOPHARMACEUTICALS IN PCa

The FDA approval of  $^{223}\text{Ra}$ -dichloride and the success of the recent phase III VISION trial assessing  $^{177}\text{Lu}$ -PSMA-617 provide a pathway and a model for future development of radiopharmaceuticals in PCa. Careful adherence to published FDA regulations pertaining to radiopharmaceuticals (7), the principles for trial conduct outlined in the PCWG3 recommendations, and considerations in recommended FDA trial design are critical.

From the recent experiences, important lessons have been learned that may optimize future radiopharmaceuticals. Given the variation in regulatory processes globally, improved international collaboration may improve efficiency in the conduct of phase II and III trials. Many patients may be treated outside clinical trial protocols, particularly in countries with less restrictive regulatory

oversight; however, publishing such retrospective data provides limited value in the context of regulatory approval. Thus, it is paramount that early experience with novel agents be published in the context of trial protocols to add to the body of knowledge while providing robust clinical data that are beneficial for regulatory approval. With respect to study design, there is a need to reach consensus on an optimal control arm with which to compare radiopharmaceuticals. The respective control arm treatment should be commensurate with the risks faced by the treated population. Indeed, in some scenarios, the use of passive control groups (e.g., placebo) may be suitable, though in other trial designs a suitable active control will be needed. For example, there is some role for chemotherapy control groups (e.g., docetaxel or cabazitaxel), although not all patients require chemotherapy.

At present, most studied agents have assessed the role in late PCa, typically metastatic CRPC. The role of radiopharmaceuticals at earlier times in the PCa course is of interest, though it has a unique set of challenges (Fig. 2). For example, the PSMAfore trial is a phase III, open-label, randomized trial assessing the role of  $^{177}\text{Lu}$ -PSMA-617 in taxane-naïve patients versus a change in the androgen receptor pathway inhibitor in metastatic CRPC (NCT04689828) (58). Use of such agents in even earlier disease states, such as localized disease, requires the use of more intermediate endpoints, given the prolonged follow-up required to demonstrate differences in overall survival. The fact that the optimal endpoint is currently not clear may be disruptive from a regulatory perspective. In particular, molecular imaging endpoints—be they based on response or progression—have been defined, have undergone clinical qualification as clinically relevant, and are not recognized by regulatory agencies as meritorious for drug approval. Additionally, combination therapies with radiopharmaceuticals and alternate systemic agents are being investigated, such as immunotherapy agents. Table 2 lists current radiopharmaceutical trials in PCa.

It is likely that novel radiopharmaceuticals will soon be developed and enter clinical-phase trials. Such agents may be directed to new targets that are overexpressed in PCa tumor cells or the tumor microenvironment (59). In addition to novel pathways and targets, variation in therapeutic radionuclides is a likely avenue of development. Although the most common radioisotopes are frequently  $\beta$ -particle emitters,  $\alpha$ -emitters such as  $^{225}\text{Ac}$ ,  $^{213}\text{Bi}$ ,  $^{212}\text{Pb}$ , and  $^{211}\text{At}$  are attractive because they provide more energy across a shallower depth of penetration (25). Future trial designs may require demonstration of superiority or noninferiority compared with previously approved radiopharmaceutical agents.

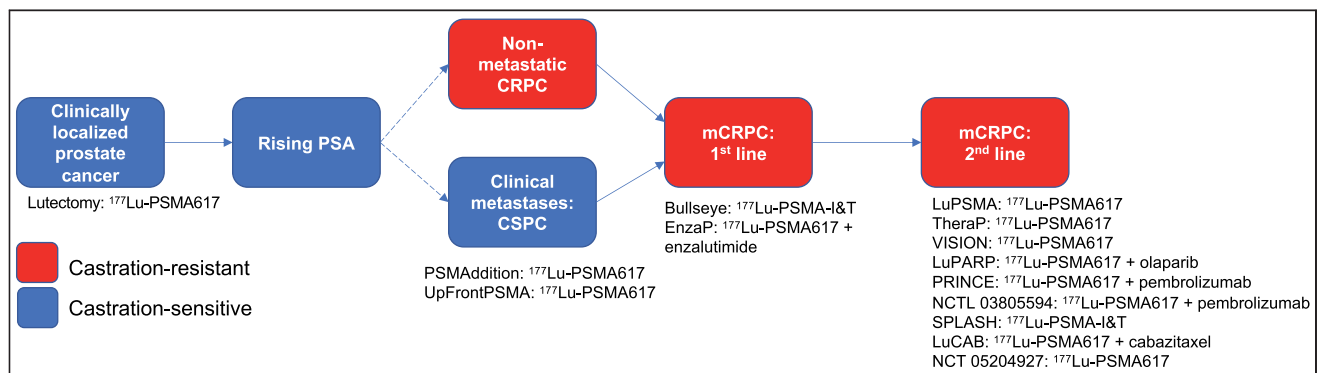


**FIGURE 2.** Trials assessing  $^{177}\text{Lu}$ -PSMA-617 therapy in various stages of PCa.

**TABLE 2**  
Current Radiopharmaceutical Trials in PCa

Trial name	ClinicalTrials.gov number	Phase	Size (n)	Regimen	Geographic region
<b>High-risk localized or oligometastatic PCa</b>					
Lutectomy	NCT04430192	II	20	<sup>177</sup> Lu-PSMA-617 before prostatectomy	Australia
Bullseye	NCT04443062	II	58	<sup>177</sup> Lu-PSMA-617 vs. standard of care	The Netherlands
PROQUIRE-1	NCT05162573	I	18	EBRT + <sup>177</sup> Lu-PSMA-617	The Netherlands
<b>Metastatic CRPC</b>					
UpFrontPSMA	NCT04343885	II	140	Docetaxel ± <sup>177</sup> Lu-PSMA-617	Australia
ProstACT TARGET	NCT05146973	II	50	EBRT + <sup>177</sup> Lu-DOTA-TLX591	Australia
PSMAAddition	NCT04720157	III	1,126	Standard of care ± <sup>177</sup> Lu-PSMA-617	United States, Europe, Korea, Singapore, Taiwan
NA	NCT04206319	II	26	<sup>223</sup> Ra	United States
NA	NCT05079698	I	6	<sup>177</sup> Lu-PSMA-617 + stereotactic radiotherapy	United States
<b>First-line therapy for metastatic CRPC</b>					
EnzaP	NCT04419402	II	160	Enzalutamide ± <sup>177</sup> Lu-PSMA-617	Australia
PSMAfore	NCT04689828	III	450	<sup>177</sup> Lu-PSMA-617 vs. change in ARSI	North America, Europe
<b>Second-line therapy for metastatic CRPC</b>					
LuPARP	NCT03874884	I	52	<sup>177</sup> Lu-PSMA-617 + olaparib	Australia
PRINCE	NCT03658447	I/II	37	<sup>177</sup> Lu-PSMA-617 + pembrolizumab	Australia
NA	NCT03805594	I	43	<sup>177</sup> Lu-PSMA-617 + pembrolizumab	United States
NA	NCT04946370	I/II	76	<sup>225</sup> Ac-J591 + pembrolizumab	United States
SPLASH	NCT04647526	III	415	<sup>177</sup> Lu-PSMA-I&T vs. second-line ARSI	North America, Europe
NA	NCT04506567	I/II	105	<sup>225</sup> Ac-J591	United States
ARROW	NCT03939689	II	120	Enzalutamide ± MIP 1095 <sup>131</sup> I	North America
NA	NCT04644770	I	70	<sup>225</sup> Ac h11B6	United States
SECURE	NCT04868604	I/II	44	<sup>64</sup> Cu-SAR-bisPSMA	United States
LuCAB	NCT05340374	I/II	44	<sup>177</sup> Lu-PSMA-617 + cabazitaxel	Australia
NA	NCT04071236	I/II	24	<sup>223</sup> Ra ± M3814 ± avelumab	United States
TATCIST	NCT05219500	II	100	<sup>225</sup> Ac-PSMA-I&T	United States
NA	NCT04886986	I/II	33	<sup>225</sup> Ac + <sup>177</sup> Lu-PSMA-I&T	United States
ECLIPSE	NCT05204927	III	400	<sup>177</sup> Lu-PSMA-I&T	United States
NA	NCT04597411	I	30	<sup>225</sup> Ac-PSMA-617	Australia, South Africa
PROSTACT	NCT04876651	III	387	<sup>177</sup> Lu-J591	Australia

EBRT = external beam radiotherapy; ARSI = androgen receptor signaling inhibitor; NA = not applicable.

## CONCLUSION

Although radiopharmaceuticals are currently in their infancy, they represent a promising treatment pathway that warrants careful interrogation. Presently, significant barriers to entry exist in the realms of radiopharmaceutical development and progression through to clinical trials and eventual FDA approval. Despite these barriers, agents have been approved largely because of the clear regulatory guides published by the FDA. In metastatic CRPC, adherence to the framework provided by PCWG facilitated the successful designs of the phase III ALYSMPCA and VISION trials. As such, these recent approvals provide optimism and highlight a clear pipeline toward NDA application for novel radiopharmaceuticals. The roles of radiopharmaceuticals using alternative targeting ligands and radioactive nuclides, and at different disease points in PCa, are an area of future research.

## REFERENCES

1. Sgouros G, Bodei L, McDevitt MR, Nedrow JR. Radiopharmaceutical therapy in cancer: clinical advances and challenges. *Nat Rev Drug Discov*. 2020;19:589–608.
2. Bentzen SM, Constine LS, Deasy JO, et al. Quantitative Analyses of Normal Tissue Effects in the Clinic (QUANTEC): an introduction to the scientific issues. *Int J Radiat Oncol Biol Phys*. 2010;76(suppl):S3–S9.
3. Kiess AP, Minn I, Chen Y, et al. Auger radiopharmaceutical therapy targeting prostate-specific membrane antigen. *J Nucl Med*. 2015;56:1401–1407.
4. Sgouros G, Roeske JC, McDevitt MR, et al. MIRD pamphlet no. 22 (abridged): radiobiology and dosimetry of alpha-particle emitters for targeted radionuclide therapy. *J Nucl Med*. 2010;51:311–328.
5. Suominen MI, Wilson T, Käkönen SM, Scholz A. The mode-of-action of targeted alpha therapy radium-223 as an enabler for novel combinations to treat patients with bone metastasis. *Int J Mol Sci*. 2019;20:3899.
6. Jentzen W, Hobbs RF, Stahl A, Knust J, Sgouros G, Bockisch A. Pre-therapeutic <sup>124</sup>I PET/CT dosimetry confirms low average absorbed doses per administered <sup>131</sup>I activity to the salivary glands in radioiodine therapy of differentiated thyroid cancer. *Eur J Nucl Med Mol Imaging*. 2010;37:884–895.
7. Guidance for industry: developing medical imaging drug and biological products—part 1: conducting safety assessments. U.S. Food and Drug Administration website. <https://www.fda.gov/media/72295/download>. Published June 2004. Accessed November 4, 2022.
8. Hofling AA, Fotenos AF, Niu G, et al. Prostate cancer theranostics: concurrent approvals by the Food and Drug Administration of the first diagnostic imaging drug indicated to select patients for a paired radioligand therapeutic drug. *J Nucl Med*. 2022;63:1642–1643.
9. Sherman M, Levine R. Nuclear medicine and wall street: an evolving relationship. *J Nucl Med*. 2019;60(suppl 2):20S–24S.
10. do Pazo C, Webster RM. The prostate cancer drug market. *Nat Rev Drug Discov*. 2021;20:663–664.
11. Sweeney CJ, Chen YH, Carducci M, et al. Chemohormonal therapy in metastatic hormone-sensitive prostate cancer. *N Engl J Med*. 2015;373:737–746.
12. de Bono JS, Oudard S, Ozguroglu M, et al. Prednisone plus cabazitaxel or mitoxantrone for metastatic castration-resistant prostate cancer progressing after docetaxel treatment: a randomised open-label trial. *Lancet*. 2010;376:1147–1154.
13. Ryan CJ, Smith MR, de Bono JS, et al. Abiraterone in metastatic prostate cancer without previous chemotherapy. *N Engl J Med*. 2013;368:138–148.
14. de Bono J, Mateo J, Fizazi K, et al. Olaparib for metastatic castration-resistant prostate cancer. *N Engl J Med*. 2020;382:2091–2102.
15. Content details: 21 U.S.C. 9—federal food, drug, and cosmetic act. GovInfo website. <https://www.govinfo.gov/app/details/USCODE-2011-title21/USCODE-2011-title21-chap9/summary>. Published 2011. Accessed November 3, 2022.
16. Gieringer DH. The safety and efficacy of new drug approval. *Cato J*. 1985;5:177–201.
17. Wouters OJ, McKee M, Luyten J. Estimated research and development investment needed to bring a new medicine to market, 2009–2018. *JAMA*. 2020;323:844–853.
18. Guidance for industry: content and format of investigational new drug applications (INDs) for phase 1 studies of drugs, including well-characterized, therapeutic, biotechnology-derived products. U.S. Food and Drug Administration website. <https://www.fda.gov/media/72057/download>. Published November 1995. Accessed November 4, 2022.
19. Van Norman GA. Drugs, devices, and the FDA: part 1—an overview of approval processes for drugs. *JACC Basic Transl Sci*. 2016;1:170–179.
20. CFR—Code of Federal Regulations Title 21: Sec. 312.21, phases of an investigation. U.S. Food and Drug Administration website. <https://www.accessdata.fda.gov/scripts/cdrh/cfdocs/cfcfr/cfrsearch.cfm?fr=312.21>. Updated March 29, 2022. Accessed November 4, 2022.
21. 22 case studies where phase 2 and phase 3 trials had divergent results. U.S. Food and Drug Administration website. <https://www.fda.gov/media/102332/download>. Published January 2017. Accessed November 4, 2022.
22. Rahbar K, Ahmadzadehfar H, Kratochwil C, et al. German multicenter study investigating <sup>177</sup>Lu-PSMA-617 radioligand therapy in advanced prostate cancer patients. *J Nucl Med*. 2017;58:85–90.
23. CFR—Code of Federal Regulations title 21: sec. 314.126, adequate and well-controlled studies. U.S. Food and Drug Administration website. <https://www.accessdata.fda.gov/scripts/cdrh/cfdocs/cfcfr/cfrsearch.cfm?fr=314.126>. Updated March 29, 2022. Accessed November 4, 2022.
24. Fast track, breakthrough therapy, accelerated approval, priority review. U.S. Food and Drug Administration website. <https://www.fda.gov/patients/learn-about-drug-and-device-approvals/fast-track-breakthrough-therapy-accelerated-approval-priority-review>. Revised February 23, 2018. Accessed November 4, 2022.
25. Herrmann K, Schwaiger M, Lewis JS, et al. Radiotheranostics: a roadmap for future development. *Lancet Oncol*. 2020;21:e146–e156.
26. Institute of Medicine and National Research Council. *Advancing Nuclear Medicine Through Innovation*. National Academies Press; 2007:119–130.
27. Keppler JS, Conti PS. A cost analysis of positron emission tomography. *AJR*. 2001;177:31–40.
28. Mottet N, van den Bergh RCN, Briers E, et al. EAU-EANM-ESTRO-ESUR-SIOG guidelines on prostate cancer: 2020 update. Part 1: screening, diagnosis, and local treatment with curative intent. *Eur Urol*. 2021;79:243–262.
29. Scher HI, Halabi S, Tannock I, et al. Design and end points of clinical trials for patients with progressive prostate cancer and castrate levels of testosterone: recommendations of the Prostate Cancer Clinical Trials Working Group. *J Clin Oncol*. 2008;26:1148–1159.
30. Fleming MT, Morris MJ, Heller G, Scher HI. Post-therapy changes in PSA as an outcome measure in prostate cancer clinical trials. *Nat Clin Pract Oncol*. 2006;3:658–667.
31. Bubley GJ, Carducci M, Dahut W, et al. Eligibility and response guidelines for phase II clinical trials in androgen-independent prostate cancer: recommendations from the Prostate-Specific Antigen Working Group. *J Clin Oncol*. 1999;17:3461–3467.
32. Scher HI, Morris MJ, Stadler WM, et al. Trial design and objectives for castration-resistant prostate cancer: updated recommendations from the Prostate Cancer Clinical Trials Working Group 3. *J Clin Oncol*. 2016;34:1402–1418.
33. Pollen JJ, Witzum KF, Ashburn WL. The flare phenomenon on radionuclide bone scan in metastatic prostate cancer. *AJR*. 1984;142:773–776.
34. Morris MJ, Molina A, Small EJ, et al. Radiographic progression-free survival as a response biomarker in metastatic castration-resistant prostate cancer: COU-AA-302 results. *J Clin Oncol*. 2015;33:1356–1363.
35. Porter AT, McEwan AJ, Powe JE, et al. Results of a randomized phase-III trial to evaluate the efficacy of strontium-89 adjuvant to local field external beam irradiation in the management of endocrine resistant metastatic prostate cancer. *Int J Radiat Oncol Biol Phys*. 1993;25:805–813.
36. Sartor O, Reid RH, Hoskin PJ, et al. Samarium-153-lexidronam complex for treatment of painful bone metastases in hormone-refractory prostate cancer. *Urology*. 2004;63:940–945.
37. Morris MJ, Corey E, Guise TA, et al. Radium-223 mechanism of action: implications for use in treatment combinations. *Nat Rev Urol*. 2019;16:745–756.
38. Henriksen G, Breistol K, Bruland OS, Fodstad Ø, Larsen RH. Significant antitumor effect from bone-seeking, alpha-particle-emitting <sup>223</sup>Ra demonstrated in an experimental skeletal metastases model. *Cancer Res*. 2002;62:3120–3125.
39. Suominen MI, Fagerlund KM, Rissanen JP, et al. Radium-223 inhibits osseous prostate cancer growth by dual targeting of cancer cells and bone microenvironment in mouse models. *Clin Cancer Res*. 2017;23:4335–4346.
40. FDA approves radiopharmaceutical for metastatic prostate cancer. *Cancer Discov*. 2013;3:OF1.
41. Nilsson S, Larsen RH, Fosså SD, et al. First clinical experience with alpha-emitting radium-223 in the treatment of skeletal metastases. *Clin Cancer Res*. 2005;11:4451–4459.
42. Nilsson S, Franzén L, Parker C, et al. Bone-targeted radium-223 in symptomatic, hormone-refractory prostate cancer: a randomised, multicentre, placebo-controlled phase II study. *Lancet Oncol*. 2007;8:587–594.
43. Parker C, Nilsson S, Heinrich D, et al. Alpha emitter radium-223 and survival in metastatic prostate cancer. *N Engl J Med*. 2013;369:213–223.
44. FDA updates: approval for Xofigo for advanced prostate cancer; new indication for Tarceva, along with companion diagnostic test. *Oncology Times*. 2013;35:12.
45. Smith M, Parker C, Saad F, et al. Addition of radium-223 to abiraterone acetate and prednisone or prednisolone in patients with castration-resistant prostate cancer

- and bone metastases (ERA 223): a randomised, double-blind, placebo-controlled, phase 3 trial. *Lancet Oncol.* 2019;20:408–419.
46. EMA restricts use of prostate cancer medicine Xofigo. European Medicines Agency website. <https://www.ema.europa.eu/en/news/ema-restricts-use-prostate-cancer-medicine-xofigo>. Published July 27, 2018. Accessed November 4, 2022.
  47. Gillissen S, Choudhury A, Rodriguez-Vida A, et al. Decreased fracture rate by mandating bone protecting agents in the EORTC 1333/PEACEIII trial combining Ra223 with enzalutamide versus enzalutamide alone: an updated safety analysis [abstract]. *J Clin Oncol.* 2021;39(suppl):5002.
  48. Novartis Pluvicto™ approved by FDA as first targeted radioligand therapy for treatment of progressive, PSMA positive metastatic castration-resistant prostate cancer. Novartis website. <https://www.novartis.com/news/media-releases/novartis-pluvictotm-approved-fda-first-targeted-radioligand-therapy-treatment-progressive-psma-positive-metastatic-castration-resistant-prostate-cancer>. Published March 23, 2022. Accessed November 4, 2022.
  49. Afshar-Oromieh A, Hetzheim H, Kratochwil C, et al. The theranostic PSMA ligand PSMA-617 in the diagnosis of prostate cancer by PET/CT: biodistribution in humans, radiation dosimetry, and first evaluation of tumor lesions. *J Nucl Med.* 2015;56:1697–1705.
  50. Silver DA, Pellicer I, Fair WR, Heston WD, Cordon-Cardo C. Prostate-specific membrane antigen expression in normal and malignant human tissues. *Clin Cancer Res.* 1997;3:81–85.
  51. Pienta KJ, Gorin MA, Rowe SP, et al. A phase 2/3 prospective multicenter study of the diagnostic accuracy of prostate specific membrane antigen PET/CT with <sup>18</sup>F-DCFPyL in prostate cancer patients (OSPREGY). *J Urol.* 2021;206:52–61.
  52. Morris MJ, Rowe SP, Gorin MA, et al. Diagnostic performance of <sup>18</sup>F-DCFPyL-PET/CT in men with biochemically recurrent prostate cancer: results from the CONDOR phase III, multicenter study. *Clin Cancer Res.* 2021;27:3674–3682.
  53. Hofman MS, Violet J, Hicks RJ, et al. [<sup>177</sup>Lu]-PSMA-617 radionuclide treatment in patients with metastatic castration-resistant prostate cancer (LuPSMA trial): a single-centre, single-arm, phase 2 study. *Lancet Oncol.* 2018;19:825–833.
  54. Hofman MS, Emmett L, Sandhu S, et al. <sup>177</sup>Lu-PSMA-617 versus cabazitaxel in patients with metastatic castration-resistant prostate cancer (TheraP): a randomised, open-label, phase 2 trial. *Lancet.* 2021;397:797–804.
  55. Calais J, Czernin J, Thin P, et al. Safety of PSMA-targeted molecular radioligand therapy with <sup>177</sup>Lu-PSMA-617: results from the prospective multicenter phase 2 trial RESIST-PC (NCT03042312). *J Nucl Med.* 2021;62:1447–1456.
  56. Calais J, Gafita A, Eiber M, et al. Prospective phase 2 trial of PSMA-targeted molecular Radiotherapy with <sup>177</sup>Lu-PSMA-617 for metastatic castration-resistant prostate cancer (RESIST-PC): efficacy results of the UCLA cohort. *J Nucl Med.* 2021;62:1440–1446.
  57. Sartor O, de Bono J, Chi KN, et al. Lutetium-177-PSMA-617 for metastatic castration-resistant prostate cancer. *N Engl J Med.* 2021;385:1091–1103.
  58. Sartor AO, Morris MJ, Chi KN, et al. PSMAfore: a phase 3 study to compare <sup>177</sup>Lu-PSMA-617 treatment with a change in androgen receptor pathway inhibitor in taxane-naïve patients with metastatic castration-resistant prostate cancer [abstract]. *J Clin Oncol.* 2022;40(suppl 6):TPS211.
  59. Cheever MA, Allison JP, Ferris AS, et al. The prioritization of cancer antigens: a National Cancer Institute pilot project for the acceleration of translational research. *Clin Cancer Res.* 2009;15:5323–5337.

# Nanoparticle Diagnostics and Theranostics in the Clinic

Roger M. Pallares<sup>1</sup>, Felix M. Mottaghy<sup>2,3</sup>, Volkmar Schulz<sup>1,4</sup>, Fabian Kiessling<sup>1</sup>, and Twan Lammers<sup>1</sup>

<sup>1</sup>Institute for Experimental Molecular Imaging, RWTH Aachen University Hospital, Aachen, Germany; <sup>2</sup>Department of Nuclear Medicine, RWTH Aachen University Hospital, Aachen, Germany; <sup>3</sup>Department of Radiology and Nuclear Medicine, Maastricht University Medical Center, Maastricht, The Netherlands; and <sup>4</sup>Physics Institute III B, RWTH Aachen University, Aachen, Germany

Nanoparticles possess unique features that may be useful for disease diagnosis and therapy. Preclinically, many different nanodiagnostics have been explored, but only a few have made it to the market. We here provide an overview of nanoparticle-based imaging agents currently used and evaluated in the clinic and discuss preclinical progress and translational avenues for the use of nanoparticles for diagnostic and theranostic applications.

**Key Words:** molecular imaging; oncology; nanodiagnostics; nanomedicine; nanoparticles; theranostics

**J Nucl Med 2022; 63:1802–1808**  
DOI: 10.2967/jnumed.122.263895

**I**maging plays an important role in disease diagnosis, prediction of prognosis, and monitoring of therapeutic responses. Imaging modalities used in routine practice are ultrasound, radiography, CT, PET, SPECT, MRI, and combinations of these (i.e., SPECT/CT, PET/CT, and PET/MRI). Optical imaging and photoacoustic imaging are also gradually finding their way into the clinic, mainly in the setting of intraoperative imaging approaches. To improve the distinction between pathologic and normal tissues, contrast agents and radiolabeled probes are frequently used. In the last 2 decades, nanoparticles have received a lot of interest as imaging probes. Some nanoparticles are intrinsically magnetically or optically imageable, whereas others can be imaged only indirectly, after being labeled with radiotracers or dyes (1).

Nanoparticles tend to circulate for prolonged periods (compared with small-molecule agents) and display passive accumulation at pathologic sites such as tumors, metastases, and sites of inflammation, because of leaky vasculature and a high population of phagocytes (2). Furthermore, nanoparticles can be functionalized with targeting ligands to promote engagement with and uptake by target cells or tissues. It is because of these features that, beyond applications in imaging, nanoparticles are also extensively used for drug delivery. The therapeutic performance of drug-loaded nanomedicines relies on their ability to reach the pathologic site, which in the case of tumors usually relies on the enhanced permeability and retention (EPR) effect (3). Because EPR is a highly heterogeneous phenomenon, companion nanodiagnostics or theranostic nanoparticles are needed to stratify patients during translation, to ensure that only patients presenting good tumor accumulation are included in clinical

trials (4). At the preclinical level, imaging techniques assist in better understanding nanoparticle behavior in vivo, providing fundamental insights to improve drug delivery formulations.

In this perspective, we discuss the development of nanoparticles as imaging agents, either as purely diagnostic probes for clinical disease diagnosis and staging or as imaging allies of nanoparticle therapeutics for improved formulation design, patient stratification, and nanomedicine translation.

## NANOPARTICLE-BASED IMAGING

### Nanoparticle-Based Diagnostics in the Clinic

Despite large numbers of preclinical studies using nanoparticles as imaging probes, only a few have moved to clinical settings (5) (Supplemental Tables 1 and 2; supplemental materials are available at <http://jnm.snmjournals.org>). This is because the particular pharmacokinetic properties of nanoparticles limit their use to very specific applications. For instance, nanoparticles tend to circulate for relatively long periods, have a small volume of distribution, and are taken up by phagocytes. They consequently reside and accumulate mainly in well-perfused and macrophage-rich tissues, such as liver, spleen, and lymph nodes. Hence, traditional diagnostic applications of nanoparticles include imaging of liver lesions after intravenous administration or localization of sentinel lymph nodes (SLNs) after local injection. Moreover, because of their potent contrast generation properties, nanoparticles have been used to label stem cells and track their migration to or retention in pathologic tissues. Recent clinical work has furthermore explored the use of stimulus-responsive nanoparticles, which can change their behavior or contrast generation depending on their environment. Such approaches may gradually expand nanoparticle-based imaging beyond traditional clinical applications.

<sup>99m</sup>Tc-Colloids for SLN Mapping and for Inflammation and Bone Marrow Imaging. The first nanoparticles used in the clinic were <sup>99m</sup>Tc-colloids for planar scintigraphy and later SPECT imaging (6). They have been administered since the mid-1960s and are based primarily on radiolabeled sulfur colloids. <sup>99m</sup>Tc-colloids are used to identify SLNs in various tumor entities (e.g., breast cancer, melanoma, oral cavity tumors, prostate cancer, and cervical cancer) and to image lymphatic flow. Moreover, these colloids are also used for radiolabeling of leukocytes to locate sites of infection and inflammation and for imaging of bone marrow distribution. In the European Union, radiolabeled albumin nanocolloids are more commonly used than the sulfur counterparts. Although sulfur colloids have a wide range of sizes (from 10 to 1,000 nm, with filtration removing particles larger than 200 nm), albumin nanoparticles are much smaller (~30 nm) and have a narrower size distribution (between 6 and 80 nm), which results in faster migration through the lymphatic system. Currently, these nanoparticles are still broadly used in daily clinical practice (Supplemental Table 1).

Received May 26, 2022; revision accepted Oct. 19, 2022.  
For correspondence or reprints, contact Roger M. Pallares (rmolltopallar@ukaachen.de) or Twan Lammers (tlammers@ukaachen.de).  
Published online Oct. 27, 2022.  
COPYRIGHT © 2022 by the Society of Nuclear Medicine and Molecular Imaging.

*Superparamagnetic Iron Oxide Nanoparticles (SPIONs) for MRI of Liver Tumors.* In 1996, ferumoxide became the first SPION-based imaging formulation approved by the U.S. Food and Drug Administration (Supplemental Table 1) (6). The large magnetic moment of SPIONs alter the transverse relaxation times ( $T_2$ ) of water protons, changing their signal properties in MRI. Because around 80% of intravenously injected SPIONs are cleared by Kupffer cells in the liver, and because liver tumors generally have altered vascularization and a much lower phagocytic capacity, SPIONs were initially used for carcinoma detection and dysplastic nodule evaluation. Subsequent applications outside the liver included atheroma imaging, stem cell tracking to identify postadministration location and engraftment, and dendritic cell labeling to monitor vaccine administration and lymph node trafficking. Given the more favorable pharmacokinetics and excretion profiles of gadolinium-based contrast agents (i.e., SPIONs show poor excretion and strong accumulation in the liver and spleen), as well as their positive signal generation properties, most clinical SPION applications have been discontinued, except for very specific applications such as MR angiography in patients with renal failure and use as a drug in iron-deficiency anemia (5,7). Interestingly, in recent years, the use of SPIONs has again increased in clinical settings, for new specific niche applications.

*SPIONs for Imaging Tumor-Associated Macrophages (TAMs).* TAMs are involved in tumor progression and considered to be biomarkers for an unfavorable prognosis (8). Several new therapeutic agents target leukocytes, diminishing macrophage infiltration in tumors. Thus, it is important to identify tumors that present high levels of TAMs and to monitor how they respond to treatments. SPIONs (ferumoxytol) have been used to image macrophages in high-grade glioma patients (9). MRI measurements have shown a good correlation with iron-containing TAMs at tumor sites, where SPIONs were localized inside macrophages and not in tumor cells or astrocytes, as confirmed by histopathology.

*SPIONs for Identifying Lymphoid Tissue.* In breast cancer and melanoma, SLNs can be mapped with  $^{99m}\text{Tc}$ -colloids and blue dyes. The use of these agents is limited by several factors, including the lack of strong optical signal in tissue (blue dye), artifacts originating from shine-through phenomena (if the SLN is too close to the primary lesion), poor spatial resolution (e.g., 10 mm for lymphoscintigraphy with  $^{99m}\text{Tc}$ ), and the need for using radioisotopes. Hence, SPIONs have been clinically explored as alternative mapping probes for SLN detection, showing diagnostic performance similar to  $^{99m}\text{Tc}$ -based methods (10). SPIONs have also been used to identify lymph node metastases in prostate cancer patients via nanoparticle-enhanced MRI. Compared with PET/CT imaging with  $^{68}\text{Ga}$ -PSMA-HBED-CC, SPION-enhanced MRI was found to be superior in identifying smaller suggestive lymph nodes (11).

*Fluorescent Silica Dots for Mapping SLNs.* Ultrasmall integrin-targeted fluorescent core-shell silica nanoparticles (also known as Cornell dots) are being explored in the clinic to locate SLNs. Their size of less than 8 nm allows for fast renal excretion, resulting in whole-body clearance half-times of between 13 and 21 h. This rapid removal from the body favors specific molecular imaging applications and minimizes safety concerns, such as long-term accumulation in the liver. A phase I/IIa clinical study has demonstrated the feasibility and safety of Cornell dot-based SLN biopsy mapping in patients with melanoma in the head and neck area (Fig. 1A) (12). Moreover, Cornell dots radiolabeled with  $^{124}\text{I}$ ,  $^{89}\text{Zr}$ , or  $^{64}\text{Cu}$  have also been used as hybrid probes for PET and fluorescence-based imaging for staging tumors in clinical settings (13).

*pH-Sensitive Fluorescent Polymeric Nanoparticles for Intraoperative Imaging.* ONM-100 is a micellar fluorescent nanoparticle imaging agent composed of a pH-sensitive amphiphilic polymer conjugated to indocyanine green. The polymeric micelles irreversibly dissociate in the acidic extracellular tumor microenvironment, and they fluoresce as a result. In a recent clinical study, ONM-100 enabled intraoperative imaging of 4 different solid tumor types (e.g. head and neck squamous cell carcinoma, esophageal cancer, breast cancer, and colorectal cancer) both in vivo and ex vivo in 30 patients (Fig. 1B) (14). ONM-100 furthermore promoted the detection of tumor-positive resection margins in 9 (of 9) patients. Moreover, nanoparticle fluorescence was observed in 4 occult lesions missed by standard-of-care surgery or pathologic analysis.

*Nanoparticle-Based Surface-Enhanced Raman Spectroscopy (SERS) for Identification of Surgical Tumor Margin Surfaces.* Lumpectomy (also known as partial mastectomy) is a standard intervention for breast cancer. Unfortunately, additional surgery is required in up to 50% of patients if pathologic analysis reveals the presence of carcinoma in the resection margins. Intraoperative identification of residual carcinoma at the surgical margin surface holds promise to reduce the number of reexcision surgeries. Recently, a raman-encoded molecular imaging technique based on gold nanoparticles topically applied to the excised tissue has been developed (15). This SERS technique allows visualization of the expression of multiple cell surface biomarkers at surgical margins. In a proof-of-concept study, 57 freshly removed specimens were imaged to characterize the expression of 4 biomarkers (i.e., human epidermal growth factor receptor-2 [HER2], estrogen receptor, epidermal growth factor receptor, and CD44), and the detection of breast carcinoma was achieved with a sensitivity and specificity of 89% and 92%, respectively.

#### **Promising Nanoparticle-Based Imaging Approaches at the Preclinical Stage**

While the amount of preclinical research focusing on developing novel nanoparticles for imaging applications is vast, only very few nanodiagnostics are heading toward clinical use. This discordance is because research is driven mostly by materials science, in which developing new multifunctional nanomaterials with exotic properties prevails over trying to overcome key current pitfalls of nanoparticle imaging agents. Nonetheless, it is worth highlighting several preclinical initiatives that are trying to move toward translation. For example, some efforts have focused on already-approved SPIONs, either minimizing some of the features that resulted in their discontinuation as MRI contrast agents or exploiting them as probes for new imaging modalities previously not used for diagnostics. Beyond SPIONs, nanoparticles emitting in the second near-infrared window (NIR-II) have recently expanded the applicability of fluorescence imaging, as their deeper tissue penetration and higher spatial resolution potentially allow for more precise functional and molecular imaging.

*SPIONs for Longitudinal Relaxation Time ( $T_1$ )-Based MR Angiography.* Despite initial approval in the United States and European Union, most SPIONs were discontinued as  $T_2$  contrast agents because of poorer pharmacokinetic properties and performance than for the much smaller gadolinium-based contrast agents.  $T_2$  MRI contrast agents have inherent limitations, including dark signal (negative contrast) and the blooming effect. Hence,  $T_1$  contrast agents tend to be preferred by clinicians. Expanding on a pioneer work in which small SPIONs were used as  $T_1$  blood-pool contrast agents, a study used extremely small SPIONs as contrast agents for high-resolution  $T_1$  MR angiography in beagle dogs and

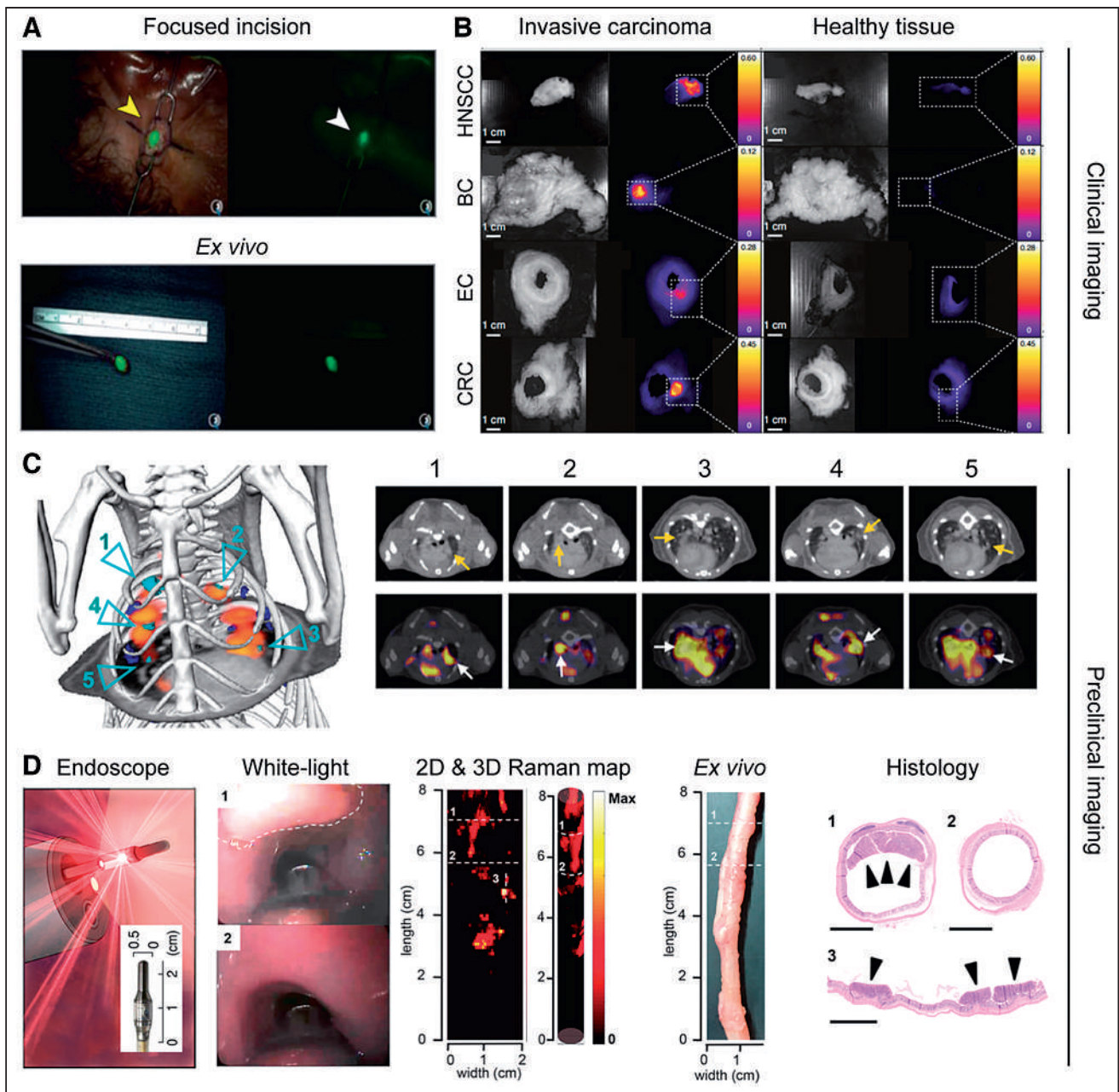


**FIGURE 1.** Nanoparticle-based imaging for diagnosis. (A) Real-time transcutaneous imaging of SLNs using fluorescent silica dots. (Adapted with permission of (12).) (B) Fluorescence images of different surgically removed tumor and healthy-tissue specimens after ONM-100 administration. (Adapted with permission of (14).) (C) Use of  $^{64}\text{Cu}$ -macrin to image tumor-associated macrophages in orthotopic mouse model of lung adenocarcinoma via PET/CT. Cyan arrows highlight tumors with high  $^{64}\text{Cu}$ -macrin uptake. Arrows are used to further highlight those regions in corresponding transverse sections. (Adapted with permission of (19).) (D) Endoscopy imaging premalignant colorectal lesions using nanoparticle-based SERS. Lesion is highlighted by the white dashed line in white-light image. Raman signals correlated with presence of lesions (regions 1 and 3), whereas no raman signals were detected in lesion-free region (region 2). (Adapted with permission of (22).) BC = breast cancer; EC = esophageal cancer; CRC = colorectal cancer; HNSCC = head and neck squamous cell carcinoma.

macaques (16). As a proof of concept, cerebral ischemia was imaged and identified in these large animals. Regarding a potential clinical future, SPIONs showing  $T_1$  contrast may benefit current niche applications in which conventional SPIONs are used as  $T_2$  contrast agents (e.g., SLN imaging and cell tracking), as long as SPION clustering, which can result in signal quenching, is minimized. Compared with current small-molecule gadolinium chelates, SPIONs have diagnostically less optimal pharmacokinetics

(i.e., slower tissue accumulation, slower compartment exchange, and slower excretion) and are therefore unlikely to replace them as general MRI probes.

*SPIONs for Magnetic Particle Imaging (MPI) of Perfusion.* Invented in 2001 and commercialized in 2013, MPI has emerged as a promising imaging technique. MPI provides 3-dimensional images of SPION distribution and has distinct advantages over conventional MRI, such as quantitative imaging of nanoparticles

as positive contrasts, shorter acquisition times, higher temporal resolution, and absence of signal from tissue. Hence, MPI has been used for real-time functional imaging, such as detecting perfusion deficits in ischemic brains in mice (17). Regarding its clinical future, MPI faces 2 main challenges. First, most current MPI systems are designed for animal imaging, and efforts to upscale MPI scanners to the appropriate size (while providing sufficient imaging capabilities) are still ongoing and continue to be a challenge. Second, whereas MPI may outperform SPION-based MRI, MPI is still limited by the distinct pharmacokinetic features of SPIONs (i.e., slower accumulation in tissue of interest, slower compartment exchange, and slower excretion than for small molecules). Moreover, many MPI studies have focused on imaging the vascular system. Reliable (and cheaper) techniques for imaging perfusion already exist, including CT and ultrasound, questioning the need for a more expensive imaging technique. Taking everything together, the future of MPI as a general diagnostic tool is disputable, and MPI may be limited to specific applications such as hot-spot imaging of labeled stem cells (as long as the cell properties are not disrupted).

*SPIONs for Monitoring Immunotherapy.* Chimeric antigen receptor T-cell therapy is approved by the Food and Drug Administration for the treatment of chemotherapy-resistant leukemia. However, in patients with solid tumors, chimeric antigen receptor T-cell therapy has shown mixed results. As with nanomedicines, one challenge facing this therapy is monitoring infiltration and accumulation of the therapeutic entities, that is, the ex vivo engineered T cells, into the tumor region on intravenous administration, as the therapeutic response strongly depends on this accumulation. Hence, there may be a need to track the location of T cells noninvasively. Following the steps of a pioneer study that monitored dendritic cell therapy with SPIONs in melanoma patients, a recent study demonstrated that SPIONs could also be used to label chimeric antigen receptor T cells, and their accumulation and distribution could be determined in osteosarcoma-bearing mice by MRI and MPI (18). From the different SPION applications described in this article, tracking of circulating cells is one with decent clinical potential, as nanoparticles are more suited than small molecule-based contrast agents for labeling and tracking stem and immune cells.

*<sup>64</sup>Cu-Labeled Macrin Nanoparticles for PET Imaging of Macrophages.* TAM density correlates with cancer progression and drug response (8), especially during nano- and immunotherapy. However, imaging the dynamic spatiotemporal distribution of TAMs is challenging, particularly noninvasively. In this context, <sup>64</sup>Cu-labeled macrin nanoparticles were developed to image TAMs and their response to therapy via PET. Macrin nanoparticles comprise a 20-nm polyglucose core, which prevents renal clearance and promotes macrophage uptake (>90% of the administered dose). In a proof-of-concept study, macrin nanoparticles were used to characterize macrophage responses to chemotherapy and radiotherapy (Fig. 1C) (19). Furthermore, TAM-rich tumors identified by macrin nanoparticle-based imaging showed over a 700% higher nanomedicine accumulation than in TAM-deficient tumors. This observation corroborates that TAM imaging is useful for patient stratification in cancer nanomedicine. Beyond cancer, <sup>64</sup>Cu-macrin nanoparticles have also been used to monitor macrophages during infections in mice, rabbits, and pigs (20). Regarding their clinical translation, a phase I clinical trial is currently recruiting participants to further study <sup>64</sup>Cu-macrin nanoparticles. The aim of this study is to evaluate the pharmacokinetics, whole-body distribution, and safety in healthy individuals, as well as nanoparticle accumulation in disease sites in patients with cancer, sarcoidosis, and myocardial infarction.

*Nanoparticles with NIR-II Emission for Imaging Immune Responses.* The NIR-II ranges from 1,000 to 1,700 nm. It has become an attractive optical region for biologic imaging, as tissues show lower autofluorescence, absorption, and scattering, resulting in higher spatial resolution and deeper tissue penetration. Taking advantage of these characteristics, molecular imaging based on NIR-II has been explored to study immunotherapy responses (21). Down-converting nanoparticles functionalized with polymers and antibodies allowed the imaging of programmed death ligand 1 and CD8 in mice with colon cancer, with an impressive tumor-to-normal-tissue signal ratio of 40. Molecular imaging revealed the presence of cytotoxic T cells in tumors in response to immunotherapy. Regarding translation, NIR-II fluorescence imaging holds promise for several niche applications. However, most work done thus far has relied on quantum dots, carbon nanotubes, and lanthanide-based down-converting nanoparticles, which are unlikely to be translated because they are incompletely excreted from the body and possess intrinsic tolerability issues. Conversely, although organic dyes and polymeric nanoparticles loaded with NIR-II fluorophores have somewhat lower quantum yields, they typically display better excretion profiles and currently are the NIR-II imaging probes with the brightest clinical future.

*Nanoparticle-Based SERS for Intraoperative Imaging.* Intraoperative imaging of precursor lesions in live animals has been performed by contrast-enhanced raman endoscopy (Fig. 1D) (22). The nanoparticles used as SERS probes were similar to the ones used in the clinic for the identification of surgical margin tumor surfaces via SERS. With this technique, highly sensitive detection of precursor lesions of gastrointestinal tract cancer in clinically relevant transgenic animal models was achieved. Furthermore, real-time raman endoscopy systems have already been used in the clinic in humans, although not for SERS-based imaging. In this regard, although SERS is one of the most sensitive techniques for detection and analysis, it requires the use of gold (or silver) nanoparticles. At the moment, the future of gold nanoparticles in the clinic is unclear (several clinical trials are ongoing), as a fraction of the injected nanoparticles tends to remain in the liver and spleen of patients for prolonged periods. Therefore, the clinical future of gold nanoparticle-enhanced SERS remains uncertain.

## IMAGING OF NANOPARTICLES

### Patient Stratification in Cancer Nanomedicine

While nanomedicines usually display strong antitumor effects in preclinical studies, their benefits in clinical settings tend to be modest, primarily reducing the side effects of drugs (4). To facilitate clinical translation, oncology practice routinely uses different strategies for patient stratification, including biopsy-based companion diagnostics (e.g., in vitro testing assays) and imaging-based companion diagnostics (e.g., nontherapeutic imageable nanoparticles). For example, in the clinical trials resulting in the approval of trastuzumab and pertuzumab, only patients with high expression levels of human epidermal growth factor receptor 2 (HER2, the antigen for both antibodies) were included, as they were most likely to benefit from treatments. In the case of nanomedicines in the clinic, such strategies are not routinely used to identify patients who should be included in trials and treated with the formulations in question. This is stunning, since nanomedicine performance is known to be strongly affected by the extent of tumor accumulation (i.e., EPR effect), which is highly variable both intra- and interindividually. This lack of stratification may explain multiple recent failures of cancer nanomedicines in

clinical trials (23). Taking these notions into account, several recent studies have now gradually started to explore the use of companion nanodiagnostics and nanotheranostics to visualize and quantify tumor accumulation of nanomedicines in patients (Supplemental Tables 1 and 2).

**SPIONs as Companion Nanodiagnostics.** Ferumoxytol is Food and Drug Administration–approved for the treatment of anemia in patients with kidney disease and can be used to characterize nanoparticle tumor accumulation and EPR heterogeneity via MRI (24). Ferumoxytol accumulation was studied in patients with different types of malignancy. As anticipated, higher levels of ferumoxytol accumulation in tumors correlated with a greater reduction in lesion size on treatment with liposomal irinotecan (which is approved for pancreatic cancer therapy). This pragmatic way of visualizing and quantifying nanoparticle accumulation in tumors via SPION application holds significant clinical potential for use as a companion diagnostic in cancer nanomedicine.

**Radiolabeled Nanoparticles as Nanotheranostic Agents.** An alternative to using a companion nanodiagnostic is coloaded nanomedicines with both drugs and imaging agents. For example, a clinical study showed that PET/CT can assess the tumor accumulation of  $^{64}\text{Cu}$ -labeled HER2-targeted liposomal doxorubicin in metastatic breast cancer patients (25). A retrospective exploratory analysis of

patient outcome confirmed that the tumor deposition of  $^{64}\text{Cu}$ -labeled liposome correlated favorably with therapy outcome. This approach has recently been expanded to other nanoparticle platforms. For instance, the tumor accumulation of docetaxel-loaded polymeric micelles has been studied using PET/CT in 7 patients with solid tumors via radiolabeling of the theranostic nanomedicine formulations with  $^{89}\text{Zr}$  (Fig. 2A) (26). Looking into the future, there are several theranostic radioisotopes, such as  $^{177}\text{Lu}$  and  $^{131}\text{I}$  ( $\beta^-$  and  $\gamma$  emitters), that provide both therapeutic and imaging capabilities. These isotopes have also already been loaded into nanoformulations; however, they have thus far been tested only in preclinical settings (27).

**Gadolinium Nanoparticles as Nanotheranostic Agents.** AGuIX (NH TherAguix SA) nanoparticles are ultrasmall (5 nm) polysiloxane-based nanoformulations that contain approximately a dozen chelated gadolinium ions per particle and are being evaluated in the clinic, particularly for whole-brain radiotherapy enhancement (Supplemental Table 1). AGuIX nanoparticles rely on the potent radiosensitizing properties of gadolinium, which (like other elements with a high atomic number) has a high photoelectric absorption coefficient, delivering a high dose to the surrounding tissue when exposed to ionizing radiation. Thus far, the results of only a phase I completed clinical trial have been published (28), in which single intravenous administrations of AGuIX nanoparticles (doses

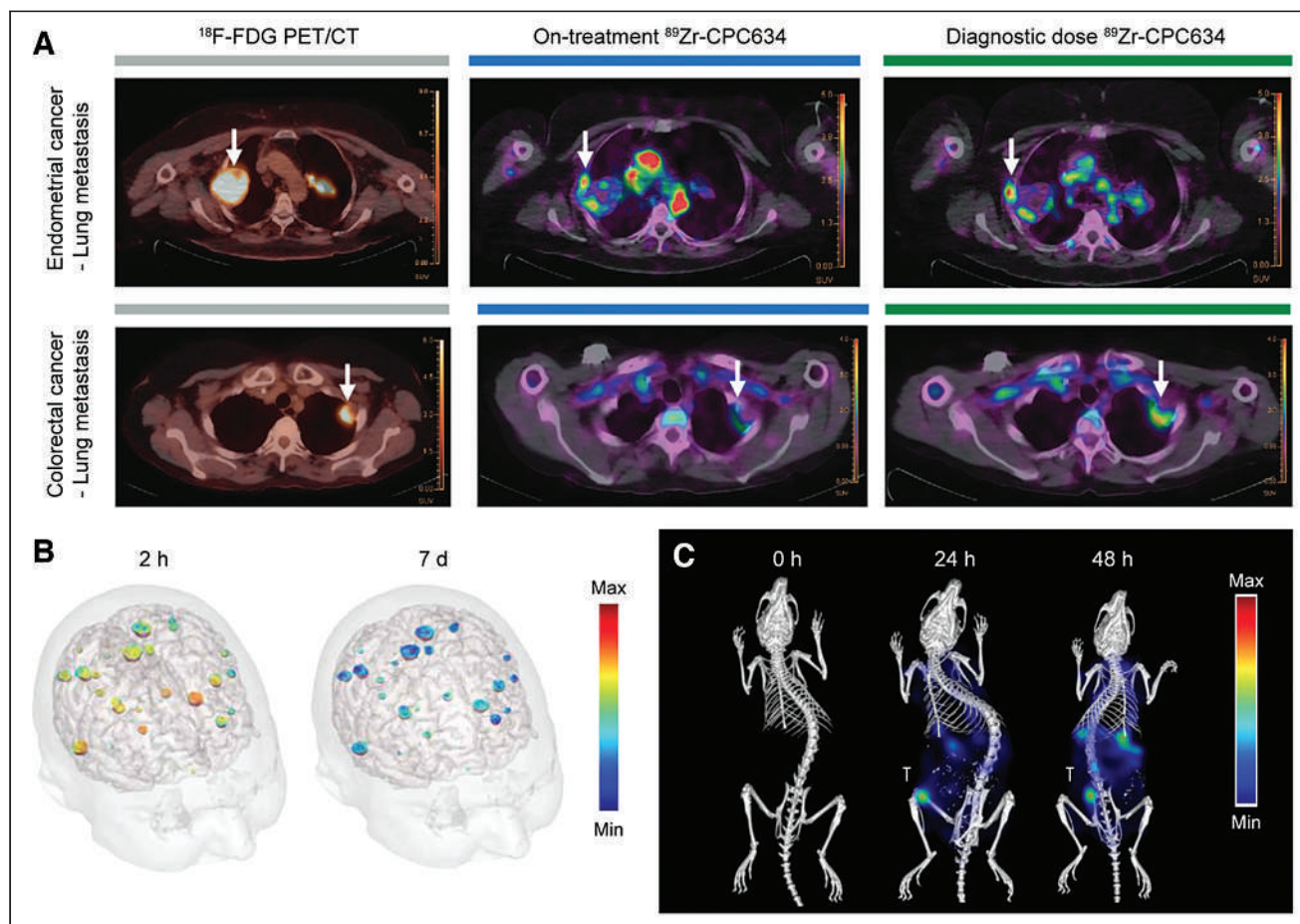


**FIGURE 2.** Imaging of companion diagnostic nanomedicines and nanotheranostics. (A) PET/CT imaging of accumulation of  $^{89}\text{Zr}$ -labeled docetaxel-loaded polymeric micelles ( $^{89}\text{Zr}$ -CPC634) in lung metastases at 96 h after intravenous injection. Arrows indicate tumors. (Adapted with permission of (26).) (B) Color-coded signal-enhanced MRI of upper half of the head of patient with brain metastases resulting from non–small cell lung cancer after intravenous injection of AGuIX. (Adapted with permission of (28).) (C) Biodistribution images of fluorophore-labeled polymeric micelles obtained using hybrid micro-CT fluorescence tomography. (Adapted with permission of (32).) T = orthotopically induced triple-negative breast cancer tumor.

of 15–100 mg/kg of body weight) were studied in 15 patients with 4 types of brain metastases (melanoma, lung, colon, and breast). AGuIX nanoparticles prominently accumulated in and increased image contrast in all types of brain metastases for up to a week after administration (Fig. 2B). At the moment, 7 open clinical trials (phase I/II or II) are ongoing, in which the benefits of AGuIX as a radiosensitizer against several cancers (therapeutic performance), as well as its ability to guide radiotherapy (theranostic performance), are being explored. The results of these studies will define the clinical future of AGuIX nanoparticles.

**Imaging of Therapeutic Nanoparticles.** In addition to nanoparticles specifically developed as imaging or theranostic probes, several nanoparticles that are approved for clinical use as therapeutics also possess intrinsic imaging properties (Supplemental Table 1). For example, NanoTherm (MagForce AG) is a SPION-based nanoformulation used for the treatment of localized cancers with magnetic hyperthermia. These nanoparticles were approved in Europe for the treatment of glioblastoma in 2011 and recently received the green light from the Food and Drug Administration to move to a stage IIb trial for the focal ablation of prostate cancer. SPIONs can be imaged via MRI and MPI, allowing the study of NanoTherm tumor accumulation, retention, or distribution if necessary. Another type of imageable therapeutic nanoparticle is the hafnium oxide nanoparticle (NBTXR3; Nanobiotix), which in 2019 was approved by the European Medicines Agency as an intratumorally injected radiosensitizer for the treatment of soft-tissue sarcoma. NBTXR3 is also in clinical trials for the treatment of other types of cancer (Supplemental Table 2). Hafnium is a high-atomic-number element and (like gadolinium) has a strong photoelectric absorption coefficient, which causes hafnium oxide nanoparticles to display both strong radiosensitizing properties and strong CT contrast. Similarly, gold nanoparticles, which are currently in clinical trials for nucleic acid delivery to glioblastomas and for photothermal ablation therapy of solid tumors (29), also show strong contrast in CT, as well as in photoacoustic imaging. Thus, whereas these nanoformulations were not initially designed as imaging probes, their intrinsic imaging capabilities may assist in promoting their clinical expansion or translation, via providing noninvasive and quantitative information on tumor accumulation and distribution and, thereby, via promoting potential patient stratification.

### **Preclinical Imaging of Nanoparticles for Improved In Vivo Performance**

When not used as tools for clinical diagnosis and decision making, nanoparticle imaging can be performed to better understand and refine nanoparticle behavior and performance in vivo. Efforts in this regard include characterizing nanoparticle pharmacokinetics and biodistribution, performing mechanistic studies on the principles of nanoparticle tumor accumulation, and monitoring local drug release from nanoparticles on external stimuli. In the last couple of years, new studies relying heavily on multiimaging setups have challenged some of the long-standing paradigms in nanomedicine and drug delivery.

**Imaging Nanoparticles in Circulation and During Extravasation.** The accumulation of nanomedicines in tumors is widely believed to be caused by passive diffusion of nanoparticles through the gaps between endothelial cells in tumor blood vessels. This notion, which is an essential component of the EPR effect, has been one of the driving forces for the development of nanocarriers that can maximize convection or diffusion through interendothelial gaps. Recently, new research has questioned the prominence of this extravasation

mechanism by identifying new transport processes, such as phagocyte hijacking in the bloodstream (30). By combining transmission electron microscopy, 3-dimensional microscopy, and dynamic intravital microscopy, it has been reported that although gaps between endothelial cells occur, they are not frequent and their role in nanoparticle tumor accumulation may thus be overestimated. Similar multiimaging efforts have set out to measure nanoparticle uptake rates by Kupffer cells in vivo, identifying a concentration threshold above which Kupffer cells get overwhelmed and liver clearance decreases, prolonging nanoparticle circulation and enhancing the therapeutic effect of nanotherapies (31).

**Multiscale Imaging of the Biodistribution of Nanomedicines.** Clinical-stage polymeric micelles were fluorophore-labeled to investigate their biodistribution and target site accumulation (32). The micelles were imaged at the whole-body, tissue, and cellular level by multimodal and multiscale optical imaging approaches (Fig. 2C), including 3-dimensional micro-CT fluorescence tomography and 2-dimensional fluorescence reflectance imaging, among others. The polymeric micelles achieved a high tumor accumulation, with values twice as high as those observed in liver and spleen. Moreover, from the observation that 66% of intratumoral polymeric micelles were extracellularly located, the authors concluded that the anticancer efficacy of polymeric micelles is likely caused by release of the drugs in the tumor microenvironment, providing key information for the design of nanoformulations. Regarding the remaining 33% of intratumoral polymeric micelles, they predominantly accumulated in phagocytes, which may provide new opportunities for nanoimmunotherapy.

**Monitoring Drug Release from Nanomedicines.** Nanomedicines need to release their payload at the tumor site to achieve proper therapeutic outcomes. To study drug release in vivo, different imaging strategies have been explored. One possible approach relies on the inherent fluorescence emission of chemotherapeutic drugs, such as topotecan (topoisomerase I inhibitor), which is an anticancer agent and shows strong pH-dependent fluorescence (33). Alternatively, triggerable nanomedicine formulations can be coloaded with drugs and imaging agents that are released at the same time as the drugs. In such setups, gadolinium chelates have been used on multiple occasions to monitor drug release from (thermo-, sono-, and pH-) responsive liposomes via MRI (34), confirming that therapeutic cargo is released at the tumor site. These efforts are valuable to optimize formulation design and confirm preclinical performance and clinical potential, but because of their unpragmatic nature and insufficient cost efficiency and time efficiency, it is unlikely that they will be widely implemented in the clinic.

### **SUMMARY AND OUTLOOK**

After several decades of preclinical and clinical progress, successes, and setbacks, nanoparticle-based imaging agents are slowly but steadily making a mark in disease diagnosis and clinical decision making (Supplemental Tables 1 and 2). Initial paradigms based on smart, multimodal, or multifunctional nanomaterials that are universally useful for the detection of all sorts of diseases have shifted to more pragmatic and realistic approaches in which nanoparticles are used for very specific diagnostic applications. On the one hand, these applications are strongly dictated by the pharmacokinetic properties of the nanoparticles, as well as by their propensity to accumulate in specific tissues and cells. On the other hand, the applicability of nanoparticle-based imaging agents strongly depends on the

availability of alternative diagnostic probes and protocols, or more explicitly, the lack thereof.

Theranostic nanoparticles, which combine diagnostic and therapeutic features in a single formulation, can provide information about their biodistribution and about target site accumulation, distribution, and retention. This is a potential avenue toward patient stratification, which is performed routinely in the development of oncologic treatments but hardly ever in nanomedicine. Advances in this direction will increasingly profit from combination with machine-learning techniques, which can contribute to many aspects of basic, translational, and clinical nanoparticle research, such as via formulation optimization or via pathologic and radiomic feature identification related to nanomedicine target site accumulation and efficacy. Novel nanoparticle formats are furthermore developed to align with advances in the engineering of novel imaging instrumentation, including ones implemented in surgical theaters, giving rise to new diagnostic and theranostic methods. Finally, nanoparticles are also extensively explored for ex vivo sensing applications, such as in point-of-care devices and in coronavirus self-tests.

Altogether, it can be concluded that nanoparticles are increasingly impacting clinical imaging and diagnostic decision making and that there is promising preclinical progress toward the development of novel nanoparticle-based imaging protocols.

## DISCLOSURE

This work is funded under the Excellence Strategy of the Federal Government and the Länder, by the European Research Council (ERC COG Meta-Targeting; 864121), by the German Federal Ministry of Research and Education (BMBF; 16GW0319K), and by the German Research Foundation (DFG; GRK2375 [331065168], LA2937/4-1, and SFB1066). No other potential conflict of interest relevant to this article was reported.

## REFERENCES

- Kim J, Lee N, Hyeon T. Recent development of nanoparticles for molecular imaging. *Philos Trans A Math Phys Eng Sci.* 2017;375:20170022.
- Rizzo LY, Theek B, Storm G, Kiessling F, Lammers T. Recent progress in nanomedicine: therapeutic, diagnostic and theranostic applications. *Curr Opin Biotechnol.* 2013;24:1159–1166.
- Golombek SK, May J-N, Theek B, et al. Tumor targeting via EPR: strategies to enhance patient responses. *Adv Drug Deliv Rev.* 2018;130:17–38.
- van der Meel R, Sulheim E, Shi Y, Kiessling F, Mulder WJM, Lammers T. Smart cancer nanomedicine. *Nat Nanotechnol.* 2019;14:1007–1017.
- Anselmo AC, Mitragotri S. Nanoparticles in the clinic: an update post COVID-19 vaccines. *Bioeng Transl Med.* 2021;6:e10246.
- Thakor AS, Jokerst JV, Ghanouni P, Campbell JL, Mitra E, Gambhir SS. Clinically approved nanoparticle imaging agents. *J Nucl Med.* 2016;57:1833–1837.
- Kallianos K, Henry TS, Yeghiazarians Y, et al. Ferumoxytol MRA for transcatheter aortic valve replacement planning with renal insufficiency. *Int J Cardiol.* 2017;231:255–257.
- Pathria P, Louis TL, Varner JA. Targeting tumor-associated macrophages in cancer. *Trends Immunol.* 2019;40:310–327.
- Iv M, Samghabadi P, Holdsworth S, et al. Quantification of macrophages in high-grade gliomas by using ferumoxytol-enhanced MRI: a pilot study. *Radiology.* 2019;290:198–206.
- Taruno K, Kurita T, Kuwahata A, et al. Multicenter clinical trial on sentinel lymph node biopsy using superparamagnetic iron oxide nanoparticles and a novel handheld magnetic probe. *J Surg Oncol.* 2019;120:1391–1396.
- Schilham MGM, Zamecnik P, Privé BM, et al. Head-to-head comparison of  $^{68}\text{Ga}$ -prostate-specific membrane antigen PET/CT and ferumoxtran-10-enhanced MRI for the diagnosis of lymph node metastases in prostate cancer patients. *J Nucl Med.* 2021;62:1258–1263.
- Zanoni DK, Stambuk HE, Madajewski B, et al. Use of ultrasmall core-shell fluorescent silica nanoparticles for image-guided sentinel lymph node biopsy in head and neck melanoma: a nonrandomized clinical trial. *JAMA Netw Open.* 2021;4:e211936.
- Janjua TI, Cao Y, Yu C, Popat A. Clinical translation of silica nanoparticles. *Nat Rev Mater.* 2021;6:1072–1074.
- Voskuil FJ, Steinkamp PJ, Zhao T, et al. Exploiting metabolic acidosis in solid cancers using a tumor-agnostic pH-activatable nanoprobe for fluorescence-guided surgery. *Nat Commun.* 2020;11:3257.
- Wang YW, Reder NP, Kang S, et al. Raman-encoded molecular imaging with topically applied SERS nanoparticles for intraoperative guidance of lumpectomy. *Cancer Res.* 2017;77:4506–4516.
- Lu Y, Xu Y-J, Zhang G-B, et al. Iron oxide nanoclusters for T1 magnetic resonance imaging of non-human primates. *Nat Biomed Eng.* 2017;1:637–643.
- Ludewig P, Gdaniec N, Sedlacik J, et al. Magnetic particle imaging for real-time perfusion imaging in acute stroke. *ACS Nano.* 2017;11:10480–10488.
- Kiru L, Zlitni A, Tousley Aidan M, et al. In vivo imaging of nanoparticle-labeled CAR T cells. *Proc Natl Acad Sci USA.* 2022;119:e2102363119.
- Kim H-Y, Li R, Ng TSC, et al. Quantitative imaging of tumor-associated macrophages and their response to therapy using  $^{64}\text{Cu}$ -labeled macrin. *ACS Nano.* 2018;12:12015–12029.
- Nahrendorf M, Hoyer FF, Meerwaldt AE, et al. Imaging cardiovascular and lung macrophages with the positron emission tomography sensor  $^{64}\text{Cu}$ -macrin in mice, rabbits, and pigs. *Circ Cardiovasc Imaging.* 2020;13:e010586.
- Zhong Y, Ma Z, Wang F, et al. In vivo molecular imaging for immunotherapy using ultra-bright near-infrared-IIb rare-earth nanoparticles. *Nat Biotechnol.* 2019;37:1322–1331.
- Harmsen S, Rogalla S, Huang R, et al. Detection of premalignant gastrointestinal lesions using surface-enhanced resonance Raman scattering–nanoparticle endoscopy. *ACS Nano.* 2019;13:1354–1364.
- He H, Liu L, Morin EE, Liu M, Schwendeman A. Survey of clinical translation of cancer nanomedicines: lessons learned from successes and failures. *Acc Chem Res.* 2019;52:2445–2461.
- Ramanathan RK, Kom RL, Raghunand N, et al. Correlation between ferumoxytol uptake in tumor lesions by MRI and response to nanoliposomal irinotecan in patients with advanced solid tumors: a pilot study. *Clin Cancer Res.* 2017;23:3638–3648.
- Lee H, Shields AF, Siegel BA, et al.  $^{64}\text{Cu}$ -MM-302 positron emission tomography quantifies variability of enhanced permeability and retention of nanoparticles in relation to treatment response in patients with metastatic breast cancer. *Clin Cancer Res.* 2017;23:4190–4202.
- Miedema IHC, Zwezerijnen GJC, Huisman MC, et al. PET-CT imaging of polymeric nanoparticle tumor accumulation in patients. *Adv Mater.* 2022;34:2201043.
- Pallares RM, Abergel RJ. Nanoparticles for targeted cancer radiotherapy. *Nano Rev.* 2020;13:2887–2897.
- Verry C, Dufort S, Lemasson B, et al. Targeting brain metastases with ultrasmall theranostic nanoparticles, a first-in-human trial from an MRI perspective. *Sci Adv.* 2020;6:eaay5279.
- Zhang R, Kiessling F, Lammers T, Pallares RM. Clinical translation of gold nanoparticles. *Drug Deliv Transl Res.* August 31, 2022 [Epub ahead of print].
- Sofias AM, Toner YC, Meerwaldt AE, et al. Tumor targeting by  $\alpha_v\beta_3$ -integrin-specific lipid nanoparticles occurs via phagocyte hitchhiking. *ACS Nano.* 2020;14:7832–7846.
- Ouyang B, Poon W, Zhang Y-N, et al. The dose threshold for nanoparticle tumour delivery. *Nat Mater.* 2020;19:1362–1371.
- Biancacci I, Sun Q, Möckel D, et al. Optical imaging of the whole-body to cellular biodistribution of clinical-stage PEG-b-pHPMA-based core-crosslinked polymeric micelles. *J Control Release.* 2020;328:805–816.
- Centelles MN, Wright M, So P-W, et al. Image-guided thermosensitive liposomes for focused ultrasound drug delivery: using NIRF-labelled lipids and topotecan to visualise the effects of hyperthermia in tumours. *J Control Release.* 2018;280:87–98.
- Reeßing F, Szymanski W. Following nanomedicine activation with magnetic resonance imaging: why, how, and what's next? *Curr Opin Biotechnol.* 2019;58:9–18.

# Validation of $^{18}\text{F}$ -rhPSMA-7 and $^{18}\text{F}$ -rhPSMA-7.3 PET Imaging Results with Histopathology from Salvage Surgery in Patients with Biochemical Recurrence of Prostate Cancer

Markus Kroenke<sup>1,2</sup>, Lilit Schweiger<sup>1,3</sup>, Thomas Horn<sup>4</sup>, Bernhard Haller<sup>5</sup>, Kristina Schwamborn<sup>6</sup>, Alexander Wurzer<sup>1,7</sup>, Tobias Maurer<sup>8</sup>, Hans-Jürgen Wester<sup>7</sup>, Matthias Eiber<sup>\*1,3</sup>, and Isabel Rauscher<sup>\*1,3</sup>

<sup>1</sup>Department of Nuclear Medicine, School of Medicine, Technical University of Munich, Munich, Germany; <sup>2</sup>Department of Radiology and Nuclear Medicine, German Heart Center Munich, Technical University of Munich, Munich, Germany; <sup>3</sup>Bavarian Cancer Research Center (BZKF), Munich, Germany; <sup>4</sup>Department of Urology, School of Medicine, Technical University of Munich, Munich, Germany; <sup>5</sup>Institute of Medical Informatics, Statistics and Epidemiology, School of Medicine, Technical University of Munich, Munich, Germany; <sup>6</sup>Department of Pathology, School of Medicine, Technical University of Munich, Munich, Germany; <sup>7</sup>Chair of Radiopharmacy, School of Medicine, Technical University of Munich, Munich, Germany; and <sup>8</sup>Martini-Klinik and Department of Urology, University Hospital Hamburg-Eppendorf, Hamburg, Germany

$^{18}\text{F}$ -rhPSMA-7, and its single diastereoisomer form,  $^{18}\text{F}$ -rhPSMA-7.3, are prostate-specific membrane antigen (PSMA)-targeting radiopharmaceuticals. Here, we investigated their accuracy for the assessment of lymph node (LN) metastases validated by histopathology. **Methods:** Data from 58 patients with biochemical recurrence of prostate cancer after radical prostatectomy receiving salvage surgery after PET imaging with  $^{18}\text{F}$ -rhPSMA-7 or  $^{18}\text{F}$ -rhPSMA-7.3 were retrospectively reviewed. Two nuclear medicine physicians reviewed all PET scans and morphologic imaging in consensus. Readers were masked from the results of histopathology. PET and morphologic imaging were correlated with histopathology from resected LNs. **Results:** In 75 of 150 resected regions in 54 of 58 patients, tumor lesions were present in histopathology. The template-based specificity of PET ( $^{18}\text{F}$ -rhPSMA-7 and  $^{18}\text{F}$ -rhPSMA-7.3 combined) and morphologic imaging was 93.3% and 100%, respectively. However,  $^{18}\text{F}$ -rhPSMA-7 and  $^{18}\text{F}$ -rhPSMA-7.3 PET detected metastases in 61 of 75 histopathologically proven metastatic LN fields (81.3%) whereas morphologic imaging was positive in only 9 of 75 (12.0%). The positive predictive value was 92.4% for  $^{18}\text{F}$ -rhPSMA-7 and  $^{18}\text{F}$ -rhPSMA-7.3 PET and 100% for morphologic imaging.  $^{18}\text{F}$ -rhPSMA-7 and  $^{18}\text{F}$ -rhPSMA-7.3 PET performance was significantly superior to morphologic imaging (difference in the areas under the receiver-operating-characteristic curves, 0.222; 95% CI, 0.147–0.298;  $P < 0.001$ ). The mean size of PET-positive and histologically confirmed LN metastases was  $6.3 \pm 3.1$  mm (range, 2–15 mm) compared with a mean size of  $9.8 \pm 2.5$  mm (range, 7–15 mm) on morphologic imaging. **Conclusion:**  $^{18}\text{F}$ -rhPSMA-7 and  $^{18}\text{F}$ -rhPSMA-7.3 PET offer a high positive predictive value comparable to that reported for  $^{68}\text{Ga}$ -PSMA-11 and represent a valuable tool for guiding salvage lymphadenectomy.

**Key Words:**  $^{18}\text{F}$ -rhPSMA-7;  $^{18}\text{F}$ -rhPSMA-7.3; prostate cancer; salvage surgery; biochemical recurrence; prostate-specific membrane antigen

J Nucl Med 2022; 63:1809–1814  
DOI: 10.2967/jnumed.121.263707

Received Dec. 25, 2021; revision accepted Mar. 28, 2022.  
For correspondence or reprints, contact Isabel Rauscher (isabel.rauscher@tum.de).

\*Contributed equally to this work.

Published online Apr. 7, 2022.

COPYRIGHT © 2022 by the Society of Nuclear Medicine and Molecular Imaging.

Up to one third of all patients with prostate cancer (PC) will experience biochemical recurrence after initial curative-intended treatment (1). Salvage therapies such as salvage surgery and other metastasis-directed treatments can prolong the interval until systemic therapy is needed (2–4). To perform any localized treatment, for either metastasis or local recurrence, accurate diagnostic imaging is of utmost importance. Several studies have already proven the superiority of PET targeting the prostate-specific membrane antigen (PSMA) compared with morphologic imaging (e.g., CT and MRI) for localization of recurrent disease or for primary N staging (5,6). In this context,  $^{68}\text{Ga}$ -PSMA-11 has been the PSMA-ligand most extensively assessed in several retrospective and prospective studies, leading to its approval and recommendation by various guidelines as the preferred imaging tool for restaging (7–11).

However,  $^{18}\text{F}$ -labeled PSMA-targeting ligands are becoming increasingly used in preference to  $^{68}\text{Ga}$ -labeled counterparts because of the principal advantages of radiofluorinated tracers (e.g., longer half-life and large batch production in cyclotrons leading to the possibility of centralized production and distribution as well as lower positron energy of  $^{18}\text{F}$  compared with  $^{68}\text{Ga}$ ) (12).

$^{18}\text{F}$ -rhPSMA-7 is one such  $^{18}\text{F}$ -labeled PSMA-targeting ligand representing a class of radiohybrid PSMA (rhPSMA) ligands that can be labeled with  $^{18}\text{F}$  for imaging purposes but also with other radioactive isotopes such as  $^{177}\text{Lu}$  for endoradiotherapy (13).  $^{18}\text{F}$ -rhPSMA-7 is composed of 4 diastereoisomers ( $^{18}\text{F}$ -rhPSMA-7.1–7.4) (14). Of these,  $^{18}\text{F}$ -rhPSMA-7.3 was selected for clinical development on the basis of its superior characteristics in preclinical studies, including fast clearance from blood pool, liver, and kidneys as well as high tumor accumulation in LNCaP tumor-bearing mice (14).  $^{18}\text{F}$ -rhPSMA-7.3 is currently under investigation in 2 multicenter phase III trials for PET imaging (NCT04186845 and NCT04186819); it shows properties similar to those of the isomeric mixture  $^{18}\text{F}$ -rhPSMA-7, with both PSMA-ligands demonstrating high detection rates in patients with biochemical recurrence of PC (15,16).

However, to date, no histopathology-validated study on the use of  $^{18}\text{F}$ -rhPSMA-7.3 in patients with biochemical recurrence of PC has been published. Thus, the aim of this retrospective analysis was to assess the performance of  $^{18}\text{F}$ -rhPSMA-7 and  $^{18}\text{F}$ -rhPSMA-7.3 PET

in patients with biochemical recurrence after radical prostatectomy undergoing subsequent salvage surgery for histopathologic comparison.

## MATERIALS AND METHODS

### Patients

We retrospectively reviewed the institution's database for all patients with biochemical recurrence of PC who underwent either  $^{18}\text{F}$ -rhPSMA-7 or  $^{18}\text{F}$ -rhPSMA-7.3 PET and subsequent salvage surgery between November 2017 and June 2020. Patients were excluded if they had not undergone radical prostatectomy as a primary treatment. In total, 58 patients were identified. The retrospective analysis was approved by the local ethics committee (permit 290/18S and 99/19). Administration of  $^{18}\text{F}$ -rhPSMA-7 and  $^{18}\text{F}$ -rhPSMA-7.3 complied with the German Medicinal Products Act, AMG §13 2b, and the responsible regulatory body (government of Oberbayern).

### $^{18}\text{F}$ -rhPSMA Synthesis, Administration, and PET Imaging

$^{18}\text{F}$ -rhPSMA-7 and  $^{18}\text{F}$ -rhPSMA-7.3 were synthesized and used as previously reported (13,17,18). Twenty-three (40%) patients received  $^{18}\text{F}$ -rhPSMA-7, and 35 (60%) patients received the single-isomer  $^{18}\text{F}$ -rhPSMA-7.3.  $^{18}\text{F}$ -rhPSMA-7 and  $^{18}\text{F}$ -rhPSMA-7.3 were administered (median activity, 320 MBq; range, 239–399 MBq) as an intravenous bolus a median of 72 min (range, 60–148 min) before scanning. In total, 49 patients underwent contrast-enhanced PET/CT (Biograph mCT Flow [Siemens Healthineers]; contrast agent: Imeron 300 [Bracco Imaging]), and 9 patients underwent PET/MRI (Biograph mMR; Siemens Healthineers). The fully diagnostic PET/CT and PET/MRI examinations were conducted as previously reported (19,20). Furosemide (20 mg intravenously) was administered to all patients at the time of tracer application, and patients were asked to void urine before the scan.

All PET/CT scans were acquired in 3-dimensional mode with time of flight and in continuous table motion (flowMotion technology, Siemens (21)) with 1.1 mm/s, equal to 2 min per bed position. The PET/MRI scans were acquired in 3-dimensional mode and step-and-shoot with 4 min per bed position for PET/MRI. Emission data were corrected for randoms, dead time, scatter, and attenuation and were reconstructed iteratively by an ordered-subsets expectation maximization algorithm (4 iterations, 8 subsets) followed by a postreconstruction smoothing gaussian filter (5 mm in full width at half maximum).

### Image Analysis

All  $^{18}\text{F}$ -rhPSMA-7 and  $^{18}\text{F}$ -rhPSMA-7.3 PET/CT and PET/MRI datasets were reviewed by 2 experienced board-certified nuclear medicine specialists in consensus. The readers were masked to the results of histopathology. First, the CT dataset of the PET/CT or the dedicated high-resolution axial T2-weighted turbo spin echo sequence of the pelvis up to the aortic bifurcation (slice thickness, 5 mm each) of the PET/MRI were analyzed. Second, after an interval of at least 4 wk, the corresponding  $^{18}\text{F}$ -rhPSMA-7 and  $^{18}\text{F}$ -rhPSMA-7.3 PET scans were read by the same readers, with the morphologic imaging only being used for anatomic allocation. Findings were rated using a 5-point Likert scale as described previously (22): PET rating of 5 indicates a tumor manifestation (intense, focal uptake, uptake higher than in the liver); 4, probable tumor manifestation (uptake clearly higher than the background level in vessels but less than in the liver); 3, equivocal findings (faint uptake between muscle and vessels uptake); 2, probable benign findings (uptake equal to the adjacent muscle); 1, benign findings (no uptake).

For both CT and MRI, the same Likert scale was applied with a rating of 5 indicating tumor manifestation (lymph node short-axis diameter > 10 mm); 4, probable tumor manifestation (short-axis diameter of 8–10 mm or a round configuration or a regional grouping); 3, equivocal findings (short-axis diameter of 8–10 mm, an oval configuration, and no regional grouping); 2, probable benign findings (short-axis diameter

< 8 mm); and 1, benign findings (short-axis diameter < 5 mm). Finally,  $\text{SUV}_{\text{max}}$  and size (short-axis diameter) of the largest lymph node per template region rated with a score 4 or 5 were measured.

### Surgery and Histopathology

The patients were selected for salvage surgery by an interdisciplinary tumor board based on clinical characteristics and the initial clinical reads of  $^{18}\text{F}$ -rhPSMA-7 or  $^{18}\text{F}$ -rhPSMA-7.3 PET. The salvage surgery was planned based on the information on PET and the surgical fields were limited to the pelvis including potential local recurrence. Depending on the location, adjacent lymph node template regions were resected as well. The lymph node template regions were separately collected. Uropathologists were masked to imaging results.

### Statistical Analysis

The histopathologic results from resected lymph nodes were correlated with the results of morphologic imaging (MRI or CT) and  $^{18}\text{F}$ -rhPSMA-7 and  $^{18}\text{F}$ -rhPSMA-7.3 PET in a patient- and template-based manner. Further, a separate template-based analysis of  $^{18}\text{F}$ -rhPSMA-7 and  $^{18}\text{F}$ -rhPSMA-7.3 was performed. Results from the 5-point Likert scale were dichotomized to allow estimation of sensitivity, specificity, positive predictive value (PPV), and accuracy. For the statistical analysis, we decided that only scores indicating definitive or probable tumor manifestation on PET and morphologic imaging (scores  $\geq$  4) were counted as positive. This decision was based on a clinical consideration that invasive procedures (e.g., secondary lymphadenectomy and associated general anesthesia) with their potential risks are not justified if only equivocal findings (score 3) are present.

The overall diagnostic accuracy of template-based data was assessed using receiver-operating-characteristic (ROC) analyses. ROC curves were calculated for both modalities. Areas under the ROC curves with 95% CIs were calculated and compared with each other. The approach proposed by Obuchowski was considered for region-based analyses to account for correlations of multiple findings within 1 patient with the help of generalized estimating equations extension of linear regression model (23). A significance level of 5% was considered for all tests. All statistical analyses were performed using the statistical software R with its packages pROC and geepack (24–26).

## RESULTS

### Patient Characteristics and Histopathologic Results

The data for 58 patients were reviewed. The patients were a median age of 68.5 y (age range, 51–85 y) and presented with a median prostate-specific antigen (PSA) level of 0.71 ng/mL (range, 0.16–8.39 ng/mL) before the PET scan. Detailed patient characteristics are presented in Table 1. Supplemental Tables 1 and 2 (supplemental materials are available at <http://jnm.snmjournals.org>) provide detailed per-patient information on patient characteristics, imaging methods, and results.

In 54 of 58 patients, pelvic tumor lesions were confirmed by histopathology. Overall, 150 template regions were resected, with 75 of these harboring tumor lesions (50%). Most ( $n = 129$ ) were part of the typical pelvic lymph node template. Other resected regions were 9 retroperitoneal locations ( $n = 6$  positive on histopathology) and 12 local regions due to suspicion of local recurrence ( $n = 10$  positive on histopathology).

### Imaging Results

The template-based areas under the ROC curves for  $^{18}\text{F}$ -rhPSMA-7 and  $^{18}\text{F}$ -rhPSMA-7.3 were 0.891 (95% CI, 0.838–0.944) and for morphologic imaging 0.669 (95% CI, 0.595–0.742, Fig. 1).  $^{18}\text{F}$ -rhPSMA-7 and  $^{18}\text{F}$ -rhPSMA-7.3 PET performed significantly better than morphologic imaging for the detection of lymph node metastases

**TABLE 1**  
Patient Characteristics (*n* = 58)

Characteristic	Data (%)
Age (y)	
Median	68.5
Range	51–85
iPSA (ng/mL)*	
Median	10.00
Range	1.9–57.9
ISUP grade ( <i>n</i> )	
1–2	17 (29)
3–4	27 (47)
5	10 (17)
Missing	4 (6.9)
Pathologic T stage at primary RPE ( <i>n</i> )	
≤pT2c	23 (40)
pT3a	11 (19)
≥pT3b	18 (31)
Missing	6 (10)
Pathologic N stage at primary RPE ( <i>n</i> )	
pN0	39 (67)
pN1	10 (17)
Missing	9 (16)
Time between primary surgery and PET (mo)	
Median	48
Range	1–278
Prescan PSA (ng/mL) <sup>†</sup>	
Median	0.71
Range	0.16–8.39
Time between PET and salvage surgery (d)	
Median	59
Range	19–117
Lymph node regions removed at salvage LAE	
N	150
Median	2
Range	1–9
Lymph node regions with metastases at salvage LAE	
N	75
Median	1
Range	0–4

\*Not available in 12 cases.

<sup>†</sup>Not available in 1 case.

iPSA = initial PSA concentration; ISUP = International Society of Urological Pathology; RPE = radical prostatectomy; PSA = prostate-specific antigen; LAE = lymphadenectomy.

Data in parentheses are percentages unless otherwise specified.

(difference in areas under the ROC curves, 0.222; 95% CI, 0.147–0.298; *P* < 0.001).

On the template-based analysis, specificity was 93.3% (95% CI, 85.9%–97.0%) and 100% (95% CI, not available) for <sup>18</sup>F-

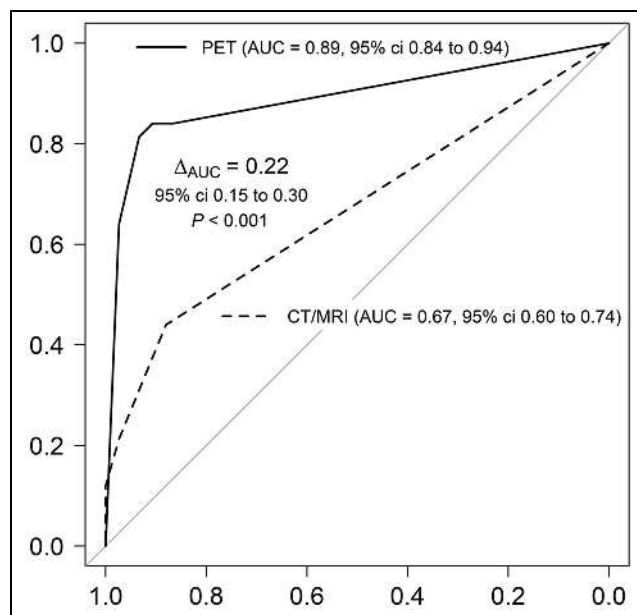


**FIGURE 1.** Template-based ROC curves for combined data of <sup>18</sup>F-rhPSMA-7 and <sup>18</sup>F-rhPSMA-7.3 PET (black line) and morphologic imaging (CT/MRI) (dotted line) for assessment of lymph node metastases in all 150 lymph node regions. AUC = area under the curve.

rhPSMA-7 and <sup>18</sup>F-rhPSMA-7.3 PET and morphologic imaging, respectively. <sup>18</sup>F-rhPSMA-7 and <sup>18</sup>F-rhPSMA-7.3 PET detected lymph node metastases in 61 of 75 histopathologically proven metastatic lymph node template regions (sensitivity, 81.3%; 95% CI, 70.1%–89.0%) whereas morphologic imaging was positive in only 9 of 75 lymph node templates (sensitivity, 12.0% 95% CI, 6.3%–21.6%). The PPV was 92.4% for <sup>18</sup>F-rhPSMA-7 and <sup>18</sup>F-rhPSMA-7.3 PET and 100% for morphologic imaging. The diagnostic accuracy was 87.3% (95% CI, 80.5%–92.0%) for <sup>18</sup>F-rhPSMA-7 and <sup>18</sup>F-rhPSMA-7.3 PET and 64.5% (95% CI, 47.2%–64.5%) for morphologic imaging (Table 2).

In detail, 75 template regions were free of tumor invasion after histopathologic evaluation, with 70 of them being correctly identified as negative with PET and 75 of them being correctly identified as negative with morphologic imaging. Five template regions (in 3 patients) were classified as suspicious on PET, with no correlation on histopathology (false-positive), whereas morphologic imaging resulted in no template regions being judged as false positive. Follow-up was available in 2 of the patients with false-positive results on PET with slightly increasing PSA levels after surgery but no sign of metastasis in the follow-up <sup>18</sup>F-rhPSMA-7 and <sup>18</sup>F-rhPSMA-7.3 PET scan.

Fourteen template regions were false-negative on PET, whereas 66 template regions resulted in a false-negative finding on morphologic imaging. Data for the patient-based analysis are presented in Supplemental Table 3. A separate analysis of <sup>18</sup>F-rhPSMA-7 and <sup>18</sup>F-rhPSMA-7.3 is presented in Supplemental Table 4; in this table, <sup>18</sup>F-rhPSMA-7 and <sup>18</sup>F-rhPSMA-7.3 PET presented with a similar PPV (92.3% for <sup>18</sup>F-rhPSMA-7 and 92.5% for <sup>18</sup>F-rhPSMA-7.3).

#### Uptake in <sup>18</sup>F-rhPSMA-7 and <sup>18</sup>F-rhPSMA-7.3 PET and Lesion Size

The mean SUV<sub>max</sub> of histologically confirmed pelvic lymph node metastases rated as suspicious on PET was 16.7 ± 24.7 (range,

**TABLE 2**  
Template-Based Analysis

<sup>18</sup> F-rhPSMA-7.3 PET/CT rating	Histology: lymph node metastasis		Proportions
	Positive	Negative	
Combined data for <sup>18</sup> F-rhPSMA-7 and <sup>18</sup> F-rhPSMA-7.3			
Positive	61	5	PPV: 92.4% (95% CI, 83.3%–96.8%)
Negative	14	70	NPV: 83.3% (95% CI, 72.2%–90.6%)
Total	75	75	150
	Sensitivity: 81.3% (95% CI, 70.1%–89.0%)	Specificity: 93.3% (95% CI, 85.9%–97.0%)	Accuracy: 87.3% (95% CI, 80.5–92.0)
Morphologic imaging (CT/MRI)			
Positive	9	0	PPV: 100% (95% CI, N/A)
Negative	66	75	NPV: 53.2% (95% CI, 44.5%–61.6%)
Total	75	75	150
	Sensitivity: 12.0% (95% CI, 6.3%–21.6%)	Specificity: 100% (95% CI, N/A)	Accuracy: 64.5% (95% CI, 47.2%–64.5%)

Scores  $\geq 4$  in PET and morphologic imaging rated positive.

NPV = negative predictive value; N/A = not available as cannot be calculated (there exists no CI for point estimator of 1 in a generalized estimating equation).

3.3–146.6). The corresponding mean lesion size of these PET-positive, histologically confirmed lymph nodes was  $6.3 \pm 3.1$  mm (range, 2–15 mm). The mean size of histologically confirmed lymph nodes rated as suspicious on morphologic imaging was  $10.6 \pm 2.7$  mm (range, 7–15 mm). The mean size of histologically confirmed lymph nodes not rated as suspicious on morphologic imaging was  $5.3 \pm 2.3$  mm (range, 2–14 mm).

A representative example of a correctly classified lymph node metastases by PET/CT is shown in Figure 2.

## DISCUSSION

The value of PSMA PET for imaging patients with recurrence of PC after primary treatment has been extensively reported (5,6,20, 27–29). Here, we reviewed real-world clinical data supporting the utility of the novel PSMA-targeting radiopharmaceuticals <sup>18</sup>F-rhPSMA-7 and <sup>18</sup>F-rhPSMA-7.3. To date, the efficacy of both <sup>18</sup>F-rhPSMA-7 and <sup>18</sup>F-rhPSMA-7.3 for imaging PC patients has been demonstrated by several retrospective studies (15,16,30), including their high accuracy for lymph node staging in patients with primary PC (22,31). The presented data demonstrate a high specificity and PPV of <sup>18</sup>F-rhPSMA-7 and <sup>18</sup>F-rhPSMA-7.3 PET for lymph node metastases in patients with recurrent PC after radical prostatectomy validated by histopathology. On a template-based analysis, <sup>18</sup>F-rhPSMA-7.3 offers a higher accuracy and sensitivity than morphologic imaging.

These results are in line with a similar, histopathologically validated analysis using <sup>68</sup>Ga-PSMA-11 that showed a sensitivity, specificity, and PPV of 77.9%, 97.3%, and 94.6%, respectively, compared with 81.3%, 93.3%, and 92.4% in our analysis, respectively (5). Further, the difference in the areas under the receiver-operating-characteristic curves for morphologic images was 0.139 with <sup>68</sup>Ga-PSMA-11 compared with 0.222 with <sup>18</sup>F-rhPSMA-7 and <sup>18</sup>F-rhPSMA-7.3 in our analysis (5). Similar to <sup>68</sup>Ga-PSMA-11 PET, our data show

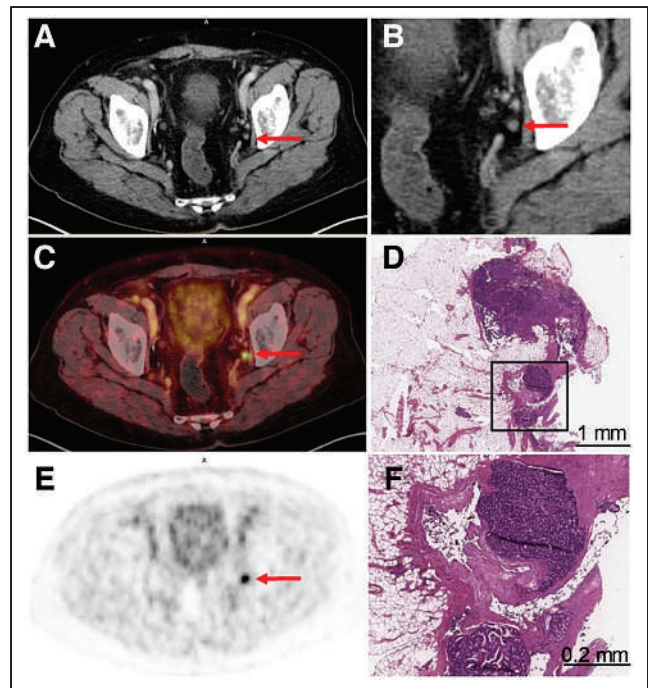


**FIGURE 2.** A 75-y-old patient with biochemical recurrence after radical prostatectomy (ISUP grade group 4, pT3b pN0 cM0, iPSA level: 11 ng/mL, PSA level at time of PET examination: 1.02 ng/mL) and a correctly classified lymph node metastasis by <sup>18</sup>F-rhPSMA-7.3 PET. A morphologically nonsuspicious lymph node, 5 mm in diameter, is visible in left obturator fossa on CT (A and B) that shows intense, focal and suggestive tracer uptake in <sup>18</sup>F-rhPSMA-7.3 PET and fused PET/CT (C and E). Salvage lymphadenectomy with histologic evaluation confirmed a single lymph node metastasis (D and F). Arrow shows lymph node metastasis. iPSA = initial PSA concentration; ISUP = International Society of Urological Pathology.

that these novel tracers can detect small lymph node metastasis (a lesion size smaller than 10 mm) in the recurrent PC setting (5). Salvage lymph node surgery represents a therapeutic option for patients experiencing biochemical recurrence after radical prostatectomy, and previous  $^{11}\text{C}$ -choline PET-guided data suggest that up to 40% of patients may experience recurrence-free survival after PET-guided salvage lymph node dissection (32). More recently, Horn et al. showed that in a subgroup of patients with recurrent PC undergoing PSMA PET-guided salvage surgery, complete biochemical response was achieved in 66% of patients (2). Moreover, it is believed that PET-guided salvage lymph node dissection may prolong the time until initiation of hormonal treatment, which is associated with significant morbidity (33,34). For salvage surgery with potential complications, a high specificity and PPV are of utmost importance to avoid unnecessary interventions. Interestingly, the specificity of morphologic imaging on a template base was also excellent, which is most likely related to the strict criteria for the determination of metastases. However, as known from the literature, the sensitivity of morphologic imaging is rather low as it can detect only lymph node metastases with already enlarged (>10 mm) lesions.

The pure enantiomeric form of  $^{18}\text{F}$ -rhPSMA-7,  $^{18}\text{F}$ -rhPSMA-7.3, has been selected as the lead rhPSMA compound for clinical development on the basis of preclinical assessments showing favorable safety and kinetic profiles for diagnostic imaging of PC (14,18). Because of the limited numbers, no sound comparison of the diagnostic performance of  $^{18}\text{F}$ -rhPSMA-7 versus  $^{18}\text{F}$ -rhPSMA-7.3 is possible in the present study. However, we note similar PPVs for the 2 compounds, which is the only descriptive statistical value to be unaffected by the potential selection bias that results from the present study design. Another limitation of this retrospective analysis is its potential selection bias due to the selection of patients and the lymph node template regions to be removed on the basis of the clinical reads of the  $^{18}\text{F}$ -rhPSMA-7 and  $^{18}\text{F}$ -rhPSMA-7.3 PET scans. Possible imaging-negative nodes could have been missed, which would impact the sensitivity estimate. Therefore, PPV is the only descriptive statistical value independent of this bias. Of note, specificity on the patient-based analysis was only informed by 4 cases (Supplemental Table 3). For different reasons, it was not always feasible to perform surgery shortly after PET examination (median time between PET and surgery, 59 d; range, 19–117 d). Thus, in principle, it cannot be excluded that there was tumor progression or even new tumor lesions at the time of surgery. The data presented in the supplemental materials for separate analyses of  $^{18}\text{F}$ -rhPSMA-7 and  $^{18}\text{F}$ -rhPSMA-7.3 should be interpreted with caution given the limited number of patients in each group. Further prospective studies with  $^{18}\text{F}$ -rhPSMA-7.3 are warranted to confirm the diagnostic accuracy for lymph node staging and to avoid potential bias.

## CONCLUSION

$^{18}\text{F}$ -rhPSMA-7 and  $^{18}\text{F}$ -rhPSMA-7.3 PET are superior to morphologic imaging for detecting pelvic lymph node metastases and helping guide salvage lymph node surgery. They offer a high PPV, comparable to that reported for  $^{68}\text{Ga}$ -PSMA-11, while yielding the benefits of a radiofluorinated tracer such as the potential for scale production and wide-range distribution.

## DISCLOSURE

Hans-Jürgen Wester, Alexander Wurzer, and Matthias Eiber have a patent application for rhPSMA. Hans-Jürgen Wester and

Matthias Eiber received funding from Blue Earth Diagnostics Ltd. (Oxford, U.K., Licensee for rhPSMA) as part of an academic collaboration. Matthias Eiber reports prior consulting activities for Blue Earth Diagnostics Ltd., Novartis, Telix, Progenics, Bayer, Point Biopharma, and Janssen. Hans-Jürgen Wester is founder, shareholder, and advisor board member of Scintomics GmbH (Fuerstenfeldbruck, Germany). Siemens Medical Solutions (Erlangen, Germany) supported the application of Biograph mCT flow as part of an academic collaboration. Tobias Maurer reports prior consulting activities for Blue Earth Diagnostics Ltd., Novartis, Telix, ROTOP Pharma, Advanced Accelerator Applications International S.A., GEMoAb, and Astellas. No other potential conflict of interest relevant to this article was reported.

## KEY POINTS

**QUESTION:** What is the value of the radiopharmaceuticals  $^{18}\text{F}$ -rhPSMA-7 and  $^{18}\text{F}$ -rhPSMA-7.3 for assessing the presence of lymph node metastases before potential salvage lymphadenectomy?

**PERTINENT FINDINGS:** This histopathologically validated, retrospective study shows that  $^{18}\text{F}$ -rhPSMA-7 and  $^{18}\text{F}$ -rhPSMA-7.3 are superior to morphologic imaging and comparable to  $^{68}\text{Ga}$ -PSMA-11 for N staging of biochemical recurrent prostate cancer.

**IMPLICATIONS FOR PATIENT CARE:**  $^{18}\text{F}$ -rhPSMA-7 and  $^{18}\text{F}$ -rhPSMA-7.3 can detect small soft-tissue metastases with a high, template-based specificity of 93%.

## REFERENCES

1. Freedland SJ, Presti JC Jr, Amling CL, et al. Time trends in biochemical recurrence after radical prostatectomy: results of the SEARCH database. *Urology*. 2003;61:736–741.
2. Horn T, Kroenke M, Rauscher I, et al. Single lesion on prostate-specific membrane antigen-ligand positron emission tomography and low prostate-specific antigen are prognostic factors for a favorable biochemical response to prostate-specific membrane antigen-targeted radioguided surgery in recurrent prostate cancer. *Eur Urol*. 2019;76:517–523.
3. Bandini M, Fossati N, Briganti A. Salvage surgery for nodal recurrent prostate cancer. *Curr Opin Urol*. 2017;27:604–611.
4. Steuber T, Jilg C, Tennstedt P, et al. Standard of care versus metastases-directed therapy for PET-detected nodal oligorecurrent prostate cancer following multimodality treatment: a multi-institutional case-control study. *Eur Urol Focus*. 2019;5:1007–1013.
5. Rauscher I, Maurer T, Beer AJ, et al. Value of  $^{68}\text{Ga}$ -PSMA HBED-CC PET for the assessment of lymph node metastases in prostate cancer patients with biochemical recurrence: comparison with histopathology after salvage lymphadenectomy. *J Nucl Med*. 2016;57:1713–1719.
6. Maurer T, Gschwend JE, Rauscher I, et al. Diagnostic efficacy of  $^{68}\text{Ga}$ -PSMA positron emission tomography compared to conventional imaging for lymph node staging of 130 consecutive patients with intermediate to high risk prostate cancer. *J Urol*. 2016;195:1436–1443.
7. Eder M, Schafer M, Bauder-Wust U, et al.  $^{68}\text{Ga}$ -complex lipophilicity and the targeting property of a urea-based PSMA inhibitor for PET imaging. *Bioconjug Chem*. 2012;23:688–697.
8. Afshar-Oromieh A, Malcher A, Eder M, et al. PET imaging with a [ $^{68}\text{Ga}$ ]gallium-labelled PSMA ligand for the diagnosis of prostate cancer: biodistribution in humans and first evaluation of tumour lesions. *Eur J Nucl Med Mol Imaging*. 2013;40:486–495.
9. Perera M, Papa N, Christidis D, et al. Sensitivity, specificity, and predictors of positive  $^{68}\text{Ga}$ -prostate-specific membrane antigen positron emission tomography in advanced prostate cancer: a systematic review and meta-analysis. *Eur Urol*. 2016;70:926–937.
10. Cornford P, Bellmunt J, Bolla M, et al. EAU-ESTRO-SIOG guidelines on prostate cancer. Part II: Treatment of relapsing, metastatic, and castration-resistant prostate cancer. *Eur Urol*. 2017;71:630–642.

11. Fendler WP. Assessment of  $^{68}\text{Ga}$ -PSMA-11 PET accuracy in localizing recurrent prostate cancer: a prospective single-arm clinical trial. *JAMA Oncol.* 2019;5:856–863.
12. Oh SW, Wurzer A, Teoh EJ, et al. Quantitative and qualitative analyses of biodistribution and PET image quality of novel radiohybrid PSMA,  $^{18}\text{F}$ -rhPSMA-7, in patients with prostate cancer. *J Nucl Med.* 2020;61:702–709.
13. Wurzer A, DiCarlo D, Schmidt A, et al. Radiohybrid ligands: a novel tracer concept exemplified by  $^{18}\text{F}$ - or  $^{68}\text{Ga}$ -labeled rhPSMA-inhibitors. *J Nucl Med.* 2020;61:735–742.
14. Wurzer A, Parzinger M, Konrad M, et al. Preclinical comparison of four [ $^{18}\text{F}$ ,  $^{68}\text{Ga}$ ]rhPSMA-7 isomers: influence of the stereoconfiguration on pharmacokinetics. *EJNMMI Res.* 2020;10:149.
15. Rauscher I, Karimzadeh A, Schiller K, et al. Detection efficacy of  $^{18}\text{F}$ -rhPSMA-7.3 PET/CT and impact on patient management in patients with biochemical recurrence of prostate cancer after radical prostatectomy and prior to potential salvage treatment. *J Nucl Med.* 2021;62:1719–1726.
16. Eiber M, Kronke M, Wurzer A, et al.  $^{18}\text{F}$ -rhPSMA-7 positron emission tomography for the detection of biochemical recurrence of prostate cancer following radical prostatectomy. *J Nucl Med.* 2020;61:696–701.
17. Wurzer A, Di Carlo D, Herz M, et al. Automated synthesis of [ $^{18}\text{F}$ ]Ga-rhPSMA-7/7.3: results, quality control and experience from more than 200 routine productions. *EJNMMI Radiopharm Chem.* 2021;6:4.
18. Tolvanen T, Kalliokoski KK, Malaspina S, et al. Safety, biodistribution and radiation dosimetry of  $^{18}\text{F}$ -rhPSMA-7.3 in healthy adult volunteers. *J Nucl Med.* 2021;62:679–684.
19. Souvatzoglou M, Eiber M, Martinez-Moeller A, et al. PET/MR in prostate cancer: technical aspects and potential diagnostic value. *Eur J Nucl Med Mol Imaging.* 2013;40(suppl 1):S79–S88.
20. Eiber M, Maurer T, Souvatzoglou M, et al. Evaluation of hybrid  $^{68}\text{Ga}$ -PSMA ligand PET/CT in 248 patients with biochemical recurrence after radical prostatectomy. *J Nucl Med.* 2015;56:668–674.
21. Rausch I, Cal-Gonzalez J, Dapra D, et al. Performance evaluation of the Biograph mCT Flow PET/CT system according to the NEMA NU2-2012 standard. *EJNMMI Phys.* 2015;2:26.
22. Kroenke M, Wurzer A, Schwamborn K, et al. Histologically-confirmed diagnostic efficacy of  $^{18}\text{F}$ -rhPSMA-7 positron emission tomography for N-staging of patients with primary high risk prostate cancer. *J Nucl Med.* 2020;61:710–715.
23. Obuchowski NA. Nonparametric analysis of clustered ROC curve data. *Biometrics.* 1997;53:567–578.
24. The R project for statistical computing. The R project website. <https://www.R-project.org/>. Accessed September 14, 2022.
25. Robin X, Turck N, Hainard A, et al. pROC: an open-source package for R and S+ to analyze and compare ROC curves. *BMC Bioinformatics.* 2011;12:77.
26. Hojsgaard S, Halekoh U, Yan J. The R package geeppack for generalized estimating equations. *J Stat Softw.* 2005;15:1–11.
27. Afshar-Oromieh A, Avtzi E, Giesel FL, et al. The diagnostic value of PET/CT imaging with the  $^{68}\text{Ga}$ -labelled PSMA ligand HBED-CC in the diagnosis of recurrent prostate cancer. *Eur J Nucl Med Mol Imaging.* 2015;42:197–209.
28. Hijazi S, Meller B, Leitsmann C, et al. Pelvic lymph node dissection for nodal oligometastatic prostate cancer detected by  $^{68}\text{Ga}$ -PSMA-positron emission tomography/computerized tomography. *Prostate.* 2015;75:1934–1940.
29. Herlemann A, Wenter V, Kretschmer A, et al.  $^{68}\text{Ga}$ -PSMA positron emission tomography/computed tomography provides accurate staging of lymph node regions prior to lymph node dissection in patients with prostate cancer. *Eur Urol.* 2016;70:553–557.
30. Chantadisai M, Buschner G, Kronke M, et al. Positive predictive value and correct detection rate of  $^{18}\text{F}$ -rhPSMA-7 PET in biochemically recurrent prostate cancer validated by composite reference standard. *J Nucl Med.* 2021;62:968–974.
31. Langbein T, Kroenke M, Rauscher I, et al. Preliminary data on the diagnostic efficacy of F-18-rhPSMA-7.3 PET imaging for N-staging of patients with intermediate and high-risk prostate cancer compared to histopathology [abstract]. *J Nucl Med.* 2020;61(suppl 1):1267.
32. Suardi N, Gandaglia G, Gallina A, et al. Long-term outcomes of salvage lymph node dissection for clinically recurrent prostate cancer: results of a single-institution series with a minimum follow-up of 5 years. *Eur Urol.* 2015;67:299–309.
33. Saigal CS, Gore JL, Krupski TL, et al. Androgen deprivation therapy increases cardiovascular morbidity in men with prostate cancer. *Cancer.* 2007;110:1493–1500.
34. Tsai HK, D'Amico AV, Sadetsky N, Chen MH, Carroll PR. Androgen deprivation therapy for localized prostate cancer and the risk of cardiovascular mortality. *J Natl Cancer Inst.* 2007;99:1516–1524.

---

---

# Using $^{68}\text{Ga}$ -PSMA-11 PET/CT for Therapy Response Assessment in Patients with Metastatic Castration-Resistant Prostate Cancer: Application of EAU/EANM Recommendations in Clinical Practice

Chloé S. Denis<sup>1</sup>, François Cousin<sup>2</sup>, Bram De Laere<sup>3,4</sup>, Roland Hustinx<sup>2,5</sup>, Brieuc R. Sautois<sup>\*1</sup>, and Nadia Withofs<sup>\*2,5</sup>

<sup>1</sup>Medical Oncology Department, University Hospital of Liège, Liège, Belgium; <sup>2</sup>Division of Nuclear Medicine and Oncological Imaging, Department of Medical Physics, University Hospital of Liège, Liège, Belgium; <sup>3</sup>Department of Medical Epidemiology and Biostatistics, Karolinska Institutet, Stockholm, Sweden; <sup>4</sup>Department of Human Structure and Repair, Ghent University, Ghent, Belgium; and <sup>5</sup>GIGA-CRC In Vivo Imaging, University of Liège, Liège, Belgium

---

J Nucl Med 2022; 63:1815–1821  
DOI: 10.2967/jnumed.121.263611

---

For patients with metastatic castration-resistant prostate cancer (mCRPC), no reliable biomarkers for predicting therapeutic response or assisting in treatment selection and sequencing are currently available. Using the recent European Association of Urology and European Association of Nuclear Medicine recommendations, we aimed to compare response assessment between prostate-specific membrane antigen (PSMA) PET/CT and conventional imaging in mCRPC patients starting first-line treatment with a novel hormonal agent (NHA) and to perform a sequential comparative analysis of PSMA PET/CT-derived parameters after 4 and 12 wk of therapy. **Methods:** Data from 18 mCRPC patients who started NHA treatment and underwent  $^{68}\text{Ga}$ -PSMA-11 PET/CT before therapy initiation (baseline), at week 4 (W4), and at week 12 (W12) in addition to conventional imaging (bone scintigraphy, CT) at baseline and W12 were retrospectively included. PET/CT images were quantitatively analyzed for maximum and mean SUV and total PSMA ligand-positive lesions. Comparative analysis of PET/CT-derived parameters was performed, and patients were classified as having non-progressive disease or progressive disease (PD) according to  $^{68}\text{Ga}$ -PSMA-11 PET/CT, prostate-specific antigen, and conventional imaging criteria. **Results:** Treatment response was evaluable by  $^{68}\text{Ga}$ -PSMA-11 PET/CT in 16 of 18 patients (89%) and by conventional imaging in 11 of 18 patients (61%). Five of 16 patients classified as having PD by  $^{68}\text{Ga}$ -PSMA-11 PET/CT at W12 had already met progression criteria at W4, and substantial agreement was observed between W4 and W12 ( $\kappa$ , 0.74)  $^{68}\text{Ga}$ -PSMA-11 PET/CT results. Nonetheless, 2 of 16 patients (13%) were incorrectly classified as having PD because of a flare phenomenon on PSMA PET/CT that disappeared at W12. **Conclusion:** Volumetric assessments of  $^{68}\text{Ga}$ -PSMA-11 PET/CT imaging can improve response evaluation in NHA-treated patients with mCRPC. Although early response assessments at W4 need to be approached with caution because of flare,  $^{68}\text{Ga}$ -PSMA-11 PET/CT imaging at W4 and W12 revealed substantial agreement in therapy response assessments; these findings warrant further investigation to distinguish PD from flare at W4 and help improve the understanding of resistance to therapy.

**Key Words:** mCRPC; prostate cancer; tumor quantification; PSMA PET/CT; flare

Although new imaging modalities using radionuclides have become available to—for example—evaluate tumor burden, a practical tool for improved staging and clinical decision making in metastatic castration-resistant prostate cancer (mCRPC) is urgently needed. In current clinical practice, therapy response assessment by means of conventional imaging, encompassing CT and bone scintigraphy (BS), is typically performed after 12–16 wk of therapy. However, conventional imaging has limited sensitivity and specificity for small lymph node and bone metastases, especially at low prostate-specific antigen (PSA) levels (1,2). Because of its higher accuracy, prostate-specific membrane antigen (PSMA) PET/CT has gained momentum in staging and recurrence localization compared with conventional imaging (3–5).

Recently, the European Association of Urology (EAU) in collaboration with the European Association of Nuclear Medicine (EANM) recruited a panel of international experts to reach a consensus statement for the use of PSMA PET/CT in assessing therapy response for patients with metastatic disease (6). However, semi-quantitative parameters that should be used for PSMA PET/CT interpretation were not clearly defined. Moreover, the expert panel raised awareness for potential “tumor flare” phenomena after the initiation of androgen deprivation therapy and discouraged the use of PSMA PET/CT within 12 wk to avoid the misinterpretation of potential flare as progressive disease (PD).

As PSMA imaging is more widely used in clinical practice, understanding the factors underlying PSMA expression modulation is becoming increasingly important. Interestingly, factors other than exposure to androgen deprivation therapy, such as a DNA damage response gene defect (7) or activation of the PI3K-Akt pathway (8), may modulate PSMA expression. Thus, PSMA PET/CT imaging may indirectly reflect underlying molecular biology and—besides being a prognostic tool—may also serve as a predictive biomarker before biochemical progression or PD on conventional imaging (8–11). Consequently, exploring response endpoints with PSMA PET/CT might improve clinical decision making in—for example—treatment intensification for oligoresistant or oligoprogressive lesions to delay disease progression (11–13).

---

Received Dec. 2, 2021; revision accepted Apr. 18, 2022.  
For correspondence or reprints, contact Chloé S. Denis (chloe.denis@chuliege.be).  
\*Contributed equally to this work.  
Published online Apr. 21, 2022.  
COPYRIGHT © 2022 by the Society of Nuclear Medicine and Molecular Imaging.

In the present work, we evaluated  $^{68}\text{Ga}$ -PSMA-11 PET/CT for the baseline assessment and monitoring of treatment response in a retrospective series of patients who had mCRPC and were starting first-line treatment with a novel hormonal agent (NHA). Additionally, the therapy response determined by  $^{68}\text{Ga}$ -PSMA-11 PET/CT at 12 wk was compared with the earlier response obtained at 4 wk, and individual analysis of  $^{68}\text{Ga}$ -PSMA-11 PET/CT-derived parameters using the proposed criteria from the expert-based consensus was performed.

## MATERIALS AND METHODS

### Patients

From a large internal database, files from mCRPC patients who started first-line treatment with an NHA between January 2018 and May 2021 at the University Hospital of Liège (Liège, Belgium) were retrospectively extracted and reviewed. Additional inclusion criteria comprised patients having undergone  $^{68}\text{Ga}$ -PSMA-11 PET/CT before NHA initiation (baseline), at week 4 (W4,  $\pm 7$  d), and at week 12 (W12,  $\pm 7$  d) along with conventional imaging at baseline and W12; having histologically confirmed prostate adenocarcinoma; having progressive castration-resistant disease, as defined by castration levels of testosterone ( $<1.7$  nmol/L) and clinical, biologic, or radiographic progression conforming to Prostate Cancer Clinical Trials Working Group 3 (PCWG3) criteria (14); and having documented evidence of metastatic disease (on conventional imaging or  $^{68}\text{Ga}$ -PSMA-11 PET/CT) before NHA initiation. Patients who did not meet all inclusion criteria were excluded. This study was approved by the Institutional Review Board of the University Hospital of Liège, and written informed consent was obtained from all patients.

### $^{68}\text{Ga}$ -PSMA-11 PET/CT

$^{68}\text{Ga}$ -PSMA-11 PET/CT images were analyzed by a nuclear medicine specialist (15 y of experience, including 7 y with PSMA PET/CT) who was unaware of the clinical data and BS results (MIM Software, version 7.0.5; MIM Software Inc.).  $^{68}\text{Ga}$ -PSMA-11 radiolabeling was performed as previously described (15). Image acquisition and tumor volume delineation techniques are summarized in the supplemental materials (supplemental materials are available at <http://jnm.snmjournals.org>) (16–19). The following semiquantitative variables were extracted for each patient:  $\text{SUV}_{\text{max}}$  of the hottest lesion, total PSMA ligand-positive tumor volume (PSMA-TV),  $\text{SUV}_{\text{mean}}$  of PSMA-TV, and total PSMA ligand-positive lesions (PSMA-TL, the product of  $\text{SUV}_{\text{mean}}$  and PSMA-TV) (20,21). In accordance with EAU/EANM recommendations, the parameters used to assess therapy response for tracer uptake and tumor volume were  $\text{SUV}_{\text{max}}$  and PSMA-TL, respectively.

### Conventional Imaging

CT (chest–abdomen–pelvis) and BS images were analyzed according to PCWG3 recommendations (14) by a nuclear medicine specialist and a radiologist (10 y of experience) who were unaware of the clinical data and  $^{68}\text{Ga}$ -PSMA-11 PET/CT results. To enable therapy response assessment, patients needed to have measurable disease, defined as the presence of bone lesions on BS or at least 1 measurable lesion on CT, according to RECIST v1.1 (2).

All retrospective image interpretations ( $^{68}\text{Ga}$ -PSMA-11 PET/CT and conventional imaging) were compared with the protocols issued prospectively as part of the follow-up: if discordances were observed, another nuclear medicine specialist and radiologist who were unaware of the clinical and imaging data were to interpret the images to reach a consensus majority (2 vs. 1).

## Therapy Response Assessment

Therapy response was assessed by  $^{68}\text{Ga}$ -PSMA-11 PET/CT and conventional imaging using EAU/EANM PSMA PET/CT (6) and PCWG3 (2,14) criteria, respectively (Table 1). The clinical response rates after 4 wk ( $^{68}\text{Ga}$ -PSMA-11 PET/CT) and 12 wk ( $^{68}\text{Ga}$ -PSMA-11 PET/CT and conventional imaging) of therapy were calculated for patients with PD and those with nonprogressive disease (non-PD) by adding the numbers of patients with a complete response, a partial response, and a stable response. A biochemical response was defined according to PCWG3 criteria, and patients without PSA progression were classified as having non-PD.

## Statistical Analysis

Categoric variables were described using relative frequencies and percentages. Mean, SD, median, range, and interquartile range (IQR) were used to describe normally and nonnormally distributed data. The primary outcome measure of PSMA PET/CT response endpoints was reported as changes at W4 and W12 by means of waterfall plots. The percentage changes in PSA,  $\text{SUV}_{\text{max}}$ ,  $\text{SUV}_{\text{mean}}$ , and PSMA-TL between baseline and W4 or W12 were calculated using the following formula:

$$\text{Change from baseline (\%)} = 100 \left( \frac{\text{New value}}{\text{Baseline value}} - 1 \right)$$

Additionally, the proportions of patients categorized with non-PD or PD using PSA or conventional imaging response endpoints at 4–12 wk were reported and compared with  $^{68}\text{Ga}$ -PSMA-11 PET/CT response rates. Cooccurrences of W4  $^{68}\text{Ga}$ -PSMA-11 PET/CT, W12  $^{68}\text{Ga}$ -PSMA-11 PET/CT, PSA, and conventional imaging response categories were tested using the Cohen  $\kappa$ -coefficient. All statistical tests were performed with RStudio (version 1.1.463; RStudio), and a 2-sided  $P$  value of  $<0.05$  was considered statistically significant.

## RESULTS

### Patients and Imaging

From our database, data for 165 patients who had mCRPC and were starting a first-line treatment with an NHA were extracted. A total of 144 patients were first excluded because  $^{68}\text{Ga}$ -PSMA-11 PET/CT was not performed or not at the required time points. Of the 21 remaining patients, 3 were further excluded for the following reasons: 2 patients were registered as having mCRPC by the clinician, but no metastatic disease was detected by either conventional imaging or  $^{68}\text{Ga}$ -PSMA-11 PET/CT at the time of NHA initiation, and 1 patient was found to have started his NHA therapy with a 1-mo delay, so the imaging no longer fit the inclusion criteria. Overall, 18 patients could be included for further analysis (Supplemental Fig. 1; Table 2).

PET/CT scans were obtained  $76.5 \pm 14.8$  min (mean  $\pm$  SD) after intravenous injection of  $154 \pm 6.6$  MBq of  $^{68}\text{Ga}$ -PSMA-11. Median time intervals between NHA initiation and baseline  $^{68}\text{Ga}$ -PSMA-11 PET/CT, BS, and CT scans were 10 (IQR, 6–27), 5 (IQR, 4–10), and 5 (IQR, 4–12) d, respectively. Follow-up  $^{68}\text{Ga}$ -PSMA-11 PET/CT scans at 4 and 12 wk from NHA initiation were obtained after median time intervals of 29 (IQR, 28–29) and 85 (IQR, 85–85) d, respectively. BS and CT scans at W12 were both acquired at a median time interval of 86 d (IQR for BS scan, 86–86; IQR for CT scan, 86–87). No disagreement was observed in the prospective and retrospective image interpretations.

**TABLE 1**  
Therapy Response Assessment Criteria Based on Imaging

Response criteria	Non-PD			
	Imaging	Complete response	Partial response	Stable response
PCWG3 imaging	CT (2)	Disappearance of all lesions	Decrease of $\geq 30\%$ in sum of target lesions (without new lesion or nontarget lesion progression)	Not meeting criteria for partial response, complete response, or progressive disease
EAU/EANM PSMA	PSMA PET/CT (6)	Disappearance of any lesion with tracer uptake	Reduction of uptake and tumor PET volume by $> 30\%$	Change in uptake and tumor PET volume by $\leq 30\%$ , without evidence of new lesions
BS (14)		Disappearance of all suggestive lesions	No new lesion or appearance of $< 2$ new lesions	No new lesion or appearance of $< 2$ new lesions
			Decrease of $\geq 20\%$ in sum of target lesions, unequivocal progression of nontarget lesions, or appearance of new lesions	Increase of $\geq 20\%$ in sum of target lesions, unequivocal progression of nontarget lesions, or appearance of new lesions
			Appearance of at least $\geq 2$ new lesions confirmed on subsequent scan	Appearance of at least $\geq 2$ new lesions confirmed on subsequent scan
			Disappearance of all suggestive lesions	Appearance of at least $\geq 2$ new lesions confirmed on subsequent scan

**TABLE 2**  
Characteristics of 18 Patients at Study Entry

Characteristic	Value*
Age (y)	
Mean	73.1
SD	6.1
PSA at baseline (ng/mL)	
Median	8.04
IQR	5.96–24.8
Time between initiation of first-generation ADT and mCRPC status (mo)	
Median	47.5
IQR	27.0–79.0
Patients with prior local treatment	14 (78)
RP only	4 (22)
RP + ePLND	3 (17)
Exclusive RT only	5 (28)
ePLND + aborted RP + RT	2 (11)
Type of prior systemic therapy before resistance to castration	
First-generation ADT	16 (89)
Up-front chemotherapy	2 (11)
ISUP grade group version 8.0 at time of diagnosis	
Grade 1	2 (11)
Grade 2	2 (11)
Grade 3	3 (17)
Grade 4	6 (33)
Grade 5	4 (22)
Unknown	1 (6)
First-line treatment initiated for mCRPC	
Enzalutamide (160 mg daily)	17 (94)
Abiraterone (1,000 mg daily)	1 (6)

\*Unless otherwise indicated, values are reported as numbers of patients, with percentages in parentheses.

ADT = androgen deprivation therapy; RP = radical prostatectomy; ePLND = extended pelvic lymph node dissection; RT = radiotherapy; ISUP = International Society of Urological Pathology.

**Baseline Assessment of Tumor Burden and PCWG3 Clinical Subtypes**

At baseline,  $^{68}\text{Ga}$ -PSMA-11 PET/CT detected metastatic disease in all 18 patients (100%), whereas conventional imaging identified 14 of 18 patients with metastases (78%). Overall, baseline tumor burden quantification (Supplemental Table 1) and subsequent therapy response assessment by  $^{68}\text{Ga}$ -PSMA-11 PET/CT could be performed in 16 of 18 patients. Two patients were not evaluable by PSMA PET: for 1 (UPN7), parameters could not be extracted because his PSMA-avid lesions were below the fixed volume threshold for delineation; the unique residual lung nodule for the other (UPN19)—highly suggestive given the diagnosis of biopsy-confirmed lung metastases from prostate cancer 3 y before the

study—was visible on CT but did not show PSMA tracer uptake. Individual imaging data are listed in Supplemental Figure 2.

Finally, we determined the PCWG3 clinical subtypes using conventional imaging and <sup>68</sup>Ga-PSMA-11 PET/CT (14,22). In 14 of 18 patients (78%), <sup>68</sup>Ga-PSMA-11 PET/CT and conventional imaging resulted in concordant PCWG3 subtypes. <sup>68</sup>Ga-PSMA-11 PET/CT upstaged the results for 4 of 18 patients (22%) from non-metastatic by conventional imaging to nodal involvement. Moreover, the results for 3 patients (UPN5, UPN18, and UPN20) were upstaged from oligometastatic by conventional imaging to polymetastatic by <sup>68</sup>Ga-PSMA-11 PET/CT.

### Comparison of Therapy Response Assessments at W12

On the basis of PSA values at W12, 17 of 18 patients (94%) and 1 of 18 patients (6%) were classified as having non-PD and PD, respectively (Supplemental Table 2). Patients for whom metastatic disease was not detectable by conventional imaging at baseline (4/18) still showed no lesions at W12.

Overall, 16 of 18 patients (89%) had disease measurable by <sup>68</sup>Ga-PSMA-11 PET/CT; this result allowed for treatment response assessment in a larger proportion of patients than conventional imaging (11/18 [61%]). The patients who were not evaluable by conventional imaging either had no metastases (4/18 [22%]) or had nonmeasurable disease (3/18 [17%]) (Table 3). Among patients who were evaluable by conventional imaging, 4 of 18 (22%) had RECIST v1.1-measurable disease; in 7 of 18 patients (39%), response assessment was BS driven because disease was not measurable on CT (2/18 [11%]) or was present only in bone (5/18 [28%]).

Among the 11 patients who were evaluable by conventional imaging and <sup>68</sup>Ga-PSMA-11 PET/CT at W12, we observed discordances between imaging techniques in the response categorization for 4 patients (36%) (Table 3). Three patients categorized as having PD by <sup>68</sup>Ga-PSMA-11 PET/CT were responding to therapy according to conventional imaging, and 1 patient was categorized as having PD by conventional imaging but not by <sup>68</sup>Ga-PSMA-11 PET/CT. The latter patient (UPN21) demonstrated a 38% increase in the sum of the largest-diameter liver metastases at W12 despite a 42% decline in PSA from baseline. The distinction between true progression and size progression related to necrosis will be clarified with follow-up. Overall, treatment responses according to conventional imaging, <sup>68</sup>Ga-PSMA-11 PET/CT, and PSA change were concordantly categorized in 5 of 11 patients (45%). Discordant results were observed in 6 of 11 patients (55%) with PD on either conventional imaging or <sup>68</sup>Ga-PSMA-11 PET/CT, despite a PSA response in all but 1 patient (UPN16). Individual patient data are shown in Supplemental Table 2.

Next, changes in <sup>68</sup>Ga-PSMA-11 PET/CT–derived parameters at W12 were compared with baseline data (Fig. 1A), and concordances in response categorization according to each parameter were investigated (Supplemental Table 3A). PSMA-TL was concordant with tracer uptake (SUV<sub>max</sub> and SUV<sub>mean</sub>) and with the appearance of ≥2 new lesions in most cases (88%; 14/16 cases), whereas the latter was concordant with SUV<sub>max</sub> in only 12 of 16 patients (75%).

### Early Therapy Response Assessments (W4) Using PSMA PET/CT

At W4, 17 of 18 patients (94%) were classified as having PSA non-PD, whereas 1 of 18 patients (6%) had PSA PD (Supplemental Table 2). As at W12, 16 of 18 patients (89%) were evaluable by <sup>68</sup>Ga-PSMA-11 PET/CT at W4. Although only fair agreement was observed in the response categorization between <sup>68</sup>Ga-PSMA-11 PET/CT at W4 and conventional imaging or PSA at W12,

**TABLE 3**  
Therapy Response Assessment at W12 According to PCWG3 Conventional Imaging, Biochemical (PSA), and EAU/EANM PSMA PET/CT Response Criteria

Unique patient designation	Conventional Imaging	PSA	PSMA PET/CT
7	NE <sub>0</sub>	Non-PD	NE <sub>nt</sub>
11	NE <sub>0</sub>	Non-PD	Non-PD
14	NE <sub>0</sub>	Non-PD	Non-PD
6	NE <sub>0</sub>	Non-PD	Non-PD
5	NE <sub>nm</sub>	Non-PD	Non-PD
18	NE <sub>nm</sub>	Non-PD	Non-PD
19	NE <sub>nm</sub>	Non-PD	NE <sub>nt</sub>
1	Non-PD*	Non-PD	PD
4	Non-PD*	Non-PD	Non-PD
9	Non-PD*	Non-PD	PD
15	Non-PD*	Non-PD	Non-PD
16	Non-PD*	PD	PD
2	Non-PD <sup>†</sup>	Non-PD	Non-PD
17	Non-PD <sup>†</sup>	Non-PD	Non-PD
20	Non-PD <sup>†</sup>	Non-PD	Non-PD
12	PD*	Non-PD	PD
13	PD*	Non-PD	PD
21	PD <sup>†</sup>	Non-PD	Non-PD

\*Patient for whom response assessment was BS driven.

<sup>†</sup>Patient with measurable lesions according to RECIST v1.1.

NE<sub>0</sub> = not evaluable, if no metastases were detected since baseline; NE<sub>nt</sub> = not evaluable, if lesions were visible but not evaluable by PSMA imaging; NE<sub>nm</sub> = not evaluable, if no measurable lesions were visible on CT and without bone lesions on BS.

substantial agreement ( $\kappa = 0.74$ ;  $P < 0.005$ ) was observed between <sup>68</sup>Ga-PSMA-11 PET/CT at W4 and <sup>68</sup>Ga-PSMA-11 PET/CT at W12 (Supplemental Table 4). Overall, 7 of 16 patients (44%) were classified as having PD at W4; 5 of 16 (31%) were so classified at W12. Importantly, the 5 patients classified as having PD by <sup>68</sup>Ga-PSMA-11 PET/CT at W12 had already fulfilled PD criteria at W4.

When <sup>68</sup>Ga-PSMA-11 PET/CT–derived parameters were compared at W4 and W12, a larger number of discordant results was observed at W4, especially between PSMA-TL and SUV<sub>max</sub> (Supplemental Table 3). At W4, 4 of 16 patients (25%) demonstrated an increase in the SUV<sub>max</sub> of greater than 30%; this increase was sustained until W12 in only 1 patient (UPN12). This flare phenomenon led to incorrectly classifying 2 patients (UPN2 and UPN17) as having PD at W4 (Fig. 1B). For both patients, this flare phenomenon resolved by W12, and the patients were classified as having non-PD (Fig. 1A). Finally, unlike SUV<sub>max</sub>, SUV<sub>mean</sub> showed few modifications at W4 (IQR, −1.0% to +10.8%) and showed no discordance between W4 and W12. It was significant only in patient UPN1, who was confirmed to have PD at W12.

### DISCUSSION

Despite EAU/EANM consensus statements on PSMA PET/CT response assessment criteria (6), recommendations or guidelines on

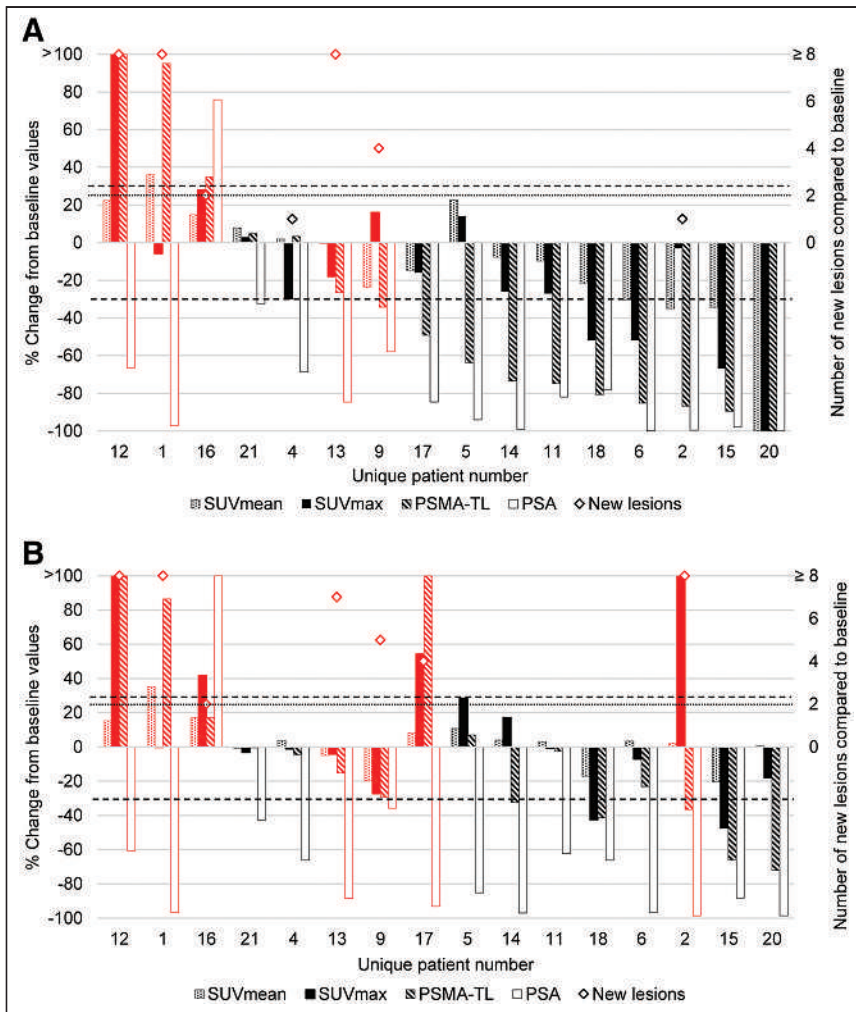


**FIGURE 1.** Waterfall plots of changes in PSMA PET/CT–derived parameters ( $SUV_{mean}$ ,  $SUV_{max}$ , PSMA-TL, PSA, and number of new lesions) at W12 (A) and W4 (Fig. 1B) in comparison to baseline PSMA PET/CT ( $n = 16$ ), stratified according to PSMA-TL and therapy response assessment (i.e., non-PD in black and PD in red, as defined in Table 1). Horizontal dashed line represents  $\pm 30\%$  cut-off. Dotted line represents cutoff at  $n = 2$  lesions. Patients are presented in same order in A and B.

which segmentation algorithm or PSMA PET/CT–derived parameter(s) should be used are lacking. Various thresholding techniques, such as using fixed thresholds (mostly,  $SUV_{max}$  of greater than 3) or relative thresholds (e.g., 40%–45% of the  $SUV_{max}$  of the selected lesion), also exist for PET image segmentation (16–18,23). Here, we applied a combined fixed  $SUV_{max}$  of greater than 3 and a lesion volume threshold of greater than 0.5 mL to select and delineate PSMA-positive lesions. Although potential misinterpretation of background foci as small lesions was avoided in this way, this approach underestimated the number of liver metastases in 2 of 16 patients (12.5%) because of the difficulties in delineating lesions from the intense normal liver background activity. Combining liver-based and relative thresholds to limit image sampling errors and compensate for the spillover effect might also overcome the liver background–lesion discrimination issue (20,21). Moreover, as low-dose CT may underestimate small visceral lesions that can also be PSMA negative (24), PSMA imaging should be combined with thin-slice contrast-enhanced CT to optimize tumor burden enumeration and monitoring.

In contrast to tracer intensity of uptake, volumetric parameters were the most adequate for assessing treatment response using EAU/

EANM PSMA PET/CT criteria in our dataset and the least influenced by the flare phenomenon (Supplemental Table 3). The underlying mechanism behind PSMA “flare” after androgen deprivation therapy is poorly understood. Similar to BS tumor flare definitions (25), the increase in  $SUV_{max}$  on  $^{68}\text{Ga}$ -PSMA-11 PET/CT may also lead to a concomitant increase in PSMA-TV (and, thus, PSMA-TL) because of activity spillover or emergence of previously invisible or non-significant lesions at baseline and may result in the misinterpretation of PD, which is why the EAU/EANM did not recommend PSMA PET/CT imaging before 12 wk. The volumetric changes associated with a flare phenomenon may be significant but remain transitory; for example, for patient UPN17, the increase in  $SUV_{max}$  by 54% at W4 led to the appearance of 4 new lesions and an increase in PSMA-TL by 163%. By W12, the  $SUV_{max}$  had decreased by 70% (i.e., 16% lower than baseline), the previously observed new lesions disappeared completely, and PSMA-TL decreased by 49% from baseline (Fig. 1).

When comparing PSMA PET/CT at W4 and W12, we made 3 observations. First, an increase in  $SUV_{max}$  at W4 with a decrease in PSMA-TL, with or without new lesions, was confirmed at W12 to be linked to a flare phenomenon (e.g., for patients UPN2 and UPN14). Second, new lesions at W4 without an increase of greater than 30% in  $SUV_{max}$ , independently of PSMA-TL, were confirmed to be progressive at W12 (e.g., for patients UPN1 and UPN13). Third, when both  $SUV_{max}$  and PSMA-TL increased at W4, with or without new lesions, PD could not be distinguished from flare (e.g., for patients UPN12 and UPN17). Thus, defining PD on the basis of  $SUV_{max}$  alone does not seem to be feasible, and  $SUV_{max}$  should always be evaluated in combination with the other parameters to limit misinterpretation of flare as PD. Although at early time points  $SUV_{max}$  may provide a hint to a nuclear medicine specialist of the presence of a flare phenomenon, no flare was observed after W12, and  $SUV_{max}$  at W12 did not change the therapeutic response evaluation in our cohort.

Furthermore, the EAU/EANM recommendations on the use of uptake thresholds based on PERCIST were arbitrarily chosen, as these have been validated only for  $^{18}\text{F}$ -FDG PET. Even though tracer uptake in PSMA imaging does not reflect direct metabolic activity, modified PERCIST criteria were shown to perform better than morphologic criteria such as RECIST in metastatic PC—as molecular changes appeared earlier than morphologic ones (26). Although the aim of the present study was not to validate PERCIST criteria in PSMA imaging, we observed that caution should be taken when those criteria are used, especially for early imaging. Indeed, changes in tracer uptake are not synonymous with PD but rather seem to reflect biomolecular changes leading to modifications in PSMA expression, as indicated by the heterogeneous

responses at the patient level, and further highlight the fact that additional data are needed to shed light on the mechanisms of PSMA expression and tracer uptake. Besides flare, the modulation of PSMA expression may also reflect intrinsic tumor tissue modifications conferring potential treatment resistance (10). In our data, the 5 of 16 patients (31%) with PD at W12 according to PSMA PET/CT had already met progression criteria at W4. Two of those patients (UPN12 and UPN13) had PD according to conventional imaging, and 1 patient (UPN16) had PSA progression.

With these EAU/EANM recommendations, patients with non-PD may be further subdivided into those with a stable response, those with a partial response, and those with a complete response, depending on the reductions in both  $SUV_{max}$  and PSMA-TL (Table 1). However, these criteria may need to be revised, as the extent of reduction in  $SUV_{max}$  and volumetric parameters rarely seemed comparable (Fig. 1). For example, at W12, 4 of 11 patients would be classified with a partial response (>30% reductions in both  $SUV_{max}$  and volumetric parameters) and 7 of 11 patients would be classified with a stable response even though 5 of the 7 achieved a significant (>30%) reduction in PSMA-TL. Data are also lacking on the thresholds that should be used, especially to define PD. For example, according to the current recommendations, PD may be defined by a 30% increase in tumor volume, but the recently proposed RECIP criteria have set a lower threshold of 20%; in addition, these parameters have been shown to carry prognostic value after  $^{177}\text{Lu}$ -PSMA therapy (27). Moreover, in contrast to PERCIST, RECIP does not include tracer uptake modifications for evaluating response to  $^{177}\text{Lu}$ -PSMA therapy. Nonetheless, this parameter could be of potential use for improving patient stratification before therapy initiation and was recently shown to predict a higher likelihood of a response to  $^{177}\text{Lu}$ -PSMA therapy than to cabazitaxel (28).

The integration of minimally invasive molecular biomarkers, such as circulating tumor DNA, with novel imaging might facilitate discrimination between PD and flare and guide therapeutic intervention at early response assessment time points. As shown in a recent work, circulating tumor DNA does not seem to rise in patients with an increase in PSA or bone flare on conventional imaging (29). Additionally, the introduction of PSMA PET/CT in mCRPC might improve disease control rates by identifying oligoresistant or oligoprogressive lesions, which could be subjected to—for example—metastasis-directed therapy, while preserving the antitumoral effect of the systemic agent on the responsive lesions (12,13).

Overall, molecular imaging parameters have the potential to act as predictive biomarkers of response to treatment, but whether modifying a treatment plan according to them improves patient outcomes has yet to be determined in larger prospective trials. The main limitations of the present study were the small number of patients who were retrospectively included and the absence of validated criteria for the interpretation of PSMA PET/CT scans and the delineation method.

## CONCLUSION

Volumetric assessments of PSMA PET/CT imaging can improve metastasis detection and image-based response assessment in NHA-treated patients with mCRPC. At early imaging time points, flare phenomena can be observed, typically denoted by an increase in  $SUV_{max}$  that resolves by W12. Overall, although early response assessments at W4 need to be approached with caution, our

comparative analysis of PSMA PET/CT imaging at W4 and W12 revealed substantial agreement in the therapy response assessments, thus warranting further investigation to distinguish PD from flare at W4.

## DISCLOSURE

The study was funded by a Belgium Multidisciplinary Meeting on Urological Cancers (BMUC) research grant. No other potential conflict of interest relevant to this article was reported.

## KEY POINTS

**QUESTION:** Is the use of EAU/EANM recommendations for PSMA PET/CT feasible for therapy assessment of mCRPC patients, and can early imaging detect resistance to treatment?

**PERTINENT FINDINGS:** EAU/EANM recommendations improve PSMA imaging reporting and evaluation of NHA-treated mCRPC patients, but caution should be taken in the interpretation of  $SUV_{max}$  in early imaging. Early PSMA uptake modifications occurred as early as 4 wk after therapy and showed substantial agreement with imaging at W12.

**IMPLICATIONS FOR PATIENT CARE:** Early imaging may contribute to improving therapy selection and sequencing in the mCRPC context, and adding biologic biomarkers may provide further insight into the biology behind PSMA expression and help distinguish early progressive disease from flare.

## REFERENCES

1. Abuzalouf S, Dayes I, Lukka H. Baseline staging of newly diagnosed prostate cancer: a summary of the literature. *J Urol*. 2004;171:2122–2127.
2. Eisenhauer EA, Therasse P, Bogaerts J, et al. New response evaluation criteria in solid tumors: revised RECIST guideline (version 1.1). *Eur J Cancer*. 2009;45:228–247.
3. Hofman MS, Lawrentschuk N, Francis RJ, et al. Prostate-specific membrane antigen PET-CT in patients with high-risk prostate cancer before curative-intent surgery or radiotherapy (proPSMA): a prospective, randomised, multi-centre study. *Lancet*. 2020;395:1208–1216.
4. Perera M, Papa N, Christidis D, et al. Sensitivity, specificity, and predictors of positive  $^{68}\text{Ga}$ -prostate-specific membrane antigen positron emission tomography in advanced prostate cancer: a systematic review and meta-analysis. *Eur Urol*. 2016;70:926–937.
5. Mottet N, Cornford P, Van den Bergh RCN, et al. EAU-ESTRO-ESUR-SIOG guidelines on prostate cancer. Paper presented at: EAU Annual Congress Amsterdam; July 17–26, 2020; Arnhem, The Netherlands.
6. Fanti S, Goffin K, Hadaschik BA, et al. Consensus statements on PSMA PET/CT response assessment criteria in prostate cancer. *Eur J Nucl Med Mol Imaging*. 2021;48:469–476.
7. Paschalis A, Sheehan B, Riisnaes R, et al. Prostate-specific membrane antigen heterogeneity and DNA repair defects in prostate cancer. *Eur Urol*. 2019;76:469–478.
8. Kaittani S, Andreou C, Hieronymus H, et al. Prostate-specific membrane antigen cleavage of vitamin B9 stimulates oncogenic signaling through metabotropic glutamate receptors. *J Exp Med*. 2018;215:159–175.
9. Emmett L, Yin C, Crumbaker M, et al. Rapid modulation of PSMA expression by androgen deprivation: serial  $^{68}\text{Ga}$ -PSMA-11 PET in men with hormone-sensitive and castrate-resistant prostate cancer commencing androgen blockade. *J Nucl Med*. 2019;60:950–954.
10. Mei R, Bracarda S, Emmett L, et al. Androgen deprivation therapy and its modulation of PSMA expression in prostate cancer: mini review and case series of patients studied with sequential  $^{68}\text{Ga}$ -PSMA-11 PET/CT. *Clin Transl Imaging*. 2021;9:215–220.
11. Kyriakopoulos CE, Heath EI, Ferrari A, et al. Exploring spatial-temporal changes in  $^{18}\text{F}$ -sodium fluoride PET/CT and circulating tumor cells in metastatic castration-resistant prostate cancer treated with enzalutamide. *J Clin Oncol*. 2020;38:3662–3671.

12. Berghen C, Joniau S, Ost P, et al. Progression-directed therapy for oligoprogression in castration-refractory prostate cancer. *Eur Urol Oncol*. 2021;4:305–309.
13. Triggiani L, Mazzola R, Magrini SM, et al. Metastasis-directed stereotactic radiotherapy for oligoprogressive castration-resistant prostate cancer: a multicenter study. *World J Urol*. 2019;37:2631–2637.
14. Scher HI, Morris MJ, Stadler WM, et al. Trial design and objectives for castration-resistant prostate cancer: updated recommendations from the prostate cancer clinical trials working group 3. *J Clin Oncol*. 2016;34:1402–1418.
15. Derwael C, Lavergne O, Lovinfosse P, et al. Interobserver agreement of <sup>68</sup>Ga-Ga-PSMA-11 PET/CT images interpretation in men with newly diagnosed prostate cancer. *EJNMMI Res*. 2020;10:15.
16. Acar E, Özdoğan Ö, Aksu A, Derebek E, Bekiş R, Kaya GC. The use of molecular volumetric parameters for the evaluation of Lu-177 PSMA I&T therapy response and survival. *Ann Nucl Med*. 2019;33:681–688.
17. Ferdinandus J, Violet J, Sandhu S, et al. Prognostic biomarkers in men with metastatic castration-resistant prostate cancer receiving [<sup>177</sup>Lu]-PSMA-617. *Eur J Nucl Med Mol Imaging*. 2020;47:2322–2327.
18. Violet J, Jackson P, Ferdinandus J, et al. Dosimetry of <sup>177</sup>Lu-PSMA-617 in metastatic castration-resistant prostate cancer: correlations between pretherapeutic imaging and whole-body tumor dosimetry with treatment outcomes. *J Nucl Med*. 2019;60:517–523.
19. Sheikhbahaei S, Afshar-Oromieh A, Eiber M, et al. Pearls and pitfalls in clinical interpretation of prostate-specific membrane antigen (PSMA)-targeted PET imaging. *Eur J Nucl Med Mol Imaging*. 2017;44:2117–2136.
20. Seifert R, Herrmann K, Kleesiek J, et al. Semiautomatically quantified tumor volume using <sup>68</sup>Ga-PSMA-11 PET as a biomarker for survival in patients with advanced prostate cancer. *J Nucl Med*. 2020;61:1786–1792.
21. Gafita A, Bieth M, Kronke M, et al. qPSMA: semiautomatic software for whole-body tumor burden assessment in prostate cancer using <sup>68</sup>Ga-PSMA11 PET/CT. *J Nucl Med*. 2019;60:1277–1283.
22. Farolfi A, Hirmas N, Gafita A, et al. PSMA-PET identifies PCWG3 target populations with superior accuracy and reproducibility when compared to conventional imaging: a multicenter retrospective study. *J Nucl Med*. 2021;62:675–678.
23. Schmuck S, von Klot CA, Henkenberens C, et al. Initial experience with volumetric <sup>68</sup>Ga-PSMA I&T PET/CT for assessment of whole-body tumor burden as a quantitative imaging biomarker in patients with prostate cancer. *J Nucl Med*. 2017;58:1962–1968.
24. Noto B, der Springe KA, Huss S, Allkemper T, Stegger L. Prostate-specific membrane antigen-negative metastases: a potential pitfall in prostate-specific membrane antigen PET. *Clin Nucl Med*. 2018;43:e186–e188.
25. Cook GJR, Venkitaraman R, Sohaib AS, et al. The diagnostic utility of the flare phenomenon on bone scintigraphy in staging prostate cancer. *Eur J Nucl Med Mol Imaging*. 2011;38:7–13.
26. Gupta M, Choudhury PS, Rawal S, Goel HC, Rao SA. Evaluation of RECIST, PERCIST, EORTC, and MDA criteria for assessing treatment response with Ga68-PSMA PET-CT in metastatic prostate cancer patient with biochemical progression: a comparative study. *Nucl Med Mol Imaging*. 2018;52:420–429.
27. Andrei G, Isabel R, Manuel W, et al. Novel framework for treatment response evaluation using PSMA-PET/CT in patients with metastatic castration-resistant prostate cancer (RECIP): an international multicenter study. *J Clin Oncol*. 2022;40(6 suppl):42.
28. Buteau PJ, Martin JA, Louise E, et al. PSMA PET and FDG PET as predictors of response and prognosis in a randomized phase 2 trial of <sup>177</sup>Lu-PSMA-617 (LuP-SMA) versus cabazitaxel in metastatic, castration-resistant prostate cancer (mCRPC) progressing after docetaxel (TheraP ANZUP 1603). *J Clin Oncol*. 2022;40(6 suppl):10.
29. Conteduca V, Wetterskog D, Scarpi E, et al. Plasma tumor DNA as an early indicator of treatment response in metastatic castration-resistant prostate cancer. *Br J Cancer*. 2020;123:982–987.

---

---

# <sup>68</sup>Ga-PSMA-11 PET/MRI in Patients with Newly Diagnosed Intermediate- or High-Risk Prostate Adenocarcinoma: PET Findings Correlate with Outcomes After Definitive Treatment

Farshad Moradi<sup>1</sup>, Heying Duan<sup>1</sup>, Hong Song<sup>1</sup>, Guido A. Davidzon<sup>1</sup>, Benjamin I. Chung<sup>2</sup>, Alan E. C. Thong<sup>2</sup>, Andreas M. Loening<sup>3</sup>, Pejman Ghanouni<sup>3</sup>, Geoffrey Sonn<sup>2</sup>, and Andrei Iagaru<sup>1</sup>

<sup>1</sup>Division of Nuclear Medicine and Molecular Imaging, Department of Radiology, Stanford University, Stanford, California;

<sup>2</sup>Department of Urology, Stanford University, Stanford, California; and <sup>3</sup>Division of Body MRI, Department of Radiology, Stanford University, Stanford, California

---

Prostate-specific membrane antigen (PSMA) PET offers an accuracy superior to other imaging modalities in initial staging of prostate cancer and is more likely to affect management. We examined the prognostic value of <sup>68</sup>Ga-PSMA-11 uptake in the primary lesion and presence of metastatic disease on PET in newly diagnosed prostate cancer patients before initial therapy. **Methods:** In a prospective study from April 2016 to December 2020, <sup>68</sup>Ga-PSMA-11 PET/MRI was performed in men with a new diagnosis of intermediate- or high-grade prostate cancer who were candidates for prostatectomy. Patients were followed up after initial therapy for up to 5 y. We examined the Kendall correlation between PET (intense uptake in the primary lesion and presence of metastatic disease) and clinical and pathologic findings (grade group, extraprostatic extension, nodal involvement) relevant for risk stratification, and examined the relationship between PET findings and outcome using Kaplan–Meier analysis. **Results:** Seventy-three men (age, 64.0 ± 6.3 y) were imaged. Seventy-two had focal uptake in the prostate, and in 20 (27%) PSMA-avid metastatic disease was identified. Uptake correlated with grade group and prostate-specific antigen (PSA). Presence of PSMA metastasis correlated with grade group and pathologic nodal stage. PSMA PET had higher per-patient positivity than nodal dissection in patients with only 5–15 nodes removed (8/41 vs. 3/41) but lower positivity if more than 15 nodes were removed (13/21 vs. 10/21). High uptake in the primary lesion (SUV<sub>max</sub> > 12.5, *P* = 0.008) and presence of PSMA metastasis (*P* = 0.013) were associated with biochemical failure, and corresponding hazard ratios for recurrence within 2 y (4.93 and 3.95, respectively) were similar to or higher than other clinicopathologic prognostic factors. **Conclusion:** <sup>68</sup>Ga-PSMA-11 PET can risk-stratify patients with intermediate- or high-grade prostate cancer before prostatectomy based on degree of uptake in the prostate and presence of metastatic disease.

**Key Words:** oncology; GU; PET; PET/MRI; prostate cancer; biochemical recurrence; prostate-specific membrane; antigen; prostatectomy

**J Nucl Med 2022; 63:1822–1828**

DOI: 10.2967/jnumed.122.263897

---

**P**atients diagnosed with localized prostate adenocarcinoma have generally prolonged natural history, although some patients

experience rapid progression after initial curative intent prostatectomy or radiation therapy. Initial risk stratification affects treatment decisions and subsequent management of prostate cancer patients. Risk stratification is primarily based on clinical tumor stage, histologic grade group, and the prostate-specific antigen (PSA) level (1), although incorporating molecular markers is increasingly being considered (2). Imaging is indicated in all men with unfavorable intermediate-, high-, or very-high-risk disease (3,4). The presence of nodal or distant metastatic disease on cross-sectional imaging or bone scintigraphy affects management and prognosis. Prostate-specific membrane antigen (PSMA) PET/CT or PET/MRI has significantly better sensitivity and higher diagnostic yield for detection of metastatic disease (5,6). Unfortunately, the outcome data on patients with metastasis that is occult on anatomic imaging and bone scintigraphy are sparse. Extrapolation of data from prostatectomy and pelvic nodal dissection suggests that prognosis of patients with nodal metastasis could be variable (7). After prostatectomy, even in node-positive patients, 75% achieve complete biochemical response and are at low risk for recurrence and cancer specific mortality (8). There is a need for prognostic models to identify patients at risk for persistent or recurrent disease based on PET versus others who do not benefit from overtreatment.

We and others have examined the clinical utility of pretherapy vertex to mid-thigh <sup>68</sup>Ga-PSMA-11 PET as a part of PET/MRI in newly diagnosed prostate cancer patients and correlation with histopathology (9–11). We now examine the association between PET findings and outcomes/biochemical recurrence after initial therapy.

## MATERIALS AND METHODS

### Patient Population

The study protocol was approved by the Stanford University Institutional Review Board, and all subjects signed a written informed consent form. Patients with newly diagnosed intermediate- or high-risk prostate cancer (PSA ≥ 10 ng/mL, cT2b or greater, or Gleason score ≥ 7) who were scheduled for radical prostatectomy were enrolled from April 2016 until December 2020 (NCT02678351). The protocol has been described previously (11). Exclusion criteria were androgen deprivation therapy, neoadjuvant chemotherapy, or radiation therapy before the planned prostatectomy.

### PET/MR Imaging Protocol

<sup>68</sup>Ga-PSMA-11 was prepared as described previously (11,12). The mean ± SD administered dosage was 160.8 ± 31.1 MBq (range, 91.4–236.4 MBq). After an uptake time of 50.0 ± 8.9 min (range,

Received Feb. 18, 2022; revision accepted Apr. 22, 2022.

For correspondence or reprints, contact Farshad Moradi (fmoradi@stanford.edu).

Published online May 5, 2022.

COPYRIGHT © 2022 by the Society of Nuclear Medicine and Molecular Imaging.

40–108 min), patients were imaged from mid-thighs to vertex using a time-of-flight simultaneous PET/MR scanner (SIGNA; GE Healthcare) in 3-dimensional mode for 4 min per bed position in 5–9 beds. Delayed pelvic PET/MRI including prostate multiparametric MRI (mpMRI) was obtained after voiding, at  $70.5 \pm 13.4$  min (range, 43–108 min) after the initial scan. A 2-point Dixon 3-dimensional T1-weighted spoiled gradient-echo MR sequence was acquired using the volume coil for MR-attenuation correction.

### Image Analysis

PET images acquired before October 2017 (33 patients) were independently reviewed in correlation with MRI by 2 nuclear medicine physicians with 13 and 5 y of experience (11). Subsequent studies were reviewed by one of the original nuclear physicians (with more than 13 y of experience) using MIM (version 7; MIM Software Inc.). PET findings were communicated with the referring surgeon and the information was used as a part of clinical decision making. SUVs normalized based on body weight were measured for prostate lesions and physiologic activity in liver, spleen, right parotid gland, and mediastinal blood pool separately by a radiologist/nuclear medicine physician (with 10 y of experience). For prostate lesions,  $SUV_{max}$  and  $SUV_{peak}$  were recorded for initial images, and  $SUV_{max}$  was recorded for delayed images. Physiologic activity was recorded using  $SUV_{mean}$  per Prostate Cancer Molecular Imaging Standardized Evaluation recommendations (13). Lesion PSMA index was calculated using  $SUV_{peak}$  comparison with blood pool and liver activity (14).

### Outcome Analysis

Biochemical persistence and recurrence were assessed via review of all available electronic medical records (including PSA results and clinical notes). Biochemical failure was defined as PSA  $\geq 0.4$  ng/mL after prostatectomy or persistent PSA that was followed by adjuvant therapy. Recurrence was defined as a rise in PSA at least 6 wk after radical prostatectomy with or without adjuvant therapy measuring  $\geq 0.2$  ng/mL that was subsequently confirmed by a follow-up measurement (15) or any rise in PSA that was treated with salvage therapy.

### Statistical Analysis

Analysis was performed using MATLAB (R2021B) Statistics and Machine Learning toolbox (The MathWorks). A multistep analysis was performed. PET findings were dichotomized (low vs. high uptake in the primary lesion, presence of metastatic disease). We next examined the correlation between PET findings and clinical and pathologic parameters in prostate cancer risk stratification. Finally, we examined the relationship between PET findings and outcomes.

There is no a priori threshold for dichotomizing uptake in prostate although uptake higher than twice activity in normal liver parenchyma has been suggested for metastatic lesions (13,14). To explore a basis for thresholding of the primary prostate lesion (or the dominant lesion if more than one lesion were present), we used histogram and cluster analysis. The Shapiro–Wilk test was used to examine normality of  $SUV_{max}$  distribution. We subsequently used cluster analysis of the  $SUV_{max}$  based on L1-norm ( $k$ -medians) with  $k = 2$ . The resulting categories (low vs. high uptake) were stable for  $SUV_{max} < 12.5$  ( $n = 40$ ) or  $SUV_{max} > 20$  ( $n = 13$ ), but classification was variable for  $SUV_{max}$  between 12.5 and 20 (i.e.,  $k$ -median results depended on initial state,  $n = 20$ ). We used an SUV of 12.5 as the cutoff threshold for future analysis, which is close to twice average normal liver activity (11.88 g/mL) in our patients, and more evenly divided the patients into low- and high-uptake groups compared with a higher cutoff value.

We also explored reliability of physiologic uptake that can define an internal reference per subject (16). Coefficient of variation was used to examine the variability of physiologic uptake. Person correlation coefficient was used to estimate the contribution of factors that

systematically affect physiologic uptake in different organs to the overall variability of physiologic uptake.

Metastatic disease on  $^{68}\text{Ga}$ -PSMA-11 PET/MRI was categorized as absent versus present (regardless of number of metastases). For clinical parameters, conventional categories were used (PSA level:  $<10$ , 10–20,  $>20$ ; clinical tumor stage: T1–2a, T2b/c,  $\geq T3$ ; grade group: 2, 3,  $\geq 4$ ) (17).

Kendall  $\tau$  was used to assess correlation between PET findings and clinical and pathologic parameters. A cutoff value of  $P < 0.05$  was used for significance. The Kruskal–Wallis H test was used to examine whether a similar number of nodes were sampled during pelvic dissection between various groups.

**Survival Analysis.** The relationship between PET findings and outcomes was analyzed using Kaplan–Meier survival plots and log-rank test using MatSurv (<https://github.com/aebergl/MatSurv>) (18).

## RESULTS

### Patient Characteristics and Pathologic Findings

Seventy-five men were enrolled in this study (Fig. 1). One patient was excluded because of equipment failure. No imaging could be done in one patient, and PET/MRI was terminated early (after acquisition of pelvis and lower abdomen) in another patient because of claustrophobia. The data for prostate lesions and regional lymph nodes include 73 patients (Tables 1 and 2). The data for distant metastasis and physiologic uptake include 72 patients.

Sixty-five patients underwent prostatectomy  $12.4 \pm 15.4$  d (median, 7 d; range, 1–95 d) after PET. In all cases, clinically significant prostate cancer was confirmed. On average,  $14.83 \pm 10.84$  lymph nodes (median, 13; range, 0–54) from 64 patients were submitted for pathologic examination. The Gleason grade group after prostatectomy correlated with grade group based on initial biopsy (Kendall  $\tau = 0.42$ ,  $P = 0.0002$ ), and was unchanged, revised up, or revised down after prostatectomy in 32, 26, and 5 patients, respectively (Table 3).

In 72 of 73 patients, follow-up data were available (34.4  $\pm$  15.49 mo after PET; median, 35.91 mo; range, 4.86–60.7 mo). Persistent disease (based on PSA failure) was documented in 10 patients after prostatectomy and 4 after other treatments. Biochemical

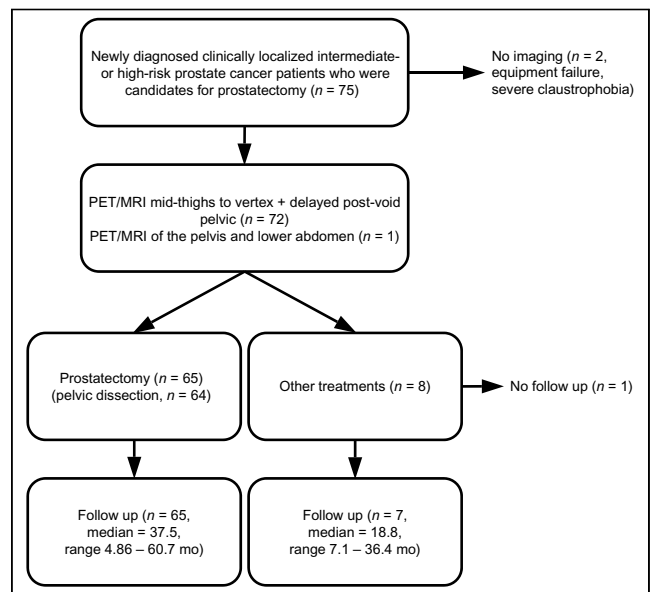


FIGURE 1. Study diagram.

**TABLE 1**  
Clinical Characteristics of Patients Included in Study  
(*n* = 73)

Characteristic	Mean ± SD	Median and range
Age at time of PET (y)	64.0 ± 6.3	66; range, 44–75
Weight (kg)	86.0 ± 13.3	85.3; range, 62.1–138.3
Body mass index (kg)	27.2 ± 3.4	26.6; range, 20.9–43.8
PSA (ng/mL)*	12.9 ± 21.1	8.6; range, 3.0–176

\*PSA data not available in 1 patient.

recurrence (after initial complete response) was documented in 14 patients after prostatectomy and in 6 patients after prostatectomy and adjuvant therapy.

**PET Findings**

Except for 1 patient, focal uptake was identified within the prostate gland. In 7 patients (including a patient with negative PET results) MI showed more lesions, and in 26 patients PET showed more lesions. For the remaining patients, a PET-positive lesion was congruent with mpMRI in 36 patients and incongruent in 1 (Table 4). In 20 patients (27.4%), PET showed focal uptake outside the prostate consistent with metastatic disease in 66 lesions (3.3 ± 4.6 sites per patient; median, 1; range, 1–19) (Table 5).

**Metastatic Disease on PET Versus Pelvic Dissection**

Of 16 patients with pathologically proven N1 disease, 9 had PSMA metastasis (56% per patient sensitivity). There were 9 patients for whom nodal dissection did not reveal metastasis (pN0) but who had PSMA metastasis. The extent of a pelvic lymph node dissection confounds the probability of positive lymph nodes. Patients with PSMA metastasis and negative pelvic dissection had

**TABLE 2**  
Gleason Score and Clinical Stage of Patients Included in Study

Primary tumor	<i>n</i>
Gleason score (biopsy)*	
3 + 4	14 (19.2%)
4 + 3	20 (27.4%)
4 + 4 or 3 + 5	18 (24.7%)
4 + 5	19 (26%)
Clinical T stage†	
T1c	33 (45.2%)
T2a	13 (17.8%)
T2b	7 (9.6%)
T2c	6 (8.2%)
T3a	8 (11%)

\*Not known in 2 patients.  
†Not known in 6 individuals.

**TABLE 3**  
Initial Biopsy Versus Prostatectomy

Final grade group	Grade group based on initial biopsy		
	2	3	4/5
2	9	5	0
3	6	9	0
4/5	8	12	14

on average less than half of the number of lymph nodes sampled compared with patients for whom both PET and pelvic dissection showed metastatic disease, or only pelvic dissection showed metastatic disease (11.7 ± 5.2 vs. 24.4 ± 13.1 and 27.3 ± 15.7, respectively, *P* = 0.012, Kruskal–Wallis test). The per-patient <sup>68</sup>Ga-PSMA-11 PET/MRI positivity rate was 2.5 times higher than pelvic nodal dissection when 5–15 nodes were surgically sampled (Table 5).

*Degree of <sup>68</sup>Ga-PSMA-11 Uptake.* For prostate lesions (dominant lesion if multiple lesions are present), the SUV<sub>max</sub> was 14.53 ± 10.42 (median, 10.64; range, 3.61–50.12 g/mL) and the SUV<sub>peak</sub> was 9.18 ± 7.21 (median, 6.69; range, 2.13–40.24 g/mL). Figure 2A depicts the histogram of SUV<sub>max</sub> of the dominant prostate lesion in our dataset. The distribution is asymmetric and nongaussian (*P* < 0.001, Shapiro–Wilk test). A cutoff value of 12.5 (~55th percentile) was used for subsequent analysis as the threshold for high uptake. Uptake on initial PET and delayed pelvic PET was highly correlated (*r* = 0.968, Fig. 2B) and followed a similar distribution, with the equivalent delayed SUV cutoff of 13.5.

The average uptake in liver, spleen, blood pool, and parotid gland were 5.94 ± 1.53, 9.33 ± 3.11, 1.26 ± 0.24, and 16.08 ± 3.94 g/mL, respectively (corresponding to interpatient coefficients of variation of 0.26, 0.34, 0.19, and 0.25, respectively; Fig. 2C). SUV<sub>max</sub> or SUV<sub>peak</sub> of the prostate lesion did not correlate with physiologic uptake in the liver, spleen, blood pool, or parotid gland (*r* < 0.12 for all tests). Correlation between physiologic uptake in various organs was weak, with the highest between liver and spleen (*r* = 0.224, *P* = 0.058; Fig. 2D).

**Relationship Between PET Findings and Clinicopathologic Risk Factors**

Uptake in the primary lesion and presence of PSMA metastasis correlated with several clinical and pathologic factors as detailed in Table 6. The notable exception was a nonsignificant correlation between clinical or pathologic T stage (extraprostatic extension) and

**TABLE 4**  
Laterality of PSMA-Avid Lesion Versus PIRADS 4 or 5 Lesions on Prostate mpMRI

PSMA PET	mpMRI			
	No lesion	R	L	Bilateral
No lesion	0	0	1	0
R	1	13	1	3
L	1	0	10	3
Bilateral	5	10	9	13

**TABLE 5**  
Positivity Versus Number of Lymph Nodes Removed During Pelvic Nodal Dissection

No. of nodes removed	Pelvic dissection			PSMA PET		
	pN0	pN1	Positivity rate	No metastasis	Metastatic disease	Positivity rate
1–2	2	0	0	2	0	0
5–15	38	3	7.3%	33	8	19.5%
>15	8	13	61.9%	11	10	52.4%

PET findings (in contrast to the study of Lima et al. (19)). High uptake in the primary lesion correlated more with preprostatectomy PSA level and D’Amico risk category whereas PSMA metastasis correlated more with grade group and nodal involvement.

#### Relationship Between PET Findings and Outcome

High uptake ( $SUV_{max} > 12.5$ ) and presence of PSMA metastasis were associated with biochemical failure or rapid recurrence within 2 y after prostatectomy. In contrast, patients with low uptake in the primary lesion who did not have evidence of metastatic disease on PET had low likelihood of experiencing recurrence within the follow-up period (Fig. 3). The outcomes were worse in patients with high uptake in the primary lesion and PSMA metastasis (Fig. 4). Results were similar when the analysis included all patients rather than only patients who underwent prostatectomy ( $P = 0.008$  for uptake in primary,  $P = 0.0135$  for PSMA metastasis, and  $P = 0.001$  for the combination of the two). Alternative measures of uptake using body surface area and lean body mass also showed significant differences in survival ( $P < 0.05$ ) between high and low uptake when a comparable cutoff threshold (about 55 percentile of corresponding population values) was used. Neither  $SUV_{peak}$  nor lesion index (14) (defined based on  $SUV_{peak}$ ) reached statistical significance.

PET findings correlated with the duration of biochemical response after initial therapy (including adjuvant therapy) (Fig. 5). The hazard ratio for PET compared with clinicopathologic factors for biochemical recurrence within the first 24 mo are depicted in Table 7. High uptake in the primary cancer and presence of PSMA-avid metastasis were associated with higher hazard ratios for early recurrence compared with clinicopathologic factors, although our sample is too small to allow for statistical comparison and testing independence. Kaplan–Meier survival analysis showed worse outcome for patients with bilateral disease in the prostate (based on either PET or MRI) or if PET and MRI results were incongruent ( $P = 0.125$ , not significant).

#### DISCUSSION

In patients with newly diagnosed intermediate- or high-risk prostate cancer who were candidates for radical prostatectomy,  $^{68}Ga$ -PSMA-11 PET/MRI findings were closely linked with clinical and pathologic risk factors. High  $^{68}Ga$ -PSMA-11 uptake in the primary lesion and presence of PSMA-avid metastatic disease were negatively associated with response to initial therapy and duration of biochemical response. Our findings add to the evidence of the utility of PSMA PET in the initial workup of prostate cancer and correlation between PSMA expression and tumor behavior (20).

Dedicated prostate MRI was performed in the same session in conjunction with PET and helped identify prostate lesions (particularly lesions with very low uptake). Uptake and conspicuity increase on delayed PET. Nonetheless, most lesions were readily visible on the initial PET, including lesions that were identified only on PET or lesions with indeterminate appearance on mpMRI that were not prospectively called. Although survival analysis did not use MRI findings, scanner hardware, attenuation correction methodology, and postprocessing affect image quality and SUV measurements, which should be considered before applying our results to data from PET/CT or other PET/MRI systems.

A PSMA PET sensitivity of 56% for nodal involvement here is in line with that of other studies (21,22). Therefore, the absence of PSMA metastasis does not indicate that a pelvic nodal dissection is not required (23). Several patients had nodal involvement on PET that was not confirmed pathologically. PSMA PET has high specificity (23–26), so we suspected undersampling, corroborated by our analysis. Accurate surgical staging requires extensive lymphadenectomy, which increases surgical morbidity. The positivity rate of PET in our study was 2.5 times higher than limited pelvic dissection (sampling up to 15 lymph nodes), and only slightly lower than extensive pelvic nodal dissection (52% vs. 62%). Therefore, PSMA PET could be supplementary to surgical pathology in staging patients undergoing nodal dissection, particularly if for any reason extensive nodal dissection is not performed. Our survival analysis also suggests that despite limited sensitivity, the

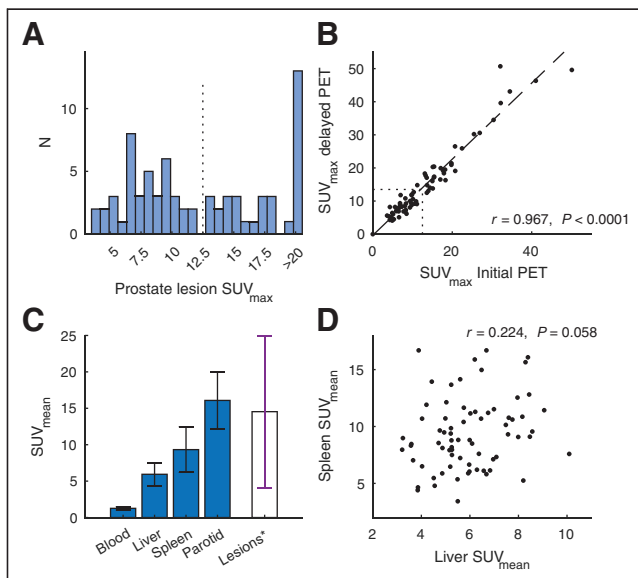


**FIGURE 2.** Uptake in primary prostate cancer versus physiologic uptake. (A) Histogram of  $SUV_{max}$  of primary lesion on initial PET. (B) Correlation between early and delayed  $SUV_{max}$ . (C) Average uptake in blood pool, liver, spleen, and right parotid gland (error bars indicate SD). \*Lesion uptake (using  $SUV_{max}$ ) is also plotted for comparison (white bar). (D) Poor within-subject correlation between liver and spleen uptake.

**TABLE 6**

Cross-Tabulation of the Relationship Between PET Findings and Clinical or Pathologic Risk Factors in Prostate Cancer

Prognostic factor	SUV <sub>max</sub>		Kendall $\tau$	PSMA-avid metastasis		Kendall $\tau$
	<12.5	>12.5		Absent	Present	
D'Amico risk category			0.35 ( <i>P</i> = 0.0027)			0.15 ( <i>P</i> = 0.2)
Intermediate	21	6		22	5	
High	19	27		31	15	
Grade group			0.24 ( <i>P</i> = 0.034)			0.31 ( <i>P</i> = 0.0058)
2	17	6		20	3	
3	15	16		24	7	
4/5	8	11		9	10	
PSA			0.33 ( <i>P</i> = 0.0037)			0.21 ( <i>P</i> = 0.068)
<10	30	15		36	9	
10–20	8	12		14	6	
>20	1	6		3	5	
Clinical T stage			0.23 ( <i>P</i> = 0.052)			0.08 ( <i>P</i> = 0.48)
T1c	19	14		23	10	
T2a	9	4		13	0	
T2b/c	8	5		8	5	
≥T3	1	8		7	2	
Extraprostatic extension			0.02 ( <i>P</i> = 0.85)			0.07 ( <i>P</i> = 0.57)
Negative	16	13		22	7	
Positive	19	17		25	11	
Nodal involvement			0.18 ( <i>P</i> = 0.12)			0.34 ( <i>P</i> = 0.0036)
pN0	29	19		39	9	
pN1	6	10		7	9	

Number of patients in each group is specified.

prognostic value of PSMA PET (in terms of hazard ratio of biochemical recurrence) can be comparable to pathologic nodal staging given variable prognosis of pN1 disease (7).

PSMA expression and histologic tumor grade are linked (27) and PSMA plays a complex role in tumor progression (28), which is consistent with our finding of slower progression in patients with low uptake in the primary tumor. Low PSMA expression could reduce the sensitivity of PET for metastatic disease but might have

little impact on the overall prognostic value of PSMA PET if cancers with low PSMA expression would have low probabilities for metastatic spread in the first place. <sup>68</sup>Ga-PSMA-11 uptake and grade group were correlated in our data (Table 6), which partially explains

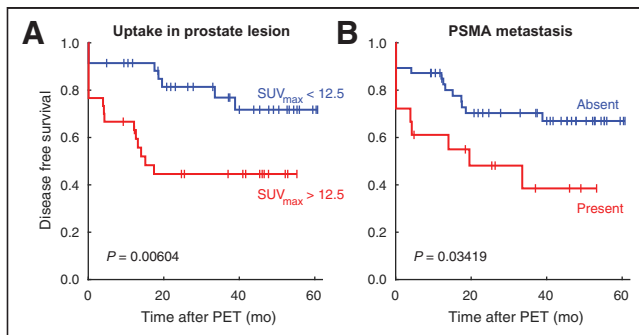


**FIGURE 3.** Kaplan–Meier Analysis for disease free survival after prostatectomy according to uptake of primary lesion (A) (SUV<sub>max</sub> on initial PET), and presence of metastatic disease on PET (B). Censored events are marked with a tick.

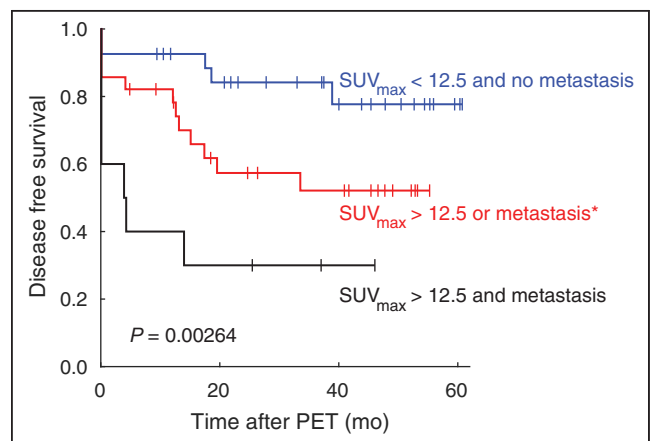


**FIGURE 4.** Kaplan–Meier Analysis for disease-free survival after prostatectomy as a function of uptake in primary cancer and presence of metastatic disease. Patient with both high uptake in primary cancer and metastatic disease on PET had worse survival than patient who had no or only 1 risk factor. \*Exclusive disjunction.

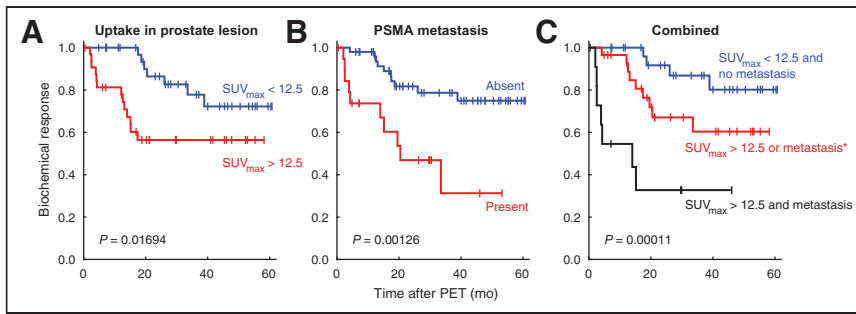


**FIGURE 5.** Proportion of patients without biochemical progression after initial treatment with or without adjuvant radiation therapy over time according to uptake of primary prostate lesion (A), presence of metastatic disease on PET (B), or combination of them (C). \*Exclusive disjunction.

better prognosis in patients with low uptake in the prostate. Nonetheless, for every grade group, we noticed that those with an  $SUV_{max} < 12.5$  tended to have longer recurrence-free survivals. Larger studies could shed light into the value of incorporating PSMA uptake in prognostic models of prostate cancer in addition to histologic grade. This question could be particularly relevant in patients who decide not to undergo prostatectomy because in nearly half our patients, the grade group based on initial biopsy changed after prostatectomy.

To simplify our analysis, we categorized uptake to low versus high. Variations on how this was done (e.g., normalizing based on lean body mass instead of weight) did not affect our results, although using  $SUV_{peak}$  (which could underestimate uptake in small lesions) did have an impact on the results. Uptake categorization and Kaplan–Meier analysis was reproducible on repeated PET/MRI of the pelvis performed after voiding, suggesting that  $SUV_{max}$  was a sufficiently robust measure in our study (29). Dichotomizing a continuous variable is, however, associated with certain issues such as loss of information (30), and further studies may be needed to confirm the relationship between SUV and duration of biochemical response.

A limitation of our study is that we did not examine how PET findings affected management. Heterogeneity in initial treatment strategies in prostate cancer can confound survival analysis. A few

**TABLE 7**  
Prognostic Factors for Biochemical Recurrence Within 24 Months After Initial Response

Factor	Hazard ratio (95% CI) (n = 72)	Hazard ratio in patients who underwent prostatectomy (n = 65)
$SUV_{max} > 12.5$	4.93 (1.87–13.04)	5.148 (1.94–13.66)
PSMA metastasis	3.95 (1.26–12.42)	4.14 (1.30–13.19)
D’Amico high risk	1.06 (0.39–2.83)	1.11 (0.42–2.96)
Grade group > 2	2.74 (1.03–7.34)	3.12 (1.18–8.24)
PSA > 10 ng/dL	1.48 (0.56–3.96)	1.72 (0.63–4.69)
$\geq cT2b$	3.53 (1.08–11.56)	4.12 (1.19–14.29)
$\geq pT3$	1.35 (0.52–3.53)	1.35 (0.52–3.53)
pN1	3.57 (1.09–11.72)	3.22 (1.01–10.21)

Unadjusted log-rank hazard ratio; ratio > 1 indicates increased probability of recurrence.

patients elected not to undergo prostatectomy and pursued other treatments after PET. Exclusion of these patients did not change the survival analysis results. As the role of PSMA PET in initial evaluation of patients with prostate cancer evolves, our results point to opportunities for optimizing treatment strategies in patients with high uptake in the primary lesion or with metastatic disease on PET.

## CONCLUSION

PSMA PET in initial evaluation of patients with intermediate- and high-risk prostate cancer correlates with the probability of biochemical failure or recurrence at least as well as clinical and pathologic factors. Patients with low uptake in prostate lesions and no evidence of metastatic disease on PET are unlikely to have recurrence within the first 2 y after initial treatment. Patients with high uptake in prostate cancer and metastatic disease are at risk for early recurrence and may require frequent surveillance and aggressive treatments.

## DISCLOSURE

This study was partially supported by GE Healthcare. No other potential conflict of interest relevant to this article was reported.

## ACKNOWLEDGMENTS

We thank Simon John Christoph Soerensen and Tie Liang for comments and suggestions on earlier versions of the manuscript.

## KEY POINTS

**QUESTION:** Is  $^{68}\text{Ga}$ -PSMA-11 PET useful in the assessment of risk for failure after prostatectomy or early biochemical recurrence?

**PERTINENT FINDINGS:** High  $^{68}\text{Ga}$ -PSMA-11 uptake in primary prostate cancer and the presence of PSMA-avid metastatic disease on PET are significant adverse prognostic factors after initial therapy.

**IMPLICATION FOR PATIENT CARE:**  $^{68}\text{Ga}$ -PSMA-11 PET has higher positivity rate than limited pelvic lymphadenectomy for metastatic disease and identifies patients who could benefit from additional treatment or frequent surveillance.

## REFERENCES

- D’Amico AV, Whittington R, Malkowicz SB, et al. Biochemical outcome after radical prostatectomy, external beam radiation therapy, or interstitial radiation therapy for clinically localized prostate cancer. *JAMA*. 1998;280:969–974.
- Egger SE, Rumble RB, Armstrong AJ, et al. Molecular biomarkers in localized prostate cancer: ASCO guideline. *J Clin Oncol*. 2020;38:1474–1494.
- Sanda MG, Cadeddu JA, Kirkby E, et al. Clinically localized prostate cancer: AUA/ASTRO/SUO guideline. Part I: risk stratification, shared decision making, and care options. *J Urol*. 2018;199:683–690.
- Bekelman JE, Rumble RB, Chen RC, et al. Clinically localized prostate cancer: ASCO clinical practice guideline endorsement of an American Urological Association/American Society for Radiation Oncology/Society of Urologic Oncology guideline. *J Clin Oncol*. 2018;36:3251–3258.

5. Moradi F, Farolfi A, Fanti S, Iagaru A. Prostate cancer: molecular imaging and MRI. *Eur J Radiol*. 2021;143:109893.
6. Hofman MS, Lawrentschuk N, Francis RJ, et al. Prostate-specific membrane antigen PET-CT in patients with high-risk prostate cancer before curative-intent surgery or radiotherapy (proPSMA): a prospective, randomised, multicentre study. *Lancet*. 2020;395:1208–1216.
7. Schumacher MC, Burkhard FC, Thalmann GN, Fleischmann A, Studer UE. Good outcome for patients with few lymph node metastases after radical retropubic prostatectomy. *Eur Urol*. 2008;54:344–352.
8. Bianchi L, Nini A, Bianchi M, et al. The role of prostate-specific antigen persistence after radical prostatectomy for the prediction of clinical progression and cancer-specific mortality in node-positive prostate cancer patients. *Eur Urol*. 2016;69:1142–1148.
9. Fassbender TF, Schiller F, Zamboglou C, et al. Voxel-based comparison of [<sup>68</sup>Ga]Ga-RM2-PET/CT and [<sup>68</sup>Ga]Ga-PSMA-11-PET/CT with histopathology for diagnosis of primary prostate cancer. *EJNMMI Res*. 2020;10:62.
10. Mapelli P, Ghezzi S, Samanes Gajate AM, et al. Preliminary results of an ongoing prospective clinical trial on the use of <sup>68</sup>Ga-PSMA and <sup>68</sup>Ga-DOTA-RM2 PET/MRI in staging of high-risk prostate cancer patients. *Diagnostics (Basel)*. 2021;11:2068.
11. Park SY, Zacharias C, Harrison C, et al. Gallium 68 PSMA-11 PET/MR imaging in patients with intermediate- or high-risk prostate cancer. *Radiology*. 2018;288:495–505.
12. Eder M, Neels O, Müller M, et al. Novel preclinical and radiopharmaceutical aspects of [<sup>68</sup>Ga]Ga-PSMA-HBED-CC: a new PET tracer for imaging of prostate cancer. *Pharmaceuticals (Basel)*. 2014;7:779–796.
13. Eiber M, Herrmann K, Calais J, et al. Prostate Cancer Molecular Imaging Standardized Evaluation (PROMISE): proposed miTNM classification for the interpretation of PSMA-ligand PET/CT. *J Nucl Med*. 2018;59:469–478.
14. Nickols N, Anand A, Johnsson K, et al. aPROMISE: a novel automated PROMISE platform to standardize evaluation of tumor burden in <sup>18</sup>F-DCFPyL images of veterans with prostate cancer. *J Nucl Med*. 2022;63:233–239.
15. Lowrance WT, Breau RH, Chou R, et al. Advanced prostate cancer: AUA/ASTRO/SUO guideline part 1. *J Urol*. 2021;205:14–21.
16. Davis K, Tann M. Which reference tissue is best for semiquantitative determination of <sup>68</sup>Ga-PSMA-11 activity in PET/CT? *J Nucl Med* [abstract]. 2020;61:100.
17. National Comprehensive Cancer Network. NCCN clinical practice guidelines in oncology (NCCN guidelines®): prostate cancer (version 3.2020). [https://www.nccn.org/professionals/physician\\_gls/pdf/prostate.pdf](https://www.nccn.org/professionals/physician_gls/pdf/prostate.pdf). Accessed September 14, 2022.
18. Creed JH, Gerke TA, Berglund AE. MatSurv: survival analysis and visualization in MATLAB. *J Open Source Softw*. 2020;5:1830.
19. P Lima J, Carvalho J, Quaresma V, et al. The role of Ga-68-PSMA PET/CT in the initial staging of prostate cancer - a single center 4 year experience. *Res Rep Urol*. 2021;13:479–485.
20. von Eyben FE, Picchio M, von Eyben R, Rhee H, Bauman G. <sup>68</sup>Ga-labeled prostate-specific membrane antigen ligand positron emission tomography/computed tomography for prostate cancer: a systematic review and meta-analysis. *Eur Urol Focus*. 2018;4:686–693.
21. Ferraro DA, Muehlethaler UJ, Garcia Schüler HI, et al. <sup>68</sup>Ga-PSMA-11 PET has the potential to improve patient selection for extended pelvic lymph node dissection in intermediate to high-risk prostate cancer. *Eur J Nucl Med Mol Imaging*. 2020;47:147–159.
22. Klingenberg S, Jochimsen MR, Ulhoi BP, et al. <sup>68</sup>Ga-PSMA PET/CT for primary lymph node and distant metastasis NM staging of high-risk prostate cancer. *J Nucl Med*. 2021;62:214–220.
23. Hope TA, Eiber M, Armstrong WR, et al. Diagnostic accuracy of <sup>68</sup>Ga-PSMA-11 PET for pelvic nodal metastasis detection prior to radical prostatectomy and pelvic lymph node dissection: a multicenter prospective phase 3 imaging trial. *JAMA Oncol*. 2021;7:1635–1642.
24. Luiting HB, van Leeuwen PJ, Busstra MB, et al. Use of gallium-68 prostate-specific membrane antigen positron-emission tomography for detecting lymph node metastases in primary and recurrent prostate cancer and location of recurrence after radical prostatectomy: an overview of the current literature. *BJU Int*. 2020;125:206–214.
25. Jansen BHE, Bodar YJL, Zwezerijnen GJC, et al. Pelvic lymph-node staging with <sup>18</sup>F-DCFPyL PET/CT prior to extended pelvic lymph-node dissection in primary prostate cancer: the SALT trial. *Eur J Nucl Med Mol Imaging*. 2021;48:509–520.
26. Scholte M, Barentsz JO, Sedelaar JPM, Gotthardt M, Grutters JPC, Rovers MM. Modelling study with an interactive model assessing the cost-effectiveness of <sup>68</sup>Ga Prostate-specific membrane antigen positron emission tomography/computed tomography and nano magnetic resonance imaging for the detection of pelvic lymph node metastases in patients with primary prostate cancer. *Eur Urol Focus*. 2020;6:967–974.
27. Bravaccini S, Puccetti M, Bocchini M, et al. PSMA expression: a potential ally for the pathologist in prostate cancer diagnosis. *Sci Rep*. 2018;8:4254.
28. Hyvärkkä A, Virtanen V, Kemppainen J, Grönroos TJ, Minn H, Sundvall M. More than meets the eye: scientific rationale behind molecular imaging and therapeutic targeting of prostate-specific membrane antigen (PSMA) in metastatic prostate cancer and beyond. *Cancers (Basel)*. 2021;13:2244.
29. Lodge MA, Chaudhry MA, Wahl RL. Noise considerations for PET quantification using maximum and peak standardized uptake value. *J Nucl Med*. 2012;53:1041–1047.
30. Altman DG, Royston P. The cost of dichotomising continuous variables. *BMJ*. 2006;332:1080.

---

---

# Correlation of <sup>68</sup>Ga-RM2 PET with Postsurgery Histopathology Findings in Patients with Newly Diagnosed Intermediate- or High-Risk Prostate Cancer

Heying Duan<sup>1</sup>, Lucia Baratto<sup>1</sup>, Richard E. Fan<sup>2</sup>, Simon John Christoph Soerensen<sup>2,3</sup>, Tie Liang<sup>1</sup>, Benjamin Inbeh Chung<sup>2</sup>, Alan Eih Chih Thong<sup>2</sup>, Harcharan Gill<sup>2</sup>, Christian Kunder<sup>4</sup>, Tanya Stoyanova<sup>5</sup>, Mirabela Rusu<sup>6</sup>, Andreas M. Loening<sup>7</sup>, Pejman Ghanouni<sup>7</sup>, Guido A. Davidzon<sup>1</sup>, Farshad Moradi<sup>1</sup>, Geoffrey A. Sonn<sup>2</sup>, and Andrei Iagaru<sup>1</sup>

<sup>1</sup>Division of Nuclear Medicine and Molecular Imaging, Department of Radiology, Stanford University, Stanford, California; <sup>2</sup>Department of Urology, Stanford University, Stanford, California; <sup>3</sup>Department of Epidemiology and Population Health, Stanford University, Stanford, California; <sup>4</sup>Department of Pathology, Stanford University, Stanford, California; <sup>5</sup>Radiology, Canary Center at Stanford for Cancer Early Detection, Stanford University, Stanford, California; <sup>6</sup>Division of Integrative Biomedical Imaging, Department of Radiology, Stanford University, Stanford, California; and <sup>7</sup>Division of Body MRI, Department of Radiology, Stanford University, Stanford, California

<sup>68</sup>Ga-RM2 targets gastrin-releasing peptide receptors (GRPRs), which are overexpressed in prostate cancer (PC). Here, we compared preoperative <sup>68</sup>Ga-RM2 PET to postsurgery histopathology in patients with newly diagnosed intermediate- or high-risk PC. **Methods:** Forty-one men, 64.0 ± 6.7 y old, were prospectively enrolled. PET images were acquired 42–72 min (median ± SD, 52.5 ± 6.5 min) after injection of 118.4–247.9 MBq (median ± SD, 138.0 ± 22.2 MBq) of <sup>68</sup>Ga-RM2. PET findings were compared with preoperative multiparametric MRI (mpMRI) (*n* = 36) and <sup>68</sup>Ga-PSMA11 PET (*n* = 17) and correlated to postprostatectomy whole-mount histopathology (*n* = 32) and time to biochemical recurrence. Nine participants decided to undergo radiation therapy after study enrollment. **Results:** All participants had intermediate- (*n* = 17) or high-risk (*n* = 24) PC and were scheduled for prostatectomy. Prostate-specific antigen was 8.8 ± 77.4 (range, 2.5–504) and 7.6 ± 5.3 ng/mL (range, 2.5–28.0 ng/mL) when participants who ultimately underwent radiation treatment were excluded. Preoperative <sup>68</sup>Ga-RM2 PET identified 70 intraprostatic foci of uptake in 40 of 41 patients. Postprostatectomy histopathology was available in 32 patients in which <sup>68</sup>Ga-RM2 PET identified 50 of 54 intraprostatic lesions (detection rate = 93%). <sup>68</sup>Ga-RM2 uptake was recorded in 19 nonenlarged pelvic lymph nodes in 6 patients. Pathology confirmed lymph node metastases in 16 lesions, and follow-up imaging confirmed nodal metastases in 2 lesions. <sup>68</sup>Ga-PSMA11 and <sup>68</sup>Ga-RM2 PET identified 27 and 26 intraprostatic lesions, respectively, and 5 pelvic lymph nodes each in 17 patients. Concordance between <sup>68</sup>Ga-RM2 and <sup>68</sup>Ga-PSMA11 PET was found in 18 prostatic lesions in 11 patients and 4 lymph nodes in 2 patients. Noncongruent findings were observed in 6 patients (intraprostatic lesions in 4 patients and nodal lesions in 2 patients). Sensitivity and accuracy rates for <sup>68</sup>Ga-RM2 and <sup>68</sup>Ga-PSMA11 (98% and 89% for <sup>68</sup>Ga-RM2 and 95% and 89% for <sup>68</sup>Ga-PSMA11) were higher than those for mpMRI (77% and 77%, respectively). Specificity was highest for mpMRI with 75% followed by <sup>68</sup>Ga-PSMA11 (67%) and <sup>68</sup>Ga-RM2 (65%). **Conclusion:** <sup>68</sup>Ga-RM2 PET accurately detects intermediate- and high-risk primary PC, with a detection rate of 93%. In addition, <sup>68</sup>Ga-RM2 PET showed significantly higher specificity and accuracy than mpMRI and a performance similar to <sup>68</sup>Ga-PSMA11 PET. These findings need to be confirmed in

larger studies to identify which patients will benefit from one or the other or both radiopharmaceuticals.

**Key Words:** <sup>68</sup>Ga-RM2; <sup>68</sup>Ga-PSMA11; PET; prostate cancer; histopathology

**J Nucl Med 2022; 63:1829–1835**  
DOI: 10.2967/jnumed.122.263971

**P**rostate cancer (PC) remains the most common noncutaneous cancer in American men and the second highest cause of cancer-related mortality (1). Cancer stage at diagnosis defines subsequent management. Although low-risk PC (Gleason score 6, pretreatment prostate-specific antigen [PSA] < 10 ng/mL, and clinical stage T1–T2a) may be managed with active surveillance, patients with higher grade, clinically significant cancers typically receive treatment. Imaging plays a crucial role in initial staging. Multiparametric MRI (mpMRI) is widely used for initial evaluation. However, mpMRI may miss clinically significant PC in 5%–8% (2) to 35% (3) of cases.

Molecular imaging with PET and CT (PET/CT) or PET/MRI is changing the landscape of PC staging with the development and regulatory approval of new radiopharmaceuticals. The most promising radiopharmaceuticals target prostate-specific membrane antigen (PSMA). PSMA is highly overexpressed in 90%–95% of PC (4–7). However, it is not specific to PC (8,9) and false-positive (FP) findings have been reported (10–13). Thus, there is a continued need for other imaging targets. <sup>68</sup>Ga-RM2 is a bombesin receptor antagonist that targets the gastrin-releasing peptide receptor (GRPR) with high affinity (14). GRPR is highly overexpressed in several cancers including breast (15,16), small cell lung cancer (17), gastrointestinal stromal and neuroendocrine tumors (18,19) and in PC (20–24), especially in earlier stages, making it an attractive target for initial staging (20).

In this study we compared preoperative <sup>68</sup>Ga-RM2 PET and mpMRI with histopathology after radical prostatectomy (RP) in patients with newly diagnosed intermediate- or high-risk PC. In a subgroup of patients, comparison with <sup>68</sup>Ga-PSMA11 PET was also available.

---

Received Feb. 2, 2022; revision accepted May 10, 2022.  
For correspondence or reprints, contact Andrei Iagaru (aiagaru@stanford.edu).  
Published online May 12, 2022.  
COPYRIGHT © 2022 by the Society of Nuclear Medicine and Molecular Imaging.

**TABLE 1**  
Patients' Characteristics ( $n = 41$ )

Characteristic	Data
Age (y)	64 ± 6.7 (50–78)
PSA (ng/mL)	8.8 ± 77.4 (2.5–504)
PSA (excluding radiation therapy patients [ng/mL])	7.6 ± 5.3 (2.5–28.0)
Risk (n)	
Intermediate	17 (41.5%)
High	24 (58.5%)
Gleason score from preoperative biopsy* (n)	
7	18 (45%)
8	12 (30%)
9	10 (25%)
Clinical stage (n)	cT1b: 2 (5%); cT1c: 18 (43.9%)
	cT2a: 6 (14.6%); cT2b: 6 (14.6%); cT2c: 3 (7.3%)
	cT3a: 6 (14.6%)
Preoperative biopsy available (n patients)	40
mpMRI (n patients)	36
<sup>68</sup> Ga-PSMA11 PET (n patients)	17
Postoperative histopathology available (n patients)	32

\*Gleason score of 1 patient was unavailable.  
Numeric factors are expressed as median ± SD (range).

## MATERIALS AND METHODS

### Participants

Patients scheduled to undergo RP for newly diagnosed, nontreated, intermediate- or high-risk PC were prospectively enrolled in 2 clinical trials evaluating the performance of <sup>68</sup>Ga-RM2 (NCT03113617) and <sup>68</sup>Ga-PSMA11 (NCT02678351). This study was approved by the local

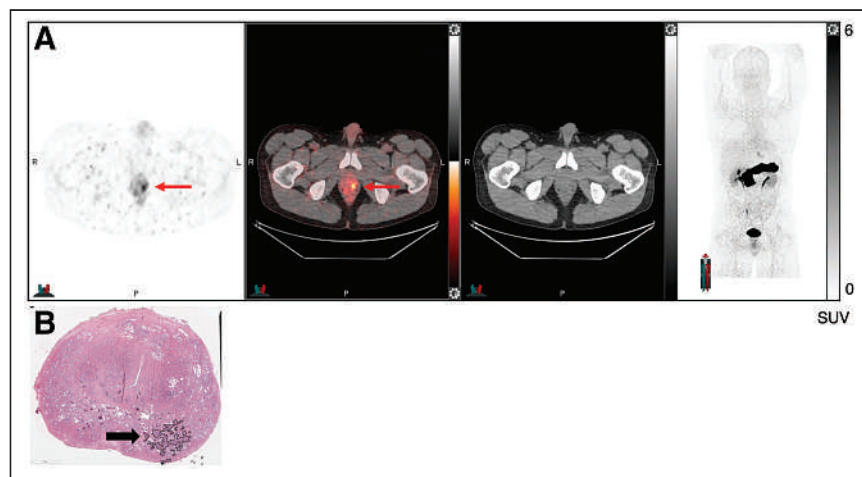


**FIGURE 1.** A 50-y-old patient with intermediate-risk PC and PSA of 5.27 ng/mL. <sup>68</sup>Ga-RM2 PET/CT (A, axial PET, fused PET/CT, CT, and maximum-intensity-projection images, respectively) shows focal uptake in left mid gland (red arrows) correlating to Gleason 4 + 3 prostate cancer (black arrow) on histology (B).

institutional review board. Written informed consent was obtained from all participants. Presurgical clinical assessments included serum PSA, Gleason score, clinical stage, and risk assessment according to the D'Amico classification (25). Patients were followed up to evaluate time to biochemical recurrence (BCR).

### Scanning Protocols

<sup>68</sup>Ga-RM2 PET. Discovery 690 PET/CT ( $n = 19$ ), Discovery MI PET/CT ( $n = 19$ ), or SIGNA PET/MRI ( $n = 3$ ) scanners (GE Healthcare) were used for <sup>68</sup>Ga-RM2 PET. Details of PET/CT and PET/MRI acquisitions were previously described (26,27). The choice of PET/CT or PET/MRI was dictated by the funding available to support the clinical trials. Discovery MI PET/CT and SIGNA PET/MRI use the same silicon photomultiplier-based detectors, and we previously reported their clinical evaluation (28,29).

<sup>68</sup>Ga-PSMA11 PET. A SIGNA PET/MRI scanner (GE Healthcare) was used for <sup>68</sup>Ga-PSMA11 PET. Details of PET/MR image acquisition were previously described (27).

<sup>68</sup>Ga-RM2 and <sup>68</sup>Ga-PSMA11 were synthesized as previously reported (30).

### mpMRI Protocol

The protocol consisted of T2-weighted imaging, diffusion-weighted imaging, and dynamic contrast-enhanced imaging sequences using a 3T scanner (MR750; GE Healthcare). Details of mpMR image acquisition were previously described (31).

### Histopathology

Hematoxylin-eosin-stained slides from whole-mount prostate specimens were analyzed according to standard of care. The slides were annotated by a genitourinary pathologist to outline areas of cancer across the entire gland.

### Fusion of Histology and PET/MRI

The RAPSODI registration framework was used to align corresponding preoperative axial T2-weighted imaging, whole-mount histopathology, and <sup>68</sup>Ga-PSMA11 PET/MRI using rigid, affine, and deformable transformations (32). This registration ensures a slice-to-slice alignment between histology—including ground-truth cancer labels—mpMRI, and PET/MRI. The methodology relies on precise prostate segmentations, automatically generated by a validated deep learning model, and its accuracy was evaluated using a Dice Similarity coefficient (33).

### Image Analysis

Two nuclear medicine physicians reviewed and analyzed PET images independently and in a random, masked fashion with the knowledge that participants were scheduled to undergo RP for known PC. Any focal uptake of <sup>68</sup>Ga-RM2 or <sup>68</sup>Ga-PSMA11 higher than the adjacent background and not associated with physiologic accumulation was deemed suggestive of PC (34,35). The number and location of each lesion and its SUV<sub>max</sub> were recorded. A visual comparison was performed between annotated suggestive lesions on PET and cancer-annotated histology slides. A lesion was deemed true-positive when annotations on PET and histopathology matched and considered true-negative when uptake on PET was not above background and when there was no cancer annotation on corresponding histopathology slides.

mpMRI was interpreted as standard of care using PI-RADS criteria version 2 (36). Lesions with a PI-RADS score ≥ 3 were

**TABLE 2**

SUV<sub>max</sub> of <sup>68</sup>Ga-RM2 in Verified Intraprostatic Lesions and Lymph Node Metastases Compared with Benign Prostate and Lymph Node Uptake

<sup>68</sup> Ga-RM2	SUV <sub>max</sub>	P
SUV <sub>max</sub> prostate cancer	6.1 ± 5.9 (2.3–32.2)	0.04
SUV <sub>max</sub> lymph node metastases	4.7 ± 3.3 (1.9–12.2)	
SUV <sub>max</sub> prostate cancer	6.1 ± 5.9 (2.3–32.2)	<0.001
SUV <sub>max</sub> benign prostate	1.8 ± 0.5 (0.5–3.3)	
SUV <sub>max</sub> lymph node metastases	4.7 ± 3.3 (1.9–12.2)	<0.001
SUV <sub>max</sub> benign lymph nodes	0.5 ± 0.2 (0.1–0.9)	

Numeric factors are expressed as median ± SD (range).

recorded. A PI-RADS score of 3 was considered equivocal, PI-RADS 4 likely, and 5 highly likely for PC.

**Statistical Analysis**

A logistic regression model was used to determine the predictive value of preoperative biopsy, mpMRI, <sup>68</sup>Ga-RM2, and <sup>68</sup>Ga-PSMA11 PET for final histopathology and risk prediction. Sensitivity, specificity, and accuracy were stratified to intermediate- and high-risk groups for <sup>68</sup>Ga-RM2 and <sup>68</sup>Ga-PSMA11. A McNemar test determined difference between <sup>68</sup>Ga-RM2 and mpMRI for sensitivity, specificity, and accuracy. A Wilcoxon signed-rank test was performed to determine differences between SUV<sub>max</sub>. Concordance correlation was used for <sup>68</sup>Ga-RM2 and <sup>68</sup>Ga-PSMA11 SUV<sub>max</sub>. The degrees of correlation are: > 0.99, almost perfect; 0.95–0.99, substantial; 0.90–0.95, moderate; and < 90, poor agreement. Spearman correlation was used for evaluation of SUV<sub>max</sub> and time to BCR. Statistical analyses were performed with Stata (version 16.1; Stata Corp. LLC). Continuous data are presented as median ± SD, with minimum–maximum values. A P value of <0.05 was considered significant except when Bonferroni adjustment was applied for concordance analyses (P value < 0.0025 significant) and risk prediction (P value < 0.017 significant).

**RESULTS**

Forty-one men (age, 64.0 ± 6.7 y [range, 50–78 y]) scheduled to undergo RP for PC were prospectively enrolled. Seventeen (41.5%) participants had intermediate-risk and 24 (58.5%) had high-risk PC. PSA was 8.8 ± 77.4 ng/mL (range, 2.5–504 ng/mL) and 7.6 ± 5.3 ng/mL (range 2.5–28.0 ng/mL) when participants who received radiation therapy (RT) were excluded. PSA was undetectable 3 mo after RP in all but 3 patients. In 1 patient, preoperative biopsy was not available and PC was diagnosed by imaging and PSA. All participants (n = 41) were imaged with <sup>68</sup>Ga-RM2 PET, 36 of 41 underwent additional mpMRI, and 17 of 41 underwent <sup>68</sup>Ga-PSMA11 PET. Of these 41 patients, 32 underwent RP and 9 opted for RT after enrollment in the protocol and completion of the scan. Patient characteristics are shown in Table 1.

**<sup>68</sup>Ga-RM2 PET**

<sup>68</sup>Ga-RM2 PET identified 70 intraprostatic foci in 40 of 41 and focal uptake in 19 nonenlarged pelvic lymph nodes in 6 of 41 patients. One participant had a negative <sup>68</sup>Ga-RM2 PET scan result.

**TABLE 3**  
Lesion Detection Rates with Histopathologic Confirmation Among modalities

Modality	Presurgical			Postsurgical whole-mount pathology					Patient (n)	
	Prostate lesions	Patient (n)	Lymph nodes	Prostate lesions (%)	Lymph nodes (%)	FP prostate	FN prostate	FP lymph nodes		FN lymph nodes
<sup>68</sup> Ga-RM2	70	40	19	50/54 (92.5%)	16/19 (88.9%)	4	4	2	1	32
<sup>68</sup> Ga-PSMA11	26	17	5	17/18 (94.4%)	4/5 (80%)	1	2	1	1	13
mpMRI	49	36	1	38/42 (90.5%)	1/1 (100%)	4	10	—	—	30
PIRADS 3	43	33	—	—	—	—	—	—	—	—
PIRADS ≥ 4	6	3	—	—	—	—	—	—	—	—
Biopsy	151	40	—	—	—	—	—	—	—	—
Gleason score 6	34	16	—	—	—	—	—	—	—	—
Gleason score ≥ 7	116	40	—	—	—	—	—	—	—	—

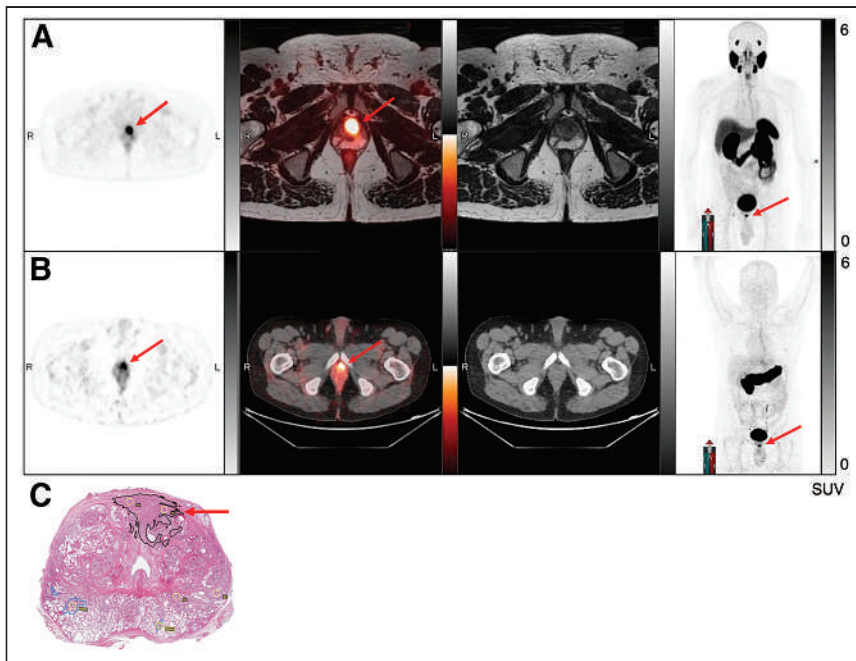


**FIGURE 2.** A 65-y-old man, presenting with PSA of 9.5 ng/mL and Gleason 3 + 4 lesion on presurgery biopsy.  $^{68}\text{Ga}$ -PSMA11 PET/MRI (A) and  $^{68}\text{Ga}$ -RM2 PET/CT (B) axial PET, fused PET/CT, CT, and maximum-intensity-projection images, respectively, show concordant focal uptake in left anterior apex of prostate (arrows), correlating to Gleason 3 + 3 on histology (C, arrow).

In the 32 patients who underwent RP,  $^{68}\text{Ga}$ -RM2 identified 54 intraprostatic foci, with 50 of 54 (92.6%) confirmed by histology (example shown in Fig. 1). Four lesions in 4 patients were false-negative (FN). A total of 527 lymph nodes were removed, of which 26 of 527 proved to be metastases in 8 participants.  $^{68}\text{Ga}$ -RM2 PET identified 19 lymph nodes in 6 patients, of which 16 were verified by pathology. The 3 unverified positive lymph nodes were seen in the 3 patients whose PSA did not decrease after RP, suggesting TP for metastases. Two lesions were subsequently confirmed by standard-of-care  $^{18}\text{F}$ -fluciclovine PET after RP.

The  $\text{SUV}_{\text{max}}$  of histologically verified intraprostatic lesions was statistically significantly higher than that of verified lymph node metastases ( $P = 0.04$ ) and benign prostatic uptake ( $P < 0.001$ ).  $^{68}\text{Ga}$ -RM2 uptake in lymph node metastases was also significantly higher than that in benign nodes ( $P < 0.001$ ).  $\text{SUV}_{\text{max}}$  findings are summarized in Table 2.

#### mpMRI

mpMRI identified lesions in 36 of 41 participants: 43 PI-RADS  $\geq 4$  lesions (vs. 64 on corresponding  $^{68}\text{Ga}$ -RM2) in 33, and 6 PI-RADS 3 lesions (vs. 5 on corresponding  $^{68}\text{Ga}$ -RM2) in 3 patients. In the 30 participants who underwent RP, mpMRI detected 42 intraprostatic lesions with 38 confirmed by histopathology (vs. 50 seen and 48 verified lesions on corresponding  $^{68}\text{Ga}$ -RM2). One suggestive pelvic lymph node was seen and verified as PC metastasis on mpMRI (vs. 18 seen and 16 verified pelvic lymph nodes on corresponding  $^{68}\text{Ga}$ -RM2 PET). Four lesions were FP on histopathology, and 10 lesions were FN. Table 3 summarizes detection rates of the 3 modalities.

#### $^{68}\text{Ga}$ -PSMA11 and $^{68}\text{Ga}$ -RM2 PET

In 17 participants,  $^{68}\text{Ga}$ -RM2 and  $^{68}\text{Ga}$ -PSMA11 PET identified 27 and 26 intraprostatic lesions, respectively, and 5 positive pelvic

lymph nodes each. Concordance was seen in 18 intraprostatic lesions (example shown in Fig. 2) and 3 lymph nodes. Histopathology was available in 13 patients and confirmed 18 of 19 and 17 of 18 intraprostatic lesions and 4 of 5 and 3 of 5 lymph node metastases for  $^{68}\text{Ga}$ -RM2 and  $^{68}\text{Ga}$ -PSMA11, respectively. On a per-lesion analysis,  $^{68}\text{Ga}$ -RM2 had 1 FP and 2 FN intraprostatic lesions, whereas  $^{68}\text{Ga}$ -PSMA11 had 1 FP and 3 FN. Six patients had incongruent uptake (examples shown in Supplemental Figs. 1 and 2; supplemental materials are available at <http://jnm.snmjournals.org>): cancer was present in 5 of 6 lesions on  $^{68}\text{Ga}$ -RM2 versus 3 of 4 on  $^{68}\text{Ga}$ -PSMA11.

$^{68}\text{Ga}$ -PSMA11  $\text{SUV}_{\text{max}}$  of verified PC was significantly higher than that of lymph node metastases ( $P = 0.002$ ). No statistically significant differences were noted when comparing  $\text{SUV}_{\text{max}}$  for  $^{68}\text{Ga}$ -RM2 with  $^{68}\text{Ga}$ -PSMA11 for intraprostatic cancers ( $P = 0.43$ ) or lymph node metastases ( $P = 0.25$ ).  $^{68}\text{Ga}$ -RM2 and  $^{68}\text{Ga}$ -PSMA11 were poorly correlated between the left and right prostate. Table 4 summarizes  $^{68}\text{Ga}$ -RM2 and  $^{68}\text{Ga}$ -PSMA11 findings.

#### Sensitivity, Specificity, and Accuracy

All 3 modalities— $^{68}\text{Ga}$ -RM2,  $^{68}\text{Ga}$ -PSMA11 PET, and mpMRI—were significant predictors for PC ( $P \leq 0.0025$ ). For intraprostatic lesions, both  $^{68}\text{Ga}$ -RM2 and  $^{68}\text{Ga}$ -PSMA11 had higher sensitivity and accuracy rates than mpMRI, whereas specificity was highest for mpMRI (Supplemental Table 1). For intraprostatic and lymph node lesions, specificity increased for both radiopharmaceuticals, whereas sensitivity decreased for  $^{68}\text{Ga}$ -PSMA11 (Supplemental Table 2). Significantly higher sensitivity ( $P = 0.01$ ) and accuracy ( $P < 0.01$ ) were seen for  $^{68}\text{Ga}$ -RM2 PET than for mpMRI.

Sensitivity, specificity, and accuracy for  $^{68}\text{Ga}$ -RM2 were slightly higher for the high-risk than for the intermediate-risk group. For  $^{68}\text{Ga}$ -PSMA11, the opposite was found (Supplemental Table 3).

For the relationship and predictive value of PSA (grouped into  $<5$ , 5–10, 10.1–15, and  $\geq 15$  ng/mL), PI-RADS (3,  $\geq 4$ ), and  $\text{SUV}_{\text{max}}$  for histopathologic outcome, the only significance found was a higher  $\text{SUV}_{\text{max}}$  of  $^{68}\text{Ga}$ -RM2 in PSA  $\geq 5$  versus PSA  $< 5$  ( $P < 0.0025$ , Fig. 3).

#### Follow-up

Six patients were lost in follow-up. After RP, patients ( $n = 26$ ) were followed for  $28.6 \pm 11.7$  mo (range, 7.0–47.3 mo). PSA remained undetectable in 15 patients, whereas 11 developed BCR  $17.7 \pm 10.8$  mo (range, 2.8–32.0 mo) after RP.  $^{68}\text{Ga}$ -RM2  $\text{SUV}_{\text{max}}$  of intraprostatic lesions and time to BCR were negatively correlated ( $r = -0.34$ ), meaning the lower the  $\text{SUV}_{\text{max}}$ , the longer the time to BCR. The correlation of PSA and time to BCR was also negatively correlated ( $r = -0.25$ ), indicating the lower the PSA, the longer the time to BCR.

#### DISCUSSION

In this study, we prospectively compared GRPR-targeting  $^{68}\text{Ga}$ -RM2 PET with whole-mount histopathology after RP in patients

**TABLE 4**  
Correlation of <sup>68</sup>Ga-RM2 and <sup>68</sup>Ga-PSMA11 PET in 17 Patients and Comparison to Histopathologic Outcome in 13 Patients

Variable	<sup>68</sup> Ga-RM2		<sup>68</sup> Ga-PSMA11		Postsurgical pathology	
	n	P	Confirmed/total (%)	FP/FN	Confirmed/total (%)	FP/FN
Injected activity (MBq)	178.7 ± 31.7 (124.3–233.8)					
Time to scan (min)	140.6 ± 11.7 (125.1–162.8)					
SUV <sub>max</sub> prostatic lesion (verified)	53.5 ± 7.4 (46–72)					
SUV <sub>max</sub> lymph node lesion verified)	6.1 ± 4.6 (2.3–19.3)	0.43				
SUV <sub>max</sub> lymph node lesion verified)	3.9 ± 3.4 (1.9–10.7)	0.25				
Prostatic lesions			18/19 (94.7%)	1/2	17/18 (94.4%)	1/3
Lymph node lesions			4/5 (80%)	1/1	3/5 (60%)	2/2
Incongruent prostatic lesions			5/6 (83%)	1/0	3/4 (75%)	1/0
Incongruent lymph node lesions			1/1 (100%)	0/2	0/1 (0%)	1/2

Numeric factors are expressed as median ± SD, (range) and as mean (95% CI). Time between <sup>68</sup>Ga-RM2 and <sup>68</sup>Ga-PSMA11 PET = 3.0 ± 5.6 d (1–21 d) (n = 17); PSA = 7.5 ± 3.6 ng/mL (2.5–14.7 ng/mL) (n = 17). Concordance correlation between <sup>68</sup>Ga-RM2 and <sup>68</sup>Ga-PSMA11 PET for left prostatic lesions was 0.77 (95% CI, 0.56–0.98) and for right prostatic lesions 0.68 (95% CI, 0.41–0.95), respectively; agreement was poor.

with newly diagnosed PC. Sensitivity and accuracy were high for <sup>68</sup>Ga-RM2 at 98% and 89%, respectively, and were comparable to those for <sup>68</sup>Ga-PSMA11 and superior to those for mpMRI. However, a specificity of 65% was lower than that for mpMRI. These results were comparable to previously reported sensitivity, specificity, and accuracy rates of 89%, 81%, and 83% for prostatic lesions and sensitivity of 70% for lymph node metastases for <sup>68</sup>Ga-RM2 PET/CT in a smaller cohort of 14 men with primary PC and 3 with BCR (37).

<sup>68</sup>Ga-RM2 and <sup>68</sup>Ga-PSMA11 both showed high detection rates for primary PC and lymph node metastases but were poorly correlated. A recently published study compared <sup>68</sup>Ga-RM2 and <sup>68</sup>Ga-PSMA11 PET/MRI in staging of 19 men with biopsy-proven high-risk PC, with histopathology available in 12 patients. Although the detection rate of 95% for the primary tumor is similar that in to our study, the positivity rates for lymph nodes were lower (37% for <sup>68</sup>Ga-PSMA11, 21% for <sup>68</sup>Ga-RM2). Apart from a negative <sup>68</sup>Ga-RM2 finding in 1 participant, concordant uptake was seen between <sup>68</sup>Ga-RM2 and <sup>68</sup>Ga-PSMA11 (38). The incongruent uptake pattern in our cohort might be due to our more heterogeneous groups of intermediate- and high-risk PC. However, the difference in expression pattern of PSMA and GRPR is consistent with our previous findings in BCR PC (30,39) and is supported by immunohistochemistry showing that GRPR and PSMA expression are not correlated (40). Fassbender et al. found in a voxel-based approach that <sup>68</sup>Ga-RM2 and <sup>68</sup>Ga-PSMA11 in 8 patients with primary PC showed similar averaged SUV<sub>mean</sub>; however, on a per-patient basis, they found a different intensity, revealing again a different expression pattern of GRPR and PSMA (41).

We found no correlation between <sup>68</sup>Ga-RM2 uptake and Gleason score or tumor volume, but a positive correlation between PSA and <sup>68</sup>Ga-RM2 SUV<sub>max</sub>. SUV<sub>max</sub> was also negatively correlated to time to BCR. This negative correlation is supported by previous findings in patients with BCR PC showing a positive correlation between <sup>68</sup>Ga-RM2 positivity and PSA and PSA velocity and, conversely, a negative correlation of SUV<sub>max</sub> and PSA with time to BCR indicating that the higher <sup>68</sup>Ga-RM2 SUV<sub>max</sub> and PSA, the shorter the time to BCR (27). However, there is controversy (24) as to whether GRPR density is related to a better prognosis of PC (20,21) or found in high-risk tumors as our results indicate. Larger studies with a longer follow-up are needed to understand these possible correlations.

The need now is to understand if and how these radiopharmaceuticals may provide complementary and useful information in patients with PC at various stages and risks. Given the high tumor heterogeneity in PC, and that neither <sup>68</sup>Ga-RM2 nor <sup>68</sup>Ga-PSMA11 are 100% sensitive or specific and hence attributing to FP and FN lesions, a bispecific tracer that targets GRPR and PSMA simultaneously may present a promising imaging option (42).

Limitations of this study include the relatively small number of patients, especially of participants undergoing both <sup>68</sup>Ga-RM2 and <sup>68</sup>Ga-PSMA11 PET, and the different imaging modalities used, that is, different PET/CT scanners and PET/MRI. In addition, not all participants had histopathology data available because some elected to undergo RT. Correlating lymph node positivity to histopathology is a challenge because not all lymph nodes seen on PET were resected. PET data were analyzed by readers who were aware that participants were scheduled to undergo RP for known PC, whereas readers for mpMRI were unaware that participants were scheduled for RP as mpMRI was part of clinical care for PC diagnosis.

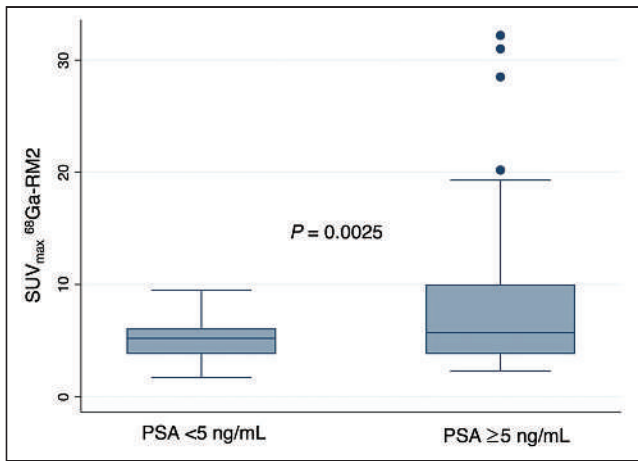


**FIGURE 3.** Boxplot of  $^{68}\text{Ga}$ -RM2  $\text{SUV}_{\text{max}}$  stratified to PSA < 5 ng/mL and  $\geq$  5 ng/mL. Patients with PSA  $\geq$  5 ng/mL had a statistically significantly higher  $\text{SUV}_{\text{max}}$  ( $P = 0.0025$ ).

## CONCLUSION

$^{68}\text{Ga}$ -RM2 PET accurately detects intermediate- and high-risk primary PC with a significantly higher specificity and accuracy than mpMRI and a performance similar to  $^{68}\text{Ga}$ -PSMA11 PET. The poor correlation between  $^{68}\text{Ga}$ -RM2 and  $^{68}\text{Ga}$ -PSMA11 underline the different expression patterns of GRPR and PSMA and the complex tumor biology of PC. Larger prospective studies are needed to identify which patients will benefit from one, the other, or both radiopharmaceuticals.

## DISCLOSURE

The study was partially supported by GE Healthcare. No other potential conflict of interest relevant to this article was reported.

## KEY POINTS

**QUESTION:** Is  $^{68}\text{Ga}$ -RM2 PET a useful tool in the initial staging of PC?

**PERTINENT FINDINGS:** Forty-one patients with newly diagnosed PC underwent  $^{68}\text{Ga}$ -RM2 PET; a subgroup also underwent mpMRI ( $n = 36$ ) and  $^{68}\text{Ga}$ -PSMA11 PET ( $n = 17$ ).  $^{68}\text{Ga}$ -RM2 PET showed high sensitivity, accuracy, and detection rates of 98%, 89%, and 93%, respectively. Specificity at 65% was lower than that of mpMRI (75%). Poor correlation to  $^{68}\text{Ga}$ -PSMA11 indicates the different expression patterns of GRPR and PSMA in PC.

**IMPLICATIONS FOR PATIENT CARE:**  $^{68}\text{Ga}$ -RM2 PET accurately detected intermediate- and high-risk primary PC with a significantly higher sensitivity and accuracy than that mpMRI and a performance similar to that of  $^{68}\text{Ga}$ -PSMA11 PET. Larger prospective studies are needed to identify which patients will benefit from one, the other, or both radiopharmaceuticals.

## REFERENCES

- Siegel RL, Miller KD, Fuchs HE, Jemal A. Cancer statistics, 2021. *CA Cancer J Clin.* 2021;71:7–33.
- Rouvière O, Puech P, Renard-Penna R, et al. Use of prostate systematic and targeted biopsy on the basis of multiparametric MRI in biopsy-naive patients

- (MRI-FIRST): a prospective, multicentre, paired diagnostic study. *Lancet Oncol.* 2019;20:100–109.
- Johnson DC, Raman SS, Mirak SA, et al. Detection of individual prostate cancer foci via multiparametric magnetic resonance imaging. *Eur Urol.* 2019;75:712–720.
- Bostwick DG, Pacelli A, Blute M, Roche P, Murphy GP. Prostate specific membrane antigen expression in prostatic intraepithelial neoplasia and adenocarcinoma: a study of 184 cases. *Cancer.* 1998;82:2256–2261.
- Mannweiler S, Amersdorfer P, Trajanoski S, Terrett JA, King D, Mehes G. Heterogeneity of prostate-specific membrane antigen (PSMA) expression in prostate carcinoma with distant metastasis. *Pathol Oncol Res.* 2009;15:167–172.
- Budäus L, Leyh-Bannurah SR, Salomon G, et al. Initial Experience of  $^{68}\text{Ga}$ -PSMA PET/CT imaging in high-risk prostate cancer patients prior to radical prostatectomy. *Eur Urol.* 2016;69:393–396.
- Maurer T, Gschwend JE, Rauscher I, et al. Diagnostic efficacy of  $^{68}\text{Ga}$ -PSMA positron emission tomography compared to conventional imaging for lymph node staging of 130 consecutive patients with intermediate to high risk prostate cancer. *J Urol.* 2016;195:1436–1443.
- Sathekge M, Lengana T, Modiselle M, et al.  $^{68}\text{Ga}$ -PSMA-HBED-CC PET imaging in breast carcinoma patients. *Eur J Nucl Med Mol Imaging.* 2017;44:689–694.
- Patel D, Loh H, Le K, Stevanovic A, Mansberg R. Incidental detection of hepatocellular carcinoma on  $^{68}\text{Ga}$ -labeled prostate-specific membrane antigen PET/CT. *Clin Nucl Med.* 2017;42:881–884.
- Demirkol MO, Kiremit MC, Acar O, Sag AA, Kapran Y. False-positive pancreatic uptake detected on  $^{68}\text{Ga}$ -PSMA PET/CT: a priority changing incidental finding while assessing the need for a prostate biopsy. *Clin Nucl Med.* 2017;42:e475–e477.
- Sasikumar A, Joy A, Nanabala R, Pillai MR, T AH.  $^{68}\text{Ga}$ -PSMA PET/CT false-positive tracer uptake in Paget disease. *Clin Nucl Med.* 2016;41:e454–e455.
- Noto B, Vrachimis A, Schafers M, Stegger L, Rahbar K. Subacute stroke mimicking cerebral metastasis in  $^{68}\text{Ga}$ -PSMA-HBED-CC PET/CT. *Clin Nucl Med.* 2016;41:e449–e451.
- Hermann RM, Djannatian M, Czech N, Nitsche M. Prostate-Specific membrane antigen PET/CT: false-positive results due to sarcoidosis? *Case Rep Oncol.* 2016;9:457–463.
- Ischia J, Patel O, Shulkes A, Baldwin GS. Gastrin-releasing peptide: different forms, different functions. *Biofactors.* 2009;35:69–75.
- Stoykow C, Erbes T, Maecke HR, et al. Gastrin-releasing peptide receptor imaging in breast cancer using the receptor antagonist  $^{68}\text{Ga}$ -RM2 and PET. *Theranostics.* 2016;6:1641–1650.
- Dalm SU, Martens JW, Sieuwerts AM, et al. In vitro and in vivo application of radiolabeled gastrin-releasing peptide receptor ligands in breast cancer. *J Nucl Med.* 2015;56:752–757.
- Mattei J, Achcar RD, Cano CH, et al. Gastrin-releasing peptide receptor expression in lung cancer. *Arch Pathol Lab Med.* 2014;138:98–104.
- Reubi JC, Komer M, Waser B, Mazzucchelli L, Guillou L. High expression of peptide receptors as a novel target in gastrointestinal stromal tumours. *Eur J Nucl Med Mol Imaging.* 2004;31:803–810.
- Reubi JC. Peptide receptor expression in GEP-NET. *Virchows Arch.* 2007;451(suppl 1):S47–S50.
- Körner M, Waser B, Rehmann R, Reubi JC. Early over-expression of GRP receptors in prostatic carcinogenesis. *Prostate.* 2014;74:217–224.
- Beer M, Montani M, Gerhardt J, et al. Profiling gastrin-releasing peptide receptor in prostate tissues: clinical implications and molecular correlates. *Prostate.* 2012;72:318–325.
- Markwalder R, Reubi JC. Gastrin-releasing peptide receptors in the human prostate: relation to neoplastic transformation. *Cancer Res.* 1999;59:1152–1159.
- Wieser G, Mansi R, Grosu AL, et al. Positron emission tomography (PET) imaging of prostate cancer with a gastrin releasing peptide receptor antagonist—from mice to men. *Theranostics.* 2014;4:412–419.
- Ischia J, Patel O, Bolton D, Shulkes A, Baldwin GS. Expression and function of gastrin-releasing peptide (GRP) in normal and cancerous urological tissues. *BJU Int.* 2014;113(suppl 2):40–47.
- D’Amico AV, Whittington R, Malkowicz SB, et al. A multivariable analysis of clinical factors predicting for pathological features associated with local failure after radical prostatectomy for prostate cancer. *Int J Radiat Oncol Biol Phys.* 1994;30:293–302.
- Song H, Harrison C, Duan H, et al. Prospective evaluation of  $^{18}\text{F}$ -DCFPyL PET/CT in biochemically recurrent prostate cancer in an academic center: a focus on disease localization and changes in management. *J Nucl Med.* 2020;61:546–551.
- Minamimoto R, Sonni I, Hancock S, et al. Prospective Evaluation of  $^{68}\text{Ga}$ -RM2 PET/MRI in patients with biochemical recurrence of prostate cancer and negative findings on conventional imaging. *J Nucl Med.* 2018;59:803–808.
- Igaru A, Mittra E, Minamimoto R, et al. Simultaneous whole-body time-of-flight  $^{18}\text{F}$ -FDG PET/MRI: a pilot study comparing  $\text{SUV}_{\text{max}}$  with PET/CT and assessment of MR image quality. *Clin Nucl Med.* 2015;40:1–8.

29. Baratto L, Park SY, Hatami N, et al.  $^{18}\text{F}$ -FDG silicon photomultiplier PET/CT: a pilot study comparing semi-quantitative measurements with standard PET/CT. *PLoS One*. 2017;12:e0178936.
30. Minamimoto R, Hancock S, Schneider B, et al. Pilot Comparison of  $^{68}\text{Ga}$ -RM2 PET and  $^{68}\text{Ga}$ -PSMA-11 PET in patients with biochemically recurrent prostate cancer. *J Nucl Med*. 2016;57:557–562.
31. Sonn GA, Fan RE, Ghanouni P, et al. Prostate magnetic resonance imaging interpretation varies substantially across radiologists. *Eur Urol Focus*. 2019;5: 592–599.
32. Rusu M, Shao W, Kunder CA, et al. Registration of presurgical MRI and histopathology images from radical prostatectomy via RAPSODI. *Med Phys*. 2020;47: 4177–4188.
33. Soerensen SJC, Fan RE, Seetharaman A, et al. Deep learning improves speed and accuracy of prostate gland segmentations on magnetic resonance imaging for targeted biopsy. *J Urol*. 2021;206:604–612.
34. Baratto L, Duan H, Laudicella R, et al. Physiological  $^{68}\text{Ga}$ -RM2 uptake in patients with biochemically recurrent prostate cancer: an atlas of semi-quantitative measurements. *Eur J Nucl Med Mol Imaging*. 2020;47:115–122.
35. Fanti S, Minozzi S, Morigi JJ, et al. Development of standardized image interpretation for  $^{68}\text{Ga}$ -PSMA PET/CT to detect prostate cancer recurrent lesions. *Eur J Nucl Med Mol Imaging*. 2017;44:1622–1635.
36. Weinreb JC, Barentsz JO, Choyke PL, et al. PI-RADS Prostate Imaging – Reporting and Data System: 2015, version 2. *Eur Urol*. 2016;69:16–40.
37. Kähkönen E, Jambor I, Kemppainen J, et al. In vivo imaging of prostate cancer using [ $^{68}\text{Ga}$ ]-labeled bombesin analog BAY86-7548. *Clin Cancer Res*. 2013;19: 5434–5443.
38. Mapelli P, Ghezzi S, Samanes Gajate AM, et al.  $^{68}\text{Ga}$ -PSMA and  $^{68}\text{Ga}$ -DOTA-RM2 PET/MRI in recurrent prostate cancer: diagnostic performance and association with clinical and histopathological data. *Cancers (Basel)*. 2022;14:334.
39. Baratto L, Song H, Duan H, et al. PSMA- and GRPR-targeted PET: results from 50 patients with biochemically recurrent prostate cancer. *J Nucl Med*. 2021;62: 1545–1549.
40. Touijer KA, Michaud L, Alvarez HAV, et al. Prospective study of the radiolabeled GRPR antagonist BAY86-7548 for positron emission tomography/computed tomography imaging of newly diagnosed prostate cancer. *Eur Urol Oncol*. 2019;2: 166–173.
41. Fassbender TF, Schiller F, Zamboglou C, et al. Voxel-based comparison of [ $^{68}\text{Ga}$ ]-RM2-PET/CT and [ $^{68}\text{Ga}$ ]-PSMA-11-PET/CT with histopathology for diagnosis of primary prostate cancer. *EJNMMI Res*. 2020;10:62.
42. Mitran B, Varasteh Z, Abouzayed A, et al. Bispecific GRPR-antagonistic anti-PSMA/GRPR heterodimer for PET and SPECT diagnostic imaging of prostate cancer. *Cancers (Basel)*. 2019;11:1371.

# Joint EANM, SNMMI, and IAEA Enabling Guide: How to Set up a Theranostics Center

Ken Herrmann<sup>1,2</sup>, Luca Giovanella<sup>3</sup>, Andrea Santos<sup>4</sup>, Jonathan Gear<sup>5</sup>, Pinar Ozgen Kiratli<sup>6</sup>, Jens Kurth<sup>7</sup>, Ana M. Denis-Bacelar<sup>8</sup>, Roland Hustinx<sup>9,10</sup>, Marianne Patt<sup>11</sup>, Richard L. Wahl<sup>12</sup>, Diana Paez<sup>13</sup>, Francesco Giammarile<sup>13</sup>, Hossein Jadvar<sup>14</sup>, Neeta Pandit-Taskar<sup>15</sup>, Munir Ghesani<sup>16</sup>, and Jolanta Kunikowska<sup>17</sup>

<sup>1</sup>Department of Nuclear Medicine, University of Duisburg-Essen, Duisburg, Germany; <sup>2</sup>German Cancer Consortium (DKTK)-University Hospital Essen, Essen, Germany; <sup>3</sup>Clinic for Nuclear Medicine and Molecular Imaging, Imaging Institute of Southern Switzerland, Ente Ospedaliero Cantonale, Bellinzona, Switzerland; <sup>4</sup>Department of Nuclear Medicine, Hospital Cuf Descobertas, Lisbon, Portugal; <sup>5</sup>Joint Department of Physics, Royal Marsden NHS Foundation Trust, Sutton, Sutton, United Kingdom; <sup>6</sup>Department of Nuclear Medicine, Hacettepe University, Ankara, Turkey; <sup>7</sup>Department of Nuclear Medicine, Rostock University Medical Center, Rostock, Germany; <sup>8</sup>National Physical Laboratory, Teddington, United Kingdom; <sup>9</sup>Division of Nuclear Medicine and Oncological Imaging, University Hospital of Liège, Liège, Belgium; <sup>10</sup>GIGA-CRC in vivo imaging, University of Liège, Liège, Belgium; <sup>11</sup>Department for Nuclear Medicine, University Hospital Leipzig, Leipzig, Germany; <sup>12</sup>Department of Radiology, Washington University School of Medicine, St. Louis, Missouri; <sup>13</sup>Nuclear Medicine and Diagnostic Imaging Section, Division of Human Health, Department of Nuclear Sciences and Application, International Atomic Energy Agency, Vienna, Austria; <sup>14</sup>Division of Nuclear Medicine, Department of Radiology, University of Southern California, Los Angeles, California; <sup>15</sup>Department of Radiology, Memorial Sloan Kettering Cancer Center, New York, New York; <sup>16</sup>Diagnostic, Molecular & Interventional Radiology, Icahn School of Medicine at Mount Sinai, New York, New York; and <sup>17</sup>Nuclear Medicine Department, Medical University of Warsaw, Warsaw, Poland

J Nucl Med 2022; 63:1836–1843

DOI: 10.2967/jnumed.122.264321

The theranostics concept using the same target for both imaging and therapy dates back to the middle of the last century, when radioactive iodine was first used to treat thyroid diseases. Since then, radioiodine has become broadly established clinically for diagnostic imaging and therapy of benign and malignant thyroid disease, worldwide. However, only since the approval of SSTR2-targeting theranostics following the NETTER-1 trial in neuroendocrine tumors, and the positive outcome of the VISION trial has theranostics gained substantial attention beyond nuclear medicine. The roll-out of radioligand therapy for treating a high-incidence tumor such as prostate cancer requires the expansion of existing and the establishment of new theranostics centers. Despite wide global variation in the regulatory, financial and medical landscapes, this guide attempts to provide valuable information to enable interested stakeholders to safely initiate and operate theranostic centers. This enabling guide does not intend to answer all possible questions, but rather to serve as an overarching framework for multiple, more detailed future initiatives. It recognizes that there are regional differences in the specifics of regulation of radiation safety, but common elements of best practice valid globally.

**Key Words:** theranostics; radionuclide theranostics; nuclear medicine; PSMA; PRRT

Received Apr. 20, 2022; revision accepted Apr. 20, 2022.

For correspondence or reprints, contact Ken Herrmann (ken2404@web.de).

This article was originally published in **Herrmann K, Giovanella L, Santos A, Gear J, et al. Joint EANM, SNMMI and IAEA enabling guide: how to set up a theranostics center. Eur J Nucl Med Mol Imaging. 2022 Apr 11. doi: 10.1007/s00259-022-05785-x** under a Creative Commons Attribution 4.0 International License (<http://creativecommons.org/licenses/by/4.0/>), which permits use, sharing, adaptation, distribution and reproduction in any medium or format, as long as appropriate credit is provided to the original author(s) and source, a link is provided to the Creative Commons license, and indication of changes is provided. This version was submitted to *The Journal of Nuclear Medicine* by the authors and has been adapted for publication in *JNM*.

Published online Apr. 21, 2022.

COPYRIGHT © 2022 by the Society of Nuclear Medicine and Molecular Imaging.

The theranostics concept—that is, using the same target for both imaging and therapy—has been the cornerstone of therapeutic nuclear medicine since the introduction for treatment of thyroid disease in the early 1940s. Despite the fact that iodine-131 (<sup>131</sup>I) and yttrium-90 (<sup>90</sup>Y)-radiolabeled anti-CD20 antibodies showed excellent long-term clinical outcomes in low-grade non-Hodgkin lymphomas (1–3), these agents have largely been replaced by nonradioactive therapies, mainly due to market forces and the relative ease of delivering nonradioactive treatments. The success story of iodine theranostics in thyroid diseases and the recent approval of lutetium-177 [<sup>177</sup>Lu]Lu-DOTATATE following the landmark NETTER-1 (1) trial have increased the applications of targeted radionuclide therapies. The expansion of the theranostics concept beyond thyroid cancer and neuroendocrine tumors toward higher incidence diseases like prostate cancer (and subsequently to other tumors) shifts nuclear medicine and radionuclide therapy into the spotlight of modern cancer therapies. VISION, a prospective randomized phase 3 trial, showed that in prostate cancer, the most common and second most fatal cancer in men, the use of up to 6 cycles of [<sup>177</sup>Lu]Lu-PSMA-617 increased the median overall survival by 4 mo (15.3 vs. 11.3 mo, HR 0.62; 95% CI 0.52 – 0.74; *P* < 0.001) (2) in patients with metastatic castration-resistant prostate cancer (mCRPC).

A tremendous increase in the demand for theranostics procedures can be expected in anticipation of FDA and EMA approval of [<sup>177</sup>Lu]Lu-PSMA-617, and this projected surge in demand for both theranostics infrastructure and appropriately skilled professional staff will pose a challenge and opportunity for healthcare systems. Even in countries with a strong track record in radionuclide theranostics, the existing infrastructure may be insufficient to

meet the growing demand (3,4). Thus, theranostics and radionuclide therapy need to get ready for the demand from cancer patients, referring physicians and society. Here we provide an enabling guide for p stakeholders interested in setting up a dedicated theranostics center. Special attention is given to regulatory considerations and requirements, logistical and technical challenges, medical considerations including training, collaboration with clinical partners and treatment indications and important lessons learnt from early adopters of theranostics. We also provide advice for troubleshooting during creating a theranostics service. This guide does not cover the specific requirements associated with the in-house production of radiopharmaceuticals since there is no global harmonization, and national laws differ considerably.

## REGULATORY, LOGISTICAL AND TECHNICAL CONSIDERATIONS

The design, construction and subsequent operation of a theranostics service has to be guided by the fundamentals of radiation protection established by the appropriate regulatory agencies. In Europe, the International Atomic Energy Agency (IAEA) through the International Basic Safety Standards (BSS) (5) are a set of consensus requirements derived from knowledge of radiation biology and radiation protection, respectively (6). In the USA, the Nuclear Regulatory Commission (NRC) governs safety standards and delegates' responsibilities to specific states (Agreement States) in many instances. The European Commission Directive 2013/59/EURATOM is a legal act that establishes the recommendations and requirements of the BSS and ICRP for EU countries, which have been transposed into national law by the Member States. Sections 2 and 3 of the BSS specify that requirements that apply to all existing and planned exposure situations must be considered when establishing and operating a theranostics center.

The BSS requires that legal entities apply to the regulatory authority for a license. Therefore, the regulatory basis for operating a theranostics center is a radioactive material license (RAM), in accordance with the national regulations and laws governing the handling of radioactive materials for medical applications, as defined in ICRP Publication 105 (7). This must cover all aspects of both diagnostic and therapeutic use of radiopharmaceuticals. Prerequisites for applying for a RAM license include the existence of adequate infrastructure, sufficient personnel (including trained physicians, technologists, nursing staff, a Radiation Safety Officer (RSO), a Medical Physics Expert (MPE)), sufficient means of radiation protection, and processes for discharge management of treated patients and handling of radioactive waste and sewage. To this end, several requirements must be met, depending on the respective spectrum of diagnostics and therapies applied and the radiopharmaceuticals used. In the US, regulations differ but require a suitable radiation license and appropriately qualified authorized users to allow administration of the radiopharmaceutical therapies.

## RADIONUCLIDES AND RADIOPHARMACEUTICALS USED

A commonly used theranostic pair is gallium-68 ( $^{68}\text{Ga}$ ) for PET/CT diagnostics and  $^{177}\text{Lu}$  for therapy. In the US, [ $^{64}\text{Cu}$ ] $^{64}\text{Cu}$ -DOTA-TATE is commonly used in addition to [ $^{68}\text{Ga}$ ] $^{68}\text{Ga}$ -DOTA-TATE or DOTA-TOC. However,  $^{90}\text{Y}$  is also occasionally therapeutically, as are fluorine-18 ( $^{18}\text{F}$ )- and technetium-99 m ( $^{99\text{m}}\text{Tc}$ )-labeled diagnostic compounds. Table 1 summarizes the main properties of these radionuclides.

With  $^{177}\text{Lu}$ , attention must be paid to the underlying manufacturing pathway, which may result in unwanted long-lived accompanying nuclides that require special consideration in terms of storage and disposal of waste depending on local regulations.  $^{177}\text{Lu}$  is made either by direct neutron irradiation of  $^{176}\text{Lu}$  targets ( $^{176}\text{Lu}$  (n, $\gamma$ ) reaction) or indirectly as a decay product of the neutron irradiation of ytterbium-176 ( $^{176}\text{Yb}$  (n, $\gamma$ ) reaction), which produces  $^{177}\text{Yb}$  that decays to  $^{177}\text{Lu}$ . In the indirect reaction, no long-lived contaminants are created. However, in the direct reaction, small quantities of metastable lutetium-177 ( $^{177\text{m}}\text{Lu}$ ) with a half-life of 161 d may be present (7). In this case,  $^{177\text{m}}\text{Lu}$  may account for approximately 0.02% of the total amount of  $^{177}\text{Lu}$  in the final radiopharmaceutical.  $^{68}\text{Ga}$  may either be obtained from a radionuclide generator ( $^{68}\text{Ge}/^{68}\text{Ga}$ -generator) or produced by proton irradiation of zinc-68 ( $^{68}\text{Zn}$ (p,n) $^{68}\text{Ga}$ ). The different production pathways of the radionuclides are associated with different radionuclidic impurities that must be taken into account, i.e. germanium-68 and gallium-67, respectively (8). The  $^{90}\text{Y}$  currently available for radiolabeling is of high radionuclidic purity with no relevant amounts of accompanying nuclides (9). Long-lived radioactive contaminants may require specific regulatory attention.

## RADIATION PROTECTION, SHIELDING

Shielding of syringes and vials, as well as in some jurisdictions, waste and storage containers, is an important aspect of reducing external exposure among staff, the public and patients. After administration of the radiopharmaceutical, it may be necessary (mainly in Europe, and in some cases in the US depending on exposure rates) to isolate the patient from other persons, either within the hospital or in the public domain. The type of radiation emitted from the theranostics compound will dictate the extent of shielding required. This can vary from PMMA (polymethyl methacrylate) storage boxes for vials and waste containers, lead pots and tungsten syringe shields, to concrete waste bunkers or lead-lined treatment rooms. This infrastructure must be prepared according to local regulation and must be in place before any activity involving radiation is carried out. Appropriateness of the control measures must also be demonstrated, usually in the form of a written radiation risk assessment that considers radiation protection of both employees and patients. Established risk analysis methods such as failure mode and effects analysis (FMEA) or fault tree analysis (FTA) should be used for this purpose. Compliance with NRC and/or state radiation safety regulations is required in the US.

## STORAGE OF RADIOPHARMACEUTICALS

Radiopharmaceuticals must be stored in a safe, secure, and environmentally appropriate (such as refrigerated or frozen) place to which only the licensee and appropriate staff may have access. In addition, provisions for the safe storage and custody of radioactive materials must be in place, including protection against theft, fire, and chemicals. Transport and movement of radioactive materials to, from, and within the hospital must be carefully documented so that any radioactive material can be tracked from source to final use and disposal.

## ADMINISTRATION OF RADIOPHARMACEUTICALS

Accurate quantification of the radioactivity administered to the patient is the first step of the radiopharmaceutical administration and traceability chain. A radionuclide calibrator measures the activity and cross-calibrates other equipment. It is therefore essential to

**TABLE 1**  
Physical Characteristics of the Commonly Used Theranostics Pairs  $^{68}\text{Ga}/^{177}\text{Lu}$  and  $^{68}\text{Ga}/^{90}\text{Y}$

Radionuclides	Physical characteristics*		Half-life	Pharmaceuticals <sup>†</sup>	Use
	Energy [keV]				
	Gamma	Beta or Alpha			
$^{68}\text{Ga}$	511 (caused by annihilation)	1899 ( $\beta^+$ )	1.13 h	$^{68}\text{Ga}$ ]Ga-PSMA-11 $^{68}\text{Ga}$ ]Ga-PSMA-I&T $^{68}\text{Ga}$ ]Ga-DOTA-TATE (NETSPOT <sup>TM</sup> ) $^{68}\text{Ga}$ ]Ga-DOTA-TOC (SomaKIT TOC <sup>®</sup> )	Diagnostic
$^{18}\text{F}$	511 (caused by annihilation)	634 ( $\beta^+$ )	1.83 h	Piflufolastat F18 (Pylarify <sup>®</sup> ) $^{18}\text{F}$ ]F PSMA-1007 $^{18}\text{F}$ ]DCFPyL	
$^{177}\text{Lu}$	113 (6%) 208 (11%)	498 ( $\beta^-$ )	6.73 d	$^{177}\text{Lu}$ ]Lu-PSMA-617 $^{177}\text{Lu}$ ]Lu-PSMA-I&T $^{177}\text{Lu}$ ]Lu-DOTA-TATE (Lutathera <sup>®</sup> )	Therapy
$^{90}\text{Y}$	Bremsstrahlung	2280 ( $\beta^-$ )	2.67 d	$^{90}\text{Y}$ ]Y-DOTA-TOC	
$^{99\text{m}}\text{Tc}$	140 (89%)	not relevant	6.01 h	$^{99\text{m}}\text{Tc}$ ]Tc-MDP $^{99\text{m}}\text{Tc}$ ]Tc-DPD $^{99\text{m}}\text{Tc}$ ]Tc-HDP	Diagnostic
$^{223}\text{Ra}$	154 (6%) 269 (14%)	5716 ( $\alpha$ ), 5606 ( $\alpha$ ), 6819 ( $\alpha$ ), 7386 ( $\alpha$ ), 6623 ( $\alpha$ ) 1370 ( $\beta^-$ ) 1420 ( $\beta^-$ )	11.44 d	$^{223}\text{RaCl}_2$ (Xofigo <sup>®</sup> )	Therapy

\*Data are extracted from The Lund/LBNL Nuclear Data Search V 2.0 (<http://nucleardata.nuclear.lu.se/toi/>).

<sup>†</sup>Without claim to completeness.

ensure that calibration is traceable to primary standards when these are available (10–12).

A well-documented program for quality assurance (QA) and quality control (QC) is essential to ensure the dependable performance of safe, accurate and reproducible equipment operation and the appropriate clinical administration of radiopharmaceuticals (10,13,14). Following installation of any new instrument, acceptance testing must confirm that the system meets the performance specifications and to provide a baseline for comparison during routine QC. The type and frequency of QC tests should follow national guidelines.

The theranostics compounds can be administered in several ways:

Adequate shielding must be ascertained to avoid undesirable beta and gamma irradiation and to minimize the risk of contamination, e.g., by using hybrid shielding consisting of layers of PMMA and lead/tungsten, which results in attenuation of both beta and gamma radiation and minimizes the occurrence of bremsstrahlung. A syringe is prepared with the therapeutic agent, and the qualified operator administers the drug via correctly placed and patent intravenous access. This is followed by flushing with saline. This method is particularly used for drugs such as PSMA ligands, which do not require specific administration as a bolus. Alternatively, the syringe content can be administered via perfusor or injection pump. To minimize staff radiation exposure it is recommended to use automatic dispensing and semi- or fully automated infusion pumps for the administration of the radiopharmaceuticals.

## RADIOACTIVE WASTE

Storage for decay is essential for the clearance of radioactive waste containing short-lived radioisotopes, with a half-life of less than 100 d. “Clearance is the removal of radioactive material from regulatory control provided that the radionuclide concentrations are below specific clearance levels” (12).

Waste may be stored for decay and subsequent discharge in a locked, ventilated and properly demarcated room. It is recommended to segregate radionuclides according to the expected time required for their decay (e.g., initial activity and physical half-life). For example, the shorter lived waste from PET/CT diagnostics (syringes, swabs, vials, etc.) should be separated from that of the longer lived radionuclides used for the therapy. There should also be sufficient space in these rooms for interim storage of potentially contaminated items (e.g., patient clothing, patient diapers, perfusors, etc.). The origin of the waste should be recorded to ensure proper identification.

Disposal of aqueous radioactive wastes must strictly follow the recommendations set out in the national regulations. These may allow a limited amount of highly diluted wastewater to be disposed of into the public sewage system or require specific processing such as filtration and/or specific storage systems before release. Local regulatory authorities may also additionally require the facility to regularly assess the environmental and radiologic impact of radiation work being undertaken.

If long-lived contaminants such as  $^{177\text{m}}\text{Lu}$  ( $t_{1/2} = 160$  d) are present in the radiopharmaceutical, the waste (e.g., vials, cannula,

infusion lines, swabs, etc.) should be stored separately from other waste until the time limit for disposal according to national law is reached. Specific attention must be paid to isolation, storage and disposal of biohazardous and radioactive waste which may contain patient fluids. Potential contamination of liquid waste (i.e., excreta) with  $^{177\text{m}}\text{Lu}$  must also be considered, and any wastewater treatment or storage facilities used—if applicable—must be inspected for capacity and compliance with regulatory limits. Installation of separate toilets for patients treated with theranostics compounds potentially containing  $^{177\text{m}}\text{Lu}$  is also an option.

## RELEASE OF PATIENTS AFTER TREATMENT

Prior to injection of a radioactive substance, radiation safety guidance should be given to the patient and family (where applicable) regarding rules of conduct to reduce the potential radiation exposure to others. Release of patients after diagnostic procedures does not require extensive or any (USA) measures, since the physical and effective half-life of radiotracers involved is usually only a few hours. With  $^{68}\text{Ga}$ -,  $^{64}\text{Cu}$ -, or  $^{18}\text{F}$ -based tracers it is therefore usually sufficient to restrict direct contact between the patient and vulnerable individuals (pregnant women, children) during the hours immediately after patient release. In the US, no or limited radiation specific discharge instructions are given following diagnostic procedures. The situation is somewhat different for patient discharged after therapeutic administrations, as the activity levels here are significantly higher. ICRP Publication 94 (15,16) and IAEA Safety Report no. 63 (17) comment on the release of patients after radionuclide therapy. A dose limit of 1 mSv/y for the public and a dose constraint of 5 mSv/episode for caregivers (a family member or paid helper who regularly looks after a child or a sick, elderly, or disabled person) have been proposed as acceptable limits. However, in many countries there are different limits and specifications that must be followed after therapeutic administration of radionuclides. In [ $^{177}\text{Lu}$ ]Lu-PSMA-617 therapy, for instance, patients are typically treated with an activity of 7.4 GBq and the initial dose rate from the patient after the injection is in the order of 50  $\mu\text{Sv/h}$  at a distance of 1 m. If, as in many countries, a dose rate threshold of 30  $\mu\text{Sv/h}$  at a distance of 1 m is used as release criterion, the therapy can be applied as an outpatient treatment and patients can return home within 6 h of administration (18). Consideration must be taken when more than one radionuclide therapy per year is administered. For example, if a patient is treated with 6 cycles of PSMA-targeted therapy per year, the cumulative exposure received by the family members, the caregivers and the public must be considered. In this case, exposure to members of the public that the patient has frequent contact with (such as family members, children or co-workers) should be kept below one sixth of the annual limit after each cycle. The same considerations can be applied to [ $^{177}\text{Lu}$ ]Lu-DOTATATE therapies.

For both therapies, the high excretion rate in the first hours after therapy administration must be considered: after 4 h, approximately 50% of the activity may be renally excreted (19,20). To be compliant with the dose limits, a system needs to be established to measure or estimate activity in patients before discharge and calculate the exposure that members of the household and public may receive (European standards do not apply in other parts of the world). The result should be recorded. One method of estimating the acceptable activity of radiopharmaceuticals in patients upon discharge from hospital is to calculate the time integral of the ambient equivalent dose rate and compare it with the dose limits.

Direct measurement of patient activity before discharge is commonly performed and can be used as a patient-specific guide to minimize radiation exposure to caregivers and the general public. The patient should be given written instructions on precautions for the first few days after discharge. In particular, contact with pregnant women and small children should be avoided. Special attention should be given to the risk of contamination via urine, especially in the case of incontinent patients and children. In some cases, it may be appropriate to mandate hospital isolation due to this risk, even if the external dose rate is deemed adequately low. In some countries, including Germany, Austria and Italy, hospitalization is in any case mandatory following radionuclide therapy.

## HANDLING OF DECEASED PERSONS

Despite careful patient selection, death of patients, while receiving therapy or soon after, could happen. Such cases could increase as the use of radiopharmaceutical treatments becomes more widely used. If such situations arise, appropriate measures must be taken to handle the corpse. This includes restricted access to the room occupied by the deceased until a proper decontamination and survey have been completed. Radioactive corpses must be identified as a potential hazard using proper identifiers. In case of leakage of radioactive substances, a body bag is needed. In addition, surveillance may be needed in all stages of disposal (17). None of this however is currently required in the US but careful discussions are commonly held with funeral homes regarding safe handling of patients who have died soon after receiving a radiopharmaceutical therapy.

Handling (preparation for burial or cremation) of a body containing significant radioactivity must be performed under the supervision of a radiation protection officer (17). Depending on the national regulations, cremation may be postponed for several days or even weeks. Autopsy is not advisable in such cases and must be kept to a minimum. In consultation with the radiation protection officer, all necessary radiation protection and decontamination measures must be undertaken for personnel, instruments and the workplace.

## TREATMENT PLANNING, OPTIMIZATION AND VERIFICATION

Council Directive 2013/59/Euratom calls for the planning, optimization and verification of all radiotherapy exposures in the geographical areas of the EU. The EANM recently provided guidance on how to interpret the Directive's statements for NM treatments (21). Theranostics procedures are the epitome of such exposures, allowing the appropriateness of therapy to be determined via companion diagnostic imaging, followed by post-administration therapy imaging for treatment verification, followed by further diagnostic response imaging.  $^{68}\text{Ga}$ - is generally accepted as the favored diagnostic companion for  $^{177}\text{Lu}$ -based therapies although copper-64 ( $^{64}\text{Cu}$ ) is seeing increased application in some settings. Most countries in the EU, North America and the Far East show a fairly high density of PET centers, that is, at least 1/million (22). The short half-life of  $^{68}\text{Ga}$  can make transport to centers difficult unless the production site is a short distance away or production is carried out within an in-house radiopharmacy facility. With the emerging availability of licensed kits for  $^{68}\text{Ga}$ -labeled tracers, the clinical availability of these compounds and the longer lived tracers such as  $^{64}\text{Cu}$  will increase as well. Considering the many advantages of PET/CT imaging as a companion diagnostic tool, all efforts should be made to equip the countries still lacking so that equal access to therapies can be achieved, as highlighted by the Lancet Oncology Commission

on Medical Imaging and Nuclear Medicine (22). Scaling up access of imaging, treatment, and care quality will produce substantial health and economic benefits, and avert millions of death, but will require initial investment before a return is observed (22).

The complexity of the task and the resources required to implement theranostics will vary depending on the respective radiopharmaceutical, application and desired clinical end-point (23). Commercial software applications are now available, some of which have FDA/EMA approval and are intended to perform dosimetric evaluation (24). However, in many centers, software developed in-house is still widely used and remains a valuable option for research purposes and post-therapy dosimetry.

Dosimetry calculations require measurements of the distribution of activity in the targets of interest at different time-points to determine the time-integrated activity (25,26). Methods requiring less resourcing include whole-body, blood and bone marrow dosimetry, which use external probe measurements of the activity in a tissue biopsy, blood sample or whole body (27). The number and frequency of activity measurements require careful consideration and should match the desired biological and clinical endpoint. For wider implementation, there is growing interest in minimizing the number of imaging sessions while having a sufficient level of accuracy to achieve the desired treatment outcome and reduce patient burden and hospital costs. Nearly all radiopharmaceutical therapies approved in the US do not require dosimetry as a part of the product labeling.

Publications on general principles and practice of PET/CT imaging as well as information about the EARL accreditation program for the harmonization of  $^{18}\text{F}$ ,  $^{68}\text{Ga}$  and  $^{89}\text{Zr}$  imaging are provided by the EANM (28,29). The EANM guidelines provide recommendations on setting up quantitative SPECT/CT imaging with examples of potential clinical applications and include details on scanner calibration, image acquisition parameters, and reconstruction and correction methods (30,31). The EANM also provides general guidance on documenting and reporting dosimetry data to facilitate the reproducibility of results (32), as well as a detailed methodology on the evaluation and calculation of uncertainties in absorbed dose calculations (33). Guidance on logistical and technical considerations when developing quantitative imaging and dosimetry protocols is available for  $^{131}\text{I}$  (34–38),  $^{177}\text{Lu}$  (39–41),  $^{90}\text{Y}$  (42),  $^{223}\text{Ra}$  (43–45). The Radiological Society of North America QIBA profiles can inform PET and SPECT applications as can use of the SNMMI Clinical Trials Network Phantoms.

## MEDICAL CONSIDERATIONS AND REFLECTIONS

Application of radionuclide therapies requires the involvement and coordination of multiple stakeholders—inter- but also intra-professionally. Whereas in regular patient care the treating physician is also the referring physician, patients undergoing radionuclide therapy are typically followed by clinicians who are not nuclear medicine physicians. In the case of prostate cancer patients, the majority are seen and followed by urologists and medical oncologists. However, radioligand therapies are delivered by authorized users, most typically within nuclear medicine departments. Accordingly, coordination and communication with the treating physician are of utmost importance, especially as the indication of radioligand therapies must be appropriately sequenced in the disease journey of a patient. An active presence and participation of nuclear medicine specialists in the multidisciplinary team is mandatory to ensure acceptance and awareness of radioligand therapies. While in the past our contribution

to multidisciplinary teams was often limited to presenting diagnostic images, we now must play a more active role in providing our expertise for potential treatment. Overall, a proactive approach promoting theranostics methods will facilitate the adoption and acceptance of our field by our clinical colleagues. This role change also needs to be reflected in the training of junior doctors and the continued education of board-certified nuclear medicine specialists.

## INTEGRATED CARE

The success of a theranostic center highly depends on the level of integration within an oncologic practice. Indeed both diagnostic imaging as well as radioligand therapy have to be embedded within the oncologic workflows to facilitate access to the patient flow controlling clinicians. Not surprisingly the currently most successful theranostic centers are embedded in strong cancer centers focusing on neuroendocrine tumors and prostate cancer. Accordingly in anticipation of an ever growing number of theranostic indications, a close collaboration with all clinical domains managing cancer patients is very important.

## INTRA-PROFESSIONAL STAKEHOLDERS

Apart from the interprofessional complexity of theranostics, it is also important to address the multiple specialties and skill sets involved in the successful operation of a theranostics center. In addition to medical expertise including both physicians and well-trained support staff such as nurses, the administration of either commercially or locally produced theranostics agents requires the involvement of medical physicists, radiochemists/radiopharmacists and radiation safety experts. Whereas many of the skill sets required for theranostics resemble those needed for diagnostic nuclear medicine procedures, the higher activity levels needed for therapy, the different radionuclides involved and the multiple steps in the process, from validating the indication to delivering the radiopharmaceutical, often calls for a significantly higher degree of knowledge but also requires more time. The less infrastructure and local expertise that is already in place, the more demanding the transition to a state-of-the-art theranostics center will be. Needless to say, the adjustments required from a center with experience in delivering high-activity radioiodine therapies will be less onerous than those for a site currently only dealing with diagnostic outpatient procedures or  $^{223}\text{Ra}$  outpatient treatments.

## TRAINING AND EDUCATION

The expected surge in demand for theranostics centers entails numerous challenges. Accessibility and availability of a skilled, well-trained workforce represent one of the greatest unmet needs, alongside upscaling of the healthcare system to accommodate the expected demand for radionuclide therapies. Training and education of existing board-certified nuclear medicine specialists is of high importance, as is the incorporation of radionuclide therapy and the concept of theranostics into the curricula of the ongoing training programs for junior doctors. Besides learning how to apply radionuclide therapy, understand the right timing for theranostics and the alternative treatments that could be available, deal with typical toxicity profiles and manage the corresponding side effects, there is also an overall shift toward being more actively involved in patient treatment. While cross-training in radiology is helpful for the diagnostic nuclear medicine procedures, the spectrum of radionuclide therapies rather demands a profound expertise

in internal medicine, oncology and/or urology. Experienced theranostics centers in countries such as The Netherlands, Switzerland, Germany, the United Kingdom and others should accommodate interested nuclear medicine specialists from elsewhere to acquaint them with the application of radionuclide therapies. In the US, radiation oncologists can become authorized users, but current training for such practitioners in radiopharmaceutical therapy is often quite limited as their focus is external beam therapy in most centers. Practical training of nuclear medicine technologists is also needed, along with continuous education programs for the development of skills and dissemination of best practice principles. The success of theranostics and the independence of nuclear medicine are directly dependent on our success in meeting patient demand. In parallel, the introduction of theranostics fellowships mutually accepted by national and international nuclear medicine and clinical societies needs to be pursued. Nuclear medicine physicians who have attained expertise in theranostics will in turn be able to inform the clinicians about all specific aspects of the new treatments with radionuclides. The goal is for medical oncologists and urologists to reach a similar level of comfort with referring patients for these treatments as that reached by clinicians dealing with clinical indications of  $^{131}\text{I}$  in care of thyroid diseases. In the US, the SNMMI has endorsed the usage of the term “nuclear oncologist” to refer to nuclear medicine physicians with special expertise in treating cancer patients with targeted radiopharmaceuticals. This term associated with appropriate training and experience may better reflect the critical role of the oncology focused nuclear medicine physician and warrants further use.

## LESSONS LEARNT

Based on our experience, the most important aspect in preparation for the likely surge in theranostics treatments is to seek advice and experience from centers already actively involved in such treatments. Of the lessons learnt, by far the most important is that careful preparation and planning are key to successful implementation.

With an increase in the breadth of theranostics services being delivered comes a larger variety of patients with a wider range of comorbidities and potential complications in safely delivering a radionuclide therapy. Historically, with I-131 thyroid treatments we have been privileged in treating relatively young and healthy patients. While Xofigo® ( $^{223}\text{Ra}$ ]RaCl<sub>2</sub>) treatments brought in an older, frailer population, the reduced radiation risks from the alpha-emitter meant that therapies could still be safely delivered in high numbers as an outpatient service in most countries.

PSMA ligand treatments, particularly when radiolabeled with Lu-177, do not necessarily benefit from the same logistical advantages, and thought should be given to the potential complications that could arise from treating such patients. Most notable, from experience, is the increase in the number of patients presenting with some form of lower urinary tract symptom. The degree of incontinence will vary from patient to patient and may be controllable through the wearing of absorbent diapers, or through external, self-inserted or semipermanent catheterization. Artificial sphincters and other interventions have also been observed. For a treatment where the primary form of excretion is via the urinary system, this aspect should not be overlooked. A thorough and clear patient history is required so that control measures can be put in place to deal with these complications and there are no surprises on the day of therapy and once the patient returns home.

Consideration should also be given to the patient after treatment. Responsibility for the radiation and potential risks that may

occur to the patient, the public and the environment do not stop after the patient has left the hospital. Contingency planning is required to deal with the unexpected, be it disease, treatment, or unrelated emergency care. Examples that have been experienced include blood transfusions for anemia, orthopedic surgical interventions and even patient death (46). It should be recognized that theranostics treatments will impact surrounding and local hospitals in addition to those delivering the radionuclide therapy. It is also likely that the receiving center and staff will not have the expert knowledge or facilities to deal with radioactive patients or potentially will not possess the required licenses to administer radioactivity or to handle such a patient on site. Good communication and coordination between centers are therefore paramount.

With the expected demand for treatments, outpatient or day case administrations are appealing with a view to increasing patient throughput. However, patient preparation and treatment delivery should not be rushed. Even in centers and countries where treatments can be delivered as a day case, preparations should be in place to respond to delays and contingency plans should be in place to admit the patient overnight, should the need arise. Until the number of theranostics centers increases, extended patient travel time can be expected as current centers cover a wider geographical area. Radiation restrictions during this period should be considered and guidance given as to whether it is more appropriate for the patient to stay in local accommodation rather than undertake a lengthy journey home immediately after therapy.

## PROVIDING POINTS OF CONTACT

Promoting theranostics and the scale-up of sites providing access to radionuclide therapy is a joint effort involving multiple professional societies such as EANM and SNMMI, international agencies such as IAEA, but also multiple industry-driven initiatives. A very solid source of information are procedural guidelines promoting the use of innovative diagnostic and therapeutic radionuclides such as [ $^{68}\text{Ga}$ ]Ga-PSMA ligands (47), [ $^{177}\text{Lu}$ ]Lu-PSMA ligands (48), [ $^{223}\text{Ra}$ ]RaCl<sub>2</sub> (49), and on a more general level peptide receptor radionuclide therapy (31), among many others. The leading professional societies generally attempt to provide early guidance on how to use novel theranostics, even in cases where clinical evidence is still lacking. For detailed review, both EANM and SNMMI provide direct access to an overview of procedural guidelines (46,50). In addition, several EANM committees, such as the EANM Oncology & Theranostics Committee, or the SNMMI Therapy Centre of Excellence serve as an entry point for individuals requesting assistance or information on how to promote theranostics at local level. More recently, multiple joint initiatives have been launched, paving the way for an understanding of theranostics within the oncologic community and facilitating the increased exchange between clinicians and nuclear medicine experts. A pioneering example of this is the joint ESMO/EANM initiative offering advanced courses on diagnostic and therapeutic applications of nuclear medicine in oncology. Additional industry-driven initiatives have recently been announced and will also provide very valuable sources of education and training.

## SUMMARY

The expansion of theranostics applications beyond thyroid cancer and neuroendocrine tumors to a higher-incidence disease such as prostate cancer is triggering the up-scaling of existing and new theranostics centers. This guide establishes an overarching framework

helping practitioners to understand what is needed and required to set up a theranostics center. Despite a widely varying regulatory, financial and medical landscape, the nuclear medicine community will doubtless prove capable of responding to the expanding practice in this field. The era of theranostics offers a great opportunity to improve patient care, and theranostics will become a mainstay of personalized cancer treatment. As a community we have the experience and facilities to deliver, with careful preparation and collaboration we will see expansion, and will be ready and able to respond to the demand placed on us as theranostics continues to develop.

## DECLARATIONS

**Informed consent:** This manuscript does not contain proprietary human data; accordingly an informed consent is not applicable.

**Conflicts of interest:** KH reports personal fees from Bayer, personal fees and other from Sofie Biosciences, personal fees from SIRTEX, non-financial support from ABX, personal fees from Adacap, personal fees from Curium, personal fees from Endocyte, grants and personal fees from BTG, personal fees from IPSEN, personal fees from Siemens Healthineers, personal fees from GE Healthcare, personal fees from Amgen, personal fees from Novartis, personal fees from ymabs, all outside the submitted work. LG reports personal fees from Roche Diagnostics and SNIBE for advisory board participation, and research support from Roche Diagnostics., all outside the submitted work. AMDB is supported by the National Measurement System of the UK Department for Business, Energy and Industrial Strategy. RLW has research contracts from Siemens, Bayer, Actinium Pharmaceuticals, and serves (with compensation) on the scientific advisory boards of Seno Medical and Clarity Pharmaceuticals. HJ serves on the advisory board of Radiomedix, is a consultant to Bayer and Blue Earth Diagnostics, an investigator for ImaginAb, and on the speaker's bureau of Lantheus. MG reports fee for speakers bureau of Novartis, Blue Earth and Ionetix (not active currently). The remaining authors have no relevant conflict of interest to declare with regards to this comment.

**Research involving human participants and/or animals:** This manuscript does not contain proprietary research involving neither humans nor animals.

**Liability:** This guideline summarizes the views of the co-authoring EANM Committee members, SNMMI representatives and IAEA co-authors. It reflects recommendations for which the EANM, the SNMMI and the IAEA cannot be held responsible. The recommendations should be taken into the context of good practice of nuclear medicine and do not substitute for national and international legal or regulatory provisions.

## ACKNOWLEDGMENTS

This guideline was only possible thanks to the tremendous support of the EANM headquarters and especially Nuria Serra. The authors want to eternally thank them for their support, help and patience.

## REFERENCES

- Kaminski MS, Zasadny KR, Francis IR, et al. Radioimmunotherapy of B-cell lymphoma with [<sup>131</sup>I]anti-B1 (anti-CD20) antibody. *N Engl J Med*. 1993;329:459–465.
- Morschhauser F, Radford J, Van Hoof A, et al. 90Yttrium-ibritumomab tiuxetan consolidation of first remission in advanced-stage follicular non-Hodgkin lymphoma: updated results after a median follow-up of 7.3 years from the International, Randomized, Phase III First-Line Indolent trial. *J Clin Oncol*. 2013;31:1977–1983.
- Zippel C, Giesel FL, Kratochwil C, et al. PSMA radioligand therapy could pose infrastructural challenges for nuclear medicine: results of a basic calculation for the capacity planning of nuclear medicine beds in the German hospital sector. *Nucl Med (Stuttg)*. 2021;60:216–223.
- Czermin J, Sonni I, Razmaria A, Calais J. The future of nuclear medicine as an independent specialty. *Journal of nuclear medicine: official publication, Society of Nuclear Medicine*. 2019;60(suppl 2):3S–12S.
- Radiation Protection and Safety of Radiation Sources: International Basic Safety Standards. Vienna: INTERNATIONAL ATOMIC ENERGY AGENCY; 2014.
- The 2007 Recommendations of the International Commission on Radiological Protection. ICRP publication 103. *Ann ICRP*. 2007;37:1–332.
- ICRP Publication 105. Radiation protection in medicine. *Ann ICRP*. 2007;37:1–63.
- Thisgaard H, Kumlin J, Langkjaer N, et al. Multi-curie production of gallium-68 on a biomedical cyclotron and automated radiolabelling of PSMA-11 and DOTATATE. *EJNMMI Radiopharm Chem*. 2021;6:1.
- Radchenko V, Morgenstern A, Jalilian AR, et al. Production and Supply of alpha-Particle-Emitting Radionuclides for Targeted alpha-Therapy. *Journal of nuclear medicine: official publication, Society of Nuclear Medicine*. 2021; 62(11):1495–1503.
- Gadd R, Baker M, Nijran KS, et al. Protocol for Establishing and Maintaining the Calibration of Medical Radionuclide Calibrators and their Quality Control, 2006.
- AAPM. The selection, use, calibration and quality assurance of radionuclide calibrators used in nuclear medicine: American Association of Physicist in Medicine, 2012.
- IAEA. Quality assurance for radioactivity measurement in nuclear medicine. Vienna: International Atomic Energy Agency, 2006.
- EANM PC, Busemann Sokole E, Plachcinska A, et al. Routine quality control recommendations for nuclear medicine instrumentation. *Eur J Nucl Med Mol Imaging*. 2010;37:662–671.
- Busemann Sokole E, Plachcinska A, Britten A, Committee EP. Acceptance testing for nuclear medicine instrumentation. *Eur J Nucl Med Mol Imaging*. 2010; 37:672–681.
- ICRP. Release of patients after therapy with unsealed radionuclides. *Ann ICRP*. 2004;34:v–vi, 1–79.
- Erratum to “ICRP Publication 94: Release of patients after therapy with unsealed radionuclides.” *Ann ICRP* [Ann ICRP 34(2)]. 2004;34:281.
- IAEA. Release of Patients After Radionuclide Therapy. Vienna: International Atomic Energy Agency; 2009.
- Demir M, Abuqbeitah M, Uslu-Besli L, et al. Evaluation of radiation safety in (177)Lu-PSMA therapy and development of outpatient treatment protocol. *J Radiol Prot*. 2016;36:269–278.
- Kurth J, Krause BJ, Schwarzenbock SM, Stegger L, Schafers M, Rahbar K. External radiation exposure, excretion, and effective half-life in (177)Lu-PSMA-targeted therapies. *EJNMMI Res*. 2018;8:32.
- Levart D, Kalogianni E, Corcoran B, Mulholland N, Vivian G. Radiation precautions for inpatient and outpatient (177)Lu-DOTATATE peptide receptor radionuclide therapy of neuroendocrine tumours. *EJNMMI Phys*. 2019;6:7.
- Konijnenberg M, Herrmann K, Kobe C, et al. EANM position paper on article 56 of the Council Directive 2013/59/Euratom (basic safety standards) for nuclear medicine therapy. *Eur J Nucl Med Mol Imaging*. 2021;48:67–72.
- Hricak H, Abdel-Wahab M, Atun R, et al. Medical imaging and nuclear medicine: a Lancet Oncology Commission. *Lancet Oncol*. 2021;22:e136–e72.
- Craig AJ, Rojas B, Wevrett JL, Hamer E, Fenwick A, Gregory R. IPEM topical report: current molecular radiotherapy service provision and guidance on the implications of setting up a dosimetry service. *Phys Med Biol*. 2020;65:245038.
- Mora-Ramirez E, Santoro L, Cassol E, et al. Comparison of commercial dosimetric software platforms in patients treated with (177) Lu-DOTATATE for peptide receptor radionuclide therapy. *Med Phys*. 2020;47:4602–4615.
- Bolch WE, Eckerman KF, Sgouros G, Thomas SR. MIRD Pamphlet No. 21: A Generalized Schema for Radiopharmaceutical Dosimetry—Standardization of Nomenclature. *J Nucl Med*. 2009;50:477–484.
- Dewaraja YK, Frey EC, Sgouros G, et al. MIRD pamphlet No. 23: quantitative SPECT for patient-specific 3-dimensional dosimetry in internal radionuclide therapy. *Journal of nuclear medicine: official publication, Society of Nuclear Medicine*. 2012;53(8):1310–1325.
- Hindorf C, Glatting G, Chiesa C, Linden O, Flux G, Committee ED. EANM Dosimetry Committee guidelines for bone marrow and whole-body dosimetry. *Eur J Nucl Med Mol Imaging*. 2010;37:1238–1250.
- EARL. 2022. <https://earl.eanm.org/>. Accessed 28 Feb 2022.
- Committee ET. Technologists' Guide. 2022. <https://www.eanm.org/publications/technologists-guide/>. Accessed 28 Feb 2022.

30. Ljungberg M, Celler A, Konijnenberg MW, et al. MIRDO Pamphlet No. 26: Joint EANM/MIRD Guidelines for Quantitative  $^{177}\text{Lu}$  SPECT Applied for Dosimetry of Radiopharmaceutical Therapy. *J Nucl Med*. 2016;57:151–162.
31. Bodei L, Mueller-Brand J, Baum RP, et al. The joint IAEA, EANM, and SNMMI practical guidance on peptide receptor radionuclide therapy (PRRT) in neuroendocrine tumours. *Eur J Nucl Med Mol Imaging*. 2013;40:800–816.
32. Lassmann M, Chiesa C, Flux G, Bardies M, Committee ED. EANM Dosimetry Committee guidance document: good practice of clinical dosimetry reporting. *Eur J Nucl Med Mol Imaging*. 2011;38:192–200.
33. Gear JI, Cox MG, Gustafsson J, et al. EANM practical guidance on uncertainty analysis for molecular radiotherapy absorbed dose calculations. *Eur J Nucl Med Mol Imaging*. 2018;45:2456–2474.
34. Dewaraja YK, Ljungberg M, Green AJ, et al. MIRDO pamphlet No. 24: Guidelines for quantitative  $^{131}\text{I}$  SPECT in dosimetry applications. *Journal of nuclear medicine: official publication, Society of Nuclear Medicine*. 2013;54(12):2182–2188.
35. Taprogge J, Leek F, Schurrat T, et al. Setting up a quantitative SPECT imaging network for a European multi-centre dosimetry study of radioiodine treatment for thyroid cancer as part of the MEDIRAD project. *EJNMMI Phys*. 2020;7:61.
36. Hanscheid H, Canzi C, Eschner W, et al. EANM Dosimetry Committee series on standard operational procedures for pre-therapeutic dosimetry II. Dosimetry prior to radioiodine therapy of benign thyroid diseases. *Eur J Nucl Med Mol Imaging*. 2013;40:1126–1134.
37. Lassmann M, Hanscheid H, Chiesa C, et al. EANM Dosimetry Committee series on standard operational procedures for pre-therapeutic dosimetry I: blood and bone marrow dosimetry in differentiated thyroid cancer therapy. *Eur J Nucl Med Mol Imaging*. 2008;35:1405–1412.
38. Gear J, Chiesa C, Lassmann M, et al. EANM Dosimetry Committee series on standard operational procedures for internal dosimetry for  $^{131}\text{I}$  mIBG treatment of neuroendocrine tumours. *EJNMMI Phys*. 2020;7:15.
39. Ljungberg M, Celler A, Konijnenberg MW, et al. MIRDO Pamphlet No. 26: Joint EANM/MIRD Guidelines for Quantitative  $^{177}\text{Lu}$  SPECT Applied for Dosimetry of Radiopharmaceutical Therapy. *Journal of nuclear medicine: official publication, Society of Nuclear Medicine*. 2016;57(1):151–162.
40. Tran-Gia J, Denis-Bacelar AM, Ferreira KM, et al. A multicentre and multinational evaluation of the accuracy of quantitative Lu-177 SPECT/CT imaging performed within the MRTDOSIMETRY project. *EJNMMI Phys*. 2021;8:55.
41. Peters SMB, van der Werf NR, Segbers M, et al. Towards standardization of absolute SPECT/CT quantification: a multi-center and multi-vendor phantom study. *EJNMMI Phys*. 2019;6:29.
42. Chiesa C, Sjogreen-Gleisner K, Walrand S, et al. EANM dosimetry committee series on standard operational procedures: a unified methodology for  $(99\text{m})\text{Tc}$ -MAA pre- and  $(90\text{Y})$  peri-therapy dosimetry in liver radioembolization with  $(90\text{Y})$  microspheres. *EJNMMI Phys*. 2021;8:77.
43. Hindorf C, Chittenden S, Aksnes AK, Parker C, Flux GD. Quantitative imaging of  $^{223}\text{Ra}$ -chloride (Alpharadin) for targeted alpha-emitting radionuclide therapy of bone metastases. *Nucl Med Commun*. 2012;33:726–732.
44. Murray I, Chittenden SJ, Denis-Bacelar AM, et al. The potential of  $(223)\text{Ra}$  and  $(18)\text{F}$ -fluoride imaging to predict bone lesion response to treatment with  $(223)\text{Ra}$ -dichloride in castration-resistant prostate cancer. *Eur J Nucl Med Mol Imaging*. 2017;44:1832–1844.
45. Chittenden SJ, Hindorf C, Parker CC, et al. A Phase 1, Open-Label Study of the Bio-distribution, Pharmacokinetics, and Dosimetry of  $^{223}\text{Ra}$ -Dichloride in Patients with Hormone-Refractory Prostate Cancer and Skeletal Metastases. *Journal of nuclear medicine: official publication, Society of Nuclear Medicine*. 2015;56(9):1304–1309.
46. SNMMI. Procedure Standards. <https://www.snmmi.org/ClinicalPractice/content.aspx?ItemNumber=64142021>. Accessed 28 Feb 2022.
47. Fendler WP, Eiber M, Beheshti M, et al.  $(68)\text{Ga}$ -PSMA PET/CT: Joint EANM and SNMMI procedure guideline for prostate cancer imaging: version 1.0. *Eur J Nucl Med Mol Imaging*. 2017;44:1014–1024.
48. Kratochwil C, Fendler WP, Eiber M, et al. EANM procedure guidelines for radionuclide therapy with  $(177)\text{Lu}$ -labelled PSMA-ligands ( $(177)\text{Lu}$ -PSMA-RLT). *Eur J Nucl Med Mol Imaging*. 2019;46:2536–2544.
49. Poeppel TD, Handkiewicz-Junak D, Andreeff M, et al. EANM guideline for radionuclide therapy with radium-223 of metastatic castration-resistant prostate cancer. *Eur J Nucl Med Mol Imaging*. 2018;45:824–845.
50. EANM. Guidelines. <https://www.eanm.org/publications/guidelines/2021>. Accessed 28 Feb 2022.

---

---

# Repetitive Early $^{68}\text{Ga}$ -FAPI PET Acquisition Comparing $^{68}\text{Ga}$ -FAPI-02, $^{68}\text{Ga}$ -FAPI-46, and $^{68}\text{Ga}$ -FAPI-74: Methodologic and Diagnostic Implications for Malignant, Inflammatory/Reactive, and Degenerative Lesions

Frederik M. Glatting<sup>1,3</sup>, Jorge Hoppner<sup>1,4</sup>, Dawn P. Liew<sup>1</sup>, Antonia van Genabith<sup>1</sup>, Anna-Maria Spektor<sup>1</sup>, Levin Steinbach<sup>1</sup>, Alexander Hubert<sup>1</sup>, Clemens Kratochwil<sup>1</sup>, Frederik L. Giesel<sup>1,5</sup>, Katharina Dendl<sup>1</sup>, Hendrik Rathke<sup>1,6</sup>, Hans-Ulrich Kauczor<sup>4,7</sup>, Peter E. Huber<sup>2,3</sup>, Uwe Haberkorn<sup>1,7,8</sup>, and Manuel Röhrich<sup>1,7</sup>

<sup>1</sup>Department of Nuclear Medicine, University Hospital Heidelberg, Heidelberg, Germany; <sup>2</sup>Clinical Cooperation Unit Molecular and Radiation Oncology, German Cancer Research Center, Heidelberg, Germany; <sup>3</sup>Department of Radiation Oncology, University Hospital Heidelberg, Heidelberg, Germany; <sup>4</sup>Department of Diagnostic and Interventional Radiology, University of Heidelberg, Heidelberg, Germany; <sup>5</sup>Department of Nuclear Medicine, University Hospital Düsseldorf, Düsseldorf, Germany; <sup>6</sup>Department of Nuclear Medicine, Inselspital, Bern University Hospital, University of Bern, Bern, Switzerland; <sup>7</sup>Translational Lung Research Center Heidelberg, Member of the German Center for Lung Research DZL, Heidelberg, Germany; and <sup>8</sup>Clinical Cooperation Unit Nuclear Medicine, German Cancer Research Center, Heidelberg, Germany

$^{68}\text{Ga}$ -labeled fibroblast activation protein (FAP) inhibitor ( $^{68}\text{Ga}$ -FAPI) PET targets  $^{68}\text{Ga}$ -FAPI-positive activated fibroblasts and is a promising imaging technique for various types of cancer and nonmalignant pathologies. However, discrimination between malignant and nonmalignant  $^{68}\text{Ga}$ -FAPI-positive lesions based on static PET with a single acquisition time point can be challenging. Additionally, the optimal imaging time point for  $^{68}\text{Ga}$ -FAPI PET has not been identified yet, and different  $^{68}\text{Ga}$ -FAPI tracer variants are currently used. In this retrospective analysis, we evaluate the diagnostic value of repetitive early  $^{68}\text{Ga}$ -FAPI PET with  $^{68}\text{Ga}$ -FAPI-02,  $^{68}\text{Ga}$ -FAPI-46, and  $^{68}\text{Ga}$ -FAPI-74 for malignant, inflammatory/reactive, and degenerative lesions and describe the implications for future  $^{68}\text{Ga}$ -FAPI imaging protocols. **Methods:** Whole-body PET scans of 24 cancer patients were acquired at 10, 22, 34, 46, and 58 min after the administration of 150–250 MBq of  $^{68}\text{Ga}$ -FAPI tracer molecules (8 patients each for  $^{68}\text{Ga}$ -FAPI-02,  $^{68}\text{Ga}$ -FAPI-46, and  $^{68}\text{Ga}$ -FAPI-74). Detection rates and SUVs (SUV<sub>max</sub> and SUV<sub>mean</sub>) for healthy tissues, cancer manifestations, and nonmalignant lesions were measured, and target-to-background ratios (TBR) versus blood and fat were calculated for all acquisition time points. **Results:** For most healthy tissues except fat and spinal canal, biodistribution analysis showed decreasing uptake over time. We analyzed 134 malignant, inflammatory/reactive, and degenerative lesions. Detection rates were minimally reduced for the first 2 acquisition time points and remained at a constant high level from 34 to 58 min after injection. The uptake of all 3 variants was higher in malignant and inflammatory/reactive lesions than in degenerative lesions.  $^{68}\text{Ga}$ -FAPI-46 showed the highest uptake and TBRs in all pathologies. For all variants, TBRs versus blood constantly increased over time for all pathologies, and TBRs versus fat were constant or decreased slightly. **Conclusion:**  $^{68}\text{Ga}$ -FAPI PET/CT is a promising imaging modality for malignancies and benign lesions. Repetitive early PET acquisition added diagnostic value for the discrimination of malignant from nonmalignant  $^{68}\text{Ga}$ -FAPI-positive lesions. High detection rates and TBRs over time confirmed that PET acquisition earlier than 60 min after injection delivers

high-contrast images. Additionally, considering clinical feasibility, acquisition at 30–40 min after injection might be a reasonable compromise. Different  $^{68}\text{Ga}$ -FAPI variants show significant differences in time-dependent biodistributional behavior and should be selected carefully depending on the clinical setting.

**Key Words:** fibroblast activation protein; FAPI; PET; cancer; biodistribution

**J Nucl Med 2022; 63:1844–1851**

DOI: 10.2967/jnumed.122.264069

**P**ET using fibroblast activation protein (FAP) inhibitor labeled with  $^{68}\text{Ga}$  ( $^{68}\text{Ga}$ -FAPI) targets  $^{68}\text{Ga}$ -FAPI-positive fibroblasts that occur in the tumor microenvironment as cancer-associated fibroblasts (1–3), as well as in benign pathologies, such as fibrotic (4,5), reactive (6), and degenerative (7) processes. Numerous studies have demonstrated the great potential of  $^{68}\text{Ga}$ -FAPI PET/CT for imaging of various malignant (8,9) and nonmalignant diseases, especially fibrotic and inflammatory (10–13) and degenerative (14,15) diseases.

In most of these studies, static PET images were acquired 1 h after injection of the  $^{68}\text{Ga}$ -FAPI tracer, in analogy to  $^{18}\text{F}$ -FDG PET. Some studies have evaluated  $^{68}\text{Ga}$ -FAPI PET/CT at different acquisition time points or dynamic  $^{68}\text{Ga}$ -FAPI PET (13,16–19), but the reported results are based on small numbers of patients and are partially conflicting. To date, it is not clear which time point should be considered optimal for  $^{68}\text{Ga}$ -FAPI PET acquisition. Moreover, a large variety of  $^{68}\text{Ga}$ -FAPI tracer variants is currently in use at different centers, and only a small number of preclinical (20) and clinical (6,8,16) studies have compared different  $^{68}\text{Ga}$ -FAPI variants regarding their biodistribution and imaging properties for different pathologies.

In this retrospective analysis, we evaluated a repetitive early  $^{68}\text{Ga}$ -FAPI PET protocol with PET acquisition at 10, 22, 34, 46, and 58 min after tracer application, wherein 3  $^{68}\text{Ga}$ -FAPI variants ( $^{68}\text{Ga}$ -FAPI-02,  $^{68}\text{Ga}$ -FAPI-46, and  $^{68}\text{Ga}$ -FAPI-74) were applied in 8 patients. The aim of this study was to describe the differential biodistribution and imaging

---

Received Feb. 25, 2022; revision accepted May 16, 2022.  
For correspondence or reprints, contact Manuel Röhrich (manuel.roehrich@med.uni-heidelberg.de).  
Published online May 26, 2022.  
COPYRIGHT © 2022 by the Society of Nuclear Medicine and Molecular Imaging.

properties of the 3 variants over time for malignant, degenerative, and inflammatory/reactive lesions and to determine an optimal time point for  $^{68}\text{Ga}$ -FAPI PET acquisition with respect to optimal imaging quality, detection rate, and workflow.

## MATERIALS AND METHODS

### Patient Characterization

Twenty-four patients (aged 34–83 y; average, 61 y) with different types of cancer were examined by  $^{68}\text{Ga}$ -FAPI PET/CT. To avoid potential therapy effects on  $^{68}\text{Ga}$ -FAPI PET signaling, only patients without surgery, radiotherapy, or chemotherapy within the last 4 wk were examined. Median intervals between treatments and  $^{68}\text{Ga}$ -FAPI PET were 13 mo (range, 1–240 mo) for surgery, 29 mo (range, 2–260 mo) for radiotherapy, and 7 mo (range, 1–240 mo) for chemotherapy. All patients were referred by their treating physicians for  $^{68}\text{Ga}$ -FAPI PET/CT because of clinical indications. All patients gave written informed consent to the scientific evaluation of their personal data. This study was approved by the local institutional review board (study S-115/2020). Patient characteristics and tracer variants for each patient are given in Supplemental Table 1 (supplemental materials are available at <http://jnm.snmjournals.org>).

### Repetitive $^{68}\text{Ga}$ -FAPI PET/CT

Diagnostic imaging was performed under the conditions of the updated declaration of Helsinki, §37 (Unproven Interventions in Clinical

Practice), and in accordance with the German Pharmaceuticals Law §13 (2b) for medical reasons. FAPI tracers (FAPI-02, FAPI-46, and FAPI-74; 8 patients each) were labeled with  $^{68}\text{Ga}$  as previously described (20) and applied intravenously (80 nmol/GBq). Within the first 10 min after tracer injection, CT scans were performed with a Biograph mCT Flow PET/CT scanner (Siemens Medical Solutions) using the following parameters: slice thickness of 5 mm, increment of 3–4 mm, soft-tissue reconstruction kernel, and CARE Dose4D. PET scans were acquired exactly 10, 22, 34, 46, and 58 min after tracer administration (named as time points 1, 2, 3, 4, and 5) with a standardized field of view allowing whole-body scans within 12 min in 3 dimensions (matrix,  $200 \times 200$ ) in FlowMotion at 1.6 cm/min. Emission data were corrected for random events, scatter, and decay. Reconstruction used an ordered-subset expectation maximization algorithm with 2 iterations and 21 subsets, gauss-filtered to a transaxial resolution of 5 mm in full width at half maximum. Attenuation correction was performed using low-dose non-enhanced CT data.

### Image Analysis and Quantification

*Volumes of Interest (VOIs).* SUVs using a VOI technique were quantitatively assessed by 2 of the authors independently at first, followed by a consensus reading between them. Tracer biodistribution in patients and uptake at pathologic sites were quantified by  $\text{SUV}_{\text{mean}}$  and  $\text{SUV}_{\text{max}}$ . Normal organs were evaluated using a sphere, placed inside the organ parenchyma, with a diameter of 5 mm for oral

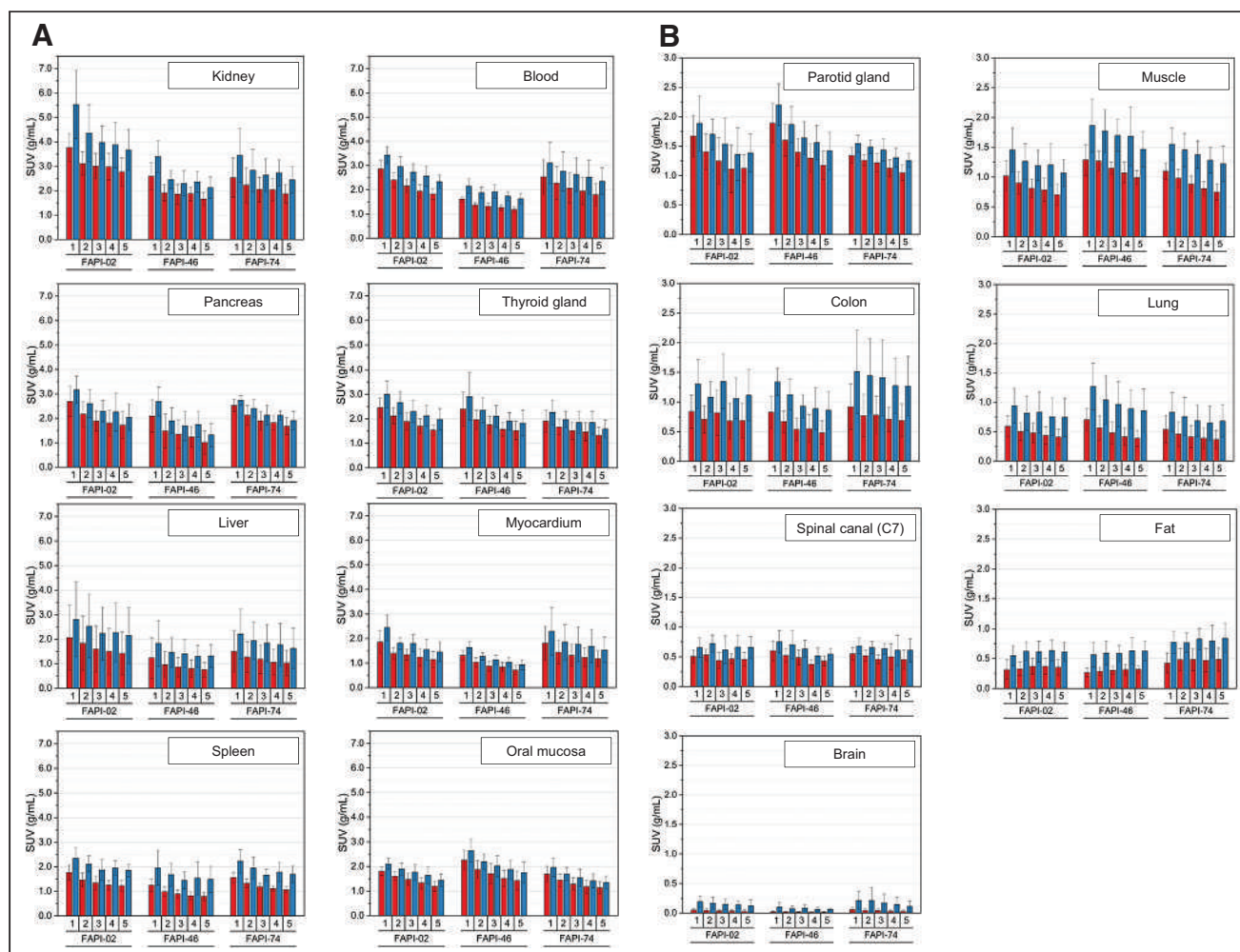


**FIGURE 1.** Biodistribution analysis ( $\text{SUV}_{\text{mean}}$  [red] and  $\text{SUV}_{\text{max}}$  [blue]  $\pm$  SD) of 24 patients, 8 patients per  $^{68}\text{Ga}$ -FAPI variant, with high-uptake (A) and low-uptake (B) tissues over time at acquisition time points of 10 min (1), 22 min (2), 34 min (3), 46 min (4), and 58 min (5) after application of  $^{68}\text{Ga}$ -FAPI variants of  $^{68}\text{Ga}$ -FAPI-02,  $^{68}\text{Ga}$ -FAPI-46, or  $^{68}\text{Ga}$ -FAPI-74.

mucosa, parotid glands, thyroid, myocardium, pancreas, kidneys, and spinal canal (C7); 10 mm for blood, colon, and fat tissue; and 15 mm for brain, lungs, liver, spleen, and muscles. VOIs for blood were drawn at the beginning of the descending aorta on the first axial slice on which the aortic arch was no longer visible, and VOIs for fat were drawn within gluteal fat tissue at the height of the acetabulum. Respecting SUV calculation for pathologies, spheric regions of interest were drawn around the lesions on  $^{68}\text{Ga}$ -FAPI PET images acquired at 58 min after injection and were automatically adapted to a 3-dimensional volume by PMOD software (PMOD Technologies LLC) at a 50%–70% isocontour. All VOIs for normal tissues and pathologies were automatically transferred to the previous time points by PMOD software in order to achieve identical intraindividual VOIs.

We determined dominating tracer variants for each tissue by evaluating the mean absolute  $\text{SUV}_{\text{max}}$  and  $\text{SUV}_{\text{mean}}$  at the initial and following time points. Variants with the highest values and marked differences from the other 2 variants were considered dominant. If the differences between different  $^{68}\text{Ga}$ -FAPI tracers were not distinct, they were considered approximately equal.

Lesions were classified as malignant, inflammatory/reactive, or degenerative on the basis of clinical information and CT morphology. Only lesions with highly suggestive characteristics for 1 of these classes were analyzed. Detection rates for all classes of lesions were determined by 3 of the authors as previously described (18).

An increase, constant level, or decrease in  $^{68}\text{Ga}$ -FAPI uptake was determined on the basis of visual assessment and the trends in mean absolute  $\text{SUV}_{\text{max}}$  or  $\text{SUV}_{\text{mean}}$  over time.

### Statistical Analysis

We performed descriptive analyses for patients and their characteristics. For determination of SUVs, median and range were used. The correlation of  $^{68}\text{Ga}$ -FAPI uptake within or outside the lesions was determined using a 2-sided  $t$  test. A  $P$  value of less than 0.05 was defined as statistically significant. Excel (version 2111; Microsoft) and Origin (version 2021b; OriginLab Corp.) were used for statistical analyses.

## RESULTS

### Patient Cohort

Supplemental Table 1 summarizes the demographic and clinical data of all patients. Overall, 1 patient was treatment-naïve, having metastasis at the initial presentation. Of the 23 patients with suspected recurrence or progression after resection, chemotherapy, or radiotherapy, some patients showed evidence of a local tumor only (6 patients), metastasis only (8 patients), both local tumor and metastasis (6 patients), or no tumor (3 patients).

### Biodistribution

Figure 1 shows the biodistribution in terms of  $\text{SUV}_{\text{max}}$  and  $\text{SUV}_{\text{mean}}$  over time for all physiologic tissues. Organs were categorized as having high or low  $^{68}\text{Ga}$ -FAPI avidity (B). For most tissues,  $\text{SUV}_{\text{max}}$  and  $\text{SUV}_{\text{mean}}$  decreased continuously, whereas  $\text{SUV}_{\text{max}}$  and  $\text{SUV}_{\text{mean}}$  tended to increase for fat tissue and to remain constant for the spinal canal. By comparing tissue uptake for the 3 variants, Figure 2 shows the dominating variant for each tissue.

For each variant, Figure 3 shows representative maximum-intensity projections and axial  $^{68}\text{Ga}$ -FAPI PET/CT images of blood pool, lungs, and muscles. In accordance with the data of Figure 2, these typical examples underline the biodistribution of the variants and show that the highest uptake by blood was for  $^{68}\text{Ga}$ -FAPI-02. However, the highest uptake by muscle tissue was for  $^{68}\text{Ga}$ -FAPI-46, according to the kinetics shown in Figure 1 and the data of Figure 2.

Tissue	Tracer variant - uptake		
	FAPI-02	FAPI-46	FAPI-74
Blood	Red	Green	Yellow
Kidney	Red	Orange	Orange
Liver	Red	Green	Yellow
Pancreas	Red	Green	Yellow
Spleen	Red	Green	Yellow
Thyroid	Red	Yellow	Green
Lungs	Yellow	Red	Green
Muscle	Green	Red	Yellow
Oral mucosa	Yellow	Red	Green
Parotid gland	Yellow	Red	Green
Brain	Yellow	Green	Red
Colon	Yellow	Green	Red
Fat tissue	Orange	Orange	Red
Myocardium	Orange	Green	Orange
Spinal canal (C7)	Orange	Orange	Orange

**FIGURE 2.** Dominating  $^{68}\text{Ga}$ -FAPI variant for each considered tissue, with red indicating highest uptake; yellow, medium uptake; green, lowest uptake; and orange, approximately equal uptake.

Supplemental Figure 1 shows an intertissue comparison of the biodistribution at 34 and 58 min after injection.

### Detection Rate

On the basis of clinical information and CT morphology, 134 lesions were classified as malignant, inflammatory/reactive, or degenerative and were used for further analysis. Three lesions were labeled “other” because they could not be matched with 1 of the 3 classes and were not further analyzed. Table 1 summarizes all 137 lesions. Lesions rated as malignant numbered 34 of 49 (69.4%) for  $^{68}\text{Ga}$ -FAPI-02, 21 of 52 (40.4%) for  $^{68}\text{Ga}$ -FAPI-46, and 16 of 36 (44.4%) for  $^{68}\text{Ga}$ -FAPI-74.

Respecting  $^{68}\text{Ga}$ -FAPI-02 and  $^{68}\text{Ga}$ -FAPI-74, 2 malignant lesions of 47 total lesions (4.3%) and 1 malignant lesion of 36 total lesions (2.8%), respectively, could not be detected on imaging at the first time point but were detectable at the following 4 time points. For  $^{68}\text{Ga}$ -FAPI-46, a retroperitoneal liposarcoma remained undetected over all 5 time points. Two degenerative lesions of 52 total lesions (3.8%) were not detected at the first time point, and 1 of these (1.9%) was not seen at the second time point either. Both were detectable at the following time points. All inflammatory/reactive lesions were detected at all 5 time points for each variant (Table 2).

### Uptake over Time in Malignant, Inflammatory/Reactive, and Degenerative Lesions

The different types of lesions differed in their time-dependent uptake. Figure 4 provides an overview of the  $\text{SUV}_{\text{max}}$  and  $\text{SUV}_{\text{mean}}$

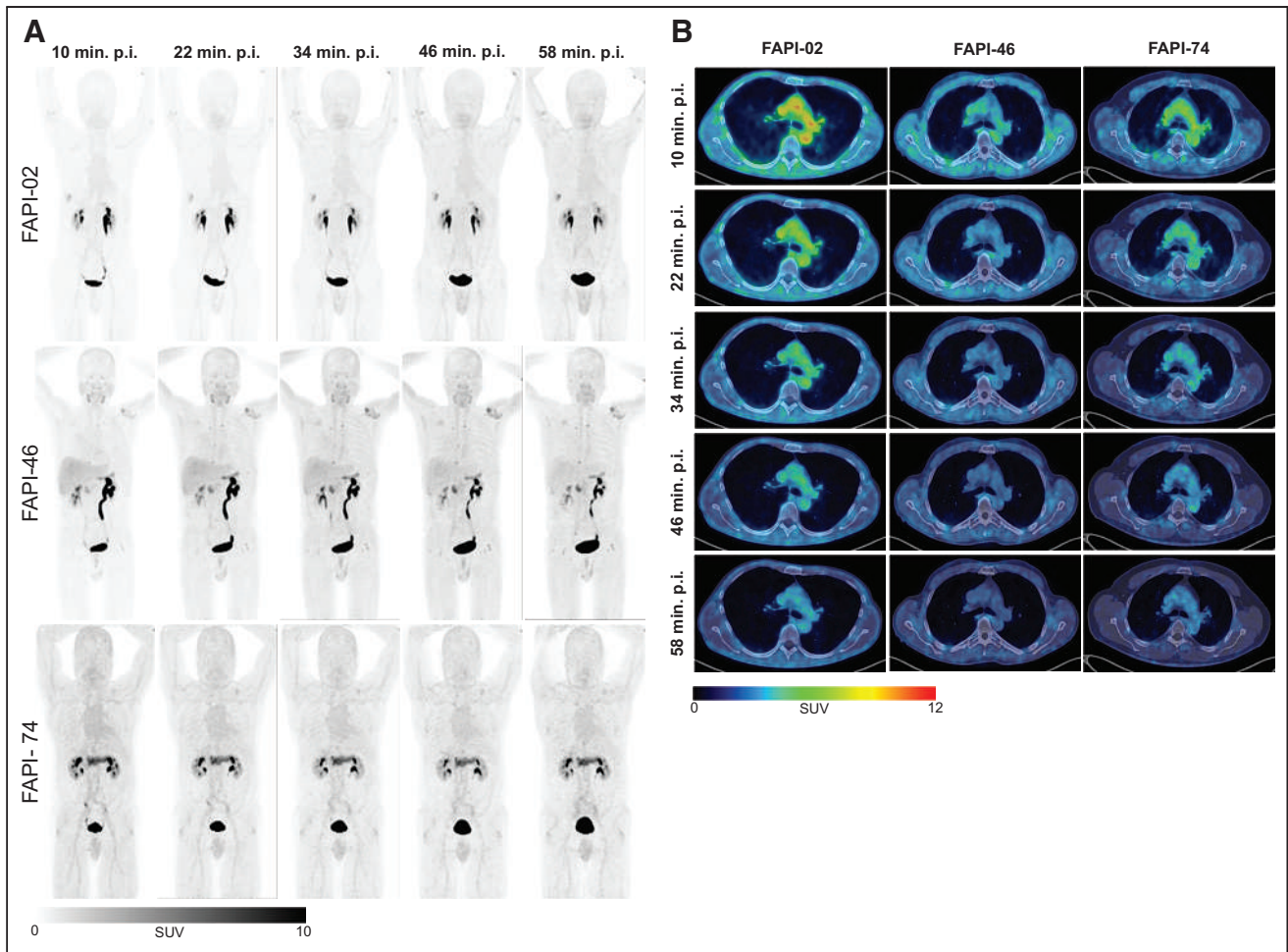


**FIGURE 3.** (A) Representative maximum-injection projections of  $^{68}\text{Ga}$ -FAPI PET/CT for  $^{68}\text{Ga}$ -FAPI-02 (top row, 56-y-old man with resected pancreatic carcinoma, staging for metastases, no local recurrence, single hepatic metastasis),  $^{68}\text{Ga}$ -FAPI-46 (middle row, 64-y-old man with pancreatic cancer, staging for suspected local recurrence, no metastases), and  $^{68}\text{Ga}$ -FAPI-74 (bottom row, 60-y-old man with pancreatic carcinoma, staging in advance of radiation therapy, primary, single hepatic metastasis) over time with acquisition time points of 10 min (1), 22 min (2), 34 min (3), 46 min (4), and 58 min (5) after application. (B) Representative axial  $^{68}\text{Ga}$ -FAPI PET/CT images of upper thorax showing uptake for blood, muscle, and lungs over time with acquisition time points of 10 min (1), 22 min (2), 34 min (3), 46 min (4), and 58 min (5) after application of  $^{68}\text{Ga}$ -FAPI-02 (left column, 56-y-old man with resected pancreatic carcinoma, staging for metastases, no local recurrence, single hepatic metastasis),  $^{68}\text{Ga}$ -FAPI-46 (middle column, 58-y-old man with retroperitoneal liposarcoma, staging in advance of neoadjuvant radiation therapy, primary, 3 metastases), and  $^{68}\text{Ga}$ -FAPI-74 (60-y-old man with pancreatic carcinoma, staging in advance of radiation therapy, primary, single hepatic metastasis). p.i. = after injection.

kinetics of different types of lesions at the 5 acquisition times, allowing a comparison between variants. Respecting  $^{68}\text{Ga}$ -FAPI-02, malignant lesions showed a slightly increasing uptake over time whereas benign lesion tended to be constant or slightly decreasing. The absolute values among the 3 lesion types were similar.

For  $^{68}\text{Ga}$ -FAPI-46, malignant and inflammatory/reactive lesions show higher uptake than degenerative lesions. Moreover, the uptake within these lesions was higher than for  $^{68}\text{Ga}$ -FAPI-02 or  $^{68}\text{Ga}$ -FAPI-74. Additionally, regarding  $^{68}\text{Ga}$ -FAPI-46, malignant and inflammatory/reactive lesions featured a slope over time, whereas uptake by degenerative lesions remained roughly unchanged.

$^{68}\text{Ga}$ -FAPI-74 showed higher uptake in malignant and inflammatory/reactive lesions than in degenerative lesions. The uptake remained constant or increased only slowly for malignant and inflammatory/reactive lesions over time. However, the degenerative pathologies showed an increasing uptake over time, finally approaching the level of the 2 other types of pathologies. This

finding is demonstrated in Figure 5 by a  $^{68}\text{Ga}$ -FAPI-74 PET/CT scan of a patient with a solitary hepatic metastasis, pancreatitis, and an insertion-related tendinopathy in the right trochanter region. The uptake associated with the insertion-related tendinopathy increased over time, whereas the uptake by the hepatic metastasis and pancreatitis decreased slightly (Supplemental Table 2).

#### Target-to-Background Ratios (TBRs) over Time in Malignant, Inflammatory/Reactive, and Degenerative Lesions

Because fat tissue showed an increasing  $^{68}\text{Ga}$ -FAPI uptake for all 3 variants over time, contrary to the other healthy tissues, and because uptake by fat can easily be measured in a clinical setting, the  $\text{SUV}_{\text{max}}$  and  $\text{SUV}_{\text{mean}}$  of fat tissue were used to calculate TBRs versus fat tissue in addition to TBRs versus blood. The corresponding graphs are in Figure 6.

In comparison with  $^{68}\text{Ga}$ -FAPI-02 and  $^{68}\text{Ga}$ -FAPI-74,  $^{68}\text{Ga}$ -FAPI-46 showed a higher TBR versus blood and versus fat for

**TABLE 1**  
Number of Malignant, Inflammatory/Reactive, and Degenerative Pathologies for Each Radiotracer

Variant	Pathology	n
<sup>68</sup> Ga-FAPI-02	Total	49 (100.0%)
	Malignant	34 (69.4%)
	Inflammatory/reactive	4 (8.2%)
	Degenerative	9 (18.4%)
	Other	2 (4.1%)
<sup>68</sup> Ga-FAPI-46	Total	52 (100.0%)
	Malignant	21 (40.4%)
	Inflammatory/reactive	8 (15.4%)
	Degenerative	22 (42.3%)
	Other	1 (1.9%)
<sup>68</sup> Ga-FAPI-74	Total	36 (100.0%)
	Malignant	16 (44.4%)
	Inflammatory/reactive	9 (25.0%)
	Degenerative	11 (30.6%)
	Other	0 (0.0%)

malignant, inflammatory/reactive, and degenerative lesions at all acquisition times. In contrast to the curve progression of TBR versus blood, which increased over time for all variants at different slopes for all 3 kinds of lesions, TBR versus fat tended to remain constant or to decrease slightly. This behavior was particularly evident for <sup>68</sup>Ga-FAPI-02 in inflammatory/reactive pathologies, whereas <sup>68</sup>Ga-FAPI-74 still showed an increase in TBR versus fat over time only for degenerative lesions.

## DISCUSSION

In this retrospective analysis, we found different time-dependent biodistributions for the 3 variants <sup>68</sup>Ga-FAPI-02, <sup>68</sup>Ga-FAPI-46, and <sup>68</sup>Ga-FAPI-74, implicating the benefit of careful selection of the variant depending on the tissue of interest and the clinical setting. Furthermore, this study demonstrated the differential behavior of malignant, inflammatory/reactive, and degenerative lesions over time by considering the uptake and TBR versus blood and fat tissue.

### Time-Dependent Biodistribution of <sup>68</sup>Ga-FAPI Variants

Biodistribution analysis showed that SUV<sub>max</sub> and SUV<sub>mean</sub> declined over time for all tissues except fat tissue (increase) and spinal cord (constant). The detection rate for each variant was slightly reduced at 10 min after injection for all variants; for <sup>68</sup>Ga-FAPI-46, the detection rate was still reduced at 22 min but was stable at a high level between 34 and 58 min. To optimize the selection of <sup>68</sup>Ga-FAPI variants, we identified the dominating variant for each tissue. The variant showing the lowest uptake, and thus lowest background, within healthy tissue is considered a potential optimal variant. Given the differential muscle-to-fat ratio between female and male patients and the variability in body mass, it might be of interest to analyze fat and muscle signaling with respect to the sexes and body mass index in order to minimize background activity through optimal variant selection. This analysis may also be interesting with respect to reduction of radiation exposure but would require a larger cohort than ours. However, as the magnitude of uptake by malignant and benign lesions, and thereby the TBRs, also affects the suitability of a variant for a certain clinical context, uptake and TBR over time were analyzed in malignant, inflammatory/reactive, and degenerative lesions. Generally, the uptake was higher in malignant and inflammatory/reactive lesions than in degenerative lesions for all 3 variants. However, different trends could be observed for the different variants. The slightly increasing or constant uptake of <sup>68</sup>Ga-FAPI-02 over

**TABLE 2**  
Detection Rates and Undetected Lesions at Different Acquisition Time Points

Variant	Detection rate and undetected lesions				
	10 min	22 min	34 min	46 min	58 min
<sup>68</sup> Ga-FAPI-02	95.7	100.0	100.0	100.0	100.0
Malignant	2/34	0/31*	0/34	0/34	0/34
Inflammatory/reactive	0/4	0/4	0/4	0/9	0/4
Degenerative	0/9	0/6*	0/9	0/9	0/9
<sup>68</sup> Ga-FAPI-46	94.1	96.1	98.0	98.0	98.0
Malignant	1/21	1/21	1/21	1/21	1/21
Inflammatory/reactive	0/8	0/8	0/8	0/8	0/8
Degenerative	2/22	1/22	0/22	0/22	0/22
<sup>68</sup> Ga-FAPI-74	97.2	100.0	100.0	100.0	100.0
Malignant	1/1	0/16	0/16	0/16	0/16
Inflammatory/reactive	0/9	0/9	0/9	0/9	0/9
Degenerative	0/11	0/11	0/11	0/11	0/11

\*In 1 patient with 3 malignant and 3 degenerative lesions, image acquisition failed at time point 2. Data are percentages.

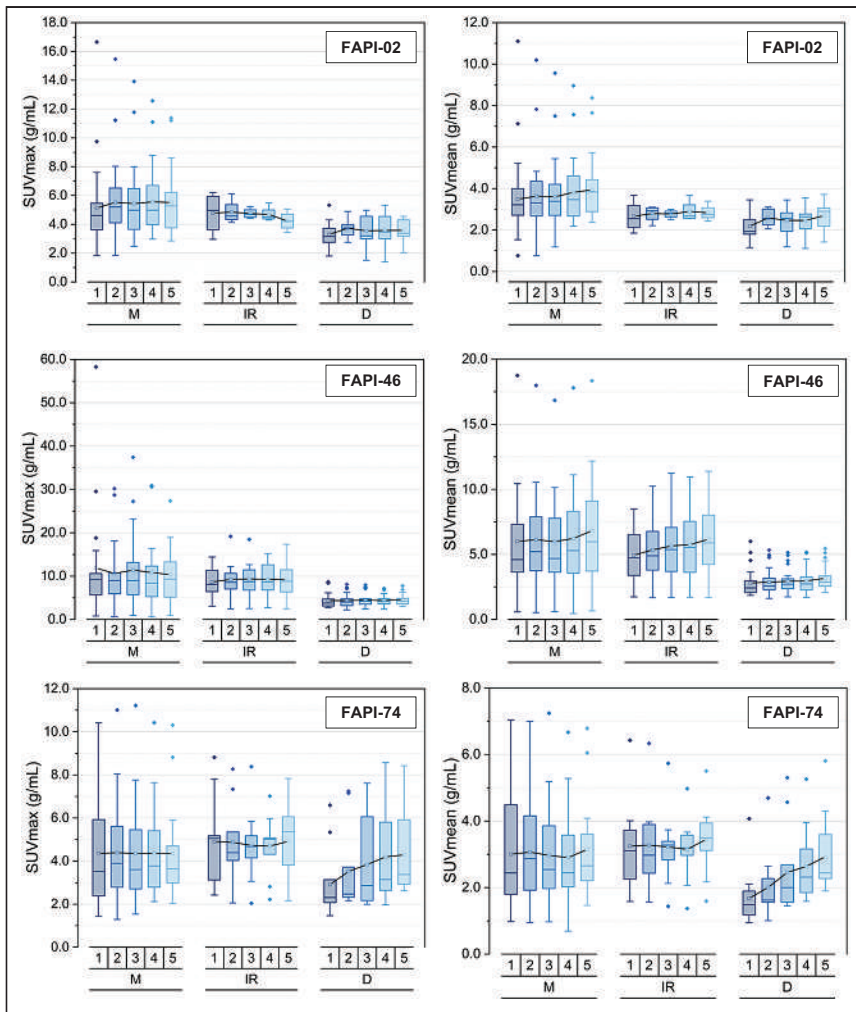


**FIGURE 4.**  $SUV_{max}$  and  $SUV_{mean}$  for malignant (M), inflammatory/reactive (IR), or degenerative (D) pathologies over time at 10 min (1), 22 min (2), 34 min (3), 46 min (4), and 58 min (5) after injection of 3  $^{68}\text{Ga}$ -FAPI variants ( $^{68}\text{Ga}$ -FAPI-02,  $^{68}\text{Ga}$ -FAPI-46, and  $^{68}\text{Ga}$ -FAPI-74). Boxes represent interquartile range, whiskers represent interquartile range of 1.5, horizontal line within box indicates median, and small box indicates mean. Data outliers are shown separately within graph. Trending lines regarding mean are shown.

time might indicate rapid uptake within the lesions and only a slow washout. Notably, in pathologies,  $^{68}\text{Ga}$ -FAPI-46 showed the highest uptake of all variants. Along with the observation that  $^{68}\text{Ga}$ -FAPI-46 showed a lower background activity in blood and other tissues, this variant also manifested the highest TBRs. Although  $^{68}\text{Ga}$ -FAPI-46 featured a slightly increasing uptake within malignant and inflammatory/reactive lesions, there was an approximately constant uptake for degenerative lesions over time.  $^{68}\text{Ga}$ -FAPI-74 showed an approximately constant level of uptake over time for malignant and inflammatory/reactive lesions but an increase for degenerative lesions.

#### Uptake and TBRs in Pathologies over Time

Most previous studies analyzing several acquisition time points demonstrated that time-dependent differences are small from 10 to 180 min after injection (6,13,18,21). Hu et al. observed a nonsignificant increase in  $SUV_{max}$  over time between 10 and 60 min after injection but calculated a significant increase in TBRs versus blood over time (16). In our study, we found only small differences in uptake

among the 5 acquisition time points from 10 to 58 min after injection. Nevertheless, some trends could be concluded from the time-dependent uptake curves. First, uptake was higher in malignant and inflammatory/reactive lesions than in degenerative lesions for all 3 variants. Additionally, the malignant, inflammatory/reactive, and degenerative pathologies were distinguishable from one another by their absolute values and by their uptake progression over time. TBRs versus blood for all pathologies constantly increased over time for all variants, but at different slopes. In addition to the data presented here, we are planning to perform a separate analysis of this dataset focused on different subclasses of malignant, inflammatory/reactive, and degenerative lesions to identify further subgroups with differential uptake behaviors over time.

#### Diagnostic Value of Repetitive $^{68}\text{Ga}$ -FAPI Imaging and Implications for $^{68}\text{Ga}$ -FAPI PET Acquisition

$^{68}\text{Ga}$ -FAPI PET/CT is a promising imaging modality for the detection of both malignant and benign pathologies. Nevertheless, the optimal acquisition time has not been clearly determined yet. The current level of knowledge is ambiguous and inconsistent. On the one hand, a recent study on  $^{18}\text{F}$ -FAPI-42-PET/CT in 22 patients concluded that the optimal acquisition time was 60 min after injection, arguing that TBR versus blood was small initially and increased over time and that some lesions were undetected early after tracer application because of the small initial TBR versus blood (16). At the same time, the authors postulated that it might not be necessary to postpone the acquisition because tumor detection was not improved at later time points. On the other hand, Ferdinandus et al. reasoned—on the basis of a retrospective study including 69 patients who underwent  $^{68}\text{Ga}$ -FAPI-46 PET 10 and 60 min after injection—that detection rates at the 2 acquisition times did not differ (18). Because of the improved feasibility and scan volume, the authors decided to implement early acquisition time points in future PET protocols.

Contrary to this conclusion and partly agreeing with the results of Hu et al., our study showed that the detection rate was slightly reduced at 10 min after injection (mainly caused by undetected malignant and degenerative lesions), thus arguing against performing clinical interpretation based on an early acquisition at 10 min after injection only. Along with the increasing TBR versus blood and the constant TBR versus fat over time, our finding suggested that the later time points would favor optimal clinical interpretations of PET/CT. Taking clinical practicability and feasibility into account along with a sufficient detection rate, acquisition at 30–40 min after injection is what we recommend and appears to be a reasonable compromise.

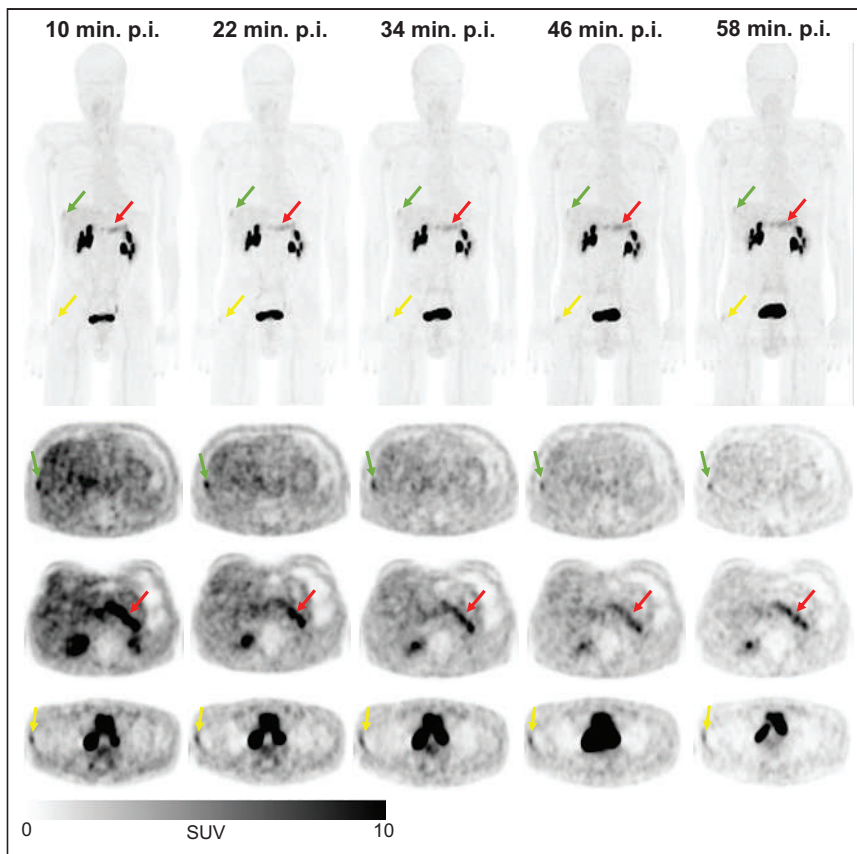


**FIGURE 5.** Example maximum-intensity projection (top) and axial PET/CT images of  $^{68}\text{Ga}$ -FAPi-74 PET/CT scans (bottom) of 56-y-old man with pancreatic carcinoma after resection (no local recurrence, 4 metastases) over time with acquisition time points of 10 min (1), 22 min (2), 34 min (3), 46 min (4), and 58 min (5) after application. Clinically, patient showed hepatic metastasis (green arrows, second row, malignant manifestation), pancreatitis-related uptake (red arrows, third row, inflammatory lesion), and insertion-related tendinopathy in right trochanter region (yellow arrows, fourth row, degenerative lesion). p.i. = after injection.

### Limitations

Several limitations of our analysis must be considered. One arises from the relatively low number (24) of patients included. Thus, conclusions on our data should be drawn with caution. A second limitation is that the lesions were not histologically confirmed. Our classification of pathologies had to be based on morphologic CT anomalies. Third, VOIs for the biodistribution analysis and for pathologies were defined using the dataset of the last acquisition time point and subsequently transferred to the previous time points in order to achieve identical intraindividual VOIs. This method can lead to uncertainty caused by movement artifacts within the first 4 acquisition time points, even though datapoints with visually obvious spatial differences were excluded from the dataset. Furthermore, because of the only small number of degenerative lesions examined using  $^{68}\text{Ga}$ -FAPi-74, the surprising finding of markedly increasing uptake over time for degenerative lesions has to be interpreted carefully. Another limitation is the heterogeneity of the patient cohorts per variant. Although emphasis was put on pancreatic carcinoma within the patient groups, rarer malignancies such as liposarcomas, which are known to show FAP expression not only by cancer-associated fibroblasts but also by neoplastic cells, (22) were included and may have reduced the intergroup comparability. Since the results among tumor entities did not differ markedly, our conclusions might be relevant beyond the considered tumor entities.

### CONCLUSION

$^{68}\text{Ga}$ -FAPi PET/CT is a promising, innovative imaging modality for various malignancies and for various benign conditions. Repetitive early PET acquisition added diagnostic value for discrimination of malignant from nonmalignant  $^{68}\text{Ga}$ -FAPi-positive lesions. TBRs and high detection rates over time confirmed that PET acquisition earlier than 60 min after injection delivers high-contrast images. According to our findings, by taking clinical practicability and feasibility into consideration along with a sufficient detection rate, we recommend acquisition at 30–40 min after injection. Different  $^{68}\text{Ga}$ -FAPi variants show significant differences in their time-dependent biodistributional behavior and should be selected carefully depending on the clinical setting.

### DISCLOSURE

This work was funded by grant 13341 from the Federal Ministry of Education and Research. Uwe Haberkorn, Clemens Kratochwil, and Frederik Giesel have filed a patent application for quinoline-based FAP-targeting agents for imaging and therapy in nuclear medicine and have shares of a consultancy group for iTheragnostics. No other potential conflict of interest relevant to this article was reported.

### ACKNOWLEDGMENT

We thank Oda Landmann-Fothergill for her language corrections.

### KEY POINTS

**QUESTION:** What is the rationale for selection of optimal tracer variants and acquisition times for  $^{68}\text{Ga}$ -FAPi PET?

**PERTINENT FINDINGS:** The background activity of most tissues decreased over time, and the detection rates for pathologies were minimally reduced at early acquisition times.  $^{68}\text{Ga}$ -FAPi-46 showed the highest uptake in all pathologies. For all variants and pathologies, TBRs versus blood increased over time and TBRs versus fat were constant or decreased slightly.

**IMPLICATIONS FOR PATIENT CARE:**  $^{68}\text{Ga}$ -FAPi variants show significant differences in their time-dependent biodistributional behavior and should be selected carefully depending on the clinical setting.

### REFERENCES

1. LeBleu VS, Kalluri R. A peek into cancer-associated fibroblasts: origins, functions and translational impact. *Dis Model Mech*. 2018;11:dmm029447.
2. Kalluri R. The biology and function of fibroblasts in cancer. *Nat Rev Cancer*. 2016;16:582–598.
3. Sahai E, Astsaturov I, Cukierman E, et al. A framework for advancing our understanding of cancer-associated fibroblasts. *Nat Rev Cancer*. 2020;20:174–186.

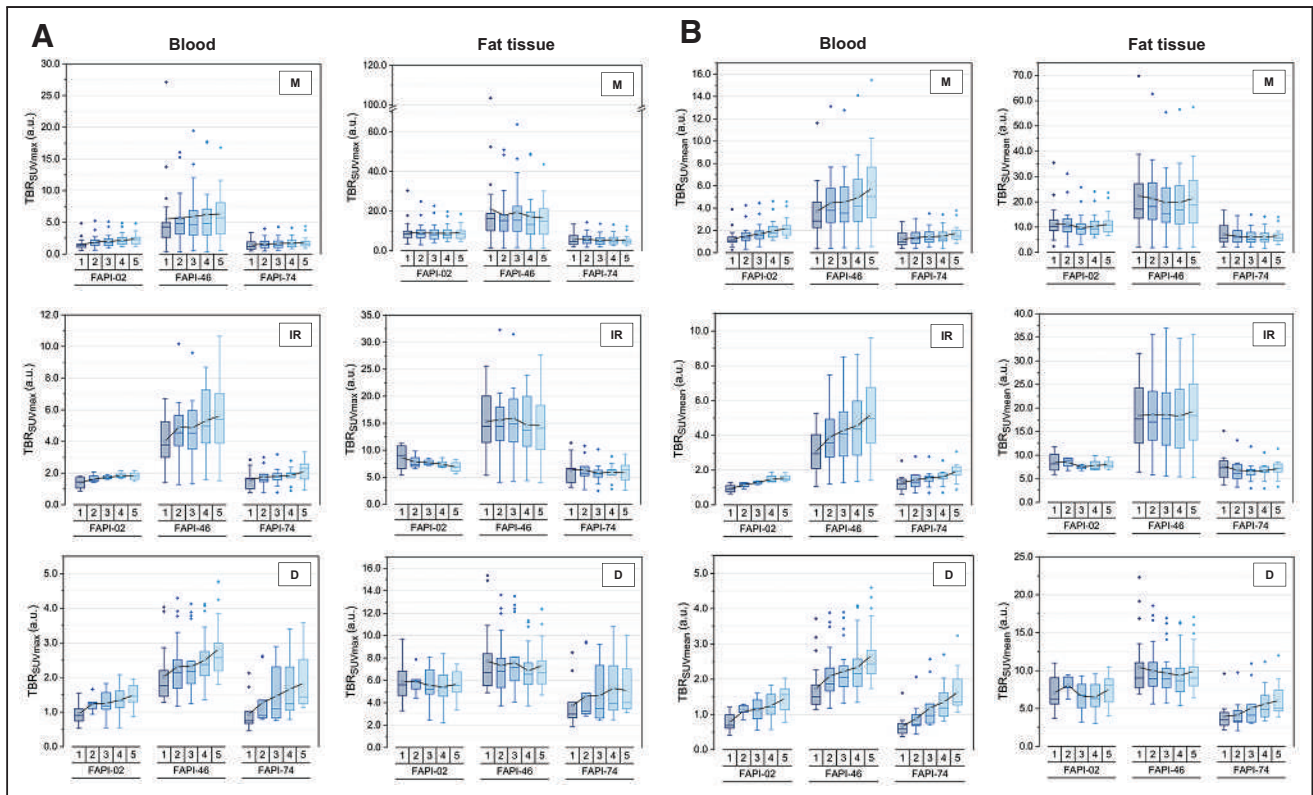


**FIGURE 6.** TBRs for  $SUV_{max}$  (A) and  $SUV_{mean}$  (B) regarding malignant (M), inflammatory/reactive (IR), and degenerative (D) pathologies vs. blood and vs. fat tissue for 3  $^{68}\text{Ga}$ -FAPI variants ( $^{68}\text{Ga}$ -FAPI-02,  $^{68}\text{Ga}$ -FAPI-46, and  $^{68}\text{Ga}$ -FAPI-74) over time, with acquisition time points of 10 min (1), 22 min (2), 34 min (3), 46 min (4), and 58 min (5) after injection. Boxes represent interquartile range, whiskers represent interquartile range of 1.5, horizontal line within box indicates median, and small box indicates mean. Data outliers are shown separately within graph. Trending lines regarding mean are shown. a.u. = arbitrary units.

- Henderson NC, Rieder F, Wynn TA. Fibrosis: from mechanisms to medicines. *Nature*. 2020;587:555–566.
- Affo S, Yu LX, Schwabe RF. The role of cancer-associated fibroblasts and fibrosis in liver cancer. *Annu Rev Pathol*. 2017;12:153–186.
- Röhrich M, Naumann P, Giesel FL, et al. Impact of  $^{68}\text{Ga}$ -FAPI PET/CT imaging on the therapeutic management of primary and recurrent pancreatic ductal adenocarcinomas. *J Nucl Med*. 2021;62:779–786.
- Pap T, Dankbar B, Wehmeyer C, Korb-Pap A, Sherwood J. Synovial fibroblasts and articular tissue remodelling: role and mechanisms. *Semin Cell Dev Biol*. 2020;101:140–145.
- Kratochwil C, Flechsig P, Lindner T, et al.  $^{68}\text{Ga}$ -FAPI PET/CT: tracer uptake in 28 different kinds of cancer. *J Nucl Med*. 2019;60:801–805.
- Chen H, Pang Y, Wu J, et al. Comparison of [ $^{68}\text{Ga}$ ]Ga-DOTA-FAPI-04 and [ $^{18}\text{F}$ ]FDG PET/CT for the diagnosis of primary and metastatic lesions in patients with various types of cancer. *Eur J Nucl Med Mol Imaging*. 2020;47:1820–1832.
- Luo Y, Pan Q, Yang H, Peng L, Zhang W, Li F. Fibroblast activation protein-targeted PET/CT with  $^{68}\text{Ga}$ -FAPI for imaging IgG4-related disease: comparison to  $^{18}\text{F}$ -FDG PET/CT. *J Nucl Med*. 2021;62:266–271.
- Schmidkonz C, Rauber S, Atzinger A, et al. Disentangling inflammatory from fibrotic disease activity by fibroblast activation protein imaging. *Ann Rheum Dis*. 2020;79:1485–1491.
- Zhou Y, Yang X, Liu H, et al. Value of [ $^{68}\text{Ga}$ ]Ga-FAPI-04 imaging in the diagnosis of renal fibrosis. *Eur J Nucl Med Mol Imaging*. 2021;48:3493–3501.
- Röhrich M, Leitz D, Glatting FM, et al. Fibroblast activation protein-specific PET/CT imaging in fibrotic interstitial lung diseases and lung cancer: a translational exploratory study. *J Nucl Med*. 2022;63:127–133.
- Qin C, Song Y, Liu X, et al. Increased uptake of  $^{68}\text{Ga}$ -DOTA-FAPI-04 in bones and joints: metastases and beyond. *Eur J Nucl Med Mol Imaging*. 2022;49:709–720.
- Liu H, Wang Y, Zhang W, Cai L, Chen Y. Elevated [ $^{68}\text{Ga}$ ]Ga-DOTA-FAPI-04 activity in degenerative osteophyte in a patient with lung cancer. *Eur J Nucl Med Mol Imaging*. 2021;48:1671–1672.
- Hu K, Wang L, Wu H, et al. [ $^{18}\text{F}$ ]FAPI-42 PET imaging in cancer patients: optimal acquisition time, biodistribution, and comparison with [ $^{68}\text{Ga}$ ]Ga-FAPI-04. *Eur J Nucl Med Mol Imaging*. 2022;49:2833–2843.
- Wang S, Zhou X, Xu X, et al. Dynamic PET/CT Imaging of  $^{68}\text{Ga}$ -FAPI-04 in Chinese subjects. *Front Oncol*. 2021;11:651005.
- Ferdinandus J, Kessler L, Hirmas N, et al. Equivalent tumor detection for early and late FAPI-46 PET acquisition. *Eur J Nucl Med Mol Imaging*. 2021;48:3221–3227.
- Geist BK, Xing H, Wang J, et al. A methodological investigation of healthy tissue, hepatocellular carcinoma, and other lesions with dynamic  $^{68}\text{Ga}$ -FAPI-04 PET/CT imaging. *EJNMMI Phys*. 2021;8:8.
- Loktev A, Lindner T, Burger EM, et al. Development of fibroblast activation protein-targeted radiotracers with improved tumor retention. *J Nucl Med*. 2019;60:1421–1429.
- Röhrich M, Syed M, Liew DP, et al.  $^{68}\text{Ga}$ -FAPI-PET/CT improves diagnostic staging and radiotherapy planning of adenoid cystic carcinomas: imaging analysis and histological validation. *Radiother Oncol*. 2021;160:192–201.
- Dohi O, Ohtani H, Hatori M, et al. Histogenesis-specific expression of fibroblast activation protein and dipeptidylpeptidase-IV in human bone and soft tissue tumours. *Histopathology*. 2009;55:432–440.

---

---

# A Dimeric FAP-Targeting Small-Molecule Radioconjugate with High and Prolonged Tumor Uptake

Andrea Galbiati\*<sup>1</sup>, Aureliano Zana\*<sup>1</sup>, Matilde Bocci<sup>1</sup>, Jacopo Millul<sup>1</sup>, Abdullah Elsayed<sup>1,2</sup>, Jacqueline Mock<sup>1</sup>, Dario Neri<sup>2,3</sup>, and Samuele Cazzamalli<sup>1</sup>

<sup>1</sup>Research and Development Department, Philochem AG, Otelfingen, Switzerland; <sup>2</sup>Department of Chemistry and Applied Biosciences, Swiss Federal Institute of Technology, Zurich, Switzerland; and <sup>3</sup>Philogen S.p.A., Siena, Italy

Imaging procedures based on small-molecule radioconjugates targeting fibroblast activation protein (FAP) have recently emerged as a powerful tool for the diagnosis of a wide variety of tumors. However, the therapeutic potential of radiolabeled FAP-targeting agents is limited by their short residence time in neoplastic lesions. In this work, we present the development and in vivo characterization of BiOncoFAP, a new dimeric FAP-binding motif with an extended tumor residence time and favorable tumor-to-organ ratio. **Methods:** The binding properties of BiOncoFAP and its monovalent OncoFAP analog were assayed against recombinant human FAP. Preclinical experiments with <sup>177</sup>Lu-OncoFAP-DOTAGA (<sup>177</sup>Lu-OncoFAP) and <sup>177</sup>Lu-BiOncoFAP-DOTAGA (<sup>177</sup>Lu-BiOncoFAP) were performed on mice bearing FAP-positive HT-1080 tumors. **Results:** OncoFAP and BiOncoFAP displayed comparable subnanomolar dissociation constants toward recombinant human FAP in solution, but the bivalent BiOncoFAP bound more avidly to the target immobilized on solid supports. In a comparative biodistribution study, <sup>177</sup>Lu-BiOncoFAP exhibited a more stable and prolonged tumor uptake than <sup>177</sup>Lu-OncoFAP (~20 vs. ~4 percentage injected dose/g, respectively, at 24 h after injection). Notably, <sup>177</sup>Lu-BiOncoFAP showed favorable tumor-to-organ ratios with low kidney uptake. Both <sup>177</sup>Lu-OncoFAP and <sup>177</sup>Lu-BiOncoFAP displayed potent antitumor efficacy when administered at therapeutic doses to tumor-bearing mice. **Conclusion:** <sup>177</sup>Lu-BiOncoFAP is a promising candidate for radioligand therapy of cancer, with favorable in vivo tumor-to-organ ratios, a long tumor residence time, and potent anticancer efficacy.

**Key Words:** fibroblast activation protein; theranostics; OncoFAP; targeted radiotherapy; dimeric targeting ligands

**J Nucl Med 2022; 63:1852–1858**  
DOI: 10.2967/jnumed.122.264036

**S**mall-molecule radioconjugates (SMRCs) are pharmaceutical products comprising a small organic ligand that acts as a tumor-targeting agent and a radionuclide payload that can be exploited for both diagnostic and therapeutic applications (1–3). The therapeutic potential of SMRCs—that is, the possibility to perform imaging and therapy with the same product—facilitates the clinical development of this new class of drugs (4–7). Patients who can predictably benefit from targeted radioligand therapy are accurately selected through dosimetry studies (8). <sup>177</sup>Lu-DOTATATE

(Lutathera; Advanced Accelerator Applications), a radioligand therapeutic targeting somatostatin receptor type 2, is the first SMRC product that gained marketing authorization for therapy of neuroendocrine tumors (9). The use of this drug has consistently shown high response rates and long median progression-free survival in a multicenter phase III clinical trial (10). More recently, a second product, named <sup>177</sup>Lu-PSMA-617, was shown to provide therapeutic benefit to PSMA-positive metastatic castration-resistant prostate cancer patients in a large phase III clinical trial (11). Radioligand therapy with <sup>177</sup>Lu-PSMA-617 prolonged imaging-based progression-free survival and overall survival when added to standard care (11).

In the last few years, a new category of pan-tumoral tumor-targeting SMRCs specific to fibroblast activation protein (FAP) has been successfully implemented for the diagnosis of solid tumors (12–15). FAP is a membrane-bound enzyme highly expressed on the surface of cancer-associated fibroblasts in the stroma of more than 90% of human epithelial cancers. FAP expression in healthy tissues is negligible (12,13,16,17). We have recently reported the discovery of OncoFAP, the small-molecule FAP-targeting agent with the highest affinity reported so far (18). Proof-of-concept targeting studies with <sup>68</sup>Ga-OncoFAP-DOTAGA (<sup>68</sup>Ga-OncoFAP), a PET tracer based on OncoFAP, have confirmed excellent biodistribution in patients with different primary and metastatic solid malignancies (19).

The efficacy of radioligand therapeutics correlated strongly with their residence time in tumors (9,20–23). Although <sup>177</sup>Lu-DOTATATE and PSMA-617 are characterized by a sustained tumor residence time in patients (i.e., ~61 h for <sup>177</sup>Lu-PSMA-617 and ~88 h for <sup>177</sup>Lu-DOTATATE) (24,25), SMRCs based on FAP-targeting agents are typically cleared from solid lesions in a few hours (26,27). In preclinical biodistribution experiments, <sup>177</sup>Lu-OncoFAP selectively localized on neoplastic lesions (~38 percentage injected dose [%ID]/g 1 h after systemic administration), but half the dose delivered to the tumor was lost within 8–12 h (18). A comparable tumor-targeting performance and pharmacokinetic profile have been reported for other FAP-targeting SMRCs by Loktev et al. (e.g., the tumor uptake of <sup>177</sup>Lu-FAPI-46 decreased from 12.5 %ID/g at 1 h to 2.5 %ID/g at 24 h after administration) (28). Importantly, a rapid washout from tumors was observed not only in mice but also in patients treated with <sup>177</sup>Lu-FAPI-46 (26,29).

In an attempt to extend the tumor residence time of FAP-targeting SMRCs and to maximize the exposure of cancer cells to biocidal radiation, we developed BiOncoFAP, a dimeric FAP-targeting OncoFAP derivative. In this work, we describe the in vitro characterization of BiOncoFAP and we report the first preclinical biodistribution and therapy studies with a radiolabeled preparation of this novel dimeric FAP-targeting compound.

---

Received Feb. 21, 2022; revision accepted May 10, 2022.  
For correspondence or reprints, contact Samuele Cazzamalli (samuele.cazzamalli@philochem.ch) or Dario Neri (neri@pharma.ethz.ch).  
\*Contributed equally to this work.  
Published online May 19, 2022.  
COPYRIGHT © 2022 by the Society of Nuclear Medicine and Molecular Imaging.

## MATERIALS AND METHODS

### Chemistry and Radiochemistry

(*S*)-4-((4-(2-(2-cyano-4,4-difluoropyrrolidin-1-yl)-2-oxoethyl)carbamoyl)quinolin-8-yl)amino-4-oxobutanoic acid (named OncoFAP-COOH), OncoFAP-fluorescein, OncoFAP-Alexa488, and OncoFAP-IRDye750 were synthesized as previously reported by Millul et al. (18). OncoFAP-DOTAGA (compound 1) and BiOncoFAP-DOTAGA (compound 4) were labeled with cold lutetium by incubation with [<sup>nat</sup>Lu]LuCl<sub>3</sub> in acetate buffer at 90°C for 15 min to obtain <sup>nat</sup>Lu-OncoFAP-DOTAGA (compound 2) and <sup>nat</sup>Lu-BiOncoFAP-DOTAGA (compound 5), which were used as reference compounds for in vitro characterization (inhibition assay and serum stability). The structures of OncoFAP and BiOncoFAP conjugates are depicted in Figure 1. Detailed experimental chemical procedures are described in the supplemental material (available at <http://jnm.snmjournals.org>).

OncoFAP-DOTAGA (compound 1) and BiOncoFAP-DOTAGA (compound 4) were radiolabeled with <sup>177</sup>Lu using different specific activities for the different studies (biodistribution and therapy). Before the biodistribution study, precursors (compound 1 or 4, 100 nmol) were dissolved in 100 μL of phosphate-buffered saline (PBS) and diluted with 200 μL of sodium acetate (1 M in water, pH 8). Twenty megabecquerels of <sup>177</sup>Lu solution were added, and the mixture was heated at 90°C for 15 min, followed by dilution with 1,600 μL of PBS to achieve a final volume of 2 mL. Before the therapy studies, precursors (compound 1 or 4, 5 nmol) were dissolved in 5 μL of PBS, and then sodium acetate buffer (30 μL, 1 M in water) and 15 or 70 MBq of <sup>177</sup>Lu solution were added. The mixture was heated at 90°C for 15 min, followed by dilution with 130 μL of PBS to afford a final volume of 200 μL. Quality control of the radiosynthesis was performed using radio-high-performance liquid chromatography. The possibility of forming a stable complex between the so-obtained <sup>177</sup>Lu-radiolabeled derivatives and the target antigen was tested by coinubating the compounds with recombinant human FAP (hFAP) and loading the mixture onto a desalting PD-10 column run by gravity (Supplemental Fig. 1).

### In Vitro Inhibition Assay on hFAP

The enzymatic activity of hFAP on the Z-Gly-Pro-AMC substrate was measured at room temperature on a microtiter plate reader, monitoring the fluorescence at an excitation wavelength of 360 nm and

an emission wavelength of 465 nm. The reaction mixture contained substrate (20 μM), protein (200 pM, constant), assay buffer (50 mM Tris, 100 mM NaCl, and 1 mM ethylenediaminetetraacetic acid, pH 7.4), and inhibitors (compounds 1, 2, 4, and 5) with serial dilution from 1.67 μM to 800 fM, 1:2 in a total volume of 20 μL. Experiments were performed in triplicate, and the mean fluorescence values were fitted using Prism, version 7 (GraphPad) [ $y = \text{bottom} + (\text{top} - \text{bottom}) / (1 + 10^{(\text{LogIC}_{50} - X) * \text{HillSlope}})$ ]. The value is defined as the concentration of inhibitor required to reduce the enzyme activity by 50% after addition of the substrate (Fig. 2).

### Affinity Measurement to hFAP by Fluorescence Polarization

Fluorescence polarization experiments were performed in 384-well plates (nonbinding, polystyrene, flat-bottom, black, high volume, 30 μL final volume). Stock solutions of proteins were serially diluted (1:2) with buffer (50 mM Tris, 100 mM NaCl, and 1 mM ethylenediaminetetraacetic acid, pH 7.4), whereas the final concentration of the binders (OncoFAP-fluorescein and BiOncoFAP-fluorescein) was kept constant at 10 nM. The fluorescence anisotropy was measured on a microtiter plate reader (Tecan Life Sciences). Experiments were performed in triplicate, and the mean anisotropy values were fitted using Prism  $y = \text{bottom} + (\text{top} - \text{bottom}) / (1 + 10^{(\text{LogIC}_{50} - X) * \text{HillSlope}})$ . The data are reported in Supplemental Figure 2.

### Affinity Measurement to hFAP by Enzyme-Linked Immunosorbent Assay (ELISA)

Recombinant hFAP (1 μM, 5 mL) was biotinylated with biotin-LC-*N*-hydroxysuccinimide (100 equivalents) by incubation at room temperature under gentle agitation in 50 mM 4-(2-hydroxyethyl)-1-piperazineethanesulfonic acid (HEPES; VWR) and 100 mM NaCl buffer (pH 7.4). After 2 h, biotinylated hFAP was purified via a PD-10 column and dialyzed overnight in HEPES buffer. The following day, a StreptaWell (Roche) (transparent 96-well plate) was incubated with biotinylated hFAP (100 nM, 100 μL/well) for 1 h at room temperature and washed with PBS (3 times, 200 μL/well). The protein was blocked by adding 4% milk in PBS (200 μL/well, 30 min at room temperature) and then washed with PBS (3 times, 200 μL/well). Immobilized hFAP was incubated for 30 min in the dark with serial dilutions of OncoFAP-fluorescein (compound 7) and BiOncoFAP-fluorescein (compound 8) and then washed with PBS (3 times, 200 μL/well). A solution of rabbit anti-fluorescein isothiocyanate antibody (1 μg/mL, product 4510-7804; Bio-Rad) in 2% milk-PBS was added to each well (100 μL/well) and incubated for an additional 30 min in the dark. The resulting complex was washed with PBS (3 times, 200 μL/well) and incubated for an additional 30 min with protein A-horseradish peroxidase (1 μg/mL in 2% milk-PBS, 100 μL/well). Each well was washed with PBS with 0.1% polysorbate (3 times, 200 μL/well) and PBS (3 times, 200 μL/well). The substrate (3,3',5,5'-tetramethylbenzidine) was added (100 μL/well) and developed in the dark for 2 min. The reaction was stopped by adding 50 μL of 1 M sulfuric acid. The absorbance was measured at 450 nm (reference level, 620–650 nm) with a Spark multimode microplate reader (Tecan Life Sciences).

### Internalization Studies by Confocal Microscopy Analysis

SK-RC-52.hFAP and HT-1080.hFAP cells were seeded into 4-well coverslip chamber plates (Sarstedt, Inc.) at a density of 10<sup>4</sup> cells

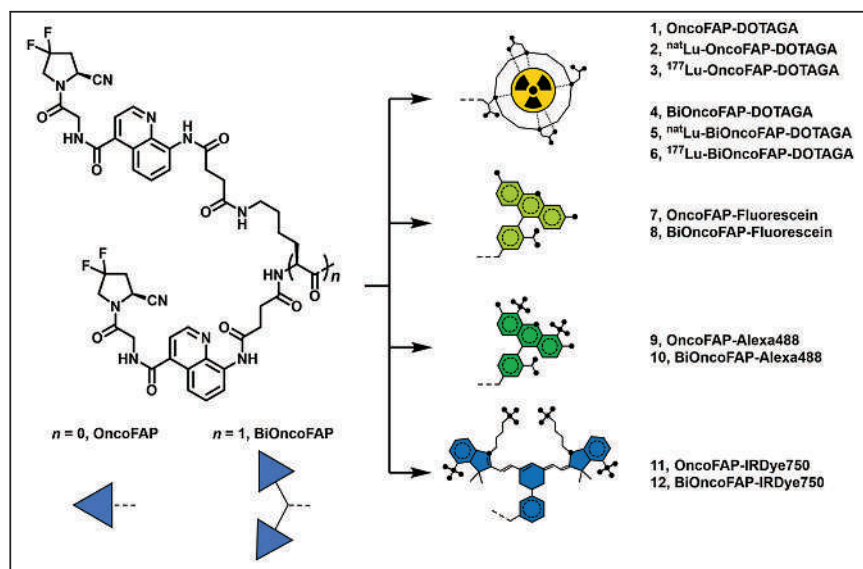


**FIGURE 1.** BiOncoFAP and OncoFAP and their DOTAGA, fluorescein, Alexa488, and IRDye750 conjugates.

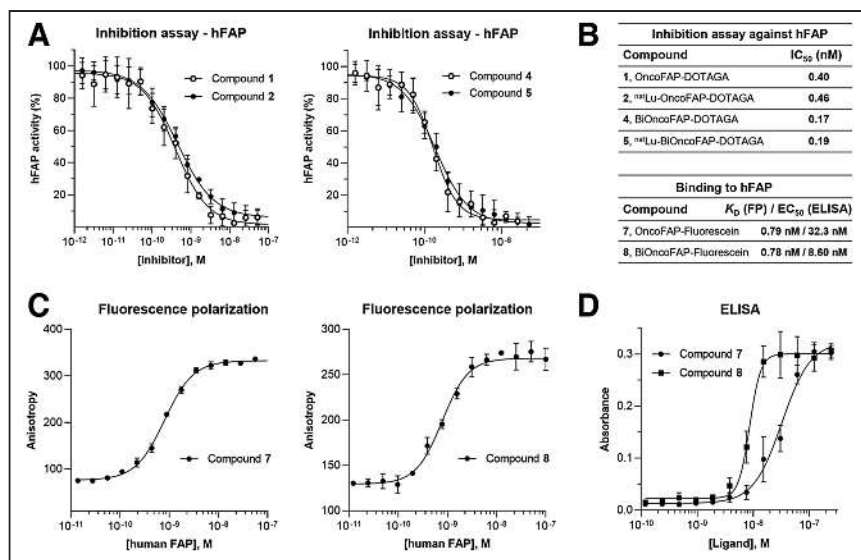


**FIGURE 2.** (A) Enzymatic assays performed with OncoFAP-DOTAGA (compound 1), BiOncoFAP-DOTAGA (compound 2), and their corresponding cold <sup>125</sup>I-labeled derivatives (compounds 4 and 5). (B) Binding affinity and IC<sub>50</sub> values for OncoFAP and BiOncoFAP derivatives toward hFAP. (C) Affinity measurement of OncoFAP-fluorescein (compound 7) and BiOncoFAP-fluorescein (compound 8) to recombinant hFAP by fluorescence polarization. Both compounds showed ultrahigh affinity for FAP target. (D) ELISA experiment on OncoFAP-fluorescein (compound 7) and BiOncoFAP-fluorescein (compound 8) against hFAP. FP = fluorescence polarization; K<sub>D</sub> = affinity constant.

per well in RPMI-1640 medium (Gibco) or Dulbecco modified Eagle medium (Gibco), respectively (1 mL; Invitrogen) supplemented with 10% fetal bovine serum (Gibco), Antibiotic-Antimycotic (Gibco), and 10 mM HEPES. Cells were allowed to grow overnight under standard culture conditions. The culture medium was replaced with fresh medium containing the suitable Alexa488-conjugated probes (100 nM) and Hoechst 33342 nuclear dye (Invitrogen, 1 μg/mL). Colonies were randomly selected and imaged 30 min after incubation on an SP8 confocal microscope equipped with an acoustooptical beam splitter (Leica Microsystems) (Fig. 3).

### Animal Studies

All animal experiments were conducted in accordance with Swiss animal welfare laws and regulations under license ZH006/2021 granted by the Veterinäramt des Kantons Zürich.

### Implantation of Subcutaneous Tumors

Tumor cells were grown to 80% confluence in Dulbecco modified Eagle medium or RPMI-1640 medium with 10% fetal bovine serum and 1% Antibiotic-Antimycotic and detached with trypsin-ethylenediaminetetraacetic acid, 0.05%. Tumor cells were resuspended in Hank's balanced salt solution medium. Aliquots of 5 × 10<sup>6</sup> cells (100 μL of suspension) were injected subcutaneously in the flank of female athymic BALB/c AnNRj-Foxn1 mice (6–8 wk old; Janvier).

### Quantitative Biodistribution of <sup>177</sup>Lu-OncoFAP and <sup>177</sup>Lu-BiOncoFAP in Tumor-Bearing Mice

OncoFAP-DOTAGA (compound 1) and BiOncoFAP-DOTAGA (compound 4) were

radiolabeled with <sup>177</sup>Lu (as described in the supplemental material). Tumors were allowed to grow to an average volume of 500 mm<sup>3</sup>. Mice were randomized (4 or 5 per group) and injected intravenously with radiolabeled preparations of <sup>177</sup>Lu-OncoFAP and <sup>177</sup>Lu-BiOncoFAP (250 nmol/kg; 50 MBq/kg). The mice were euthanized by CO<sub>2</sub> asphyxiation at different time points (1, 4, 17, and 24 h) after the intravenous injection. Tumors, organs, and blood were harvested and weighed, and radioactivity was measured with a Packard Cobra γ-counter. Values are expressed as %ID/g ± SD (Fig. 4). The %ID/g in the tumors was corrected by tumor growth rate (30).

### Therapy Studies with <sup>177</sup>Lu-OncoFAP and <sup>177</sup>Lu-BiOncoFAP in Tumor-Bearing Mice

The anticancer efficacy of <sup>177</sup>Lu-OncoFAP and <sup>177</sup>Lu-BiOncoFAP was assessed in athymic BALB/c AnNRj-Foxn1 mice bearing HT-1080.hFAP (right flank) and HT-1080.wt (wild type, left flank). <sup>177</sup>Lu-OncoFAP or <sup>177</sup>Lu-BiOncoFAP was intravenously administered at a dose of 250 nmol/kg, with 15 or 70 MBq/mouse (single administration, following the schedule indicated in Fig. 5). Therapy experiments started when the average volume of established tumors had reached 100–150 mm<sup>3</sup>.

The body weight of the animals and tumor volume were measured daily and recorded. Tumor dimensions were measured with an electronic caliper, and tumor volume was calculated with the formula (long side, mm) × (short side, mm) × (short side, mm) × 0.5. The animals were euthanized when one or more termination criteria indicated by the experimental license were reached (e.g., weight loss > 15%). Prism software was used for data analysis.

## RESULTS

### Preparation of OncoFAP and BiOncoFAP Conjugates

The dimeric ligand (BiOncoFAP-COOH, compound 13) was chemically synthesized exploiting L-lysine for the multimerization

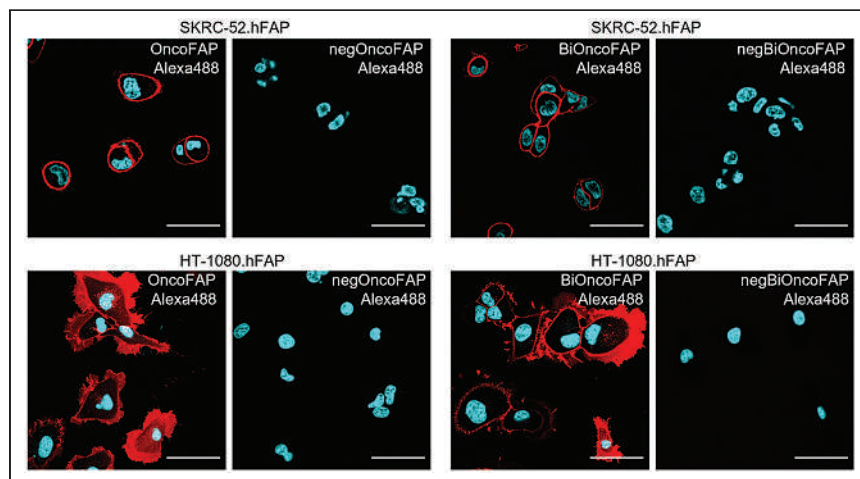


**FIGURE 3.** Confocal microscopy images after incubation of OncoFAP-Alexa488 (compound 9) and BiOncoFAP-Alexa488 (compound 10) with SK-RC-52.hFAP or HT-1080.hFAP. Red = fluorescein derivative staining; blue = Hoechst 33342 staining; scale bar = 50 μm.

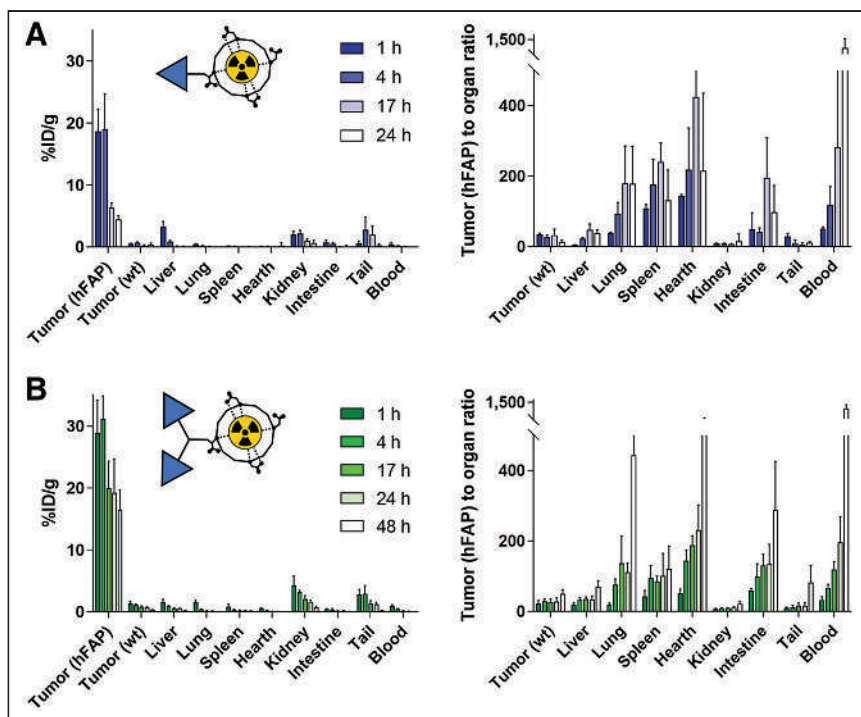


**FIGURE 4.** Quantitative in vivo biodistribution and tumor-to-organ ratio of <sup>177</sup>Lu-OncoFAP (compound 3) (A) and <sup>177</sup>Lu-BiOncoFAP (compound 6) (B) at different time points after intravenous administration (250 nmol/kg, 50 MBq/kg) in mice bearing HT-1080.wt and HT-1080.hFAP tumors.

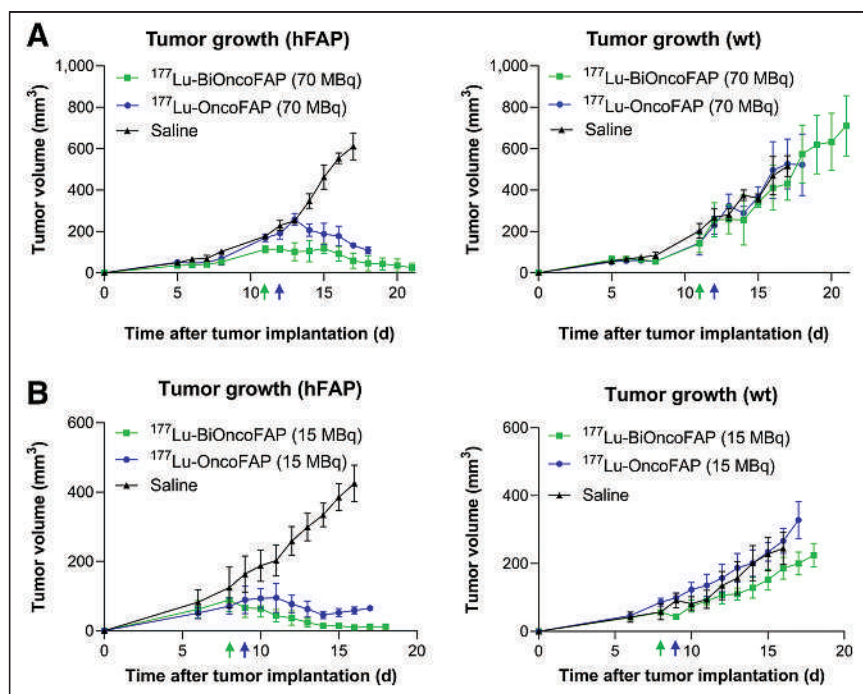


**FIGURE 5.** Therapeutic activity after single administration (250 nmol/kg) of <sup>177</sup>Lu-OncoFAP (compound 3) and <sup>177</sup>Lu-BiOncoFAP (compound 6) in BALB/c nu/nu-mice bearing HT-1080.hFAP tumor in right flank and HT-1080.wt tumor in left flank at dose of 70 MBq/mouse (A) or 15 MBq/mouse (B). Efficacy of different treatments was assessed by daily measurement of tumor volume (mm<sup>3</sup>) after administration of different compounds. Data points represent mean tumor volume  $\pm$  SEM.

of the OncoFAP targeting moiety. The free carboxylic acid served as a functional group for the conjugation of fluorophores (BiOncoFAP-fluorescein, compound 8; BiOncoFAP-Alexa488, compound 10; and BiOncoFAP-IRDye750, compound 12) and of DOTAGA chelator (compound 4). All compounds were produced in high yields and purities (supplemental material). Monovalent OncoFAP and the corresponding conjugates (OncoFAP-fluorescein, compound 7; OncoFAP-Alexa488, compound 9; and OncoFAP-IRDye750, compound 11) were synthesized following established procedures (18). The chemical structures of OncoFAP and BiOncoFAP derivatives are illustrated in Figure 1 and in the supplemental material. Radiolabeling of OncoFAP-DOTAGA (compound 1) and BiOncoFAP-DOTAGA (compound 4) with <sup>177</sup>Lu was achieved in high yield and purity (supplemental material). After radiolabeling, <sup>177</sup>Lu-OncoFAP and <sup>177</sup>Lu-BiOncoFAP retained the ability to form stable complexes with recombinant hFAP, as assessed by a PD-10 coelution experiment. Both compounds were highly hydrophilic, with experimental  $\text{Log}D_{7.4}$  values of  $-4.02 \pm 0.22$  ( $n = 5$ ) and  $-3.60 \pm 0.31$  ( $n = 5$ ), respectively (supplemental material).

#### In Vitro Inhibition Assay Against hFAP

We evaluated the inhibitory activity of OncoFAP-DOTAGA (compound 1), BiOncoFAP-DOTAGA (compound 4), and their <sup>nat</sup>Lu cold-labeled derivatives (compounds 2 and 5, respectively) against hFAP. Compounds 4 and 5 displayed enhanced inhibitory activity against the target ( $\text{IC}_{50}$ , 168 and 192 pM, respectively), compared with their monovalent counterparts (OncoFAP-DOTAGA:  $\text{IC}_{50}$ , 399 pM; <sup>nat</sup>Lu-OncoFAP-DOTAGA:  $\text{IC}_{50}$ , 456 pM) (Figs. 2A and 2B).

#### Assessment of Binding Properties of BiOncoFAP to Soluble and Immobilized hFAP

To study the binding properties of OncoFAP and BiOncoFAP to soluble hFAP, we measured the affinity constant of the corresponding fluorescein conjugates (compound 8, OncoFAP-fluorescein, and compound 9, BiOncoFAP-fluorescein) in fluorescence polarization assays (Fig. 2C). Compounds 8 and 9 exhibited comparable subnanomolar affinity constants against hFAP (respectively, 795 and 781 pM). Moreover, both compounds were selective for FAP and did not bind to a set of nontarget proteins up to micromolar concentrations (Supplemental Fig. 2). Our data confirm that the

dimerization does not impair the affinity and selectivity of BiOncoFAP for its target. Then, we studied the binding affinity to hFAP immobilized on a solid support of the dimeric ligand. In a comparative ELISA, BiOncoFAP-fluorescein exhibited a lower affinity constant than OncoFAP-fluorescein (8.60 vs. 32.3 nM, respectively) (Figs. 2B and 2D).

#### Confocal Microscopy Analysis on Tumor Cells

Binding of BiOncoFAP to FAP-positive SK-RC-52 and HT-1080 cancer cells and internalization were assessed by confocal microscopy analysis using the corresponding Alexa-488 conjugate (compound 10). OncoFAP-Alexa488 (compound 9) was used in the same experiment as a positive control, whereas untargeted analogs were included as nonbinding negative controls (chemical structures are depicted in the supplemental material). OncoFAP and BiOncoFAP displayed comparable binding features on living tumor cells. Both compounds showed lack of internalization on FAP-positive SK-RC-52 cells, whereas high membrane trafficking was observed when compounds were incubated on HT-1080.hFAP cells (Fig. 3).

#### Stability Studies

The stability of cold-labeled  $^{nat}\text{Lu}$ -BiOncoFAP-DOTAGA was assessed in human and mouse serum after incubation at 37°C for 24, 48, 72 and 120 h. The test compound exhibited a half-life longer than 5 d in all experimental conditions. No loss of lutetium ( $^{nat}\text{Lu}$ ) from the DOTAGA chelator was detected (Supplemental Fig. 3).

#### Biodistribution of OncoFAP and BiOncoFAP in Tumor-Bearing Mice

The qualitative biodistribution of OncoFAP and BiOncoFAP was assessed in tumor-bearing mice using a near-infrared fluorophore (IRDye750) as a detection agent. Macroscopic imaging of mice implanted with SK-RC-52.hFAP (right flank) and SK-RC-52.wt (left flank) tumors revealed that both OncoFAP-IRDye750 (compound 11) and BiOncoFAP-IRDye750 (compound 12) selectively accumulated in FAP-positive tumors (Supplemental Figs. 4 and 5). Interestingly, the BiOncoFAP-IRDye750 conjugate exhibited a longer residence time at the site of disease. Encouraged by these results, we studied the quantitative biodistribution of  $^{177}\text{Lu}$ -BiOncoFAP in athymic BALB/c mice bearing HT-1080.hFAP (right flank) and HT-1080.wt (left flank) tumors. A direct comparison with  $^{177}\text{Lu}$ -OncoFAP was included in the experiment (Fig. 4). Both compounds accumulated selectively in FAP-positive tumors shortly after intravenous administration. The dimeric  $^{177}\text{Lu}$ -BiOncoFAP product exhibited a more stable and prolonged tumor uptake than its monovalent counterpart ( $\sim 20$  vs.  $\sim 4$  %ID/g, 24 h after systemic administration). Notably,  $^{177}\text{Lu}$ -BiOncoFAP did not show significant uptake in healthy organs, with a favorable tumor-to-organ ratio (e.g., 22-to-1 tumor-to-kidney ratio and 70-to-1 tumor-to-liver ratio, at the 48-h time point) (Supplemental Tables 1–4).

#### In Vitro Cell Binding and Efflux Assays with $^{177}\text{Lu}$ -OncoFAP and $^{177}\text{Lu}$ -BiOncoFAP on HT-1080.hFAP Cells

Cell binding of  $^{177}\text{Lu}$ -OncoFAP and  $^{177}\text{Lu}$ -BiOncoFAP was assessed on HT-1080.hFAP cells, following literature procedures (29). Both compounds showed high binding properties toward the FAP-positive cell line. The binding was efficiently antagonized by a large excess of cold competitors (OncoFAP-DOTAGA or BiOncoFAP-DOTAGA) (Supplemental Fig. 6A). Cell efflux experiments revealed a longer half-life for  $^{177}\text{Lu}$ -BiOncoFAP ( $\sim 36$  h) than for the monovalent counterpart ( $\sim 18$  h) (Supplemental Fig. 6B).

#### Therapy Study

The therapeutic efficacy of  $^{177}\text{Lu}$ -OncoFAP and of  $^{177}\text{Lu}$ -BiOncoFAP was assessed in mice bearing HT-1080.hFAP tumors on the right flank and HT-1080.wt tumors on the left flank (Fig. 5; Supplemental Fig. 7). Systemic administration of both compounds at therapeutic doses (15 or 70 MBq/mouse, 250 nmol/kg) resulted in selective and potent anticancer activity against the growth of HT-1080.hFAP as compared with mice injected with saline. The most active compound in our therapy studies was  $^{177}\text{Lu}$ -BiOncoFAP. Tumor growth of FAP-negative lesions (HT-1080.wt) was not influenced by the treatment with  $^{177}\text{Lu}$ -OncoFAP or with  $^{177}\text{Lu}$ -BiOncoFAP. No significant change in mouse body weight was detected with either the 15- or the 70-MBq dose (Supplemental Fig. 8).

#### DISCUSSION

FAP-targeting radiopharmaceuticals may revolutionize the field of radioligand imaging of cancer because of their applicability to many types of malignancies and their excellent tumor selectivity, which has already been proven at the clinical level (12,13,19). Other SMRC products— $^{177}\text{Lu}$ -PSMA-617 and  $^{177}\text{Lu}$ -DOTATATE—are limited to certain specific cancer indications and may be taken up by certain normal organ structures (31,32). FAP is expressed mainly in the stroma of solid malignancies and on the tumor cell surface of mesenchymal tumors, thus adding a new element of differentiation compared with previously established targeting platforms, based on somatostatin receptor type 2 and PSMA (12,13,16,17), which are expressed on the surface of cancer cells. In this context, accurate selection of the radionuclide payload is crucial to the success of FAP-targeting radiotherapy. Although  $\alpha$ -emitters are characterized by a short range, typically more than 100  $\mu\text{m}$  (33) which may be insufficient, the use of a  $\beta$ -emitter radionuclide such as  $^{177}\text{Lu}$  (pathlength of  $\sim 1.5$  mm) (33) may enable the killing of stromal cells and surrounding tumor cells (34,35).

Sustained accumulation of SMRCs in tumors is fundamental to the effective delivery of high radiation doses over time at the site of disease and, therefore, to the success of the treatment. Among different approaches used in the past, dimerization of high-affinity ligands has been proposed as a strategy to enhance residence time in antigen-positive structures (i.e., in FAP-positive tumors) (23,36–39). Dimeric ligands present higher chances of rebinding to their target, with slower off-rates than are seen with their monovalent counterparts (40). However, an increase in the binding valency typically leads to higher uptake in healthy tissues (21,38,39). To the best of our knowledge, only 3 dimeric FAP-targeting radionuclides—DOTA/DOTAGA.(SA.FAPi)<sub>2</sub> (41,42), DOTA-2P(FAPi)<sub>2</sub> (21), and ND-bisFAPi (29)—have recently been described. Although preclinical biodistribution data are not available for DOTA/DOTAGA.(SA.FAPi)<sub>2</sub>, DOTA-2P(FAPi)<sub>2</sub> was extensively characterized in an HCC-PDX-1 mouse model. Despite its slightly increased tumor uptake compared with the monovalent FAPi-46 ( $\sim 9\%$  vs.  $\sim 4$  %ID/g 1 h after injection), the dimeric ligand presents low tumor-to-organ ratios both at 1 h and 4 h, with a particular liability for the kidney ( $\sim 1.2$ -to-1 and  $\sim 1.5$ -to-1 tumor-to-kidney ratios, respectively) (21). Similarly, ND-bisFAPi exhibited increased tumor uptake in A549-FAP xenografts, with low tumor-to-organ ratios at all investigated time points (i.e., from 1 to 72 h after systemic administration) (29). BiOncoFAP, the novel homodimeric FAP-targeting small organic ligand described in this article, shows specific and persistent tumor uptake ( $\sim 30$  %ID/g 1 h after injection and  $\sim 16$  %ID/g at 48 h after injection) in HT-1080.hFAP tumor-bearing mice. Remarkably,

<sup>177</sup>Lu-BiOncoFAP presents a clean preclinical biodistribution profile with high tumor-to-organ ratios even at early time points (e.g., ~7-to-1 and ~10-to-1 tumor-to-kidney ratio and ~20-to-1 and ~34-to-1 tumor-to-liver ratio at the 1 and 4 h time points, respectively).

The in vivo anticancer activity of <sup>177</sup>Lu-FAPI-46 (β-emitter) and <sup>225</sup>Ac-FAPI-46 (α-emitter) has recently been evaluated in PANC-1 tumor-bearing mice, a xenograft model of pancreatic cancer characterized by high stromal expression of FAP (35). Both products showed only limited tumor growth suppression even at the highest dose (i.e., 30 kBq/mouse for <sup>225</sup>Ac-FAPI-46 and 30 MBq/mouse for <sup>177</sup>Lu-FAPI-46).

Collectively, our biodistribution and therapy results show that both <sup>177</sup>Lu-OncoFAP and <sup>177</sup>Lu-BiOncoFAP are able to efficiently localize at the tumor site and produce a potent anticancer effect in mice bearing subcutaneous FAP-positive tumors, after a single administration at a dose of 70 MBq (~2 mCi)/mouse or 15 MBq (~0.4 mCi)/mouse. Compared with the monomeric <sup>177</sup>Lu-OncoFAP, our new bivalent <sup>177</sup>Lu-BiOncoFAP displayed an enhanced in vivo antitumor activity. As expected, lack of tumor suppression was observed for the FAP-negative tumors (HT-1080.wt), which were used as an internal control to appreciate the specificity of OncoFAP-based theranostic products toward FAP-positive solid lesions. In this article, we have presented the favorable biodistribution profile and therapeutic efficacy of <sup>177</sup>Lu-OncoFAP and <sup>177</sup>Lu-BiOncoFAP obtained in xenograft models with stable, homogeneous expression of hFAP on the surface of tumor cells. Further investigations in tumor models with a stromal pattern of FAP expression (e.g., patient-derived xenografts) will be of pivotal importance to predict the therapeutic performance of OncoFAP and BiOncoFAP-based therapeutics in the view of future clinical studies.

Considering the exquisite selectivity for cancer lesions and pan-tumoral properties of FAP-targeting radioligand therapeutics, this new class of radiopharmaceutical products may represent a breakthrough in cancer therapy (12). Interim reports on the efficacy of the FAP-targeting peptides and small organic ligands developed so far have shown this therapeutic strategy to have limitations (26,43). Escalation of the dose of radiolabeled FAP-targeting peptides is limited by their intrinsically high kidney uptake at late time points (43–45). Therapy with small organic ligands based on FAPI-46 may be limited by their short residence time in the tumor (26,46). We have developed <sup>177</sup>Lu-BiOncoFAP, a new radioligand therapeutic product with prolonged in vivo tumor uptake and highly favorable tumor-to-kidney ratios. Future clinical studies on a basket of indications will provide clarity on the therapeutic efficacy of this novel FAP-targeting product.

## CONCLUSION

<sup>177</sup>Lu-BiOncoFAP is a promising FAP-targeting SMRC product for tumor therapy. This novel bivalent FAP-targeting compound binds its target with high affinity and shows a long residence time in tumor lesions, with favorable tumor-to-organ ratios. Once administered at therapeutic doses, <sup>177</sup>Lu-BiOncoFAP potently inhibits growth of FAP-positive tumors in mice. Our data support clinical development of <sup>177</sup>Lu-BiOncoFAP in the frame of targeted radioligand therapy.

## DISCLOSURE

Dario Neri is a cofounder and shareholder of Philogen (<http://www.philogen.com/en/>), a Swiss–Italian Biotech company that operates in the field of ligand-based pharmacodelivery. Andrea

Galbiati, Aureliano Zana, Matilde Bocci, Jacopo Millul, Abdullah Elsayed, Jacqueline Mock, and Samuele Cazzamalli are employees of Philochem AG, the daughter company of Philogen that owns and has patented OncoFAP (PCT/EP2021/053494) and BiOncoFAP (PCT/EP2022/053404). No other potential conflict of interest relevant to this article was reported.

## ACKNOWLEDGMENTS

We thank Ettore Gilardoni for performing an exact mass analysis of compounds presented in this article, and Frederik Peisert and Luca Prati for their support with small-molecule ELISA experiments.

## KEY POINTS

**QUESTION:** Does ligand dimerization enhance the tumor retention time and therapeutic potential of FAP-targeting radioconjugates?

**PERTINENT FINDINGS:** Compared with its OncoFAP monovalent counterpart, dimeric <sup>177</sup>Lu-BiOncoFAP shows higher and longer tumor uptake in tumor-bearing mice. <sup>177</sup>Lu-BiOncoFAP displays a potent in vivo anticancer effect in preclinical murine models.

**IMPLICATIONS FOR PATIENT CARE:** The prolonged tumor uptake of <sup>177</sup>Lu-BiOncoFAP supports clinical development for the targeted radioligand therapy of multiple FAP-positive cancer lesions.

## REFERENCES

1. Dal Corso A. Targeted small-molecule conjugates: the future is now. *ChemBioChem*. 2020;21:3321–3322.
2. Sun X, Li Y, Liu T, Li Z, Zhang X, Chen X. Peptide-based imaging agents for cancer detection. *Adv Drug Deliv Rev*. 2017;110–111:38–51.
3. Siva S, Udovicich C, Tran B, Zargar H, Murphy DG, Hofman MS. Expanding the role of small-molecule PSMA ligands beyond PET staging of prostate cancer. *Nat Rev Urol*. 2020;17:107–118.
4. Ballinger JR. Theranostic radiopharmaceuticals: established agents in current use. *Br J Radiol*. 2018;91:20170969.
5. Turner JH. An introduction to the clinical practice of theranostics in oncology. *Br J Radiol*. 2018;91:20180440.
6. Lenzo NP, Meyrick D, Turner JH. Review of gallium-68 PSMA PET/CT imaging in the management of prostate cancer. *Diagnostics (Basel)*. 2018;8:16.
7. Turner JH. Recent advances in theranostics and challenges for the future. *Br J Radiol*. 2018;91:20170893.
8. Herrero Álvarez N, Bauer D, Hernández-Gil J, Lewis JS. Recent advances in radiometals for combined imaging and therapy in cancer. *ChemMedChem*. 2021;16:2909–2941.
9. Henrich U, Kopka K. Lutathera®: the first FDA- and EMA-approved radiopharmaceutical for peptide receptor radionuclide therapy. *Pharmaceuticals (Basel)*. 2019;12:114.
10. Strosberg J, El-Haddad G, Wolin E, et al. Phase 3 trial of <sup>177</sup>Lu-DOTATATE for midgut neuroendocrine tumours. *N Engl J Med*. 2017;376:125–135.
11. Sartor O, de Bono J, Chi KN, et al. Lutetium-177-PSMA-617 for metastatic castration-resistant prostate cancer. *N Engl J Med*. 2021;385:1091–1103.
12. Calais J. FAP: the next billion dollar nuclear theranostics target? *J Nucl Med*. 2020;61:163–165.
13. Kratochwil C, Flechsig P, Lindner T, et al. <sup>68</sup>Ga-FAPI PET/CT: tracer uptake in 28 different kinds of cancer. *J Nucl Med*. 2019;60:801–805.
14. Backhaus P, Burg M, Roll W, et al. A new horizon for breast cancer staging: first evidence from simultaneous PET-MRI targeting the fibroblast activating protein (FAP) [abstract]. *Nuklearmedizin*. 2021;60:L10.
15. Backhaus P, Burg MC, Roll W, et al. Simultaneous FAPI PET/MRI targeting the fibroblast-activation protein for breast cancer. *Radiology*. 2022;302:39–47.
16. Lo A, Wang LCS, Scholler J, et al. Tumour-promoting desmoplasia is disrupted by depleting FAP-expressing stromal cells. *Cancer Res*. 2015;75:2800–2810.
17. Mona CE, Benz MR, Hikmat F, et al. Correlation of <sup>68</sup>Ga-FAPI-46 PET biodistribution with FAP expression by immunohistochemistry in patients with solid

- cancers: interim analysis of a prospective translational exploratory study. *J Nucl Med*. 2022;63:1021–1026.
18. Millul J, Bassi G, Mock J, et al. An ultra-high-affinity small organic ligand of fibroblast activation protein for tumour-targeting applications. *Proc Natl Acad Sci USA*. 2021;118:e2101852118.
  19. Backhaus P, Gierse F, Burg MC, et al. Translational imaging of the fibroblast activation protein (FAP) using the new ligand [<sup>68</sup>Ga]Ga-OncoFAP-DOTAGA. *Eur J Nucl Med Mol Imaging*. 2022;49:1822–1832.
  20. Mansi R, Fani M. Radiolabeled peptides for cancer imaging and therapy: from bench-to bedside. *Chimia (Aarau)*. 2021;75:500–504.
  21. Zhao L, Niu B, Fang J, et al. Synthesis, preclinical evaluation, and a pilot clinical PET imaging study of <sup>68</sup>Ga-labeled FAPI dimer. *J Nucl Med*. 2022;63:862–868.
  22. Jones W, Griffiths K, Barata PC, Paller CJ. PSMA theranostics: review of the current status of PSMA-targeted imaging and radioligand therapy. *Cancers (Basel)*. 2020;12:1367.
  23. Schäfer M, Bauder-Wüst U, Leotta K, et al. A dimerized urea-based inhibitor of the prostate-specific membrane antigen for <sup>68</sup>Ga-PET imaging of prostate cancer. *EJNMMI Res*. 2012;2:23.
  24. Gupta SK, Singla S, Thakral P, Bal CS. Dosimetric analyses of kidneys, liver, spleen, pituitary gland, and neuroendocrine tumours of patients treated with <sup>177</sup>Lu-DOTATATE. *Clin Nucl Med*. 2013;38:188–194.
  25. Schuchardt C, Zhang J, Kulkarni HR, Chen X, Müller D, Baum RP. Prostate-specific membrane antigen radioligand therapy using <sup>177</sup>Lu-PSMA I&T and <sup>177</sup>Lu-PSMA-617 in patients with metastatic castration-resistant prostate cancer: comparison of safety, biodistribution, and dosimetry. *J Nucl Med*. 2022;63:1199–1207.
  26. Kaghazchi F, Aghdam RA, Haghighi S, Vali R, Adinehpour Z. <sup>177</sup>Lu-FAPI therapy in a patient with end-stage metastatic pancreatic adenocarcinoma. *Clin Nucl Med*. 2022;47:e243–e245.
  27. Meyer C, Dahlbom M, Lindner T, et al. Radiation dosimetry and biodistribution of <sup>68</sup>Ga-FAPI-46 PET imaging in cancer patients. *J Nucl Med*. 2020;61:1171–1177.
  28. Loktev A, Lindner T, Burger EM, et al. Development of fibroblast activation protein-targeted radiotracers with improved tumour retention. *J Nucl Med*. 2019;60:1421–1429.
  29. Li H, Ye S, Li L, et al. <sup>18</sup>F- or <sup>177</sup>Lu-labeled bivalent ligand of fibroblast activation protein with high tumor uptake and retention. *Eur J Nucl Med Mol Imaging*. 2022;49:2705–2715.
  30. Tarli L, Balza E, Viti F, et al. A high-affinity human antibody that targets tumoural blood vessels. *Blood*. 1999;94:192–198.
  31. Tönnemann R, Meyer PT, Eder M, Baranski AC. [<sup>177</sup>Lu]Lu-PSMA-617 salivary gland uptake characterized by quantitative in vitro autoradiography. *Pharmaceuticals (Basel)*. 2019;12:18.
  32. Geenen L, Nonnekens J, Konijnenberg M, Baatout S, De Jong M, Aerts A. Overcoming nephrotoxicity in peptide receptor radionuclide therapy using [<sup>177</sup>Lu]Lu-DOTA-TATE for the treatment of neuroendocrine tumours. *Nucl Med Biol*. 2021;102–103:1–11.
  33. Navalkissoor S, Grossman A. Targeted alpha particle therapy for neuroendocrine tumours: the next generation of peptide receptor radionuclide therapy. *Neuroendocrinology*. 2019;108:256–264.
  34. Frey K, Neri D. Antibody-based targeting of tumor vasculature and stroma. In: *Tumor-Associated Fibroblasts and Their Matrix*. Springer; 2011:419–450.
  35. Liu Y, Watabe T, Kaneda-Nakashima K, et al. Fibroblast activation protein targeted therapy using [<sup>177</sup>Lu]FAPI-46 compared with [<sup>225</sup>Ac]FAPI-46 in a pancreatic cancer model. *Eur J Nucl Med Mol Imaging*. 2022;49:871–880.
  36. Gaertner FC, Kessler H, Wester HJ, Schwaiger M, Beer AJ. Radiolabelled RGD peptides for imaging and therapy. *Eur J Nucl Med Mol Imaging*. 2012;39(suppl):S126–S138.
  37. Liu S. Radiolabeled cyclic RGD peptides as integrin  $\alpha v \beta 3$ -targeted radiotracers: maximizing binding affinity via bivalency. *Bioconjug Chem*. 2009;20:2199–2213.
  38. Krall N, Pretto F, Neri D. A bivalent small molecule-drug conjugate directed against carbonic anhydrase IX can elicit complete tumour regression in mice. *Chem Sci*. 2014;5:3640–3644.
  39. Liu S. Radiolabeled multimeric cyclic RGD peptides as integrin  $\alpha v \beta 3$  targeted radiotracers for tumour imaging. *Mol Pharm*. 2006;3:472–487.
  40. Chittasupho C. Multivalent ligand: design principle for targeted therapeutic delivery approach. *Ther Deliv*. 2012;3:1171–1187.
  41. Ballal S, Yadav MP, Moon ES, et al. First-in-human results on the biodistribution, pharmacokinetics, and dosimetry of [<sup>177</sup>Lu]Lu-DOTA.SA.FAPi and [<sup>177</sup>Lu]Lu-DOTAGA.(SA.FAPi)<sub>2</sub>. *Pharmaceuticals (Basel)*. 2021;14:1212.
  42. Qin C, Song Y, Cai W, Lan X. Dimeric FAPI with potential for tumour theranostics. *Am J Nucl Med Mol Imaging*. 2021;11:537–541.
  43. Baum RP, Schuchardt C, Singh A, et al. Feasibility, biodistribution, and preliminary dosimetry in peptide-targeted radionuclide therapy of diverse adenocarcinomas using <sup>177</sup>Lu-FAP-2286: first-in-humans results. *J Nucl Med*. 2022;63:415–423.
  44. Zhao L, Shang Q, Wu H, Lin Q. Fibroblast activation protein-based theranostics in cancer research: a state-of-the-art review. *Theranostics*. 2022;12:1557–1569.
  45. Nishio M, Okamoto I, Murakami H, et al. Preclinical evaluation of FAP-2286, a peptide-targeted radionuclide therapy (PRT) to fibroblast activation protein alpha (FAP) [abstract]. *Ann Oncol*. 2020;31(suppl 4):S488.
  46. Assadi M, Rekabpour SJ, Jafari E, et al. Feasibility and therapeutic potential of <sup>177</sup>Lu-fibroblast activation protein inhibitor-46 for patients with relapsed or refractory cancers: a preliminary study. *Clin Nucl Med*. 2021;46:e523–e530.

# Improved Tumor Responses with Sequential Targeted $\alpha$ -Particles Followed by Interleukin 2 Immunocytokine Therapies in Treatment of CEA-Positive Breast and Colon Tumors in CEA Transgenic Mice

Megan Minnix\*<sup>1</sup>, Maciej Kujawski\*<sup>1</sup>, Erasmus Poku<sup>2</sup>, Paul J. Yazaki<sup>1</sup>, Jeffrey Y. Wong<sup>3</sup>, and John E. Shively<sup>1</sup>

<sup>1</sup>Department of Immunology and Theranostics, Riggs Institute of Diabetes and Metabolic Research, Beckman Research Institute of the City of Hope, Duarte, California; <sup>2</sup>Radiopharmacy, Beckman Research Institute of the City of Hope, Duarte, California; and <sup>3</sup>Department of Radiation Oncology, City of Hope National Medical Center, Duarte, California

Targeted  $\alpha$ -therapy (TAT) delivers high-linear-transfer-energy  $\alpha$ -particles to tumors with the potential to generate tumor immune responses that may be augmented by antigen-targeted immunotherapy. **Methods:** This concept was evaluated in immunocompetent carcinoembryonic antigen (CEA) transgenic mice bearing CEA-positive mammary or colon tumors. Tumors were targeted with humanized anti-CEA antibody M5A labeled with <sup>225</sup>Ac for its 10-d half-life and emission of 4  $\alpha$ -particles, as well as being targeted with the immunocytokine M5A–interleukin 2. **Results:** A dose response (3.7, 7.4, and 11.1 kBq) to TAT only, for orthotopic CEA-positive mammary tumors, was observed, with a tumor growth delay of 30 d and an increase in median survival from 20 to 36 d at the highest dose. Immunocytokine (4 times daily) monotherapy gave a tumor growth delay of 20 d that was not improved by addition of 7.4 kBq of TAT 5 d after the start of immunocytokine. However, TAT (7.4 kBq) followed by immunocytokine 10 d later led to a tumor growth delay of 38 d, with an increase in median survival to 45 d. Similar results were seen for TAT followed by immunocytokine at 5 versus 10 d. When a similar study was performed with subcutaneously implanted CEA-positive MC38 colon tumors, TAT (7.4 kBq) monotherapy gave an increase in median survival from 29 to 42 d. The addition of immunocytokine 10 d after 7.4 kBq of TAT increased median survival to 57 d. Immunophenotyping showed increased tumor-infiltrating interferon- $\gamma$ -positive, CD8-positive T cells and an increased ratio of these cells to Foxp3-positive, CD4-positive regulatory T cells with sequential therapy. Immunohistochemistry confirmed there was an increase in tumor-infiltrating CD8-positive T cells in the sequential therapy group, strongly suggesting that immunocytokine augmented TAT can lead to an immune response that improves tumor therapy. **Conclusion:** Low-dose (7.4 kBq) TAT followed by a 4-dose immunocytokine regimen 5 or 10 d later gave superior tumor reductions and survival curves compared with either monotherapy in breast and colon cancer tumor models. Reversing the order of therapy to immunocytokine followed by TAT 5 d later was equivalent to either monotherapy in the breast cancer model.

**Key Words:** radionuclide therapy; carcinoembryonic antigen; breast cancer; colon cancer; targeted alpha therapy; targeted immunotherapy

**J Nucl Med 2022; 63:1859–1864**  
DOI: 10.2967/jnumed.122.264126

**C**arcinoembryonic antigen (CEA) is a pancarcinoma antigen highly expressed in colon (1) and breast cancers. Radiolabeled CEA antibodies have been used to image a variety of CEA-expressing tumors (2–4), confirming their tumor-targeting specificity. Since most anti-CEA antibodies are not cytotoxic, they require conjugation to drugs or radionuclides for therapeutic applications. In this respect, radioimmunotherapy with anti-CEA antibodies radiolabeled with the  $\beta$ -emitters <sup>131</sup>I (5–7) or <sup>90</sup>Y (8,9) have met with some success in the clinic. In the case of immunotherapy, anti-CEA bifunctional antibodies have shown promising preclinical results (10,11). In addition, there are also several clinical trials (NCT04513431, NCT04348643, NCT02349724) investigating chimeric antigen receptor (CAR) T-cell therapy targeting CEA—trials that have met with mixed results (12). Thus, there is an unmet need for improvement in CEA-targeted therapies.

Sequential targeted radiotherapy followed by targeted immunotherapy is a promising approach in that it may stimulate an immune response. In this respect, we have recently shown that stereotactic body radiotherapy (SBRT) plus a CEA-targeted immunocytokine gave tumor reduction superior to that from either monotherapy (13). Those studies were performed with humanized anti-CEA antibody M5A (14) and an M5A–interleukin 2 fusion protein (13). We now extend those studies to sequential targeted  $\alpha$ -therapy (TAT) plus immunocytokine. The choice of  $\alpha$ - over  $\beta$ -based radionuclide therapy is based on the fact that  $\alpha$ -emitters deliver more energy to the tumor and tumor vasculature because of their high linear-energy transfer (15), with a potential increase in tumor cytotoxicity due to stimulation of an immune response. In addition, their low tissue penetration is expected to reduce the hematologic toxicity of the systemic radiolabeled antibody, one of the major off-target effects of  $\beta$ -emitter-based radioimmunotherapy (16). For this study, we chose the  $\alpha$ -emitter <sup>225</sup>Ac for its long half-life (10 d) and emission of 4  $\alpha$ -particles (17). We have previously investigated the use of <sup>225</sup>Ac-based TAT in the treatment of ovarian cancer (18) and multiple myeloma (19), finding that in one study, <sup>225</sup>Ac-radionuclide TAT was superior to <sup>177</sup>Lu-radionuclide radioimmunotherapy (19).

We hypothesized that TAT was more likely to stimulate a tumor immune response when followed by targeted immunotherapy. To test this hypothesis, it was necessary to perform these studies on immune-competent mice that expressed the target antigen of interest in normal tissues. For this reason, we used CEA transgenic mice in which the entire human CEA gene was expressed, conferring

Received Mar. 22, 2022; revision accepted May 25, 2022.

For correspondence or reprints, contact John E. Shively (jshively@coh.org).

\*Contributed equally to this work.

Published online Jun. 30, 2022.

COPYRIGHT © 2022 by the Society of Nuclear Medicine and Molecular Imaging.

tissue-specific CEA expression that mimics that found in humans (20). We have previously shown that an all-murine anti-CEA immunocytokine significantly reduced CEA-positive tumor growth in this CEA transgenic model (21) and, more recently, that an all-murine anti-CEA CAR T-cell therapy plus the humanized immunocytokine reduced tumor growth in the same model (22). We now show that sequential TAT followed by immunocytokine therapy significantly improves tumor responses in both breast and colon tumors compared with either monotherapy in the CEA transgenic model.

## MATERIALS AND METHODS

M5A, DOTA-M5A, immunocytokine, and the cell lines E0771/CEA and MC38/CEA were previously described (13).

### Radiolabeling

DOTA-M5A (50  $\mu\text{g}$ ) was incubated with  $^{225}\text{Ac}$  at a labeling ratio of 1.85 kBq/ $\mu\text{g}$  for 45 min at 43°C, chased with 1 mM diethylenetriaminepentaacetic acid and purified by size-exclusion high-performance liquid chromatography.

### Immunohistochemistry, Blood Analysis, and Flow Cytometry

Details of immunohistochemistry staining blood analysis and flow cytometry are provided in the supplemental materials (available at <http://jnm.snmjournals.org>).

### Animal Studies

Animals were handled in accordance with institutional animal care and use committee protocol 91037, approved by the City of Hope Institutional Animal Care and Use Committee. CEA transgenic mice were previously described (20). E0771/CEA cells ( $10^5$  in Matrigel [Corning]:phosphate-buffered saline 1:1) were injected into the mammary fat pad, and MC38/CEA ( $10^6$ ) were injected subcutaneously.

### Statistical Analysis

Two-way ANOVA was used to analyze tumor growth curves, and the log-rank Mantel-Cox test was used to analyze survival curves, using Prism, version 8.3.0 (GraphPad Software). Survival was the time at which the tumor reached 1,500 mm<sup>3</sup>. Treated groups were compared with untreated, unless otherwise stated. Differences were considered significant if *P* values were 0.05 or less.

## RESULTS

### TAT of E0771/CEA Mammary Tumors

Murine mammary cancer cells E0771 transfected with CEA (13) were injected into the mammary fat pad of CEA transgenic mice (20) to establish mammary tumors in an immunocompetent model that expressed the human CEA gene. Since we have previously shown that these tumors do not respond to naked humanized anti-CEA antibody M5A (13), we tested their response to TAT using  $^{225}\text{Ac}$ -DOTA-M5A (Fig. 1A). Increasing doses from 3.7 to 11.1 kBq showed a significant dose response compared with untreated controls (Fig. 1B; Supplemental Table 1), with the highest dose leading to a delay in tumor growth of about 30 d and a significant increase in median survival from about 20 to 36 d

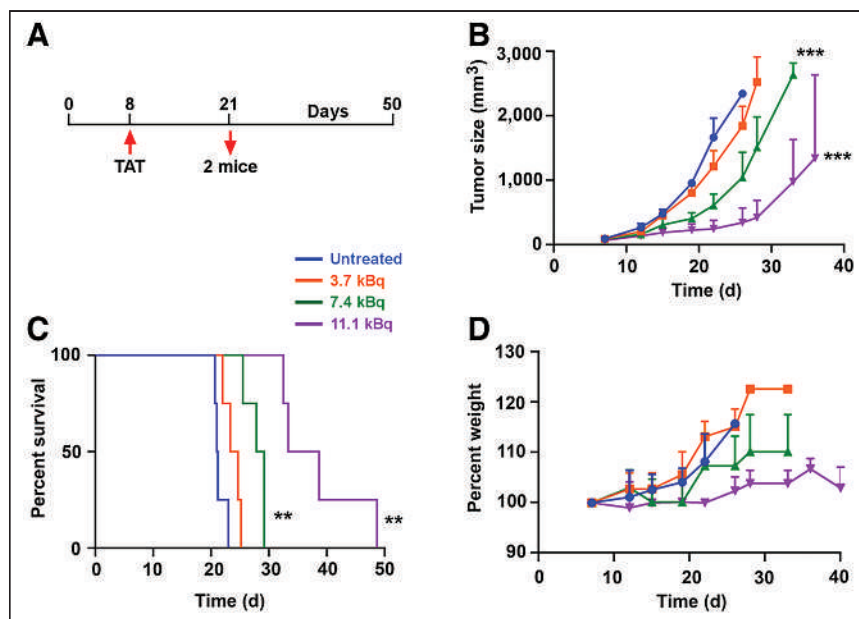


**FIGURE 1.** (A) Treatment schema and color codes for TAT  $^{225}\text{Ac}$ -DOTA-M5A TAT doses in orthotopic breast cancer model. (B) Tumor growth curves. (C) Kaplan-Meier survival plot. (D) Weight loss. Groups contained 8 mice, with 2 mice removed at days 21 and 22 for blood analysis. \*\**P* < 0.01. \*\*\**P* < 0.001.

compared with untreated controls (Fig. 1C; Supplemental Table 1). Whole-body toxicity as measured by weight loss ( $\geq 20\%$  loss) was not observed at all doses (Fig. 1D). In addition, there was no evidence of acute liver or kidney toxicity as measured by enzymes at the end of the study (Supplemental Table 2).

Flow cytometry analysis of the blood on day 21 indicated a significant decrease in CD8 T cells and B cells for the 2 highest doses of TAT, with no effect on CD11b myeloid cells (Supplemental Fig. 1A). The highest dose of TAT significantly reduced tumor infiltration of both CD4 and CD8 T cells (Supplemental Fig. 1B), and there was an increase in tumor-infiltrating neutrophils by 7.4 and 11.1 kBq of TAT (Supplemental Fig. 1C). These results suggest the possibility that TAT had a major effect on the immune response to the tumor, but it was unclear if the effect was immunosuppressive or immunostimulatory.

### Comparison of Immunocytokine Plus TAT Versus TAT Plus Immunocytokine in E0771/CEA Mammary Tumors

The order of sequential therapy was tested since it was likely that TAT could kill tumor-resident CD8 cells that would otherwise respond to immunocytokine given first (Fig. 2A). The immunocytokine therapy schedule of 4 daily doses of 1 mg/kg starting 8 d after tumor inoculation into the mammary fat pad, adopted from our previous study (13), significantly delayed tumor growth by about 20 d, compared with untreated tumors (Fig. 2B; Supplemental Table 1). Interestingly, the delay in tumor growth for immunocytokine therapy alone was equivalent to the 7.4 kBq of TAT only (Fig. 2B). When immunocytokine was given before TAT (Fig. 2B), the results were similar to either monotherapy. Thus, the addition of TAT to immunocytokine given first did not boost the antitumor response.

For TAT first followed by immunocytokine, we chose 10 d later for the start of immunocytokine, based on the 2- to 4-d half-life of the circulating antibody in the blood (23) and the 10-d half-life of  $^{225}\text{Ac}$ . When TAT was followed by immunocytokine 10 d later,

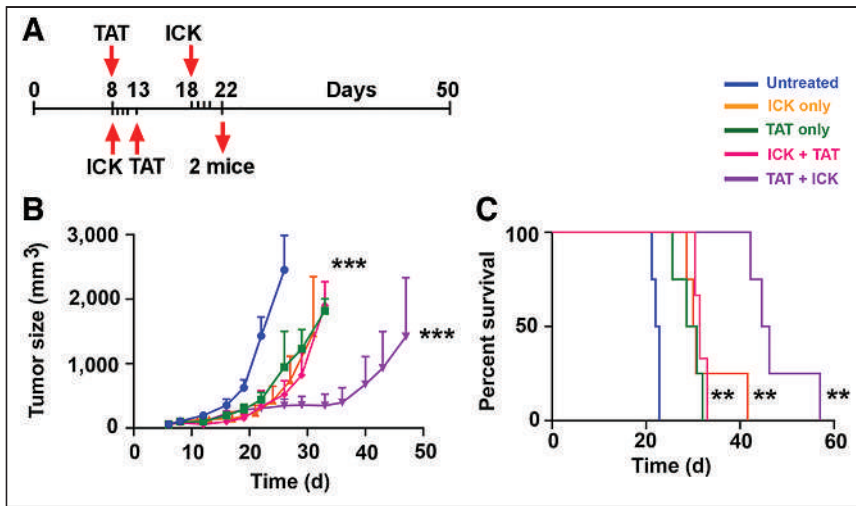


**FIGURE 2.** (A) Treatment schema for immunocytokine first followed by TAT (bottom) or TAT first followed by immunocytokine (top) in breast cancer model. Groups contained 8 mice, with 2 mice removed at days 21 and 22 for blood analysis. (B and C) Tumor growth curves (B) and Kaplan-Meier survival plot (C) for immunocytokine-first vs. TAT-first sequential therapy. *P* values are vs. untreated controls. \*\**P* < 0.01. \*\*\**P* < 0.001. ICK = immunocytokine.

tumor growth was reduced to 38 d (Fig. 2B), with an increase in median survival to 45 d compared with about 30 d for either monotherapy (Fig. 2C; Supplemental Tables 1 and 3). In addition, sequential therapy did not result in significant loss of whole-body weight (Supplemental Fig. 2A) or liver and kidney toxicity (Supplemental Table 2). White blood cell analysis of TAT followed by immunocytokine showed a 50% reduction early after therapy (21 d) that recovered at the late time point (30–50 d) (Supplemental Fig. 2B). A breakdown of white blood cells into component cells revealed that early effects in this group were mostly on lymphocytes and neutrophils, with recovery in the TAT-plus-immunocytokine group by the later time point (Supplemental Figs. 2C and 2D). There was no effect on red blood cells in any group (Supplemental Fig. 2E), and there was about a 50% reduction in platelets immediately after therapy that recovered at the end of the study (Supplemental Fig. 2F). Overall, the toxicities of the sequential therapies were transient and minimal.

TAT alone or TAT plus immunocytokine affected the cellular viability of treated tumors at 21 d as shown by flow cytometry (Supplemental Fig. 3A). Although the percentage of tumor-infiltrating CD8 or CD4 T cells was reduced by TAT only and increased by immunocytokine monotherapy, the changes were not statistically significant. However, when analyzed for interferon- $\gamma$  (IFN $\gamma$ ) production, there was a significant increase in tumor-infiltrating IFN $\gamma$ -positive, CD8-positive T cells at 21 d (Supplemental Fig. 3B), of which IFN $\gamma$ -positive, PD-1-positive tumor-infiltrating CD8-positive T cells also increased, followed by a significant decrease in IFN $\gamma$ -negative, PD-1-positive exhausted T cells (Supplemental Fig. 3C). In addition, the ratio of CD8-positive, IFN $\gamma$ -positive to CD4-positive regulatory T cells (Tregs) increased in both the immunocytokine-

only and the sequential therapy groups (Supplemental Fig. 3D), suggesting that the Tregs play a more important role in tumor response than does the percentage of PD1-positive, CD8-positive T cells. This analysis confirmed that TAT followed by immunocytokine was superior to immunocytokine followed by TAT, suggesting that TAT adversely affected immunocytokine given first in sequential therapy.

#### Timing of Immunocytokine After TAT in E0771/CEA Mammary Tumors

Since TAT can adversely affect immunocytokine therapy when immunocytokine is given first but not when immunocytokine was given 10 d after TAT, we tested the possibility of administering immunocytokine 5 d after TAT (Fig. 3A). Five days was chosen as a time point when circulating M5A is at about 25% of initial levels (24) and total <sup>225</sup>Ac would be at about 50% of its initial levels. Although the tumor reduction and survival curves showed slight differences

between immunocytokine at 5 versus 10 d after TAT, the results overall were statistically identical to untreated controls and monotherapies (Figs. 3B–3C; Supplemental Table 1). A comparison of median survivals for all the mammary tumor studies shows increased survivals for the +5-d and +10-d groups out to 44–45 d (Supplemental Table 3). Flow analysis of infiltrating leukocytes in the tumor were also similar between the 2 sequential therapy groups (Supplemental Figs. 4A–4C). Notably, the percentage of CD4-positive, Foxp3-positive Tregs was reduced (Supplemental Fig. 4C), and the percentage of IFN $\gamma$ -positive, CD8-positive cells to Tregs was higher in the +10-d and +5-d immunocytokine groups (Supplemental Fig. 4D). We conclude that delaying immunocytokine after TAT may prove to be beneficial as early as 5 d after TAT. This result suggests that immunocytokine may have its greatest effects on tumors that are damaged by prior radiation therapy, whether SBRT or TAT.

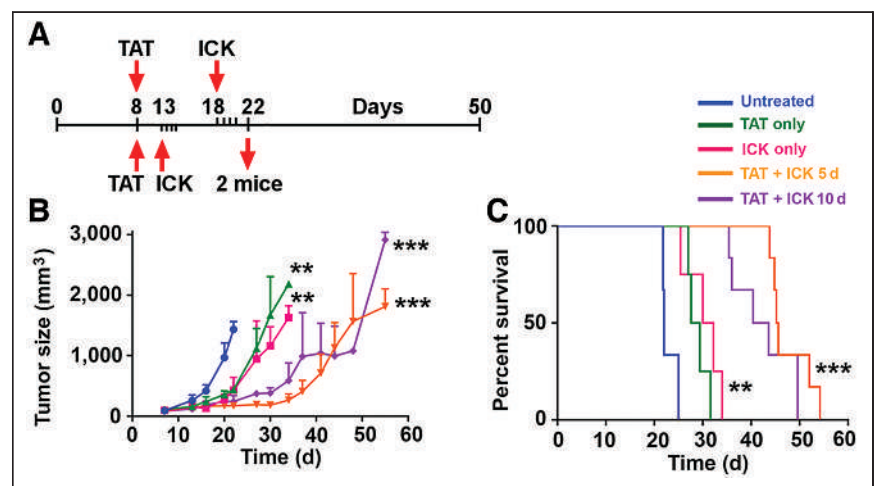


**FIGURE 3.** (A) Treatment schema for TAT followed by immunocytokine 5 d later (top) or 10 d later (bottom) in breast cancer model. Groups contained 8 mice, with 2 mice removed at days 21 and 22 for blood analysis. (B and C) Tumor growth curves (B) and Kaplan-Meier survival plot (C). *P* values are vs. untreated controls. \*\**P* < 0.01. \*\*\**P* < 0.001. ICK = immunocytokine.

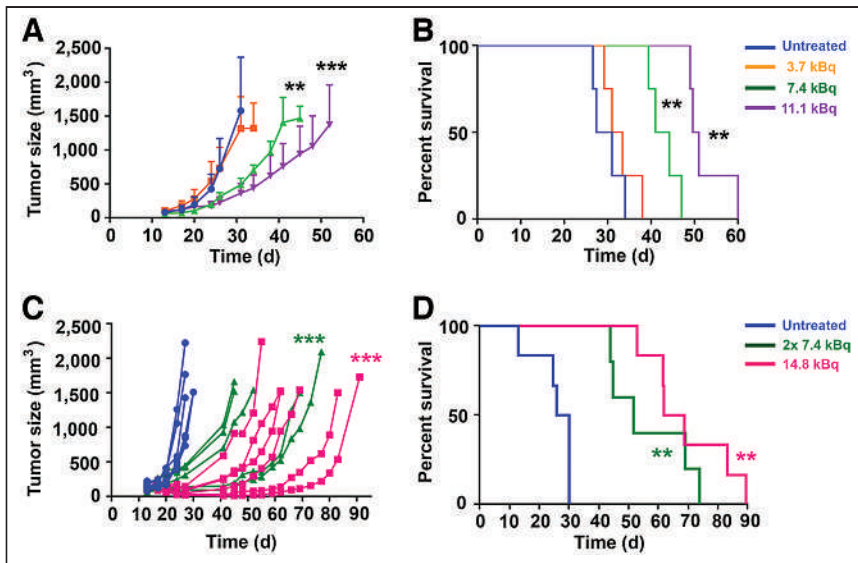


**FIGURE 4.** (A and B) Tumor growth curves (A) and Kaplan–Meier survival plot (B) for TAT dose response in colon cancer model (6 per group, with 2 removed at day 27). (C and D) Tumor growth curves (C) and Kaplan–Meier survival plot (D) for  $2 \times 7.4$  kBq vs. 14.8 kBq of TAT ( $n = 5$ –6).  $P$  values are vs. untreated controls. \*\* $P < 0.01$ . \*\*\* $P < 0.001$ .

The timing of immunocytokine after TAT had minimal effect on whole-body toxicity (Supplemental Fig. 5) or liver and kidney toxicity (Supplemental Table 2). Hematologic analysis was similar between the 2 studies, showing a reduction in lymphocytes with TAT only at the early time point and recovery in the TAT-plus-immunocytokine group at the late time point (Supplemental Figs. 5A–5D). There were no effects on red blood cells (Supplemental Fig. 5E), and there was a transient effect on platelets (Supplemental Fig. 5F).

#### TAT of CEA-Positive MC38/CEA Colon Tumors

To confirm the efficacy of TAT in a second tumor model, CEA-transfected murine colon carcinoma MC38 cells were engrafted subcutaneously in CEA transgenic mice. In a dose response study of 3.7–11.1 kBq, there was little difference in tumor reduction or survival between control and treated tumors at the lowest dose (Figs. 4A and 4B; Supplemental Table 1), but at the middle (7.4 kBq) and highest (11.1 kBq) doses, there was a significant reduction in tumor growth and increase in median survival from 29 d (no treatment) to 50 d for the highest dose (Supplemental Table 4). In the colon cancer model, we evaluated the effects of increased TAT by changing the dose in 2 ways, first by raising the maximum dose to 14.8 kBq, and second by administering the 7.4-kBq dose twice, once at 13 d after tumor inoculation and again 10 d later. The tumor growth curves for individual mice shown in Figure 4C reveal an interesting spread in response to TAT, suggesting that minor differences in tumor sizes or microenvironment affect the responses to TAT that are not apparent in the control tumors. However, both the tumor growth (Fig. 4C; Supplemental Table 1) and the survival curves (Fig. 4D; Supplemental Tables 1 and 4) demonstrate

that the single 14.8-kBq dose was superior to the fractionated  $2 \times 7.4$ -kBq dose. No significant whole-body (Supplemental Fig. 6A), liver or kidney (Supplemental Table 5), or chronic hematologic (Supplemental Figs. 6B–6F) toxicities were noted in this TAT monotherapy model.

#### Sequential TAT Plus Immunocytokine Therapy of MC38/CEA Colon Tumors

To directly compare the 2 tumor model responses to sequential therapy, the identical TAT dose of 7.4 kBq was chosen with a delay of 10 d for the start of immunocytokine (Fig. 5A). The tumor growth curves for TAT or immunocytokine monotherapy were identical until 35 d, after which immunocytokine monotherapy showed tumor regrowth (Fig. 5B; Supplemental Table 1). Even though some of the mice treated with TAT had prolonged tumor growth inhibition and survival, the sequential therapy showed an improved tumor growth reduction out to about 45 d, after which tumor regrowth became obvious (Fig. 5B; Supplemental

Table 1). Median survival for sequential therapy was 57 versus 29 d for untreated controls (Fig. 5C; Supplemental Tables 1 and 4). No whole-body (Supplemental Fig. 7A) or liver or kidney (Supplemental Table 5) toxicities were noted in the TAT-plus-immunocytokine group; however, early lymphocyte and platelet numbers and percentages were reduced but recovered at the late time point (Supplemental Figs. 7B–7F).

Surprisingly, there was a significant increase in tumor-infiltrating CD4-positive and CD8-positive T cells only in mice treated with immunocytokine as analyzed by flow cytometry at 27 d (Supplemental Fig. 8A). However, both IFN $\gamma$ -positive, CD4-positive T cells and CD8-positive T cells were significantly increased by sequential therapy (Supplemental Fig. 8B). Since these findings did not explain the significant improvement in tumor growth inhibition and survival in the TAT-plus-immunocytokine group, an

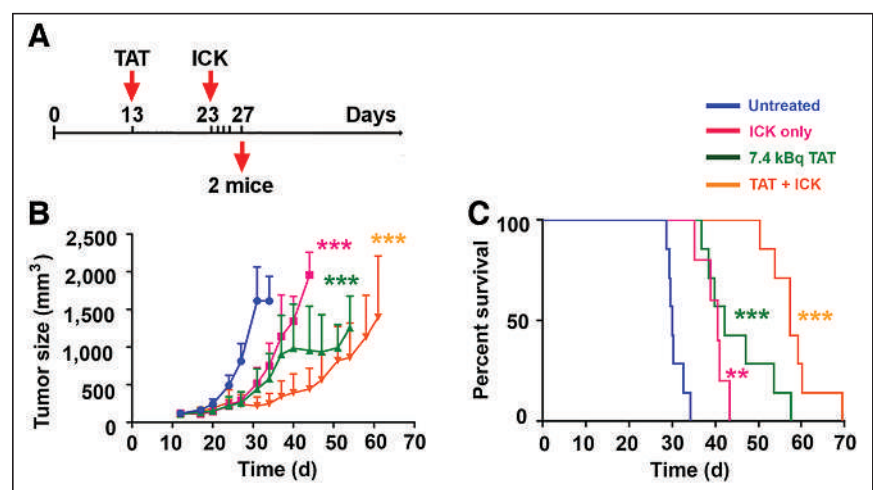


**FIGURE 5.** Treatment schema and TAT doses (A), tumor growth curves (B), and Kaplan–Meier survival plot (C) for TAT first followed by immunocytokine therapy in colon cancer model (7 per group).  $P$  values are vs. untreated controls. \*\* $P < 0.01$ . \*\*\* $P < 0.001$ . ICK = immunocytokine.

additional study was performed in which tumors were collected and analyzed on days 1, 5, and 8 after the last dose of immunocytokine in the sequential therapy group. The results of this study showed a gradual increase in CD8-positive T-cell infiltration into tumors (Supplemental Fig. 8C). The increase in tumor-infiltrating IFN $\gamma$ -positive, CD8-positive T cells on days 5 and 8 after the last dose of immunocytokine in the sequential therapy group was especially evident (Supplemental Fig. 8D). As in the other sequential therapy model, the change in the ratio of IFN $\gamma$ -positive, CD8-positive T cells to regulatory T cells on days 5 and 8 after the last dose of immunocytokine in the sequential therapy group was significant (Supplemental Fig. 8E).

We conclude that both tumor models show a similar augmented response to TAT followed by immunocytokine, in which the increase in cytotoxic infiltrating T cells and decrease in tumor Tregs are due to the addition of immunocytokine, suggesting an immunologic mechanism.

### Immunohistochemistry Analysis of Therapies

A limited number of tumors were harvested 21 or 27 d (for breast or colon cancer models, respectively) after tumor injection to study tumor morphology, vascularity, CEA expression, and lymphocyte infiltration. In the orthotopic mammary tumor model, vascularity as measured by CD31 staining was most affected by sequential therapy, as evidenced by increased staining and vessel size, especially at the tumor periphery (Supplemental Figs. 9A–9D). In the colon cancer model, the vascularity of untreated tumors showed even CD31 staining across the entire tumor that was greatly disrupted in all therapy groups (Supplemental Figs. 9E–9H).

CD8 numbers were lowest in the TAT-alone breast cancer group, with similar expression in the untreated control and immunocytokine groups, and were highest in the TAT-plus-immunocytokine group (Supplemental Figs. 10A–10D). CEA expression was largely limited to the tumor periphery in untreated controls and was markedly decreased toward the tumor center (Supplemental Fig. 10E), indicating an *in vivo* effect on CEA expression in this tumor model. Interestingly, TAT greatly reduced CEA expression only at the tumor periphery while preserving expression toward the tumor center (Supplemental Fig. 10F), whereas the opposite was true for immunocytokine-only therapy (Supplemental Fig. 10G). CEA expression in the sequential therapy tumors was similar to TAT only (Supplemental Fig. 10H), suggesting that TAT was most efficient in killing CEA-positive cells at the tumor periphery, a result that may be explained by the low tissue penetration of  $\alpha$ -particles. In addition, breast tumors were stained for macrophages with the antibody F4/80 (Supplemental Fig. 11). In this series, F4/80 staining was most intense at the tumor periphery and was relatively unchanged for immunocytokine-only therapy. However, TAT alone or TAT plus immunocytokine greatly increased myeloid staining throughout the tumor, suggesting that TAT mobilized myeloid infiltration.

For CD8 staining of colon cancer tumors, untreated controls had large numbers of resident CD8 cells (Supplemental Fig. 12A), which were greatly reduced by TAT only (Supplemental Fig. 12B). The profile in immunocytokine-only therapy was intermediate, with clusters of CD8 cells observed in regions of the tumor (Supplemental Fig. 12C), suggesting a redistribution or elimination of CD8 subtypes. Sequential therapy was similar to TAT only (Supplemental Fig. 12D). CEA staining was uniformly intense throughout the tumor in untreated controls (Supplemental Fig. 12E), but with islands of low staining in TAT-only tumors (Supplemental Fig. 8F).

Conversely, controls treated with immunocytokine only stained lightly for CEA, with islands of CEA-negative cells (Supplemental Fig. 12G). The sequential therapy tumors showed intense CEA staining at the periphery, with a centralized area of less intense staining (Supplemental Fig. 12H). Myeloid cell staining with F4/80 exhibited a profile different from the mammary tumors, with intense sporadic staining throughout the untreated controls changing to peripheral tumor staining in the treated groups (Supplemental Fig. 13).

### DISCUSSION

Both tumor models responded similarly to targeted monotherapies, in which higher doses caused transient white blood cell and platelet reduction. Although no early kidney toxicity was observed, we did not test for delayed kidney toxicity, a potential problem with  $^{225}\text{Ac}$ -based therapy (17). In the case of the colon cancer model, an even higher dose (14.7 kBq), divided into a single-treatment or a split-treatment regimen, showed that the single higher dose increased the median survival to 65 d, versus 51 d for the split dose.

The order of sequential therapy in the breast cancer model showed that immunocytokine first followed by TAT was no better than either monotherapy, but TAT followed by immunocytokine increased survival from 30 to 45 d. Since immunocytokine therapy increases CD8 infiltration into both tumor models, these cells may be killed by subsequent TAT, which is cytotoxic to all cells in the tumor and T cells in particular. This may explain the controversial results of tumor-targeted radiation therapy, which was found to either suppress or stimulate the immune response (25,26). Although antibody-targeted radiation therapy can deliver significant tumor doses (27,28), they are accompanied by hematologic doses that are unavoidable because of circulating antibody. However, hematologic doses can be reduced by the short range of  $\alpha$ -particles used in TAT (17). In a previous study with the same breast cancer model, tumor regrowth with SBRT plus immunocytokine occurred at 23 d, versus 15 d with SBRT alone (13). Tumor regrowth with TAT plus immunocytokine occurred at 40 d, versus 20 d for TAT alone. Thus, TAT plus immunocytokine may have advantages over SBRT plus immunocytokine. Clinical studies with SBRT plus anti-PD-1 or anti-PD-L1 immunotherapy demonstrate modest improvements in tumor response and suggest that the toxicities associated with these immunotherapies is limiting (29). The use of targeted immunotherapy with agents such as immunocytokine may improve outcomes.

Immunohistochemistry staining of tumors showed that tumors responded spatially differently for vascular effects, immune cell infiltration, and target antigen expression. Notably, TAT was more effective than immunocytokine in destroying or modifying tumor vasculature. CEA expression was most affected by TAT. However, effective therapy was observed in both models, suggesting that loss of CEA expression was not the major factor. Thus, in a single targeted treatment regimen, the initial antigen expression played the dominant role.

Myeloid cell infiltration was pronounced for TAT only or for TAT plus immunocytokine versus immunocytokine only in both models, but TAT caused little, if any, increase in CD8 cell infiltration, whereas immunocytokine therapy had a greater effect on CD8 infiltration, whether alone or followed by TAT in both models. A role for myeloid cell infiltration after TAT was also noted by Dabagian et al. (30), who ascribed this effect to immunosuppression. Thus, immunotherapy may increase the effectiveness of TAT by

reducing myeloid infiltration. In a study by Dabagian et al. (30), anti-PD-1 immunotherapy was more effective than TAT, making comparisons to our study difficult.

## CONCLUSION

In 2 tumor models, we showed comparable tumor reduction by TAT or immunocytokine monotherapy, which, when performed sequentially with TAT followed by immunocytokine, produced improved therapy. Both monotherapy and sequential therapies have minimal whole-body, hematologic, liver, and kidney toxicities. Increased infiltration of IFN $\gamma$ -positive CD8 lymphocytes and an increased ratio of IFN $\gamma$ -positive CD8 T cells to Foxp3-positive CD4 T cells is a mechanistic observation for immunocytokine-only or sequential TAT-plus-immunocytokine therapy in both tumor models.

## DISCLOSURE

This research was partially supported by NIH cancer center support grant P30CA033572. No other potential conflict of interest relevant to this article was reported.

## KEY POINTS

**QUESTION:** Is sequential TAT plus targeted immunocytokine therapy more effective than either monotherapy, and what is the best order for sequential targeted therapies?

**PERTINENT FINDINGS:** In an immunocompetent animal model, TAT followed by immunocytokine was more effective than either monotherapy, and TAT before immunocytokine performed better than immunocytokine followed by TAT. A major effect of immunocytokine was to improve the effector CD8 T-cell-to-Treg ratio.

**IMPLICATIONS FOR PATIENT CARE:** The effect of targeted radiotherapy on the immune system is controversial, making it hard to predict whether and when targeted immunotherapy should be added to the treatment regimen. Our study suggests that TAT followed by immunocytokine may be effective because of the limited tissue range of  $\alpha$ -particles, which cause less hematologic immune suppression.

## REFERENCES

1. Tong G, Xu W, Zhang G, et al. The role of tissue and serum carcinoembryonic antigen in stages I to III of colorectal cancer: a retrospective cohort study. *Cancer Med*. 2018;7:5327–5338.
2. Buchegger F, Mach JP, Pelegrin A, et al. Radiolabeled chimeric anti-CEA monoclonal antibody compared with the original mouse monoclonal antibody for surgically treated colorectal carcinoma. *J Nucl Med*. 1995;36:420–429.
3. Goldenberg DM. Cancer imaging with CEA antibodies: historical and current perspectives. *Int J Biol Markers*. 1992;7:183–188.
4. Wong JY, Thomas GE, Yamauchi D, et al. Clinical evaluation of indium-111-labeled chimeric anti-CEA monoclonal antibody. *J Nucl Med*. 1997;38:1951–1959.
5. Behr TM, Sharkey RM, Juweid ME, et al. Phase I/II clinical radioimmunotherapy with an iodine-131-labeled anti-carcinoembryonic antigen murine monoclonal antibody IgG. *J Nucl Med*. 1997;38:858–870.
6. Juweid ME, Sharkey RM, Behr T, et al. Radioimmunotherapy of patients with small-volume tumors using iodine-131-labeled anti-CEA monoclonal antibody NP-4 F(ab')<sub>2</sub>. *J Nucl Med*. 1996;37:1504–1510.
7. Ychou M, Azria D, Menkarios C, et al. Adjuvant radioimmunotherapy trial with iodine-131-labeled anti-carcinoembryonic antigen monoclonal antibody F6 F(ab')<sub>2</sub> after resection of liver metastases from colorectal cancer. *Clin Cancer Res*. 2008;14:3487–3493.
8. Akhavan D, Yazaki P, Yamauchi D, et al. Phase I study of yttrium-90 radiolabeled M5A anti-carcinoembryonic antigen humanized antibody in patients with advanced carcinoembryonic antigen producing malignancies. *Cancer Biother Radiopharm*. 2020;35:10–15.
9. Wong JY, Chu DZ, Williams LE, et al. A phase I trial of <sup>90</sup>Y-DOTA-anti-CEA chimeric T84.66 (cT84.66) radioimmunotherapy in patients with metastatic CEA-producing malignancies. *Cancer Biother Radiopharm*. 2006;21:88–100.
10. Oberst MD, Fuhrmann S, Mulgrew K, et al. CEA/CD3 bispecific antibody MEDI-565/AMG 211 activation of T cells and subsequent killing of human tumors is independent of mutations commonly found in colorectal adenocarcinomas. *MABS*. 2014;6:1571–1584.
11. Bacac M, Fauti T, Sam J, et al. A novel carcinoembryonic antigen T-cell bispecific antibody (CEA TCB) for the treatment of solid tumors. *Clin Cancer Res*. 2016;22:3286–3297.
12. Zhang C, Wang Z, Yang Z, et al. Phase I escalating-dose trial of CAR-T therapy targeting CEA(+) metastatic colorectal cancers. *Mol Ther*. 2017;25:1248–1258.
13. Kujawski M, Sherman M, Hui S, et al. Potent immunomodulatory effects of an anti-CEA-IL-2 immunocytokine on tumor therapy and effects of stereotactic radiation. *Oncimmunology*. 2020;9:1724052.
14. Yazaki PJ, Sherman MA, Shively JE, et al. Humanization of the anti-CEA T84.66 antibody based on crystal structure data. *Protein Eng Des Sel*. 2004;17:481–489.
15. Morgenstern A, Apostolidis C, Kratochwil C, Sathekge M, Krolicki L, Bruchertseifer F. An overview of targeted alpha therapy with <sup>225</sup>actinium and <sup>213</sup>bismuth. *Curr Radiopharm*. 2018;11:200–208.
16. Ferrer L, Kraeber-Bodere F, Bodet-Milin C, et al. Three methods assessing red marrow dosimetry in lymphoma patients treated with radioimmunotherapy. *Cancer*. 2010;116:1093–1100.
17. Scheinberg DA, McDevitt MR. Actinium-225 in targeted alpha-particle therapeutic applications. *Curr Radiopharm*. 2011;4:306–320.
18. Minnix M, Li L, Yazaki PJ, et al. TAG-72-targeted  $\alpha$ -radionuclide therapy of ovarian cancer using <sup>225</sup>Ac-labeled DOTAylated-huCC49 antibody. *J Nucl Med*. 2021;62:55–61.
19. Minnix M, Adhikarla V, Caserta E, et al. Comparison of CD38-targeted  $\alpha$ - versus  $\beta$ -radionuclide therapy of disseminated multiple myeloma in an animal model. *J Nucl Med*. 2021;62:795–801.
20. Clarke P, Mann J, Simpson JF, Rickard-Dickson K, Primus FJ. Mice transgenic for human carcinoembryonic antigen as a model for immunotherapy. *Cancer Res*. 1998;58:1469–1477.
21. Xu X, Clarke P, Szalai G, et al. Targeting and therapy of carcinoembryonic antigen-expressing tumors in transgenic mice with an antibody-interleukin 2 fusion protein. *Cancer Res*. 2000;60:4475–4484.
22. Cha SE, Kujawski M, J Yazaki P, Brown C, Shively JE. Tumor regression and immunity in combination therapy with anti-CEA chimeric antigen receptor T cells and anti-CEA-IL2 immunocytokine. *Oncimmunology*. 2021;10:1899469.
23. Li L, Crow D, Turatti F, et al. Site-specific conjugation of monodispersed DOTA-PEGn to a thiolated diabody reveals the effect of increasing PEG size on kidney clearance and tumor uptake with improved 64-copper PET imaging. *Bioconjug Chem*. 2011;22:709–716.
24. Yazaki PJ, Sherman MA, Shively JE, et al. Humanization of the anti-CEA T84.66 antibody based on crystal structure data. *Protein Eng Des Sel*. 2004;17:481–489.
25. Grass GD, Krishna N, Kim S. The immune mechanisms of abscopal effect in radiation therapy. *Curr Probl Cancer*. 2016;40:10–24.
26. Sridharan V, Schoenfeld JD. Immune effects of targeted radiation therapy for cancer. *Discov Med*. 2015;19:219–228.
27. Muylle K, Flamen P, Vugts DJ, et al. Tumour targeting and radiation dose of radioimmunotherapy with <sup>90</sup>Y-rituximab in CD20+ B-cell lymphoma as predicted by <sup>89</sup>Zr-rituximab immuno-PET: impact of preloading with unlabelled rituximab. *Eur J Nucl Med Mol Imaging*. 2015;42:1304–1314.
28. DeNardo SJ, Williams LE, Leigh BR, Wahl RL. Choosing an optimal radioimmunotherapy dose for clinical response. *Cancer*. 2002;94:1275–1286.
29. Chen Y, Gao M, Huang Z, Yu J, Meng X. SBRT combined with PD-1/PD-L1 inhibitors in NSCLC treatment: a focus on the mechanisms, advances, and future challenges. *J Hematol Oncol*. 2020;13:105.
30. Dabagian H, Taghvaei T, Martorano P, et al. PARP targeted alpha-particle therapy enhances response to PD-1 immune-checkpoint blockade in a syngeneic mouse model of glioblastoma. *ACS Pharmacol Transl Sci*. 2021;4:344–351.

---

---

# <sup>18</sup>F-DOPA PET/CT at the Forefront of Initial or Presurgical Evaluation of Small-Intestine Neuroendocrine Tumors

Eric Ouvrard<sup>1</sup>, Louis De Mestier<sup>2</sup>, Caroline Boursier<sup>3</sup>, Boumediene Lachachi<sup>4</sup>, Nicolas Sahakian<sup>5</sup>, Elodie Chevalier<sup>3</sup>, Nidaa Mikail<sup>6</sup>, Josefina Carullo<sup>1,7</sup>, Aurélie Bando-Delaunay<sup>6</sup>, Thomas Walter<sup>8</sup>, Gabriel G. Malouf<sup>9</sup>, Pietro Addeo<sup>10</sup>, Gilles Poncet<sup>11</sup>, Frederic Sebag<sup>12</sup>, Rachida Lebtahi<sup>6</sup>, Bernard Goichot<sup>13</sup>, David Taïeb<sup>5,14</sup>, and Alessio Imperiale<sup>1,15</sup>

<sup>1</sup>Nuclear Medicine and Molecular Imaging, Institut de Cancérologie Strasbourg Europe, University Hospitals of Strasbourg, University of Strasbourg, Strasbourg, France; <sup>2</sup>Department of Pancreatology and Digestive Oncology, ENETS Centre of Excellence, Beaujon Hospital, Université de Paris, and INSERM U1149, Centre of Research in Inflammation, Paris, France; <sup>3</sup>Nuclear Medicine, University Hospital of Nancy, Nancy, France; <sup>4</sup>Nuclear Medicine, Hospices Civils de Lyon, Lyon, France; <sup>5</sup>Nuclear Medicine, La Timone University Hospital, Aix-Marseille University, Marseille, France; <sup>6</sup>Nuclear Medicine, ENETS Centre of Excellence, Beaujon Hospital, Université de Paris, Paris, France; <sup>7</sup>Nuclear Medicine, Sanatorio Allende S.A., Cordoba, Argentina; <sup>8</sup>Medical Oncology, Edouard Herriot Hospital, Hospices Civils de Lyon, Université Lyon 1, Lyon, France; <sup>9</sup>Oncology, Institut de Cancérologie Strasbourg Europe, Strasbourg, France; <sup>10</sup>Hepato-Pancreato-Biliary Surgery and Liver Transplantation, University Hospitals of Strasbourg, Strasbourg, France; <sup>11</sup>Digestive and Oncologic Surgery, Edouard-Herriot University Hospital, Claude-Bernard Lyon 1 University, Lyon, France; <sup>12</sup>Endocrine Surgery, Conception University Hospital, Aix-Marseille University, Marseille, France; <sup>13</sup>Diabetes and Metabolic Disorders, Internal Medicine, University Hospitals of Strasbourg, Strasbourg University, Strasbourg, France; <sup>14</sup>European Center for Research in Medical Imaging, Aix-Marseille University, Marseille, France; and <sup>15</sup>Molecular Imaging-DRHIM, IPHC, UMR 7178, CNRS/Unistra, Strasbourg, France

---

Our objective was to compare the respective value of <sup>68</sup>Ga-DOTATOC and <sup>18</sup>F-DOPA PET/CT for initial staging or presurgical work-up of patients with small-intestine neuroendocrine tumors (SiNETs). **Methods:** This was a retrospective, multicenter, noninterventive investigation involving 53 non-surgically treated SiNET patients who underwent both <sup>68</sup>Ga-DOTATOC and <sup>18</sup>F-DOPA PET/CT within a 6-mo interval without surgical intervention or therapeutic change between the 2 PET/CT studies. Percentage detection rate was calculated according to per-region and per-lesion analyses. Sensitivity for primary tumor detection was assessed in 37 surgically treated patients, taking surgical results (76 SiNETs) as the diagnostic gold standard. **Results:** <sup>68</sup>Ga-DOTATOC PET/CT and <sup>18</sup>F-DOPA PET/CT individually identified at least 1 primary SiNET in 92% (34/37) of the patients. Intestinal tumor multifocality was confirmed by histology in 8 patients. <sup>68</sup>Ga-DOTATOC and <sup>18</sup>F-DOPA PET/CT were concordantly positive for tumor multifocality in 5 patients, discordantly positive in 2 patients, and concordantly negative in 1 patient. The detection rate for subdiaphragmatic nodal metastases on per-region-based analysis was 91% and 98% for <sup>68</sup>Ga-DOTATOC and <sup>18</sup>F-DOPA PET/CT, respectively ( $P = 0.18$ ). <sup>18</sup>F-DOPA PET/CT detected a higher number of abnormal subdiaphragmatic nodes ( $P = 0.009$ ). Regarding mesenteric nodes only, <sup>18</sup>F-DOPA PET/CT detected more positive regions ( $P = 0.005$ ) and nodal lesions ( $P = 0.003$ ) than <sup>68</sup>Ga-DOTATOC PET/CT, including nodes at the origin of mesenteric vessels. For detection of distant metastases, <sup>68</sup>Ga-DOTATOC and <sup>18</sup>F-DOPA PET/CT performed equally well on a per-region-based analysis. As compared with <sup>68</sup>Ga-DOTATOC, <sup>18</sup>F-DOPA PET/CT detected more hepatic ( $P < 0.001$ ), peritoneal ( $P < 0.001$ ), and lung metastases ( $P < 0.001$ ). **Conclusion:** <sup>18</sup>F-DOPA PET/CT detected more lesions than <sup>68</sup>Ga-DOTATOC PET/CT in the studied patients. The respective roles of the two should be discussed in terms of disease staging and treatment selection.

**Key Words:** <sup>68</sup>Ga-DOTATOC; <sup>18</sup>F-DOPA; PET; neuroendocrine; small intestine; carcinoid; staging

**J Nucl Med 2022; 63:1865–1870**  
DOI: 10.2967/jnumed.122.263984

---

**N**euroendocrine tumors (NETs) originating from the gastroenteropancreatic system account for approximately 60% of all NETs. The small intestine, mainly the ileum, is the most common site of primary tumor origin. Despite their slow pace of progression, small-intestine NETs (SiNETs) can extensively spread to mesenteric nodal stations, liver, and bone and can cause pronounced fibrosis locally in the mesentery and at distant sites, as in the heart, leading to extremely serious complications. Surgery is the only potentially curative treatment for nonmetastatic SiNETs (1,2). Identification of distant metastases usually does not prevent (if indicated) surgical resection of primary SiNETs, mesenteric lymph nodes, and mesenteric fibrosis to avoid potential complications (2,3). If curative surgery is possible, the extent of lymph node metastasis must be carefully evaluated because a complete lymphadenectomy decreases the risk of recurrence (4–6). In addition, a 19% rate of missed metastases was reported in the retropancreatic area, a region not systematically explored during surgery (7).

Imaging plays a central role in initial diagnosis for staging (screening for primary multifocality, lymph nodes, systemic metastases, and fibrosis) and for determining operability, the latter being related to the location of nodal lesions or mesenteric fibrosis with regard to the mesenteric arteries (8). Functional imaging can be performed in addition to whole-body CT and liver MRI (9). <sup>68</sup>Ga-labeled somatostatin analogs used for somatostatin receptor (SSTR) PET/CT have achieved consensus or near consensus among expert panels as a forefront radio-pharmaceutical for SiNETs. <sup>68</sup>Ga-somatostatin analog PET/CT has indeed been shown to provide results comparable to those of <sup>18</sup>F-DOPA PET/CT at the patient-based level, adding information on

---

Received Feb. 9, 2022; revision accepted Apr. 27, 2022.  
For correspondence or reprints, contact Alessio Imperiale (a.imperiale@icans.eu).  
Published online May 19, 2022.  
COPYRIGHT © 2022 by the Society of Nuclear Medicine and Molecular Imaging.

SSTR expression status for theranostic application, which is tightly linked to tumor differentiation and patient prognosis. However, a systematic review (10) has shown that despite similar high patient- and region-based pooled sensitivities (83% and 89%, respectively, for  $^{18}\text{F}$ -DOPA PET; 88% and 92%, respectively, for SSTR PET),  $^{18}\text{F}$ -DOPA was superior in lesion detection (lesion-based pooled sensitivity, 95% vs. 82%). These data agree with 2017 European Association of Nuclear Medicine guidelines positioning  $^{18}\text{F}$ -DOPA and  $^{68}\text{Ga}$ -somatostatin analogs as first-choice radiotracers for SiNETs, except when evaluation of SSRT expression is mandatory before treatment (11). Moreover, the most accurate modality should be required when the assessment of tumor extension needs to be as precise as possible. To this end, in the present study we compared  $^{68}\text{Ga}$ -DOTATOC and  $^{18}\text{F}$ -DOPA PET/CT in initial staging or in the presurgical work-up of patients with SiNETs.

## MATERIALS AND METHODS

### Patient Population

This was a retrospective, multicenter, noninterventional investigation conducted in the department of nuclear medicine of 5 academic NET centers in France (Beaujon, Lyon, Marseille, Nancy, and Strasbourg), involving patients with SiNETs evaluated by PET/CT between 2017 and 2021. Patients were retrospectively included according to the following criteria: well-differentiated SiNETs, PET investigations performed for initial staging or presurgical work-up,  $^{68}\text{Ga}$ -DOTATOC and  $^{18}\text{F}$ -DOPA PET/CT performed within a 6-mo period, and absence of any surgical intervention or therapeutic change between the 2 PET studies. Patients with a history of oncologic intestinal surgery for SiNETs were not considered for the study. Demographics, presence of carcinoid syndrome, imaging results, and pathologic results after surgical resection were collected. Values of serum chromogranin-A (CgA) and 24-h urinary 5-hydroxyindoleacetic acid (5-HIAA) were collected when available. Tumors were graded according to the 2019 World Health Organization classification (12). In accordance with local guidelines, all patients gave written informed consent to the use of anonymous data extracted from their medical records for scientific or epidemiologic purposes. The institutional review board approved this study (Comité d'Ethique 2021-93).

### $^{68}\text{Ga}$ -DOTATOC and $^{18}\text{F}$ -DOPA PET/CT: Acquisition/Reconstruction Parameters

All examinations were performed on combined PET/CT devices equipped with 3-dimensional time-of-flight technology and without iodinated contrast medium. Patients in a given center were scanned on the same instrument regarding the 2 tracers. Patients were injected with a 2–3 MBq/kg dose of  $^{68}\text{Ga}$ -DOTATOC and a 3–4 MBq/kg dose of  $^{18}\text{F}$ -DOPA.  $^{68}\text{Ga}$ -DOTATOC (SomaKit TOC; Advanced Accelerator Applications) and  $^{18}\text{F}$ -DOPA (Dopacis; Cisbio International) were used in the setting of marketing authorization. In cases of concurrent octreotide therapy,  $^{68}\text{Ga}$ -DOTATOC PET/CT was performed just before the next octreotide injection. Carbidopa premedication (200 mg orally) was done in 24 cases (45%) 60–90 min before  $^{18}\text{F}$ -DOPA intravenous injection. The PET/CT protocol included an acquisition from the upper thigh to the top of the skull (3–5 min/step or continuous bed motion when available), starting approximately 60 or 30 min after injection of  $^{68}\text{Ga}$ -DOTATOC or  $^{18}\text{F}$ -DOPA, respectively. PET image datasets were reconstructed iteratively (ordered-subset expectation maximization algorithm) using non-contrast-enhanced data for attenuation correction. CT, PET (attenuation-corrected), and PET/CT were independently interpreted by 1 experienced nuclear medicine physician who was aware of patients' clinical data and the results of biologic, pathologic, and anatomic imaging investigations but not the results of the other PET study.  $^{68}\text{Ga}$ -DOTATOC and  $^{18}\text{F}$ -DOPA PET/CT from the same patients were analyzed more than 7 d apart.

### Interpretation Criteria of PET Studies

PET findings were interpreted as either positive or negative. A positive PET result was defined as detection of at least 1 focus of pathologically increased uptake relative to surrounding tissue and physiologic biodistribution. For per-region analysis, the following 9 anatomic regions were analyzed: small intestine (i.e., primary tumors), peritoneum, liver, abdominal lymph nodes, left-sided supraclavicular lymph nodes, supradiaphragmatic lymph nodes (excluding the left supraclavicular region), lungs/pleura, bones, and others. Moreover, mesenteric lymph nodes were analyzed independently, according to the Pasquer et al. (7) classification: group 1 included those in contact with the small bowel; group 2, in the middle of the mesentery; and group 3, at the origin of the mesenteric vessels under the pancreatic uncus. A region was considered positive when it contained at least 1 focal uptake abnormality, regardless of the number of positive foci. Finally, for per-lesion analysis, the number of lesions in each region was recorded. If the number exceeded 20, the count was fixed at 20.

### Statistical Analysis

Results for continuous variables were expressed as mean and SD or range, as appropriate, whereas categoric variables were expressed as frequencies and percentages. For ethical reasons, histologic proof of all potentially metastatic lesions was not possible, and pathologic  $^{68}\text{Ga}$ -DOTATOC or  $^{18}\text{F}$ -DOPA uptake was considered a true-positive result. The sum of positive regions and lesions on either  $^{68}\text{Ga}$ -DOTATOC or  $^{18}\text{F}$ -DOPA PET/CT was considered the total number of involved regions and lesions. The percentage detection rate (DR) of  $^{68}\text{Ga}$ -DOTATOC and  $^{18}\text{F}$ -DOPA PET/CT was calculated according to per-region and per-lesion analyses.  $^{68}\text{Ga}$ -DOTATOC and  $^{18}\text{F}$ -DOPA PET/CT sensitivity for primary tumor detection was assessed in surgically treated patients using surgical findings as the diagnostic gold standard. Region-to-region and lesion-to-lesion comparisons between  $^{68}\text{Ga}$ -DOTATOC and  $^{18}\text{F}$ -DOPA PET/CT were performed using the McNemar test. Correlations were assessed using the Spearman  $\rho$ -correlation test. A 2-sided *P* value of less than 0.05 was considered significant. Statistical analyses were performed using freely available statistical software (Jamovi, version 1.8).

## RESULTS

### Patient Population

Of 59 screened patients, 2 were excluded because they had undergone surgery before PET/CT, 2 because of more than a 6-mo delay between the 2 PET/CT studies, 1 because  $^{18}\text{F}$ -DOPA PET/CT data were not available, and 1 because there were more than 100 SiNETs. Hence, 53 patients were included in the analysis. Their characteristics are summarized in Table 1. The population comprised 31 (58%) women and 22 (42%) men, with a mean age of  $65 \pm 13$  y (range, 33–89 y). Fifteen patients (28%) were referred because of clinical and radiologic suspicion of SiNETs (afterward histologically confirmed), and 38 (72%) patients presented with biopsy-proven metastatic SiNETs.

Tumors were classified as grade 1 in 23 (43%) patients, grade 2 in 25 (47%) patients, and well-differentiated grade 3 in 3 (6%) patients (mean Ki-67,  $5.8\% \pm 8.7\%$ ; median Ki-67, 3.7%; range, 1%–44%). The Ki-67 index was not available for 2 (4%) patients with well-differentiated tumors. Nineteen (36%) patients had carcinoid syndrome. Serum CgA and urinary 5-HIAA were elevated in 28 (53%) and 14 (26%) patients, respectively. At the time of PET/CT, 13 (25%) patients were treated by long-acting somatostatin analogs. The mean interval between the 2 modalities was  $29 \pm 76$  d (range, 1–161 d), and 68% of patients had the 2 examinations within 28 d. After PET/CT, 37 of 53 (70%) patients

**TABLE 1**  
Patient Population and Tumor Characteristics

Characteristic	Data
Patients	53 (100%)
Women	31 (58%)
Age (y)	65 (13)
PET/CT indication	
Suspicion of SiNETs	15 (28%)
Staging of histologically proven metastatic SiNETs	38 (72%)
World Health Organization grade, 2019	
1	23 (43%)
2	25 (47%)
3	3 (6%)
Ki-67	5.8 (8.7) (median, 3.7)
Biochemical tumor markers	
Elevated serum CgA	28 (53%)
Elevated 24-h urinary 5-HIAA	14 (26%)
Long-acting somatostatin analogs	13 (25%)

Qualitative data are number and percentage; continuous data are median and SD.

underwent oncologic surgery, and histology revealed a total of 76 primary SiNETs.

#### Similar Primary SiNET Detection Rates Shown by <sup>18</sup>F-DOPA and <sup>68</sup>Ga-DOTATOC PET/CT

<sup>68</sup>Ga-DOTATOC and <sup>18</sup>F-DOPA PET/CT sensitivity for primary SiNET detection was assessed from the analysis of 37 surgically treated patients and 76 histologically detected SiNETs. The ability of both imaging modalities to detect a multifocal intestinal disease was also evaluated.

In 32 (86%) patients, <sup>68</sup>Ga-DOTATOC and <sup>18</sup>F-DOPA PET/CT were concordant and identified at least 1 primary SiNET. PET/CT was discordant in an additional 4 (11%) patients: 2 patients showed positive uptake on <sup>68</sup>Ga-DOTATOC PET/CT only, and 2 other patients showed positive uptake on <sup>18</sup>F-DOPA PET/CT only. The Ki-67 of tumors detected by <sup>18</sup>F-DOPA PET (44% and 10%) was higher than that of tumors revealed by <sup>68</sup>Ga-DOTATOC PET (1% and 2%). However, no statistical considerations were possible.

In the remaining case (3%), no primary SiNET was revealed by either PET/CT modality despite 2 SiNETs detected by pathology. Accordingly, per-region sensitivity was 94% for both techniques (Supplemental Table 1; supplemental materials are available at <http://jnm.snmjournals.org>).

According to a lesion-based analysis, 45 of 76 (59%) histologically confirmed SiNETs were detected by both modalities, 13 (17%) by <sup>68</sup>Ga-DOTATOC only, and 8 (11%) exclusively by <sup>18</sup>F-DOPA. Ten (13%) tumors were not detected by either modality. The sensitivity of <sup>68</sup>Ga-DOTATOC and <sup>18</sup>F-DOPA was, respectively, 76% and 70% ( $P = 0.275$ ) (Table 2). CgA and 5-HIAA did not differ with metabolic tumor imaging profile ( $P = 0.73$  for CgA,  $P = 0.80$  for 5-HIAA). Tumor intestinal multifocality was confirmed by histology in 8 (16%) patients. Among them, <sup>68</sup>Ga-DOTATOC and <sup>18</sup>F-DOPA PET/CT

were concordantly positive for tumor multifocality in 5 (63%) patients. In 2 patients (25%), PET/CT studies were discordantly positive (1 patient with only <sup>68</sup>Ga-DOTATOC PET/CT positivity, and 1 patient with only <sup>18</sup>F-DOPA PET/CT positivity). In the last patient, both <sup>68</sup>Ga-DOTATOC and <sup>18</sup>F-DOPA PET/CT failed to detect multifocal disease.

#### Better Performance of <sup>18</sup>F-DOPA Than of <sup>68</sup>Ga-DOTATOC PET/CT for the Evaluation of LN Metastases

*Mesenteric Lymph Nodes.* Three lymph node groups were considered (7), group 1 being lymph nodes in contact with the small bowel; group 2, in the middle of the mesentery; and group 3, at the origin of the mesenteric vessels under the pancreatic uncus. Pathologic data about nodal PET/CT positivity according to this 3-scale classification were available for 32 selected patients (Fig. 1) from Strasbourg and Beaujon University Hospitals.

On a per-region analysis, 33 of the 96 (34%) analyzed regions were considered positive by both modalities and 5 (5%) were only <sup>18</sup>F-DOPA-positive. No regions showed an exclusively <sup>68</sup>Ga-DOTATOC abnormality. <sup>18</sup>F-DOPA detected significantly more positive regions than did <sup>68</sup>Ga-DOTATOC (100% vs. 87%;  $P = 0.025$ ). Regarding subgroup analysis, 2 group 1 regions (17%) ( $P = 0.157$ ), 2 group 2 regions (10%) ( $P = 0.157$ ), and 1 group 3 region (17%) ( $P = 0.317$ ) were positive only on <sup>18</sup>F-DOPA PET/CT (Supplemental Table 1).

Per-lesion-based analysis revealed a total of 67 nodal mesenteric pathologic foci of either <sup>68</sup>Ga-DOTATOC or <sup>18</sup>F-DOPA uptake, of which 58 (87%) were common to both modalities: 14 of 16 (88%) for group 1, 33 of 36 (92%) for group 2, and 11 of 14 (79%) for group 3. No lymph node was positive only on <sup>68</sup>Ga-DOTATOC PET/CT, and 9 (14%) were positive only on <sup>18</sup>F-DOPA PET/CT. Global DR of <sup>18</sup>F-DOPA PET/CT was significantly higher than that of <sup>68</sup>Ga-DOTATOC PET/CT (100% vs. 88%,  $P = 0.003$ ). Moreover, a statistically significant difference was observed for group 3 when considered independently (100% vs. 79%,  $P = 0.046$ ) or pooled with group 2 (100% vs. 86%,  $P = 0.008$ ). Finally, DR was equivalent for both group 1 (100% vs. 88%,  $P = 0.16$ ) and group 2 (100% vs. 92%,  $P = 0.32$ ) when analyzed independently. Results are summarized in Table 2.

*Subdiaphragmatic Lymph Nodes.* On a per-region analysis, 40 (75%) patients had at least 1 subdiaphragmatic lymph node detected by <sup>68</sup>Ga-DOTATOC and <sup>18</sup>F-DOPA PET/CT; 1 (2%), by <sup>68</sup>Ga-DOTATOC only; and 4 (8%), by <sup>18</sup>F-DOPA only. In 8 (15%) patients, no pathologic subdiaphragmatic lymph nodes were detected by both modalities. DR did not significantly differ between <sup>68</sup>Ga-DOTATOC and <sup>18</sup>F-DOPA (91% vs. 98%,  $P = 0.18$ ; Supplemental Table 1).

On a per-lesion analysis, 184 subdiaphragmatic foci of lymph node pathologic uptake of either <sup>68</sup>Ga-DOTATOC or <sup>18</sup>F-DOPA were revealed, and 159 (86%) were common to both modalities. Six (3%) and 19 (10%) additional nodal abnormalities were detected by <sup>68</sup>Ga-DOTATOC and by <sup>18</sup>F-DOPA PET/CT, respectively (DR, 90% vs. 97%;  $P = 0.009$ ). Results are summarized in Table 2.

#### Detection of More Distant Metastases with <sup>18</sup>F-DOPA PET/CT Than with <sup>68</sup>Ga-DOTATOC PET/CT

On a per-region-based analysis, 28 (53%) patients showed liver uptake abnormalities. Among them, 26 (93%) showed such abnormalities on both <sup>68</sup>Ga-DOTATOC and <sup>18</sup>F-DOPA PET/CT. In the remaining 2 (7%) patients, only <sup>18</sup>F-DOPA PET revealed liver metastases ( $P = 0.346$ ) (Fig. 2). No patient had hepatic lesions detectable only on <sup>68</sup>Ga-DOTATOC PET/CT. No significant difference was seen between <sup>68</sup>Ga-DOTATOC and <sup>18</sup>F-DOPA PET/CT

**TABLE 2**  
Comparison Between  $^{68}\text{Ga}$ -DOTATOC and  $^{18}\text{F}$ -DOPA PET/CT for Primary SiNETs and Metastases (DR): Per-Lesion Analysis

Parameter	$^{68}\text{Ga}$ -DOTATOC	$^{18}\text{F}$ -DOPA	Lesions	Discordant patients	<i>P</i>
All primary SiNETs	106 (91%)	103 (88%)	117	14	0.549
Excised primary SiNETs	58 (76%)	53 (70%)	76*	12	0.275
Primary multifocality	6 (75%)	6 (75%)	8 (100%)	5	1.000
All metastases	694 (81%)	811 (95%)	855	38	<0.001
Subdiaphragmatic LN	165 (90%)	178 (97%)	184	14	0.009
Mesenteric LN	58 (88%)	67 (100%)	67	7	0.003
Mesenteric LN, group 1	14 (88%)	16 (100%)	16	2	0.157
Mesenteric LN, group 2	33 (92%)	36 (100%)	36	3	0.317
Mesenteric LN, group 3	11 (79%)	15 (100%)	15	3	0.046
Liver	312 (87%)	353 (99%)	357	12	<0.001
Peritoneum	53 (47%)	107 (96%)	112	12	<0.001
Lung	13 (50%)	26 (100%)	26	4	<0.001
Bone	98 (84%)	100 (86%)	116	7	0.732
Supradiaphragmatic LN	30 (81%)	28 (76%)	37	10	0.617
Left supraclavicular LN	23 (100%)	19 (83%)	23	3	0.046

\*76 primary SiNETs detected at histology (sensitivity) in 37 surgically treated patients.  
LN = lymph nodes.

for the remaining anatomic regions (i.e., peritoneum, abdominal lymph nodes, left-sided supraclavicular lymph nodes, supradiaphragmatic lymph nodes [excluding the left supraclavicular region], lung/pleura, bones, and other metastatic sites). Results are summarized in Supplemental Table 1.

On a per-lesion-based analysis, 671 foci of pathologic uptake on either  $^{68}\text{Ga}$ -DOTATOC or  $^{18}\text{F}$ -DOPA indicating extranodal metastases were detected (Table 2). Among them, 491 (73%) were common to both modalities, 38 (6%) were detected on  $^{68}\text{Ga}$ -DOTATOC only, and 142 (21%) were detected on  $^{18}\text{F}$ -DOPA

only.  $^{18}\text{F}$ -DOPA had a better global DR for detection of distant metastases than did  $^{68}\text{Ga}$ -DOTATOC (94% vs. 79%,  $P < 0.001$ ).  $^{18}\text{F}$ -DOPA PET/CT performed better than  $^{68}\text{Ga}$ -DOTATOC PET/CT for the detection of liver metastases (98.9% vs. 87.4%,  $P < 0.001$ ), peritoneal carcinomatosis (95.5% vs. 47.3%,  $P < 0.001$ ), and lung metastases (100% vs. 50.0%,  $P < 0.001$ ).  $^{68}\text{Ga}$ -DOTATOC PET/CT detected significantly more left supraclavicular lymph nodes than did  $^{18}\text{F}$ -DOPA (100% vs. 82.6%,  $P = 0.046$ ). Finally, no statistically significant difference was observed for bone metastases and supradiaphragmatic lymph nodes.

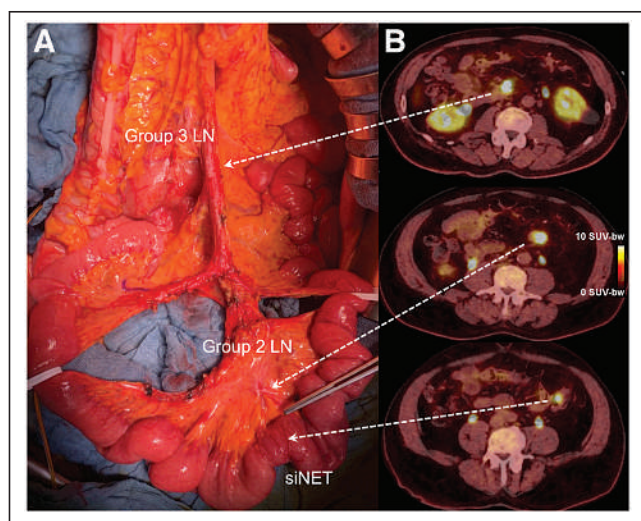


**FIGURE 1.** Correlation of surgical exploration and  $^{18}\text{F}$ -DOPA PET/CT findings in patient with grade 1 SiNETs and metastatic mesenteric lymph nodes of groups 2 and 3 according to Pasquer et al. (7).

#### Imaging Protocol, Ki-67, Tumor Grade, and Biologic Markers

Thirty-one and 22 patients underwent  $^{68}\text{Ga}$ -DOTATOC before  $^{18}\text{F}$ -DOPA PET/CT and vice versa, respectively. In both cases,  $^{18}\text{F}$ -DOPA PET revealed more lesions than did  $^{68}\text{Ga}$ -DOTATOC PET ( $P = 0.002$ ,  $^{18}\text{F}$ -DOPA first;  $P < 0.001$ ,  $^{68}\text{Ga}$ -DOTATOC first). The number of discordant lesions did not correlate with the time between the 2 PET studies ( $\rho = 0.286$ ;  $P = 0.081$ ), suggesting a minor influence of the imaging sequence on final PET/CT results.

No correlation was shown between Ki-67 index and the number of discordant lesions in the entire population ( $\rho = 0.06$ ;  $P = 0.67$ ) and only in patients with discordant PET results ( $\rho = 0.23$ ;  $P = 0.17$ ).

The lesion-based detection rate of  $^{18}\text{F}$ -DOPA PET was better than that of  $^{68}\text{Ga}$ -DOTATOC PET regardless of the tumor grade (grade 1,  $P < 0.001$ ; grade 2,  $P < 0.001$ ; grade 3,  $P < 0.004$ ) and patient treatment (long-acting somatostatin analogs,  $P < 0.001$ ; no treatment,  $P < 0.001$ ).

Quantitative values of serum CgA and urinary 5-HIAA were available for 35 (66%) and 26 (49%) patients, respectively. CgA and 5-HIAA levels were increased in 28 and 14 patients, respectively. A moderate statistically significant correlation was found between the

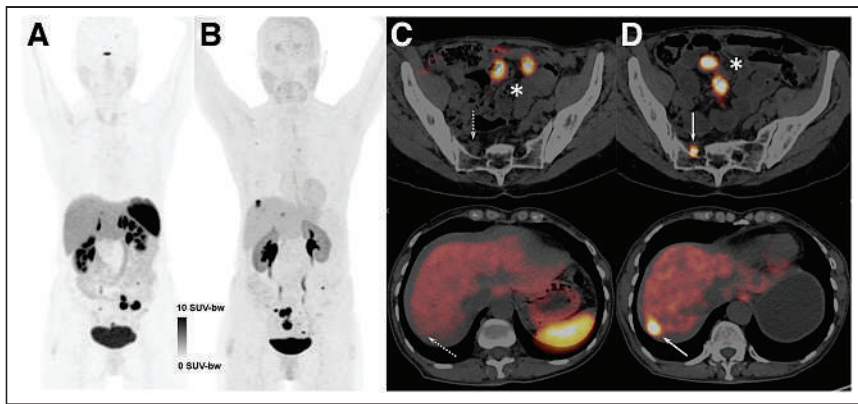


**FIGURE 2.** Head-to-head comparison between  $^{68}\text{Ga}$ -DOTATOC (A and C) and  $^{18}\text{F}$ -DOPA PET/CT (B and D) in oligometastatic patient with bifocal SiNETs (\*).  $^{68}\text{Ga}$ -DOTATOC PET/CT failed to detect hepatic and peritoneal metastases (dotted arrows), visible only on  $^{18}\text{F}$ -DOPA PET/CT (solid arrows).  $\text{SUV-bw} = (\text{PET image pixel value}) * (\text{weight in grams}) / (\text{injected dose})$ .

total number of lesions detected by either  $^{68}\text{Ga}$ -DOTATOC or  $^{18}\text{F}$ -DOPA and the level of CgA ( $\rho$  for DOTATOC = 0.32,  $P = 0.003$ ;  $\rho$  for DOPA = 0.36,  $P = 0.016$ ) and 5-HIAA ( $\rho$  for DOTATOC = 0.34,  $P = 0.043$ ;  $\rho$  for DOPA = 0.44,  $P = 0.013$ ).

## DISCUSSION

Only a few studies have compared  $^{68}\text{Ga}$ -DOTATOC and  $^{18}\text{F}$ -DOPA PET/CT in patients with SiNETs. Before further considerations, it is necessary to distinguish diagnostic from theragnostic applications.  $^{68}\text{Ga}$ -somatostatin analog PET/CT remains mandatory for selecting candidates for PRRT. By contrast, the choice of the most appropriate diagnostic imaging modality should rely on diagnostic performance. Thus, there is no reason to disqualify  $^{18}\text{F}$ -DOPA PET/CT in a purely diagnostic setting (13).

In our series,  $^{68}\text{Ga}$ -DOTATOC and  $^{18}\text{F}$ -DOPA PET/CT identified at least 1 primary SiNET in 86% of cases, achieving a similar per-lesion sensitivity of 76% and 70%, respectively. Several reasons may decrease the detectability of small primaries on PET/CT, such as the partial-volume effect and bowel peristalsis. The sensitivity of conventional presurgical diagnostic investigations remains suboptimal, and intraoperative palpation of the entire small intestine should routinely be performed to improve the detection of multifocal primary SiNETs (14).

Resection of at least 8 lymph nodes is advocated (when possible), along with resection of the primary SiNET (6,15). A systematic extensive nodal resection including the retropancreatic area around the origin of the superior mesenteric vessels has been proposed to prevent unresectable local recurrence (3,16). Moreover, up to 67% of patients could present with skip metastases, of which 19% are retropancreatic (group 3), without nodal invasion around the mesenteric vessels (7). In our study, the DR of subdiaphragmatic metastatic lymph nodes during initial staging was significantly higher for  $^{18}\text{F}$ -DOPA than for  $^{68}\text{Ga}$ -SSTR PET/CT. Moreover, when we focused exclusively on mesenteric lymph node metastases,  $^{18}\text{F}$ -DOPA PET/CT detected more positive regions (groups 1–3) and metastatic lymph nodes than did  $^{68}\text{Ga}$ -DOTATOC PET/CT ( $P = 0.005$  and  $0.003$ , respectively). Noteworthy, a statistically significant difference ( $P = 0.046$ ) was also shown for the detection of group 3 pathologic lymph nodes. This result appears to be novel, and given its potential therapeutic impact on patients with SiNETs, it will need to be confirmed by prospective clinical trials.

$^{18}\text{F}$ -DOPA performed better than  $^{68}\text{Ga}$ -DOTATOC PET/CT for the detection of lesions in the liver ( $P < 0.001$ ), peritoneum ( $P < 0.001$ ), and lung ( $P < 0.001$ ). Similar results have been recently reported by our group for the retrospective comparison of  $^{68}\text{Ga}$ -DOTATOC and  $^{18}\text{F}$ -DOPA PET/CT in a series of 41 patients with well-differentiated SiNETs during the postsurgical follow-up (17).  $^{18}\text{F}$ -DOPA PET/CT was found to have a significantly higher metastatic DR than did  $^{68}\text{Ga}$ -DOTATOC PET/CT ( $P < 0.001$ ). Of 605 lesions, 122 (20%) were revealed exclusively by  $^{18}\text{F}$ -DOPA PET/CT. The liver was the region with the highest number of discordant results. Moreover, a trend toward significance ( $P = 0.07$ ) was shown for the detection of bone metastases, in favor of  $^{18}\text{F}$ -DOPA PET/CT. In the recent study of Dele-

val et al. (18),  $^{18}\text{F}$ -DOPA PET/CT detected bone metastases in 46 of 155 (29.7%) SiNET patients, with negative prognostic impact.

Ansquer et al. (19) retrospectively compared  $^{18}\text{F}$ -DOPA and  $^{68}\text{Ga}$ -DOTANOC PET/CT in 30 patients with SiNETs. PET/CT was performed for primary staging in 9 patients, including 4 patients before surgery and 5 after surgical removal of the primary SiNET. The remaining 21 patients were investigated during regular follow-up. In total, 221 lesions were detected. Even in this case,  $^{18}\text{F}$ -DOPA PET/CT identified significantly more lesions than did  $^{68}\text{Ga}$ -DOTANOC PET/CT, with a sensitivity of 95.5% and 88.2%, respectively ( $P < 0.0001$ ).  $^{18}\text{F}$ -DOPA PET/CT detected more lesions than did  $^{68}\text{Ga}$ -DOTANOC PET/CT in 9 patients (30%) and revealed 22 additional lesions from variable locations. Concerning the detection of primary SiNETs, both imaging methods showed excellent sensitivity, with detection in all 14 patients without previous surgery. When considering only liver metastases visualized by both radiotracers, the ratio of tumor  $\text{SUV}_{\text{max}}$  to liver  $\text{SUV}_{\text{mean}}$  was higher for  $^{18}\text{F}$  DOPA than for  $^{68}\text{Ga}$ -DOTANOC for 30 of 46 lesions (62.5%). These findings could explain the better sensitivity of  $^{18}\text{F}$ -DOPA for liver metastasis detection. Perhaps the upcoming clinical availability of SSTR antagonists will allow better detection of lesions (20), warranting further head-to-head comparative studies. In these 2 comparative reports, different  $^{68}\text{Ga}$ -SSTR analogs were used for PET/CT imaging (i.e., DOTATOC and DOTANOC), but the results always remained in favor of  $^{18}\text{F}$ -DOPA. The choice of the SSTR subtype remains probably marginal without explaining the diagnostic difference between  $^{18}\text{F}$ -DOPA and  $^{68}\text{Ga}$ -SSTR PET/CT (21).

Veenstra et al. (22) retrospectively compared the detection rates of  $^{18}\text{F}$ -DOPA and  $^{68}\text{Ga}$ -DOTATOC PET/CT for the localization of primary tumor and metastases in 45 patients with NETs, including 23 (51%) SiNETs.  $^{18}\text{F}$ -DOPA revealed significantly more lesions than did  $^{68}\text{Ga}$ -DOTATOC in 16 SiNET patients (70%) with high circulating biomarker levels. The relationship between tumor markers, clinical features, and primary tumor location has been previously highlighted to optimize radiotracer selection in patients with NETs (23,24).

We acknowledge that the present study like previous ones (17,19,22), was not tailored for assessing the potential therapeutic impact of the detection of additional sites on  $^{18}\text{F}$ -DOPA PET/CT compared with SSTR PET/CT. An additional limitation of our study was the lack of an objective gold standard as an imaging comparator for all pathologic uptake findings. However, histologic proof of all metastatic lesions was neither reasonable nor feasible.

## CONCLUSION

<sup>18</sup>F-DOPA PET/CT detected more lesions than did <sup>68</sup>Ga-DOTATOC PET/CT in the studied patients. Our results provide a great impetus toward the use of <sup>18</sup>F-DOPA PET/CT in the evaluation of SiNETs at initial diagnosis or prior surgery. We believe that the respective role of <sup>18</sup>F-DOPA and <sup>68</sup>Ga-DOTATOC PET/CT should be discussed according to the expected results in terms of disease staging and treatment selection.

## DISCLOSURE

No potential conflict of interest relevant to this article was reported.

## KEY POINTS

**QUESTION:** Which is the most sensitive nuclear imaging modality for tumor metastasis assessment at initial staging or presurgical work-up in patients with SiNETs?

**PERTINENT FINDINGS:** <sup>18</sup>F-DOPA PET/CT detected more lesions than did <sup>68</sup>Ga-DOTATOC PET/CT in the studied patients. When clinically available, <sup>18</sup>F-DOPA should be considered the first-choice PET tracer for exhaustive metastasis assessment.

**IMPLICATIONS FOR PATIENT CARE:** Our results encourage the use of <sup>18</sup>F-DOPA PET/CT in the evaluation of SiNETs at initial diagnosis or prior surgery. The respective role of <sup>18</sup>F-DOPA and <sup>68</sup>Ga-DOTATOC PET/CT should be discussed according to the expected results in terms of disease staging and treatment selection.

## REFERENCES

- Niederle MB, Hackl M, Kaserer K, Niederle B. Gastroenteropancreatic neuroendocrine tumours: the current incidence and staging based on the WHO and European Neuroendocrine Tumor Society classification: an analysis based on prospectively collected parameters. *Endocr Relat Cancer*. 2010;17:909–918.
- Howe JR, Cardona K, Fraker DL, et al. The surgical management of small bowel neuroendocrine tumors: consensus guidelines of the North American Neuroendocrine Tumor Society. *Pancreas*. 2017;46:715–731.
- Van Den Heede K, Chidambaram S, Van Slycke S, et al. Effect of primary tumour resection without curative intent in patients with metastatic neuroendocrine tumours of the small intestine and right colon: meta-analysis. *Br J Surg*. 2022;109:191–199.
- Zaidi MY, Lopez-Aguilar AG, Dillhoff M, et al. Prognostic role of lymph node positivity and number of lymph nodes needed for accurately staging small-bowel neuroendocrine tumors. *JAMA Surg*. 2019;154:134–140.
- Cives M, Anaya DA, Soares H, Coppola D, Strosberg J. Analysis of postoperative recurrence in stage I-III midgut neuroendocrine tumors. *J Natl Cancer Inst*. 2018;110:282–289.
- Landry CS, Lin HY, Phan A, et al. Resection of at-risk mesenteric lymph nodes is associated with improved survival in patients with small bowel neuroendocrine tumors. *World J Surg*. 2013;37:1695–1700.
- Pasquer A, Walter T, Rousset P, et al. Lymphadenectomy during small bowel neuroendocrine tumor surgery: the concept of skip metastases. *Ann Surg Oncol*. 2016;23:804–808.
- Lardièrre-Deguelle S, de Mestier L, Appéré F, et al. Toward a preoperative classification of lymph node metastases in patients with small intestinal neuroendocrine tumors in the era of intestinal-sparing surgery. *Neuroendocrinology*. 2016;103:552–559.
- Deroose CM, Hindié E, Kebebew E, et al. Molecular imaging of gastroenteropancreatic neuroendocrine tumors: current status and future directions. *J Nucl Med*. 2016;57:1949–1956.
- Piccardo A, Fiz F, Bottoni G, Ugolini M, Noordzij W, Trimboli P. Head-to-head comparison between <sup>18</sup>F-DOPA PET/CT and <sup>68</sup>Ga-DOTA peptides PET/CT in detecting intestinal neuroendocrine tumours: a systematic review and meta-analysis. *Clin Endocrinol (Oxf)*. 2021;95:595–605.
- Bozkurt MF, Virgolini I, Balogova S, et al. Guideline for PET/CT imaging of neuroendocrine neoplasms with <sup>68</sup>Ga-DOTA-conjugated somatostatin receptor targeting peptides and <sup>18</sup>F-DOPA. *Eur J Nucl Med Mol Imaging*. 2017;44:1588–1601.
- Nagtegaal ID, Odze RD, Klimstra D, et al. The 2019 WHO classification of tumours of the digestive system. *Histopathology*. 2020;76:182–188.
- Imperiale A, Meuter L, Pacak K, Taïeb D. Imaging of small intestine neuroendocrine neoplasms: is SSTR PET the Holy Grail? *J Nucl Med*. 2021;62:1347–1348.
- Pasquer A, Walter T, Milot L, Hervieu V, Poncet G. Principles of surgical management of small intestinal NET. *Cancers (Basel)*. 2021;13:5473.
- Niederle B, Pape U-F, Costa F, et al. ENETS consensus guidelines update for neuroendocrine neoplasms of the jejunum and ileum. *Neuroendocrinology*. 2016;103:125–138.
- Pasquer A, Walter T, Hervieu V, et al. Surgical management of small bowel neuroendocrine tumors: specific requirements and their impact on staging and prognosis. *Ann Surg Oncol*. 2015;22(suppl 3):S742–S749.
- Ouvrard E, Chevalier E, Addeo P, et al. Intraindividual comparison of <sup>18</sup>F-FDOPA and <sup>68</sup>Ga-DOTATOC PET/CT detection rate for metastatic assessment in patients with ileal neuroendocrine tumours. *Clin Endocrinol (Oxf)*. 2021;94:66–73.
- Deleval N, Pesque L, Dieudonné A, et al. Prognostic impact of bone metastases detected by <sup>18</sup>F-DOPA PET in patients with metastatic midgut neuroendocrine tumors. *Eur Radiol*. 2021;31:4166–4174.
- Ansquer C, Touchefeu Y, Faivre-Chauvet A, et al. Head-to-head comparison of <sup>18</sup>F-DOPA PET/CT and <sup>68</sup>Ga-DOTANOC PET/CT in patients with midgut neuroendocrine tumors. *Clin Nucl Med*. 2021;46:181–186.
- Zhu W, Cheng Y, Wang X, et al. Head-to-head comparison of <sup>68</sup>Ga-DOTA-JR11 and <sup>68</sup>Ga-DOTATATE PET/CT in patients with metastatic, well-differentiated neuroendocrine tumors: a prospective study. *J Nucl Med*. 2020;61:897–903.
- Poeppel TD, Binse I, Petersenn S, et al. <sup>68</sup>Ga-DOTATOC versus <sup>68</sup>Ga-DOTATATE PET/CT in functional imaging of neuroendocrine tumors. *J Nucl Med*. 2011;52:1864–1870.
- Veenstra EB, de Groot DJA, Brouwers AH, Walenkamp AME, Noordzij W. Comparison of <sup>18</sup>F-DOPA versus <sup>68</sup>Ga-DOTATOC as preferred PET imaging tracer in well-differentiated neuroendocrine neoplasms. *Clin Nucl Med*. 2021;46:195–200.
- Fiebrich H-B, de Jong JR, Kema IP, et al. Total <sup>18</sup>F-dopa PET tumour uptake reflects metabolic endocrine tumour activity in patients with a carcinoid tumour. *Eur J Nucl Med Mol Imaging*. 2011;38:1854–1861.
- Imperiale A, Rust E, Gabriel S, et al. <sup>18</sup>F-fluorodihydroxyphenylalanine PET/CT in patients with neuroendocrine tumors of unknown origin: relation to tumor origin and differentiation. *J Nucl Med*. 2014;55:367–372.

---

---

# First-in-Humans PET Imaging of Tissue Factor in Patients with Primary and Metastatic Cancers Using $^{18}\text{F}$ -labeled Active-Site Inhibited Factor VII ( $^{18}\text{F}$ -ASIS): Potential as Companion Diagnostic

Mathias Loft<sup>\*1</sup>, Camilla Christensen<sup>\*1</sup>, Malene M. Clausen<sup>1,2</sup>, Esben A. Carlsen<sup>1</sup>, Carsten P. Hansen<sup>3</sup>, Niels Kroman<sup>4</sup>, Seppo W. Langer<sup>2,5</sup>, Claus Høgdall<sup>6</sup>, Jacob Madsen<sup>1</sup>, Nic Gillings<sup>1</sup>, Carsten H. Nielsen<sup>1,7</sup>, Thomas L. Klausen<sup>1</sup>, Søren Holm<sup>1</sup>, Annika Loft<sup>1</sup>, Anne K. Berthelsen<sup>1</sup>, and Andreas Kjaer<sup>1</sup>

<sup>1</sup>Department of Clinical Physiology and Nuclear Medicine & Cluster for Molecular Imaging, Copenhagen University Hospital – Rigshospitalet & Department of Biomedical Sciences, University of Copenhagen, Denmark; <sup>2</sup>Department of Oncology, Copenhagen University Hospital – Rigshospitalet, Denmark; <sup>3</sup>Department of Surgery, Copenhagen University Hospital – Rigshospitalet, Denmark; <sup>4</sup>Department of Breast Surgery, Copenhagen University Hospital – Rigshospitalet, Denmark; <sup>5</sup>Department of Clinical Medicine, University of Copenhagen, Denmark; <sup>6</sup>Department of Gynecology, Copenhagen University Hospital – Rigshospitalet, Denmark and <sup>7</sup>Minerva Imaging ApS, Denmark

---

Tissue factor (TF) expression in cancers correlates with poor prognosis. Recently, the first TF-targeted therapy was approved by the U.S. Food and Drug Administration for cervical cancer. To unfold the potential of TF-targeted therapies, correct stratification and selection of patients eligible for treatments may become important for optimization of patient outcomes. TF-targeted PET imaging based on  $^{18}\text{F}$ -radiolabeled active-site inhibited versions of the TF natural ligand coagulation factor VII ( $^{18}\text{F}$ -ASIS) has in preclinical models convincingly demonstrated its use for noninvasive quantitative measurements of TF expression in tumor tissue.  $^{18}\text{F}$ -ASIS PET imaging thus has the potential to act as a diagnostic companion for TF-targeted therapies in the clinical setting.

**Methods:** In this first-in-humans trial, we included 10 cancer patients (4 pancreatic, 3 breast, 2 lung, and 1 cervical cancer) for  $^{18}\text{F}$ -ASIS PET imaging. The mean and SD of administered  $^{18}\text{F}$ -ASIS activity was  $157 \pm 35$  MBq (range, 93–198 MBq). PET/CT was performed after 1, 2, and 4 h. The primary objectives were to establish the safety, biodistribution, pharmacokinetics, and dosimetry of  $^{18}\text{F}$ -ASIS. Secondary objectives included quantitative measurements of SUVs in tumor tissue with PET and evaluation of the correlation (Pearson correlation) between tumor SUV<sub>max</sub> and ex vivo TF expression in tumor tissue. **Results:** Administration of  $^{18}\text{F}$ -ASIS was safe, and no adverse events were observed. No clinically significant changes in vital signs, electrocardiograms, or blood parameters were observed after injection of  $^{18}\text{F}$ -ASIS. Mean  $^{18}\text{F}$ -ASIS plasma half-life was  $3.2 \pm 0.6$  h, and the radiotracer was predominantly excreted in the urine. For injection activity of 200 MBq of  $^{18}\text{F}$ -ASIS, effective whole-body dose was 4 mSv and no prohibitive organ-specific absorbed doses were found. Heterogeneous radiotracer uptake was observed across patients and within tumors. We found a trend of a positive correlation between tumor SUV<sub>max</sub> and ex vivo TF expression ( $r = 0.84$ ,  $P = 0.08$ ,  $n = 5$ ). **Conclusion:**  $^{18}\text{F}$ -ASIS can be safely administered to cancer patients for PET imaging of TF expression in tumors. The trial marks the first test of a TF-targeted PET radiotracer in humans (first-in-class). The findings represent important first steps toward clinical implementation of  $^{18}\text{F}$ -ASIS PET imaging of TF expression.

**Key Words:** active site inhibited factor VII (ASIS); tissue factor; PET/CT; first-in-humans; phase I clinical trial

**J Nucl Med 2022; 63:1871–1879**  
DOI: 10.2967/jnumed.122.264068

---

**P**ersonalized medicine based on targeted therapies is predicted to shape the future of oncology in the coming decades. An emerging oncologic target is the transmembrane glycoprotein tissue factor (TF) that functions as the main initiator of the extrinsic coagulation cascade (1). In addition to its role in coagulation, TF expression is also linked to several cancer hallmarks including tumor growth, angiogenesis, and metastatic potential (2,3). Abundant TF expression has been reported in most solid tumors, and TF expression levels are associated with disease stage and overall survival in pancreatic cancer (4), cervical cancer (5), non-small cell lung cancer (6–8), and breast cancer (9).

TF-targeted therapies are currently under translation into the clinical treatment of cancer patients. In 2019, reports from the first phase 1–2 clinical trial of the TF-targeted antibody–drug conjugate tivotumab vedotin in patients with recurrent, advanced, or metastatic solid tumors showed an objective tumor response in 16% of the patients (10). Recently, a 24% response rate was demonstrated in a phase 2 trial in previously treated recurrent or metastatic cervical cancer patients (11), and the U.S. Food and Drug Administration approved the therapy in September 2021 for this indication (12).

With the emergence of TF-targeted therapies, robust methods for quantifying TF expression in primary tumors and metastases are needed for efficient patient selection and stratification. Whole-body PET imaging can reduce the risk of sampling error from within tumor and between tumor heterogeneity seen in ex vivo analyses of tumor biopsies (13). Hence, PET imaging of TF expression is attractive as a companion imaging diagnostic agent for identifying patients eligible for TF-targeted therapies and may have the potential to increase response rates.

---

Received Mar. 4, 2022; revision accepted May 10, 2022.

For correspondence or reprints, contact Andreas Kjaer (akjaer@sund.ku.dk).

\*Contributed equally to this work.

Published online May 19, 2022.

COPYRIGHT © 2022 by the Society of Nuclear Medicine and Molecular Imaging.

We have developed a TF-targeted PET radiotracer based on the natural ligand, factor VII (FVII). When vascular injury occurs, FVII is activated to FVIIa by the exposed TF on the endothelial cells and sets off the coagulation cascade (1). Through inhibition of the active site in FVIIa, the resulting active-site inhibited FVIIa (ASIS) binds to TF with an affinity approximately 5-fold higher than FVIIa without activating the coagulation system (14). For TF-targeted PET imaging, ASIS is radiolabeled with *N*-succinimidyl 4-[<sup>18</sup>F]fluorobenzoate (<sup>18</sup>F-SFB) to form <sup>18</sup>F-ASIS (15). Preclinical studies with xenograft tumor-bearing mice have demonstrated high and specific <sup>18</sup>F-ASIS uptake in tumor tissue that reflects the level of TF expression determined *ex vivo* (16). Spurred on by the promising preclinical results, we moved forward with the clinical translation of <sup>18</sup>F-ASIS PET imaging to cancer patients.

Here we report our first-in-humans trial on <sup>18</sup>F-ASIS PET in cancer patients. The primary objectives were to demonstrate the safety, biodistribution, pharmacokinetics, and dosimetry of <sup>18</sup>F-ASIS. As a secondary objective, we investigated radiotracer accumulation in tumors with PET and its correlation with TF expression in *ex vivo* analyses of matched tumor samples.

## MATERIALS AND METHODS

### Study Design

We performed the study as an open-label, phase 1 clinical trial approved by the Danish Medicines Agency (EudraCT no. 2015-005583-42) and the Ethical Committee of the Capital Region of Denmark (protocol H-18015477). Patients signed a written informed consent form before inclusion. The study was conducted in accordance with the requirements for good clinical practice including independent monitoring by the Good Clinical Practice unit of Copenhagen University Hospital, and the trial was registered at ClinicalTrials.gov (NCT03790423). Eligible patients were 18 y or older; diagnosed with breast, lung, pancreatic, cervical, or ovarian cancer; and capable of understanding the patient information in Danish and giving full informed consent. Exclusion criteria were pregnancy/breastfeeding, weight above 140 kg, or history of allergic reaction attributable to compounds of similar chemical or biologic composition to <sup>18</sup>F-ASIS.

From January to November 2019, after giving informed consent, 10 patients with pancreatic cancer (*n* = 4), breast cancer (*n* = 3), lung cancer (*n* = 2), and cervical cancer (*n* = 1) were included in the study and referred to a <sup>18</sup>F-ASIS PET/CT imaging series. The mean and SD of the administered mass of <sup>18</sup>F-ASIS was 0.67 ± 0.12 mg (range, 0.41–0.84 mg). The mean administered activity was 157 ± 35 MBq (range, 93–198 MBq), yielding a mean specific activity of 245 ± 84 MBq/mg (range, 126–412 MBq/mg) at the time of injection. Sequential whole-body PET/CT imaging was performed 1, 2, and 4 h after injection of <sup>18</sup>F-ASIS. Patients were monitored for changes in vital signs, electrocardiograms, and blood parameters before and after radiotracer administration. Adverse events were registered up to 48 h after administration of <sup>18</sup>F-ASIS and coded according to the Common Terminology Criteria for Adverse Events (version 5.0). Blood sampling and urine collection was performed for pharmacokinetic analyses. The study design is summarized in Figure 1. A detailed study description is provided in the supplemental information (supplemental materials are available at <http://jnm.snmjournals.org>). When available, tumor biopsies or surgically excised primary tumor tissue and local lymph nodes were collected, and TF expression was analyzed with immunohistochemistry and enzyme-linked immunosorbent assay (ELISA).

### Inhibition of FVIIa

FVIIa (Novo Nordisk A/S) was dissolved in water and 5 equivalents of *D*-Phe-Phe-Arg-chloromethyl ketone (fFR-cmk; Bachem) were added for inhibition of FVIIa to produce ASIS. After inhibition (1 h, 4°C), excess of inhibitor was removed by dialysis (Slide-a-lyzer,

MWCO 10; Thermo Fisher Scientific) in 50 mM *N*-2-hydroxyethylpiperazine-*N'*-2-ethanesulfonic acid (HEPES, 150 mM NaCl, 10 mM CaCl<sub>2</sub>, pH 7.4; Sigma-Aldrich) overnight. The content of fFR-cmk and the concentration of ASIS were analyzed by high-pressure liquid chromatograph (HPLC) using an Aeris C4 column (3.6 μm, 150 × 4.6 mm; Phenomenex) and 1.5 mL/min solvent flow with a gradient method: 0–2 min 17% B, 2–5 min 60% B, 5–6 min 60% B, 6–7 min 17% B, 7–8 min 17% B with solvent phases 0.1% trifluoroacetic acid (TFA) in H<sub>2</sub>O (A) and 0.1% TFA in acetonitrile (MeCN) (B). Aliquots (500 μL) were stored at –80°C before labeling.

### Synthesis of <sup>18</sup>F-ASIS

ASIS was labeled with the <sup>18</sup>F-containing prosthetic group <sup>18</sup>F-SFB. <sup>18</sup>F-SFB was produced in a 3-step, 1-pot synthesis on a qualified Tracer-Lab<sub>MX</sub> module (GE Healthcare) with a final solid-phase extraction purification in 80% MeCN. <sup>18</sup>F-SFB was subsequently evaporated to dryness in a single vial. ASIS (500 μL) was added to the vial for labeling at room temperature for 30 min followed by purification with a PD10 column (Sigma-Aldrich) into formulation buffer (10 mM GlyGly, 150 mM NaCl, and 10 mM CaCl<sub>2</sub>, pH 7.5). The final product was sterile-filtered in a laminar airflow bench, and a sample was drawn for quality control. The shelf-life of <sup>18</sup>F-ASIS was evaluated up to 4 h after the end of synthesis.

### Quality Control of <sup>18</sup>F-ASIS

All analytic methods were validated according to the International Council of Harmonization guidelines (17). The radiochemical purity, unspecified <sup>18</sup>F-labeled impurities, and <sup>18</sup>F-fluoride were determined with radio-HPLC, and the content of ASIS was determined by ultraviolet-detector HPLC, both using the same gradients as described in the “Inhibition of FVIIa” section. Residual MeCN from the <sup>18</sup>F-SFB synthesis was determined by gas chromatography. Color spot tests were used to determine the content of tetrabutylammonium hydrogen carbonate and HEPES in the final product. The immunoreactivity of <sup>18</sup>F-ASIS was determined by Lindmo assay using a high TF-expressing cell line (BxPC-3, CRL-1687; American Type Culture Collection) according to previously described procedures (18). Quality control parameters are summarized in Supplemental Table 1.

### Plasma and Urine Pharmacokinetics

The activity of urine, whole blood, and plasma samples was measured on a Cobra II TM γ-Counter (Packard). The plasma samples were prepared from whole-blood samples by centrifugation (3,500 rpm, 4 min) and filtering of the supernatant plasma through a 0.45-μm syringe filter. The radiotracer plasma half-life was determined from the activity concentrations in plasma decay-corrected to the blood sampling time points (approximately 1, 2, and 4 h after injection). The accumulated percentages of excreted radiotracer in urine were determined from the ratio between the accumulated activity in urine and the injected radiotracer activity dose decay-corrected to the urine sampling time points (approximately 1, 2, and 5 h after injection). Metabolites in plasma and urine samples were analyzed by radio-HPLC with a Posi-RAM Module (LabLogic) 4 using the same gradients as described in the “Inhibition of FVIIa” section.

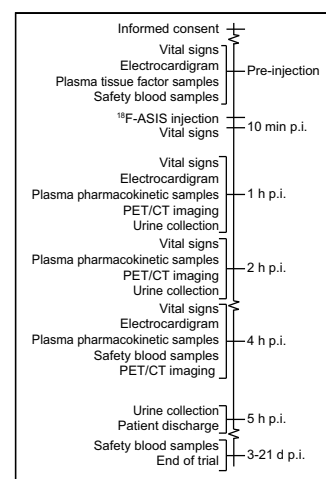


**FIGURE 1.** Schematic overview of study design. p.i. = postinjection.

**TABLE 1**  
Patient Characteristics

Characteristic	Patient									
	1	2	3	4	5	6	7	8	9	10
Sex	Female	Female	Female	Female	Male	Female	Female	Female	Female	Female
Age (y)	88	67	69	79	65	58	54	59	43	73
Primary tumor	Pancreas	Pancreas	Pancreas	Pancreas	Lung†	Lung	Breast	Breast	Cervix	Breast
Type [stage]*	PT: DAC	PT: PAC [pT2pN2M0]	PT†: DAC	PT: DAC [pT2N0M0]	PT†: AC MET: AC	PT: AC [pT2bN0M0]	PT: IDC (HER2+1/ ER100%), SN without MET (0/1 LN), [M0]	PT: ILC (HER2+1/ ER100%), SN without MET (0/2 LN), [M0]	PT: SCC	PT†: ISPC SN with micro MET (1/2 LN), [M0]
Prior cancer treatment	None	None	CTX	None	Surgery and CTX	CTX	None	None	None	None
Concomitant cancer treatment	None	None	None	None	CTX	RDX	None	None	None	None

\*Pathology TNM staging is reported in square brackets when available.

†Primary tumor removed.

‡Two separate tumors without connection; Tumor 1: HER2+1/ER100%; Tumor 2: HER2-/ER100%.

AC = adenocarcinoma; CTX = chemotherapy; DAC = ductal adenocarcinoma; ER = estrogen receptor; HER2 = human epidermal growth factor receptor 2; IDC = invasive ductal carcinoma; ILC = invasive lobular carcinoma; ISPC = invasive solid papillary carcinoma; LN = lymph nodes; MET = metastases; PAC = pancreaticobiliary adenocarcinoma; PT = primary tumor; RDX = radiation therapy; SCC = squamous cell carcinoma; SN = sentinel nodes.

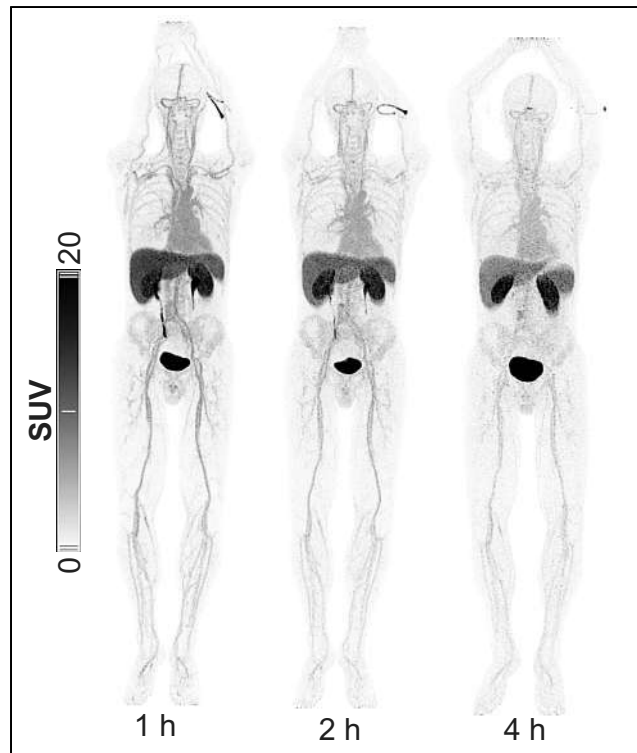


**FIGURE 2.** Representative maximum-intensity projection showing distribution of  $^{18}\text{F}$ -ASIS for patient 5.

### Image Acquisition

Images were acquired on a Biograph 128 mCT PET/CT (Siemens Healthineers) with PET acquisition commenced 1, 2, and 4 h after injection of  $^{18}\text{F}$ -ASIS. Unless otherwise contraindicated, patients were injected with intravenous iodine-based contrast (Optiray [Guerbet] 300 mg I/mL, 70–100 mL, injection rate 1.5–2.5 mL/s) using an automated Medrad Stellant injection system (Bayer). Detailed descriptions of the PET and CT imaging parameters (including acquisition times and reconstruction parameters) are provided in the supplemental materials.

### Biodistribution and Dosimetry

Dosimetry was based on the PET images ( $n = 10$ ) supplemented with sampled urine data ( $n = 8$ ). For each patient, organ, and time point, tissue activity concentration was calculated as the average of the mean values from 3 volumes of interests drawn in the following organs/regions: adrenal, bone, brain, blood pool, ascending and descending colon, heart wall, kidney, liver, lung, red marrow (L3–L5 vertebrae), small intestines, spleen, stomach contents, and thyroid using MIRADA DBx, version 1.2.0 (Mirada Medical). OLINDA/EXM 2.0 software (Vanderbilt University and HERMES Medical Solutions) was used for calculation of dosimetry parameters using the organ masses of the OLINDA male adult phantom (19,20) and the absorbed doses for organs and effective dose with tissue-weighting factors according to International Commission on Radiological Protection (ICRP) 103 (21). A detailed description of the dosimetry calculation and biodistribution data processing is provided in the supplemental materials.

### Image Analysis

The PET/CT images were evaluated by a highly experienced team consisting of a nuclear medicine specialist and a radiologist. Size measurements of the primary tumor and metastases (if any) were performed on the diagnostic CT. In tumor lesions identified on the CT, radiotracer accumulation was measured on the PET images and reported as SUVs.

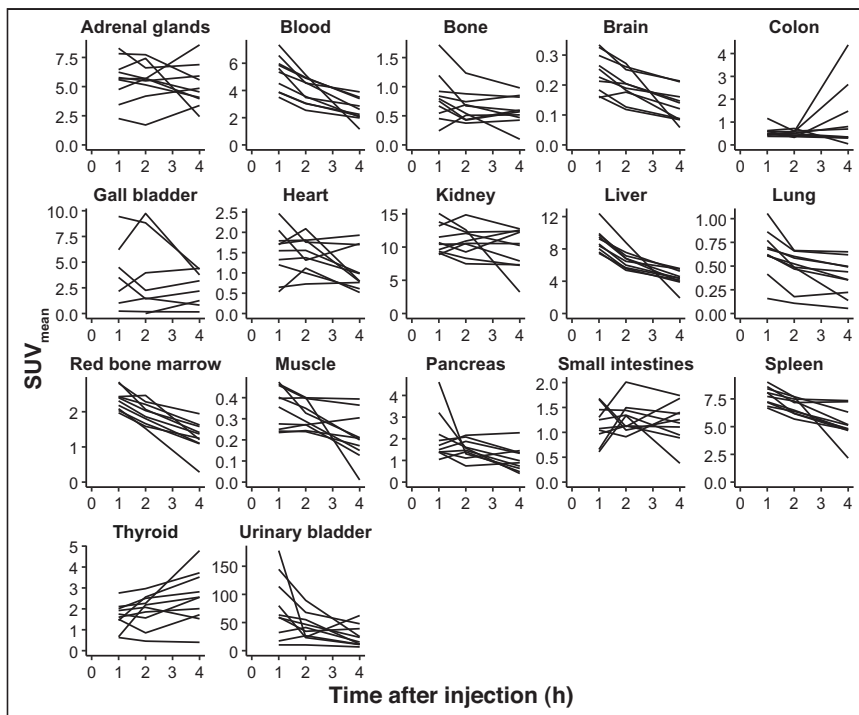


**FIGURE 3.** Distribution of  $^{18}\text{F}$ -ASIS in organs ( $n = 10$ ).

Spheric volumes of interest maximizing a volume encompassed by the tumor lesion perimeter based on the CT images were used for uptake quantification, and the tumor lesion  $\text{SUV}_{\text{max}}$  and  $\text{SUV}_{\text{mean}}$  were recorded on the PET images. Tumor-to-blood ratios were calculated as tumor lesion  $\text{SUV}_{\text{max}}$  divided by the blood pool  $\text{SUV}_{\text{mean}}$ . Any additional foci identified only on PET, judged indicative of a primary tumor or metastases by the readers, were recorded. SyngoVIA (version VB30A-HF04; Siemens Healthineers) was used for the image analysis.

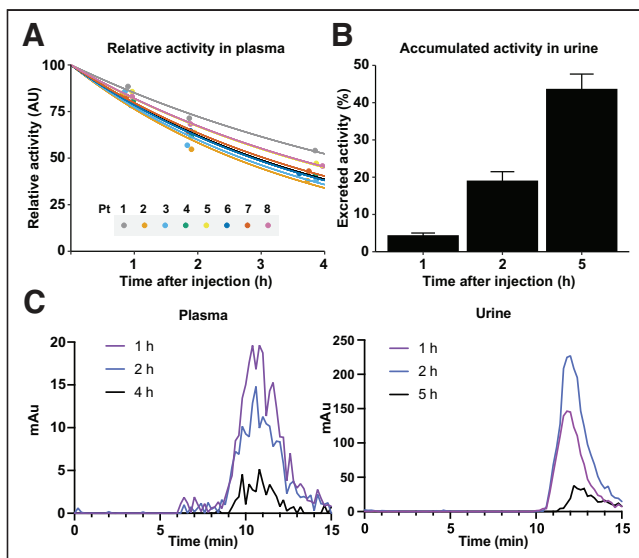


**FIGURE 4.** (A) Normalized time-activity curves of plasma samples with monoexponential fits ( $n = 8$ ). (B) Accumulated percentages of activity excreted in urine ( $n = 8$ ). (C) Representative radio-HPLC from plasma showing no major metabolites (left) and representative radio-HPLC from urine showing urinary excretion of a smaller  $^{18}\text{F}$ -radiolabeled fragment (right). AU = arbitrary units; mAu = absorbance units.

### Ex Vivo Tumor Tissue Samples

Tumor tissue samples were obtained from surgically resected tissue or from tumor biopsies performed in relation to routine clinical procedures. Samples were processed for measurement of TF expression with ELISA and immunohistochemistry. Details on tissue preparation, ELISA measurements, and immunohistochemistry preparation are provided in the supplemental materials. TF expression on immunohistochemistry was stratified as low, intermediate, or high based on visual assessment.

### Statistical Methods

The radiotracer plasma half-life was determined from monoexponential linear regression models (1-compartment models) fitted to the decay-corrected time-activity curves in plasma ( $n = 8$ ). The relationship between the 4-h PET tumor  $\text{SUV}_{\text{max}}$  and ex vivo measurements of TF expression by ELISA was analyzed with Pearson correlation ( $n = 5$ ). Two-sided  $P$  values of less than 0.05 were considered statistically significant. Data are presented as mean  $\pm$  SD unless otherwise noted. All statistical analyses were performed using R, version 3.6.1 (R Foundation for Statistical Computing).

## RESULTS

### Radiochemistry

$^{18}\text{F}$ -SFB was prepared in  $29.4\% \pm 25.9\%$  non-decay-corrected radiochemical yield ( $n = 10$  batches).  $^{18}\text{F}$ -ASIS was achieved in  $221 \pm 58$  MBq non-decay-corrected activity yield ( $n = 10$  batches).  $^{18}\text{F}$ -ASIS was produced with a radiochemical purity  $\geq 95\%$ , and unspecified  $^{18}\text{F}$ -labeled impurities and  $^{18}\text{F}$ -fluoride were both determined to be  $\leq 2\%$ . The concentration of ASIS was  $0.08 \pm 0.01$  mg/mL. Tetrabutylammonium hydrogen carbonate and HEPES content were  $< 0.1$  mg/mL and  $< 20$   $\mu\text{g/mL}$ , respectively. An immunoreactivity of  $\geq 75\%$  was found for all 10 batches. Summary results of all quality control parameters are provided in Supplemental Table 1.

### Patient Characteristics and Safety

The characteristics of the patients are shown in Table 1. There were no adverse events and no clinically significant changes in vital signs (Supplemental Table 2), blood parameters (Supplemental Table 3), or electrocardiograms observed in any of the 10 patients.

### Biodistribution, Pharmacokinetics, and Dosimetry

**Biodistribution.** A representative imaging series demonstrating the radiotracer distribution on the 1-, 2-, and 4-h PET on the maximum-intensity projection is shown in Figure 2 for patient 5. The maximum-intensity projections for the additional 9 patients are shown in Supplemental Figure 1. Organ-specific radiotracer uptake expressed as  $\text{SUV}_{\text{mean}}$  is shown in Figure 3. The highest uptake was observed in the urinary bladder followed by the kidneys and the liver. The brain, bone, muscle, red bone marrow, and lung had low and decreasing uptake, suggesting no radiotracer accumulation.

**Pharmacokinetics and Dosimetry.** Time-activity curves measured in plasma ( $n = 8$ ) are shown in Figure 4A. The plasma half-life was  $3.2 \pm 0.6$  h. Urinary excretion accounted for most of the  $^{18}\text{F}$ -ASIS elimination, and more than 40% of the injected

**TABLE 2**  
Organ-Based Dosimetry

Organ	Total mean absorbed dose ( $\mu\text{Gy}/\text{MBq}$ )
Adrenals	56
Brain	4
Breasts	8
Esophagus	12
Eyes	6
Gallbladder wall	22
Left colon	21
Small intestine	25
Stomach wall	15
Right colon	13
Rectum	17
Heart wall	17
Kidneys	76
Liver	67
Lungs	10
Ovaries	15
Pancreas	17
Prostate	15
Salivary glands	7
Red marrow	15
Osteogenic cells	16
Spleen	60
Testes	8
Thymus	9
Thyroid	17
Urinary bladder wall	118
Uterus	22
Total body	12
Effective dose ( $\mu\text{Sv}/\text{MBq}$ )	20

activity was accumulated in the urine within 5 h after injection (Fig. 4B). Radio-HPLC run on plasma samples showed no major metabolites. Radio-HPLC run on urine samples showed urinary excretion of a smaller  $^{18}\text{F}$ -radiolabeled fragment, suggesting renal metabolism of  $^{18}\text{F}$ -ASIS. Representative chromatograms of plasma samples collected 1, 2, and 4 h after injection and urine samples collected 1, 2, and 5 h after injection are shown in Figure 4C. The dosimetry output from the OLINDA/EXM dosimetry software is shown in Table 2. The highest dose was received by the urinary bladder wall (118  $\mu\text{Gy}/\text{MBq}$ ) followed by the kidneys (76  $\mu\text{Gy}/\text{MBq}$ ), liver (67  $\mu\text{Gy}/\text{MBq}$ ), and spleen (60  $\mu\text{Gy}/\text{MBq}$ ). The effective dose was 20  $\mu\text{Sv}/\text{MBq}$  corresponding to 4 mSv for a target activity of 200 MBq.

#### Radiotracer Accumulation in Tumor and Correlation with Ex Vivo Tumor Tissue

$^{18}\text{F}$ -ASIS accumulation in tumor lesions quantified as  $\text{SUV}_{\text{max}}$  and tumor-to-blood ratios are shown in Figure 5. Heterogeneous  $\text{SUV}_{\text{max}}$  patterns between patients were observed: for patients 3 and 4 (both primary pancreatic tumors) and 5 (lung metastasis)

$\text{SUV}_{\text{max}}$  increased on the 2- to 4-h PET compared with the 1-h PET. Contrary, in patients 7 and 8 (both primary breast tumors), low uptake was observed at all 3 time points. The remaining patients showed relatively intermediate  $\text{SUV}_{\text{max}}$  that remained stable or slightly increased with time. Compared with the other patients, for patients 3 and 4 the 4-h PET  $\text{SUV}_{\text{max}}$  was relatively high. The tumor-to-blood ratios showed a similar pattern.

Within tumor and within patient heterogeneity in radiotracer accumulation was also observed. Patient 10 (breast cancer) had heterogeneous radiotracer accumulation in the primary tumor (Fig. 6A), with 4-h PET  $\text{SUV}_{\text{max}}$  in the intermediate range (2.86).

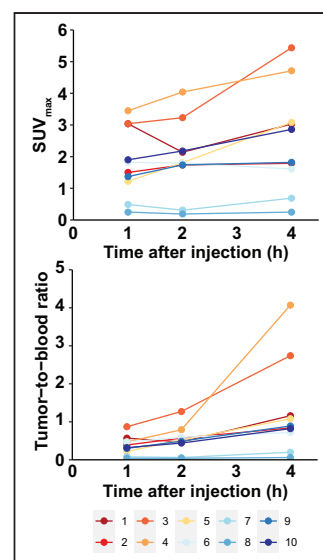


**FIGURE 5.** Tumor  $\text{SUV}_{\text{max}}$  (top) and tumor-to-blood ratios (tumor  $\text{SUV}_{\text{max}}$  divided by blood pool  $\text{SUV}_{\text{mean}}$ ) on 1-, 2-, and 4-h PET (bottom). Colors refer to patient numbers.

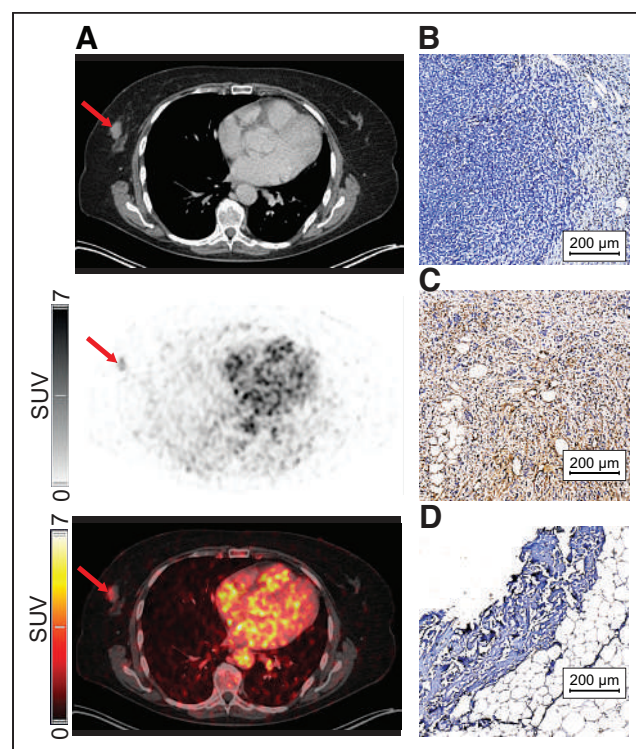


**FIGURE 6.** Patient 10 with breast cancer. (A) Primary breast tumor with relatively intermediate 4-h PET  $\text{SUV}_{\text{max}}$  (2.86) shown on (from top to bottom) CT, PET, and fused PET/CT. Arrows mark tumor location. (B) Small sample taken from tumor lesion immediately after surgery with low TF expression on immunohistochemistry. (C) Portion of mastectomy specimen showing intermediate TF expression in the tumor on immunohistochemistry performed after pathology examination. (D) Axillary sentinel node metastasis with low TF expression on immunohistochemistry without apparent focal accumulation in corresponding axillary area on PET or lymph node enlargement on CT (not shown).

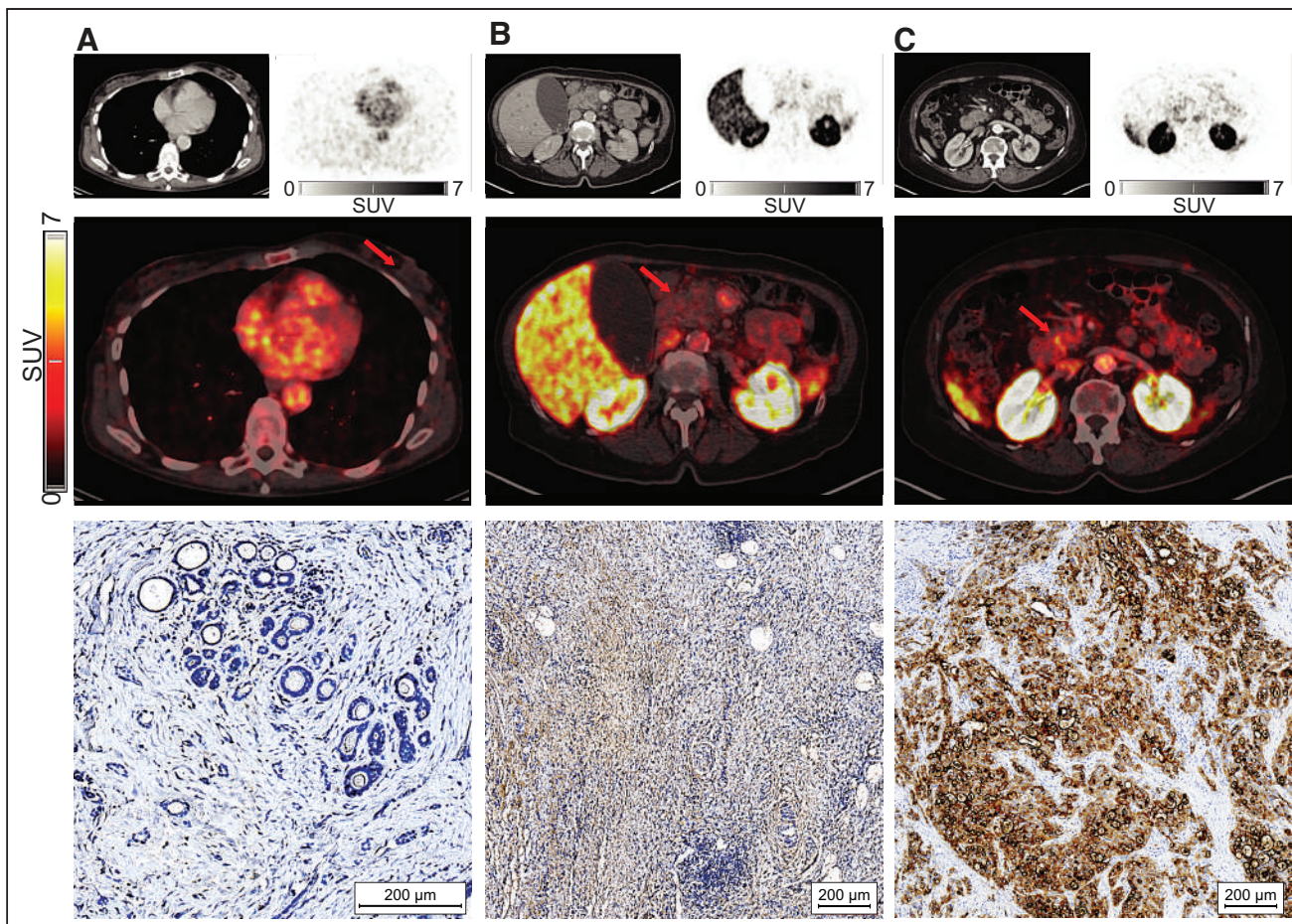


**FIGURE 7.** (A) Patient 7: breast tumor with low 4-h PET  $SUV_{max}$  (0.69) and low TF expression on immunohistochemistry ex vivo. (B) Patient 2: pancreatic tumor with relatively intermediate 4-h PET  $SUV_{max}$  (1.79) and intermediate TF expression on immunohistochemistry. (C) Patient 4: pancreatic tumor with relatively high 4-h PET  $SUV_{max}$  (4.71) and high TF expression on immunohistochemistry. Images from top to bottom are: 4-h CT, PET and fused PET/CT, and immunohistochemistry. Arrows mark tumor location on PET/CT.

A corresponding small tissue sample taken immediately from the surgically resected tumor showed low ex vivo TF expression measured with both ELISA and immunohistochemistry (Fig. 6B). However, TF immunohistochemistry staining of the tumor from the full mastectomy specimen, performed after the pathology examination, showed areas with intermediate TF expression (Fig. 6C). The pathology examination demonstrated 2 separate primary tumors. This patient also had an axially sentinel node metastasis that was not enlarged on CT, showed no apparent focal accumulation on PET, and had low TF expression on immunohistochemistry (Fig. 6D).

There was a trend of a positive correlation between 4-h PET  $SUV_{max}$  and TF expression measured ex vivo on matched tumor tissue samples, although not statistically significant ( $r = 0.84$ ,  $P = 0.08$ ,  $n = 5$ ). TF immunohistochemistry stains in matched tumor tissue samples were available for 7 patients. Representative examples of low, intermediate, and high TF expression on immunohistochemistry with corresponding 4-h PET/CT images are shown in Figure 7. A summary of the PET/CT findings, quantitative plasma and ex vivo tumor TF expression, and TF immunohistochemistry staining patterns is shown in Table 3.

## DISCUSSION

We report here the first-in-humans experience of the TF-targeted radiotracer  $^{18}F$ -ASIS in cancer patients. The trial marks the first

test in humans of a PET radiotracer targeting TF (first-in-class). Our main finding was that injection of  $^{18}F$ -ASIS was safe, and no adverse events were observed. The effective radiation dose of 4 mSv from administration of 200 MBq of  $^{18}F$ -ASIS is lower than that received after a standard  $^{18}F$ -FDG injection (22). None of the calculated organ-specific absorbed doses were prohibitive for administration of 200 MBq of  $^{18}F$ -ASIS. As an indication of the specific tumor-targeting ability of  $^{18}F$ -ASIS, we observed a trend of a positive correlation between tumor  $SUV_{max}$  and quantitative TF expression determined ex vivo ( $r = 0.84$ ,  $P = 0.08$ ). These initial findings represent important first steps toward the clinical implementation of  $^{18}F$ -ASIS PET imaging as a companion diagnostic tool for TF-targeted therapies.

The biodistribution and pharmacokinetic data indicated that the primary elimination route of  $^{18}F$ -ASIS was through the kidneys. The low bone uptake is supportive of high metabolic stability, as freely circulating  $^{18}F$ -fluoride would expectedly result in high bone accumulation (23). The 3.2-h  $^{18}F$ -ASIS plasma half-life was comparable to the 3.8-h plasma half-life observed for an unlabeled version of ASIS at similar dose (24), suggesting that the radiolabeling does not fundamentally alter the elimination of the radiotracer from plasma. Compared with antibody- and antibody fragment-based TF-targeted radiotracers with long circulation time resulting in optimal tumor-to-background contrast after several days in preclinical

**TABLE 3**  
PET/CT Image Findings and Ex Vivo Tissue Factor Measurements

Characteristic	Patient									
	1	2	3	4	5	6	7	8	9	10
Primary tumor	Pancreas	Pancreas	Pancreas	Pancreas	Lung <sup>  </sup>	Lung	Breast	Breast	Cervix	Breast
Radiotracer mass (mg)	0.84	0.69	0.71	0.71	0.74	0.41	0.76	0.56	0.74	0.58
Injected activity (MBq)	135	187	198	189	93	169	145	187	117	145
Specific activity* (MBq/mg)	161	271	279	266	126	412	191	334	158	250
Metastases (Pathology/PET/CT) <sup>†</sup>	÷/÷/÷	÷/÷/÷	÷/÷/÷	÷/÷/÷	+ / + / +	÷ / ÷ / ÷	÷ / ÷ / ÷	÷ / ÷ / ÷	÷ / ÷ / ÷	+ / ÷ / ÷ <sup>¶</sup>
Tumor size (cm)	3.6 × 3.3	3.5 × 3.1	4.9 × 3.8	2.6 × 2.2	1.2 × 0.9 <sup>  </sup>	3.6 × 3.4	2.8 × 1.4	0.7 × 0.8	3.2 × 2.9	2.4 × 1.4
Tumor SUV <sub>max</sub>										
1 h	3.04	1.50	3.04	3.45	1.22 <sup>  </sup>	1.82	0.49	0.25	1.37	1.90 <sup>#</sup>
2 h	2.14	1.74	3.23	4.04	1.81 <sup>  </sup>	1.80	0.31	0.19	1.74	2.18 <sup>#</sup>
4 h	3.03	1.79	5.44	4.71	3.08 <sup>  </sup>	1.61	0.69	0.25	1.82	2.86 <sup>#</sup>
Tumor SUV <sub>mean</sub>										
1 h	1.41	0.85	1.67	1.93	0.83 <sup>  </sup>	0.70	0.30	0.20	0.75	1.19 <sup>#</sup>
2 h	1.38	0.96	1.73	2.24	1.19 <sup>  </sup>	1.26	0.21	0.15	0.92	1.21 <sup>#</sup>
4 h	1.68	0.98	2.94	2.62	1.97 <sup>  </sup>	1.18	0.40	0.15	1.01	1.73 <sup>#</sup>
ΔT (d) <sup>‡</sup>	42	4	NA	6	NA	NA	12	5	6	4
TF <sub>tumor</sub> (μg/mg)	NA	5.93	NA	25.75	NA	NA	1.14	NA	1.27 <sup>**</sup>	PT: 0.67 MET: NA
TF <sub>tumor</sub> IHC <sup>§</sup>	Low <sup>**</sup>	Intermediate	NA	High	NA	NA	Low	Low	Low <sup>**</sup>	PT: Low/ intermediate <sup>††</sup> MET: Low
TF <sub>plasma</sub> (μg/L)	61	54	56	72	73	43	82	66	21	73

\*At time of injection.

<sup>†</sup>Presence of metastases based on pathology, PET, and CT, respectively.

<sup>‡</sup>Time between imaging and tissue collection.

<sup>§</sup>TF expression on immunohistochemistry (IHC) rated low, intermediate, or high based on visual assessment.

<sup>||</sup>Primary tumor removed. SUV and size measured on metastasis.

<sup>¶</sup>No lymph node enlargement on CT and no apparent focal accumulation on PET.

<sup>#</sup>Heterogeneous radiotracer accumulation observed.

<sup>\*\*</sup>Samples from biopsies.

<sup>††</sup>Low TF staining on IHC on tissue sample also showing low (0.67 μg/mg) TF expression. Tissue from full mastectomy, obtained from postpathology evaluation, with intermediate TF expression on IHC.

+ = metastases present; ÷ = no metastases; MET = metastases; NA = not available; PT = primary tumor.

models, for example,  $^{64}\text{Cu}$ - and  $^{89}\text{Zr}$ -labeled ALT-836 (25,26), the relatively fast elimination of  $^{18}\text{F}$ -ASIS makes this radiotracer better suited for same-day imaging.

The between-patient and cancer type heterogeneity in radiotracer tumor accumulation and ex vivo tumor TF expression observed in the study is in line with the varying degree of TF expression across cancer types reported in the literature (2,16,27). Pancreatic tumors have particularly high TF expression in agreement with our findings. The within-tumor heterogeneity seen in both radiotracer accumulation on PET and on ex vivo TF immunohistochemistry staining of the tumor from the full surgical specimens serves as an example of the potential of PET imaging for evaluation of TF expression. As PET imaging captures the whole-body tumor burden, identification of hotspots that could be otherwise missed on a biopsy is possible with PET. Importantly, the sentinel node metastasis without enlargement on CT, and with no apparent focal PET accumulation, had low TF expression on immunohistochemistry, which suggests that PET was not false-negative. Conclusions should not, of course, be inferred from single observations, but the results encourage further investigation.

The trend of a positive correlation between tumor  $\text{SUV}_{\text{max}}$  and quantitative TF expression measured ex vivo ( $r = 0.84$ ,  $P = 0.08$ ) suggests that  $^{18}\text{F}$ -ASIS accumulation depends on the levels of TF in tumors. It may be argued that the radiotracer accumulation in tumors was modest. Importantly, this does not pose a limitation to the use of  $^{18}\text{F}$ -ASIS PET as a whole-body noninvasive companion diagnostic or prognostic tool based on tumor TF expression if robust correlations between PET-derived tumor radiotracer accumulation and actual TF expression can be established. The relationship between  $\text{SUV}_{\text{max}}$  and ex vivo TF expression presented in this study suggests such a correlation. The observed trend is in line with our preclinical results in xenografted tumor mouse models that showed a strong and statistically significant positive correlation between tumor  $\text{SUV}_{\text{max}}$  on 4-h  $^{18}\text{F}$ -ASIS PET and TF expression measured in excised tumor tissue (16). The specificity of  $^{18}\text{F}$ -ASIS for targeting TF was supported by the qualitative relationship between the tumor  $\text{SUV}_{\text{max}}$  and TF immunohistochemistry staining patterns of surgical specimens that generally were in agreement. These preliminary results suggest that  $^{18}\text{F}$ -ASIS PET imaging can be used for noninvasive measurement of TF expression in tumor tissues, which may ultimately assist in identifying patients eligible for TF-targeted therapies. However, future later-phase clinical studies are needed to validate these findings in larger populations.

## CONCLUSION

$^{18}\text{F}$ -ASIS can safely be administered to cancer patients for TF-targeted PET imaging. The trial marks the first test of a TF-targeted PET radiotracer in humans (first-in-class). The effective whole-body dose from injection of 200 MBq was 4 mSv and no prohibitive organ-specific absorbed doses were observed. Plasma half-life was 3.2 h, and renal elimination accounted for most of the radiotracer excretion. The findings represent important first steps toward the clinical implementation of  $^{18}\text{F}$ -ASIS for PET imaging of TF expression, which could assist in patient prognostication and selection of eligible patients for TF-targeted therapies. Future later-phase studies are needed to validate these initial findings.

## DISCLOSURE

This project received funding from the European Union's Horizon 2020 research and innovation program under grant agreements no. 670261 (ERC Advanced Grant) and 668532 (Click-It), the

Lundbeck Foundation, the Novo Nordisk Foundation, the Innovation Fund Denmark, the Danish Cancer Society, Arvid Nilsson Foundation, the Neye Foundation, the Research Foundation of Rigshospitalet, the Danish National Research Foundation (grant 126), the Research Council of the Capital Region of Denmark, the Danish Health Authority, the John and Birthe Meyer Foundation and Research Council for Independent Research. Andreas Kjaer and Carsten H. Nielsen are inventors/hold intellectual property rights on a patent covering tissue factor imaging. Andreas Kjaer is a Lundbeck Foundation Professor. No other potential conflict of interest relevant to this article was reported.

## ACKNOWLEDGMENTS

We are grateful to the staff at the Department of Clinical Physiology and Nuclear Medicine for help with performing the PET/CT studies and for the patients for participating in the study. We also thank Katrine Qvist for performing the ex vivo immunohistochemistry staining and ELISA measurements. Novo Nordisk A/S is gratefully acknowledged for providing GMP-grade FVIIa.

## KEY POINTS

**QUESTION:** Can  $^{18}\text{F}$ -ASIS safely be administered to cancer patients for PET imaging of TF in tumors?

**PERTINENT FINDINGS:** In this first-in-humans clinical trial of 10 cancer patients, administration of  $^{18}\text{F}$ -ASIS was safe, and no adverse events were reported. The effective whole-body dose was 4 mSv for injection of a target activity of 200 MBq, and no prohibitive organ-specific absorbed doses were observed.

**IMPLICATIONS FOR PATIENT CARE:** The trial marks the first test in humans of a PET radiotracer targeting TF (first-in-class). The findings represent important first steps toward implementation of  $^{18}\text{F}$ -ASIS PET imaging of TF in cancer patients for prognostication and selection of patients for TF-targeted therapies.

## REFERENCES

1. McVey JH. Tissue factor pathway. *Baillieres Clin Haematol*. 1994;7:469–484.
2. van den Berg YW, Osanto S, Reitsma PH, Versteeg HH. The relationship between tissue factor and cancer progression: insights from bench and bedside. *Blood*. 2012;119:924–932.
3. Kasthuri RS, Taubman MB, Mackman N. Role of tissue factor in cancer. *J Clin Oncol*. 2009;27:4834–4838.
4. Nitori N, Ino Y, Nakanishi Y, et al. Prognostic significance of tissue factor in pancreatic ductal adenocarcinoma. *Clin Cancer Res*. 2005;11:2531–2539.
5. Zhao X, Cheng C, Gou J, et al. Expression of tissue factor in human cervical carcinoma tissue. *Exp Ther Med*. 2018;16:4075–4081.
6. Regina S, Valentin JB, Lachot S, Lemarie E, Rollin J, Gruel Y. Increased tissue factor expression is associated with reduced survival in non-small cell lung cancer and with mutations of TP53 and PTEN. *Clin Chem*. 2009;55:1834–1842.
7. Goldin-Lang P, Tran QV, Fichtner I, et al. Tissue factor expression pattern in human non-small cell lung cancer tissues indicate increased blood thrombogenicity and tumor metastasis. *Oncol Rep*. 2008;20:123–128.
8. Chen WH, Wang C, Zhang YH, Yang YH, Zhan HY, Zhang LM. Influence of overexpressed coagulant and fibrolytic components in tumor tissues on the prognosis of non-small cell lung cancer. *Zhonghua Yi Xue Za Zhi*. 2007;87:3228–3232.
9. Ueno T, Toi M, Koike M, Nakamura S, Tominaga T. Tissue factor expression in breast cancer tissues: Its correlation with prognosis and plasma concentration. *Br J Cancer*. 2000;83:164–170.
10. de Bono JS, Concin N, Hong DS, et al. Tisotumab vedotin in patients with advanced or metastatic solid tumours (InnovaTV 201): a first-in-human, multicentre, phase 1-2 trial. *Lancet Oncol*. 2019;20:383–393.

11. Coleman RL, Lorusso D, Gennigens C, et al. Efficacy and safety of tisotumab vedotin in previously treated recurrent or metastatic cervical cancer (InnovaTV 204/GOG-3023/ENGOT-cx6): A multicentre, open-label, single-arm, phase 2 study. *Lancet Oncol.* 2021;22:609–619.
12. U.S. Food and Drug Administration (FDA). Orange book: approved drug products with therapeutic equivalence evaluations. U.S. FDA website. [https://www.accessdata.fda.gov/drugsatfda\\_docs/label/2021/761208s000lbl.pdf](https://www.accessdata.fda.gov/drugsatfda_docs/label/2021/761208s000lbl.pdf). Accessed September 30, 2022.
13. Subramaniam RM. Precision medicine and PET/computed tomography: challenges and implementation. *PET Clin.* 2017;12:1–5.
14. Sorensen BB, Persson E, Freskgard PO, et al. Incorporation of an active site inhibitor in factor VIIa alters the affinity for tissue factor. *J Biol Chem.* 1997;272:11863–11868.
15. Erlandsson M, Nielsen CH, Jeppesen TE, et al. Synthesis and characterization of <sup>18</sup>F-labeled active site inhibited factor VII (ASIS). *J Labelled Comp Radiopharm.* 2015;58:196–201.
16. Nielsen CH, Erlandsson M, Jeppesen TE, et al. Quantitative PET imaging of tissue factor expression using <sup>18</sup>F-labeled active site-inhibited factor VII. *J Nucl Med.* 2016;57:89–95.
17. European Medicines Agency (EMA). ICH harmonised tripartite guideline: validation of analytical methods[em dash]methodology. In: *ICH Topic Q2(R1) Validation of Analytical Procedures: Text and Methodology*. CPMP/ICH/381/95. London: EMEA; 2006:7–15.
18. Lindmo T, Boven E, Cuttitta F, Fedorko J, Bunn PA Jr. Determination of the immunoreactive fraction of radiolabeled monoclonal antibodies by linear extrapolation to binding at infinite antigen excess. *J Immunol Methods.* 1984;72: 77–89.
19. International Commission on Radiological Protection (ICRP). Basic anatomical and physiological data for use in radiological protection: reference values—a report of age- and gender-related differences in the anatomical and physiological characteristics of reference individuals. ICRP publication 89. *Ann ICRP.* 2002;32:5–265.
20. Stabin MG, Siegel JA. Physical models and dose factors for use in internal dose assessment. *Health Phys.* 2003;85:294–310.
21. International Commission on Radiological Protection (ICRP). The 2007 recommendations of the International Commission on Radiological Protection. ICRP publication 103. *Ann ICRP.* 2007;37:1–332.
22. Quinn B, Dauer Z, Pandit-Taskar N, Schoder H, Dauer LT. Radiation dosimetry of <sup>18</sup>F-FDG PET/CT: incorporating exam-specific parameters in dose estimates. *BMC Med Imaging.* 2016;16:41.
23. Ahuja K, Sotoudeh H, Galgano SJ, et al. <sup>18</sup>F-sodium fluoride PET: history, technical feasibility, mechanism of action, normal biodistribution, and diagnostic performance in bone metastasis detection compared with other imaging modalities. *J Nucl Med Technol.* 2020;48:9–16.
24. Erhardtsen E, Nilsson P, Johannessen M, Thomsen MS. Pharmacokinetics and safety of FFR-rFVIIa after single doses in healthy subjects. *J Clin Pharmacol.* 2001;41:880–885.
25. Hong H, Zhang Y, Nayak TR, et al. Immuno-PET of tissue factor in pancreatic cancer. *J Nucl Med.* 2012;53:1748–1754.
26. Hernandez R, England CG, Yang Y, et al. ImmunoPET imaging of tissue factor expression in pancreatic cancer with <sup>89</sup>Zr-Df-ALT-836. *J Control Release.* 2017; 264:160–168.
27. Saidak Z, Soudet S, Lottin M, et al. A pan-cancer analysis of the human tumor coagulum and its link to the tumor immune microenvironment. *Cancer Immunol Immunother.* 2021;70:923–933.

---

---

# <sup>89</sup>Zr-Labeled High-Density Lipoprotein Nanoparticle PET Imaging Reveals Tumor Uptake in Patients with Esophageal Cancer

Kang H. Zheng<sup>1</sup>, Jeffrey Kroon<sup>2</sup>, Jasper Schoormans<sup>3</sup>, Oliver Gurney-Champion<sup>4</sup>, Sybren L. Meijer<sup>5</sup>, Suzanne S. Gisbertz<sup>6</sup>, Maarten C.C.M. Hulshof<sup>7</sup>, Danielle J. Vugts<sup>8</sup>, Guus A.M.S. van Dongen<sup>8</sup>, Bram F. Coolen<sup>3</sup>, Hein J. Verberne<sup>4</sup>, Aart J. Nederveen<sup>4</sup>, Erik S.G. Stroes<sup>1</sup>, and Hanneke W.M. van Laarhoven<sup>9</sup>

<sup>1</sup>Department of Vascular Medicine, Amsterdam Cardiovascular Sciences, Amsterdam UMC, University of Amsterdam, Amsterdam, The Netherlands; <sup>2</sup>Department of Experimental Vascular Medicine, Amsterdam Cardiovascular Sciences, Amsterdam UMC, University of Amsterdam, Amsterdam, The Netherlands; <sup>3</sup>Department of Biomedical Engineering and Physics, Amsterdam Cardiovascular Sciences, Amsterdam UMC, University of Amsterdam, Amsterdam, The Netherlands; <sup>4</sup>Department of Radiology and Nuclear Medicine, Amsterdam UMC, University of Amsterdam, Amsterdam, The Netherlands; <sup>5</sup>Department of Pathology, Cancer Center Amsterdam, Amsterdam UMC, University of Amsterdam, Amsterdam, The Netherlands; <sup>6</sup>Department of Surgery, Cancer Center Amsterdam, Amsterdam UMC, University of Amsterdam, Amsterdam, The Netherlands; <sup>7</sup>Department of Radiotherapy, Cancer Center Amsterdam, Amsterdam UMC, University of Amsterdam, Amsterdam, The Netherlands; <sup>8</sup>Department of Radiology and Nuclear Medicine, Amsterdam UMC, VU University, Amsterdam, The Netherlands; and <sup>9</sup>Department of Medical Oncology, Cancer Center Amsterdam, Amsterdam UMC, University of Amsterdam, Amsterdam, The Netherlands

Nanomedicine holds promise for the delivery of therapeutic and imaging agents to improve cancer treatment outcomes. Preclinical studies have demonstrated that high-density lipoprotein (HDL) nanoparticles accumulate in tumor tissue on intravenous administration. Whether this HDL-based nanomedicine concept is feasible in patients is unexplored. Using a multimodal imaging approach, we aimed to assess tumor uptake of exogenously administered HDL nanoparticles in patients with esophageal cancer. **Methods:** The HDL mimetic CER-001 was radiolabeled using <sup>89</sup>Zr to allow for PET/CT imaging. Patients with primary esophageal cancer staged T2 and above were recruited for serial <sup>89</sup>Zr-HDL PET/CT imaging before starting chemoradiation therapy. In addition, patients underwent routine <sup>18</sup>F-FDG PET/CT and 3-T MRI scanning (diffusion-weighted imaging/intravoxel incoherent motion imaging and dynamic contrast-enhanced MRI) to assess tumor glucose metabolism, tumor cellularity and microcirculation perfusion, and tumor vascular permeability. Tumor biopsies were analyzed for the expression of HDL scavenger receptor class B1 and macrophage marker CD68 using immunofluorescence staining. **Results:** Nine patients with adenocarcinoma or squamous cell carcinoma underwent all study procedures. After injection of <sup>89</sup>Zr-HDL (39.2 ± 1.2 [mean ± SD] MBq), blood-pool SUV<sub>mean</sub> decreased over time (11.0 ± 1.7, 6.5 ± 0.6, and 3.3 ± 0.5 at 1, 24, and 72 h, respectively), whereas liver and spleen SUV<sub>mean</sub> remained relatively constant (4.1 ± 0.6, 4.0 ± 0.8, and 4.3 ± 0.8 at 1, 24, and 72 h, respectively, for the liver; 4.1 ± 0.3, 3.4 ± 0.3, and 3.1 ± 0.4 at 1, 24, and 72 h, respectively, for the spleen) and kidney SUV<sub>mean</sub> markedly increased over time (4.1 ± 0.9, 9.3 ± 1.4, and 9.6 ± 2.0 at 1, 24, and 72 h, respectively). Tumor uptake (SUV<sub>peak</sub>) increased over time (3.5 ± 1.1 and 5.5 ± 2.1 at 1 and 24 h, respectively [*P* = 0.016]; 5.7 ± 1.4 at 72 h [*P* = 0.001]). The effective dose of <sup>89</sup>Zr-HDL was 0.523 ± 0.040 mSv/MBq. No adverse events were observed after the administration of <sup>89</sup>Zr-HDL. PET/CT and 3-T MRI measures of tumor glucose metabolism,

tumor cellularity and microcirculation perfusion, and tumor vascular permeability did not correlate with tumor uptake of <sup>89</sup>Zr-HDL, suggesting that a specific mechanism mediated the accumulation of <sup>89</sup>Zr-HDL. Immunofluorescence staining of clinical biopsies demonstrated scavenger receptor class B1 and CD68 positivity in tumor tissue, establishing a potential cellular mechanism of action. **Conclusion:** To our knowledge, this was the first <sup>89</sup>Zr-HDL study in human oncology. <sup>89</sup>Zr-HDL PET/CT imaging demonstrated that intravenously administered HDL nanoparticles accumulated in tumors of patients with esophageal cancer. The administration of <sup>89</sup>Zr-HDL was safe. These findings may support the development of HDL nanoparticles as a clinical delivery platform for drug agents. <sup>89</sup>Zr-HDL imaging may guide drug development and serve as a biomarker for individualized therapy.

**Key Words:** zirconium; PET/CT; high-density lipoprotein; nanomedicine; esophageal cancer

**J Nucl Med 2022; 63:1880–1886**

DOI: 10.2967/jnumed.121.263330

**E**sophageal cancer is the sixth leading cause of death from cancer worldwide and represents a major health care problem (1). This malignancy is associated with substantial morbidity and has a dismal prognosis, with a 5-y survival rate of less than 25% (2), despite advances in multimodality treatment strategies. Oncologic treatment for esophageal carcinoma invariably involves the use of (pre-operative) chemotherapy or concurrent chemoradiation (3). An important limitation of systemic chemotherapy is nonspecificity, resulting in low intratumor drug concentrations, while off-target cytotoxic effects limit the intensity of dosing. Novel treatment strategies are needed to improve efficacy and avoid toxicity in the management of esophageal carcinoma.

Nanomedicine is an emerging approach to addressing the issues of poor outcomes and limited efficacy in oncology (4). The key principle involves the use of nanometer-sized particles as vehicles for drug or imaging agents to enhance delivery to tumors and avoid

---

Received Oct. 16, 2021; revision accepted Apr. 18, 2022.  
For correspondence or reprints, contact Hanneke W.M. van Laarhoven (h.vanlaarhoven@amsterdamumc.nl).  
Published online Jun. 23, 2022.  
COPYRIGHT © 2022 by the Society of Nuclear Medicine and Molecular Imaging.

first-pass clearance by the liver. Compared with conventional therapies, such as systemic chemotherapy, nanoparticles should improve the balance between local efficacy and systemic toxicity. Several innovative nanomedicines have been approved by the U.S. Food and Drug Administration or reached the clinical stage of development (5). Nevertheless, clinical breakthroughs in terms of significantly prolonging patient survival have not yet been achieved by most nanoparticle platforms, comprising liposomes, albumin nanoparticles, or micelles. This situation may be due to inherent limitations of these nanosystems in dealing with the complexities and heterogeneity of tumor biology, including factors such as passive targeting, circulation half-life, tumor penetration, cellular uptake, and drug release. Specific toxicity associated with certain nanoparticles, such as hypersensitivity reactions, may also hamper clinical development (6).

High-density lipoproteins (HDLs) have received considerable interest because of their potential for drug delivery and imaging (7). HDLs are endogenous nanometer-sized particle carriers of cholesterol, and one of their main physiologic functions is considered to be the targeting and removal of cholesterol from peripheral tissues, including lipid-laden macrophages, followed by transportation to the liver for excretion (8). To exercise their function, HDLs have a natural conduit for interaction with peripheral cells through specific receptors, including scavenger receptor class B1 (SR-B1). HDLs can be formulated to carry, within their hydrophilic core or surface, therapeutic payloads, including hydrophobic drugs, controlled-released polymers, and short interfering RNAs (9). These characteristics and the absence of specific toxicity may allow HDLs to overcome the barriers to other nanosystems. In support of this notion, the administration of radiolabeled HDL nanoparticles in a mouse model of breast cancer resulted in accumulation in tumors through uptake in tumor-associated macrophages (10).

We aimed to investigate this concept in patients and set out to assess whether administered HDL nanoparticles accumulate in primary esophageal tumors. To this end, we labeled the HDL mimetic CER-001 with  $^{89}\text{Zr}$  ( $^{89}\text{Zr}$ -HDL) to allow for in vivo tracing using serial PET/CT imaging (11). Furthermore, we explored whether tumor uptake of radiolabeled HDL was associated with tumor metabolism, as assessed with routine  $^{18}\text{F}$ -FDG PET/CT; with tumor diffusion and microcirculation perfusion, as assessed with diffusion-weighted imaging/intravoxel incoherent motion imaging (DWI/IVIM); and with tumor vascular permeability, as assessed with dynamic contrast-enhanced MRI (DCE-MRI). Finally, we investigated the presence of the HDL receptor SR-B1 and macrophages in tumor biopsies using immunofluorescence.

## MATERIALS AND METHODS

### Study Design

This study was a single-center prospective trial and was conducted in accordance with the principles of the Declaration of Helsinki. The protocol was approved by the local ethics committee, and all participants provided written informed consent. Patients with esophageal cancer were included and visited the study center 3 times. All patients received a single injection of  $^{89}\text{Zr}$ -HDL (CER-001; 10 mg; 37 MBq) and underwent serial PET/CT scanning at 1, 24, and 72 h after administration. In addition, all patients were scanned on a 3-T MRI scanner during 1 of the study visits.

### Study Population

Eligible patients were adults with a primary esophageal carcinoma in situ before treatment, a histopathologically proven diagnosis, and a

tumor staged as at least locally advanced T2 (according to the TNM classification). Patients were recruited from the Gastro-Intestinal Oncology Center Amsterdam, Amsterdam, The Netherlands.

### $^{89}\text{Zr}$ -HDL and $^{18}\text{F}$ -FDG PET/CT

$^{89}\text{Zr}$ -HDL was synthesized according to current good manufacturing practice guidelines. The procedure for  $^{89}\text{Zr}$  radiolabeling of CER-001 and the quality and stability tests were described previously (11,12). The specific activity was 3.7 MBq of  $^{89}\text{Zr}$  per mg of CER-001. Radiochemical purity was determined using size exclusion high-performance liquid chromatography ( $100\% \pm 0\%$  [mean  $\pm$  SD]) and spin filters ( $99.3\% \pm 0.4\%$ ). We demonstrated that covalent coupling of the bifunctional chelator *p*-isothiocyanatobenzyl desferrioxamine to CER-001 and subsequent labeling with zirconium did not affect its functionality in vitro and in vivo. Whole-body  $^{89}\text{Zr}$ -HDL PET/CT scans were acquired on a Siemens Biograph mCT Flow system (Siemens). A low-dose CT scan was acquired with automatic modulation of current and voltage (reference values: 120 kV, 50 mA,  $128 \times 0.6$  collimation, and 0.9 pitch). PET imaging was performed with continuous bed motion at 1.1 mm/s (legs) and 0.7 mm/s (body) in the 3-dimensional acquisition mode. CT data were used for PET attenuation correction, and PET data were reconstructed with the TrueX algorithm (3-dimensional ordered-subsets expectation maximization iterative reconstruction with time-of-flight and point spread function compensation, 21 subsets, 2 iterations, and a 5-mm gaussian postprocessing filter) in  $4 \times 4 \times 5 \text{ mm}^3$  voxels.

$^{18}\text{F}$ -FDG PET/CT scans were acquired in accordance with the local clinical protocol on the Siemens Biograph mCT Flow system. Patients were instructed to drink 2 L of water and to not perform strenuous physical activities in the 24 h preceding the scan. Patients fasted for at least 6 h, except for glucose-free oral hydration before the intravenous administration of  $^{18}\text{F}$ -FDG. Fasting capillary blood glucose concentrations were measured with a blood glucose meter (StatStrip; Nova Biomedical Corp.) before  $^{18}\text{F}$ -FDG administration. Dosages of  $^{18}\text{F}$ -FDG ranged from 180 to 400 MBq, depending on the body mass index. PET/CT scanning was performed 60 min after the injection of  $^{18}\text{F}$ -FDG. A diagnostic CT scan was acquired with automatic modulation of current and voltage (reference values: 120 kV, 160 mA,  $128 \times 0.6$  collimation, and 0.9 pitch) after the intravenous administration of iodinated contrast medium (100 mL of Ultravist 300; Bayer Healthcare Pharmaceuticals) with a flow of 3 mL/s and a 65-s delay (portal phase). PET imaging was performed with continuous bed motion at 1.5 mm/s in the 3-dimensional acquisition mode. CT data were used for PET attenuation correction, and PET data were reconstructed with the TrueX algorithm (3-dimensional ordered-subsets expectation maximization iterative reconstruction with time-of-flight and point spread function compensation, 21 subsets, 2 iterations, and a 5-mm gaussian postprocessing filter) in  $4 \times 4 \times 5 \text{ mm}^3$  voxels.

Image analysis was performed on a dedicated commercially available workstation (OsiriX [Pixmeo] and OLINDA/EXM [Hermes Medical Solutions]). Tumor uptake and organ uptake were assessed by manually drawing regions of interest delineating the whole tumor or organ (in all slices where visible) on the coregistered CT image. Blood-pool activity was determined by drawing regions of interest in 5 contiguous axial slices in the lumen of the superior vena cava. The  $\text{SUV}_{\text{max}}$  was calculated as the maximal pixel activity within each region of interest. For tumors, the  $\text{SUV}_{\text{peak}}$  was calculated as the mean pixel activity within a volume of interest ( $1 \text{ cm}^3$ ) centered around the hottest pixel value. The target-to-blood pool ratio was calculated by dividing the SUV by the mean blood-pool activity. The internal radiation dosimetry for the adult human was evaluated through the normalized cumulated activities for each patient, provided as input to the OLINDA/EXM code. Residence times were calculated for the liver, kidney, lungs, spleen, and remainder of the body by entering the percentage of the

**TABLE 1**  
Baseline Characteristics of Included Patients

Patient	Age (y)	Sex	Body mass index (kg/m <sup>2</sup> )	Tumor type	Tumor size (cm <sup>3</sup> )	Tumor stage
1	73	M	26.7	Adenocarcinoma	20.4	T2N1M0
2	62	M	31.4	Adenocarcinoma	71.2	T3N1M0
3	68	M	19.4	Adenocarcinoma	16.2	T3N0M0
4	67	M	24.7	Squamous cell	97.3	T2N1M0
5	57	M	24.4	Adenocarcinoma	49.0	T3N2M1
6	66	M	26.1	Adenocarcinoma	53.7	T3N2M0
7	82	M	28.1	Adenocarcinoma	52.8	T3N1M0
8	51	M	28.1	Squamous cell	19.2	T3N2M0
9	66	M	30.4	Adenocarcinoma	52.8	T3N0M0

Tumors were classified according to TNM staging system.

injected dose at each time point for each patient in OLINDA/EXM and fitting these data using a monoexponential function.

### 3-T MRI Acquisition and Analysis

Patients were scanned on a 3-T MRI scanner (Philips Ingenia) with an anterior 16-channel phased-array coil and a posterior 16-channel phased-array coil. The maximum gradient strength of the scanner was 45 mT/m, and the maximum slew rate was 200 T/m/s. Three-dimensional T1-weighted 3-point Dixon and multislice T2-weighted turbo spin-echo images were obtained for reference.

**DWI/IVIM.** Axial diffusion-weighted 2-dimensional multislice single-shot echoplanar imaging with selective partial inversion recovery fat suppression was performed with the following acquisition settings: repetition time/echo time = 4600/70, field of view = 350 × 160 mm, resolution = 2.2 × 2.2 mm<sup>2</sup> (1.8 × 1.8 mm<sup>2</sup> reconstructed), number of slices = 20, slice thickness = 4.5 mm (slice gap = 0.5 mm), SENSE factor = 1.4, echoplanar imaging bandwidth = 16.5 Hz/voxel, and b values = 0 (3 averages), 100 (6 averages), and 800 (10 averages) s/mm<sup>2</sup>. Scans were respiration triggered by means of a liver–lung interface navigator signal.

From the diffusion-weighted images, parameter maps were calculated for the diffusivity and perfusion fraction in MATLAB 2016a (The MathWorks, Inc.) on the basis of in-house software (13,14) adapted to work for 3 b values. Diffusivity was calculated voxelwise by applying a least-squares fit to the diffusion-weighted imaging data from the b values 100 and 800 s/mm<sup>2</sup>:

$$S(b) = S0' \times e^{-b \times D}, \quad \text{Eq. 1}$$

where  $S(b)$  is the signal ( $S$ ) at b value  $b$  and  $S0'$  is the extrapolated signal at  $b = 0$  s/mm<sup>2</sup> for monoexponential data. The difference between the measured  $S$  ( $b = 0$  s/mm<sup>2</sup>) and  $S0'$ , in turn, relates to the perfusion fraction as:

$$f = 1 - \frac{S0'}{S(b=0)}. \quad \text{Eq. 2}$$

Regions of interest were drawn on  $b = 800$  s/mm<sup>2</sup> and propagated to the parameter maps to assess parameter values inside the tumor regions.

**DCE-MRI.** For DCE-MRI, a highly accelerated golden-angle radial stack-of-stars TFE sequence (15) was performed continuously at a temporal resolution of 8.7 s per time frame. Two minutes after the start of the scan, a gadolinium-based contrast agent (Gadovist; Bayer) at a dose of 0.1 mmol/kg of body weight was injected intravenously at 2 mL/s.

Other relevant scan parameters were repetition time/echo time = 7.5/3.4, flip angle = 11°, and spatial resolution = 1 × 1 × 2 mm<sup>3</sup>.

The undersampled data were reconstructed in MATLAB 2016a using compressed sensing (ref) with total variation regularization in the time domain ( $\lambda = 0.01$ ) and 100 iterations. Frame-by-frame tumor segmentation was performed on the dynamic data with ImageJ (National Institutes of Health). Signal intensity curves were obtained from the time series, and the area under the curve (AUC) was calculated for the first 2 min after contrast injection as a semiquantitative measure of tumor permeability.

### Histology and Immunohistochemistry

Tumor biopsies were obtained during routine clinical workup before the start of neoadjuvant treatment and cut into slices. All samples were stained with hematoxylin and eosin for general morphology. For immunohistochemistry, the slides were dewaxed to remove the paraffin. Antigen retrieval was done using the LabVision PT module (ThermoFisher Scientific) at pH 6.0 for 20 min at 98°C. Next, the slides were washed with phosphate-buffered saline 3 times and blocked with Ultravision

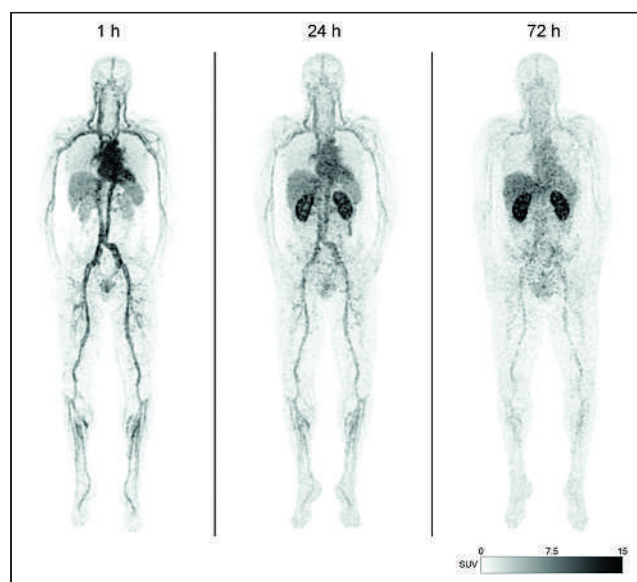


**FIGURE 1.** Maximum-intensity projections of serial <sup>89</sup>Zr-HDL PET images from patient 1.

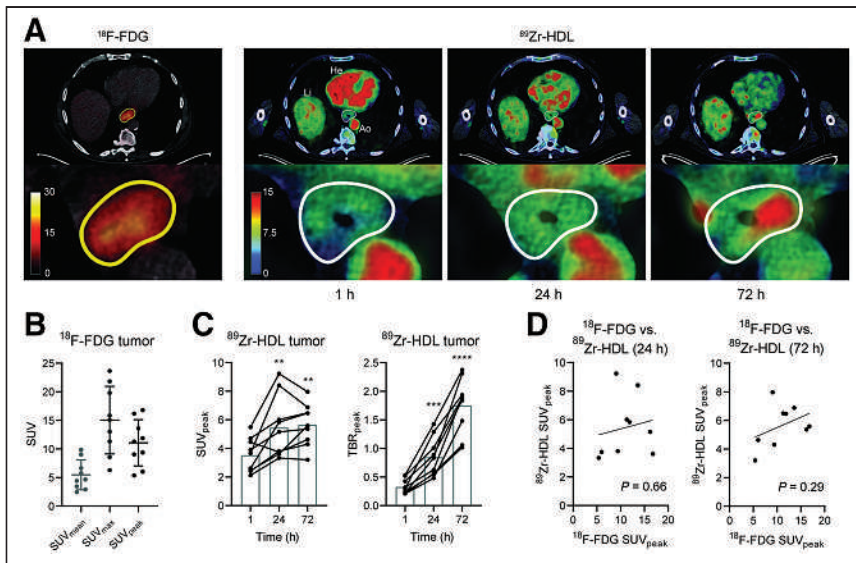


**FIGURE 2.** PET/CT images from patient 6 with esophageal adenocarcinoma. (A and B)  $^{18}\text{F}$ -FDG uptake was clearly increased in tumors. On administration of  $^{89}\text{Zr}$ -HDL, signal intensity in esophageal tumor increased over time, and focal uptake pattern was clearly visualized at 72 h. (C) Tumor SUVs and target-to-blood pool ratios increased over time, indicating accumulation of  $^{89}\text{Zr}$ -HDL particles in tumors. (D) There was no association between  $^{18}\text{F}$ -FDG uptake and  $^{89}\text{Zr}$ -HDL uptake in tumors. Ao = aorta, He = heart, Li = liver; TBR = target-to-blood pool ratio.

protein block (TA-125-PBQ; ThermoFisher Scientific) for 10 min at room temperature. The slides were incubated with primary antibodies: for SR-B1, NB400-101 (Novus Biologicals), and for CD68, clone KP-1 (catalog number Ab955; Abcam). Subsequently, secondary antibodies Alexa Fluor-488 (A21121; Invitrogen) and Alexa Fluor-568 (A11036; Invitrogen) were used. Cells were embedded using Prolong-gold (P36935; ThermoFisher Scientific) containing 4,6-diamidino-2-phenylindole. Imaging was performed on a Leica DMI6000 (SP8) confocal microscope with a  $\times 63$  objective. Pixels positive for either SR-B1 or CD68 per tumor biopsy were normalized for nuclear content using 4,6-diamidino-2-phenylindole to normalize the cellular biopsy area using Fiji (ImageJ v2.1.0/1.53c). The percentage of colocalization between SR-B1 and CD68 refers to the percentage of pixels from the total number of pixels per image and was determined using the Fiji Coloc 2 plugin.

### Statistical Analysis

All data are presented as mean and SD. For the evaluation of  $^{89}\text{Zr}$ -HDL uptake over time, a repeated-measures 1-way ANOVA was performed (significance level,  $\alpha = 0.05$ ). If significance was found, then post hoc testing with Bonferroni adjustment was performed to assess the difference in uptake compared with the first time point. The correlations of  $^{89}\text{Zr}$ -HDL uptake, MRI parameters, and immunohistochemistry data were tested using Pearson correlation coefficients. Statistical analyses were performed using SPSS Statistics package version 26 (IBM).

## RESULTS

We recruited 9 male patients with a mean age of  $66 \pm 9$  y; 7 (78%) of them were recently diagnosed with adenocarcinoma and 2 (22%) had squamous cell carcinoma of the esophagus. Baseline characteristics are listed in Table 1. All patients received an injection of 10 mg of  $^{89}\text{Zr}$ -HDL (mean,  $39.2 \pm 1.2$  MBq) and underwent serial PET/CT and 3-T MRI scanning before starting chemoradiation therapy. PET/CT scanning was performed at 1 h ( $1\text{ h } 3\text{ min} \pm 0\text{ h } 7\text{ min}$ ), 24 h ( $24\text{ h } 41\text{ min} \pm 0\text{ h } 28\text{ min}$ ), and 72 h

( $71\text{ h } 11\text{ min} \pm 2\text{ h } 6\text{ min}$ ) after the injection of  $^{89}\text{Zr}$ -HDL.  $^{89}\text{Zr}$ -HDL was well tolerated during the study, and no adverse events were reported.

### Biodistribution and Radiation Dosimetry of $^{89}\text{Zr}$ -HDL

Serial PET/CT imaging was performed at 1, 24, and 72 h after the injection of  $^{89}\text{Zr}$ -HDL. Visual inspection revealed a clear radiotracer signal in the blood pool, liver, spleen, and kidneys (Fig. 1). The uptake of  $^{89}\text{Zr}$ -HDL was measured in selected source organs (Supplemental Fig. 1) (supplemental materials are available at <http://jnm.snmjournals.org>). The blood-pool  $\text{SUV}_{\text{mean}}$  was  $11.0 \pm 1.7$  at 1 h after administration and decreased to  $6.5 \pm 0.6$  at 24 h and  $3.3 \pm 0.5$  at 72 h (both  $P$ s  $< 0.0001$ ). The liver  $\text{SUV}_{\text{mean}}$  was  $4.1 \pm 0.6$  at 1 h and remained constant over time, whereas the spleen signal decreased slightly from  $4.1 \pm 0.3$  to  $3.4 \pm 0.3$  and  $3.1 \pm 0.4$  after 24 and 72 h, respectively ( $P < 0.001$ ). The kidney  $\text{SUV}_{\text{mean}}$  markedly increased from  $4.1 \pm 0.9$  to  $9.3 \pm 1.4$  after 24 h and remained elevated at 72 h ( $P < 0.0001$ ), confirming

that the kidneys were the major site of catabolism of HDL. Organ dosimetry data and residence times are listed in Supplemental Table 1. The organs with the highest absorbed dose were the stomach ( $0.086 \pm 0.013$  mSv/MBq), lungs ( $0.070 \pm 0.008$  mSv/MBq), and liver ( $0.053 \pm 0.010$  mSv/MBq).

### PET/CT Imaging of Esophageal Tumors

We used clinical  $^{18}\text{F}$ -FDG PET/CT scans to assist in delineating the esophageal tumors; intense  $^{18}\text{F}$ -FDG uptake was demonstrated, as expected (Figs. 2A and 2B). On colocalized  $^{89}\text{Zr}$ -HDL PET/CT scans, focal uptake patterns in the esophageal tumors could clearly be observed from 24 h onward (Fig. 2A). Given the relatively small size of the esophageal tumors (mean,  $48.0 \pm 26.6\text{ cm}^3$ ) and the focal uptake patterns, tumor uptake of  $^{89}\text{Zr}$ -HDL was reported using the  $\text{SUV}_{\text{peak}}$  for more robust quantification than the  $\text{SUV}_{\text{max}}$ . Tumor uptake of  $^{89}\text{Zr}$ -HDL was significantly higher for all tumors at 24 and 72 h than at 1 h after injection (for  $\text{SUV}_{\text{max}}$ ,  $6.1 \pm 1.4$  and  $9.2 \pm 4.2$  at 1 and 24 h, respectively [ $P = 0.036$ ], and  $10.2 \pm 3.4$  at 72 h [ $P = 0.023$ ]; for  $\text{SUV}_{\text{peak}}$ ,  $3.5 \pm 1.1$  and  $5.5 \pm 2.1$  at 1 and 24 h, respectively [ $P = 0.016$ ], and  $5.7 \pm 1.4$  at 72 h [ $P = 0.001$ ]) (Fig. 2C). When corrected for the blood pool, the tumor target-to-blood pool ratio increased significantly over time (peak tumor-to-blood pool ratio,  $0.3 \pm 0.1$  and  $0.9 \pm 0.3$  at 1 and 24 h, respectively [ $P < 0.001$ ], and  $1.8 \pm 0.5$  at 72 h [ $P < 0.001$ ]). There was no association between tumor uptake values for  $^{18}\text{F}$ -FDG and  $^{89}\text{Zr}$ -HDL (Fig. 2D).

### DWI/IVIM and DCE-MRI of Esophageal Tumors

To explore whether characteristics of the tumor microenvironment affect the ability of HDL nanoparticles to penetrate tumors, all patients underwent DWI/IVIM and DCE-MRI scanning. We localized the tumors using T2-weighted turbo spin-echo images (Fig. 3A). DWI/IVIM images were acquired, and parameter maps of diffusivity and perfusion fraction were generated (Fig. 3B). The mean values for diffusivity and perfusion fraction of the tumors were not associated with tumor uptake of  $^{89}\text{Zr}$ -HDL (Fig. 3C).

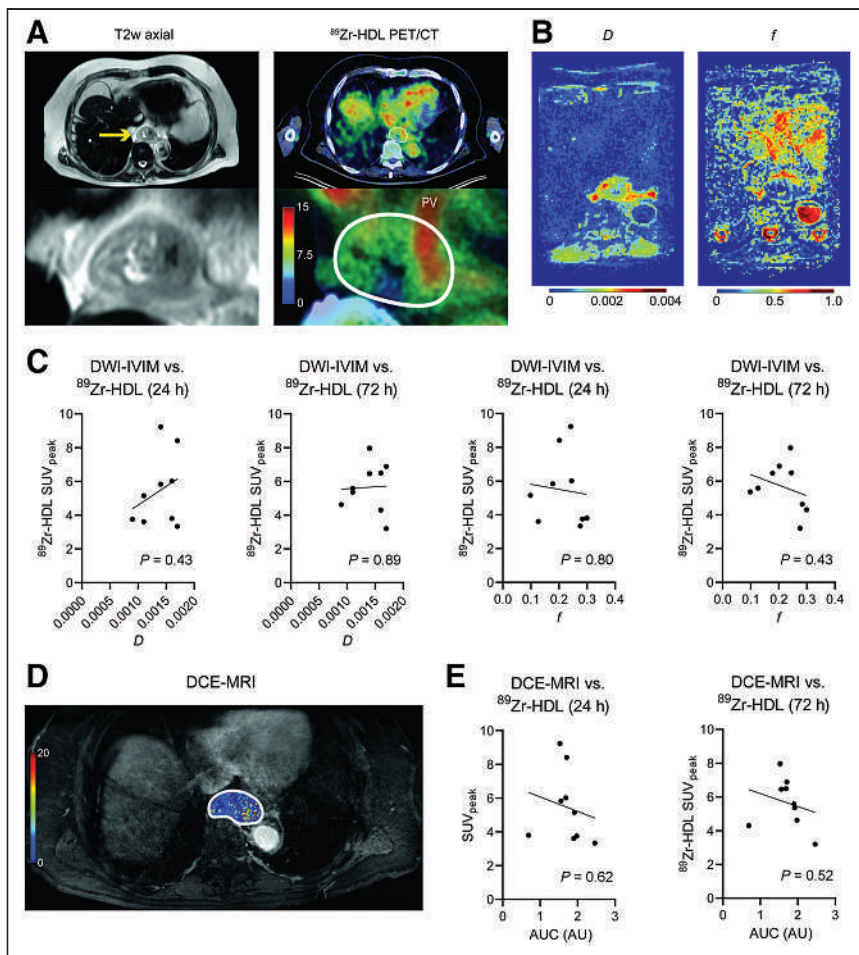


**FIGURE 3.** DWI/IVIM and DCE-MRI scanning of patient 7. (A) (Left) T2-weighted (T2w) turbo spin-echo images were obtained to localize tumors. Yellow arrow indicates tumor. (Right) Corresponding  $^{89}\text{Zr}$ -HDL PET/CT at 72 h, with focal uptake in tumor delineated with white line, as well as intravascular signal from adjacent pulmonary vein (PV). (B) DWI/IVIM images were acquired to generate diffusivity ( $D$ ) and perfusion fraction ( $f$ ) maps. (C) Mean  $D$  and  $f$  values calculated from parameter maps were not associated with tumor uptake of  $^{89}\text{Zr}$ -HDL. (D) Quantitative AUC maps resulting from DCE-MRI time series. (E) Mean AUC values were not associated with tumor uptake of  $^{89}\text{Zr}$ -HDL. AU = arbitrary units.

DCE-MRI time series were obtained, and quantitative pixelwise AUC maps were calculated from the first 2 min after the injection of a gadolinium-based contrast agent (Fig. 3D). The mean AUC values of the tumors, as a measure of permeability, were not associated with tumor uptake of  $^{89}\text{Zr}$ -HDL (Fig. 3E).

#### HDL Receptor Expression in Tumor Biopsies

Histologic analysis of tumor biopsies from all patients was performed to assess general morphology (Fig. 4A), the expression of the HDL receptor SR-B1, and the presence of macrophage marker CD68 (Fig. 4B). We established and quantified the presence of SR-B1-positive cells and macrophages by CD68 expression (Fig. 4C) as well as cells with double positivity for these markers (Fig. 4D). There was no relationship between semiquantitative measures of SR-B1 and CD68 expression and tumor uptake of  $^{89}\text{Zr}$ -HDL (Supplemental Fig. 2).

#### DISCUSSION

To our knowledge, this is the first report of the uptake of HDL nanoparticles in tumors of patients with primary esophageal

cancer. After the administration of  $^{89}\text{Zr}$ -HDL, serial PET/CT demonstrated the accumulation of HDL nanoparticles in the esophageal tumors over time. Tumor uptake could be quantified in all patients, and no adverse events occurred. These findings herald the clinical utility of HDL-based nanomedicine to target esophageal tumors for the delivery of anticancer drugs.

In this proof-of-concept study, we applied  $^{89}\text{Zr}$  labeling to the HDL mimetic CER-001, which consists of recombinant apolipoprotein A-I and phospholipids. Our data indicated relatively low uptake in the liver and spleen, whereas the radiotracer signal increased in the kidneys over time. This finding is in line with the known renal catabolism of apolipoprotein A-I (16). Importantly, focal accumulation patterns of  $^{89}\text{Zr}$ -HDL were observed in all esophageal tumors after 24 and 72 h. These data highlight the translational potential of HDL nanoparticles as a tool for altering the biodistribution of drugs of interest, to achieve higher intratumor concentrations, and to avoid systemic toxicity. This concept is supported by previous experimental studies in cardiovascular disease, which established that HDL nanoparticles effectively delivered their drug payload to atherosclerotic plaques (17,18).

The extravasation of nanoparticles to tumors is traditionally considered to depend on passive accumulation via the enhanced permeability and retention (EPR) effect (19). This phenomenon dictates that drug penetration in tumors is dependent on features of the tumor microenvironment, including the degree of cellularity and composition of the extracellular matrix, as well as vascular permeability. Nevertheless, we found that tumor uptake of  $^{89}\text{Zr}$ -HDL was not associated with imaging measures of tumor diffusivity (DWI/IVIM), tumor perfusion (DWI/IVIM), or vascular permeability (DCE-MRI). These findings suggest the contribution of a specific mechanism mediating the accumulation of HDL nanoparticles in esophageal cancer, rather than dependence on only passive vascular leakage.

We substantiated the presence of the HDL receptor SR-B1 in tumor biopsies from the studied patients—which could facilitate a specific mechanism for the accumulation of HDL. Enhanced expression of SR-B1 has been suggested to be a mechanism for tumor cells to satisfy their increased demand for cholesterol to allow for proliferation and increased metabolic cellular processes (20). The level of SR-B1 expression in human breast and prostate cancers is associated with tumor aggressiveness and adverse prognosis (21,22), and a variety of malignant cell lines overexpress SR-B1 (20). Yet, we did not find an association between tumor uptake of  $^{89}\text{Zr}$ -HDL and tumor glycolytic activity (related to cellular proliferation), as measured with  $^{18}\text{F}$ -FDG PET/CT. Prior studies using murine breast cancer models suggested that injected HDL nanoparticles are preferentially taken up by tumor-associated

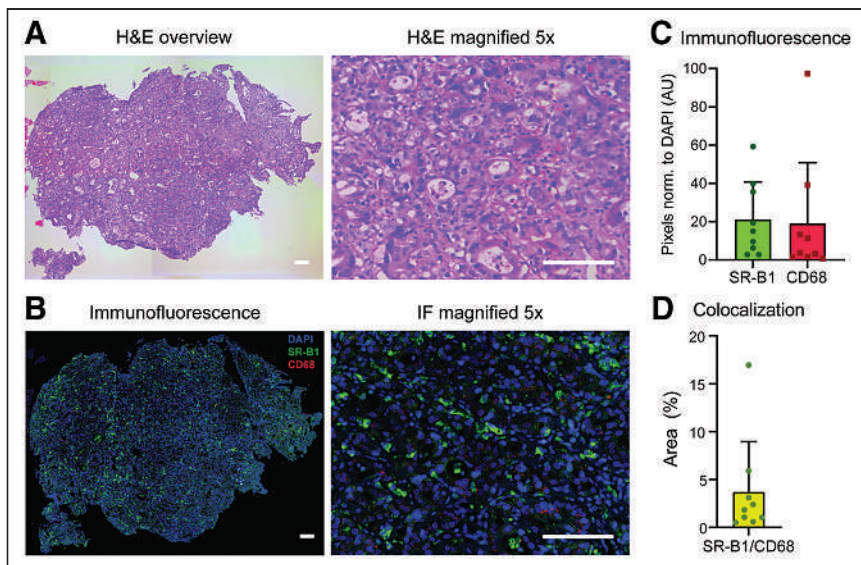


**FIGURE 4.** HDL receptor expression and macrophage presence in tumor biopsies, as shown by histology and immunofluorescence (IF) of tumor biopsies before chemoradiation therapy, in patient 3. (A and B) Hematoxylin and eosin (H&E) staining (A) with corresponding confocal microscopy image for 4,6-diamidino-2-phenylindole (DAPI) (blue), SR-B1 (green), and CD68 (red) (B). (C) Pixel count of SR-B1 and CD68 normalized (norm.) to DAPI. (D) Percentage area with double positivity for SR-B1 and CD68. AU = arbitrary units.

macrophages (10,23), which may also express SR-B1 or other scavenger receptors for HDL. However, we found that the colocalization of SR-B1 with CD68 was limited, suggesting that cells other than macrophages could be responsible for most uptake of HDL particles. Additional studies are needed to assess the cellular distribution of administered HDL particles in patients with esophageal cancer, as well as the cellular mechanisms involved. Collectively,  $^{89}\text{Zr}$ -HDL PET/CT has the potential to serve as a specific imaging biomarker for predicting the efficacy of HDL-mediated drug delivery (24).

To our knowledge, this is the first report of the radiation dosimetry of  $^{89}\text{Zr}$ -HDL. The effective dose of  $^{89}\text{Zr}$ -HDL (0.523 mSv/MBq) clearly exceeds that of the conventional diagnostic tracer  $^{18}\text{F}$ -FDG (0.019 mSv/MBq) (25), although it is comparable to those of other  $^{89}\text{Zr}$ -immuno-PET tracers (26). Although this dose may limit repetitive use, given the poor survival rate of patients with esophageal cancer, the risks of radiation may be acceptable when weighed against any potential future improvement in clinical treatment provided by this imaging modality.

We acknowledge several limitations of the present study. The sample size was small for a pilot study and carries the risk of a false-negative finding in our correlation testing of imaging modalities. The spatial heterogeneity of the tumors may have obscured MRI parameters that were calculated by averaging measurements in a region of interest. Finally, biopsies of tumors may not adequately reflect the tissue distribution of the tumors.

## CONCLUSION

$^{89}\text{Zr}$  labeling of HDL nanoparticles allowed for in vivo tracing using PET/CT in patients with esophageal cancer. The administration of  $^{89}\text{Zr}$ -HDL was safe, and the effective dose was in the range of those of other  $^{89}\text{Zr}$  tracers. Focal uptake patterns were observed within the esophageal tumors. Further studies are now needed to gain insight into the mechanisms of HDL accumulation in tumors

and to test the feasibility of HDL nanoparticles serving as a delivery system for anti-cancer drugs.

## DISCLOSURE

This work was supported by the Dutch Heart Foundation (CVON 2017–20: GENIUS-II). Jeffrey Kroon was supported by Dutch Heart Foundation Senior Scientist Dekker Grant 2021T045. This was an investigator-initiated study for which Cerenis provided CER-001. Erik S.G. Stroos also served as principal investigator for the MODE, SAMBA, and TANGO studies (involving CER-001). No other potential conflict of interest relevant to this article was reported.

## ACKNOWLEDGMENTS

We thank E. Poel, M.F. Lam, and S.R. Havik for their invaluable technical assistance.

## KEY POINTS

**QUESTION:** Do intravenously administered HDL nanoparticles accumulate in tumors in patients with primary esophageal cancer?

**PERTINENT FINDINGS:** This prospective imaging study used  $^{89}\text{Zr}$  labeling of HDL nanoparticles to demonstrate accumulation in tumors of patients with esophageal cancer after intravenous administration ( $\text{SUV}_{\text{peak}}$ :  $3.5 \pm 1.1$ ,  $5.5 \pm 2.1$ , and  $5.7 \pm 1.4$  at 1, 24, and 72 h, respectively). Tumor uptake of  $^{89}\text{Zr}$ -HDL was not associated with measures from  $^{18}\text{F}$ -FDG PET/CT, DWI/IVIM, and DCE-MRI, suggesting that a specific mechanism mediated the accumulation of  $^{89}\text{Zr}$ -HDL; analysis of tumor biopsies showed the presence of SR-B1–positive cells and macrophages, indicating a potential mechanism of action.

**IMPLICATIONS FOR PATIENT CARE:** HDL nanoparticles have the potential to serve as a delivery system for anticancer drugs in esophageal cancer.

## REFERENCES

- Smyth EC, Lagergren J, Fitzgerald RC, et al. Oesophageal cancer. *Nat Rev Dis Primers*. 2017;3:17048.
- van Putten M, de Vos-Geelen J, Nieuwenhuijzen GAP, et al. Long-term survival improvement in oesophageal cancer in the Netherlands. *Eur J Cancer*. 2018;94:138–147.
- Shah MA, Kennedy EB, Catenacci DV, et al. Treatment of locally advanced esophageal carcinoma: ASCO guideline. *J Clin Oncol*. 2020;38:2677–2694.
- Shi J, Kantoff PW, Wooster R, Farokhzad OC. Cancer nanomedicine: progress, challenges and opportunities. *Nat Rev Cancer*. 2017;17:20–37.
- Tran S, DeGiovanni P-J, Piel B, Rai P. Cancer nanomedicine: a review of recent success in drug delivery. *Clin Transl Med*. 2017;6:44.
- Szebeni J, Simberg D, Gonzalez-Fernandez A, Barenholz Y, Dobrovolskaia MA. Roadmap and strategy for overcoming infusion reactions to nanomedicines. *Nat Nanotechnol*. 2018;13:1100–1108.
- Lobatto ME, Fuster V, Fayad ZA, Mulder WJ. Perspectives and opportunities for nanomedicine in the management of atherosclerosis. *Nat Rev Drug Discov*. 2011;10:835–852.

8. Ouimet M, Barrett TJ, Fisher EA. HDL and reverse cholesterol transport. *Circ Res*. 2019;124:1505–1518.
9. Mulder WJM, van Leent MMT, Lameijer M, Fisher EA, Fayad ZA, Perez-Medina C. High-density lipoprotein nanobiologics for precision medicine. *Acc Chem Res*. 2018;51:127–137.
10. Pérez-Medina C, Tang J, Abdel-Atti D, et al. PET imaging of tumor-associated macrophages with <sup>89</sup>Zr-labeled high-density lipoprotein nanoparticles. *J Nucl Med*. 2015;56:1272–1277.
11. Zheng KH, van der Valk FM, Smits LP, et al. HDL mimetic CER-001 targets atherosclerotic plaques in patients. *Atherosclerosis*. 2016;251:381–388.
12. Vosjan MJ, Perk LR, Visser GW, et al. Conjugation and radiolabeling of monoclonal antibodies with zirconium-89 for PET imaging using the bifunctional chelate *p*-isothiocyanatobenzyl-desferrioxamine. *Nat Protoc*. 2010;5:739–743.
13. Gurney-Champion OJ, Froeling M, Klaassen R, et al. Minimizing the acquisition time for intravoxel incoherent motion magnetic resonance imaging acquisitions in the liver and pancreas. *Invest Radiol*. 2016;51:211–220.
14. Klaassen R, Gurney-Champion OJ, Engelbrecht MRW, et al. Evaluation of six diffusion-weighted MRI models for assessing effects of neoadjuvant chemoradiation in pancreatic cancer patients. *Int J Radiat Oncol Biol Phys*. 2018;102:1052–1062.
15. Zheng KH, Schoormans J, Stiekema LCA, et al. Plaque permeability assessed with DCE-MRI associates with USPIO uptake in patients with peripheral artery disease. *JACC Cardiovasc Imaging*. 2019;12:2081–2083.
16. Moestrup SK, Nielsen LB. The role of the kidney in lipid metabolism. *Curr Opin Lipidol*. 2005;16:301–306.
17. Duivenvoorden R, Tang J, Cormode DP, et al. A statin-loaded reconstituted high-density lipoprotein nanoparticle inhibits atherosclerotic plaque inflammation. *Nat Commun*. 2014;5:3065.
18. Kim Y, Lobatto ME, Kawahara T, et al. Probing nanoparticle translocation across the permeable endothelium in experimental atherosclerosis. *Proc Natl Acad Sci USA*. 2014;111:1078–1083.
19. Prabhakar U, Maeda H, Jain RK, et al. Challenges and key considerations of the enhanced permeability and retention effect for nanomedicine drug delivery in oncology. *Cancer Res*. 2013;73:2412–2417.
20. Mooberry LK, Sabnis NA, Panchoo M, Nagarajan B, Lacko AG. Targeting the SR-B1 receptor as a gateway for cancer therapy and imaging. *Front Pharmacol*. 2016;7:466.
21. Schörghofer D, Kinslechner K, Preitschopf A, et al. The HDL receptor SR-B1 is associated with human prostate cancer progression and plays a possible role in establishing androgen independence. *Reprod Biol Endocrinol*. 2015;13:88.
22. Yuan B, Wu C, Wang X, et al. High scavenger receptor class B type I expression is related to tumor aggressiveness and poor prognosis in breast cancer. *Tumour Biol*. 2016;37:3581–3588.
23. Mason CA, Kossatz S, Carter LM, et al. An <sup>89</sup>Zr-HDL PET tracer monitors response to a CSF1R inhibitor. *J Nucl Med*. 2020;61:433–436.
24. Jauw YWS, Willemien Menke-van der Houven van Oordt C, Hoekstra OS, et al. Immuno-positron emission tomography with zirconium-89-labeled monoclonal antibodies in oncology: what can we learn from initial clinical trials? *Front Pharmacol*. 2016;7:131.
25. Mattsson S, Johansson L, Leide Svegborn S, et al. Radiation dose to patients from radiopharmaceuticals: a compendium of current information related to frequently used substances. *Ann ICRP*. 2015;44(2 suppl):7–321.
26. Börjesson PK, Jauw YW, de Bree R, et al. Radiation dosimetry of <sup>89</sup>Zr-labeled chimeric monoclonal antibody U36 as used for immuno-PET in head and neck cancer patients. *J Nucl Med*. 2009;50:1828–1836.

# <sup>18</sup>F-FDG PET/CT Staging of Head and Neck Cancer: Interobserver Agreement and Accuracy—Results from Multicenter ACRIN 6685 Clinical Trial

Rathan M. Subramaniam<sup>1,2</sup>, Fenghai M. Duan<sup>3</sup>, Justin Romanoff<sup>3</sup>, Jian Qin Yu<sup>4</sup>, Twyla Bartel<sup>5</sup>, Farrokh Dehdashti<sup>6</sup>, Charles M. Intenzo<sup>7</sup>, Lilja Solnes<sup>8</sup>, JoRean Sicks<sup>3</sup>, Brendan C. Stack Jr<sup>9</sup>, and Val J. Lowe<sup>10</sup>

<sup>1</sup>Otago Medical School, University of Otago, Otago, Dunedin, New Zealand; <sup>2</sup>Duke University, Durham, North Carolina; <sup>3</sup>School of Public Health, Brown University, Providence, Rhode Island; <sup>4</sup>Fox Chase Cancer Center, Philadelphia, Pennsylvania; <sup>5</sup>Global Advanced Imaging, Little Rock, Arkansas; <sup>6</sup>Washington University School of Medicine, St Louis, Missouri; <sup>7</sup>Thomas Jefferson University, Philadelphia, Pennsylvania; <sup>8</sup>Johns Hopkins School of Medicine, Baltimore, Maryland; <sup>9</sup>Southern Illinois School of Medicine, Springfield, Illinois; and <sup>10</sup>Mayo Clinic, Rochester, Minnesota

To our knowledge, no prior multicenter clinical trial has reported interobserver agreement of <sup>18</sup>F-FDG PET/CT scans for staging of clinical N0 neck in head and neck cancer. **Methods:** A total of 287 participants were recruited. For visual analysis, positive nodal uptake of <sup>18</sup>F-FDG was defined as uptake visually greater than activity seen in the blood pool. **Results:** The negative predictive value of the <sup>18</sup>F-FDG PET/CT for N0 clinical neck was 86% or above for visual assessment (95% CI, 86%–88%) for the 2 central readers and above 90% (95% CI, 90%–95%) for SUV<sub>max</sub> for central reads and site reads dichotomized at the optimal cutoff value of 1.8 and the prespecified cutoff value of 3.5, respectively. The  $\kappa$  coefficients between the 2 expert readers and between central reads and site reads varied between 0.53 and 0.78. **Conclusion:** The NPV of the <sup>18</sup>F-FDG PET/CT for N0 clinical neck was 86% or above for visual assessment and above 90% for SUV<sub>max</sub> cut points of 1.8 and 3.5 with moderate to substantial agreements.

**Key Words:** oncology; head and neck; FDG PET/CT; head and neck cancer; staging

**J Nucl Med 2022; 63:1887–1890**  
DOI: 10.2967/jnumed.122.263902

**P**ET/CT with <sup>18</sup>F-FDG is commonly used in clinical practice for management of head and neck squamous cell carcinoma patients including for staging, treatment assessment, and detecting recurrence and metastases (1–5). We previously reported on the primary results of ACRIN 6685 trial (ClinicalTrials.gov identifier: NCT00983697) (5,6). No prior multicenter study reported interobserver agreement for staging clinical N0 neck in head and neck cancer. In this post hoc analysis study, we report on the interobserver agreement among the readers interpreting the <sup>18</sup>F-FDG PET/CT studies and their accuracy.

## MATERIALS AND METHODS

### Patient Population

As previously described, a total of 287 participants were recruited (Fig. 1) (5). A clinically N0 neck was defined as being free of palpable

lymph nodes and with neck CT or MRI neck lymph node sizes of less than 1 and 1.5 cm for jugular digastric nodes (IIa), spinal accessory nodes (IIb), or submental-submandibular nodes (Ia and Ib) or showing a lack of central lymph node necrosis in nodes of any size (5).

### Imaging Procedure and Interpretation

Imaging procedures and interpretation methods were previously described (5). PET/CT images were read at each study site by the reporting physician (i.e., site reads) and images were presented to a core reading panel of board-certified nuclear medicine or nuclear radiology certified physicians. There were 2 central readers: reader 1 and reader 2 (expert head and neck readers) who interpreted most of the PET/CT scans for the study. In addition, reader 3 and reader 4 (general readers) were used because central readers 1 and 2 were excluded from reading scans from their respective institutions and when adjudication was needed. A SUV<sub>max</sub> was required for the hottest lymph node for each nodal basin recorded as indeterminate, probably malignant, or definitely malignant. The SUV<sub>max</sub> calculation was performed using commercial software (version 5.2; MIM Software). For visual analysis, positive nodal uptake of <sup>18</sup>F-FDG was defined as uptake visually greater than background and more than that activity seen in the blood pool (Fig. 2).

### Statistical Analysis

The neck-level visual assessment <sup>18</sup>F-FDG PET/CT scan result for each central reader, for the sites and for the central adjudicated read, was compared with the neck-level pathology result. The sensitivity, specificity, positive predictive value (PPV), and negative predictive value (NPV) were calculated. Similar analyses were performed to compare the nodal basin SUV<sub>max</sub> result (dichotomized at the optimal cutoff value of 1.8 (5) and the prespecified cutoff value of 3.5) with the nodal-level pathology. Cohen's  $\kappa$  statistic was used to assess the agreement between the 2 expert readers (central readers 1 and 2) and the central reads and site reads. Because of data sparsity, agreement assessment for the 2 general readers (central readers 3 and 4) was not reported.

For all analyses, 95% CIs were calculated using the 2.5 and 97.5 percentiles of the multilevel bootstrap based on 10,000 resampled datasets (5). Analyses were performed using SAS software (version 9.4; SAS Institute) and R (version 4.0.4; R Foundation for Statistical Computing).

## RESULTS

### Patient Demographics

Patient characteristics are included in Supplemental Table 1 (supplemental materials are available at <http://jnm.snmjournals.org>),

Received Jan. 25, 2022; revision accepted Apr. 27, 2022.  
For correspondence or reprints, contact Rathan M. Subramaniam (rathan.subramaniam@otago.ac.nz).  
Published online May 12, 2022.  
COPYRIGHT © 2022 by the Society of Nuclear Medicine and Molecular Imaging.

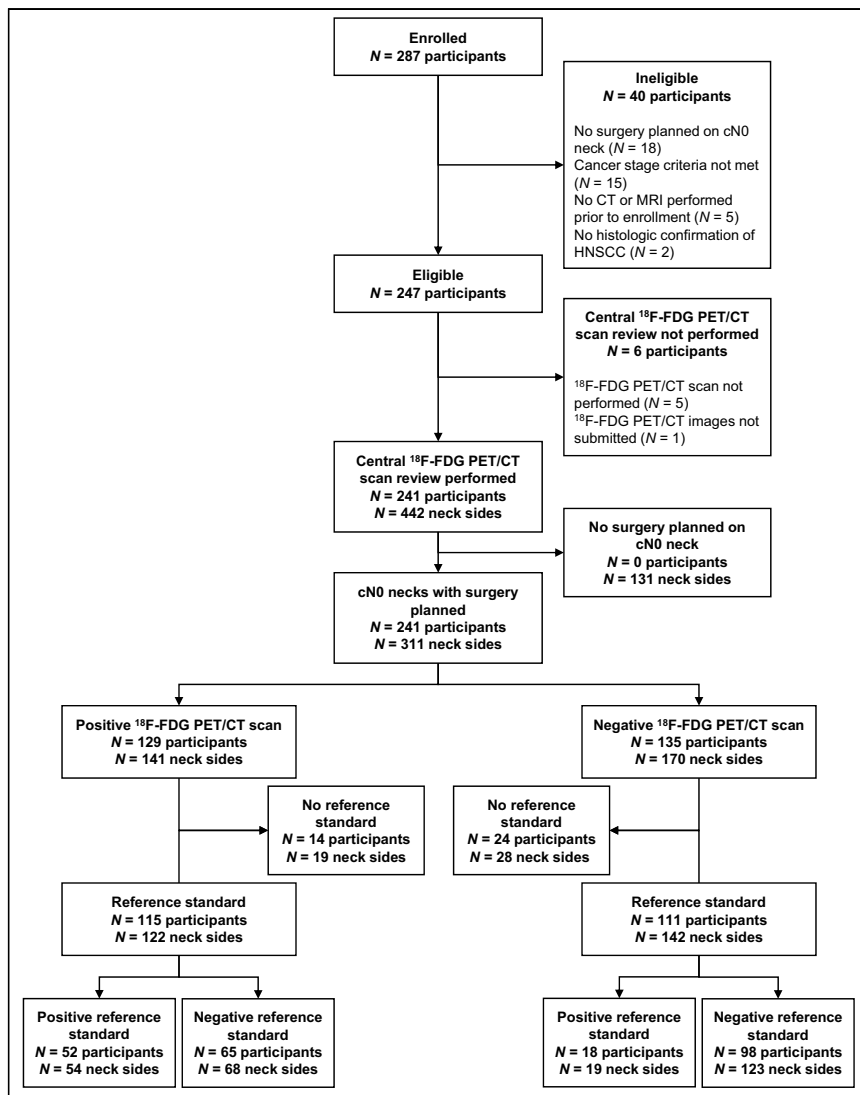


FIGURE 1. STARD flow diagram.

which include data on enrolled patients and those who were included in this post hoc analyses.

### Visual Assessment

There were 4 central readers: reader 1 and reader 2 (expert head and neck readers), and reader 3 and reader 4 (general readers). Readers 1, 2, 3, and 4 interpreted a total of 286, 273, 34, and 26 sides of necks, respectively. The site readers interpreted a total of 296 sides of neck. The sensitivity, specificity, PPV, and NPV of the visual assessment for the 2 expert central readers, the site reads, and the central adjudicated read are summarized in Table 1. The  $\kappa$  coefficients comparing reader 1 and reader 2, reader 1 and the central adjudicated read, reader 2 and the central adjudicated read, and the site reads and the central adjudicated read were 0.549 (95% CI: 0.431, 0.660), 0.756 (95% CI: 0.664, 0.837), 0.781 (95% CI: 0.696, 0.856), and 0.531 (95% CI: 0.421, 0.633), respectively.

### SUV<sub>max</sub> Reads

Readers 1, 2, 3, and 4 analyzed a total of 2,272, 2,171, 270, and 208 neck nodes measuring SUV<sub>max</sub>, respectively. The site readers

analyzed a total of 2,385 neck nodes. The sensitivity, specificity, PPV, and NPV of SUV<sub>max</sub> for the 2 expert readers and central adjudicated read are summarized in Table 2 for cut points 1.8 and 3.5. The  $\kappa$  statistics for measuring the agreement between the site SUV<sub>max</sub> and the combined central SUV<sub>max</sub> were 0.447 (95% CI: 0.363, 0.527) and 0.525 (95% CI: 0.382, 0.649), respectively, for SUV<sub>max</sub> cut points of 1.8 and SUV<sub>max</sub> 3.5. The  $\kappa$  coefficients for measuring the agreement between reader 1 and the combined central SUV<sub>max</sub> were 0.818 (95% CI: 0.758, 0.870) and 0.751 (95% CI: 0.642, 0.839), respectively, for SUV<sub>max</sub> cut points of 1.8 and SUV<sub>max</sub> 3.5. The  $\kappa$  coefficients for measuring the agreement between reader 2 and the combined central SUV<sub>max</sub> were 0.712 (95% CI: 0.640, 0.777) and 0.839 (95% CI: 0.741, 0.915), respectively, for SUV<sub>max</sub> cut points 1.8 and 3.5.

### DISCUSSION

The NPV of the <sup>18</sup>F-FDG PET/CT for N0 clinical neck was 86% or above for visual assessment (95% CI, 86%–88%) for 2 expert central readers, and above 90% (95% CI, 90%–95%) for SUV<sub>max</sub> cut points of 1.8 and 3.5 for the 2 expert readers and site reads. There was moderate to substantial agreement between readers. Increasing evidence supports the higher NPV of PET/CT to exclude nodal metastasis (5,7–9). In this study, we have provided evidence that multiple readers can achieve high NPV by visual assessment as well as by SUV<sub>max</sub> analysis. This result has significant implications, especially managing the contralateral

neck, as single-center studies have now reported on the outcome of patients managed with observation of PET-directed (negative) contralateral neck (10,11).

The interreader reliability varied between moderate and substantial agreement in this study. Using the ACRIN 6685 standardized interpretation algorithm (visual assessment) may improve the reliability of interpretation more than subjective individual reader interpretation. It is important to note that there was moderate agreement between site readers and central readers, without any training for the site readers, which simulates day-to-day clinical practice. To our knowledge, there is no other baseline interpretation schema for neck nodal assessment using <sup>18</sup>F-FDG PET/CT scans that has undergone interreader reliability assessment at a multicenter level. The standardized qualitative criteria (12), such as Hopkins criteria (2), NI-RADS (13), Deauville (14), and Porceddu (15), are for post-therapy settings. The interreader reliability for SUV<sub>max</sub> readings between central and site readers appears lower than previously reported in single-center studies for interreader and intrareader agreements (16,17), which is likely due to statistical reporting as a dichotomous (based on SUV<sub>max</sub> cut points of 1.8 and 3.5) measure than a continuous measure.

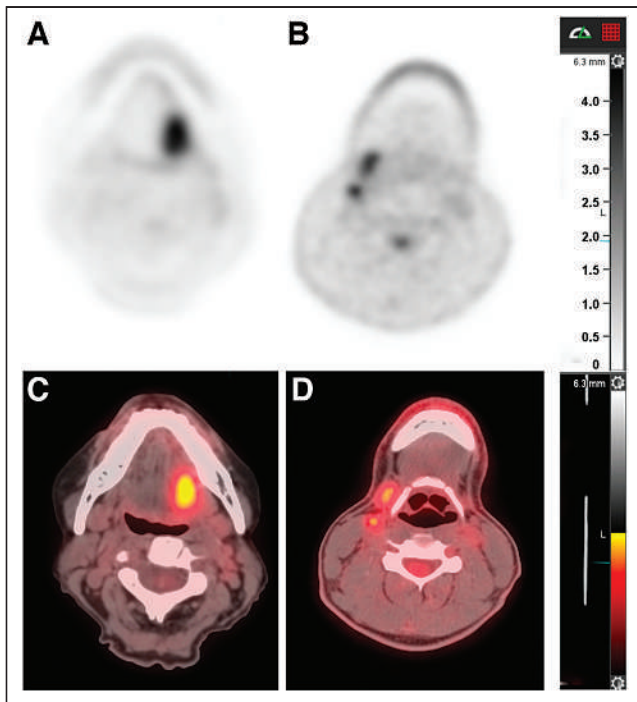


**FIGURE 2.** ACRIN 6685 visual analysis: positive and negative neck nodes. (A and C) Negative  $^{18}\text{F}$ -FDG PET and  $^{18}\text{F}$ -FDG PET/CT findings for neck nodes, with visual analysis demonstrating  $^{18}\text{F}$ -FDG uptake in left level IIA lymph nodes equal to or less than  $^{18}\text{F}$ -FDG uptake in adjacent blood vessels.  $\text{SUV}_{\text{max}}$  was 1.1. (B and D) Positive  $^{18}\text{F}$ -FDG PET and  $^{18}\text{F}$ -FDG PET/CT findings for neck nodes, with visual analysis demonstrating  $^{18}\text{F}$ -FDG uptake in right level IIA lymph node greater than  $^{18}\text{F}$ -FDG uptake in adjacent blood vessels.  $\text{SUV}_{\text{max}}$  was 3.4.

One of the limitations of the ACRIN 6685 reads was that no detailed neck nodal level visual interpretation was performed though  $\text{SUV}_{\text{max}}$  analysis was done. As the visual interpretation was recorded as side of the neck positive or negative for nodal metastasis, a global assessment was obtained. Another limitation for the  $\text{SUV}_{\text{max}}$  inter-reader agreement is readers may have recorded  $\text{SUV}_{\text{max}}$  of different lymph nodes at the same neck nodal level, which each reader considered positive and led to lower inter-reader agreement for  $\text{SUV}_{\text{max}}$  than observed in single-center studies.

## CONCLUSION

The NPV of the  $^{18}\text{F}$ -FDG PET/CT for N0 clinical neck was 86% or above for visual assessment (95% CI, 86%–88%) and

above 90% (95% CI, 90%–95%) for  $\text{SUV}_{\text{max}}$  cut points of 1.8 and 3.5. There is moderate to substantial agreement between central readers, between site reads and central adjudicated read, and central readers and central adjudicated read.

## DISCLOSURE

ACRIN 6685 was supported by the National Cancer Institute through grants U01 CA079778, U01 CA080098, CA180820, and CA180794. No other potential conflict of interest relevant to this article was reported.

## KEY POINTS

**QUESTION:** What is the NPV and reader reliability of  $^{18}\text{F}$ -FDG PET/CT for staging head and neck cancer with clinical N0 neck in a multicenter trial?

**PERTINENT FINDINGS:** The NPV of the  $^{18}\text{F}$ -FDG PET/CT for N0 clinical neck was 86% or above for visual assessment (95% CI, 86%–88%) and above 90% (95% CI, 90%–95%) for  $\text{SUV}_{\text{max}}$  cut points of 1.8 and 3.5 for the 2 expert readers and site reads, with moderate to substantial agreement between all readers.

**IMPLICATIONS FOR PATIENT CARE:**  $^{18}\text{F}$ -FDG PET/CT has very high NPV for staging clinical N0 neck and has moderate to substantial interreader reliability, especially between site and central readers, which is important for day-to-day clinical practice.

## REFERENCES

- Mehanna H, Wong W-L, McConkey CC, et al. PET-CT surveillance versus neck dissection in advanced head and neck cancer. *N Engl J Med.* 2016;374:1444–1454.
- Marcus C, Ciarallo A, Tahari AK, et al. Head and neck PET/CT: therapy response interpretation criteria (Hopkins Criteria)-interreader reliability, accuracy, and survival outcomes. *J Nucl Med.* 2014;55:1411–1416.
- Van den Wyngaert T, Helsen N, Carp L, et al. Fluorodeoxyglucose-positron emission tomography/computed tomography after concurrent chemoradiotherapy in locally advanced head-and-neck squamous cell cancer: the ECLYPS study. *J Clin Oncol.* 2017;35:3458–3464.
- Dibble EH, Lara Alvarez AC, Truong M-T, Mercier G, Cook EF, Subramaniam RM.  $^{18}\text{F}$ -FDG metabolic tumor volume and total glycolytic activity of oral cavity and oropharyngeal squamous cell cancer: adding value to clinical staging. *J Nucl Med.* 2012;53:709–715.
- Lowe VJ, Duan F, Subramaniam RM, et al. Multicenter trial of [ $^{18}\text{F}$ ]fluorodeoxyglucose positron emission tomography/computed tomography staging of head and neck cancer and negative predictive value and surgical impact in the N0 neck: results from ACRIN 6685. *J Clin Oncol.* 2019;37:1704–1712.

**TABLE 1**  
Diagnostic Test Statistics for Visual Assessment  $^{18}\text{F}$ -FDG PET/CT Scan Versus Pathology

Reader	Sensitivity	Specificity	PPV	NPV
Expert H&N reader 1	0.791 (0.677, 0.896)	0.584 (0.500, 0.665)	0.417 (0.325, 0.512)	0.881 (0.811, 0.942)
Expert H&N reader 2	0.683 (0.547, 0.810)	0.724 (0.646, 0.797)	0.466 (0.352, 0.583)	0.866 (0.801, 0.925)
Central adjudicated read	0.740 (0.629, 0.845)	0.644 (0.567, 0.716)	0.443 (0.349, 0.538)	0.866 (0.800, 0.924)
Site read	0.700 (0.581, 0.817)	0.699 (0.622, 0.774)	0.471 (0.370, 0.580)	0.859 (0.792, 0.917)

H&N = head and neck.

Data in parentheses are 95% CIs.

**TABLE 2**  
Diagnostic Test Statistics for the Dichotomized SUV<sub>max</sub> Result Versus Pathology

Reader	1.8 cutoff value for SUV <sub>max</sub>				3.5 cutoff value for SUV <sub>max</sub>			
	Sensitivity	Specificity	PPV	NPV	Sensitivity	Specificity	PPV	NPV
Expert H&N scan reader 1	0.471 (0.327, 0.623)	0.894 (0.862, 0.923)	0.268 (0.167, 0.381)	0.954 (0.931, 0.972)	0.300 (0.155, 0.459)	0.965 (0.942, 0.982)	0.412 (0.231, 0.611)	0.944 (0.919, 0.965)
Expert H&N scan reader 2	0.250 (0.109, 0.419)	0.900 (0.868, 0.929)	0.167 (0.070, 0.281)	0.938 (0.910, 0.962)	0.183 (0.062, 0.330)	0.967 (0.947, 0.983)	0.306 (0.116, 0.517)	0.937 (0.911, 0.961)
Combined central SUV <sub>max</sub>	0.507 (0.356, 0.652)	0.851 (0.814, 0.884)	0.225 (0.142, 0.315)	0.953 (0.930, 0.972)	0.267 (0.135, 0.412)	0.970 (0.952, 0.986)	0.435 (0.243, 0.634)	0.939 (0.915, 0.961)
Site read	0.395 (0.250, 0.548)	0.903 (0.874, 0.930)	0.263 (0.154, 0.383)	0.945 (0.920, 0.966)	0.250 (0.119, 0.395)	0.972 (0.955, 0.987)	0.442 (0.235, 0.658)	0.937 (0.912, 0.959)

H&N = head and neck.  
Data in parentheses are 95% CIs.

- Stack BC Jr, Duan F, Subramaniam RM, et al. FDG-PET/CT and pathology in newly diagnosed head and neck cancer: ACRIN 6685 trial, FDG-PET/CT cN0. *Otolaryngol Head Neck Surg.* 2021;164:1230–1239.
- Zheng D, Niu L, Liu W, et al. Relationship between the maximum standardized uptake value of fluoro-2-deoxyglucose-positron emission tomography/computed tomography and clinicopathological characteristics in tongue squamous cell carcinoma. *J Cancer Res Ther.* 2019;15:842–848.
- Zhao G, Sun J, Ba K, Zhang Y. Significance of PET-CT for detecting occult lymph node metastasis and affecting prognosis in early-stage tongue squamous cell carcinoma. *Front Oncol.* 2020;10:386.
- Linz C, Brands RC, Herterich T, et al. Accuracy of 18-F fluorodeoxyglucose positron emission tomographic/computed tomographic imaging in primary staging of squamous cell carcinoma of the oral cavity. *JAMA Netw Open.* 2021;4:e217083.
- Zhu F, Sun S, Ba K. Comparison between PET-CT-guided neck dissection and elective neck dissection in cT1-2N0 tongue squamous cell carcinoma. *Front Oncol.* 2020;10:720.
- Hu KS, Mourad WF, Gamez M, et al. Low rates of contralateral neck failure in unilaterally treated oropharyngeal squamous cell carcinoma with prospectively defined criteria of lateralization. *Head Neck.* 2017;39:1647–1654.
- Zhong J, Sundersingh M, Dyker K, et al. Post-treatment FDG PET-CT in head and neck carcinoma: comparative analysis of 4 qualitative interpretative criteria in a large patient cohort. *Sci Rep.* 2020;10:4086.
- Aiken AH, Rath TJ, Anzai Y, et al. ACR Neck Imaging Reporting and Data Systems (NI-RADS): a white paper of the ACR NI-RADS committee. *J Am Coll Radiol.* 2018;15:1097–1108.
- Koksel Y, Gencturk M, Spano A, Reynolds M, Roshan S, Caycı Z. Utility of Likert scale (Deauville criteria) in assessment of chemoradiotherapy response of primary oropharyngeal squamous cell cancer site. *Clin Imaging.* 2019;55:89–94.
- Porceddu SV, Pryor DI, Burmeister E, et al. Results of a prospective study of positron emission tomography-directed management of residual nodal abnormalities in node-positive head and neck cancer after definitive radiotherapy with or without systemic therapy. *Head Neck.* 2011;33:1675–1682.
- Mhlanga JC, Chirindel A, Lodge MA, Wahl RL, Subramaniam RM. Quantitative PET/CT in clinical practice: assessing the agreement of PET tumor indices using different clinical reading platforms. *Nucl Med Commun.* 2018;39:154–160.
- Shah B, Srivastava N, Hirsch AE, Mercier G, Subramaniam RM. Intra-reader reliability of FDG PET volumetric tumor parameters: effects of primary tumor size and segmentation methods. *Ann Nucl Med.* 2012;26:707–714.

# Safety and Efficacy of $^{166}\text{Ho}$ Radioembolization in Hepatocellular Carcinoma: The HEPAR Primary Study

Margot T.M. Reinders<sup>1</sup>, Karel J. van Erpecum<sup>2</sup>, Maarten L.J. Smits<sup>1</sup>, Arthur J.A.T. Braat<sup>1</sup>, Joep de Bruijne<sup>2</sup>, Rutger Bruijnen<sup>1</sup>, Dave Sprengers<sup>3</sup>, Robert A. de Man<sup>3</sup>, Erik Vegt<sup>4</sup>, Jan N.M. IJzermans<sup>5</sup>, Adriaan Moelker<sup>4</sup>, and Marnix G.E.H. Lam<sup>1</sup>

<sup>1</sup>Department of Radiology and Nuclear Medicine, University Medical Centre, Utrecht University, Utrecht, The Netherlands;

<sup>2</sup>Department of Gastroenterology and Hepatology University Medical Centre, Utrecht University, Utrecht, The Netherlands;

<sup>3</sup>Department of Gastroenterology and Hepatology, Erasmus MC–University Medical Centre, Rotterdam, The Netherlands;

<sup>4</sup>Department of Radiology and Nuclear Medicine, Erasmus MC–University Medical Centre, Rotterdam, The Netherlands; and

<sup>5</sup>Department of Surgery, Erasmus MC–University Medical Centre, Rotterdam, The Netherlands

The safety and efficacy of  $^{166}\text{Ho}$  radioembolization was first determined in the HEPAR and HEPAR II studies, which, however, excluded patients with hepatocellular carcinoma (HCC). The aim of this prospective clinical early phase II study was to establish the toxicity profile of  $^{166}\text{Ho}$  radioembolization in patients with measurable, liver-dominant HCC; Barcelona clinic liver cancer stage B or C; a Child–Pugh score of no more than B7; and an Eastern Cooperative Oncology Group performance status of 0–1 without curative treatment options. **Methods:** The primary endpoint was a rate of unacceptable toxicity defined as grade 3 hyperbilirubinemia (Common Terminology Cancer Adverse Events, version 4.03) in combination with a low albumin or ascites level in the absence of disease progression or treatment-related serious adverse events. Secondary endpoints included overall toxicity, response, survival, change in  $\alpha$ -fetoprotein, and quality of life. Thirty-one patients with Barcelona clinic liver cancer stage B (71%) or C (29%) HCC were included, mostly multifocal (87%) or bilobar (55%) disease. **Results:** Common grade 1 or 2 clinical toxicity included fatigue (71%), back pain (55%), ascites (32%), dyspnea (23%), nausea (23%), and abdominal pain (23%), with no more than 10% grade 3–5 toxicity. Grade 3 laboratory toxicity (>10%) included an aspartate transaminase and  $\gamma$ -glutamyltransferase increase (16%), hyperglycemia (19%), and lymphopenia (29%). Treatment-related unacceptable toxicity occurred in 3 of 31 patients. At 3 mo, 54% of target lesions showed a complete or partial response according to modified RECIST. Median overall survival was 14.9 mo (95% CI, 10.4–24.9 mo). No significant changes in quality of life or pain were observed. **Conclusion:** The safety of  $^{166}\text{Ho}$  radioembolization was confirmed in HCC, with less than 10% unacceptable toxicity. Efficacy data support further evaluation.

**Key Words:** hepatocellular carcinoma; radioembolization; holmium; oncology; locoregional treatment

J Nucl Med 2022; 63:1891–1898

DOI: 10.2967/jnumed.122.263823

**T**he treatment landscape for patients with hepatocellular carcinoma (HCC) consists of transplantation, resection, locoregional

treatment options (including ablation, transarterial chemoembolization, and radioembolization), and systemic treatment options (targeted therapy and immunotherapy) (1–3). Despite therapeutic advances, prognosis remains poor. Only a minority of patients is eligible for curative treatment (e.g., transplantation, resection, and in some cases ablation).  $^{90}\text{Y}$  radioembolization is often used in selected patients with HCC without curative treatment options (4).

Microspheres loaded with  $^{166}\text{Ho}$  have been commercially available since 2015 (QuiremScout and QuiremSpheres; Quirem Medical B.V.).  $^{166}\text{Ho}$  is a high-energy  $\beta$ -emitting isotope with a maximum energy of 1.85 MeV (50.0%) and 1.77 MeV (48.7%), comparable to the 2.28 MeV for  $^{90}\text{Y}$  but with a half-life of 26.8 h, which is approximately half that of  $^{90}\text{Y}$  (i.e., 64 h). The main advantage over  $^{90}\text{Y}$  is the abundance of  $\gamma$ -photons (81 keV, 6.7%) that can be used for SPECT/CT imaging (5). Furthermore, because the lanthanide  $^{166}\text{Ho}$  has paramagnetic properties, MRI can also be used to image the distribution in the liver and quantify the absorbed dose in the tumors (6). These unique characteristics improve pre- and posttherapeutic imaging options, enabling dosimetry-based individualized treatment planning. The mean diameter of  $^{166}\text{Ho}$ -microspheres is 30  $\mu\text{m}$ , with a range of 15–60  $\mu\text{m}$ , comparable to both types of  $^{90}\text{Y}$ -microspheres. The density of  $^{166}\text{Ho}$ -microspheres is 1.4  $\text{g}/\text{cm}^3$ , which is comparable to the density of resin  $^{90}\text{Y}$ -microspheres but lower than glass  $^{90}\text{Y}$ -microspheres.

The safety and efficacy of  $^{166}\text{Ho}$  radioembolization was first determined in the HEPAR and HEPAR II studies in patients with liver metastases of different types of cancer origin, excluding HCC (7,8). The aim of this clinical early phase II study was to establish the safety and toxicity profile of  $^{166}\text{Ho}$  radioembolization in patients with HCC.

## MATERIALS AND METHODS

### Study Population and Design

The HEPAR Primary study (NCT03379844) was a multicenter interventional, nonrandomized, noncomparative open-label early phase II study in patients with Barcelona clinic liver cancer (BCLC) stage B or C HCC, treated between January 28, 2018, and February 18, 2020. The study protocol was approved by the independent Medical Ethics Committee and was performed in accordance with good clinical practice and the declaration of Helsinki. All participants provided written informed consent.

The main inclusion and exclusion criteria were an age of at least 18 y with a life expectancy of at least 6 mo, a diagnosis of HCC according to

Received Jan. 15, 2022; revision accepted Apr. 18, 2022.

For correspondence, contact Margot T.M. Reinders (m.t.m.reinders@umcutrecht.nl); for reprint requests, contact Marnix G.E.H. Lam (m.lam@umcutrecht.nl).

Published online May 19, 2022.

COPYRIGHT © 2022 by the Society of Nuclear Medicine and Molecular Imaging.

the criteria of the American Association for the Study of Liver Disease (9), a measurable lesion based on RECIST (RECIST 1.1 and mRECIST), liver-dominant disease (a maximum of 5 lung nodules, all  $\leq 1.0$  cm, and mesenteric or portal lymph nodes, all  $\leq 2.0$  cm), no curative treatment options, a Child–Pugh score of B7 or less, an Eastern Cooperative Oncology Group (ECOG) performance status of 0 or 1, no prior radioembolization, and no main-branch portal vein thrombosis.

### Study Procedures

All patients were discussed by a multidisciplinary oncology board. Screening consisted of laboratory and physical examination, contrast-enhanced liver CT, liver MRI, hepatobiliary scintigraphy, and endoscopy of the upper gastrointestinal tract.

Patients received ondansetron, 8 mg, and dexamethasone, 10 mg, intravenously 1 h before angiography. Ursodeoxycholic acid, 300 mg twice daily, was given for 2 mo; prednisolone was given at a dose of 10 mg daily for the first month and 5 mg daily for the subsequent month (2 mo total), to reduce the chance of radioembolization-induced liver disease; and pantoprazole, 40 mg daily, was given for 6 wk (10).

A sheath was placed in the common femoral or radial artery, and a microcatheter was placed in the tumor-feeding artery or arteries. C-arm CT was performed at each intended target position. Then, a scout dose of  $^{166}\text{Ho}$ -microspheres was administered for treatment simulation (QuiremScout, 250 MBq,  $\sim 3$  million microspheres). The sheath stayed in situ during SPECT/CT imaging. Patients received treatment via a microcatheter at exactly the same position during a second angiography the same day.

The intended average absorbed dose in the perfused volume was 60 Gy:  $A$  (MBq) =  $3.781 \times W$  (g), where  $A$  is the prescribed activity in megabecquerels and  $W$  is the target liver mass in grams (1 mL = 1.04 g) (7,8). Approximately 24 h after treatment, MRI was performed and the patients were discharged. Three to 5 d after treatment, the patients came back for posttreatment SPECT/CT. This scan was delayed to prevent detector dead time caused by the abundance of  $\gamma$ -photons (5).

Posttreatment follow-up at 3 and 6 wk and at 3 and 6 mo included blood and physical examinations, questionnaires, hepatobiliary scintigraphy (at 3 mo), and MRI (at 3 and 6 mo) (Supplemental Table 1; supplemental materials are available at <http://jnm.snmjournals.org>). Adverse events were assessed according to the Common Terminology Criteria for Adverse Events (CTCAE), version 4.03. Furthermore, during screening, shortly after treatment, and during follow-up, the core 30 and HCC 18-question module quality-of-life questionnaires of the European Organization for Research and Treatment of Cancer were used, as well as the brief pain inventory (short form).

Two independent radiologists who were not involved in the study proceedings performed masked random response assessment. In cases of discordance, a third radiologist was consulted to determine the final response category.

Quarterly interim safety analyses were presented to an independent data safety monitoring board.

### Endpoints

The primary endpoint was the rate of unacceptable toxicity using CTCAE methodology, which was defined as grade 3 hyperbilirubinemia in combination with ascites and low albumin in the absence of disease progression (i.e., radioembolization-induced liver disease) or any serious adverse event or serious device defect possibly, probably, or causally related to treatment. Secondary endpoints included treatment efficacy, liver function, and quality of life. Dosimetric evaluation of pre- and posttreatment imaging fell outside the scope of this study.

### Statistical Analysis

As a null hypothesis, it was assumed that the probability of unacceptable toxicity was 10% and that the alternative was a probability of

unacceptable toxicity of 25%. Unacceptable toxicity of 10% or less was considered acceptable and 25% or more was not. Consequently, a sample size of 30 patients was deemed appropriate. Statistical power (85%) quantified the probability of stopping the study early if toxicity was unacceptably high (type II error, 15%), which was arguably equally as important as wrongly stopping the study in the absence of true high toxicity (type I error, 15%), in line with previous reports (7,8).

The results shown are based on the per-protocol set, comprising patients who received both scout and therapeutic  $^{166}\text{Ho}$ -microspheres. Overall survival was calculated from the date of treatment until the date of death by any cause or the end of registration (January 1, 2022). Kaplan–Meier curves and log-rank tests were used to evaluate overall survival. Responders (complete or partial response) and nonresponders (progressive or stable disease) were compared using landmark analysis with first and second response assessment. Variables with a 2-sided  $P$  value of less than 0.05 were deemed significant. Statistical analyses were performed using RStudio, version 1.2.5019.

## RESULTS

From December 15, 2017, until January 22, 2020, 41 patients were included in the study. Eight patients failed screening because of main-branch portal vein thrombosis ( $n = 2$ ), rapid tumor progression ( $n = 2$ ), alternative treatment ( $n = 1$ ), dismal liver function ( $n = 1$ ), low glomerular filtration rate ( $n = 1$ ), or worsened ECOG performance status ( $n = 1$ ). Two additional patients discontinued the study because of a significant lung shunt or because they chose an alternative treatment. In total, 31 patients were treated with a scout and therapeutic dose of  $^{166}\text{Ho}$ -microspheres (Fig. 1).

Baseline patient characteristics are given in Table 1. No cases with cavernous transformation were present. One patient previously underwent hemihepatectomy (right) followed by radiofrequency ablation of segments 2 and 3. One patient underwent resection of segments 6 and 7 and then underwent hemihepatectomy (right) followed by microwave ablation of segment 4, transarterial chemoembolization,

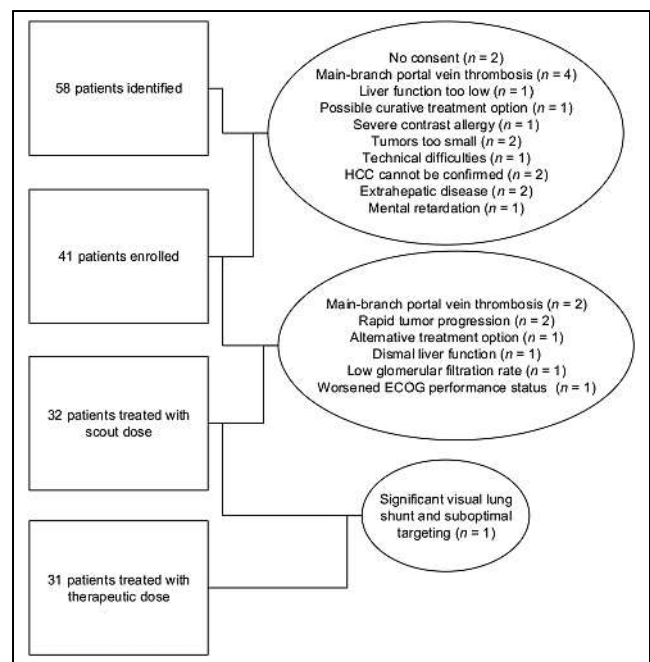


**FIGURE 1.** Flow diagram showing initial number of patients and those excluded for any given reason.

**TABLE 1**

**Baseline Characteristics of HEPAR Primary Patients (n = 31)**

Characteristic	Data	% or range
<b>Sex</b>		
Female	3	10
Male	28	90
Age (y)	73	44–85
Cirrhosis on imaging	20	65
<b>Underlying liver disease*</b>		
Alcohol abuse	20	65
Hepatitis B	1	3
Hepatitis C	4	13
Nonalcoholic fatty liver disease	3	10
Hemochromatosis	2	4
None of above	6	20
<b>BCLC</b>		
B	22	71
C	9	29
Bilirubin (μmol/L)	12	4–29
Albumin (g/L)	38.5	31–41.9
International normalized ratio	1.22	0.94–1.94
Thrombocytes (×10 <sup>9</sup> /L)	132	75–464
<b>Child–Pugh score</b>		
A5	19	61
A6	9	29
B7	3	10
Model-for-end-stage-liver-disease score	9	6–16
<b>ECOG performance status</b>		
0	18	58
1	13	42
<b>Extrahepatic lesions</b>		
None	27	87
Adrenal glands	4	13
<b>Portal hypertension</b>		
Thrombocytes < 150	18	58
<b>Varices</b>		
Small	9	29
Large	2	6
Imaging	14	45
<b>Portal vein thrombosis</b>		
Tumor thrombus	4	13
Nontumor thrombus	1	3
Mixed type	1	3
Bilobar disease†	17	55
<b>Number of tumors</b>		
1	4	13
2–3	4	13
>3	23	74
Tumor burden (%)	9.3	0.5–46.8
Largest tumor diameter (mm)	56	15 <sup>‡</sup> –195
<b>Previous treatment*</b>		
None	26	84
Resection	4	13
Ablation	4	13
Transarterial chemoembolization	1	1

\*Some patients had more than 1 underlying liver problem.

†Only Liver Imaging Reporting and Data System 5 (definitely HCC) lesions were considered.

‡Patient had more than 15 small lesions.

\*Some patients had more than 1 previous treatment.

Qualitative data are number and percentage; continuous data are median and range.

and wedge resection of segment 2. One patient underwent resection of segments 5 and 6 and microwave ablation of segment 4a. One patient underwent resection of segments 4b and 5. Finally, 1 patient previously underwent radiofrequency ablation of segments 6 and 7.

Treatment characteristics are summarized in Table 2. Unilobar treatment was performed in 20 of 31 (64%) patients, bilobar treatment (i.e., with at least 1 segment preserved) in 9 of 31 (29%), and whole-liver treatments in 2 of 31 (6%). Seven patients received a dose adjustment (median, –45%; range, –24%–56%) because of low hepatic function based on hepatobiliary scintigraphy (n = 4) or a per-procedural deviation from the planned treatment strategy (n = 3). The median absorbed dose to the target volume was 56 Gy (range, 27–90 Gy), and 23 patients received their intended dose. Twenty-eight patients received 1-d treatment. Three patients were treated at an interval of 7 d (n = 1), 35 d (reversible renal dysfunction, n = 1), or 168 d (malfunctioning aortic valve necessitating transarterial valve insertion first, n = 1). Median treatment efficiency (prescribed vs. net administered activity) was 95% (range, 74%–100%). On the basis of SPECT/CT imaging, the median anticipated lung dose resulting from shunting was 1 Gy (range, 0–16 Gy).

According to CTCAE, 120 laboratory-value adverse events were recorded, with no grade 4–5 events (Table 3). Furthermore, 168 clinical adverse events were observed, ranging from grades 1 to 5 (Table 4; Supplemental Tables 2 and 3). Most patients experienced a grade 1 or 2 increase in liver enzymes, with a maximum aspartate transaminase increase of grade 3 in 5 of 31 (16%) patients. However, the dynamic trajectory of these changes during 6 mo of follow-up did not show a clear peak or slope. Other than the expected lymphopenia, grade 2 or higher hematologic toxicity rarely occurred. Patients with type II diabetes mellitus (n = 14) experienced a high number of hyperglycemic adverse events, probably because of medication after treatment (i.e., steroids). Sixteen patients experienced grade 1 and 1 patient grade 2 back pain on the day of treatment, as they had to hold a supine position while undergoing a 1-d procedure.

Nineteen serious adverse events occurred, of which 4 events in 3 patients were related to treatment (3 possibly related and 1 definitely related). Two of these treatment-related events were from spontaneous bacterial peritonitis (both originated approximately 12 wk after treatment). One patient died of the infection after 1 d (treated with intravenous antibiotics), and the other patient recovered after 5 d (treated with intravenous and oral antibiotics). The third patient, with BCLC stage B, multifocal HCC, an ECOG performance status of 0, and previous treatment with resection and microwave ablation, experienced radiation-induced cholecystitis and cholangitis 1 mo after treatment, which developed into a biliary fistula (grade 3 bilirubin increase) and finally stabilized after endoscopic intervention. His liver function and clinical performance gradually declined until his death 1 y after treatment. Unrelated serious adverse events occurred more often in BCLC stage C patients (5/9 [56%]) than in BCLC stage B patients (4/22 [18%], P = 0.036). The treatment approach (i.e., uni- vs. bilobar) or previous liver-directed surgery could not be identified as a predictor of toxicity.

The median model-for-end-stage-liver-disease score was 9 (range, 6–16) at baseline and worsened to 10 (range, 7–20) at 6 mo after treatment. During 6 mo of follow-up, Child–Pugh scores fluctuated (Fig. 2). The 3 patients who experienced worsening of Child–Pugh score by 3 or 4 points (besides the patient with biliary fistula) had proven progression of disease. These patients received unilobar treatments and showed no signs of radioembolization-induced liver

**TABLE 2**  
Procedure Characteristics (n = 31)

Characteristic	Data	% or range
Liver volume (mL)	1,941	1,036–3,460
Treated fraction (%)	54	16–100
Anticipated perfused volume average absorbed dose		
Per protocol (60 Gy)	24	77
Dose adjustments	7	23
Actual perfused volume average absorbed dose (Gy)	50	23–69
Treatment approach; all in 1 session		
Unilobar	20	64
Bilobar (excluding some segments)	9	29
Whole liver	2	6
Number of injection positions		
1	15	48
2	16	52
Interval scout therapy (d)	0	0–168
Prescribed activity (MBq)	3,998	1,080–11,451
Net administered activity (MBq)	3,717	1,001–10,420
Treatment efficiency (%)	95	74–100
Lung shunt on SPECT/CT (Gy)	1	0–16

Qualitative data are number and percentage; continuous data are median and range.

**TABLE 3**  
Laboratory Adverse Events According to CTCAE, Version 4.03

Adverse event	Grade 1	Grade 2	Grade 3
AST increased	22/31 (71%)	2/31 (6%)	5/31 (16%)
Platelet count decreased	22/31 (71%)	1/31 (3%)	
INR increased	22/31 (71%)	2/31 (6%)	
AP increased	19/31 (61%)	5/31 (16%)	
Anemia	16/31 (52%)	5/31 (16%)	2/31 (6%)
ALT increased	15/31 (48%)	2/31 (6%)	
Hypoalbuminemia	14/31 (45%)	5/31 (16%)	1/31 (3%)
Prolonged APTT	13/31 (42%)	2/31 (6%)	
Hyponatremia	12/31 (39%)		3/31 (10%)
Hypokalemia	9/31 (29%)		
Hyperglycemia	9/31 (29%)	13/31 (42%)	6/31 (19%)
Creatinine increased	7/31 (23%)	1/31 (3%)	
Bilirubin increased	6/31 (19%)	4/31 (13%)	1/31 (3%)
GGT increased	5/31 (16%)	9/31 (29%)	14/31 (45%)
Hypoglycemia	3/31 (10%)		
Lymphopenia	1/31 (3%)	13/31 (42%)	9/31 (29%)

AST = aspartate transaminase; INR = international normalized ratio; AP = alkaline phosphatase; ALT = alanine transaminase; APTT = activated prothrombin time; GGT =  $\gamma$ -glutamyltransferase.

This table represents new and highest toxicity during 6-mo follow-up. No laboratory adverse events grade 4 or 5 were observed.

**TABLE 4**  
Clinical Adverse Events Occurring in More Than 10% Patients or Grade 3–5 According to CTCAE, Version 4.03

Adverse event	Grade 1	Grade 2	Grade 3	Grade 4	Grade 5
Back pain	16/31 (52%)	1/31 (3%)			
Fatigue	13/31 (42%)	4/31 (13%)			
Ascites	7/31 (23%)	2/31 (6%)	1/31 (3%)		
Dyspnea	7/31 (23%)				
Nausea	6/31 (19%)	1/31 (3%)			
Abdominal pain	4/31 (13%)	2/31 (6%)	1/31 (3%)		
Dizziness	4/31 (13%)				
Edema limbs	4/31 (13%)	1/31 (3%)			
Fever	4/31 (13%)				
Hepatic pain	4/31 (13%)				
Itch	3/31 (10%)	1/31 (3%)			
Abdominal infection			1/31 (3%)		
Allergic reaction			1/31 (3%)		
Arthritis			1/31 (3%)		
Atrial fibrillation			1/31 (3%)		
Bile duct stenosis			1/31 (3%)		
Biliary fistula			1/31 (3%)		
Cholecystitis			1/31 (3%)		
Endocarditis infective				1/31 (3%)	
Esophageal varices hemorrhage			2/31 (6%)		
Gastric hemorrhage			1/31 (3%)		
Hepatic failure					2/31 (6%)
Hip fracture			1/31 (3%)		
Intracranial hemorrhage					1/31 (3%)
Ischemia cerebrovascular					1/31 (3%)
Lung infection			1/31 (3%)		
Sepsis			1/31 (3%)		

This table represents new and highest toxicity during 6-mo follow-up.

disease during the first 3 mo after treatment. Two other patients died of progressive disease and hepatic failure within 6 mo (considered unlikely to be related to treatment). Stratification per Child–Pugh score or ECOG performance status did not show any significant differences.

Twenty-six patients were evaluable according to mRECIST at 3 mo (2 died, 3 had insufficient imaging quality), and 19 patients were evaluable at 6 mo (2 more died, 3 left the study because of disease progression, 2 were lost to follow-up).

Independent review of the target liver lesions on MRI at 3 mo after treatment found, according to mRECIST, that 19% had a complete response, 35% a partial response, 42% stable disease, and 4% progressive disease (Figs. 3 and 4). A variable response specifically by the tumor thrombus in the portal vein was observed in 5 patients: 1 complete response, 1 partial response, 2 stable disease, and 1 lost to follow-up.

Five patients started sorafenib treatment, and 4 patients received immunotherapy after study treatment. Median overall survival was 14.9 mo (95% CI, 10.4–24.9 mo) (Fig. 5). The median post-landmark analysis overall survival of patients with either a complete or partial response of the total body according to mRECIST

at 3 mo was 16.6 mo (95% CI, 8.72 mo–not reached); it was 13 mo for nonresponders (95% CI, 8.95 mo–not reached,  $P = 0.48$ ). The median overall survival of responders based on target liver lesions was not reached; for nonresponders, it was 12.8 mo (95% CI, 4.72–not reached,  $P = 0.046$ ) (Supplemental Fig. 1).

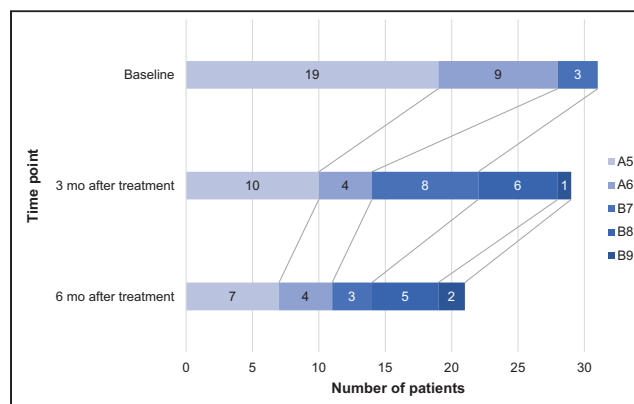


**FIGURE 2.** Child–Pugh score development over time.

The median  $\alpha$ -fetoprotein level was 20  $\mu\text{g/L}$  (range, 2.0–240,000  $\mu\text{g/L}$ ) at baseline, with a median nadir of 6.6  $\mu\text{g/L}$  (range, 2.0–120,000  $\mu\text{g/L}$ ; 67% decrease). At baseline, median liver function based on hepatobiliary scintigraphy was 5.3%/min/ $\text{m}^2$  (range, 2.0%–8.7%/min/ $\text{m}^2$ ), and 3 mo after treatment it was 4.4%/min/ $\text{m}^2$  (range, 1.8%–9.2%/min/ $\text{m}^2$ ) ( $P = 0.36$ ).

No clinically relevant change in quality of life (Supplemental Fig. 2) or pain (Supplemental Fig. 3) was observed.

## DISCUSSION

This first (to our knowledge) prospective study on  $^{166}\text{Ho}$ -microsphere radioembolization in HCC confirmed safety. During and after  $^{166}\text{Ho}$ -microsphere radioembolization, quality of life was maintained, and pain and toxicity were mild and manageable. Furthermore, a pronounced antitumor effect was found.

A low-activity scout dose of  $^{166}\text{Ho}$ -microspheres—limited enough not to cause tissue damage—can be used instead of the commonly used scout dose of  $^{99\text{m}}\text{Tc}$ -macroaggregated albumin particles ( $^{99\text{m}}\text{Tc}$ -MAA) (11). In contrast to  $^{99\text{m}}\text{Tc}$ -MAA, the scout dose of  $^{166}\text{Ho}$ -microspheres is not administered as a bolus injection, but slowly. The extrahepatic (i.e., lung shunting) and intrahepatic dose distribution can be predicted more accurately than for  $^{99\text{m}}\text{Tc}$ -MAA (12,13). A scout dose of  $^{166}\text{Ho}$ -microspheres was superior, with a median score of 4, versus 2.5 for  $^{99\text{m}}\text{Tc}$ -MAA ( $P < 0.001$ ; visually assessed from 1 to 5), which was confirmed in a quantitative

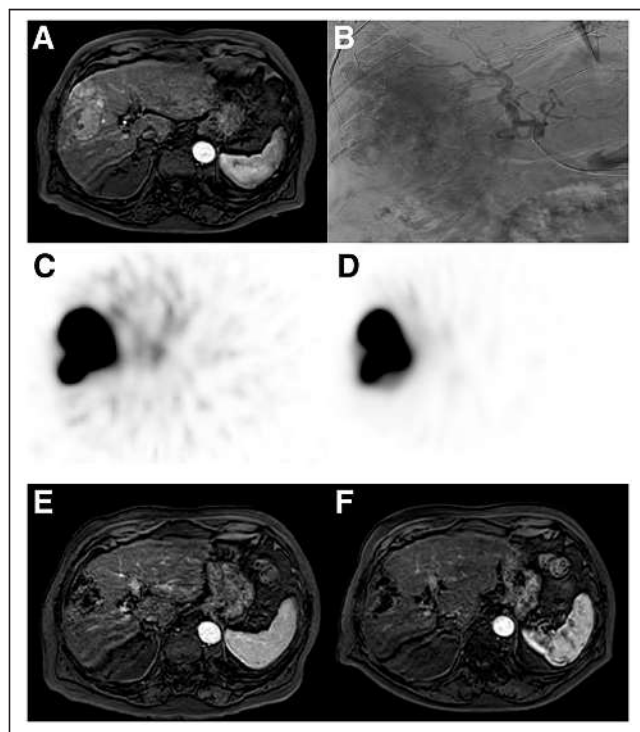


**FIGURE 3.** An 85-y-old patient with HCC, no underlying liver disease, and no previous treatment (ECOG performance status 1, Child-Pugh score A5, BCLC stage B) with large hypervascular tumor spanning segments 4–8 (A, axial contrast-enhanced MRI) that had multiple tumor-feeding vessels from right hepatic artery (B, digital subtraction angiography). He received  $^{166}\text{Ho}$ -microsphere scout procedure and SPECT (C), which showed good targeting of tumor. Scout procedure proved highly predictive for posttreatment  $^{166}\text{Ho}$ -microsphere distribution (D) and resulted in complete response of target liver lesions at 3 mo (E, axial contrast-enhanced MRI) and 6 mo (F, axial contrast-enhanced MRI).

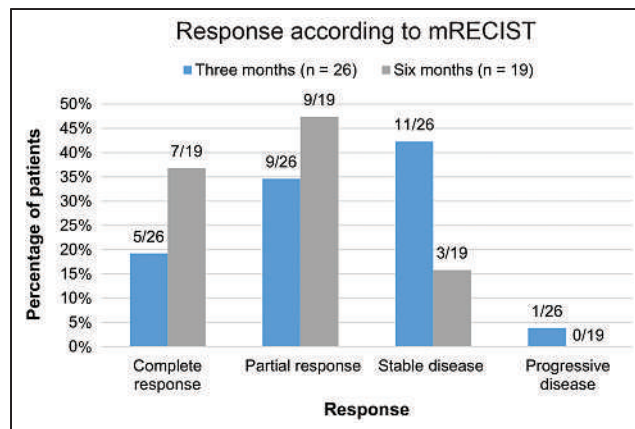


**FIGURE 4.** Response assessment of target liver lesions at 3 and 6 mo after treatment with  $^{166}\text{Ho}$ -microsphere radioembolization according to mRECIST. Some patients did not undergo imaging at 3- or 6-mo follow-up because of death ( $n = 2$  and 8, respectively) or withdrawn consent ( $n = 2$  or 0, respectively). Some patients were not evaluable because of absence of arterial enhancement of tumor or low-quality imaging (e.g., artifacts or breathing motion) ( $n = 3$  and 2, respectively).

analysis. In contrast, in the SARAH trial, in which  $^{99\text{m}}\text{Tc}$ -MAA was used as a scout, only 52% “optimal agreement” between pretreatment  $^{99\text{m}}\text{Tc}$ -MAA distribution and posttreatment resin  $^{90}\text{Y}$ -microsphere distribution was found (14).

The specific activity of  $^{166}\text{Ho}$ -microspheres (i.e.,  $\pm 340$  Bq/sphere) is higher than that of resin  $^{90}\text{Y}$ -microspheres (i.e.,  $\pm 50$  Bq/sphere) and lower than that of glass  $^{90}\text{Y}$ -microspheres (i.e.,  $\pm 1,250$ – $2,500$  Bq/sphere). At lower specific activities, a higher number of microspheres needs to be injected to reach the same absorbed dose. This is reflected in the relatively high incidence of adverse events related to the postembolization syndrome in the current study (e.g., pain [22%], nausea [22%], and fatigue [55%]). Moreover, differences in product characteristics will translate to different dose thresholds with regard to safety and efficacy, because of differences in dose distributions (15). For  $^{166}\text{Ho}$  radioembolization in HCC, these dose thresholds need to be established for patient selection and treatment planning. In 36 patients with a total of 98 tumors of different metastatic origins, a significant difference was found between patients with complete or partial response (210 Gy; 95% CI, 161–274 Gy) and patients with progressive disease (116 Gy; 95% CI, 81–165 Gy) (16). Additionally, dose

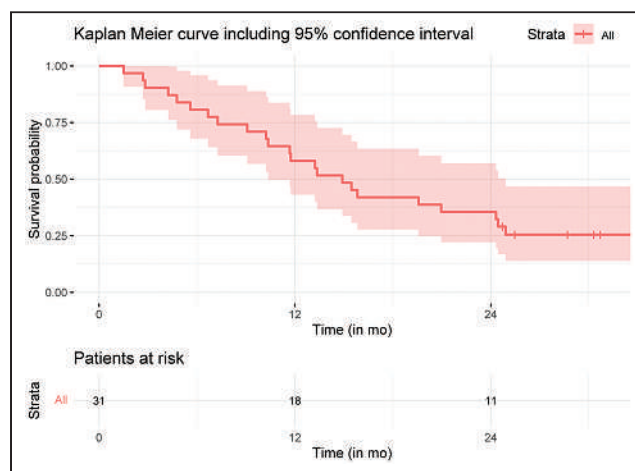


**FIGURE 5.** Overall survival of HEPAR Primary patients.

thresholds were confirmed in colorectal cancer, also looking at safety thresholds for nontumorous liver tissue. The median parenchyma-absorbed dose was 37 Gy (range, 12–55 Gy). The mean difference in parenchyma-absorbed dose for patients with CTCAE grade 0–2 versus CTCAE grade 3–5 was 12 Gy (95% CI, 3.4–19.7;  $P = 0.0070$ ) (17). For HCC patients, however, separate dose thresholds will need to be established, including considerations with regard to treatment intent (i.e., palliative setting as in the current setting vs. potential curative settings: radiation segmentectomy and lobectomy) (18,19).

These dosimetric considerations should be balanced with baseline patient characteristics such as laboratory values, Child–Pugh status, performance score, and BCLC stage. Because of the relatively low number of patients in the current study, no definite conclusions could be drawn on patient selection. At the same time, differences in patient characteristics between studies also limit direct comparison. The SARAH, SIRveNIB, and SORAMIC randomized controlled trials on resin  $^{90}\text{Y}$ -microsphere radioembolization (14,20–23), and the DOSISPHERE-01 study on glass  $^{90}\text{Y}$ -microsphere radioembolization (24), included more advanced-stage C BCLC, limiting toxicity and efficacy comparison. Nevertheless, a 23% rate of adverse events grade 3 or higher, a median overall survival of 14.9 mo, and a 3-mo response rate of 54% in the present study seem favorable. In the SARAH, SIRveNIB, and SORAMIC trials, adverse events of grade 3 or higher were observed in 27%, 28%, and 25% of the patients, respectively. The best overall response rate in the SARAH trial was 19%, the reported best tumor response in the SIRveNIB trial was 23.1%, and tumor response was not analyzed in the SORAMIC trial. The objective response rate was 35.7% in the patients in the DOSISPHERE-01 study, whose treatment was based on a predefined average absorbed dose in the perfused volume, as was used in the present study.

One of the limitations of this study was the relatively limited number of patients and the heterogeneous patient and disease characteristics, besides the fact that the study had a noncomparative design. In the current study, radioembolization treatment planning was performed according to a standard approach, regardless of tumor and functional liver dosimetry (25). A single-day treatment approach is beneficial from a patient perspective with regard to number of hospital visits, preparation, and recovery (24,26). However, a single-day treatment strategy does not allow for dosimetry-based treatment planning since patient-specific treatment activity needs to be preordered. Another limitation was that the methods used for response evaluation (modified RECIST [mRECIST]) have inherent limitations (e.g., local vs. systemic evaluation, relation to overall survival), but contrast enhancement on MRI may also be hampered by holmium-induced artifacts, since  $^{166}\text{Ho}$ -microspheres cause loss of signal on T1-weighted MRI scans and make it more difficult to measure viable tumor (6).

Concomitant use of different therapies in patients with HCC is of special interest, such as adjuvant immunotherapy after resection or ablation to decrease the chance of recurrence (27). But also of interest is the combination of immunotherapy with other local or regional treatment options, including transarterial chemoembolization and radioembolization (28,29). These combined approaches are expected to cause more toxicity, which may be seen as a clear call for more control. Radioembolization may offer that control by offering dosimetry-based individualized treatment planning.  $^{166}\text{Ho}$ -microsphere radioembolization offers the unique combination of procedural control and individualized treatment by using a predictive scout dose of the exact same  $^{166}\text{Ho}$ -microspheres and performing

treatment planning based on accurate dosimetry (12). However, dose thresholds for an effective tumor-absorbed dose and a safe functional liver-absorbed dose need to be established in larger series.

## CONCLUSION

This interventional, nonrandomized study showed an acceptable low rate of  $^{166}\text{Ho}$  radioembolization–related serious toxicity (3/31 patients; <10%) in patients with HCC. Furthermore, 54% of tumor lesions showed a response (mRECIST) at 3 mo after treatment.  $^{166}\text{Ho}$  radioembolization may be considered a safe and effective alternative treatment option in selected patients with HCC of BCLC stage B or C.

## DISCLOSURE

This study was financed mainly by a grant from the Dutch Cancer Society (KWF Kankerbestrijding, project 10307) and was financially supported by the Radiology and Nuclear Medicine Department of the University Medical Center Utrecht. Quirem Medical B.V. supplied the holmium microspheres free of charge. Margot Reinders acted as a speaker for Boston Scientific/BTG (personal fees) and was funded by the Dutch Cancer Society (KWF Kankerbestrijding) via a grant received by Marnix Lam. Karel van Erpecum was on the advisory board of AOP Orphan Pharmaceuticals AG in 2020 and is a member of HepNed and Hepatitis C Elimination in The Netherlands (CELINE—a cooperation between university medical centers in The Netherlands for elimination of hepatitis C viral infection from The Netherlands, sponsored by Gilead). Maarten Smits acted as a speaker for Boston Scientific/BTG (personal fees and nonfinancial support). Arthur Braat acted as a speaker for Boston Scientific/BTG (personal fees and nonfinancial support) and Terumo (nonfinancial support). Marnix Lam acted as a speaker for Boston Scientific/BTG (personal fees and nonfinancial support) and Terumo (nonfinancial support) and received a grant from the Dutch Cancer Society (KWF Kankerbestrijding). No other potential conflict of interest relevant to this article was reported.

## ACKNOWLEDGMENTS

We thank the patients for participating in this study; the independent radiologists Manon N.G.J.A. Braat and Frank J. Wessels for reviewing all the patient images; the Department of Radiology and Nuclear Medicine of the University Medical Centre Utrecht for cofunding this study; Tjitske Kent-Bosma (clinical research coordinator, University Medical Centre Utrecht) for contributing to study coordination; and the gastroenterology departments of both the University Medical Centre Utrecht and Erasmus MC University Medical Centre Rotterdam for recruiting patients.

## KEY POINTS

**QUESTION:** Is  $^{166}\text{Ho}$  radioembolization a safe treatment option for patients with HCC?

**PERTINENT FINDINGS:** This interventional, nonrandomized study showed an acceptably low rate of  $^{166}\text{Ho}$  radioembolization–related serious toxicity (3/31 patients; <10%) in patients with HCC. Furthermore, 54% of tumor lesions showed a response (mRECIST) at 3 mo after treatment.

**IMPLICATIONS FOR PATIENT CARE:**  $^{166}\text{Ho}$  radioembolization may be considered a safe and effective alternative treatment option in selected patients with HCC of BCLC stage B or C.

## REFERENCES

- Sangiovanni A, Colombo M. Treatment of hepatocellular carcinoma: beyond international guidelines. *Liver Int.* 2016;36(suppl 1):124–129.
- Finn RS, Qin S, Ikeda M, et al. Atezolizumab plus bevacizumab in unresectable hepatocellular carcinoma. *N Engl J Med.* 2020;382:1894–1905.
- Johnston MP, Khakoo SI. Immunotherapy for hepatocellular carcinoma: current and future. *World J Gastroenterol.* 2019;25:2977–2989.
- Kallini JR, Gabr A, Salem R, Lewandowski RJ. Transarterial radioembolization with yttrium-90 for the treatment of hepatocellular carcinoma. *Adv Ther.* 2016;33:699–714.
- Elschot M, Nijssen JFW, Dam AJ, de Jong HWAM. Quantitative evaluation of scintillation camera imaging characteristics of isotopes used in liver radioembolization. *PLoS One.* 2011;6:e26174.
- van de Maat GH, Seevinck PR, Elschot M, et al. MRI-based biodistribution assessment of holmium-166 poly(L-lactic acid) microspheres after radioembolisation. *Eur Radiol.* 2013;23:827–835.
- Smits MLJ, Nijssen JFW, van den Bosch MAAJ, et al. Holmium-166 radioembolisation in patients with unresectable, chemorefractory liver metastases (HEPAR trial): a phase 1, dose-escalation study. *Lancet Oncol.* 2012;13:1025–1034.
- Prince JF, van den Bosch MAAJ, Nijssen JFW, et al. Efficacy of radioembolization with <sup>166</sup>Ho-microspheres in salvage patients with liver metastases: a phase 2 study. *J Nucl Med.* 2018;59:582–588.
- Heimbach JK, Kulik LM, Finn RS, et al. AASLD guidelines for the treatment of hepatocellular carcinoma. *Hepatology.* 2018;67:358–380.
- Gil-Alzugaray B, Chopitea A, Iñarrairaegui M, et al. Prognostic factors and prevention of radioembolization-induced liver disease. *Hepatology.* 2013;57:1078–1087.
- Braat AJ, Prince JF, van Rooij R, Bruijnen RCG, van den Bosch M, Lam M. Safety analysis of holmium-166 microsphere scout dose imaging during radioembolisation work-up: a cohort study. *Eur Radiol.* 2018;28:920–928.
- Smits MLJ, Dassen MG, Prince JF, et al. The superior predictive value of <sup>166</sup>Ho-scout compared with <sup>99m</sup>Tc-macroaggregated albumin prior to <sup>166</sup>Ho-microspheres radioembolization in patients with liver metastases. *Eur J Nucl Med Mol Imaging.* 2020;47:798–806.
- Elschot M, Nijssen JFW, Lam MGEH, et al. <sup>99m</sup>Tc-MAA overestimates the absorbed dose to the lungs in radioembolization: a quantitative evaluation in patients treated with <sup>166</sup>Ho-microspheres. *Eur J Nucl Med Mol Imaging.* 2014;41:1965–1975.
- Hermann AL, Dieudonné A, Ronot M, et al. Relationship of tumor radiation-absorbed dose to survival and response in hepatocellular carcinoma treated with transarterial radioembolization with <sup>90</sup>Y in the SARAH study. *Radiology.* 2020;296:673–684.
- Pasciak AS, Abiola G, Liddell RP, et al. The number of microspheres in Y90 radioembolization directly affects normal tissue radiation exposure. *Eur J Nucl Med Mol Imaging.* 2020;47:816–827.
- Bastiaannet R, van Roekel C, Smits MLJ, et al. First evidence for a dose-response relationship in patients treated with <sup>166</sup>Ho radioembolization: a prospective study. *J Nucl Med.* 2020;61:608–612.
- van Roekel C, Bastiaannet R, Smits MLJ, et al. Dose-effect relationships of <sup>166</sup>Ho radioembolization in colorectal cancer. *J Nucl Med.* 2021;62:272–279.
- Salem R, Padia SA, Lam M, et al. Clinical and dosimetric considerations for Y90: recommendations from an international multidisciplinary working group. *Eur J Nucl Med Mol Imaging.* 2019;46:1695–1704.
- Levillain H, Bagni O, Deroose CM, et al. International recommendations for personalised selective internal radiation therapy of primary and metastatic liver diseases with yttrium-90 resin microspheres. *Eur J Nucl Med Mol Imaging.* 2021;48:1570–1584.
- Vilgrain V, Pereira H, Assenat E, et al. Efficacy and safety of selective internal radiotherapy with yttrium-90 resin microspheres compared with sorafenib in locally advanced and inoperable hepatocellular carcinoma (SARAH): an open-label randomised controlled phase 3 trial. *Lancet Oncol.* 2017;18:1624–1636.
- Chow PKH, Gandhi M, Tan SB, et al. SIRveNIB: selective internal radiation therapy versus sorafenib in Asia-Pacific patients with hepatocellular carcinoma. *J Clin Oncol.* 2018;36:1913–1921.
- Ricke J, Bulla K, Kolligs F, et al. Safety and toxicity of radioembolization plus sorafenib in advanced hepatocellular carcinoma: analysis of the European multicentre trial SORAMIC. *Liver Int.* 2015;35:620–626.
- Ricke J, Klumpen HJ, Amthauer H, et al. Impact of combined selective internal radiation therapy and sorafenib on survival in advanced hepatocellular carcinoma. *J Hepatol.* 2019;71:1164–1174.
- Garin E, Tselikas L, Guiu B, et al. Personalised versus standard dosimetry approach of selective internal radiation therapy in patients with locally advanced hepatocellular carcinoma (DOSISPHERE-01): a randomised, multicentre, open-label phase 2 trial. *Lancet Gastroenterol Hepatol.* 2021;6:17–29.
- Bastiaannet R, Kappadath SC, Kunnen B, Braat A, Lam M, de Jong H. The physics of radioembolization. *EJNMMI Phys.* 2018;5:22.
- van Roekel C, Harlianto NI, Braat A, et al. Evaluation of the safety and feasibility of same-day holmium-166: radioembolization simulation and treatment of hepatic metastases. *J Vasc Interv Radiol.* 2020;31:1593–1599.
- Hack SP, Spahn J, Chen M, et al. IMbrave 050: a phase III trial of atezolizumab plus bevacizumab in high-risk hepatocellular carcinoma after curative resection or ablation. *Future Oncol.* 2020;16:975–989.
- Makary MS, Khandpur U, Cloyd JM, Mumtaz K, Dowell JD. Locoregional therapy approaches for hepatocellular carcinoma: recent advances and management strategies. *Cancers (Basel).* 2020;12:1914.
- Waidmann O. Recent developments with immunotherapy for hepatocellular carcinoma. *Expert Opin Biol Ther.* 2018;18:905–910.

---

---

# Noninvasive Assessment of Acute Graft-Versus-Host Disease of the Gastrointestinal Tract After Allogeneic Hemopoietic Stem Cell Transplantation Using $^{18}\text{F}$ -FDG PET

Martin H. Cherk<sup>1,2</sup>, Robert Khor<sup>1</sup>, Thomas W. Barber<sup>1,2</sup>, Kenneth S.K. Yap<sup>1,2</sup>, Sushrut Patil<sup>2,3</sup>, Patricia Walker<sup>3</sup>, Sharon Avery<sup>2,3</sup>, Stuart Roberts<sup>2,4</sup>, William Kemp<sup>2,4</sup>, Alan Pham<sup>2,5</sup>, Michael Bailey<sup>6</sup>, and Victor Kalff<sup>1,2</sup>

<sup>1</sup>Department of Nuclear Medicine & PET, Alfred Hospital, Melbourne Australia; <sup>2</sup>Monash University, Melbourne, Australia; <sup>3</sup>Department of Haematology, Alfred Hospital, Melbourne, Australia; <sup>4</sup>Department of Gastroenterology, Alfred Hospital, Melbourne, Australia; <sup>5</sup>Department of Anatomical Pathology, Alfred Hospital, Melbourne, Australia; and <sup>6</sup>Department of Epidemiology and Preventive Medicine, Monash University, Melbourne, Australia

Acute graft-versus-host disease of the gastrointestinal tract (acute GIT-GVHD) often complicates allogeneic hemopoietic stem cell transplantation (AH SCT).  $^{18}\text{F}$ -FDG PET/CT is known to detect active inflammation and may be a useful noninvasive test for acute GIT-GVHD. The objective of this study was to evaluate the diagnostic utility of  $^{18}\text{F}$ -FDG PET/CT to noninvasively assess patients with clinically suspected acute GIT-GVHD. Fifty-one AH SCT patients with clinically suspected acute GIT-GVHD prospectively underwent  $^{18}\text{F}$ -FDG PET/CT scanning followed by upper and lower GIT endoscopy within 7 d. Endoscopic biopsies of 4 upper GIT and 4 colonic segments were obtained for histology to compare with corresponding quantitative segmental  $^{18}\text{F}$ -FDG PET/CT  $\text{SUV}_{\text{max}}$ . Receiver-operating-characteristic curve (ROC) analysis was performed to determine predictive capacity of  $^{18}\text{F}$ -FDG PET/CT  $\text{SUV}_{\text{max}}$  for acute GIT-GVHD. A separate qualitative visual  $^{18}\text{F}$ -FDG PET/CT analysis was also performed for comparison. **Results:** Twenty-three of 51 (45.1%) patients had biopsy-confirmed acute GIT-GVHD, with 19 of 23 (82.6%) having upper GIT and 22 of 22 (100%) colonic involvement. One of 23 patients did not undergo a colonoscopy. GVHD involved the entire colon contiguously in 21 of 22 patients. For quantitative analysis, histology from 4 upper GIT and 4 colonic segments were compared with  $^{18}\text{F}$ -FDG PET/CT  $\text{SUV}_{\text{max}}$ . Colonic segments positive for GVHD had a higher  $\text{SUV}_{\text{max}}$  (4.1 [95% CI, 3.6–4.5]) than did normal colonic segments (2.3 [1.9–2.7],  $P = 0.006$ ). No difference was demonstrated in upper GIT segments. Quantitative  $^{18}\text{F}$ -FDG PET/CT yielded a 69% sensitivity, 57% specificity, 73% negative predictive value, and 59% positive predictive value for the detection of GVHD compared with 70%, 76%, 76%, and 68%, respectively, for qualitative analysis. **Conclusion:**  $^{18}\text{F}$ -FDG PET is a useful noninvasive diagnostic test for acute GIT-GVHD, which when present always involves the colon and usually in its entirety, suggesting colonic biopsy obtained by sigmoidoscopy is adequate for histologic confirmation when acute GIT-GVHD is suspected. Of note,  $^{18}\text{F}$ -FDG PET cannot distinguish acute GIT-GVHD from non-GVHD inflammatory changes in the colon.

**Key Words:**  $^{18}\text{F}$ -FDG PET/CT; bone marrow transplantation; graft vs. host disease; gastrointestinal tract

**J Nucl Med 2022; 63:1899–1905**  
DOI: 10.2967/jnumed.121.263688

---

Received Jan. 3, 2022; revision accepted Apr. 8, 2022.  
For correspondence or reprints, contact Martin Cherk (m.cherk@alfred.org.au).  
Published online Apr. 21, 2022.  
COPYRIGHT © 2022 by the Society of Nuclear Medicine and Molecular Imaging.

**A**llogeneic hemopoietic stem cell transplantation (AH SCT) offers cure for various life-threatening hematologic malignancies and disorders. The number of transplants performed each year continues to increase (1). Acute graft-versus-host disease (AGVHD) is a recognized complication occurring in 30%–50% of AH SCT recipients (2). It carries significant morbidity and a 25% mortality rate within 100 d of AH SCT (3). Although AGVHD may affect any organ system, there is a strong predilection for involvement of the skin, gastrointestinal tract (GIT), and liver (4).

Acute GIT-GVHD is commonly suspected on the basis of diarrhea after AH SCT. However, the possible differentials are wide and include GVHD, infectious causes such as *Clostridioides difficile* and cytomegalovirus colitis, drug effects, and chemoradiation toxicity. The current gold standard for acute GIT-GVHD diagnosis is histology acquired via endoscopic biopsy, characterized by crypt cell apoptosis and crypt loss (5). However, endoscopy is an invasive procedure and not without risk. Anesthetic risk, bleeding, and perforation are all potential complications associated with endoscopy, particularly in post-AH SCT patients who are unwell and often thrombocytopenic (6).

Currently, there is no established role for conventional imaging in the diagnosis of acute GIT-GVHD (7). It has been observed that  $^{18}\text{F}$ -FDG PET/CT is a sensitive and specific biomarker of acute large and small bowel inflammation in inflammatory bowel disease (8). Furthermore, 2 pilot studies have reported that PET has a negative predictive value (81%–96%) in the assessment of acute GIT-GVHD (9,10), but data remain sparse in this area.

This prospective study aims to evaluate the diagnostic utility of  $^{18}\text{F}$ -FDG PET for acute GIT-GVHD and to determine its role as a noninvasive test for this condition.

## MATERIALS AND METHODS

### Study Design and Patient Selection

This study was conducted at the Alfred Hospital Melbourne, Australia. Written signed, informed consent was obtained from each participant in accordance with the Declaration of Helsinki and approval from the Alfred Hospital research ethics committee. From December 2009 to November 2014, 51 adult patients with clinically suspected acute GIT-GVHD within 180 d of AH SCT who had not commenced any treatment for GVHD, including steroids, were prospectively enrolled into a noninterventional study comparing  $^{18}\text{F}$ -FDG PET/CT, endoscopy, and histology.

Clinically suspected acute GIT-GVHD symptoms included persistent diarrhea, abdominal pain, anorexia, nausea, vomiting, or any combination of these symptoms within 180 d of AHSCT with no other apparent cause.

There were no restrictions to entry into study relating to underlying hematologic disorder, stem cell source, or conditioning regimen.

The stem cell source was peripheral blood (PBSC) in 46 cases (90%) and double umbilical cord blood in the remaining 5 cases (10%). Of the 46 PBSC donors, 2 (4%) were human leukocyte antigen (HLA)-identical sibling donors, a further 13 (28%) were HLA-matched related donors, 29 (63%) were HLA-matched unrelated donors, and 2 (4%) were mismatched unrelated donors. The 5 double umbilical cord blood donations showed variable levels of HLA matching.

Twenty-four patients (47%) received a standard myeloablative conditioning regimen (total-body irradiation based), whereas 13 patients (25%) received a reduced-intensity conditioning and 14 received nonmyeloablative conditioning (27%). Sixteen patients received equine antithymocyte globulin as part of the conditioning regimen. For GVHD prophylaxis, patients who underwent a myeloablative conditioning received cyclosporin, usually with short-course methotrexate. Patients in the reduced-intensity conditioning or nonmyeloablative groups received cyclosporin and mycophenolate mofetil or cyclosporin alone.

Patient and AHSCT characteristics are summarized in Table 1.

### <sup>18</sup>F-FDG PET/CT Evaluation

All participants with clinically suspected acute GIT-GVHD symptoms underwent <sup>18</sup>F-FDG PET/CT scanning.

Participants were asked to fast and refrain from vigorous activity for at least 6 h before imaging. Administered <sup>18</sup>F-FDG activity was 3 MBq/kg to a maximum of 400 MBq. Molecular imaging was performed on a Gemini PET/CT scanner (Philips) with scan range extending from the skull base to the proximal femora, 60–80 min after intravenous injection of <sup>18</sup>F-FDG (3 MBq/kg). Low-dose coregistered CT was used for anatomic localization and attenuation correction.

All images were interpreted independently by nuclear medicine specialists experienced in <sup>18</sup>F-FDG PET/CT masked to all investigation results including endoscopy. Results of the <sup>18</sup>F-FDG PET/CT scan were not made available to the patient's treating clinicians and did not influence subsequent clinical management of the patient.

### Quantitative <sup>18</sup>F-FDG PET/CT Analysis

For quantitative <sup>18</sup>F-FDG PET/CT analysis, the GIT was divided into 8 segments: 4 upper GIT segments (esophagus, stomach, duodenum, and terminal ileum) and 4 lower GIT segments (ascending colon, transverse colon, descending colon, and sigmoid/rectum) using the accompanying low-dose CT for anatomic localization.

The highest intensity region within each of the 8 GIT segments was ascertained visually by 2 readers and the SUV<sub>max</sub> of this region measured and recorded independently with a standardized 2-dimensional (2D) planar region of interest in the sagittal plane for the esophagus; transaxial plane for the stomach, duodenum, terminal ileum, and sigmoid/rectum; and coronal plane for the ascending, transverse, and descending colon. The size of the 2D planar region of interest varied according to the GIT segment evaluated to ensure there was no overlap of other organs, and only the SUV<sub>max</sub> in the target GIT segment was measured. A 15-mm 2D circular region of interest was placed in the central lumen of the ascending aorta and SUV<sub>mean</sub> recorded to establish background mediastinal blood-pool <sup>18</sup>F-FDG uptake as a reference. The average SUV<sub>max</sub> between both expert readers for each GIT segment was used for comparison with histology findings.

To evaluate overall <sup>18</sup>F-FDG activity in the entire colon, the parameters Min L4, Max L4, and Sum L4 were used. Min L4 and Max L4 described the lowest and highest SUV<sub>max</sub> of the ascending, transverse,

**TABLE 1**  
Patient Characteristics

Characteristic	Study population (n = 51)
Median patient age (y)	46.5 (age range, 19.6–66.8)
Patient sex	
Male	28 (54)
Female	23 (46)
CMV status	
Seronegative donor-recipient pair	12 (24)
Underlying diagnosis	
AML	21 (41)
ALL	9 (18)
MM	11 (22)
MDS	3 (6)
NHL	4 (8)
HL	1 (2)
Other (adrenoleukodystrophy and BPD)	2 (4)
Stem cell source	
PBSC	46 (90)
DUCB	5 (10)
HLA matching	
MRD	15 (29)
MUD	29 (57)
MISUD	7 (14)
Conditioning regimen	
MAC	24 (47)
RIC	13 (25)
NMAC	14 (27)
ATG	
Yes	16 (31)
No	35 (69)
GVHD prophylaxis	
CsA	10 (20)
CsA + MMF	22 (43)
CsA + MTX	19 (37)

Data in parentheses are percentages, unless otherwise indicated.

CMV = cytomegalovirus; AML = acute myeloid leukemia; ALL = acute lymphoblastic leukemia; MM = multiple myeloma; MDS = myelodysplastic syndrome; NHL = non-Hodgkin lymphoma; HL = Hodgkin lymphoma; BPD = blastic plasmacytoid dendritic cell neoplasm; PBSC = peripheral blood stem cell; DUCB = double unit cord blood; MRD = matched related donor; MUD = matched unrelated donor; MISUD = mismatched unrelated donor; MAC = myeloablative conditioning; RIC = reduced intensity conditioning; NMAC = non-myeloablative conditioning; ATG = antithymocyte globulin; CsA = cyclosporin A; MMF = mycophenolate mofetil; MTX = methotrexate.

descending, and sigmoid/rectal colon segments, respectively. Sum L4 described the combined SUV<sub>max</sub> of ascending, transverse, descending, and sigmoid/rectal colon segments.

### Qualitative <sup>18</sup>F-FDG PET/CT Analysis

For qualitative <sup>18</sup>F-FDG PET/CT analysis, the scan was considered positive for acute GIT-GVHD if there was visually increased <sup>18</sup>F-FDG uptake greater than 1.5 times background liver uptake involving at least 50% of one or more upper GIT or colonic segments. In the event of disagreement between both expert readers, a third masked expert reader was used to determine the final <sup>18</sup>F-FDG PET/CT result.

<sup>18</sup>F-FDG PET/CT findings were compared with histology, with patients considered positive for acute GIT-GVHD if they had histologic evidence of GVHD in at least 1 upper GIT or colonic segment.

### Diagnosis of Acute GIT-GVHD

Gastroscopy and colonoscopy were aimed to be performed within 7 d of the <sup>18</sup>F-FDG PET/CT examination, using a segmental unmasking method outlined as follows. Endoscopists were initially masked to the results of the <sup>18</sup>F-FDG PET/CT and were asked to macroscopically assess 4 upper GIT segments (esophagus, stomach, duodenum, and terminal ileum) and 4 colonic segments (ascending colon, transverse colon, descending colon, and sigmoid/rectum) for active inflammation.

The results of the <sup>18</sup>F-FDG PET/CT were then revealed to the endoscopists during endoscopy. Two biopsies were taken of each segment that appeared normal on both <sup>18</sup>F-FDG PET/CT and macroscopically on endoscopy. Four biopsies were taken of each segment that was abnormal on either <sup>18</sup>F-FDG PET/CT, macroscopic assessment, or both. Hence, a total of 16–32 upper to lower GIT biopsies were obtained in each participant undergoing both gastroscopy and colonoscopy. All segments able to be endoscopically visualized were biopsied.

### Histology

Each segmental GIT biopsy was deemed positive or negative for acute GVHD by a pathologist experienced in GVHD interpretation who was masked to both the <sup>18</sup>F-FDG PET/CT and the endoscopy macroscopic findings. Bacterial, viral (including cytomegalovirus), parasitic culture and *C. difficile* toxin and culture testing was also performed and documented to confirm or exclude other potential causes of non-GVHD inflammation.

### Statistical Methods

All data were assessed for normality. Group comparisons of individual location data were performed using Student *t* tests and reported as mean ( $\pm$ SD) while comparison of repeated measures data was performed using repeated-measures ANOVA with results reported as mean (with 95% CI). To further explore the predictive capacity of colonic locations, summary statistics (minimum, maximum, total) were calculated. For quantitative assessment of the relationship between acute GIT-GVHD and SUV<sub>max</sub>, sensitivity, specificity, negative predictive value (NPV) and positive predictive value (PPV) were determined from receiver-operating-characteristic curves (ROC) derived from logistic regression. Qualitative assessment was determined by consensus expert visual interpretation of scans. Statistical analysis was performed using SAS (version 9.4; SAS Institute), and a 2-sided *P* value of 0.05 was used to indicate statistical significance.

## RESULTS

### Patients

Fifty-one patients were enrolled and underwent <sup>18</sup>F-FDG PET/CT within a median of 47 d (range, 12–166 d) after AHSCT. Median time from onset of clinical symptoms suggestive of acute GIT-GVHD to <sup>18</sup>F-FDG PET/CT examination was 6 d (range, 0–69 d). Four patients had diabetes and 4 had a history of steroid induced hyperglycemia; however, none was taking metformin. Twenty-two patients had clinical evidence of cutaneous GVHD, whereas 5 patients

had elevated bilirubin suggestive of grade I-II hepatic GVHD (only 1 proven case of hepatic GVHD).

### Endoscopic Findings

Participants underwent endoscopy within an average of 3 d (range, 0–13 d) of <sup>18</sup>F-FDG PET/CT scanning. Two patients were outside the target 7-d period after <sup>18</sup>F-FDG PET/CT scanning; 1 patient at 8 d was delayed due to severe illness and the other required urgent treatment for pericardial effusion receiving endoscopy 13 d after <sup>18</sup>F-FDG PET/CT.

Eight of 51 (16%) patients did not have all 8 GIT segments biopsied due to logistical reasons or being too acutely unwell. Of these, 1 patient had a rectal biopsy only, 1 patient did not have gastroscopy, 4 patients did not have colonoscopy, and 2 patients had no biopsy of the terminal ileum. Details of endoscopic pathology data in prespecified GIT segments are presented in the Supplemental Table 1 (supplemental materials are available at <http://jnm.snmjournals.org>).

### Per-Patient Histology Findings and Treatment

Twenty-three of 51 (45.1%) patients had biopsy-confirmed acute-GIT GVHD. Nineteen of 23 (83%) had upper GIT and 22 of 23 (96%) colonic involvement. One of 23 GVHD-positive patients did not have colonic biopsies. Twenty-one of 22 (95%) patients with colonic GVHD had contiguous involvement of the entire colon. Fourteen of 51 (27%) patients had non-GVHD inflammation (6 cytomegalovirus infection, 3 *C. difficile* infection, 5 non-specific esophagitis and gastritis). Fourteen of 51 (27%) patients had normal upper GIT and colonic segments.

Twenty-one of 23 (91%) patients with histologically proven acute GIT-GVHD required steroid treatment for clinical symptoms, 13 of 21 intravenous methylprednisolone, and 8 of 21 oral budesonide or prednisolone.

### Per-GIT Segment Histology Findings

Of the intended GIT segments, 376 (191 upper GIT/185 colonic) of 408 (92%) were biopsied in 51 patients: 131 of 376 (35%) were positive for GVHD (52 upper GIT/79 colonic), 42 of 376 (11%) were positive for non-GVHD inflammation (25 upper GIT/17 colonic), 199 of 376 (53%) (113 upper GIT/86 colonic) were normal, and 4 of 376 (1.0%) were equivocal for GVHD (1 upper GIT/3 colonic).

### Relationship of <sup>18</sup>F-FDG PET/CT SUV<sub>max</sub> with Histology

No difference in SUV<sub>max</sub> was demonstrated in normal upper GIT segments (2.38 [95% CI, 2.24–2.52]) or those with GVHD (2.57 [95% CI, 2.36–2.77]) or non-GVHD inflammation (2.63 [95% CI, 2.34–2.91]) (Fig. 1A).

SUV<sub>max</sub> was significantly increased in both colonic segments with GVHD (4.06 [95% CI, 3.64–4.47]) and non-GVHD inflammation (5.03 [95% CI, 4.13–5.93]) compared with normal colonic segments (2.29 [95% CI, 1.89–2.69]) (Fig. 1B).

<sup>18</sup>F-FDG PET/CT and histology images of patient 49 are provided as an example of a positive case of acute GVHD involving both the upper GIT and colon on histology with <sup>18</sup>F-FDG uptake only visibly increased in the colon on <sup>18</sup>F-FDG PET/CT (Fig. 2).

GIT segment histology and corresponding SUV<sub>max</sub> for all 51 patients are provided in Supplemental Table 2.

### Quantitative <sup>18</sup>F-FDG PET/CT SUV<sub>max</sub> Analysis

Upper GIT and colonic segment <sup>18</sup>F-FDG PET/CT SUV<sub>max</sub> were compared between the 23 patients positive and 28 patients

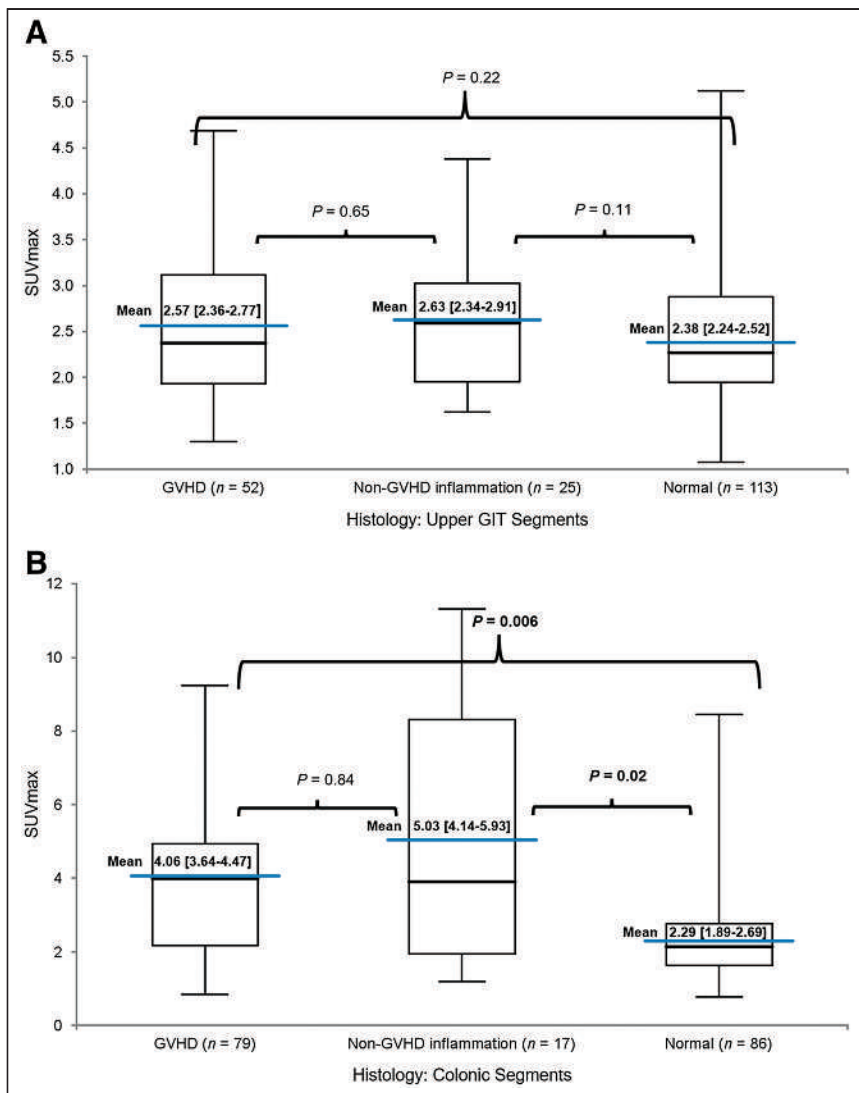


**FIGURE 1.** (A) Upper GIT segments. (B) Colonic segments.

negative for acute GIT-GVHD (Table 2). Patients positive for GVHD had significantly higher SUV<sub>max</sub> in all colonic segments other than ascending colon than did patients negative for GVHD. The minimum SUV<sub>max</sub> in any of the 4 colonic segments (Min L4) was significantly higher in GVHD-positive patients than GVHD-negative patients. Similarly, the total SUV<sub>max</sub> of all 4 colonic segments (Sum L4) was also significantly higher in GVHD-positive patients than GVHD-negative patients. No difference in SUV<sub>max</sub> was demonstrated in any of the 4 upper GIT segments between GVHD-positive and -negative patients.

Area under receiver-operating-characteristic curve (AUROC) analysis demonstrated <sup>18</sup>F-FDG PET/CT SUV<sub>max</sub> of all colonic segments other than ascending colon was independently predictive of acute GIT-GVHD (Table 3). The Min L4 ROC curve was chosen to generate sensitivity, specificity, NPV, and PPV for GVHD as it had the highest AUROC and took into account all colonic segments.

As seen from the Min L4 ROC curve in Figure 3, a Min L4 of 1.73 (uptake greater than mean background mediastinal blood-pool activity) resulted in a sensitivity of 69%, specificity of 57%, NPV of 73%, and PPV of 59% for the detection of acute GIT-GVHD.

### Qualitative <sup>18</sup>F-FDG PET/CT Analysis

<sup>18</sup>F-FDG PET/CT scans of all 51 patients were qualitatively visually assessed for acute GIT-GVHD in the upper GIT and colon. Both expert readers were concordant in their appraisal of the presence or absence of GVHD on <sup>18</sup>F-FDG PET/CT in 46 of 51 (90%) of cases. Five cases required a third expert reader for final consensus determination of <sup>18</sup>F-FDG PET/CT status. Qualitative visual assessment resulted in a <sup>18</sup>F-FDG PET/CT sensitivity of 70%, specificity of 76%, NPV of 76%, and PPV of 68% for the detection of acute GIT-GVHD.

Of the 22 acute GIT-GVHD patients with positive results who had colonic biopsies, 16 of 22 (73%) had at least 1 colonic segment, 15 of 22 (68%) at least 2 colonic segments, 13 of 22 (59%) at least 3 colonic segments, and 9 of 22 (41%) all 4 colonic segments considered <sup>18</sup>F-FDG PET/CT-positive on qualitative visual assessment.

### DISCUSSION

The main aim of our study was to determine the diagnostic utility of <sup>18</sup>F-FDG PET/CT as a noninvasive test for acute GIT-GVHD in patients with suggestive clinical symptoms after AHSCT. The few published studies (9,10) in this field have relied predominantly on qualitative assessment of <sup>18</sup>F-FDG PET/CT for detection of acute GIT-GVHD by consensus expert visual assessment, which may be difficult to reliably reproduce across institutions.

In addition to qualitative visual <sup>18</sup>F-FDG PET/CT assessment, we evaluated <sup>18</sup>F-FDG PET/CT quantitatively using SUV<sub>max</sub>. SUV<sub>max</sub> is a widely accepted and validated parameter used both clinically and for research purposes

to quantify and convey the degree/intensity of radiotracer uptake on <sup>18</sup>F-FDG PET/CT scans (11). The higher the SUV<sub>max</sub>, the higher the degree of radiotracer uptake (inflammatory activity in this clinical scenario) on the <sup>18</sup>F-FDG PET/CT scan.

Because SUV<sub>max</sub> is objective and generally reproducible across <sup>18</sup>F-FDG PET/CT cameras and institutions, it allows objective criteria and definitive thresholds to be defined when determining whether a <sup>18</sup>F-FDG PET/CT scan is considered positive or negative for acute GIT-GVHD (12). This could provide a robust standardized technique for <sup>18</sup>F-FDG PET/CT evaluation of acute GIT-GVHD that is widely applicable across all institutions with <sup>18</sup>F-FDG PET/CT.

One of the strengths of our study is the rigorous nature of data collection, which included obtaining 376 biopsies of a possible 408 upper GIT and colonic segments (92%) in 51 patients for direct correlation with <sup>18</sup>F-FDG PET/CT scan findings. This novel method of data collection provided an extremely robust dataset, which is difficult to obtain in this patient population. Twenty-three of 51 (45.1%) patients in our cohort had biopsy-confirmed acute GIT-GVHD, confirming the reasonably high prevalence of this condition when clinically suspected.

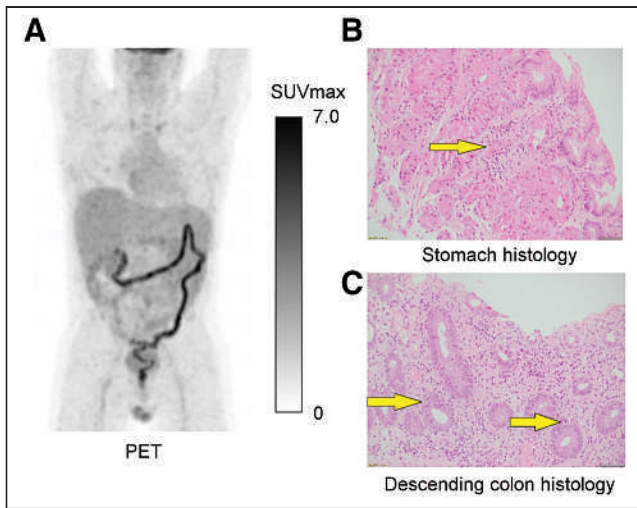


**FIGURE 2.**  $^{18}\text{F}$ -FDG PET/CT and histology images of patient 49. (A)  $^{18}\text{F}$ -FDG uptake only increased in colon and not upper GIT. (B) Lymphocytic infiltration and necrosis (arrow) of stomach crypt epithelium in keeping with acute GIT-GVHD. (C) Extensive colonic crypt destruction with frequent apoptotic bodies (arrows), the histologic hallmark of acute GIT-GVHD.

The involvement of the colon in all GVHD-positive patients and in its entirety in 96% of positive patients is a significant finding as it suggests that when acute GIT-GVHD is suspected, sigmoidoscopy alone, a less-invasive and resource-consuming procedure, may suffice for histologic confirmation. Eliminating gastroscopy and/or colonoscopy as part of work-up for acute GIT-GVHD (13) would markedly reduce the number of endoscopic procedures and the associated risk of up to 1.8% mortality and morbidity in this vulnerable patient cohort (6).

We demonstrated quantitative  $^{18}\text{F}$ -FDG PET/CT assessment using  $\text{SUV}_{\text{max}}$  is only useful for assessing the presence of GVHD in the colon because no difference in  $\text{SUV}_{\text{max}}$  was demonstrated between GVHD-positive and normal segments in the upper GIT. Stelljes et al. also reported similar findings and postulated that higher lipopolysaccharide

and microbial proinflammatory stimuli in the colon, compared with the upper GIT (9), might account for this. Interestingly, Stelljes et al. found  $^{18}\text{F}$ -FDG uptake was invariably increased in the ascending colon in patients positive for acute GIT-GVHD. On the contrary, we found the ascending colon was the only colonic segment not predictive for acute GIT-GVHD on  $^{18}\text{F}$ -FDG PET/CT.

We demonstrated GVHD and non-GVHD causes of GIT inflammation in the colon are indistinguishable and have similarly increased  $\text{SUV}_{\text{max}}$ . As such, further investigations including biopsy are required to determine the cause of inflammation when suggested on  $^{18}\text{F}$ -FDG PET/CT.

Our study yielded quantitative and qualitative  $^{18}\text{F}$ -FDG PET/CT sensitivity of 69% and 70%, specificity of 57% and 76%, NPV of 73% and 76%, and PPV of 59% and 68%, respectively, for the detection of acute GIT-GVHD. This finding suggests that quantitative analysis using  $\text{SUV}_{\text{max}}$  is no better than qualitative visual analysis and qualitative analysis alone is sufficient.

Studies by Stelljes et al. (9) and Bodet-Milin et al. (10), which both used only qualitative visual PET assessment, reported more favorable sensitivity of 82% and 81%, specificity of 100% and 90%, and NPV of 81% and 96%, respectively. They both provided limited details on how their images were standardized for review and did not have GIT segment histology datasets as comprehensive as those in our study. Interestingly, Stelljes et al. did provide quantitative  $\text{SUV}_{\text{max}}$  data as a figure, which showed findings strikingly similar to those in our Figures 1A and 1B.

Noninvasive clinical algorithms based on patient symptoms, conventional imaging, and serum biomarkers are not well established for acute GIT-GVHD, hence the low threshold for clinicians to proceed to more invasive procedures such as endoscopy (14,15).

The NPV of 73% (quantitative) and 76% (qualitative) for  $^{18}\text{F}$ -FDG PET/CT detection of acute GIT-GVHD in our study is reasonable and adds to the literature increasingly supporting the use of  $^{18}\text{F}$ -FDG PET/CT as a noninvasive diagnostic test for acute GIT-GVHD. Our findings suggest  $^{18}\text{F}$ -FDG PET/CT fills a clinical need where endoscopy may not be readily accessible, the patient too unwell, or risks of endoscopy too great.

**TABLE 2**  
Upper GIT and Colonic Segment  $\text{SUV}_{\text{max}}$ : Positive- Versus Negative-GVHD Patients

Variable	GVHD-Positive (n = 23)	GVHD-Negative (n = 28)	P
Min L4	2.96 (1.65)	1.88 (1.41)	0.02
Transverse colon $\text{SUV}_{\text{max}}$	3.72 (2.25)	2.34 (1.95)	0.02
Desc colon $\text{SUV}_{\text{max}}$	3.55 (2.16)	2.15 (1.93)	0.02
Sigmoid/rectum $\text{SUV}_{\text{max}}$	3.81 (1.96)	2.77 (1.25)	0.03
Sum L4	15.00 (7.75)	10.60 (7.31)	0.04
Terminal ileum $\text{SUV}_{\text{max}}$	2.51 (0.92)	2.12 (0.58)	0.07
Esophagus $\text{SUV}_{\text{max}}$	2.22 (0.68)	2.52 (0.62)	0.11
Ascending colon $\text{SUV}_{\text{max}}$	3.91 (1.89)	3.31 (2.48)	0.35
Max L4	4.50 (2.23)	3.61 (2.33)	0.18
Duodenum $\text{SUV}_{\text{max}}$	2.35 (0.62)	2.12 (0.49)	0.15
Stomach $\text{SUV}_{\text{max}}$	2.95 (0.69)	2.89 (0.76)	0.78

Data in parentheses denote standard deviation, unless otherwise indicated. Variables with  $P$  value < 0.05 are italicized.

Min L4/Max L4 = lowest/highest  $\text{SUV}_{\text{max}}$  out of ascending, transverse, descending and sigmoid/rectal colon; Sum L4 = combined  $\text{SUV}_{\text{max}}$  of ascending, transverse, descending and sigmoid/rectal colon.

**TABLE 3**  
AUROC Analysis:  $SUV_{max}$  as a Predictor for GVHD

Variable	<i>n</i>	Maximum	Minimum	AUROC	<i>P</i>
<i>Min L4</i>	51	7.9	0.8	0.73	0.03
<i>Descending colon <math>SUV_{max}</math></i>	51	10.3	0.8	0.72	0.03
<i>Transverse colon <math>SUV_{max}</math></i>	51	10.7	1.0	0.73	0.04
<i>Sigmoid/rectum <math>SUV_{max}</math></i>	51	8.4	1.0	0.71	0.04
Sum L4	51	40.2	5.2	0.69	0.06
Terminal ileum $SUV_{max}$	51	1.2	4.7	0.62	0.08
Esophagus $SUV_{max}$	51	4.0	1.1	0.64	0.12
Duodenum $SUV_{max}$	51	4.3	1.1	0.60	0.16
Max L4	51	11.3	1.7	0.63	0.18
Ascending colon $SUV_{max}$	51	11.3	1.1	0.63	0.35
Stomach $SUV_{max}$	51	5.1	1.5	0.57	0.78

Variables with *P* value < 0.05 are italicized.

Min L4/Max L4 = lowest/highest  $SUV_{max}$  out of ascending, transverse, descending and sigmoid/rectal colon; Sum L4 = combined  $SUV_{max}$  of ascending, transverse, descending and sigmoid/rectal colon.

A major factor that likely limits the sensitivity and specificity of  $^{18}F$ -FDG PET for acute GIT-GVHD is the marked variability in physiologic  $^{18}F$ -FDG uptake that can be seen in the GIT. It is not unusual to see intense physiologic  $^{18}F$ -FDG uptake in the GIT, which may relate to underlying peristaltic smooth muscle activity at the time of imaging.

The use of antispasmodic agents such as *N*-butylscopolamine before scanning may decrease physiologic gastrointestinal  $^{18}F$ -FDG uptake and may improve the performance of  $^{18}F$ -FDG PET/CT in this cohort of patients (16). Metformin is also well known to significantly increase physiologic gastrointestinal  $^{18}F$ -FDG uptake and should be withheld for at least 48 h when assessing the GIT on

$^{18}F$ -FDG PET/CT (17). Importantly, no patients in our study were taking metformin before their  $^{18}F$ -FDG PET/CT scan.

Combining PET with other noninvasive markers such as serum inflammatory cytokines IL-17, IFN gamma, tumor necrosis factor, and granulocyte macrophage colony-stimulating factor, which are known to be elevated in acute GIT-GVHD (18,19), may also be an option to further improve noninvasive diagnostic test performance.

Novel PET radiotracers targeting cellular apoptosis (20,21), the histologic hallmark of acute GIT-GVHD, may provide significantly improved sensitivity and specificity for detection of GVHD compared with  $^{18}F$ -FDG PET and should be explored further.

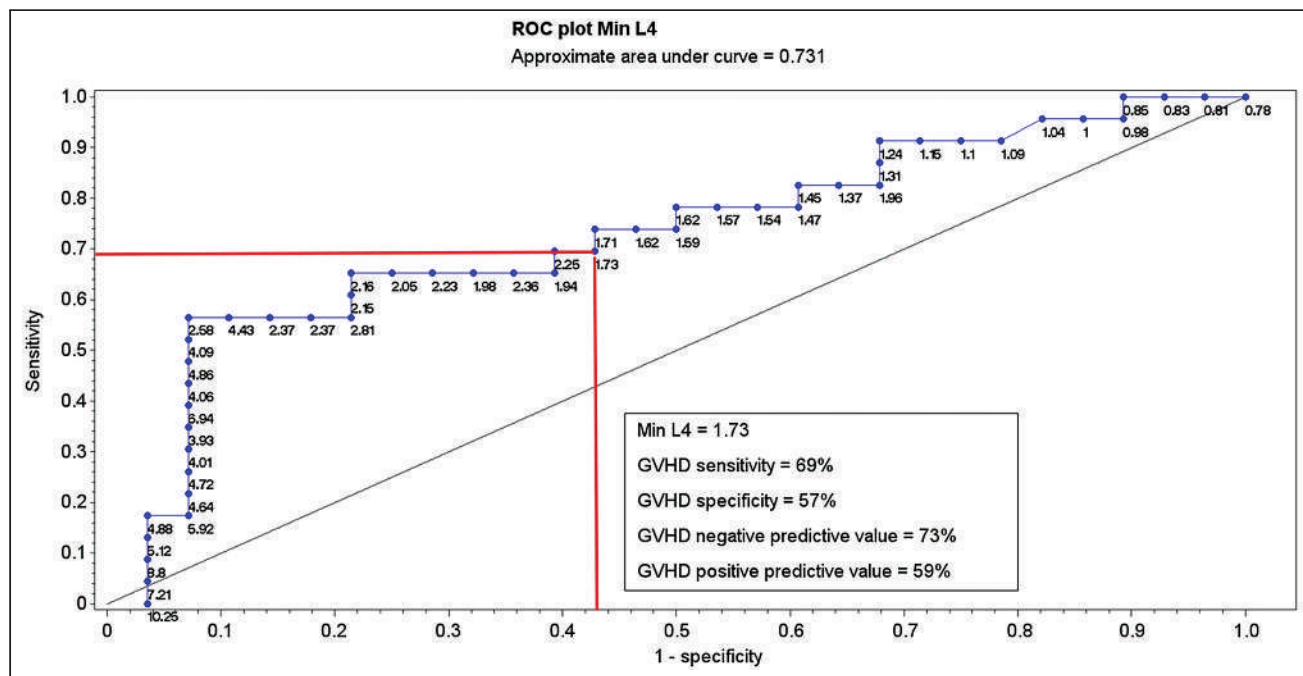


FIGURE 3. Min L4 ROC.

Limitations of our study include no formal grading of severity of acute GIT-GVHD on histology; however, 21 of 23 (91%) patients required steroid therapy (13 intravenous, 8 oral), suggesting most acute GIT-GVHD cases were at least moderately severe.

## CONCLUSION

<sup>18</sup>F-FDG PET is a useful noninvasive diagnostic test for acute GIT-GVHD particularly in the colon. Acute GIT-GVHD, when present, always involves the colon and usually in its entirety, suggesting that only colonic biopsy is required for histologic confirmation when acute GIT-GVHD is suspected. Of note, <sup>18</sup>F-FDG PET cannot distinguish acute GIT-GVHD from non-GVHD inflammatory changes in the colon.

## DISCLOSURE

The Alfred Foundation and Marian and E.H. Flack Trust provided financial support to conduct the trial. No other potential conflict of interest relevant to this article was reported.

## KEY POINTS

**QUESTION:** How useful is <sup>18</sup>F-FDG PET/CT for noninvasive assessment of patients with clinically suspected acute GIT-GVHD after allogeneic hemopoietic stem cell transplantation?

**PERTINENT FINDINGS:** In a prospective study evaluating <sup>18</sup>F-FDG PET/CT in 51 patients with clinically suspected acute GIT-GVHD with upper and lower gastrointestinal histology obtained from endoscopy, <sup>18</sup>F-FDG PET/CT was found to be a useful noninvasive test with sensitivity and specificity of 70% and 76%, respectively, for acute GIT-GVHD. The colon appears to always be involved in patients with acute GIT-GVHD and is the location of greatest increase in SUV<sub>max</sub> on <sup>18</sup>F-FDG PET/CT.

**IMPLICATIONS FOR PATIENT CARE:** <sup>18</sup>F-FDG PET/CT is a useful adjunctive noninvasive diagnostic test when acute GIT-GVHD is clinically suspected.

## REFERENCES

1. Passweg JR, Baldomero H, Peters C, et al. Hematopoietic SCT in Europe: data and trends in 2012 with special consideration of pediatric transplantation. *Bone Marrow Transplant.* 2014;49:744–750.
2. Aladağ E, Kelkitli E, Goker H. Acute graft-versus-host disease: a brief review. *Turk J Haematol.* 2020;37:1–4.
3. Jagasia M, Arora M, Flowers ME, et al. Risk factors for acute GVHD and survival after hematopoietic cell transplantation. *Blood.* 2012;119:296–307.
4. Deeg HJ, Antin JH. The clinical spectrum of acute graft-versus-host disease. *Semin Hematol.* 2006;43:24–31.
5. Washington K, Jagasia M. Pathology of graft-versus-host disease in the gastrointestinal tract. *Hum Pathol.* 2009;40:909–917.
6. Fallows G, Rubinger M, Bernstein CN. Does gastroenterology consultation change management of patients receiving hematopoietic stem cell transplantation? *Bone Marrow Transplant.* 2001;28:289–294.
7. Malard F, Mohty M. New insight for the diagnosis of gastrointestinal acute graft-versus-host disease. *Mediators Inflamm.* 2014;2014:701013.
8. Neurath MF, Vehling D, Schunk K, et al. Noninvasive assessment of Crohn's disease activity: a comparison of <sup>18</sup>F-fluorodeoxyglucose positron emission tomography, hydromagnetic resonance imaging, and granulocyte scintigraphy with labeled antibodies. *Am J Gastroenterol.* 2002;97:1978–1985.
9. Stelljes M, Hermann S, Albring J, et al. Clinical molecular imaging in intestinal graft-versus-host disease: mapping of disease activity, prediction, and monitoring of treatment efficiency by positron emission tomography. *Blood.* 2008;111:2909–2918.
10. Bodet-Milin C, Lacombe M, Malard F, et al. <sup>18</sup>F-FDG PET/CT for the assessment of gastrointestinal GVHD: results of a pilot study. *Bone Marrow Transplant.* 2014;49:131–137.
11. Lindholm H, Staaf J, Jacobsson H, Brodin F, Hatherly R, Sanchez-Crespo A. Repeatability of the maximum standard uptake value (SUV<sub>max</sub>) in FDG PET. *Mol Imaging Radionucl Ther.* 2014;23:16–20.
12. Adams MC, Turkington TG, Wilson JM, Wong TZ. A systematic review of the factors affecting accuracy of SUV measurements. *AJR.* 2010;195:310–320.
13. Scott AP, Tey SK, Butler J, Kennedy GA. Diagnostic utility of endoscopy and biopsy in suspected acute gastrointestinal graft-versus-host disease after hematopoietic progenitor cell transplantation. *Biol Blood Marrow Transplant.* 2018;24:1294–1298.
14. Ferrara JLM, Chaudhry MS. GVHD: biology matters. *Blood Adv.* 2018;2:3411–3417.
15. Naymagon S, Naymagon L, Wong SY, et al. Acute graft-versus-host disease of the gut: considerations for the gastroenterologist. *Nat Rev Gastroenterol Hepatol.* 2017;14:711–726.
16. Stahl A, Weber WA, Avril N, Schwaiger M. Effect of N-butylscopolamine on intestinal uptake of fluorine-18-fluorodeoxyglucose in PET imaging of the abdomen. *Nuklearmedizin.* 2000;39:241–245.
17. Hamidizadeh R, Eftekhari A, Wiley EA, Wilson D, Alden T, Benard F. Metformin discontinuation prior to FDG PET/CT: a randomized controlled study to compare 24- and 48-hour bowel activity. *Radiology.* 2018;289:418–425.
18. Hill GR, Koyama M. Cytokines and costimulation in acute graft-versus-host disease. *Blood.* 2020;136:418–428.
19. Zhang L, Chu J, Yu J, Wei W. Cellular and molecular mechanisms in graft-versus-host disease. *J Leukoc Biol.* 2016;99:279–287.
20. Wang X, Feng H, Zhao S, et al. SPECT and PET radiopharmaceuticals for molecular imaging of apoptosis: from bench to clinic. *Oncotarget.* 2017;8:20476–20495.
21. Reshef A, Shirvan A, Akselrod-Ballin A, Wall A, Ziv I. Small-molecule biomarkers for clinical PET imaging of apoptosis. *J Nucl Med.* 2010;51:837–840.

# Prevalence and Outcomes of Cardiac Amyloidosis in All-Comer Referrals for Bone Scintigraphy

Christian Nitsche<sup>1</sup>, Katharina Mascherbauer<sup>1</sup>, Raffaella Calabretta<sup>2</sup>, Matthias Koschutnik<sup>1</sup>, Carolina Dona<sup>1</sup>, Varius Dannenberg<sup>1</sup>, Felix Hofer<sup>1</sup>, Kseniya Halavina<sup>1</sup>, Andreas A. Kammerlander<sup>1</sup>, Tatjana Traub-Weidinger<sup>2</sup>, Georg Goliash<sup>1</sup>, Christian Hengstenberg<sup>1</sup>, Marcus Hacker<sup>2</sup>, and Julia Mascherbauer<sup>1,3</sup>

<sup>1</sup>Department of Internal Medicine II, Medical University of Vienna, Vienna, Austria; <sup>2</sup>Department of Nuclear Medicine, Medical University of Vienna, Vienna, Austria; and <sup>3</sup>Karl Landsteiner University of Health Sciences, Department of Internal Medicine 3, University Hospital St. Pölten, Krems, Austria

The prevalence of cardiac amyloidosis (CA) in the general population and associated prognostic implications remain poorly understood. We aimed to identify CA prevalence and outcomes in bone scintigraphy referrals. **Methods:** Consecutive all-comers undergoing <sup>99m</sup>Tc-3,3-diphosphono-1,2-propanodicarboxylic-acid (<sup>99m</sup>Tc-DPD) bone scintigraphy between 2010 and 2020 were included. Perugini grade 1 was defined as low-grade uptake and grade 2 or 3 as confirmed CA. All-cause mortality, cardiovascular death, and heart failure hospitalization (HHF) served as endpoints. **Results:** In total, 17,387 scans from 11,527 subjects (age, 61 ± 16 y; 63.0% women, 73.6% cancer) were analyzed. Prevalence of <sup>99m</sup>Tc-DPD positivity was 3.3% ( $n = 376/11,527$ ; grade 1: 1.8%, grade 2 or 3: 1.5%), and was higher among cardiac than non-cardiac referrals (18.2% vs. 1.7%). In individuals with more than 1 scan, progression from grade 1 to grade 2 or 3 was observed. Among patients with biopsy-proven CA, the portion of light-chain (AL)-CA was significantly higher in grade 1 than grade 2 or 3 (73.3% vs. 15.4%). After a median of 6 y, clinical event rates were: 29.4% mortality, 2.6% cardiovascular death, and 1.5% HHF, all independently predicted by positive <sup>99m</sup>Tc-DPD. Overall, adverse outcomes were driven by confirmed CA (vs. grade 0, mortality: adjusted hazard ratio [AHR] 1.46 [95% CI 1.12–1.90]; cardiovascular death: AHR 2.34 [95% CI 1.49–3.68]; HHF: AHR 2.25 [95% CI 1.51–3.37]). One-year mortality was substantially higher in cancer than noncancer patients. Among noncancer patients, also grade 1 had worse outcomes than grade 0 (HHF/death: AHR 1.45 [95% CI 1.01–2.09]), presumably because of longer observation and higher prognostic impact of early infiltration. **Conclusion:** Positive <sup>99m</sup>Tc-DPD was identified in a substantial number of consecutive <sup>99m</sup>Tc-DPD referrals and associated with adverse outcomes.

**Key Words:** transthyretin; ATTR; diagnosis; mortality; heart failure

**J Nucl Med 2022; 63:1906–1911**

DOI: 10.2967/jnumed.122.264041

**C**ardiac amyloidosis (CA) is a myocardial infiltrative disease and causes heart failure by deposition of amyloid fibrils. The 2 major amyloid proteins deposited in the myocardium are transthyretin (ATTR), which predominantly affects elderly individuals, and

immunoglobulin light chain (AL), whereas other types of CA are very rare (*1*). If left untreated, CA leads to heart failure and death, both in ATTR and AL. Formerly believed to be a rare condition, recent diagnostic advances and disease awareness have resulted in a true renaissance of CA. Increased diagnosis of CA is mainly driven by excellent sensitivity and specificity of bone scintigraphy (e.g., <sup>99m</sup>Tc-3,3-diphosphono-1,2-propanodicarboxylic acid [<sup>99m</sup>Tc-DPD]; <sup>99m</sup>Tc-pyrophosphate [<sup>99m</sup>Tc-PYP]), in particular for ATTR (*1*). Broader use of bone scintigraphy for screening of ATTR-CA has unveiled a significant proportion of (coexisting) CA for various cardiac conditions (*2–5*). Attempts to estimate the prevalence of CA in the general population using bone scintigraphy yielded substantially lower proportions of affected patients (*6–8*). However, these studies were limited either by small sample size or failure to report on prognostic implications of CA. Current diagnostic criteria require strong cardiac tracer uptake (Perugini grade  $\geq 2$ ) for ATTR-CA, whereas the clinical significance of low uptake (Perugini grade 1) is not well studied (*9*). This diagnostic gap is of particular importance because ATTR-specific treatments might be more effective at earlier stages of disease (*10*). Yet, underlying pathology and outcomes of low-grade cardiac uptake are unclear.

The present study was designed to evaluate the prevalence of cardiac tracer uptake (grades 1–3) and to investigate associated outcomes in all-comers referred to bone scintigraphy.

## MATERIALS AND METHODS

### Study Population

This study included consecutive all-comer referrals for bone scintigraphy between January 2010 and August 2020 at the Vienna General Hospital, a university-affiliated tertiary center. Bone scintigraphy was performed using <sup>99m</sup>Tc-methylene diphosphate (<sup>99m</sup>Tc-MDP) before April 2010, and <sup>99m</sup>Tc-DPD thereafter. Because <sup>99m</sup>Tc-MDP has been shown to lack sensitivity in the diagnosis of ATTR (*11*), patients evaluated with this tracer were excluded (Supplemental Fig. 1; supplemental materials are available at <http://jnm.snmjournals.org>). The remaining patients with available <sup>99m</sup>Tc-DPD scans and sufficient image quality were included in the final analysis. The institutional review board approved this retrospective study (EK 1557/2020), and the requirement to obtain informed consent was waived.

### <sup>99m</sup>Tc-DPD Bone Scintigraphy

All patients were scanned using either an Infinia Hawkeye 4 (GE Healthcare) or a Discovery 670 (GE Healthcare) hybrid  $\gamma$ -camera 3 h after intravenous administration of 700 MBq of <sup>99m</sup>Tc-DPD. Planar whole-body images were acquired at a scan speed of 10 cm/min using

Received Feb. 19, 2022; revision accepted Jun. 2, 2022.

For correspondence or reprints, contact Andreas Kammerlander (andreas.kammerlander@meduniwien.ac.at) and Christian Nitsche (christian.nitsche@meduniwien.ac.at).

Published online Jun. 16, 2022.

COPYRIGHT © 2022 by the Society of Nuclear Medicine and Molecular Imaging.

low-energy high resolution collimators (12). On clinical request, additional SPECT/CT of the chest was performed.

### Image Analysis and Diagnosis of CA

All scans were analyzed by 2 experienced nuclear imaging scan readers masked to clinical data (e.g., age, sex, and referral diagnosis). Visual assessment according to the Perugini classification was applied (11), where grade 0 represents no cardiac uptake with normal bone uptake (i.e., negative,  $^{99m}\text{Tc-DPD}$  [ $^{99m}\text{Tc-DPD}$ -]) and grades 1–3 represent increasing cardiac uptake ( $^{99m}\text{Tc-DPD}$ +) with increasing bone attenuation and soft-tissue uptake. Grade 1 was defined as low-grade uptake (Supplemental Fig. 2) and grade 2 or 3 uptake as confirmed amyloidosis. In the case of discrepant  $^{99m}\text{Tc-DPD}$  grading between the 2 readers, which occurred in 12 borderline cases, a third nuclear imaging specialist was consulted, and final diagnosis was reached by consensus (Supplemental Fig. 3). Because of the retrospective study design, CA subtype was not consistently assessed. However, organ tissue biopsy including Congo red staining and immunohistochemical analysis was available in a subset of patients. Mass spectroscopy was sought in cases with indistinct amyloid subtyping on immunohistochemistry.

### Data Acquisition

Clinical and laboratory data as well as hospitalizations for heart failure (HHF) were retrieved from medical records. All-cause mortality was captured from the Austrian-Death-Registry and served as primary study endpoint. Cardiovascular death (as determined from the cause of death in the Austrian-Death-Registry) and HHF were selected as secondary study endpoints. HHF was determined from 3 sources, covering hospitalizations in all Austrian hospitals: patient records of the Medical University of Vienna, Vienna-Health-Association data base, and the nationwide electronic health records. Outcome assessment was 100% complete. An internal expert committee adjudicated each event, masked to  $^{99m}\text{Tc-DPD}$  results. The presence of monoclonal protein was defined as positivity of serum or urine immunofixation with or without elevated serum/urine levels of the corresponding light chain.

### Statistical Analysis

All statistical analyses were computed using SPSS 27 (IBM SPSS). Continuous data are expressed as median and interquartile range (IQR), and categorical variables as numbers and percentages. Differences between groups were analyzed with the Kruskal–Wallis test. Post hoc analyses were performed using Dunn–Bonferroni tests for continuous variables.  $\chi^2$  tests or Fisher tests were used for categorical variables as appropriate. We calculated the prevalence of  $^{99m}\text{Tc-DPD}$ + and 95% CIs according to the Wilson’s score method. Kaplan–Meier estimates and Cox regression analyses were used to evaluate the prognostic significance of  $^{99m}\text{Tc-DPD}$ +. Multivariate adjustment (including age, sex, cardiovascular risk factors, and comorbidities as outlined in the respective outcome tables) was performed using a nonstepwise approach with a cutoff  $P$  value to enter the multivariate model of  $\leq 0.05$ . The proportional hazards assumption was tested with the examination of Schoenfeld residuals. Multivariate binary logistic analysis was applied to evaluate the association of parameters with the presence of  $^{99m}\text{Tc-DPD}$ +. A  $P$  value  $\leq 0.05$  was considered statistically significant.

## RESULTS

### Patient Population

In total, 17,387 consecutive  $^{99m}\text{Tc-DPD}$  bone scintigraphy scans from 11,527 patients were analyzed and included in the final analysis (Supplemental Fig. 1). The median age of the study population was 63.6 y (IQR 51.3–73.0), with 63.0% women and 73.6% cancer patients.

### Referral Diagnosis and Temporal Trends

Referral diagnoses for  $^{99m}\text{Tc-DPD}$  were noncardiac (90.6%) and cardiac (9.4%). Precise breakdown of referral diagnoses is displayed in Supplemental Figure 4 and baseline characteristics stratified according to referral indication are displayed in Supplemental Table 1. The proportion of cardiac referrals among all-comers increased consistently over time (2010–2014: 0.5%; 2015–2016: 4.5%; 2017–2018: 19.7%; 2019–2020: 28.8%;  $P < 0.001$ ).

### Prevalence and Predictors of CA

Among all-comers the prevalence of  $^{99m}\text{Tc-DPD}$ + was 3.3% (95% CI 2.9–3.6,  $n = 376/11,527$ ). Grade 1 was found in 1.8% ( $n = 209/11,527$ ) and confirmed amyloidosis (grade 2 or 3) in 1.5% ( $n = 167/11,527$ ) of patients. There was a significant increase in the prevalence of  $^{99m}\text{Tc-DPD}$  positivity with incremental age:  $<60$  y: 0.6% vs. 60–70 y: 2.2% vs. 70–80 y: 5.5% vs.  $>80$  y: 12.4% ( $P < 0.001$ ). Age distribution of  $^{99m}\text{Tc-DPD}$ + according to referral indication is shown in Figure 1. As expected,  $^{99m}\text{Tc-DPD}$ + was more common among cardiac versus noncardiac referrals (18.2%, 95% CI 16.0–20.7,  $n = 197/1,081$  vs. 1.7%, 95% CI 1.5–2.0,  $n = 179/10,446$ ;  $P < 0.001$ ). The distribution of disease burden differed significantly between cardiac and noncardiac patients. Most  $^{99m}\text{Tc-DPD}$ + cases among cardiac referrals displayed grade 2 or 3 uptake (62.9% grade 2 or 3 vs. 37.1% grade 1), whereas grade 1 uptake was predominantly observed among noncardiac referrals (24.0% grade 2 or 3 vs. 76.0% grade 1,  $P$  for differences according to referral diagnosis  $< 0.001$ ).

Independent predictors for the presence of  $^{99m}\text{Tc-DPD}$ + by multivariate binary logistic regression analysis were history of carpal tunnel syndrome (odds ratio [OR], 8.06 [95% CI 4.50–14.46]), atrial fibrillation (OR, 2.61 [95% CI 2.01–3.39]), chronic heart failure (OR, 2.05 [95% CI 1.87–3.35]), male sex (OR, 1.86 [95%

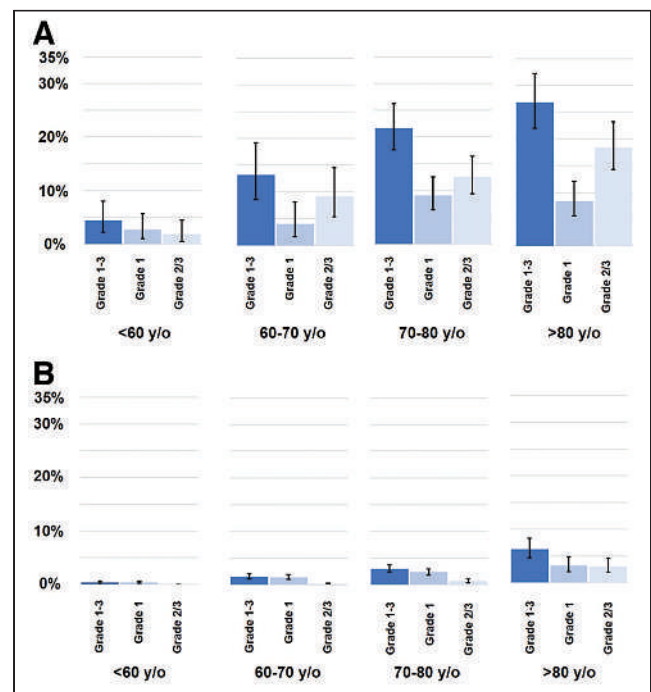


**FIGURE 1.** (A and B) Prevalence of cardiac uptake and breakdown of Perugini grading according to age levels in cardiac (A) and noncardiac referrals (B). y/o = year old.

CI 1.48–2.34]), and age (per year increase: OR, 1.08 [95% CI 1.07–1.09], all  $P < 0.001$ ).

### Grade 0 versus Low-Grade Uptake Versus Confirmed Amyloidosis

Differences in baseline characteristics according to Perugini grade are displayed in Table 1. From  $^{99m}\text{Tc}$ -DPD– to grade–1 to confirmed CA, a stepwise increase in age, male sex, and history of carpal tunnel syndrome was found ( $P$  all  $< 0.001$ ). Conversely, the proportion of cancer declined from no CA to confirmed CA ( $P < 0.001$ ). Comorbidities typically associated with age, such as arterial hypertension, coronary artery disease, and impaired kidney function, were more prevalent in  $^{99m}\text{Tc}$ -DPD+ patients (all  $P < 0.001$ ). Furthermore, atrial fibrillation and chronic heart failure were more common in  $^{99m}\text{Tc}$ -DPD+ than in  $^{99m}\text{Tc}$ -DPD– patients (all  $P < 0.001$ ). Accordingly, cardiac serum markers displayed a stepwise increase in  $^{99m}\text{Tc}$ -DPD– patients versus low-grade uptake versus confirmed CA: high-sensitive troponin T, 19 ng/mL (IQR 10–41) versus 49 (IQR 25–148) versus 60 (IQR 33–104); N-terminal pro-brain natriuretic peptide, 655 pg/mL (IQR 185–2,311) versus 2,117 (IQR 848–6,364) versus 3,043 (IQR 1,562–6,556); all  $P < 0.001$ . The presence of monoclonal protein was more prevalent in grade 1 than in  $^{99m}\text{Tc}$ -DPD– and grade 2 or 3 ( $P = 0.001$ ). Among patients who underwent echocardiography, a stepwise increase of left ventricular wall thickness from  $^{99m}\text{Tc}$ -DPD– to low-grade uptake to confirmed CA was observed: 13 mm (IQR 11–15) versus 14 (IQR 13–17) versus 20 (IQR 17–23). Also, left and right heart dimensions were increased and left ventricular function was decreased in  $^{99m}\text{Tc}$ -DPD+ compared with  $^{99m}\text{Tc}$ -DPD– ( $P$  for all  $< 0.001$ ).

### $^{99m}\text{Tc}$ -DPD Grading Trajectories

Repeated scans were available for 2,136 patients and yielded identical Perugini grades in most cases (98.9%). However, 23 patients experienced a change in cardiac tracer uptake 3.4 y (IQR 1.3–5.9) after their previous scan (Supplemental Fig. 5): grade 0 to grade 1 ( $n = 15$ ), grade 0 to grade 2 ( $n = 1$ ), grade 1 to grade 2 or 3 ( $n = 4$ ), grade 0 to grade 1 to grade 2 or 3 ( $n = 1$ ), decline in grading because of excessive bone metastasis ( $n = 2$ ).

### SPECT

Among patients with a positive scan result on planar imaging, additional SPECT of the chest was available for 19.1% ( $n = 72/376$ ). Cardiac origin of tracer uptake was verified by SPECT in 89% ( $n = 64/72$ ), which was markedly higher among patients with grade 2 or 3 (100%,  $n = 52/52$ ) than grade 1 by planar imaging (60%,  $n = 12/20$ , Supplemental Fig. 6).

### Tissue Biopsy

Organ tissue samples for amyloid detection and subtyping among patients with a positive scan result were available in 7.7% of grade 1 and in 16.8% of grade 2 or 3 (Supplemental Table 2). Confirmation rates of amyloid tissue presence were 93.8% and 92.9% for grade 1 and 2 or 3, respectively. Negative samples were derived from kidney biopsies (1 grade 1, 1 grade 2 or 3) and abdominal fat tissue aspirate (1 grade 2 or 3), whereas amyloid was confirmed in 100% of endomyocardial biopsies ( $n = 33/33$ ). Among those with confirmed amyloid on biopsy, the portion of ATTR was significantly higher in grade 2 or 3 (76.9%,  $n = 20/26$ ) than in grade 1 patients (26.7%,  $n = 4/15$ ;  $P < 0.01$ ). Hence, AL

**TABLE 1**  
Baseline Characteristics

Characteristic	Grade 0 ( $n = 11,151$ [96.7%])	Grade 1 ( $n = 209$ [1.8%])	Grade 2 or 3 ( $n = 167$ [1.5%])	$P$
Age (y)	63 (51–73)	75 (68–80)*	80 (74–84) <sup>†,‡</sup>	$< 0.001$
Sex, male (%)	36.1	53.1*	74.3 <sup>†,‡</sup>	$< 0.001$
BMI (kg/m <sup>2</sup> )	25.7 (22.8–29.4; 10,747)	27.5 (24.8–32.1; 198)*	25.3 (23.4–28.3; 163) <sup>‡</sup>	$< 0.001$
Cardiac referral (%)	7.9	34.9*	74.3 <sup>†,‡</sup>	$< 0.001$
Cancer (%)	74.6	56.5*	25.7 <sup>†,‡</sup>	$< 0.001$
Myeloma (%)	1.0	5.3*	1.2 <sup>‡</sup>	$< 0.001$
Arterial hypertension (%)	40.2	70.8*	49.9 <sup>†,‡</sup>	$< 0.001$
Diabetes (%)	12.1	24.9*	12.6 <sup>‡</sup>	$< 0.001$
Atrial fibrillation (%)	8.1	29.7*	50.3 <sup>†,‡</sup>	$< 0.001$
Past stroke (%)	5.5	7.2	10.2 <sup>†</sup>	0.019
CAD (%)	12.1	38.8*	31.1 <sup>†</sup>	$< 0.001$
Previous MI (%)	1.7	7.7*	3.0	$< 0.001$
Chronic heart failure (%)	7.2	26.3*	38.9 <sup>†,‡</sup>	$< 0.001$
PAD (%)	1.5	4.3*	1.2	0.004
COPD (%)	7.2	11.5*	10.8	0.015
CTS (%)	0.8	3.8*	6.6 <sup>†</sup>	$< 0.001$

\*DPD grade 1 vs. grade 0:  $P \leq 0.05$ .

<sup>†</sup>DPD grade 2 or 3 vs. grade 0:  $P \leq 0.05$ .

<sup>‡</sup>DPD grade 2 or 3 vs. grade 1:  $P \leq 0.05$ .

BMI = body mass index; CAD = coronary artery disease; MI = myocardial infarction; PAD = peripheral artery disease; COPD = chronic obstructive pulmonary disease; CTS = carpal tunnel syndrome.

Parenthetical data indicate number of patients with available data for parameter if not identical to column total.

was the predominant amyloid subtype in grade 1 (73.3%,  $n = 11/15$ ). Furthermore, the presence of combined ATTR/AL-CA was diagnosed in 2 grade 2 or 3 patients with endomyocardial biopsy and confirmed by mass spectroscopy.

### Mortality

After a median follow-up of 6.0 y (IQR 2.8–8.9), 29.4% ( $n = 3,385/11,527$ ) had died. Cardiovascular death accounted for 8.9% of mortality ( $n = 302/3,385$ ). Among all-comers,  $^{99m}\text{Tc-DPD}+$  was significantly associated with mortality by Cox regression analysis (crude hazard ratio [HR] 1.76 [95% CI 1.49–2.08]), which applied for both grade 1 (vs. grade 0: HR 1.61 [95% CI 1.29–1.99], and grade 2 or 3 (vs. grade 0: HR 2.02 [95% CI 1.57–2.60], all  $P < 0.001$ ). After multivariate adjustment,  $^{99m}\text{Tc-DPD}+$  remained significantly associated with mortality (Table 2), driven by confirmed CA but not low-grade uptake (adjusted HR [AHR] with  $^{99m}\text{Tc-DPD}-$  as reference: 1.20 [95% CI 1.01–1.43] for  $^{99m}\text{Tc-DPD}+$ ,  $P = 0.036$ ; AHR, 1.46 [95% CI 1.12–1.90] for confirmed CA,  $P = 0.006$ ; AHR, 1.09 [95% CI 0.87–1.35] for low-grade uptake,  $P = 0.5$ ). Results remained unchanged after exclusion of 3 grade 1 patients with documented myocardial infarction within 1 mo before scintigraphy. Also, results were consistent when cardiovascular death was analyzed separately (AHR with  $^{99m}\text{Tc-DPD}-$  as reference: 1.79 [95% CI 1.26–2.54] for  $^{99m}\text{Tc-DPD}+$ ,  $P = 0.001$ ; AHR, 2.34 [95% CI 1.49–3.68] for confirmed CA,  $P < 0.001$ ; AHR, 1.31 [95% CI 0.78–2.20] for low-grade uptake,  $P = 0.3$ ; Supplemental Table 3). The proportional hazard assumption was satisfied, and we did not detect a significant collinearity in the multivariate models. Kaplan–Meier curves illustrate increased all-cause mortality in confirmed CA versus grade 1 (log-rank,  $P = 0.039$ ; Fig. 2).

Overall, mortality rates at 1 y were more than doubled in cancer versus noncancer patients (13.4% vs. 6.0%,  $P < 0.001$ ). Unadjusted death rates for  $^{99m}\text{Tc-DPD}-$  versus  $^{99m}\text{Tc-DPD}+$  patients were

higher among both cancer (HR, 1.59 [95% CI 1.29–1.98]) and noncancer patients (HR, 3.94 [95% CI 3.03–5.11], both  $P < 0.001$ ). After multivariate adjustment,  $^{99m}\text{Tc-DPD}+$  remained significantly associated with mortality only for noncancer (AHR, 1.41 [95% CI 1.06–1.89],  $P = 0.017$ ), but not for cancer patients (AHR, 0.94 [95% CI 0.75–1.19],  $P = 0.6$ ).

### HHF

During follow-up, 1.5% of patients ( $n = 178/11,527$ ) were hospitalized for heart failure.  $^{99m}\text{Tc-DPD}+$  independently predicted the occurrence of HHF (AHR, 2.25 [95% CI 1.51–3.37],  $P < 0.001$ ). Again, patients with low-grade uptake versus  $^{99m}\text{Tc-DPD}-$  performed equally (AHR, 1.18 [95% CI 0.61–2.26],  $P = 0.6$ ), whereas confirmed CA was associated with a 3.5 times higher risk of future HHF than was  $^{99m}\text{Tc-DPD}-$  (AHR, 3.57 [95% CI 2.19–5.80],  $P < 0.001$ , Supplemental Table 4).

### Outcomes of Noncancer Patients with Low-Grade Uptake

Importantly, among noncancer patients, also grade 1 was associated with worse outcomes compared with grade 0 with a higher hazard of HHF (HR, 4.89 [95% CI 2.34–10.24]), cardiovascular (HR, 3.84 [95% CI 2.01–7.36]), and all-cause mortality (HR, 3.56 [95% CI 2.47–5.15], all  $P < 0.001$ ). Results for the composite endpoint of HHF or death remained significant after multivariate adjustment for patients with grade 1 (vs. grade 0: AHR, 1.45 [95% CI 1.01–2.09],  $P = 0.04$ ), and grade 2 or 3 (vs. grade 0: AHR, 1.40 [95% CI 1.01–1.97],  $P = 0.049$ ).

### DISCUSSION

In this large-scale study we analyzed all-comer bone scintigraphy referrals for the presence of  $^{99m}\text{Tc-DPD}$  positivity and report a prevalence of 1-in-50 among noncardiac and 1-in-5 among cardiac referrals. Repeated scans revealed an increase in the burden of cardiac

**TABLE 2**  
Cox Regression Analyses Assessing the Association of Parameters with Mortality

Parameter	Univariate		Multivariate	
	Hazard ratio	<i>P</i>	Hazard ratio	<i>P</i>
Age, per 10-y increase	1.547 (1.498–1.598)	<0.001	1.346 (1.298–1.396)	<0.001
Male sex	2.223 (2.077–2.379)	<0.001	2.097 (1.951–2.253)	<0.001
Cancer	2.515 (2.272–2.783)	<0.001	2.907 (2.620–3.225)	<0.001
Arterial hypertension	1.884 (1.761–2.016)	<0.001	1.137 (1.052–1.230)	0.001
Diabetes	1.758 (1.610–1.919)	<0.001	1.161 (1.055–1.278)	0.002
Atrial fibrillation	2.096 (1.903–2.310)	<0.001	1.095 (0.981–1.221)	0.104
Chronic heart failure	2.005 (1.808–2.225)	<0.001	1.261 (1.117–1.423)	<0.001
CAD	2.119 (1.945–2.307)	<0.001	1.065 (0.957–1.185)	0.251
Previous MI	1.633 (1.291–2.066)	<0.001	0.919 (0.718–1.177)	0.504
Past stroke	2.034 (1.812–2.284)	<0.001	1.231 (1.086–1.395)	0.001
PAD	1.837 (1.461–2.309)	<0.001	0.915 (0.722–1.159)	0.460
COPD	2.185 (1.975–2.417)	<0.001	1.585 (1.425–1.763)	<0.001
DPD positivity	1.758 (1.488–2.077)	<0.001	1.152 (1.004–1.323)	0.036

BMI = body mass index; CAD = coronary artery disease; MI = myocardial infarction; PAD = peripheral artery disease; COPD = chronic obstructive pulmonary disease; CTS = carpal tunnel syndrome.

Data in parentheses are 95% CI.

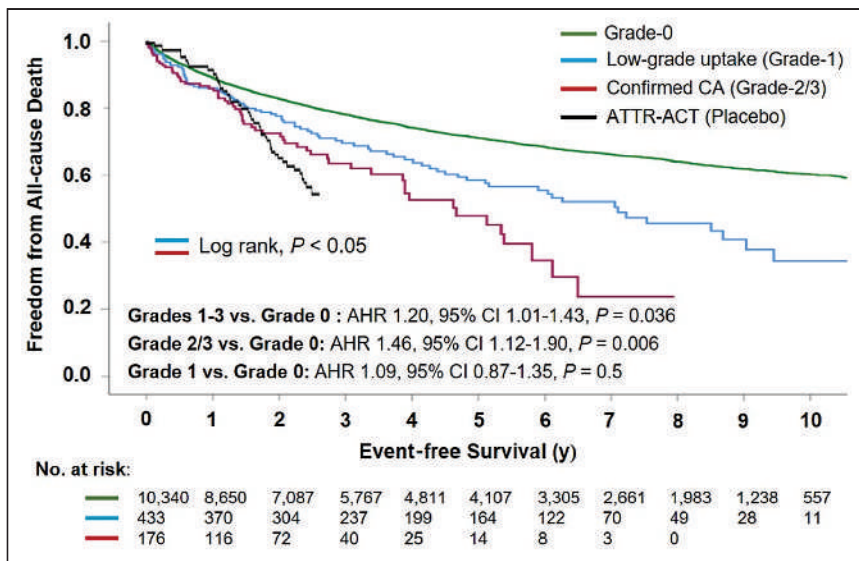


**FIGURE 2.** Association of CA with mortality. Among all-comers, grade 2 or 3 but not grade 1 was associated with increased adjusted mortality as compared with grade 0. Two-year survival rates of confirmed CA were comparable to those for patients in the placebo arm of the ATTR-ACT trial (data adapted from (10)).

tracer uptake from low- to high-grade uptake in a subgroup of patients over time, highlighting the progressive nature of the disease. Outcomes were worse in  $^{99m}\text{Tc}$ -DPD+ patients, without differences in event-free survival between grade 1 and grade 0 in the overall cohort. However, 1-y mortality was twice as high in cancer than in noncancer patients. After the exclusion of cancer patients from the analysis, grade 1 patients experienced worse outcomes than those with no uptake, presumably because of the longer observation time/life expectancy with a higher prognostic impact of early ATTR infiltration. On the basis of these results, we conclude that, particularly, patients with grade 1 tracer uptake should be examined thoroughly and receive close follow-up, as an early diagnosis may offer a window of opportunity for timely initiation of novel CA-specific treatments to prevent adverse outcomes.

We also report a 10-times higher prevalence of  $^{99m}\text{Tc}$ -DPD positivity in cardiac than noncardiac scintigraphy referrals. Active CA screening of patients with conditions typically associated with myocardial thickening, such as severe aortic stenosis and heart failure with preserved ejection fraction, have unveiled a prevalence of concomitant/underlying CA of  $\geq 10\%$  (2,3). Among elderly patients ( $\geq 80$  y) without these conditions, CA proportions ranging from less than 1% to 5% have been reported (6–8). The present data indicate an even higher CA prevalence among noncardiac patients older than 80 y of 6%.

In clinical routine, CA is generally suspected when symptoms of heart failure are reported in combination with imaging features typical for infiltrative cardiomyopathies (e.g., markedly increased wall thickness). Hence, cardiac  $^{99m}\text{Tc}$ -DPD referrals have a much higher likelihood of CA, and on average, showed more advanced disease (grade 2 or 3) than noncardiac patients, who mostly displayed grade 1 uptake. This likely relates to the clinical course of the disease. If detected incidentally, CA may be caught at an early stage where it is clinically unapparent. Conversely, the onset of clinical symptoms and transition to overt HF is more common in cases with advanced amyloid deposition (grade 2 or 3).

To our knowledge, for the first time we also report progressive amyloid deposition over time, as indicated by an increase in the

amount of cardiac tracer uptake observed in subjects with multiple scans. Most importantly, this included cases with progression from low-grade uptake to confirmed CA (grade 2 or 3). Moreover, ATTR was confirmed in approximately 25% of grade 1 patients with biopsy-proven CA. However, most grade 1 patients receiving myocardial biopsy had monoclonal protein, and tissue sampling was sought to rule out AL-CA. Hence, the proportion of ATTR among all patients with low-grade uptake on bone scintigraphy (not only in those with a likelihood of AL) might in fact be considerably higher than indicated by our data. These findings highlight the importance to recognize subtle tracer uptake as potential ATTR-CA (4,9)—especially in the absence of a plasma cell dyscrasia. In patients with monoclonal protein with or without a positive bone scan result, novel nuclear imaging tracers (e.g.,  $^{18}\text{F}$ -florbetaben) show promise to diagnose AL or reliably differentiate between AL and ATTR or mimicking conditions, respectively

(13). Distribution of late enhancement patterns by cardiac MR (CMR) may support the establishment of a CA diagnosis. Importantly, the addition of SPECT to planar imaging is recommended to discriminate cardiac from other sources of tracer uptake (e.g., ribs, residual blood-pool activity; Supplemental Fig. 6) (14). SPECT is of particular relevance in cases with subtle uptake on planar imaging to avoid false-positive results. One recent study using PYP and a 1-h imaging protocol reported false positivity in two thirds of patients with subtle uptake on planar imaging when compared with SPECT as a reference standard (15). In the present series, where scans were performed at 3 h—and therefore presumably more accurate in the verification of myocardial tracer origin—false positivity of grade 1 planar imaging was 40%, whereas grade 2 or 3 was 100% accurate. Given that SPECT was available only for a subset of patients with low-grade uptake, we assume that a relevant proportion of grade 1 patients was diagnosed because of blood pooling effects. In the case of suspected AL, endomyocardial biopsy OR extracardiac biopsy in combination with typical imaging features (echocardiography, CMR) are necessary to confirm the diagnosis (16). However, recent important improvements in cardiac imaging as outlined above have nurtured the hope that a CA diagnosis can be established purely noninvasively, thereby avoiding potential risks inherent to cardiac biopsy. Yet, on the basis of our data, grade 1 uptake currently requires comprehensive work-up (e.g., echo, CMR, SPECT, laboratory light-chain assessment, myocardial biopsy if indicated) to unmask early CA cases.

Few prospective CA registries have reported on predictors of survival (17–19). However, outcome implications of CA in the general population remain largely unknown. Here, we first describe CA as an independent predictor of clinical endpoints. After adjustment for (cardiovascular) risk factors,  $^{99m}\text{Tc}$ -DPD positivity was associated with a 20% increase in all-cause mortality, an 80% increase in cardiovascular death, and a more than 2-fold risk for HHF. Overall, adjusted risk for adverse outcomes was only increased in confirmed CA, with 2-y survival rates comparable to those for patients in the placebo arm of the ATTR-ACT trial (Fig. 2) (10). However, the present cohort comprised individuals

with a high prevalence of malignancy and, hence, substantially increased 1-y mortality rates. Thus, the impact of CA—in particular of grade 1 CA—may be much stronger in the general population, and over a longer follow-up period. Accordingly, among noncancer patients, who had a significantly longer life expectancy than those with cancer, both grade 2 or 3 and low-grade uptake predicted outcomes, as previously reported in a preliminary analysis (20). Of note, inclusion of a relevant number of grade 1 patients with blood pooling may in fact underestimate the severity of outcomes in grade 1 patients with true myocardial uptake in the present series. Hence, low-grade uptake may represent a window of opportunity for timely diagnosis and initiation of novel CA-specific treatments. In ATTR, such treatments include agents that stabilize the tetrameric TTR protein (tafamidis) or reduce TTR serum levels (inotersen, patisiran). Tafamidis is the only drug currently approved for the treatment of ATTR-CA and has been shown to improve survival compared with placebo (10). However, subgroup analysis indicated fewer benefits for those with more advanced disease (NYHA class III), where placebo was superior to Tafamidis in the prevention of cardiovascular hospitalization. Treatment should, therefore, be initiated early in the disease process to achieve prognostic improvements. Future randomized trials are necessary to clarify whether ATTR-specific drugs will improve outcomes in grade 1 ATTR-CA patients.

This study has limitations. CA subtype was not consistently assessed given the retrospective study design. Yet, available results from cardiac biopsies emphasize the importance to recognize grade 1 cardiac uptake as potential ATTR-CA. Additional SPECT/CT of the chest was not uniformly available. Grade 1 may therefore comprise a proportion of patients with blood pooling effects and outcomes of low-grade patients with true myocardial tracer origin may in reality be even worse than shown here. Also, the presence of bone metastases in this population with a high rate of malignancy may have led to an underdiagnosis of low-grade amyloid deposition because of tracer competition with other compartments (Supplemental Fig. 5). Laboratory values (including monoclonal protein assessment) were not available for all patients and therefore excluded from outcome analysis. Finally, whereas a selection bias must be considered because of the single-center nature of our study, we followed an identical protocol for <sup>99m</sup>Tc-DPD bone scintigraphy, ensuring consistency of data throughout the more than 10-y study period.

## CONCLUSION

CA is prevalent in elderly patients undergoing bone scintigraphy, both among noncardiac and even more so among cardiac referrals. Overall, the presence of confirmed CA (Perugini grade 2 or 3) was independently associated with adverse clinical outcomes. Grade 1—which we show can progress to confirmed CA over time—had increased mortality only among noncancer patients because of longer life expectancy and potentially higher prognostic impact of early ATTR infiltration. If diagnosed and treated early, outcomes of CA patients may potentially improve significantly.

## DISCLOSURE

This study received financial support from Pfizer. Christian Nitsche reports speaker fees from Pfizer. No other potential conflict of interest relevant to this article was reported.

## KEY POINTS

**QUESTION:** How prevalent is CA among all-comers referred for bone scintigraphy and is it associated with worse outcomes?

**PERTINENT FINDINGS:** <sup>99m</sup>Tc-DPD+ affects 1-in-50 noncardiac and 1-in-5 cardiac patients referred for bone scintigraphy. Confirmed CA (grade 2 or 3) has increased mortality (all-cause and cardiovascular) and risk for future heart failure; grade 1 may represent both ATTR- and AL-CA and is likewise associated with a poor prognosis if observed for a longer period.

**IMPLICATIONS FOR PATIENT CARE:** Grade 1 may offer the possibility for early CA diagnosis and treatment with new amyloid-targeting therapies.

## REFERENCES

- Ravichandran S, Lachmann HJ, Wechalekar AD. Epidemiologic and survival trends in amyloidosis, 1987-2019. *N Engl J Med*. 2020;382:1567–1568.
- González-López E, Gallego-Delgado M, Guzzo-Merello G, et al. Wild-type transthyretin amyloidosis as a cause of heart failure with preserved ejection fraction. *Eur Heart J*. 2015;36:2585–2594.
- Nitsche C, Scully PR, Patel KP, et al. Prevalence and outcomes of concomitant aortic stenosis and cardiac amyloidosis. *J Am Coll Cardiol*. 2021;77:128–139.
- Nitsche C, Aschauer S, Kammerlander AA, et al. Light-chain and transthyretin cardiac amyloidosis in severe aortic stenosis: prevalence, screening possibilities, and outcome. *Eur J Heart Fail*. 2020;22:1852–1862.
- Maurizi N, Rella V, Fumagalli C, et al. Prevalence of cardiac amyloidosis among adult patients referred to tertiary centres with an initial diagnosis of hypertrophic cardiomyopathy. *Int J Cardiol*. 2020;300:191–195.
- Longhi S, Guidalotti PL, Quarta CC, et al. Identification of TTR-related subclinical amyloidosis with <sup>99m</sup>Tc-DPD scintigraphy. *JACC Cardiovasc Imaging*. 2014;7:531–532.
- Cuscaden C, Ramsay SC, Prasad S, Goodwin B, Smith J. Estimation of prevalence of transthyretin (ATTR) cardiac amyloidosis in an Australian subpopulation using bone scans with echocardiography and clinical correlation. *J Nucl Cardiol*. 2021;28:2845–2856.
- Mohamed-Salem L, Santos-Mateo JJ, Sanchez-Serna J, et al. Prevalence of wild type ATTR assessed as myocardial uptake in bone scan in the elderly population. *Int J Cardiol*. 2018;270:192–196.
- Gillmore JD, Maurer MS, Falk RH, et al. Nonbiopsy diagnosis of cardiac transthyretin amyloidosis. *Circulation*. 2016;133:2404–2412.
- Maurer MS, Schwartz JH, Gundapaneni B, et al. Tafamidis treatment for patients with transthyretin amyloid cardiomyopathy. *N Engl J Med*. 2018;379:1007–1016.
- Perugini E, Guidalotti PL, Salvi F, et al. Noninvasive etiologic diagnosis of cardiac amyloidosis using <sup>99m</sup>Tc-3,3-diphosphono-1,2-propanodicarboxylic acid scintigraphy. *J Am Coll Cardiol*. 2005;46:1076–1084.
- Hutt DF, Quigley AM, Page J, et al. Utility and limitations of 3,3-diphosphono-1,2-propanodicarboxylic acid scintigraphy in systemic amyloidosis. *Eur Heart J Cardiovasc Imaging*. 2014;15:1289–1298.
- Genovesi D, Vergaro G, Giorgetti A, et al. [<sup>18</sup>F]-florbetaben PET/CT for differential diagnosis among cardiac immunoglobulin light chain, transthyretin amyloidosis, and mimicking conditions. *JACC Cardiovasc Imaging*. 2021;14:246–255.
- Dorbala S, Ando Y, Bokhari S, et al. ASNC/AHA/ASE/EANM/HFSA/ISA/SCMR/SNMMI expert consensus recommendations for multimodality imaging in cardiac amyloidosis: part 1 of 2—evidence base and standardized methods of imaging. *Circ Cardiovasc Imaging*. 2021;14:e000029.
- Poterucha TJ, Elias P, Bokhari S, et al. Diagnosing transthyretin cardiac amyloidosis by technetium Tc 99m pyrophosphate: a test in evolution. *JACC Cardiovasc Imaging*. 2021;14:1221–1231.
- García-Pavía P, Rapezzi C, Adler Y, et al. Diagnosis and treatment of cardiac amyloidosis: a position statement of the European Society of Cardiology Working Group on Myocardial and Pericardial Diseases. *Eur J Heart Fail*. 2021;23:512–526.
- Binder C, Duca F, Stelzer PD, et al. Mechanisms of heart failure in transthyretin vs. light chain amyloidosis. *Eur Heart J Cardiovasc Imaging*. 2019;20:512–524.
- Castano A, Haq M, Narotsky DL, et al. Multicenter study of planar technetium 99m pyrophosphate cardiac imaging: predicting survival for patients with ATTR cardiac amyloidosis. *JAMA Cardiol*. 2016;1:880–889.
- Gillmore JD, Damy T, Fontana M, et al. A new staging system for cardiac transthyretin amyloidosis. *Eur Heart J*. 2018;39:2799–2806.
- Nitsche C, Mascherbauer K, Wollenweber T, et al. The complexity of subtle cardiac tracer uptake on bone scintigraphy. *JACC Cardiovasc Imaging*. 2022;15:1516–1518.

# Evaluation of (*rac*)-, (*R*)-, and (*S*)-<sup>18</sup>F-OF-NB1 for Imaging GluN2B Subunit-Containing *N*-Methyl-D-Aspartate Receptors in Nonhuman Primates

Hazem Ahmed\*<sup>1,2</sup>, Ming-Qiang Zheng\*<sup>2</sup>, Kelly Smart<sup>2</sup>, Hanyi Fang<sup>2,3</sup>, Li Zhang<sup>2</sup>, Paul R. Emery<sup>2</sup>, Hong Gao<sup>2</sup>, Jim Ropchan<sup>2</sup>, Ahmed Haider<sup>1</sup>, Gilles Tamagnan<sup>2</sup>, Richard E. Carson<sup>2</sup>, Simon M. Ametamey<sup>1</sup>, and Yiyun Huang<sup>2</sup>

<sup>1</sup>Institute of Pharmaceutical Sciences, ETH Zurich, Zurich, Switzerland; <sup>2</sup>PET Center, Yale University, New Haven, Connecticut; and <sup>3</sup>Union Hospital, Huazhong University of Science and Technology, Wuhan, China

Despite 2 decades of research, no *N*-methyl-D-aspartate (NMDA) glutamate receptor (GluN) subtype 2B (GluN1/2B) radioligand is yet clinically validated. Previously, we reported on (*rac*)-<sup>18</sup>F-OF-NB1 as a promising GluN1/2B PET probe in rodents and its successful application for the visualization of GluN2B-containing NMDA receptors in postmortem brain tissues of patients with amyotrophic lateral sclerosis. In the current work, we report on the *in vivo* characterization of (*rac*)-, (*R*)-, and (*S*)-<sup>18</sup>F-OF-NB1 in nonhuman primates. **Methods:** PET scans were performed on rhesus monkeys. Plasma profiling was used to obtain the arterial input function. Regional brain time-activity curves were generated and fitted with the 1- and 2-tissue-compartment models and the multilinear analysis 1 method, and the corresponding regional volumes of distribution were calculated. Blocking studies with the GluN1/2B ligand Co 101244 (0.25 mg/kg) were performed for the enantiopure radiotracers. Receptor occupancy, nonspecific volume of distribution, and regional binding potential ( $BP_{ND}$ ) were obtained. Potential off-target binding toward  $\sigma_1$  receptors was assessed for (*S*)-<sup>18</sup>F-OF-NB1 using the  $\sigma_1$  receptor ligand FTC-146. **Results:** Free plasma fraction was moderate, ranging from 12% to 16%. All radiotracers showed high and heterogeneous brain uptake, with the highest levels in the cortex. (*R*)-<sup>18</sup>F-OF-NB1 showed the highest uptake and slowest washout kinetics of all tracers. The 1-tissue-compartment model and multilinear analysis 1 method fitted the regional time-activity curves well for all tracers and produced reliable regional volumes of distribution, which were higher for (*R*)- than (*S*)-<sup>18</sup>F-OF-NB1. Receptor occupancy by Co 101244 was 85% and 96% for (*S*)-<sup>18</sup>F-OF-NB1 and (*R*)-<sup>18</sup>F-OF-NB1, respectively. Pretreatment with FTC-146 at both a low (0.027 mg/kg) and high (0.125 mg/kg) dose led to a similar reduction (48% and 49%, respectively) in specific binding of (*S*)-<sup>18</sup>F-OF-NB1. Further, pretreatment with both Co 101244 and FTC-146 did not result in a further reduction in specific binding compared with Co 101244 alone in the same monkey (82% vs. 81%, respectively). Regional  $BP_{ND}$  values ranged from 1.3 in the semiovale to 3.4 in the cingulate cortex for (*S*)-<sup>18</sup>F-OF-NB1. **Conclusion:** Both (*R*)- and (*S*)-<sup>18</sup>F-OF-NB1 exhibited high binding specificity to GluN2B subunit-containing NMDA receptors. The fast washout kinetics, good regional  $BP_{ND}$  values, and high plasma free fraction render (*S*)-<sup>18</sup>F-OF-NB1 an attractive radiotracer for clinical translation.

**Key Words:** NMDA; GluN2B subunit; brain PET imaging; nonhuman primates; neurodegeneration

J Nucl Med 2022; 63:1912–1918

DOI: 10.2967/jnumed.122.263977

**G**lutamatergic *N*-methyl-D-aspartate receptors (NMDARs) are heterotetrameric ion channels ubiquitously expressed in the mammalian brain. The receptor complex is assembled from distinct subunits, namely *N*-methyl-D-aspartate (NMDA) glutamate receptor (GluN) subtypes 1a–1h (GluN1(a–h)), GluN subtypes 2A–2D (GluN2(A–D)), and GluN subtypes 3A and 3B, where each GluN2 subtype exhibits a unique spatiotemporal expression and function (*1*). NMDARs are known to be the linchpin for synaptic plasticity and transmission as well as higher cognitive functions. Notably, synaptic NMDARs are promoters of cell survival whereas extrasynaptic GluN2B subunit-enriched NMDARs are mediators of cell death. The GluN1/2B receptors are associated with several neuropathologies, such as Alzheimer’s disease, Parkinson’s disease, depression, schizophrenia, and stroke, among others (*2–5*). As such, the development of GluN1/2B antagonists has been the prime focus of therapeutic development efforts over the past 2 decades, with 19 therapeutic patent applications published in the past 5 years alone (*6,7*). Although these subtype-selective antagonists possess pharmacologic action similar to conventional NMDA ion channel blockers, they exhibit a much more favorable neurologic safety profile, as their selectivity is thought to preserve the physiologic functions of NMDARs but minimize potential undesired pharmacologic effects (*4,8*). To date, several GluN1/2B antagonists, such as CERC-301, have been evaluated in clinical trials with no-to-modest clinical benefits, whereas others are still in development (*7,9*). PET imaging is a powerful modality that can accelerate drug development—for example, to be used in target engagement and drug occupancy studies—and serve as a credible tool in patient selection and monitoring (*10,11*). Despite the longstanding interest, efforts to develop a GluN1/2B-specific PET radioligand have largely been unsuccessful. Challenges include poor brain uptake, homogeneous distribution, and the existence of brain radiometabolites, as well as binding to other brain receptors, most notably  $\sigma_1$  receptors ( $\sigma_1$ Rs) (*12*).

The 3-benzazepine structural class of compounds has recently emerged as potential PET radioligand candidates for the imaging of GluN1/2B (Fig. 1) (*13,14*). Recently, Ametamey’s group successfully developed the 3-benzazepin-1-ol derivative, (*R*)-<sup>11</sup>C-Me-NB1, for imaging GluN1/2B in humans (*15–17*). To overcome the

Received Feb. 7, 2022; revision accepted Apr. 7, 2022.  
For correspondence or reprints, contact Yiyun Henry Huang (henry.huang@yale.edu) or Simon M. Ametamey (simon.ametamey@pharma.ethz.ch).  
\*Contributed equally to this work.  
Published online Jun. 16, 2022.  
COPYRIGHT © 2022 by the Society of Nuclear Medicine and Molecular Imaging.

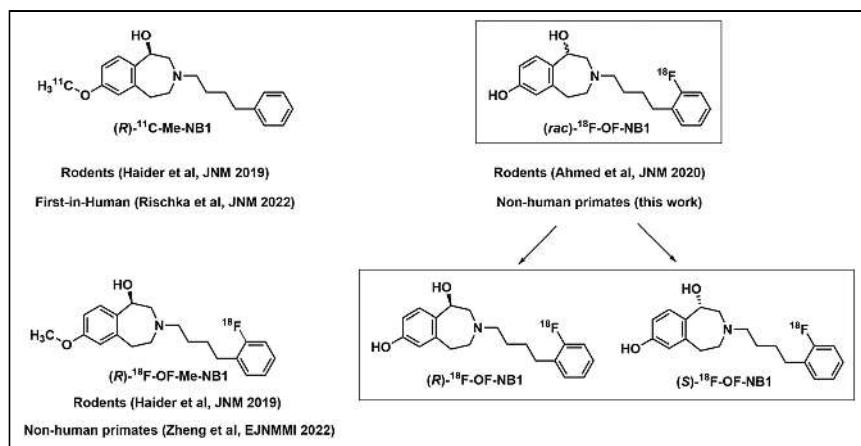


**FIGURE 1.** Structures of (*R*)-<sup>11</sup>C-Me-NB1, the lead radiotracer recently evaluated in clinical trial; (*R*)-<sup>18</sup>F-OF-Me-NB1, the first radiofluorinated derivative of (*R*)-<sup>11</sup>C-Me-NB1 evaluated in rats; and (*rac*)-, (*R*)-, and (*S*)-<sup>18</sup>F-OF-NB1 evaluated in the current work.

limitation of the short physical half-life of <sup>11</sup>C-labeled radioligands, we evaluated several radiofluorinated derivatives in animals (18–20). (*Rac*)-<sup>18</sup>F-OF-NB1 (inhibition constant  $K_i$  (GluN1/2B),  $10.4 \pm 4.7$  nM) emerged as one of the most promising candidates for evaluation in nonhuman primates (19). In the current work and for the purpose of clinical translation, we evaluated the pharmacokinetic and imaging properties of (*rac*)-, (*S*)-, and (*R*)-<sup>18</sup>F-OF-NB1 in nonhuman primates, and performed a comprehensive assessment of (*S*)-<sup>18</sup>F-OF-NB1 regarding its binding specificity to GluN1/2B receptors and selectivity over  $\sigma_1$ Rs *in vivo*.

## MATERIALS AND METHODS

### Chemistry

Synthesis of the reference compound (*rac*)-OF-NB1 and the corresponding aryl boronic ester precursors followed previously published procedures, as did their chiral high-performance liquid chromatography (HPLC) separation (18,19).

### Radiochemistry

<sup>18</sup>F-fluoride was produced via the <sup>18</sup>O(p,n)<sup>18</sup>F nuclear reaction using H<sub>2</sub><sup>18</sup>O (Huayi Isotopes) in a 16.5-MeV GE Healthcare PETtrace cyclotron. After bombardment, the activity was transferred to a shielded hot cell and trapped on an anionic-exchange resin cartridge (Chromafix PS-HCO<sub>3</sub>; Macherey-Nagel). Trapped <sup>18</sup>F<sup>-</sup> was eluted into a sealed 5-mL borosilicate glass reaction vial using a 2-mL solution of K<sub>2</sub>C<sub>2</sub>O<sub>4</sub> (1.0 mg/mL in water), K<sub>2</sub>CO<sub>3</sub> (0.1 mg/mL in water), and Kryptofix 222 (Merck) (6.3 mg/mL in acetonitrile). The solution was azeotropically dried for 5 min at 110°C under nitrogen, followed by drying twice using 0.4 mL of acetonitrile each time. Afterward, the vial was purged with 20 mL of air before the addition of 0.4 mL of the boronic ester precursor solution (6 mg of precursor and 12 mg of Cu(OTf)<sub>2</sub>(Py)<sub>4</sub> in anhydrous dimethylacetamide). The reaction mixture was stirred at 110°C for 20 min, diluted with 10 mL of deionized water, and passed through a Waters C18 SepPak cartridge. The cartridge was washed with 10 mL of deionized water. The trapped activity was eluted from the SepPak with 1 mL of ethanol into a second reaction vial. The solvent was dried at 90°C under a nitrogen stream. Dichloromethane and anhydrous BBr<sub>3</sub> were added and left to react for 15 min at room temperature. The solvent was removed by gentle nitrogen blowing, and the crude product was redissolved in the HPLC mobile phase (25% acetonitrile/75% 0.1 M ammonium formate with 0.5% acetic acid, pH 4.2). The solution was injected into a semipreparative HPLC system equipped with an Agilent Eclipse XDB-C18 (9.4 × 250 mm, 5 μm) column eluting with the above mobile phase at a flow rate of 5 mL/min. The radioactive peak

from 15 to 16 min was collected and diluted with 50 mL of water. The solution was passed through a Waters C18 SepPak cartridge. The product was eluted from the SepPak with 1 mL of ethanol and dried under gentle nitrogen blowing. The product was redissolved with the second HPLC mobile phase (32% acetonitrile/68% water with 0.05% triethylamine) and injected into the chiral semipreparative HPLC system equipped with a Regis reflect I-Amylose A column (250 × 10 mm, 5 μm) eluting with the aforementioned mobile phase at a flow rate of 5 mL/min. The radioactive peaks corresponding to (*R*)-<sup>18</sup>F-OF-NB1 (eluting from 23 to 25 min) and (*S*)-<sup>18</sup>F-OF-NB1 (eluting from 27 to 29 min) were collected in 2 separate bottles and diluted with 50 mL of water each. The solutions were passed through Waters C18 SepPak cartridges separately. Each SepPak was washed with 1 mM HCl (10 mL), dried with air, and then eluted

with 1 mL of U.S. Pharmacopeia-grade ethanol, followed by 3 mL of U.S. Pharmacopeia-grade saline, into a collection vial. The solution was then passed through a 0.22-μm Millex-GV filter (Millipore) into a 10 mL dose vial precharged with 7 mL of U.S. Pharmacopeia-grade saline for formulation.

### Measurement of Lipophilicity (log *D*<sub>7.4</sub>)

The lipophilicity (log *D*<sub>7.4</sub>) of (*S*)-<sup>18</sup>F-OF-NB1 was determined according to previously published procedures (21,22). The log *D*<sub>7.4</sub> was calculated as the ratio between the concentrations of decay-corrected radioactivity in 1-octanol and pH 7.4 phosphate-buffered saline (Dulbecco).

### PET Imaging in Rhesus Monkeys

All experimental procedures were approved by the Yale University Institutional Animal Care and Use Committee. In total, 11 dynamic PET scans (120 min each) were performed on 3 rhesus monkeys (*Macaca mulatta*, 2 males and 1 female) on the Focus 220 scanners (Siemens Medical Solutions).

Baseline scans were acquired for (*rac*)-, (*R*)-, and (*S*)-<sup>18</sup>F-OF-NB1, whereas blockade scans using the GluN1/2B antagonist Co 101244 (0.25 mg/kg; half-maximal inhibition concentration (*IC*<sub>50</sub>),  $4 \pm 1$  nM for GluN1/2B) were performed for the enantiopure radiotracers (23). Further, blockade scans using either the  $\sigma_1$ R antagonist FTC-146 (2 doses; 0.027 and 0.125 mg/kg;  $K_i$ , 0.0025 nM for  $\sigma_1$ R) alone or GluN1/2B (0.25 mg/kg dose of Co 101244) followed by  $\sigma_1$ R blockade (0.125 mg/kg dose of FTC-146) were accomplished using (*S*)-<sup>18</sup>F-OF-NB1 (24). Procedures for PET scanning, image processing, and image analysis are detailed in the supplemental materials (available at <http://jnm.snmjournals.org>).

*Arterial Input Function Measurement and Metabolite Analysis.* Plasma activity and parent fraction were determined in accordance with previously published procedures (25,26). Radioactivity was measured in whole blood and plasma from arterial samples taken at various time points after radiotracer injection using cross-calibrated  $\gamma$ -counters (Wizard 1480/2480; Perkin Elmer). The radiometabolic profile was investigated by HPLC analysis using a column-switching method with plasma samples from 0, 5, 15, 30, 60, 90, and 120 min after radiotracer injection (27). The parent fraction was calculated as the ratio of the radioactivity in parent compound-containing fractions to the total radioactivity measured. Finally, the arterial input function was calculated as the product of total plasma concentrations and the interpolated parent fraction at each time point.

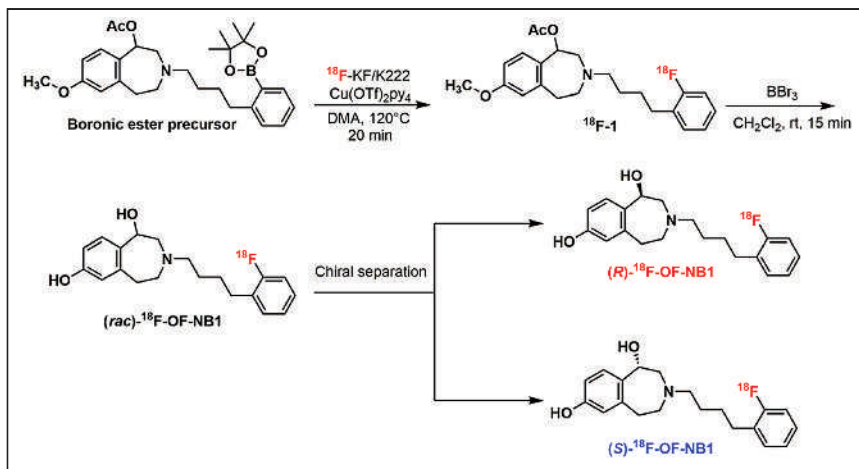


**FIGURE 2.** Radiosynthesis of (*rac*)-, (*R*)-, and (*S*)-<sup>18</sup>F-OF-NB1. DMA = dimethylacetamide; rt = room temperature.

**Measurement of Radiotracer Free Fraction in Plasma ( $f_p$ ).** Ultrafiltration was the method of choice for measuring the unbound radiotracer in plasma  $f_p$  (28). The  $f_p$  measurement was performed in triplicates per scan and was defined as the ratio of the radioactivity concentration in the filtrate to the total activity in plasma.

**Kinetic Modeling.** The regional time–activity curves and metabolite-corrected arterial input functions were analyzed with the 1- and 2-tissue compartment models, as well as the multilinear analysis 1 method (starting time, 30 min) to calculate the kinetic parameters (28). The regional volume of distribution ( $V_T$ , mL/cm<sup>3</sup>) from each model was derived and compared. Target occupancy and the nondisplaceable  $V_T$  ( $V_{ND}$ ) in the brain were derived from the Lassen plot, generated using the baseline regional  $V_T$  values and the  $V_T$  difference between baseline and blockade scans (29). Regional binding potential ( $BP_{ND}$ ) was calculated as  $BP_{ND} = (V_T - V_{ND})/V_{ND}$  using the  $V_{ND}$  value derived from the Lassen plot for the GluN1/2B blocking scan.

## RESULTS

### Chemistry

The overall chemical yields of the reference compounds (*rac*-), (*S*-), and (*R*-)OF-NB1 and the respective boronic ester precursors were comparable to those published previously (18,19).

### Radiochemistry

The radiosynthetic strategy is depicted in Figure 2. Despite starting from enantiopure precursors, racemization occurred during the deprotection step, requiring additional chiral purification. The final activities

obtained were  $1,480 \pm 185$  MBq ( $n = 5$ ) for (*rac*)-<sup>18</sup>F-OF-NB1 and  $203.7 \pm 81.4$  MBq ( $n = 10$ ) for (*S*-) and (*R*-)<sup>18</sup>F-OF-NB1. The radiotracers were prepared in more than 99% radiochemical purity. (*S*-) and (*R*-)<sup>18</sup>F-OF-NB1 were both obtained in more than 98% enantiomeric purity. Molar activity was  $143.5 \pm 127.3$  GBq/μmol ( $n = 10$ ) at the end of synthesis. The total synthesis time for (*S*-) and (*R*-)<sup>18</sup>F-OF-NB1 was 200 min on average.

### Measurement of $\log D_{7,4}$

The measured  $\log D_{7,4}$  of (*S*-)<sup>18</sup>F-OF-NB1 was  $2.05 \pm 0.08$  ( $n = 4$ ), similar to the  $\log D_{7,4}$  of (*rac*)-<sup>18</sup>F-OF-NB1, and in the optimal range for brain penetration (19,30).

### PET Imaging Experiments on Rhesus Monkeys

The amount of injected radioactivity and associated mass were  $147.1 \pm 47.4$  MBq and  $1.05 \pm 0.70$  μg, respectively ( $n = 10$ ). The parent fractions at 30 min after injection were 33% ( $n = 2$ ), 32% ( $n = 2$ ), and 57% ( $n = 1$ ) for the baseline scans of (*rac*-), (*S*-), and (*R*-)<sup>18</sup>F-OF-NB1, respectively (Fig. 3). For (*S*-) and (*R*-)<sup>18</sup>F-OF-NB1, the parent fractions decreased to 26% ( $n = 2$ ) and 27%, respectively, after pretreatment of the animals with the GluN1/2B antagonist Co 101244, whereas preblocking with the  $\sigma_1$ R antagonist FTC-146, whether at a low or a high dose, did not change the parent fraction of (*S*-)<sup>18</sup>F-OF-NB1 (32%). The  $f_p$  was  $0.12 \pm 0.01$  for (*rac*)-<sup>18</sup>F-OF-NB1 ( $n = 2$ ),  $0.16 \pm 0.01$  for (*S*-)<sup>18</sup>F-OF-NB1 ( $n = 8$ ), and 0.13 for (*R*-)<sup>18</sup>F-OF-NB1 ( $n = 1$ ).

In the monkey brain, all tracers showed a heterogeneous distribution, with uptake high in the cortex, putamen, and cerebellum; moderate in the hippocampus and thalamus; and lowest in the centrum semiovale (Fig. 4). Brain uptake of (*S*-)<sup>18</sup>F-OF-NB1 peaked at an SUV of 4–5 within 20 min after injection, followed by a relatively fast clearance. The (*R*-) enantiomer, on the other hand, displayed slow brain clearance, with uptake increasing throughout the 120-min scan. Brain uptake levels and tissue clearance of (*rac*)-<sup>18</sup>F-OF-NB1 were between those of the 2 enantiomers (Supplemental Fig. 1). Pretreatment with the GluN1/2B antagonist Co 101244 (0.25 mg/kg) reduced radioactivity levels in all regions to nearly those in the semiovale for both enantiomers at the end of the scans. Receptor occupancy by a 0.25 mg/kg dose of Co 101244 was estimated at 81% and 88% across the brain in 2 separate monkeys for (*S*-)<sup>18</sup>F-OF-NB1 and 96% for (*R*-)<sup>18</sup>F-OF-NB1 (Fig. 5). Pretreatment with a  $\sigma_1$ R antagonist reduced the uptake of (*S*-)<sup>18</sup>F-OF-NB1 across all brain regions. A low dose

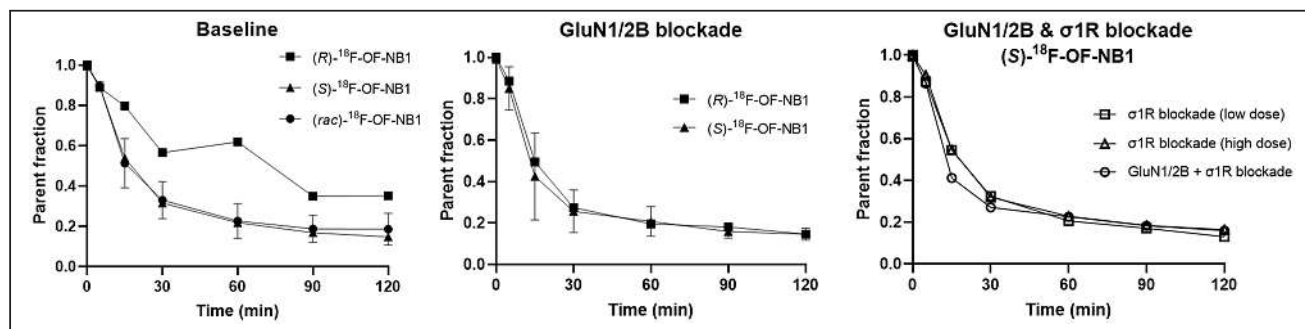


**FIGURE 3.** Parent fraction remaining of (*rac*-), (*R*-), and (*S*-)<sup>18</sup>F-OF-NB at different time points under baseline and blockade conditions. For GluN1/2B blockade, dose of 0.25 mg/kg of Co 101244 was used. For  $\sigma_1$ R blockade, either low dose (0.027 mg/kg) or high dose (0.125 mg/kg) of FTC-146 was used.

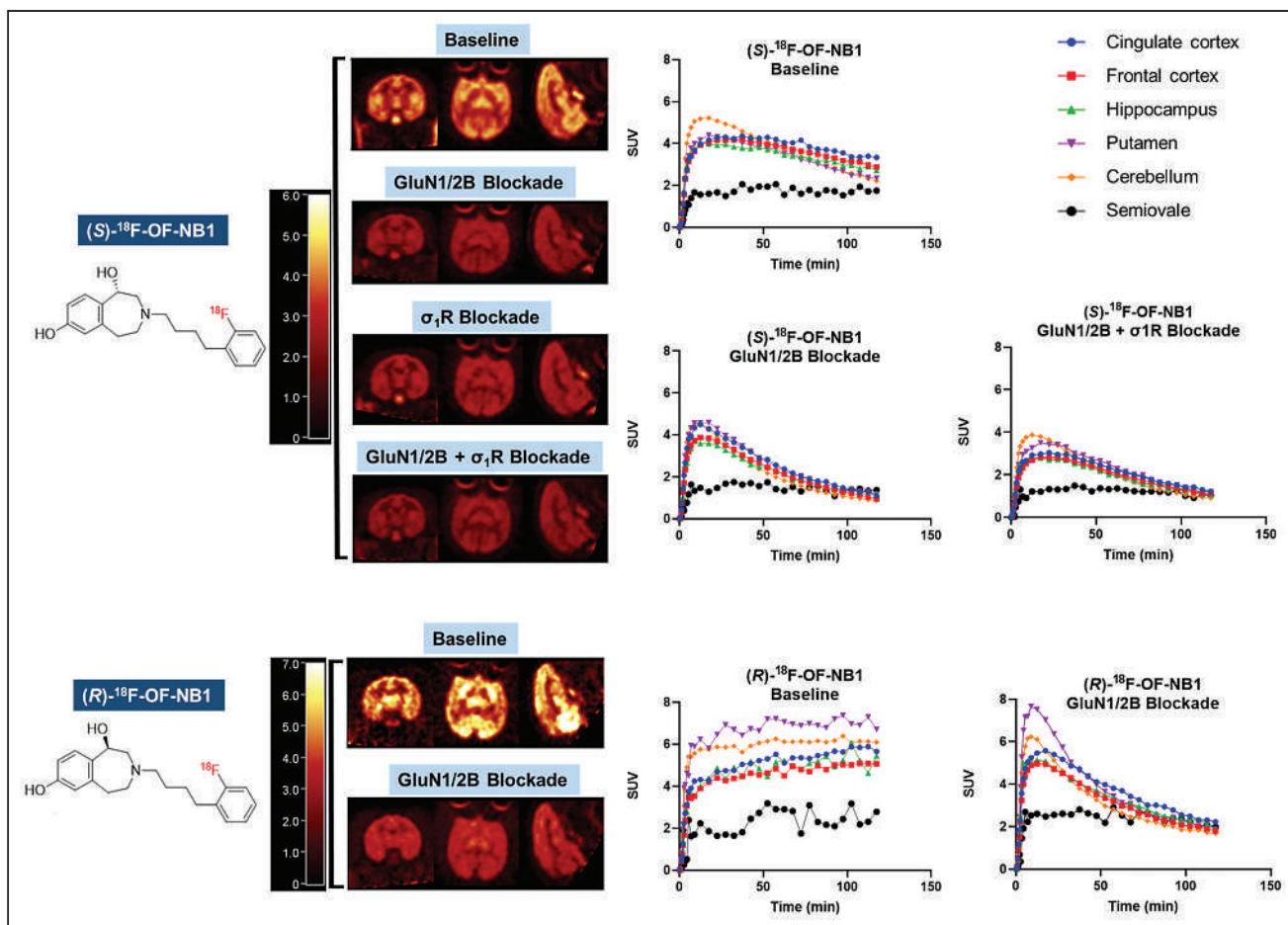


**FIGURE 4.** (Top) Representative PET SUV images (summed from 45 to 60 min) and time-activity curves in selected brain regions from baseline, GluN1/2B blockade (0.25 mg/kg dose of Co 101244),  $\sigma_1$ R blockade (0.125 mg/kg dose of FTC-146), and sequential GluN1/2B/ $\sigma_1$ R blockade (0.25 mg/kg dose of Co 101244 + 0.125 mg/kg dose FTC-146) scans of (*S*)- $^{18}\text{F}$ -OF-NB1 obtained in the same rhesus monkey (monkey 2). (Bottom) PET SUV images and time-activity curves from baseline and GluN1/2B blockade (0.25 mg/kg dose of Co 101244) scans of (*R*)- $^{18}\text{F}$ -OF-NB1 (monkey 1).

(0.027 mg/kg) and a high dose (0.125 mg/kg) of FTC-146 reduced the specific binding of (*S*)- $^{18}\text{F}$ -OF-NB1 by 48% and 49%, respectively. Double blocking with sequential administration of both Co 101244 (0.25 mg/kg) and high-dose FTC-146 (0.125 mg/kg) in 1 monkey at 25 and 15 min before the radiotracer injection, respectively, did not further reduce brain uptake of (*S*)- $^{18}\text{F}$ -OF-NB1 when compared with blocking with Co 101244 alone (82% vs. 81%).

The time-activity curves were well fitted with both the 1-tissue-compartment model and the multilinear analysis 1 method for reliable  $V_T$  estimates, with a relative SE of less than 5% (Supplemental Tables 1 and 2). On average,  $V_T$  values were similar for (*rac*)- and (*R*)- $^{18}\text{F}$ -OF-NB1 and were lower for (*S*)- $^{18}\text{F}$ -OF-NB1. Regional  $V_T$  values ranged from 17 to 39 mL/cm<sup>3</sup> for (*S*)- $^{18}\text{F}$ -OF-NB1 in the selected brain regions (Table 1). From the GluN1/2B blocking studies,  $V_{ND}$  was found to be 9.3 mL/cm<sup>3</sup> for (*S*)- $^{18}\text{F}$ -OF-NB1 in monkey 1 and 7.3 mL/cm<sup>3</sup> in monkey 2. From these  $V_{ND}$  values, regional  $BP_{ND}$  values were calculated and ranged from 1.2 (semiovale) to 3.4 (cingulate cortex) for (*S*)- $^{18}\text{F}$ -OF-NB1 (Table 1).

## DISCUSSION

Given the involvement of GluN1/2B receptors in various neuropathologies, great effort has been taken to develop therapeutic and PET

imaging agents, and several radioligands are currently in development. (*R*)- $^{11}\text{C}$ -Me-NB1 was recently evaluated in healthy volunteers and shown to have excellent brain uptake and kinetics (17). These results warrant the development of a radiofluorinated PET tracer that would allow wider use. We previously synthesized and tested several ligands, and (*rac*)- $^{18}\text{F}$ -OF-NB1 emerged as one of the most promising candidates for clinical translation, given its excellent properties in rodents (19). In the current work, we evaluated the performance characteristics of (*rac*)- $^{18}\text{F}$ -OF-NB1 and its enantiopure (*S*)- and (*R*)- $^{18}\text{F}$ -OF-NB1 with respect to their brain uptake, kinetics, and metabolism, to select the most promising candidate for clinical translation. To our knowledge, there have been no reports of clinical trials on the evaluation of a radiofluorinated probe for PET imaging of GluN1/2B in humans.

The radiosynthesis of  $^{18}\text{F}$ -OF-NB1 proceeded in 2 steps: copper-catalyzed radiofluorination of the boronic ester precursor, followed by simultaneous cleavage of the 2 hydroxyl protecting groups (19). Despite starting with enantiopure precursors, we could not obtain the respective enantiopure (*S*)- and (*R*)- $^{18}\text{F}$ -OF-NB1 without racemization during the second deprotecting step. As such, the radiosynthetic strategy was adapted to include a chiral HPLC purification step to provide enantiopure radiotracers at the end of the synthesis (Supplemental Fig. 2). This allowed the production of both enantiomers from a single radiosynthetic run. Metabolite analysis showed a higher

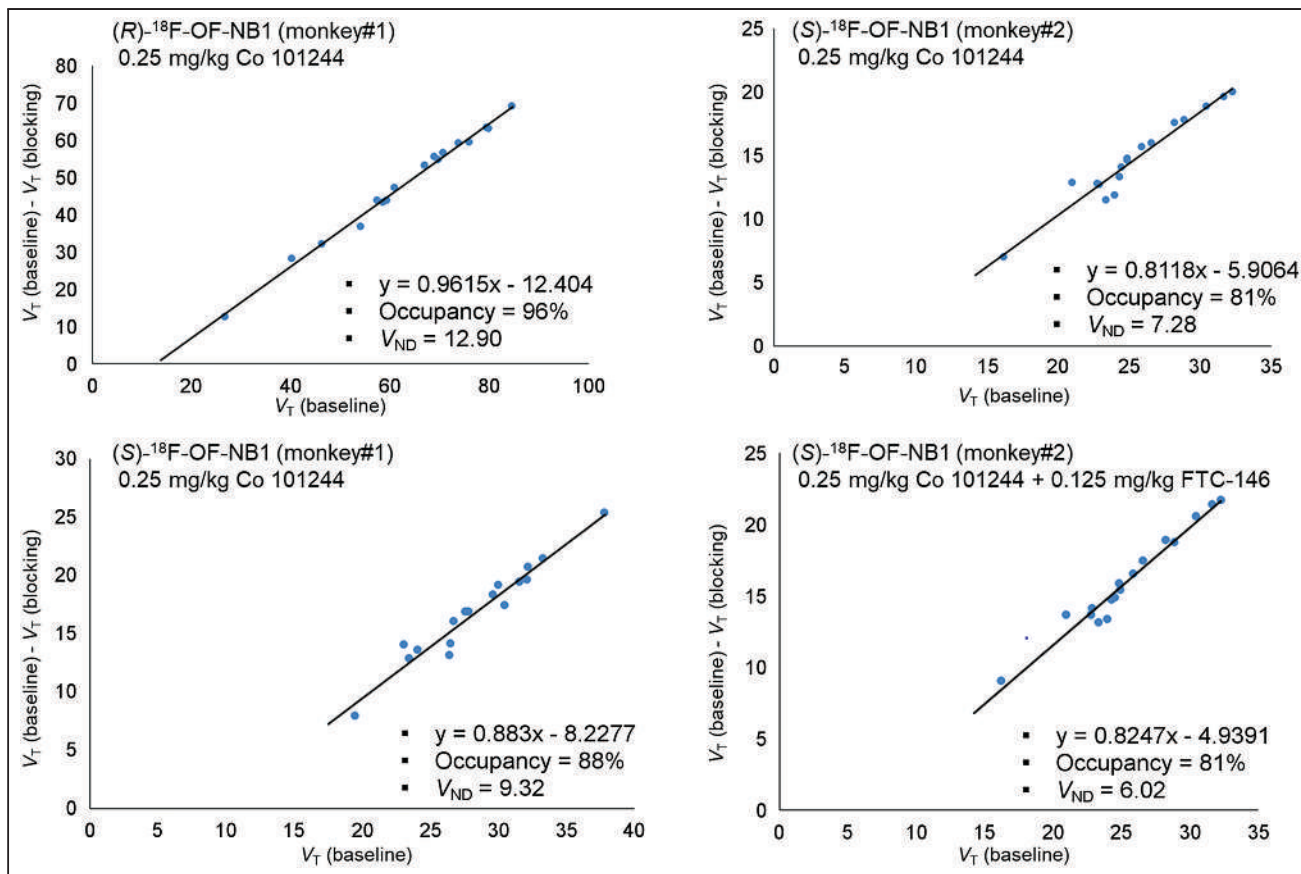


**FIGURE 5.** Lassen occupancy plots of (R)- and (S)-<sup>18</sup>F-OF-NB1 after pretreatment with either GluN1/2B ligand Co 101244 (0.25 mg/kg) only or with addition of  $\sigma_1$ R ligand FTC-146 (0.125 mg/kg). Each point represents unique brain region.

parent fraction in the plasma for (R)-<sup>18</sup>F-OF-NB1 than for the (S)-enantiomer. This phenomenon can be explained by the fact that different enantiomers can bind to enzymes with different affinities and therefore exhibit different metabolic rates (31). Further, all forms of <sup>18</sup>F-OF-NB1 presented good  $f_p$  values (0.12–0.16), offering the opportunity for high-precision measurement and

subsequently improving the accuracy of quantitative PET measurements and calculation of  $V_T/f_p$ , a potentially valuable outcome measure in clinical trials.

The brain uptake and distribution of (rac)-<sup>18</sup>F-OF-NB1 corroborated results in rodents (19). Kinetic analysis, however, is not suited for racemic mixtures unless both enantiomers exhibit identical plasma

**TABLE 1**  
One-Tissue-Compartment Model  $V_T$  and  $BP_{ND}$  Values in Selected Brain Regions Under Baseline and Blockade Conditions

Region of interest	$V_T$ (mL/cm <sup>3</sup> )						$BP_{ND}$	
	Baseline		Co 101244 (0.25 mg/kg)		FTC-146 (0.027 mg/kg)	FTC-146 (0.125 mg/kg)	$(V_T - V_{ND})/V_{ND}$	
	Monkey 1	Monkey 2	Monkey 1	Monkey 2	Monkey 1	Monkey 2	Monkey 1	Monkey 2
Thalamus	24.6 (39.6)	23.3	10.4 (13.7)	10.2	20.9	13.9	1.64 (2.1)	2.20
Cerebellum	27.3 (50.3)	25.5	10.8 (13.1)	10.2	19.6	15.5	1.93 (2.9)	2.50
Cingulate cortex	38.8 (59.5)	32.3	12.6 (16.5)	12.1	27.9	19.3	3.16 (3.6)	3.44
Frontal cortex	31.1 (49.1)	28.9	11.0 (13.8)	10.7	20.9	17.3	2.34 (2.8)	2.97
Hippocampus	32.1 (50.8)	26.3	11.5 (14.6)	10.6	24.0	16.2	2.44 (2.9)	2.61
Semiovale	20.3 (30.9)	16.9	10.6 (13.7)	9.0	15.9	11.5	1.18 (1.4)	1.32

Data in parentheses are for (R)-<sup>18</sup>F-OF-NB1 in 1 monkey; other data are for (S)-<sup>18</sup>F-OF-NB1 in 2 different monkeys.  $V_{ND}$  values were derived from GluN1/2B blocking scan using Co 101244.

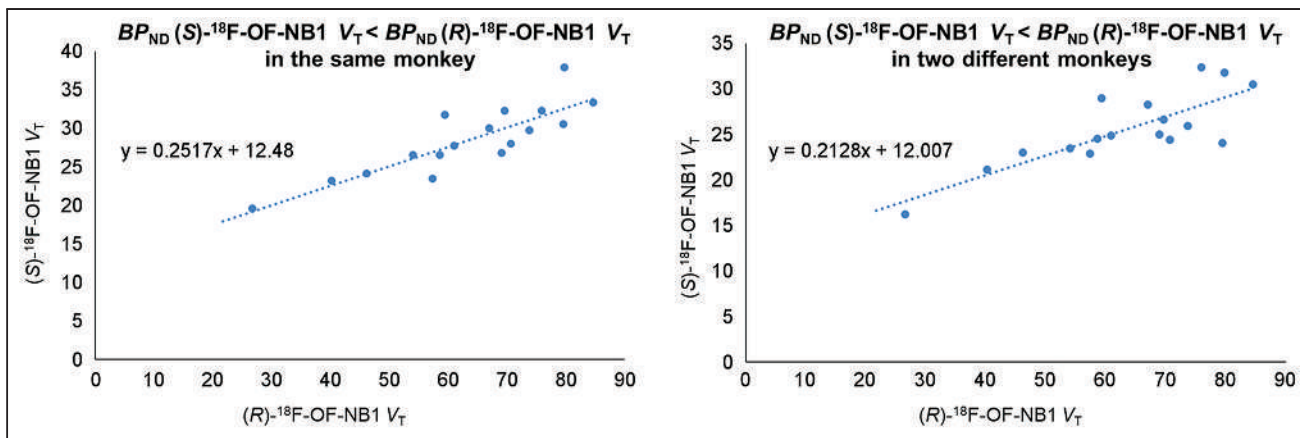


**FIGURE 6.** Guo plots (33) comparing regional  $V_T$  values of (S)- $^{18}\text{F}$ -OF-NB1 (y-axis) and (R)- $^{18}\text{F}$ -OF-NB1 (x-axis) in same monkey (left) and in 2 different monkeys (right). y-intercept is  $> 0$ , signifying higher  $BP_{\text{ND}}$  values of tracer on x-axis than on y-axis. Slope indicates relative *in vivo* binding affinity of 2 tracers, where (R)- $^{18}\text{F}$ -OF-NB1 exhibits 4- to 5-fold higher binding affinity than (S)-enantiomer.

clearance. The 2 enantiopure radiotracers displayed brain distribution and kinetics that are in line with the results in rodents. (R)- and (S)- $^{18}\text{F}$ -OF-NB1 showed high uptake in GluN1/2B-rich brain regions, with the highest uptake in the cingulate cortex. The binding of both enantiopure tracers was displaceable across all brain regions, indicating the lack of a reference region for kinetic modeling analysis. Regional time-activity curves of all 3 tracers, on the other hand, were well fitted by the 1-tissue-compartment model. The 2-tissue-compartment model also produced reasonable model fits, but the SE of  $V_T$  values was high and nonphysiologic values were generated in several gray matter regions. The multilinear analysis 1 method also provided good fits and  $V_T$  values comparable to those derived from the 1-tissue-compartment model (32). Regional  $V_T$  estimates were higher for (R)- $^{18}\text{F}$ -OF-NB1 than for the (S)-enantiomer. When plotting  $V_T$  values of (R)- and (S)- $^{18}\text{F}$ -OF-NB1 against each other to generate the Guo plot (33), the slope of this curve indicated 4- to 5-fold higher *in vivo* affinity for (R)- $^{18}\text{F}$ -OF-NB1 than for (S)- $^{18}\text{F}$ -OF-NB1 (Fig. 6).

To investigate the *in vivo* binding specificity of both enantiomers to GluN1/2B, blocking experiments with the GluN1/2B antagonist Co 101244 (0.25 mg/kg) were performed and a Lassen plot analysis for each enantiomer was undertaken. Both enantiomers showed high specific binding, with an estimated occupancy of 96% ( $n = 1$ ) across the brain by Co 101244 (0.25 mg/kg) when measured with (R)- $^{18}\text{F}$ -OF-NB1, and 85% ( $n = 2$ ) with (S)- $^{18}\text{F}$ -OF-NB1. Furthermore, both enantiomers exhibited good regional  $BP_{\text{ND}}$  values in the range of 2–3, highlighting their clinical translation potential in terms of specific binding (Table 1). The high affinity of (R)- $^{18}\text{F}$ -OF-NB1 came at the expense of a less desirable pharmacokinetic profile due to its extremely slow washout from the brain, which precluded its further development, since a very long scan might be required in humans. Pretreatment with a low dose (0.027 mg/kg) or a high dose (0.125 mg/kg) of the  $\sigma_1$ R antagonist FTC-146 led to partial blocking, with a 49% and 48% reduction in the specific binding of (S)- $^{18}\text{F}$ -OF-NB1, respectively, as calculated from the Lassen plots, and no clear dose-blockade level relationship. To address this potential off-target binding component of (S)- $^{18}\text{F}$ -OF-NB1, a sequential blockade experiment was conducted in which Co 101244 (0.25 mg/kg) was injected first, followed by the  $\sigma_1$ R antagonist FTC-146 (0.125 mg/kg). Blocking with a 0.25 mg/kg dose of Co 101244 alone resulted in 81% occupancy, and virtually no change in occupancy was observed

when FTC-146 was administered afterward. The absence of a further reduction in binding after treatment with FTC-146 suggests that (S)- $^{18}\text{F}$ -OF-NB1 binds specifically to the GluN1/2B receptors and is selective over  $\sigma_1$ Rs. The partial blockade of (S)- $^{18}\text{F}$ -OF-NB1 binding by FTC-146 when administered alone can be attributed to  $\sigma_1$ R-NMDAR cross-talk stemming from the inherent chaperone nature of  $\sigma_1$ Rs and their ability to regulate the NMDARs (34,35). Another plausible explanation might be off-target binding of FTC-146, as the  $\sigma_1$ R bears a particular binding site that is structurally similar to the ifenprodil-binding site of the GluN1/2B receptor, and thus  $\sigma_1$ R ligands are known for their off-target binding at the GluN1/2B. For example, we have reported potential off-target binding by the  $\sigma_1$ R ligand fluspidine (19). Nonetheless, further studies are warranted to clarify the nature of potential off-target binding by these novel benzazepine-based radioligands.

## CONCLUSION

We successfully synthesized and evaluated (*rac*)-, (S)-, and (R)- $^{18}\text{F}$ -OF-NB1 in rhesus monkeys. The high GluN1/2B-specific binding of (S)- $^{18}\text{F}$ -OF-NB1 (gray matter  $BP_{\text{ND}}$  values in the range of 1.6–3.4) and its attractive pharmacokinetic profile render it a promising candidate for clinical translation. Clinical PET imaging of GluN1/2B could expedite the development of GluN1/2B therapeutics through target engagement and occupancy studies. Furthermore, PET imaging of diseases in which the GluN2B subunit-containing NMDARs are implicated could potentially improve the diagnosis and treatment monitoring of these diseases.

## DISCLOSURE

This study was funded by the National Institute of Health (grant U01MH107803) and also was partly supported by the Swiss National Science Foundation (grants 310030E-160403/1 and 310030E-182872/1). Hazem Ahmed, Simon Ametamey, and Ahmed Haider hold shares in Nemosia A.G. No other potential conflict of interest relevant to this article was reported.

## ACKNOWLEDGMENTS

We thank the staff at the Yale PET Center for their expert technical support.

## KEY POINTS

**QUESTION:** Can we selectively image GluN2B subunit-containing NMDARs in nonhuman primates and identify a suitable radiofluorinated PET probe for clinical translation?

**PERTINENT FINDINGS:** (S)-<sup>18</sup>F-OF-NB1 emerged as an attractive candidate for clinical translation, as it displayed high specific binding to GluN1/2B receptors and a favorable pharmacokinetic profile.

**IMPLICATIONS FOR PATIENT CARE:** A GluN1/2B PET tracer suitable for use in humans will facilitate the investigation and diagnosis of neuropsychiatric diseases, as well as the development of therapeutics targeting GluN2B-containing NMDARs.

## REFERENCES

- Hansen KB, Yi F, Perszyk RE, et al. Structure, function, and allosteric modulation of NMDA receptors. *J Gen Physiol*. 2018;150:1081–1105.
- Hardingham GE, Bading H. Synaptic versus extrasynaptic NMDA receptor signalling: implications for neurodegenerative disorders. *Nat Rev Neurosci*. 2010;11:682–696.
- Wang R, Reddy PH. Role of glutamate and NMDA receptors in Alzheimer's disease. *J Alzheimers Dis*. 2017;57:1041–1048.
- Paoletti P, Bellone C, Zhou Q. NMDA receptor subunit diversity: impact on receptor properties, synaptic plasticity and disease. *Nat Rev Neurosci*. 2013;14:383–400.
- Adell A. Brain NMDA receptors in schizophrenia and depression. *Biomolecules*. 2020;10:947.
- Ahmed H, Haider A, Ametamey SM. N-methyl-D-aspartate (NMDA) receptor modulators: a patent review (2015-present). *Expert Opin Ther Pat*. 2020;30:743–767.
- Liu W, Jiang X, Zu Y, et al. A comprehensive description of GluN2B-selective N-methyl-D-aspartate (NMDA) receptor antagonists. *Eur J Med Chem*. 2020;200:112447.
- Kemp JA, McKernan RM. NMDA receptor pathways as drug targets. *Nat Neurosci*. 2002;5(suppl):1039–1042.
- Myers SJ, Ruppia KP, Wilson LJ, et al. A glutamate N-methyl-D-aspartate (NMDA) receptor subunit 2B-selective inhibitor of NMDA receptor function with enhanced potency at acidic pH and oral bioavailability for clinical use. *J Pharmacol Exp Ther*. 2021;379:41–52.
- Arakawa R, Takano A, Halldin C. PET technology for drug development in psychiatry. *Neuropsychopharmacol Rep*. 2020;40:114–121.
- Hargreaves RJ, Rabiner EA. Translational PET imaging research. *Neurobiol Dis*. 2014;61:32–38.
- Fuchigami T, Nakayama M, Yoshida S. Development of PET and SPECT probes for glutamate receptors. *ScientificWorldJournal*. 2015;2015:716514.
- Cai L, Liow JS, Morse CL, et al. Evaluation of <sup>11</sup>C-NR2B-SMe and its enantiomers as PET radioligands for imaging the NR2B subunit within the NMDA receptor complex in rats. *J Nucl Med*. 2020;61:1212–1220.
- Krämer SD, Betzel T, Mu L, et al. Evaluation of <sup>11</sup>C-Me-NB1 as a potential PET radioligand for measuring GluN2B-containing NMDA receptors, drug occupancy, and receptor cross talk. *J Nucl Med*. 2018;59:698–703.
- Mu L, Krämer SD, Ahmed H, et al. Neuroimaging with radiopharmaceuticals targeting the glutamatergic system. *Chimia (Aarau)*. 2020;74:960–967.
- Haider A, Herde AM, Krämer SD, et al. Preclinical evaluation of benzazepine-based PET radioligands (R)- and (S)-<sup>11</sup>C-Me-NB1 reveals distinct enantiomeric binding patterns and a tightrope walk between GluN2B- and  $\sigma_1$ -receptor-targeted PET imaging. *J Nucl Med*. 2019;60:1167–1173.
- Rischka L, Vrakas C, Pichler V, et al. First-in-humans brain PET imaging of the GluN2B-containing N-methyl-D-aspartate receptor with (R)-<sup>11</sup>C-Me-NB1. *J Nucl Med*. 2022;63:936–941.
- Haider A, Iten I, Ahmed H, et al. Identification and preclinical evaluation of a radiofluorinated benzazepine derivative for imaging the GluN2B subunit of the ionotropic NMDA receptor. *J Nucl Med*. 2018;60:259–266.
- Ahmed H, Wallimann R, Haider A, et al. Preclinical development of <sup>18</sup>F-OF-NB1 for imaging GluN2B-containing N-methyl-D-aspartate receptors and its utility as a biomarker for amyotrophic lateral sclerosis. *J Nucl Med*. 2021;62:259–265.
- Zheng M, Ahmed H, Smart K, et al. Characterization in nonhuman primates of (R)-[<sup>18</sup>F]OF-Me-NB1 and (S)-[<sup>18</sup>F]OF-Me-NB1 for imaging the GluN2B subunits of the NMDA receptor. *Eur J Nucl Med Mol Imaging*. 2022;49:2153–2162.
- Wilson AA, Jin L, Garcia A, DaSilva JN, Houle S. An admonition when measuring the lipophilicity of radiotracers using counting techniques. *Appl Radiat Isot*. 2001;54:203–208.
- Cai Z, Li S, Zhang W, et al. Synthesis and preclinical evaluation of an <sup>18</sup>F-labeled synaptic vesicle glycoprotein 2A PET imaging probe: [<sup>18</sup>F]SynVesT-2. *ACS Chem Neurosci*. 2020;11:592–603.
- Barta-Szalai G, Borza I, Bozó E, et al. Oxamides as novel NR2B selective NMDA receptor antagonists. *Bioorg Med Chem Lett*. 2004;14:3953–3956.
- James ML, Shen B, Zavaleta CL, et al. New positron emission tomography (PET) radioligand for imaging  $\sigma$ -1 receptors in living subjects. *J Med Chem*. 2012;55:8272–8282.
- Li S, Zheng MQ, Naganawa M, et al. Development and *in vivo* evaluation of a  $\kappa$ -opioid receptor agonist as a PET radiotracer with superior imaging characteristics. *J Nucl Med*. 2019;60:1023–1030.
- Zheng MQ, Nabulsi N, Kim SJ, et al. Synthesis and evaluation of <sup>11</sup>C-LY2795050 as a  $\kappa$ -opioid receptor antagonist radiotracer for PET imaging. *J Nucl Med*. 2013;54:455–463.
- Hilton J, Yokoi F, Dannals RF, Ravert HT, Szabo Z, Wong DF. Column-switching HPLC for the analysis of plasma in PET imaging studies. *Nucl Med Biol*. 2000;27:627–630.
- Ichise M, Toyama H, Innis RB, Carson RE. Strategies to improve neuroreceptor parameter estimation by linear regression analysis. *J Cereb Blood Flow Metab*. 2002;22:1271–1281.
- Cunningham VJ, Rabiner EA, Slifstein M, Laruelle M, Gunn RN. Measuring drug occupancy in the absence of a reference region: the Lassen plot re-visited. *J Cereb Blood Flow Metab*. 2010;30:46–50.
- Pike VW. PET radiotracers: crossing the blood-brain barrier and surviving metabolism. *Trends Pharmacol Sci*. 2009;30:431–440.
- Shen Z, Lv C, Zeng S. Significance and challenges of stereoselectivity assessing methods in drug metabolism. *J Pharm Anal*. 2016;6:1–10.
- Smart K, Zheng MQ, Ahmed H, et al. Comparison of three novel radiotracers for GluN2B-containing NMDA receptors in non-human primates: (R)-[<sup>11</sup>C]NR2B-Me, (R)-[<sup>18</sup>F]of-Me-NB1, and (S)-[<sup>18</sup>F]of-Me-NB1. *J Cereb Blood Flow Metab*. 2022;42:1398–1409.
- Guo Q, Owen DR, Rabiner EA, Turkheimer FE, Gunn RN. A graphical method to compare the *in vivo* binding potential of PET radioligands in the absence of a reference region: application to [<sup>11</sup>C]PBR28 and [<sup>18</sup>F]PBR111 for TSPO imaging. *J Cereb Blood Flow Metab*. 2014;34:1162–1168.
- Ryskamp DA, Korban S, Zhemkov V, Kraskovskaya N, Bezprozvanny I. Neuronal sigma-1 receptors: signaling functions and protective roles in neurodegenerative diseases. *Front Neurosci*. 2019;13:862.
- Pabba M, Wong AY, Ahlskog N, et al. NMDA receptors are upregulated and trafficked to the plasma membrane after sigma-1 receptor activation in the rat hippocampus. *J Neurosci*. 2014;34:11325–11338.

---

---

# First-in-Human Evaluation of $^{18}\text{F}$ -PF-06445974, a PET Radioligand That Preferentially Labels Phosphodiesterase-4B

Yuichi Wakabayashi<sup>1</sup>, Per Stenkrona<sup>2</sup>, Ryosuke Arakawa<sup>2</sup>, Xuefeng Yan<sup>1</sup>, Maia G. Van Buskirk<sup>1</sup>, Madeline D. Jenkins<sup>1</sup>, Jose A. Montero Santamaria<sup>1</sup>, Kevin P. Maresca<sup>3</sup>, Akihiro Takano<sup>2</sup>, Jeh-San Liow<sup>1</sup>, Thomas A. Chappie<sup>3</sup>, Andrea Varrone<sup>2</sup>, Sangram Nag<sup>2</sup>, Lei Zhang<sup>3</sup>, Zoë A. Hughes<sup>3</sup>, Christopher J. Schmidt<sup>3</sup>, Shawn D. Doran<sup>3</sup>, Andrew Mannes<sup>4</sup>, Paolo Zanotti-Fregonara<sup>1</sup>, Maarten Ooms<sup>1</sup>, Cheryl L. Morse<sup>1</sup>, Sami S. Zoghbi<sup>1</sup>, Christer Halldin<sup>2</sup>, Victor W. Pike<sup>1</sup>, and Robert B. Innis<sup>1</sup>

<sup>1</sup>Molecular Imaging Branch, NIMH-NIH, Bethesda, Maryland; <sup>2</sup>Department of Clinical Neuroscience Psychiatry Section, Karolinska Institutet, Stockholm, Sweden; <sup>3</sup>Worldwide Research, Development, and Medicine, Pfizer Inc., New York, New York; and <sup>4</sup>Anesthesia Department, NIH Clinical Center, Bethesda, Maryland

---

Phosphodiesterase-4 (PDE4), which metabolizes the second messenger cyclic adenosine monophosphate (cAMP), has 4 isozymes: PDE4A, PDE4B, PDE4C, and PDE4D. PDE4B and PDE4D have the highest expression in the brain and may play a role in the pathophysiology and treatment of depression and dementia. This study evaluated the properties of the newly developed PDE4B-selective radioligand  $^{18}\text{F}$ -PF-06445974 in the brains of rodents, monkeys, and humans. **Methods:** Three monkeys and 5 healthy human volunteers underwent PET scans after intravenous injection of  $^{18}\text{F}$ -PF-06445974. Brain uptake was quantified as total distribution volume ( $V_T$ ) using the standard 2-tissue-compartment model and serial concentrations of parent radioligand in arterial plasma. **Results:**  $^{18}\text{F}$ -PF-06445974 readily distributed throughout monkey and human brain and had the highest binding in the thalamus. The value of  $V_T$  was well identified by a 2-tissue-compartment model but increased by 10% during the terminal portions (40 and 60 min) of the monkey and human scans, respectively, consistent with radiometabolite accumulation in the brain. The average human  $V_T$  values for the whole brain were  $9.5 \pm 2.4 \text{ mL} \cdot \text{cm}^{-3}$ . Radiochromatographic analyses in knockout mice showed that 2 efflux transporters—permeability glycoprotein (P-gp) and breast cancer resistance protein (BCRP)—completely cleared the problematic radiometabolite but also partially cleared the parent radioligand from the brain. In vitro studies with the human transporters suggest that the parent radioligand was a partial substrate for BCRP and, to a lesser extent, for P-gp. **Conclusion:**  $^{18}\text{F}$ -PF-06445974 quantified PDE4B in the human brain with reasonable, but not complete, success. The gold standard compartmental method of analyzing brain and plasma data successfully identified the regional densities of PDE4B, which were widespread and highest in the thalamus, as expected. Because the radiometabolite-induced error was only about 10%, the radioligand is, in the opinion of the authors, suitable to extend to clinical studies.

**Key Words:** phosphodiesterase-4B (PDE4B); PET;  $^{18}\text{F}$ -PF-06445974

**J Nucl Med 2022; 63:1919–1924**

DOI: 10.2967/jnumed.122.263838

**P**hosphodiesterase type 4 (PDE4) metabolizes and thereby inactivates the ubiquitous second messenger 3',5'-cyclic adenosine monophosphate (cAMP). PDE4 inhibitors are approved to treat 2 peripheral inflammatory disorders (chronic obstructive pulmonary disease and psoriasis) and are being explored as treatments for several neuropsychiatric disorders (1). PDE4 has 4 isozymes: PDE4A, PDE4B, PDE4C, and PDE4D; of these, the PDE4B and PDE4D isozymes are highly expressed in the brain and may play important roles in pathophysiology and treatment. Interestingly, inhibition of the PDE4D isozyme was found to improve cognition in animals and humans (2), whereas inhibition of the PDE4B isozyme had antidepressantlike effects in animal models (3). Subtype-selective inhibitors not only may be useful in treating distinct disorders but also may avoid the nausea and vomiting associated with nonselective inhibitors. For example, antidepressant trials of the nonselective PDE4 inhibitor rolipram were discontinued because of severe nausea and vomiting.

The search for subtype-selective PDE4 inhibitors has progressed in parallel with the development of comparable PET radioligands that can measure subtype density and evaluate whether the therapeutic candidate crosses the blood–brain barrier and engages the target—that is, receptor occupancy. Subtype-selective PET radioligands have been developed for PDE4B (the subject of this article) and PDE4D. However, the most promising PDE4D radioligand,  $^{11}\text{C}$ -T1650, generated such a significant accumulation of radiometabolites in animal and human brains that it was not recommended for further study (4). Such radiometabolites are problematic because quantitation of the target density is based on the assumption that all radioactivity in the brain is parent radioligand. If radiometabolites are included in brain signal, the density of the target will be overestimated.

$^{18}\text{F}$ -PF-06445974, a new PET radioligand (Supplemental Fig. 1; supplemental materials are available at <http://jnm.snmjournals.org>), was developed to bind preferentially to PDE4B (5). This ligand was selected as a candidate on the basis of its in vitro properties and in vivo performance. In vitro,  $^{18}\text{F}$ -PF-06445974 has high affinity (<1 nM) for PDE4B and moderate-to-high selectivity relative to the other 3 PDE4 subtypes (4.7 nM for PDE4A, 17 nM for PDE4C, and 36 nM for PDE4D). In vivo, PET imaging of  $^{18}\text{F}$ -PF-06445974 in cynomolgus monkeys showed good brain uptake, a high percentage of specific (i.e., blockable) binding, and robust quantitation of enzyme density using arterial input function of

---

Received Jan. 10, 2022; revision accepted Mar. 31, 2022.  
For correspondence or reprints, contact Robert Innis (robert.innis@nih.gov).  
Published online Jun. 30, 2022.  
COPYRIGHT © 2022 by the Society of Nuclear Medicine and Molecular Imaging.

parent radioligand separated from radiometabolite (5). Because of successful imaging in monkeys, the ligand was selected for first-in-human evaluation.

## MATERIALS AND METHODS

This study sought to determine whether  $^{18}\text{F}$ -PF-06445974 could accurately quantify PDE4B in living human brain. Toward this end, PET imaging was performed in healthy human volunteers using the gold standard method of compartmental modeling and serial concentrations of arterial plasma of parent radioligand separated from radiometabolite. Five volunteers were studied: 3 at the National Institutes of Health (NIH) and 2 at the Karolinska Institutet (KI). All participants gave written informed consent, and the study was approved by the institutional review boards of the respective institutions. To address the issue of potential radiometabolite accumulation in the brain, *in vivo* studies in monkeys and *in vivo* and *ex vivo* studies in rodents were also performed after  $^{18}\text{F}$ -PF-06445974 injection and blockade by nonradioactive PF-06445974. A detailed description of the methods and the relevant references (6–11) can be found in the supplemental materials.

## RESULTS

### Brain Imaging

Uptake in the human brain was widespread (peak whole brain SUV, ~2–3) and highest in the thalamus (Figs. 1 and 2), consistent with the distribution of PDE4B (12). Plasma parent concentrations peaked immediately after injection and rapidly decreased along a curve that was well-fitted by a triexponential function (Fig. 2A). Brain activity achieved relatively stable peak values at 15–20 min and washed out slowly thereafter—that is, only 17% washout from 20 to 120 min.

To quantify the density of the target enzyme in brain regions, pharmacokinetic modeling was performed using the serial concentrations of the parent radioligand in arterial plasma as the input to the brain—that is, it was assumed that the brain contains only parent

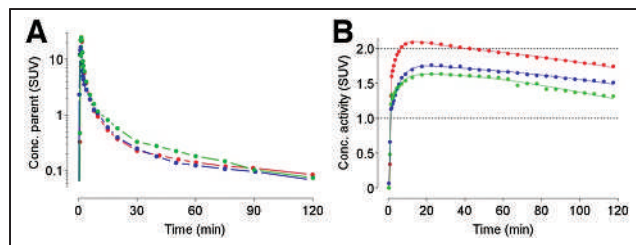


**FIGURE 2.** Concentration of plasma parent radioligand  $^{18}\text{F}$ -PF-0644974 separated from radiometabolite (A) and total radioactivity (B) in whole brain of 3 healthy human participants. The plasma time–activity curve after peak was fit to a triexponential curve. The brain time–activity curve was fit to a 2-tissue-compartment model. Concentrations in plasma and brain are expressed as SUV. Plasma parent is plotted on a log scale, and brain activity is plotted on a linear scale. Conc. = concentration.

radioligand and no radiometabolite. The standard 2-tissue-compartment model provided curves that visually fit the measured PET values in a moderately good to excellent manner (Fig. 2B). Total distribution volume ( $V_T$ ) ( $\text{mL} \cdot \text{cm}^{-3}$ ) ranged from 6.4 in the corpus callosum to 13.3 in the thalamus (Table 1). The variability (SD) of the  $V_T$  measurements was quite large and due in part to differences between the 2 institutions. For example, for the  $V_T$  ( $\text{mL} \cdot \text{cm}^{-3}$ ) of whole brain in the 5 participants reported in Table 1, the NIH values were generally slightly lower (9.9, 9.9, 5.6) than those of the KI (10.2, 12.0). We do not know the cause(s) of these institutional differences but, in such a small population of participants, they could be due to chance. The  $V_T$  in the human brain did not become stable during the 120-min scan. Instead,  $V_T$  values increased by approximately 10% during the last 40 min of the scan (80–120 min; Fig. 3A). This increase was similar in regions with high and low binding (Supplemental Fig. 2).

Brain imaging in 3 monkeys (1 rhesus monkey at the NIH and 2 cynomolgus monkeys at the KI) mirrored that in humans, including the indirect measure of radiometabolite accumulation. That is,

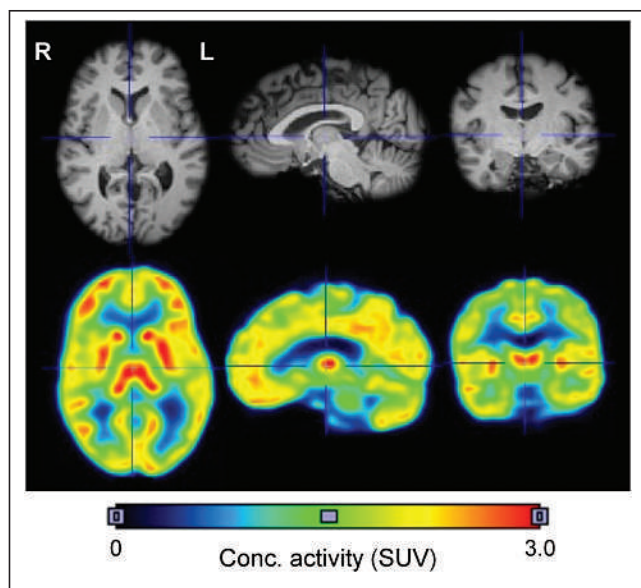


**FIGURE 1.** Distribution of radioactivity in the brain of a healthy volunteer after injection of  $^{18}\text{F}$ -PF-06445974 and the participant’s coregistered MRI scan (top). The PET image displays the mean concentration (conc.) of radioactivity from 0 to 120 min and is expressed as SUV (bottom). The highest uptake was in the thalamus, which is marked with cross hairs.

**TABLE 1**

Total Distribution Volume ( $V_T$ ) in Brain Regions for 5 Human Participants

Region	$V_T$ ( $\text{mL} \cdot \text{cm}^{-3}$ )	
	Mean	SD
Whole brain	9.5	2.4
Frontal cortex	9.5	2.6
Cingulate	9.8	3.2
Hippocampus	9.0	2.0
Amygdala	11.2	2.5
Temporal cortex	9.8	2.0
Parietal cortex	9.3	2.7
Occipital cortex	8.9	2.2
Striatum	12.1	2.7
Thalamus	13.3	3.4
Globus pallidus	12.2	5.6
Corpus callosum	6.4	3.8
Insula	10.8	2.7
Cerebellum	10.6	2.2

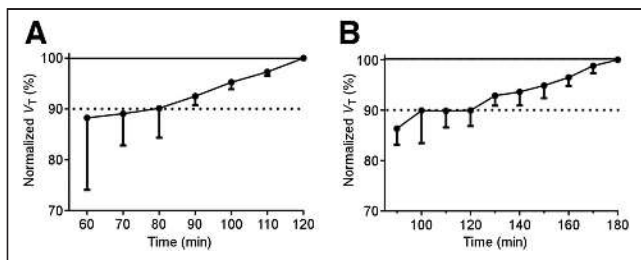


**FIGURE 3.** The apparent value of total distribution volume ( $V_T$ ) from 5 human participants (A) and 3 monkeys (B).  $V_T$  values never achieved stability during the scans.  $V_T$  values increased linearly by 10% during the last 40 min in humans and also by 10% during the last 60 min in monkeys.

$V_T$  increased by about 10% during the last 60 min of the scan (120–180 min; Fig. 3B).

### Assessing Radiometabolite Entry into Brain

The number of radiometabolite peaks in plasma varied among rats, monkeys, and humans, but all radiometabolites were less lipophilic than the parent radioligand, as shown by eluting earlier in the reversed-phase high-performance liquid chromatography (Supplemental Fig. 3). Although less lipophilic, the major radiometabolite peak (marked with an asterisk in Supplemental Fig. 3) eluted close enough to the parent radioligand that it would have been expected to enter the brain.

To directly determine whether this radiometabolite entered the brain, 3 rats were euthanized 180 min after radioligand injection, and radioactivity was extracted from the brain and plasma. Virtually all ( $98\% \pm 2\%$ ) radioactivity in brain coeluted with the parent radioligand, whereas only 32% in plasma was parent radioligand (Fig. 4). Thus, essentially none of the radiometabolite in rat plasma at 180 min was present in the brain.

To explain why rat brain had virtually no radiometabolite, brain uptake was measured in mice with a knockout of both permeability glycoprotein (P-gp) and breast cancer resistance protein (BCRP), the 2 most prevalent efflux transporters at the blood–brain barrier (13). Both the parent radioligand and the chromatographically adjacent radiometabolite were substrates for one or both efflux transporters in mice (Supplemental Fig. 4). At 120 min after  $^{18}\text{F}$ -PF-06445974 injection, the ratio of parent radioligand in brain to that in plasma was 93 in wild-type mice and 188 in knockout mice (Fig. 5); because the concentrations in brain and plasma were in the same unit (SUV), the

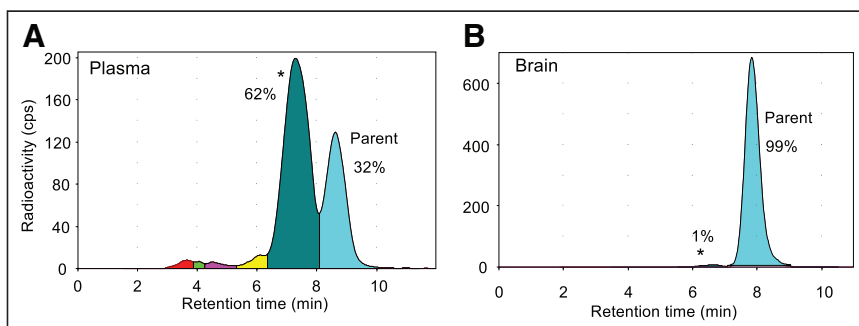


**FIGURE 4.** Radiochromatograms showing the composition of radioactivity extracted at 180 min from plasma (A) and brain (B) of a rat injected with  $^{18}\text{F}$ -PF-06445974. In plasma (A), parent radioligand (blue peak) comprised 32% of total radioactivity, and the adjacent radiometabolite (peak marked with an asterisk) was 62%. At the same time, in the brain (B), parent radioligand comprised 99% of total radioactivity, and the adjacent radiometabolite was only 1%.

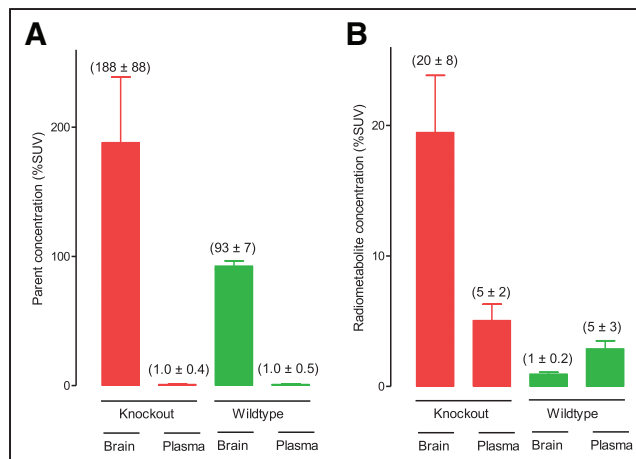


**FIGURE 5.** Concentrations of parent radioligand in brain and plasma of wild-type and efflux transporter knockout mice at 120 min after  $^{18}\text{F}$ -PF-06445974 injection. (A) For the parent radioligand, the ratio of brain-to-plasma concentration was 93 in wild-type and 188 in mice with a knockout of both BCRP and P-gp. Thus, the brain-to-plasma ratio of parent radioligand was 2 times higher in knockout mice than in wild-type mice. (B) For the radiometabolite, the ratio of brain-to-plasma concentration was 0.2 in wild-type and 4.0 in BCRP and P-gp knockout mice. Thus, the brain-to-plasma ratio of parent radioligand was 20 times higher in knockout mice than in wild-type mice. Concentrations are expressed as percent SUV (%SUV).

ratio is unitless. Thus, the brain-to-plasma ratio of parent radioligand was 2 times higher in knockout mice than in wild-type mice. Because these ratios of parent radioligand to brain to plasma were so high, this experiment was repeated in an additional set of 3 animals; similar results were obtained.

In these same mice at 180 min, the ratio of radiometabolite in brain to that in plasma was 0.2 in wild-type and 4.0 in knockout mice (i.e., a 20-fold difference), indicating that knockout of these 2 transporters had about a 10-fold greater effect (20 vs. 2) on the radiometabolite than on the parent radioligand. This differential effect on the radiometabolite versus the parent radioligand was also seen in the percentage composition of radioactivity in the brain at 120 min. Specifically, the percentage of radiometabolite in the brain was about 5-fold higher in knockout (8.8%) than in wild-type (1.8%) mice (Supplemental Table 1).

Because substrate specificity varies between species, avidity was measured *in vitro* using cloned human transporters and compared with known substrates: digoxin for P-gp and prazosin for BCRP.

For BCRP, prazosin had an efflux ratio of 9.2 whereas PF-06445974 had a ratio of 5.9 (Supplemental Table 2), suggesting that PF-06445974 was a mild/moderate substrate for BCRP. In contrast, PF-06445974 was a far less avid substrate for P-gp; specifically, digoxin had an efflux ratio of 38.1, and PF-06445974 had a ratio of only 2.5—that is, less than 1/15th that for digoxin.

Like all metabolites, radiometabolites are often pharmacologically inactive by virtue of low affinity for the target protein. Thus, any displaceable binding typically reflects parent radioligand rather than radiometabolite. Non-radioactive PF-06445974 (0.1 mg/kg intravenously injected 10 min before the radioligand) blocked almost all radioactivity in rat and

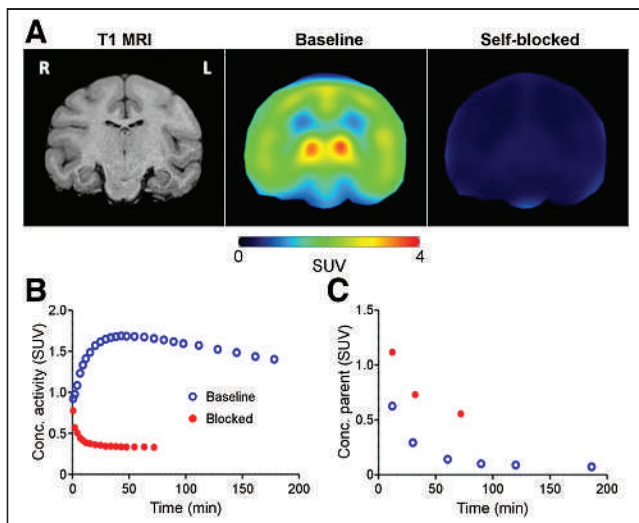


**FIGURE 6.** (A) PET and coregistered MRI of brain in a rhesus monkey. The animal was scanned at baseline and after blockade by PF-06445974 (0.1 mg/kg intravenously injected 10 min before radioligand). Because of prolonged tachycardia (heart rate up to 190 bpm), the blocked scan was terminated after 75 min. The PET images show mean concentration of radioactivity SUV from 0 to 70 min. (B) Radioactivity in whole brain after injection of  $^{18}\text{F}$ -PF-06445974. (C) Concentration in arterial plasma of plasma parent radioligand  $^{18}\text{F}$ -PF-06445974 separated from radiometabolite. Because there were so few plasma samples, compartmental modeling could not generate a reliable measure of enzyme density (total distribution volume,  $V_T$ ). Measured as average concentration of radioactivity from 10 to 60 min (SUV<sub>10-60</sub>), nonradioactive PF-06445974 blocked 92% of radioligand uptake into brain. Conc. = concentration.

monkey brain for the entire duration of the scan (Fig. 6; Supplemental Fig. 5). For the rhesus monkey, nonradioactive PF-06445974 decreased SUV<sub>10-60</sub> by 92% in the whole brain (Fig. 6). In rats, nonradioactive PF-06445974 decreased SUV<sub>10-180</sub> by 94% in the whole brain (Supplemental Fig. 5).

In summary, plasma from rats, monkeys, and humans showed a range of radiometabolites, all with lower—though sometimes only slightly lower—lipophilicities than that of  $^{18}\text{F}$ -PF-06445974. None of these radiometabolites was present in rat brain 180 min after injection. Studies in knockout mice showed that the radiometabolite (the peaks marked with an asterisk in Fig. 4 and Supplemental Fig. 3) adjacent to the radioligand was avidly cleared from the brain by P-gp or BCRP (Supplemental Fig. 4). The monkey studies showed that 92% of brain radioactivity was blocked by nonradioactive ligand, suggesting that most of the radioactivity in monkey brain, like that in rats and mice, represented parent radioligand. Thus, by analogy to rats and monkeys, it is likely that no more than a small amount of radiometabolite ( $\leq 10\%$  of total radioactivity) accumulates in the human brain. However, of particular importance to the quantitation of enzyme density, the *in vitro* studies showed that the parent radioligand is a moderate substrate for human BCRP.

#### Dosimetry Calculations in Human and Nonhuman Primates

Whole-body imaging in 2 humans and 1 monkey was notable for early distribution in the blood pool, accumulation in the target organs (i.e., brain and lung), and excretion via the urinary tract (Supplemental Fig. 6). For the human volunteers, the 4 organs with the highest exposure ( $\mu\text{Sv}/\text{MBq}$ ) were gallbladder ( $110 \pm 75$ ), upper large intestine ( $75 \pm 66$ ), urinary bladder ( $55 \pm 5.9$ ), and liver ( $44 \pm 8.1$ ). The doses in the 2 humans were 19.6 and 19.3  $\mu\text{Sv}/\text{MBq}$ ,

respectively, which were similar to those extrapolated from monkeys (16.5  $\mu\text{Sv}/\text{MBq}$ ) (Supplemental Table 3).

#### DISCUSSION

This study sought to determine whether  $^{18}\text{F}$ -PF-06445974 could accurately quantify PDE4B in human brain. Our results suggest that this radioligand quantified PDE4B reasonably well, with the exception that radiometabolite likely accumulated in the brain and that the radioligand itself may be a substrate for efflux transport from the brain. Brain uptake was moderately high (peak whole-brain SUV was 1.5), and its distribution was appropriate for the target. The PET measurements of enzyme binding ( $V_T$ ) from the human brain were reasonably well fit to a 2-tissue-compartment model that assumed input of only the parent radioligand from arterial plasma. The  $V_T$  value increased by approximately 10% over the last 60 min of the 120-min scan (Fig. 3), which may have been caused by radiometabolite accumulation in the brain.

To directly measure radiometabolite, all radioactivity was extracted from the plasma and brain of rats at 180 min and the components were separated using radio-high-performance liquid chromatography. Surprisingly, rat brain contained essentially no radiometabolite, although the plasma had several radiometabolites, one of which eluted only slightly before the parent radioligand. Knockout of 2 efflux transporters (P-gp and BCRP) in mice showed that the radiometabolite was avidly cleared from the brain and that the parent radioligand was also a substrate, but of lower avidity. Thus, either or both efflux transporters had the positive effect of “cleaning up” the brain signal by removing radiometabolite, but also the negative effect of removing some of the parent radioligand. *In vitro* studies using cloned human efflux transporters showed that PF-06445974 was a moderate substrate for BCRP and, to a lesser extent, for P-gp. Although these efflux transporters completely cleared radiometabolite from rodent brain, they likely did so only partially in humans, leading to the accumulation of the adjacent radiometabolite in human brain, as shown by increasing values of enzyme density with increasing length of scanning.

Compartmental modeling seeks to measure the specific binding ( $V_S$ ) of the radioligand for the target and is proportional to receptor density ( $B_{\text{max}}$ ) times the radioligand’s affinity ( $1/K_D$ ). Because the measurements of PET radioactivity in brain and of parent radioligand in plasma have noise, a substantial number of such measurements are required to converge on a value of specific binding, often 15–60 min for many brain radioligands. If the density of the target and the affinity of the radioligand remain constant during the scan, the converged/well-identified  $V_S$  value should not change with increasing scan duration, which will be reflected by the brain and plasma time-activity curves decreasing at the same rate. In contrast, in this study, values of total uptake ( $V_T = V_S + V_{\text{ND}}$ ) appeared to increase with increasing scan duration.

The 2 most common causes of unstable  $V_T$  values are slow kinetics of radioligand binding or the accumulation of radiometabolites in the brain. The first possible cause, slow kinetics, refers to how long the radioligand requires to reach equilibrium, which in this case usually refers to the time of peak radioactivity in brain; note that the term “peak equilibrium” refers to tissue-to-plasma ratio at the exact time of peak uptake in the brain, which varies among regions. This peak equilibrium is distinct from “transient equilibrium” (14), which refers to the tissue-to-plasma ratio after the time of peak uptake and which is typically greater than the true  $V_T$ . As a rule, the brain must be imaged before, at, and for some time after peak uptake to quantify the rates of binding and unbinding to the receptor, which themselves

are components of  $V_T$ . Here, the time to peak was about 30 min in monkeys and 20 min in humans, and our scans extended well beyond the peak (for a total of 180 min in monkeys and 120 min in humans), suggesting that slow kinetics of radioligand binding are unlikely to have caused the  $V_T$  values that increased with scan duration. Instead, radiometabolite probably accumulated in the human brain. The likely candidate is the peak marked with an asterisk in Supplemental Figure 3, which has a lipophilicity only slightly lower than that of the parent radioligand.

It should be noted that being a substrate for efflux transport is unlikely to increase  $V_T$  values over time, as it is predicted to have the opposite result. That is, the effect of efflux transport is to decrease radioactivity in the brain and, therefore, to decrease the apparent  $V_T$ . Nevertheless, the time course of efflux transport of parent ligand and radiometabolite might change in some unexpected way to contribute to increasing apparent values of  $V_T$ .

Taken together, the results suggests that the 2 pharmacologic limitations of  $^{18}\text{F}$ -PF-06445974 for quantifying PDE4B in human brain are the accumulation of a radiometabolite in the brain and partial removal of the parent radioligand by the efflux transporter BCRP. Both pharmacologic limitations will increase the variability of the measurements between individuals to the extent that individuals differ in metabolism and BCRP function. The severity of these combined limitations in humans is unknown but, in the opinion of the authors, would not preclude using this radioligand in clinical studies. An increase in  $V_T$  of  $< 5\%$  during the last hour is considered excellent, and our rate of 10% in the last 60 min (Fig. 3) is generally considered acceptable. Notably, this 10% variability mirrors what might maximally occur based on blockade studies in monkeys (Fig. 6). That is, nonradioactive PF-06445974 blocked 92% of total uptake in monkey brain, suggesting that 92% of radioactivity in brain was parent radioligand; metabolites usually, but not always, have lower affinity for the target than the parent drug.

Although these 2 limitations will increase the necessary sample size for a clinical study, we will proceed with use of this radioligand to study clinical disorders such as major depressive disorder (MDD) for 2 reasons. First, as described earlier, the error/variability of these limitations may be only about 10%. Second, PET imaging of PDE4 provides the unique ability to measure the activated (i.e., phosphorylated) form of PDE4, which is not possible in post-mortem samples (Fig. 7). Prior studies in this laboratory with  $^{11}\text{C}$ -(*R*)-rolipram, which binds to all 4 PDE4 subtypes, provide in vivo support for the notion that cAMP increases radioligand binding via phosphorylation of PDE4 by protein kinase A (15). This phosphorylation increases enzyme activity as well as the affinity of radioligand binding by about 10-fold (16). Because PDE4 is rapidly dephosphorylated after death (17), PET is uniquely capable of measuring the active form of PDE4 in living participants.

Evidence from the 1980s and 1990s suggested that rolipram might be used to treat MDD, and animal models of depression suggested that PDE4B inhibitors might have antidepressant efficacy in humans (3). In this context, a PET radioligand for PDE4B could facilitate therapeutic drug development. For instance, we predict that the current study using a PDE4B-selective radioligand will replicate results previously obtained with the nonselective radioligand  $^{11}\text{C}$ -(*R*)-rolipram (18)—namely, that PDE4B binding will be decreased in unmedicated individuals experiencing a major depressive episode but still have significant overlap with that in healthy volunteers. If so, this PDE4B radioligand could be used to identify a subgroup of MDD patients who would most benefit from PDE4B inhibition, given that low PDE4 binding implies low cAMP signaling because

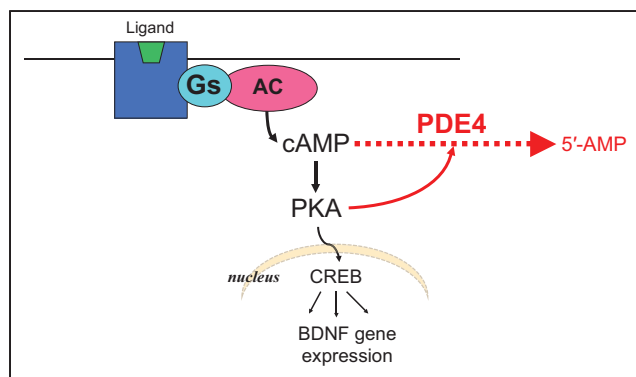


**FIGURE 7.** Schema of the cAMP cascade (black arrows) and negative feedback via protein kinase A (PKA) (red arrows). Several neurotransmitters act via receptors coupled to G proteins (Gs) to stimulate adenylyl cyclase (AC), which produces cAMP, activates PKA, and then phosphorylates cAMP response element-binding protein (CREB), which moves to the nucleus and increases expression of brain-derived neurotrophic factor (BDNF) and other genes. Negative feedback is provided by PKA, which phosphorylates and activates PDE4, which metabolizes cAMP, thereby terminating the cAMP signal.

of the negative feedback mechanism mediated by protein kinase A. The cAMP theory of the mechanism of antidepressant treatments would further suggest that increasing cAMP signaling produces antidepressant effects. Thus, those patients with low PDE4B binding might be most likely to benefit from treatment with a PDE4B inhibitor. Furthermore, numerous animal studies have shown that antidepressants of all chemical classes must be administered for several weeks in order to upregulate the cAMP cascade (19), which mirrors the therapeutic time course in humans. Because inhibiting PDE4B would immediately increase cAMP signaling, these antidepressant effects, if they exist, would occur quickly, meaning that PDE4B inhibitors may represent a new class of rapid-acting antidepressants.

In short, a PET radioligand for PDE4B may be useful in 2 ways. First, if a PDE4B inhibitor is developed as an antidepressant medication, the PET radioligand can be used to identify the appropriate dose and dosing interval of the therapeutic candidate. Indeed, PET radioligands have often been used to measure receptor occupancy and guide initial doses in therapeutic trials. Second, a PDE4B radioligand might identify a subgroup of patients most likely to respond to a PDE4B inhibitor. This selection of patients likely to respond has been referred to as patient stratification, patient enrichment, personalized medicine, and, most recently, precision medicine. Expressed in other terms, low PDE4B binding may be a biomarker to predict response to a PDE4B inhibitor.

## CONCLUSION

$^{18}\text{F}$ -PF-06445974 was able to quantify PDE4B in human brain with reasonable, but not complete, success. The gold standard compartmental method of analyzing brain and plasma data successfully identified the regional densities of PDE4B, which were widespread and highest in the thalamus, as expected. Although a radiometabolite may contaminate the signal in human brain, the amount is likely small enough ( $\sim 10\%$ ) that the authors plan to use this radioligand in clinical studies.

## DISCLOSURE

This study was funded by the Intramural Research Program of the National Institute of Mental Health (projects ZIAMH002852

and ZIAMH002793; animal protocol: MIB-02) and by a research contract from Pfizer to the Karolinska Institutet. Per Stenkrona, Ryosuke Arakawa, Akihiro Takano, Andrea Varrone, Sangram Nag, and Christer Halldin were supported by a contract with Pfizer. Kevin P. Maresca, Thomas A. Chappie, Lei Zhang, Zoë A. Hughes, Christopher J. Schmidt, and Shawn D. Doran are full-time employees of Pfizer. No other potential conflict of interest relevant to this article was reported.

## ACKNOWLEDGMENTS

We are grateful to the staff of Molecular Imaging Branch for participant recruitment; to the NIH's PET Department (Chief, Peter Herscovitch, MD) for performing the PET scans; to Ioline Henter for invaluable editorial assistance; and to Cerevel Therapeutics for obtaining the in vitro potencies of PF-06445974 at human P-gp and BCRP transporters.

## KEY POINTS

**QUESTION:** Can  $^{18}\text{F}$ -PF-06445974 accurately quantify PDE4B in living human brain?

**PERTINENT FINDINGS:**  $^{18}\text{F}$ -PF-06445974 can accurately quantify PDE4B, except for the likely presence of a small amount (probably ~10%) of radiometabolite in the brain and the removal of the radioligand from the brain via an efflux transporter.

**IMPLICATIONS FOR PATIENT CARE:** These findings have no direct implications for clinical care. However, a radioligand selective for PDE4B could measure this target in clinical disorders and facilitate the development of PDE4B-selective inhibitors as novel therapeutics.

## REFERENCES

- Menniti FS, Faraci WS, Schmidt CJ. Phosphodiesterases in the CNS: targets for drug development. *Nat Rev Drug Discov*. 2006;5:660–670.
- Berry-Kravis EM, Harnett MD, Reines SA, et al. Inhibition of phosphodiesterase-4D in adults with fragile X syndrome: a randomized, placebo-controlled, phase 2 clinical trial. *Nat Med*. 2021;27:862–870.
- Zhang C, Xu Y, Zhang H-T, Gurney ME, O'Donnell JM. Comparison of the pharmacological profiles of selective PDE4B and PDE4D inhibitors in the central nervous system. *Sci Rep*. 2017;7:40115.
- Wakabayashi Y, Telu S, Dick RM, et al. Discovery, radiolabeling, and evaluation of subtype-selective inhibitors for positron emission tomography imaging of brain phosphodiesterase-4D. *ACS Chem Neurosci*. 2020;11:1311–1323.
- Zhang L, Chen L, Beck EM, et al. The discovery of a novel phosphodiesterase (PDE) 4B-preferring radioligand for positron emission tomography (PET) imaging. *J Med Chem*. 2017;60:8538–8551.
- Hammers A, Allom R, Koeppe MJ, et al. Three-dimensional maximum probability atlas of the human brain, with particular reference to the temporal lobe. *Hum Brain Mapp*. 2003;19:224–247.
- Innis RB, Cunningham VJ, Delforge J, et al. Consensus nomenclature for in vivo imaging of reversibly binding radioligands. *J Cereb Blood Flow Metab*. 2007;27:1533–1539.
- National Research Council. *Guide for the Care and Use of Laboratory Animals*. 8th ed. Washington, DC: National Academies Press; 2011.
- Sprague DR, Fujita M, Ryu YH, Liow JS, Pike VW, Innis RB. Whole-body biodistribution and radiation dosimetry in monkeys and humans of the phosphodiesterase 4 radioligand [ $^{11}\text{C}$ ](R)-rolipram: comparison of two-dimensional planar, bisected and quadrisectioned image analyses. *Nucl Med Biol*. 2008;35:493–500.
- Terry G, Liow JS, Chemet E, et al. Positron emission tomography imaging using an inverse agonist radioligand to assess cannabinoid CB1 receptors in rodents. *Neuroimage*. 2008;41:690–698.
- Zoghbi SS, Shetty HU, Ichise M, et al. PET imaging of the dopamine transporter with  $^{18}\text{F}$ -FECNT: a polar radiometabolite confounds brain radioligand measurements. *J Nucl Med*. 2006;47:520–527.
- Richter W, Menniti FS, Zhang H-T, Conti M. PDE4 as a target for cognition enhancement. *Expert Opin Ther Targets*. 2013;17:1011–1027.
- Löscher W, Potschka H. Blood-brain barrier active efflux transporters: ATP-binding cassette gene family. *NeuroRx*. 2005;2:86–98.
- Carson RE. PET physiological measurements using constant infusion. *Nucl Med Biol*. 2000;27:657–660.
- Itoh T, Abe K, Hong J, et al. Effects of cAMP dependent protein kinase activator and inhibitor on in vivo PET rolipram binding to phosphodiesterase 4 in conscious rats. *Synapse*. 2010;64:172–176.
- Hoffmann R, Wilkinson IR, McCallum JF, Engels P, Houslay MD. cAMP-specific phosphodiesterase HSPDE4D3 mutants which mimic activation and changes in rolipram inhibition triggered by protein kinase A phosphorylation of Ser-54: generation of a molecular model. *Biochem J*. 1998;333:139–149.
- Itoh T, Abe K, Zoghbi SS, et al. PET measurement of the in vivo affinity of  $^{11}\text{C}$ -(R)-rolipram and the density of its target, phosphodiesterase-4, in brain of conscious and anesthetized rats. *J Nucl Med*. 2009;50:749–756.
- Fujita M, Richards EM, Niciu MJ, et al. cAMP signaling in brain is decreased in unmedicated depressed patients and increased by treatment with a selective serotonin reuptake inhibitor. *Mol Psychiatry*. 2017;22:754–759.
- Duman RS. Synaptic plasticity and mood disorders. *Mol Psychiatry*. 2002;7(suppl 1):S29–S34.

---

---

# <sup>18</sup>F-FDG PET Maximum-Intensity Projections and Artificial Intelligence: A Win-Win Combination to Easily Measure Prognostic Biomarkers in DLBCL Patients

Kibrom B. Girum<sup>1</sup>, Louis Rebaud<sup>1,2</sup>, Anne-Ségolène Cottureau<sup>1,3</sup>, Michel Meignan<sup>4</sup>, Jérôme Clerc<sup>3</sup>, Laetitia Vercellino<sup>5</sup>, Olivier Casanovas<sup>6</sup>, Franck Morschhauser<sup>7</sup>, Catherine Thieblemont<sup>8</sup>, and Irène Buvat<sup>1</sup>

<sup>1</sup>LITO Laboratory, U1288 Inserm, Institut Curie, University Paris-Saclay, Orsay, France; <sup>2</sup>Research and Clinical Collaborations, Siemens Medical Solutions, Knoxville, Tennessee; <sup>3</sup>Department of Nuclear Medicine, Cochin Hospital, AP-HP, Paris Descartes University, Paris, France; <sup>4</sup>Lysa Imaging, Henri Mondor University Hospital, AP-HP, University Paris East, Créteil, France; <sup>5</sup>Department of Nuclear Medicine, Saint-Louis Hospital, AP-HP, Paris, France; <sup>6</sup>Department of Hematology, University Hospital of Dijon, Dijon, France; <sup>7</sup>Department of Hematology, Claude Huriez Hospital, University Lille, EA 7365, Research Group on Injectable Forms and Associated Technologies, Lille, France; and <sup>8</sup>Department of Hematology, Saint Louis Hospital, AP-HP, Paris, France

Total metabolic tumor volume (TMTV) and tumor dissemination (Dmax) calculated from baseline <sup>18</sup>F-FDG PET/CT images are prognostic biomarkers in diffuse large B-cell lymphoma (DLBCL) patients. Yet, their automated calculation remains challenging. The purpose of this study was to investigate whether TMTV and Dmax features could be replaced by surrogate features automatically calculated using an artificial intelligence (AI) algorithm from only 2 maximum-intensity projections (MIPs) of the whole-body <sup>18</sup>F-FDG PET images. **Methods:** Two cohorts of DLBCL patients from the REMARC (NCT01122472) and LNH073B (NCT00498043) trials were retrospectively analyzed. Experts delineated lymphoma lesions from the baseline whole-body <sup>18</sup>F-FDG PET/CT images, from which TMTV and Dmax were measured. Coronal and sagittal MIP images and associated 2-dimensional reference lesion masks were calculated. An AI algorithm was trained on the REMARC MIP data to segment lymphoma regions. The AI algorithm was then used to estimate surrogate TMTV (sTMTV) and surrogate Dmax (sDmax) on both datasets. The ability of the original and surrogate TMTV and Dmax to stratify patients was compared. **Results:** Three hundred eighty-two patients (mean age  $\pm$  SD, 62.1 y  $\pm$  13.4 y; 207 men) were evaluated. sTMTV was highly correlated with TMTV for REMARC and LNH073B datasets (Spearman  $r = 0.878$  and  $0.752$ , respectively), and so were sDmax and Dmax ( $r = 0.709$  and  $0.714$ , respectively). The hazard ratios for progression free survival of volume and MIP-based features derived using AI were similar, for example, TMTV: 11.24 (95% CI: 2.10–46.20), sTMTV: 11.81 (95% CI: 3.29–31.77), and Dmax: 9.0 (95% CI: 2.53–23.63), sDmax: 12.49 (95% CI: 3.42–34.50). **Conclusion:** Surrogate TMTV and Dmax calculated from only 2 PET MIP images are prognostic biomarkers in DLBCL patients and can be automatically estimated using an AI algorithm.

**Key Words:** artificial intelligence; DLBCL; <sup>18</sup>F FDG PET/CT; dissemination; metabolic tumor volume

**J Nucl Med 2022; 63:1925–1932**  
DOI: 10.2967/jnumed.121.263501

**D**iffuse large B-cell lymphoma (DLBCL) is the most common type of non-Hodgkin lymphoma. In clinical practice, <sup>18</sup>F-FDG PET/CT is a standard of care for staging and assessing response in DLBCL patients (1). The prognostic value of the total metabolically active tumor volume (TMTV) measured from the whole-body <sup>18</sup>F-FDG PET/CT images performed before treatment has been widely demonstrated in lymphoma, especially in DLBCL (2–6). The disease dissemination reflected by the largest distance between 2 lesions in the baseline whole-body <sup>18</sup>F-FDG PET/CT image (Dmax) has been recently shown to be a complementary early prognostic factor compared with TMTV (7,8). TMTV and Dmax calculations require tumor volume delineation over the whole-body 3-dimensional (3D) <sup>18</sup>F-FDG PET/CT images, which is prone to observer variability and complicates the use of these quantitative features in clinical routine.

To address this problem, automated lesion segmentation approaches using convolutional neural networks (CNNs) have been proposed (9,10). These methods require high computational resources to be developed but have shown promising results, despite missing small lesions (7). Results from CNN still need to be validated and adjusted by an expert before they are used for further analysis (7,8). This implies a thorough visual analysis of all 3D <sup>18</sup>F-FDG PET/CT images and delineation of the lesions missed by the algorithm. Consequently, developing a pipeline that would speed up this checking/adjustment process is highly desirable in clinical practice.

Nuclear medicine physicians commonly use 2-dimensional (2D) PET maximum-intensity projection (MIP) views for visual interpretation as a synthetic representation of the 3D distribution of the tracer over the whole body. However, to the best of our knowledge, the prognostic value of PET parameters extracted from 2D MIP has never been explored. We hypothesized that tumor burden and spread could be automatically evaluated from only 2 PET MIP images corresponding to coronal and sagittal views. This would have 2 advantages: first, result checking and adjustment would be faster from 2 MIP views than the whole-body 3D <sup>18</sup>F-FDG PET/CT images, typically including more than 200 transaxial slices. Second, a deep learning model for segmenting MIP images would involve fewer parameters than when segmenting the whole-body 3D <sup>18</sup>F-FDG PET images. It is less computationally expensive and might require less data for training.

---

Received Jan. 3, 2022; revision accepted Apr. 27, 2022.

For correspondence or reprints, contact Irène Buvat (irene.buvat@u-psud.fr).  
Published online Jun. 16, 2022.

Immediate Open Access: Creative Commons Attribution 4.0 International License (CC BY) allows users to share and adapt with attribution, excluding materials credited to previous publications. License: <https://creativecommons.org/licenses/by/4.0/>. Details: <http://jnm.snmjournals.org/site/misc/permission.xhtml>.

COPYRIGHT © 2022 by the Society of Nuclear Medicine and Molecular Imaging.

The purpose of this study was to investigate whether TMTV and Dmax biomarkers could be replaced by surrogate biomarkers automatically calculated using an artificial intelligence (AI) algorithm from only 2 MIPs of the whole-body  $^{18}\text{F}$ -FDG PET images. We then determined the prognostic values of the surrogate biomarkers in terms of progression-free survival (PFS) and overall survival (OS).

## MATERIALS AND METHODS

### Patient Cohorts

The study population included DLBCL patients who had undergone a baseline (before treatment initiation) PET/CT scan from 2 independent trials: REMARC (NCT01122472) and LNH073B (NCT00498043). The characteristics of these cohorts have been published elsewhere (6,11,12). PFS and OS as defined following the revised National Cancer Institute criteria (13) were recorded. Flow diagrams for the datasets and the study design are summarized in Figure 1. All data were pseudonymized before analysis. The institutional review board approval, including ancillary studies, was obtained for the 2 trials, and all patients provided written informed consent. The demographics and staging of the patients used for the survival analysis are summarized in Table 1.

### Measurements of Reference TMTV and Dmax

For the REMARC cohort, the lymphoma regions were identified in the 3D PET images as previously described (6,14), and the LNH073B lesions were segmented as previously explained (7). In all cohorts, physicians removed the regions corresponding to physiologic uptake and added pathologic regions missed by the algorithm. The supplemental materials (section A; supplemental materials are available at <http://jnm.snmjournals.org>) provide details. Expert-validated 3D lymphoma regions were used to compute the reference TMTV and Dmax (based on the centroid of the lymphoma regions), as shown in Figure 1B (8).

### Calculation of PET MIP Images and 2D Reference Lymphoma Regions

For each patient whole-body 3D  $^{18}\text{F}$ -FDG PET images and associated 3D lymphoma regions, two 2D MIP views and associated 2D lymphoma regions were calculated (Fig. 2). The 3D PET image was projected in the coronal and sagittal directions,  $90^\circ$  apart (Fig. 2), setting each pixel value of the projection to the maximum intensity observed along the ray normal to the plane of projection. Similarly, MIPs of the expert-validated 3D lymphoma regions were calculated, resulting in binary images of 2D lymphoma regions (Fig. 2), hereafter called MIP\_masks. As described in the following section, these MIP\_masks were then used as a reference output to train a CNN-based fully automatic lymphoma segmentation method.

### Fully Automatic Lymphoma Segmentation on PET MIP Images

**Deep Learning Model Inputs and Architectures.** To automatically segment the lymphoma lesions from the sagittal and coronal PET MIP images, we adapted a previously published supervised 2D deep learning model (15). The sagittal and coronal PET MIPs were independent input images during training. The corresponding MIP\_mask was the output image. The deep learning model was trained to transform a given sagittal or coronal PET MIP image to the corresponding MIP\_mask with pixels of lymphoma regions set to 1 and pixels of the non-lymphoma regions set to 0.

**Training, Validation, and Testing Configurations.** First, using the REMARC cohort (298 patients), a 5-fold cross-validation technique was used to train and evaluate the model. Patients were randomly split

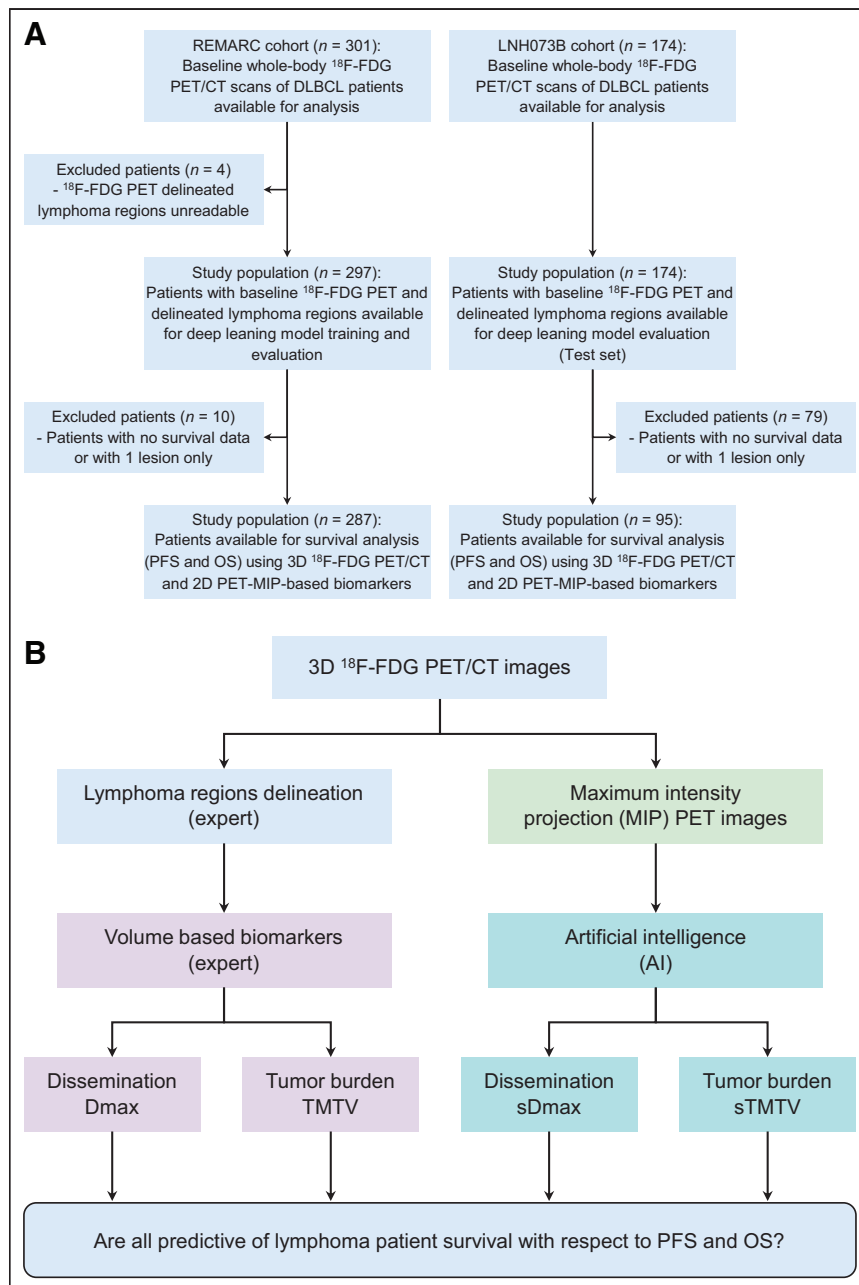
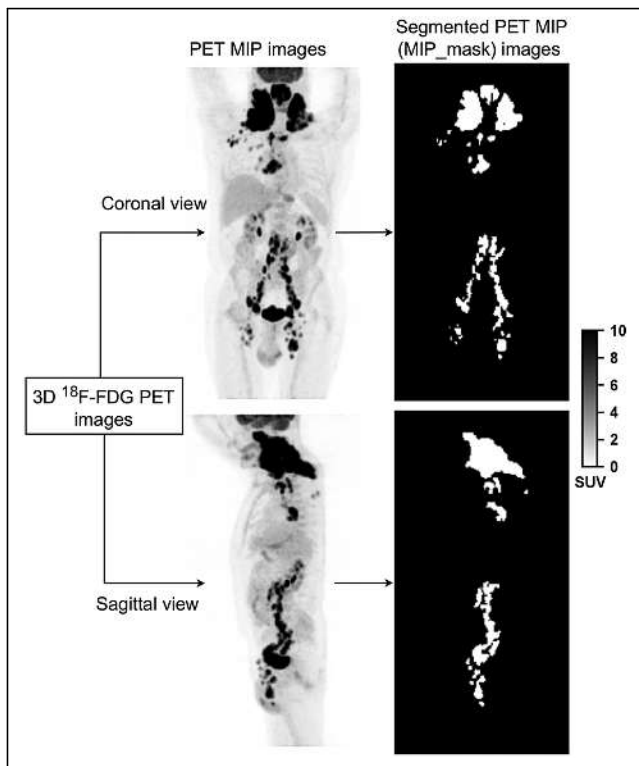


FIGURE 1. (A) Study flowchart. (B) Study design.

**TABLE 1**  
Population Characteristics

Characteristic	REMARC	LNH073B
No. of patients	287	95
Sex		
No. of men	165 (57.5%)	42 (44%)
No. of women	122 (42.5%)	53 (56%)
Median age (y)	68 (IQR, 64.0–73.0)	46 (IQR, 33.25–55.0)
Median weight (kg)	72 (IQR, 63.0–84.2)	68 (IQR, 58.0–80.0)
Median height (cm)	167.5 (IQR, 160.0–175.0) (1 case missed)	173 (IQR, 140.0–193.0)
Ann Arbor stage		
<I	1 (0.4%)	0 (0%)
≥II	286 (99.6%)	95 (100%)
Performance status		
0	115 (40%)	0 (0%)
1	121 (42%)	27 (28.4%)
2	42 (14.6%)	43 (45.3%)
3	2 (0.7%)	20 (21.1%)
4	2 (0.7%)	5 (5.3%)
Missing	5 (1.7%)	NA

IQR = interquartile range (quartile 1 to quartile 3); NA = not applicable.



**FIGURE 2.** Example of  $^{18}\text{F}$ -FDG PET MIP images (left) and associated lymphoma regions (right) based on expert delineation of the 3D  $^{18}\text{F}$ -FDG PET images.

into 5 groups, and then 5 models were trained on 80% of the population and the remaining 20% was used for validation. The detailed network architecture (15,16) and the training procedures are fully described in the supplemental materials (section B; Supplemental Fig. 1) (17), following the CLAIM guidelines (18) and Society of Nuclear Medicine and Molecular Imaging AI Task force recommendations (19). The deep learning model is publicly available at <https://github.com/KibromBerihu/ai4elife>.

Second, we tested the model trained from the REMARC cohort (298 patients) on the independent LNH073B cohort (174 patients) to characterize its generalizability and robustness. The REMARC and LNH073B cohorts were acquired from 2 different trials. The REMARC study was a double-blind, international, multicenter, randomized phase III study, which started inclusion in 2010. In contrast, the LNH073B study was a prospective multicenter, randomized phase II study that started including patients in 2007.

#### Calculation of Surrogate TMTV (sTMTV) and Surrogate Dmax (sDmax)

The sTMTV and sDmax were defined and computed from the MIP\_masks automatically segmented from the coronal and sagittal PET MIP images using the deep learning method.

**Tumor Burden Analysis.** To characterize tumor burden, we defined a surrogate tumor volume sTMTV from the MIP\_mask as the number of pixels belonging to the tumor regions in MIP\_mask multiplied by the pixel area. For a given patient, sTMTV was calculated from the coronal and the sagittal MIP\_masks as  $sTMTV = sTMTV_{\text{coronal}} + sTMTV_{\text{sagittal}}$ .

**Tumor Dissemination Analysis.** The spread of the disease was analyzed by estimating the largest distance between the tumor pixels belonging to the MIP\_mask, using a new robust largest distance estimation approach. First, we separately calculated the sum of pixels along the columns and the rows of MIP\_mask, yielding x and y profiles (Supplemental Fig. 2). Second,

in each of these 2 profiles, the distances between the 2% percentile and the 98% percentiles ( $x_{2\%}$  and  $x_{98\%}$  in the x profiles,  $y_{2\%}$  and  $y_{98\%}$  in the y profiles) were calculated, yielding ( $x_{98\%} - x_{2\%}$ ) and ( $y_{98\%} - y_{2\%}$ ), respectively. These percentiles were chosen to improve the robustness of the calculation to outliers. The largest distance was defined as  $sDmax_{sagittal/coronal} = (x_{98\%} - x_{2\%}) + (y_{98\%} - y_{2\%})$ . For a given patient, the surrogate tumor dissemination  $sDmax$  was the sum of the coronal and sagittal disseminations using  $sDmax = sDmax_{sagittal} + sDmax_{coronal}$ .

### Statistical Analysis

Using the MIP\_masks obtained from the expert-delineated 3D lymphoma regions (Fig. 2) as a reference, the segmentation performance of CNN was evaluated using the Dice score, sensitivity, and specificity. The difference between the CNN-based segmentation results and the expert-delineated 3D lymphoma regions was quantified using Wilcoxon statistical tests. Univariate and multivariate survival analyses were performed. For all biomarkers, we calculated a time-dependent area under the receiver operating characteristics curve (AUC) (20). Bootstrap resampling analysis was performed to associate CIs to the Cox model hazard ratio (HR) and the time-dependent AUC (supplemental materials, section C, provide details). Test results were considered statistically significant if the 2-sided  $P$  value was less than 0.05.

### RESULTS

A total of 475 patients from 2 different cohorts were included in this study, of which 93 patients were excluded from the biomarker and survival analysis because the provided baseline  $^{18}F$ -FDG PET/CT images were not suitable to analyze all biomarkers (no PET segmentation by an expert or less than 2 lesions). Summary statistics of patients are presented in Table 1.

### Lymphoma Segmentation

The performance of the proposed segmentation method was evaluated patientwise. The CNN segmentation method achieved a 0.80 median Dice score (interquartile range [IQR]: 0.63–0.89), 80.7% (IQR: 64.5%–91.3%) sensitivity, and 99.7% (IQR: 99.4%–99.9%) specificity for the REMARC cohort. On the testing set composed of 174 LNH073B patients, the CNN yielded a 0.86 median Dice score (IQR: 0.77–0.92), 87.9% (IQR: 74.9.0%–94.4%) sensitivity, and 99.7% (IQR: 99.4%–99.8%) specificity. In the LNH073B data, the CNN yielded a mean Dice score of  $0.80 \pm 0.17$  (mean  $\pm$  SD) on the coronal view and  $0.79 \pm 0.17$  on the sagittal view. Figure 3 shows segmentation result examples from experts (MIP\_masks)

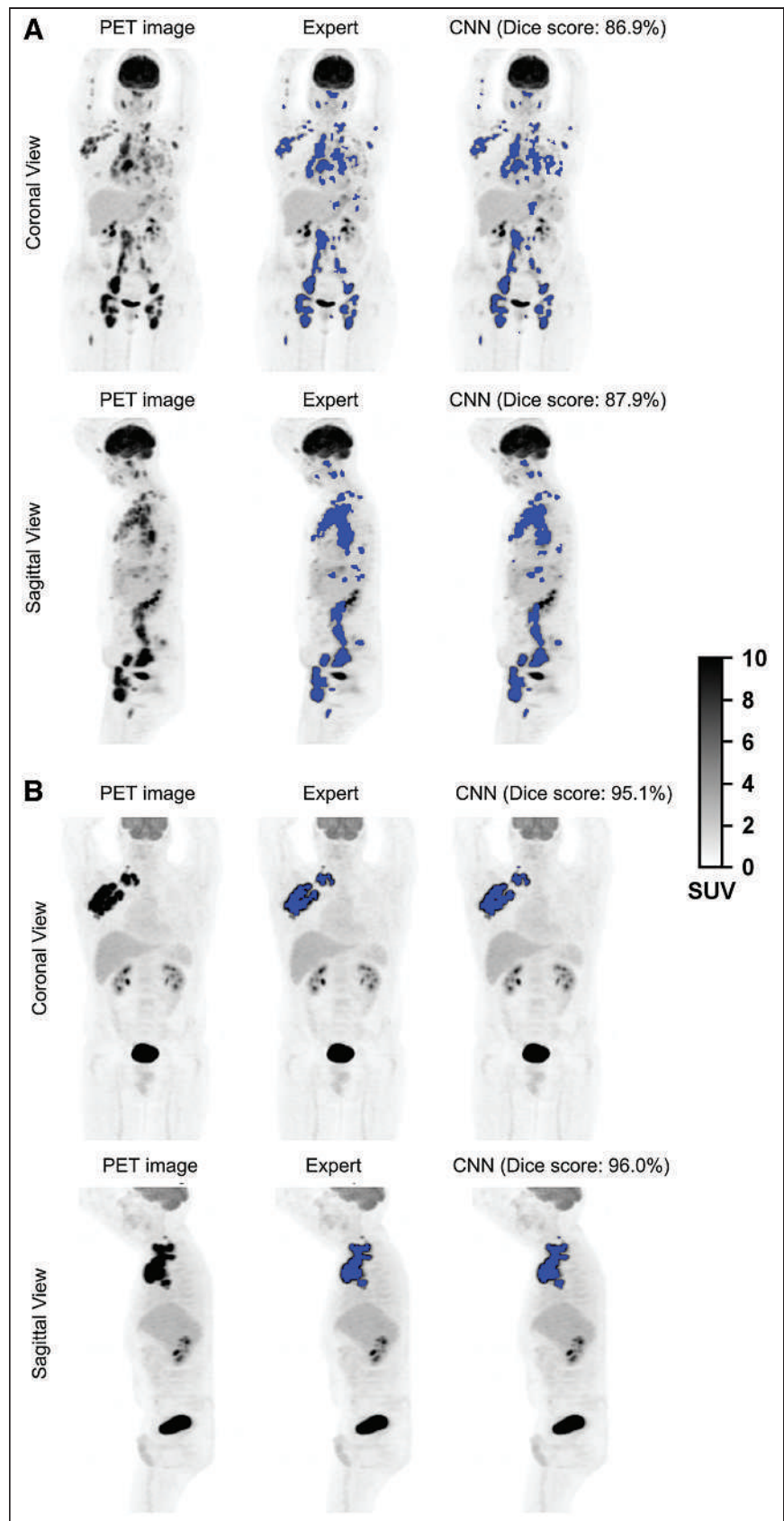


**FIGURE 3.**  $^{18}F$ -FDG PET MIP images and segmentation results (blue color overlapped over PET MIP images) by experts (MIP\_masks) and by CNN for 4 patients: from REMARC cohort (A) and from LNH073B cohort (B).

**TABLE 2**  
Statistics for Surrogate TMTV and Surrogate Dmax

Cohort	sTMTV/sDmax	Mean	SD	Minimum	Q1 (25%)	Median	Q3 (75%)	Maximum
REMARC	sTMTV (cm <sup>2</sup> )	252.27	245.75	0.48	77.04	174.24	350.56	1339.36
	sDmax (cm)	100.16	49.89	0.40	66.20	98.0	135.0	225.20
LNH073B	sTMTV (cm <sup>2</sup> )	388.12	249.91	63.68	224.48	307.2	450.08	1186.24
	sDmax (cm)	121.82	41.10	43.20	92.00	116.40	145.60	222.40

Q1 = first quartile (25% percentile); Q3 = third quartile (75% percentile).

and CNN (Supplemental Fig. 3 provides more segmentation results). The Dice score was not significantly different ( $P > 0.05$ ) between the coronal and sagittal views, both for the REMARC and the LNH073B cohorts.

In both cohorts, there was a significant correlation between ranked TMTV and Dmax values and the associated surrogate values obtained using CNN. For REMARC, TMTV was correlated with sTMTV (Spearman  $r = 0.878$ ,  $P < 0.001$ ), and Dmax was correlated with sDmax ( $r = 0.709$ ,  $P < 0.001$ ). Of 144 patients who had TMTV greater than the median TMTV (242 cm<sup>3</sup>), 121 (84.02%) patients had also sTMTV greater than the median sTMTV (174.24 cm<sup>2</sup>). One hundred forty-four patients had Dmax greater than the median Dmax (44.8 cm), and 113 (78.5%) of these patients also had sDmax greater than the median sDmax (98.0 cm).

For LNH073B, TMTV was correlated with sTMTV ( $r = 0.752$ ,  $P < 0.001$ ), and Dmax was correlated with sDmax ( $r = 0.714$ ,  $P < 0.001$ ). Of 48 patients who had TMTV greater than the median TMTV (375 cm<sup>3</sup>), 42 (87.5%) patients had also sTMTV greater than the median sTMTV (307.2 cm<sup>2</sup>). Forty-eight patients had Dmax greater than the median Dmax (44.1 cm), and 39 (81.3%) of these patients also had sDmax greater than the median sDmax (116.4 cm). Table 2 shows the descriptive statistics for the surrogate PET features.

### Survival Analysis

The time-dependent AUC and HRs with 95% CI of the metabolic tumor volume and tumor spread are shown in Table 3 for the REMARC and LNH073B data. All PET features extracted from the baseline 3D <sup>18</sup>F-FDG PET/CT images and using AI

(sTMTV and sDmax) were significant prognosticators of the PFS and OS.

When TMTV and Dmax (or their surrogates) were combined, 3 risk categories could be differentiated in the REMARC data (Fig. 4): using the 3D features, category 1 corresponded to low TMTV ( $\leq 222$  cm<sup>3</sup>) and low Dmax ( $\leq 59$  cm) (low risk,  $n = 108$ ); category 2 corresponded to either high Dmax or high TMTV (intermediate risk,  $n = 112$ ); category 3 corresponded to both high Dmax and high TMTV (high risk,  $n = 67$ ). This stratification was similar when using the MIP features-based categories using AI (Fig. 4). The accuracy of the CNN-based classification into 3 categories with respect to the 3D biomarkers-based classification was 71.4%.

In the LNH073B cohort, when TMTV and Dmax (or their surrogates) were combined, 3 risk categories could be differentiated (Fig. 5): using the 3D features, category 1 was defined as low TMTV ( $\leq 468$  cm<sup>3</sup>) and low Dmax ( $\leq 60$  cm) ( $n = 45$ ); category 2 corresponded to either high Dmax or high TMTV ( $n = 37$ ); category 3 corresponded to both high Dmax and high TMTV ( $n = 13$ ). Of the 13 patients classified as high risk, 9 (69.2%) patients had less than 4 y of OS, and 10 (76.9%) patients had less than 4 y of PFS. This stratification was similar when using the CNN-based results. The sTMTV cutoff value was 376 cm<sup>2</sup>, and the sDmax cutoff value was 122 cm. There were 38 patients in category 1, 35 in category 2, and 22 in category 3. Of the 22 patients classified as a high risk, 19 (77.3%) patients had less than 4 y of OS, and 19 (86.4%) patients had less than 4 y of PFS. The accuracy of the AI-based classification into 3 categories with respect to the 3D biomarkers-based

**TABLE 3**  
Results of the Univariate Analyses for PFS and OS Using Time-Dependent AUC Analysis and Cox Models (HR)

Data	PFS/OS	Metrics	3D <sup>18</sup> F-FDG PET/CT estimates		2D PET MIP estimates	
			TMTV	Dmax	sTMTV	sDmax
REMARC	PFS	AUC	0.67 (0.60–0.73)	0.65 (0.58–0.72)	0.65 (0.58–0.72)	0.68 (0.62–0.75)
		HR	11.24 (2.10–46.20)	9.0 (2.53–23.63)	11.81 (3.29–31.77)	12.49 (3.42–34.50)
	OS	AUC	0.67 (0.58–0.76)	0.62 (0.53–0.71)	0.67 (0.58–0.76)	0.68 (0.59–0.76)
		HR	16.43 (2.42–77.29)	8.60 (1.47–28.33)	22.14 (4.73–69.06)	22.79 (3.80–79.21)
LNH073B	PFS	AUC	0.62 (0.49–0.75)	0.56 (0.39–0.72)	0.66 (0.53–0.80)	0.58 (0.41–0.74)
		HR	13.79 (0.45–86.80)	32.83 (0.4–220.8)	9.24 (0.95–37.94)	16.79 (0.69–86.41)
	OS	AUC	0.65 (0.46–0.82)	0.51 (0.31–0.72)	0.64 (0.45–0.82)	0.50 (0.29–0.72)
		HR	64.30 (0.74–384.80)	49.21 (0.07–258.3)	14.17 (0.59–67.02)	20.39 (0.08–93.66)

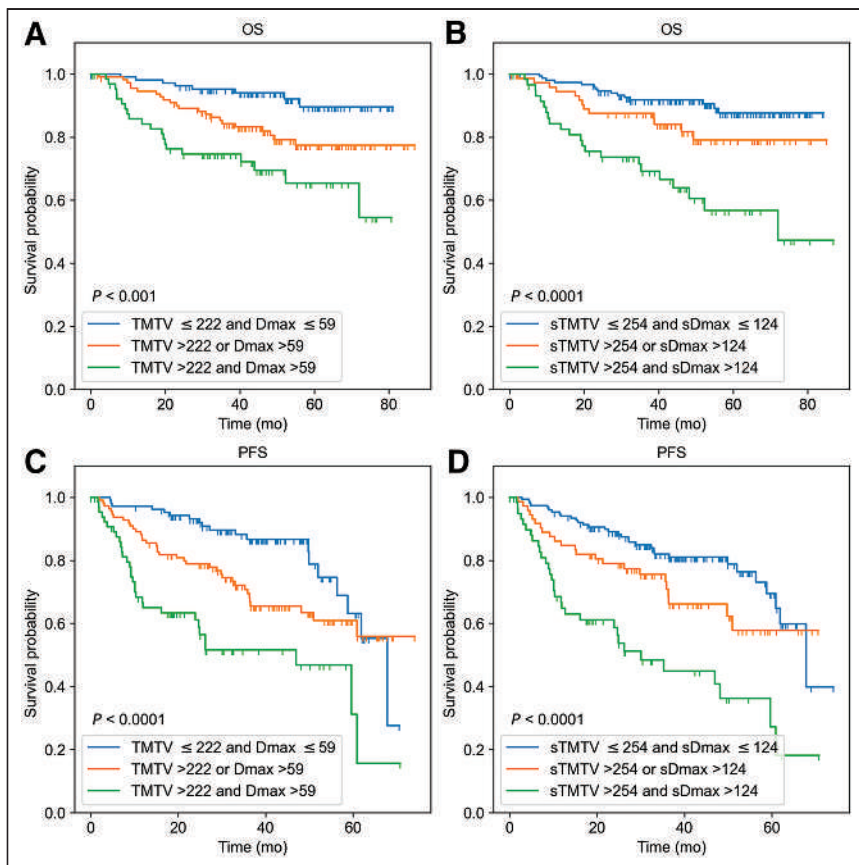


**FIGURE 4.** Kaplan–Meier estimates of OS and PFS from REMARC cohort according to 3D  $^{18}\text{F}$ -FDG PET/CT image–based features TMTV ( $\text{cm}^3$ ) and Dmax (cm) (A and C), and according to PET MIP image–based features sTMTV ( $\text{cm}^2$ ) and sDmax (cm) (B and D).

classification was 64.2%. All patients classified as high risk using the 3D biomarkers were also classified as high risk using the CNN, except 1 patient who had an OS of 36.6 mo. Of the 9 patients classified as high risk when using the CNN but not when using the 3D biomarkers, 8 (88.9%) patients had less than 4 y of OS, and the remaining 1 (11.1%) patient had 21.95 and 57.99 mo of PFS and OS, respectively.

In Supplemental Figure 4, the confusion matrices show the agreement between the 3D-based biomarkers and the surrogate MIP biomarkers in the LNH073B data. The percentage of the data classified into high, low, and intermediate risk is also shown. When a classification in 2 groups based on 1 biomarker only (either tumor burden or dissemination biomarkers) was used, the AI-based classification had a 79% accuracy compared with the 3D-based classification.

## DISCUSSION

We developed and evaluated a new framework to calculate sTMTV and sDmax (the largest distance between lymphoma sites) features from 2D PET MIP images. The motivation for considering tumor delineation on 2D MIP views instead of the 3D volume was 2-fold: first, checking lymphoma regions on 2D PET MIP images is much faster than on the 3D  $^{18}\text{F}$ -FDG PET/CT volumes. Second, training an automated AI tumor segmentation algorithm is easier in 2D than in 3D from a practical point of view (fewer parameters to be tuned, less data to be used for training, and less

computational cost). We thus investigated the prognostic values of these surrogate biomarkers using 2 independent retrospective cohorts of DLBCL patients with baseline  $^{18}\text{F}$ -FDG PET/CT. Characterizing tumor burden and its dissemination was feasible using features extracted from the 2D PET MIP images. TMTV and Dmax were highly correlated with sTMTV and sDmax, respectively.

Developing automatic and robust lymphoma segmentation methods on PET MIP images could cost less data and less computational resources than when using the whole-body  $^{18}\text{F}$ -FDG PET images. It could allow AI experts to quickly investigate appropriate segmentation approaches to tackle the challenging lymphoma segmentation task and reduce intercenter and inter-expert variations in lymphoma delineation. Experts can validate and correct, if necessary, AI results on 2D MIP images easier and faster than on their 3D volume counterparts. We also showed that a CNN could segment lymphoma lesions fully automatically from the given 2D PET MIP image with high accuracy compared with expert readers. This result was confirmed on the independent LNH073B cohort. The proposed CNN-based segmented regions enabled features extraction with predictive values comparable to when these features are calculated from the areas delineated by experts in the 3D image. The main strength

of this work was that we validated our findings using an external cohort from a different retrospective trial. However, training the proposed deep learning model from an increased training sample size, preferably from different centers and acquisition parameters, might further improve its performance. No correlations were observed between the segmentation errors made by the model and lesion size. Previous lymphoma segmentation methods used the whole-body  $^{18}\text{F}$ -FDG PET/CT images (9,10). Most of these methods involved complex preprocessing, CT and PET image alignment, and did not investigate whether both TMTV and Dmax remained good prognosticators when calculated from the automated segmentation. Recent studies have also demonstrated that CNN-based results need corrections by experts (7,8). Correction of results on 3D volume could be time-consuming, observer-dependent, and difficult. In contrast, corrections, and validations (if necessary) could be easier and faster on 2D PET MIP images, allowing easy use of these features in clinical routine.

Interestingly, the surrogate biomarkers automatically calculated using AI (sTMTV and sDmax) had strong prognostic values regarding PFS and OS, comparable to the prognostic importance of TMTV and Dmax obtained from the 3D volumes. The classification of patients into the 3 risk groups using the 3D TMTV and Dmax agreed with the patient's classification based on the 2D sTMTV and sDmax (71.4% and 64.2%, respectively, in REMARC and LNH037 cohorts). Patients classified as high-risk using 3D-based biomarkers and low-risk (or vice versa) using 2D-based biomarkers had values

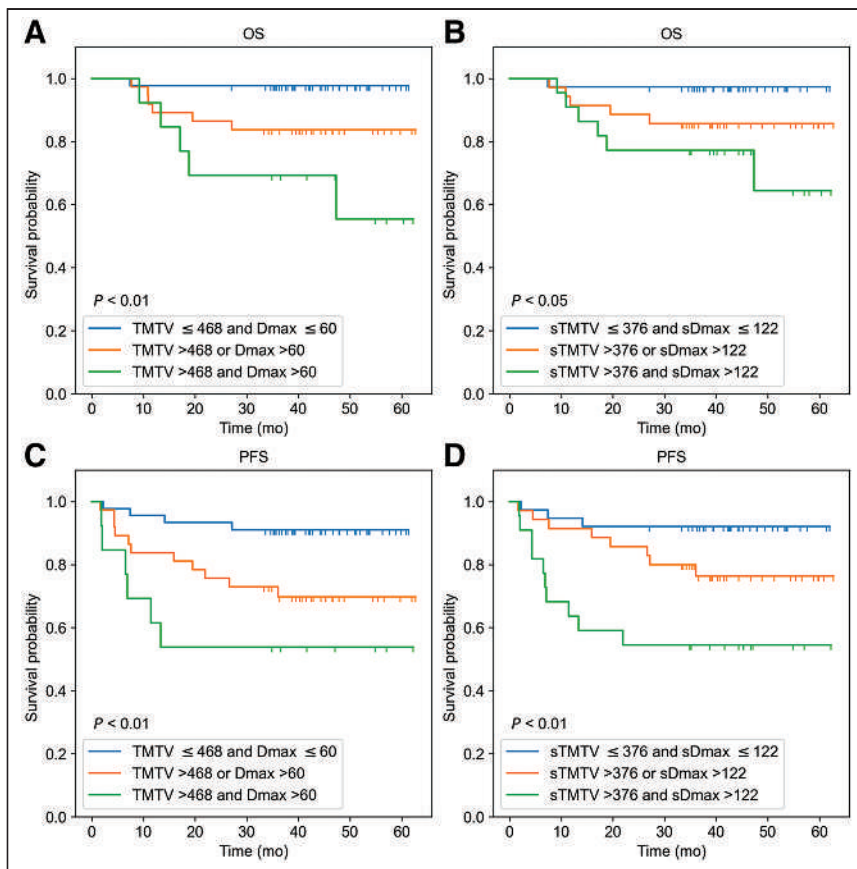


**FIGURE 5.** Kaplan-Meier estimates of OS and PFS from LNH073B cohort according to 3D  $^{18}\text{F}$ -FDG PET/CT image-based features TMTV ( $\text{cm}^3$ ) and Dmax (cm) (A and C), and according to PET MIP image-based features sTMTV ( $\text{cm}^2$ ) and sDmax (cm) estimated from AI (B and D).

close to the cutoff values. Visual assessment of the segmentation results suggested that the 2D-based biomarkers tend to perform well compared with the 3D-based biomarkers when the patient had lesions spread over the body and performed less well when the patient had a large bulky lesion.

In this work, we defined and calculated the surrogate biomarkers from both the coronal and the sagittal PET MIPs. However, experiments showed that characterizing the lymphoma disease using sTMTV and sDmax calculated from either coronal or sagittal also had good predictive values, comparable to these features obtained from 3D volumes. The same cutoff values were used to analyze the PFS and OS. The cohorts were from 2 independent studies with varying stages of cancer (Table 1). Thus the (s)TMTV cutoff values were different between the 2 cohorts. Interestingly, the cutoff values to characterize the lesion dissemination (Dmax and sDmax) in DLBCL patients on baseline PET images were almost identical on the independent cohorts. Dmax and sDmax were defined empirically, yet a recent study has shown that the distance between lesions calculated using different distance measurement methods (namely Euclidean, Manhattan, and Chebyshev) in 3D yielded similar results in predictions of the outcome (21).

Our study has limitations. Although we validated the CNN on 2 independent retrospective studies, validating the proposed CNN in larger multicenter cohorts will be required to develop it into a clinical tool. In addition, although the CNN results can be easily visually checked, they should ideally be provided with a

confidence level, which could be turned into a confidence associated with the risk classification.

## CONCLUSION

In this study, we introduced biomarkers extracted from PET MIPs as surrogates of the total metabolic tumor burden and tumor dissemination. To our knowledge, this is the first study showing that PET parameters extracted from 2D MIP images are predictive of outcome in a large series of patients with DLBCL, with results comparable to these features calculated from the 3D  $^{18}\text{F}$ -FDG PET/CT images. We demonstrated that surrogate TMTV and Dmax calculated from lymphoma regions automatically delineated on PET MIP images using AI have strong prognostic values in stratifying patients with DLBCL. This result might considerably facilitate the calculation and usage of these features in clinical practices.

## DISCLOSURE

The REMARC and LNH073B clinical studies and analyses were sponsored by the Lymphoma Academic Research Organization (LYSARC) of France. Kibrom B. Girum and Irène Buvat disclosed a research grant given to the Institut Curie by ANR (ANR-19-SYME-0005-03). Louis Rebaud disclosed employment by Siemens Medical

Solutions. No other potential conflict of interest relevant to this article was reported.

## KEY POINTS

**QUESTION:** Are surrogate tumor burden and dissemination features calculated from PET MIP images prognostic biomarkers in DLBCL patients and can they be automatically measured using an AI?

**PERTINENT FINDINGS:** sTMTV and sDmax calculated from MIP of whole-body  $^{18}\text{F}$ -FDG PET images are predictive of PFS and OS in DLBCL patients from 2 independent cohorts. A CNN could segment lymphoma lesions from 2D PET MIP images automatically and the resulting CNN-based sTMTV and sDmax estimates were predictive of PFS and OS in 2 independent cohorts.

**IMPLICATIONS FOR PATIENT CARE:** Surrogate tumor burden and dissemination features automatically calculated using AI from only 2 PET MIP images are prognostic biomarkers in DLBCL patients.

## REFERENCES

- Barrington SF, Kluge R. FDG PET for therapy monitoring in Hodgkin and non-Hodgkin lymphomas. *Eur J Nucl Med Mol Imaging.* 2017;44:97–110.
- Mikhaeel NG, Smith D, Dunn JT, et al. Combination of baseline metabolic tumour volume and early response on PET/CT improves progression-free survival prediction in DLBCL. *Eur J Nucl Med Mol Imaging.* 2016;43:1209–1219.
- Cottreau AS, Lanic H, Mareschal S, et al. Molecular profile and FDG-PET/CT total metabolic tumor volume improve risk classification at diagnosis for

- patients with diffuse large B-Cell lymphoma. *Clin Cancer Res.* 2016;22:3801–3809.
4. Kostakoglu L, Martelli M, Sehn LH, et al. Baseline PET-derived metabolic tumor volume metrics predict progression-free and overall survival in DLBCL after first-line treatment: results from the phase 3 GOYA study [abstract]. *Blood.* 2017; 130(suppl 1):824.
  5. Schmitz C, Hüttmann A, Müller SP, et al. Dynamic risk assessment based on positron emission tomography scanning in diffuse large B-cell lymphoma: post-hoc analysis from the PETAL trial. *Eur J Cancer.* 2020;124:25–36.
  6. Vercellino L, Cottreau AS, Casasnovas O, et al. High total metabolic tumor volume at baseline predicts survival independent of response to therapy. *Blood.* 2020; 135:1396–1405.
  7. Cottreau A-S, Nioche C, Dirand A-S, et al. <sup>18</sup>F-FDG PET dissemination features in diffuse large B-cell lymphoma are predictive of outcome. *J Nucl Med.* 2020;61: 40–45.
  8. Cottreau A-S, Meignan M, Nioche C, et al. Risk stratification in diffuse large B-cell lymphoma using lesion dissemination and metabolic tumor burden calculated from baseline PET/CT†. *Ann Oncol.* 2021;32:404–411.
  9. Sibille L, Seifert R, Avramovic N, et al. <sup>18</sup>F-FDG PET/CT uptake classification in lymphoma and lung cancer by using deep convolutional neural networks. *Radiology.* 2020;294:445–452.
  10. Blanc-Durand P, Jégou S, Kanoun S, et al. Fully automatic segmentation of diffuse large B cell lymphoma lesions on 3D FDG-PET/CT for total metabolic tumour volume prediction using a convolutional neural network. *Eur J Nucl Med Mol Imaging.* 2021;48:1362–1370.
  11. Casasnovas R-O, Ysebaert L, Thieblemont C, et al. FDG-PET-driven consolidation strategy in diffuse large B-cell lymphoma: final results of a randomized phase 2 study. *Blood.* 2017;130:1315–1326.
  12. Nioche C, Orhac F, Boughdad S, et al. Lifex: a freeware for radiomic feature calculation in multimodality imaging to accelerate advances in the characterization of tumor heterogeneity. *Cancer Res.* 2018;78:4786–4789.
  13. Cheson BD, Pfistner B, Juweid ME, et al. Revised response criteria for malignant lymphoma. *J Clin Oncol.* 2007;25:579–586.
  14. Capobianco N, Meignan M, Cottreau A-S, et al. Deep-learning <sup>18</sup>F-FDG uptake classification enables total metabolic tumor volume estimation in diffuse large B-cell lymphoma. *J Nucl Med.* 2021;62:30–36.
  15. Gorum KB, Crehange G, Lalande A. Learning with context feedback loop for robust medical image segmentation. *IEEE Trans Med Imaging.* 2021;40:1542–1554.
  16. He K, Zhang X, Ren S, Sun J. Deep residual learning for image recognition. In: 2016 IEEE Conference on Computer Vision and Pattern Recognition (CVPR). IEEE; 2016:770–778.
  17. Kingma DP, Ba J. Adam: a method for stochastic optimization, arxiv website, Cornell University. <https://arxiv.org/abs/1412.6980>. Revised January 30, 2017. Accessed October 18, 2022.
  18. Mongan J, Moy L, Kahn CE. Checklist for artificial intelligence in medical imaging (CLAIM): a guide for authors and reviewers. *Radiol Artif Intell.* 2020;2: e200029.
  19. Bradshaw TJ, Boellaard R, Dutta J, et al. Nuclear medicine and artificial intelligence: best practices for algorithm development. *J Nucl Med.* 2022;63: 500–510.
  20. Heagerty PJ, Lumley T, Pepe MS. Time-dependent ROC curves for censored survival data and a diagnostic marker. *Biometrics.* 2000;56:337–344.
  21. Cottreau A-S, Meignan M, Nioche C, et al. New approaches in characterization of lesions dissemination in DLBCL patients on baseline PET/CT. *Cancers (Basel).* 2021;13:3998.

---

---

# Distinction of Lymphoma from Sarcoidosis on $^{18}\text{F}$ -FDG PET/CT: Evaluation of Radiomics-Feature-Guided Machine Learning Versus Human Reader Performance

Pierre Lovinfosse<sup>1</sup>, Marta Ferreira<sup>2</sup>, Nadia Withofs<sup>1</sup>, Alexandre Jadoul<sup>1</sup>, Céline Derwael<sup>1</sup>, Anne-Noelle Frix<sup>3</sup>, Julien Guiot<sup>3</sup>, Claire Bernard<sup>1</sup>, Anh Nguyet Diep<sup>4</sup>, Anne-Françoise Donneau<sup>4</sup>, Marie Lejeune<sup>5</sup>, Christophe Bonnet<sup>5</sup>, Wim Vos<sup>6</sup>, Patrick E. Meyer<sup>7</sup>, and Roland Hustinx<sup>1</sup>

<sup>1</sup>Division of Nuclear Medicine and Oncological Imaging, CHU of Liège, Liège, Belgium; <sup>2</sup>GIGA-CRC In Vivo Imaging, University of Liège, Liège, Belgium; <sup>3</sup>Department of Respiratory Medicine, CHU of Liège, Liège, Belgium; <sup>4</sup>Biostatistics Unit, Department of Public Health, University of Liège, Liège, Belgium; <sup>5</sup>Department of Hematology, CHU of Liège, Liège, Belgium; <sup>6</sup>Radiomics SA, Liège, Belgium; and <sup>7</sup>Bioinformatics and Systems Biology Lab, University of Liège, Liège, Belgium

Sarcoidosis and lymphoma often share common features on  $^{18}\text{F}$ -FDG PET/CT, such as intense hypermetabolic lesions in lymph nodes and multiple organs. We aimed at developing and validating radiomics signatures to differentiate sarcoidosis from Hodgkin lymphoma (HL) and diffuse large B-cell lymphoma (DLBCL). **Methods:** We retrospectively collected 420 patients (169 sarcoidosis, 140 HL, and 111 DLBCL) who underwent pretreatment  $^{18}\text{F}$ -FDG PET/CT at the University Hospital of Liège. The studies were randomly distributed to 4 physicians, who gave their diagnostic suggestion among the 3 diseases. The individual and pooled performance of the physicians was then calculated. Inter-observer variability was evaluated using a sample of 34 studies interpreted by all physicians. Volumes of interest were delineated over the lesions and the liver using MIM software, and 215 radiomics features were extracted using the RadiomiX Toolbox. Models were developed combining clinical data (age, sex, and weight) and radiomics (original and tumor-to-liver TLR radiomics), with 7 different feature selection approaches and 4 different machine-learning (ML) classifiers, to differentiate sarcoidosis and lymphomas on both lesion-based and patient-based approaches. **Results:** For identifying lymphoma versus sarcoidosis, physicians' pooled sensitivity, specificity, area under the receiver-operating-characteristic curve (AUC), and accuracy were 0.99 (95% CI, 0.97–1.00), 0.75 (95% CI, 0.68–0.81), 0.87 (95% CI, 0.84–0.90), and 89.3%, respectively, whereas for identifying HL in the tumor population, it was 0.58 (95% CI, 0.49–0.66), 0.82 (95% CI, 0.74–0.89), 0.70 (95% CI, 0.64–0.75) and 68.5%, respectively. Moderate agreement was found among observers for the diagnosis of lymphoma versus sarcoidosis and HL versus DLBCL, with Fleiss  $\kappa$ -values of 0.66 (95% CI, 0.45–0.87) and 0.69 (95% CI, 0.45–0.93), respectively. The best ML models for identifying lymphoma versus sarcoidosis showed an AUC of 0.94 (95% CI, 0.93–0.95) and 0.85 (95% CI, 0.82–0.88) in lesion- and patient-based approaches, respectively, using TLR radiomics (plus age for the second). To differentiate HL from DLBCL, we obtained an AUC of 0.95 (95% CI, 0.93–0.96) in the lesion-based approach using TLR radiomics and 0.86 (95% CI, 0.80–0.91) in the patient-based approach using original radiomics and age. **Conclusion:** Characterization of sarcoidosis and lymphoma lesions is feasible using ML and radiomics, with very good to excellent performance, equivalent to or better than that of physicians, who showed significant interobserver variability in their assessment.

**Key Words:** radiomics; machine learning; sarcoidosis; lymphoma;  $^{18}\text{F}$ -FDG PET/CT

**J Nucl Med** 2022; 63:1933–1940  
DOI: 10.2967/jnumed.121.263598

**S**arcoidosis is a systemic inflammatory disease characterized by the development of granulomas, which may involve lymph nodes and various organs. Hodgkin lymphoma (HL) and diffuse large B-cell lymphoma (DLBCL), the most frequent type of non-Hodgkin lymphoma, are also characterized by enlarged invaded lymph nodes but can affect many organs. When  $^{18}\text{F}$ -FDG PET/CT is performed at diagnosis, these diseases may present with a similar pattern, that is, intense hypermetabolism in enlarged lymphadenopathies, in particular in the mediastinum. Involvement of many other nodal stations may also be observed, along with extranodal lesions, and the distribution of lesions thus helps imaging specialists in interpreting these PET/CT scans. Nonetheless, the accuracy of visual interpretation of  $^{18}\text{F}$ -FDG PET/CT scans for differentiating sarcoidosis from lymphomas is imperfect (1). Semiquantitative measurements such as  $\text{SUV}_{\text{max}}$  have not proven to be the answer either (2,3). Moreover, sarcoidosis can develop before lymphoma (sarcoidosis-lymphoma syndrome) and after lymphoma, and immunotherapy-induced sarcoidlike reactions are increasingly observed (4–7). No matter the results of the imaging studies, pathologic confirmation of the disease is mandatory in all cases before initiating treatment.

The histopathology of these entities is very different, suggesting that deep characteristics of the image might also be specific. Radiomics is a high-throughput approach allowing extraction of large amounts of data from images and characterization of the lesion phenotype (8,9). The development of artificial intelligence and machine learning (ML) combined with radiomics has gained popularity in different medical imaging tasks, including lesion identification and characterization. In lymphoma, some studies have shown the potential of  $^{18}\text{F}$ -FDG PET/CT radiomics to differentiate lymphoma from other types of cancers and to differentiate different types of lymphoma (10–14). To the best of our knowledge, no study has yet explored the use of  $^{18}\text{F}$ -FDG PET/CT radiomics to characterize sarcoidosis lesions, except one for the diagnosis of cardiac involvement (15).

---

Received Nov. 26, 2021; revision accepted May 10, 2022.  
For correspondence or reprints, contact Pierre Lovinfosse (pierre.lovinfosse@chuliege.be).  
Published online May 19, 2022.  
COPYRIGHT © 2022 by the Society of Nuclear Medicine and Molecular Imaging.

The primary objective of the present study was to develop and validate a radiomics signature to differentiate sarcoidosis, HL, and DLBCL lesions. Furthermore, we compared the ML-driven diagnosis with physician performance in categorizing the 3 diseases, taking into account interobserver variability.

## MATERIALS AND METHODS

### Patients

The study was approved by the Ethics Committee of the University Hospital of Liège. The need for written informed consent was waived because of the retrospective and noninterventional design of the study. We retrospectively collected consecutive  $^{18}\text{F}$ -FDG PET/CT scans obtained at the University Hospital of Liège between April 2010 and February 2020 of patients with HL, DLBCL, or sarcoidosis at initial diagnosis, before any treatment. The diagnosis was based on pathology in all lymphoma cases and in most cases of sarcoidosis. The diagnosis of the remaining sarcoidosis cases was based on clinical evidence and follow-up. Exclusion criteria were radiotracer extravasation, artifacts in pathologic areas, absence of a delineated volume of interest (VOI) after semiautomatic segmentation, and absence of relevant information in the DICOM files. Basic clinical data (age, sex, and weight) were collected from the information obtained routinely on the day of the PET/CT scan. Figure 1 shows the flowchart of the study.

### Imaging

$^{18}\text{F}$ -FDG PET/CT scans were acquired using 2 cross-calibrated PET/CT systems, a GEMINI TF Big Bore and a GEMINI TF 16 (Philips), 66 min on average (range, 58–92 min) after intravenous injection of  $^{18}\text{F}$ -FDG (mean injected activity, 245 MBq, depending linearly on the patient's weight). The patients fasted for at least 6 h before the injection, and the median glycemia was 92 mg/dL (range, 59–195 mg/dL). A low-dose CT scan (slice thickness, 5 mm; tube voltage, 120 kV; and tube current–time product, 50–80 mAs, depending on the patient's weight) was performed without injection of intravenous contrast agent, followed by a PET emission scan of 90 s per bed position (50% overlap), extending from the upper thighs to the skull base. All images were acquired and reconstructed according to the EARL (European Association of Nuclear Medicine Research Ltd.) guidelines for both PET/CT systems. Images were reconstructed with standard  $4 \times 4 \times 4$  mm

voxels (slice thickness, 4 mm) using an iterative list-mode algorithm (blob ordered-subset time-of-flight), and corrections for attenuation, dead time, random events, and scatter events were applied without post-reconstruction smoothing.

### Lesion Segmentation and Clinical Diagnosis

The entire cohort of anonymized patients was randomly distributed into 4 groups (groups A–D). The scans of each group were assigned to 4 different nuclear medicine physicians (observers A–D), who were unaware of any clinical information or diagnosis and had 6 y (observer A), 3 y (observer B), 15 y (observer C), and 10 y (observer D) of experience. In a first step, from visual interpretation of the PET/CT scans, the physicians attributed a diagnosis to each patient of their cohort. For that purpose, they first chose either sarcoidosis or cancer, and if the latter was selected, they chose HL or DLBCL. This evaluation was based solely on the experience of each physician. No reading guidelines or visual or semiquantitative interpretation criteria were provided to the readers within the framework of the study. For each answer, the physicians indicated their level of confidence (0, possible; 1, probable; or 2, certain).

In the next step, the physicians segmented PET VOIs for their assigned patient population using MIM software, version 7.0.5 (MIM Software Inc.), with the following 4 steps. The first was automatic selection of all regions using an absolute threshold  $\text{SUV}_{\text{max}}$  of at least 3 within a rectangular VOI manually drawn on the whole body. The second step was automatic exclusion of VOIs smaller than  $2 \text{ cm}^3$ . The third step was manual exclusion of all physiologic VOIs (e.g., brain, heart, and kidneys). The fourth step was manual modification of some pathologic VOIs, that is, removing physiologic activity in continuity with the pathologic VOI but never enlarging the VOI. In the absence of literature references for this combination of diseases, especially considering sarcoidosis, the thresholds of  $\text{SUV}_{\text{max}}$  and volume were decided after tests were performed on a sample of images with the aim of including as many lesions as possible while limiting the need for manual modifications. A VOI of  $20 \text{ cm}^3$  was also drawn on the healthy liver.

### Radiomics Extraction and Model Elaboration

Two hundred fifteen features were extracted from the segmented PET volumes using the RadiomiX Toolbox (Radiomics SA), coded with Matlab (MathWorks), and aligned with the Imaging Biomarkers Standardization Initiative, with, however, some additional features (a list of all features can be found in the supplemental materials, available at <http://jnm.snmjournals.org>). We also studied the ratio of the feature values calculated in the tumor and in the liver (tumor-to-liver ratio [TLR]), except for the shape features. For calculation of the texture matrix-based features, the intensities were discretized using 2 different methods according to the recommendations of the Imaging Biomarkers Standardization Initiative: fixed bin numbers of 32 and 64 and fixed bin widths of 0.05, 0.1, 0.2, and 0.5 SUV.

Since each patient could have more than 1 lesion, 2 radiomics approaches were tested. In a first approach (lesion-based), each lesion was considered as 1 observation and the goal was to classify each lesion as, first, belonging to the sarcoidosis or lymphoma class and, second, as belonging to the HL or DLBCL class. In the second approach (patient-based), the radiomics features of each lesion and for each patient were merged using their minimum, maximum, mean, and median values, and clinical data (age, sex, and weight) were added to the radiomics

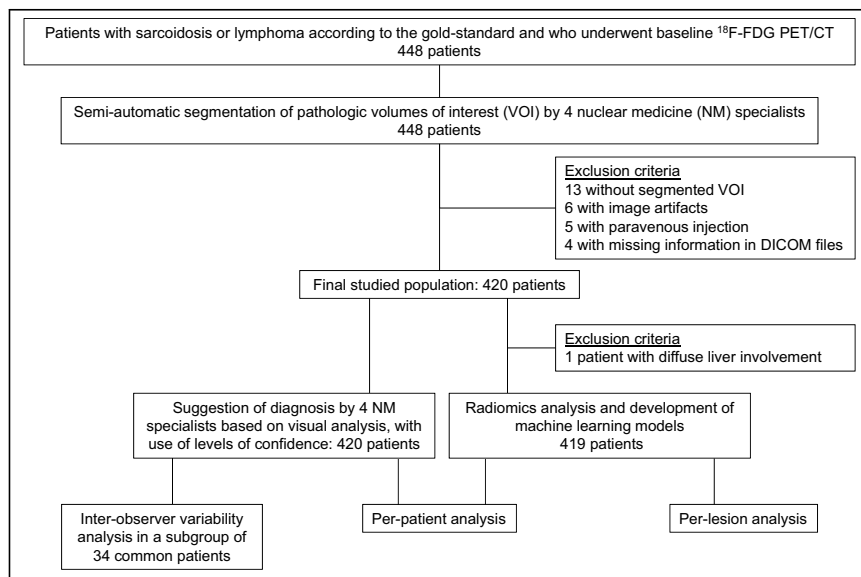


FIGURE 1. Study flowchart.

features. Here, the aim was to classify each patient into the sarcoidosis, HL, or DLBCL group.

We also evaluated whether combining different feature selection (FS) approaches and ML classifiers would allow for a radiomics signature to differentiate sarcoidosis from lymphoma patients and to differentiate HL from DLBCL. For that purpose, we tested a different set of models, which differed in feature type, that is, original radiomics or TLR radiomics; FS and ML classifier method; and the effect of adding clinical data before FS. Seven different FS methods were tested: accuracy decrease obtained from the embedded FS of the random forest (RF) classifier; Gini impurity decrease obtained from the embedded FS of the RF classifier; forward FS using the minimum redundancy maximum relevance (MRMR) method with Pearson correlation; backward FS using MRMR with Pearson correlation; forward FS using MRMR with Spearman correlation; backward FS using MRMR with Spearman correlation; and forward MRMR based on the mutual information. We also used 4 ML classifiers: RF, support vector machine with radial kernel, naive Bayes, and a logistic regression (16). The dataset was stratified with the same percentage of classes, avoiding unbalanced data, and was randomly divided into training and test sets (80% and 20%, respectively). We tested different models that differed in the FS, ML, and intensity discretization method and in the number of features, which was between 2 and 20 with intervals of 2. We used 5-fold cross validation in our training data, and we chose the best radiomics signature according to the best mean 5-fold cross validation area under the precision-recall area under the receiver-operating-characteristic curve (AUCpr). For each classifier, the default hyperparameter values were used in their respective R packages. Finally, for each of the different models with distinct selected features, all training data were bootstrapped to derive the corresponding 95% CIs for each performance metric and tested on the independent test set. The number of bootstrap repetitions was set to at least 1,000. Since images came from only 2 scanners (same manufacturer and model, same acquisition protocol), which were also cross-calibrated, we did not consider it necessary to perform data harmonization. As recently suggested by Buvat and Orlhac (17), we performed a T.R.U.E. checklist (Is it true? Is it reproducible? Is it useful? Is it explainable?) to assess the potential impact of our findings.

### Statistical Analysis

The homogeneity in age and weight across the A, B, C, and D populations was assessed by the Kruskal–Wallis nonparametric test, whereas  $\chi^2$  test association was performed for sex and the final diagnosis (gold standard). Additionally, the homogeneity in age, sex, and weight across cancer and sarcoidosis patients and between HL and DLBCL patients was also evaluated using the  $\chi^2$  and Kruskal–Wallis tests. Statistical significance was assigned for *P* values of 0.05 or less.

The diagnostic performance of all observers pooled together and each individual observer against the gold standard was calculated using sensitivity, specificity, positive predictive value (PPV), and negative predictive value (NPV). In addition, diagnostic performance was evaluated by calculating the percentage of agreement (or accuracy) and the AUC. To calculate the predicted probabilities, we fitted a logistic regression model with the observer's classification as the predictor. We additionally bootstrapped the data to measure the AUC 95% CIs. The 95% CIs for the sensitivity, specificity, PPV, and NPV were calculated using exact binomial confidence limits.

To test variability among observers, we applied the CI approach in sample size estimation for interobserver agreement with binary outcomes (18). Because of a lack of literature on the established agreement, to calculate the sample size in the case of 4 observers we assigned an expected  $\kappa$  of 0.70, indicating moderate agreement (19), a lower bound of 0.50 with an unknown upper bound, and a significance level of 0.05. With a prevalence of 0.3 for sarcoidosis versus cancer and 0.6 for HL versus DLBCL, a sample size of 27 and 23 was

required, respectively. On the basis of this estimation, we randomly selected a subgroup of 34 patients who were subsequently analyzed by all 4 observers to evaluate the interobserver variability. Because of the misclassification for the sarcoidosis versus cancer, only 21 patients remained in the evaluation of interobserver variability in the analysis of HL versus DLBCL. Fleiss  $\kappa$  was used to investigate overall agreement among 4 observers in the classification (for sarcoidosis/cancer and for HL/DLBCL) and intraclass correlation coefficients for degree of certainty. Finally, the Hotelling  $T^2$  test was used to test the difference in agreement between pairs of observers.

For radiomics, we evaluated the performance of the models using AUC, AUCpr, sensitivity, specificity, PPV, and NPV, with a 0.5 probability threshold on the test set for lesion-based and patient-based approaches. Statistical and ML analyses were performed for the 2 clinical tasks (sarcoidosis/cancer and HL/DLBCL) using R software, version 4.0.3.

## RESULTS

In total, 448 patients meeting the study inclusion criteria were initially identified. After the exclusion criteria were applied, 420 patients (mean age,  $49 \pm 18$  y; 241 men and 179 women) remained in the study (Fig. 1). According to the gold standard, 169 patients had sarcoidosis (40.2%), 140 had HL (33.3%), and 111 had DLBCL (26.4%). The Ann Arbor stages for HL were 10 cases of stage I, 1 of stage IE, 64 of stage II, 1 of stage IIE, 19 of stage III, 20 of stage IIIS, and 25 stage of IV, and the stages for DLBCL were 10 cases of stage I, 27 of stage II, 12 of stage III, 10 of stage IIIS, and 52 of stage IV. Eighty-one patients with sarcoidosis had extrathoracic lesions. Table 1 presents the patient characteristics and gold standard for the entire population and the 4 physicians' subsamples. The 4 groups were balanced except for observer D, who had significantly more sarcoidosis patients and fewer DLBCL patients. Patient age differed significantly across the 4 subsamples ( $P = 0.008$ ), with patients in group D being significantly younger than those in groups A and B, which could be explained by the difference in the distribution of diseases. There was no significant difference in weight or sex across the 4 subsamples.

### Individual and Pooled Observer Performance as Compared with Gold Standard

For identifying lymphomas (HL and DLBCL) in the entire population ( $n = 420$ ), the sensitivity and specificity were 0.99 (95% CI, 0.97–1.00) and 0.75 (95% CI, 0.68–0.81), respectively. The AUC was 0.87 (95% CI, 0.84–0.90), and accuracy was 0.893 (95% CI, 0.86–0.92). Similarly, a Cohen  $\kappa$  of 0.78 (95% CI, 0.72–0.84) revealed substantial agreement with the gold standard. Taking the certainty level into account, a significant higher agreement  $\kappa$  of 0.86 (95% CI, 0.79–0.92) was found for certainty level 2, compared with a  $\kappa$  of 0.41 (95% CI, 0.23–0.58) for level 1 ( $P < 0.001$ ).

Overall and individual observer performance for the diagnosis of cancer versus sarcoidosis for their subsample populations is listed in Table 2. All observers had an excellent sensitivity (0.97–1.00) but a lower and more variable specificity (0.58–0.81). AUC and accuracy ranged from 0.79 to 0.90 and from 0.85 to 0.92, respectively. Regarding the confidence levels, observers A, B, C, and D chose level 2 in 81%, 80%, 80%, and 65% of cases; level 1 in 15%, 19%, 12%, and 27%; and level 0 in 4%, 1%, 8%, and 8%, respectively.

For identifying HL in the cancer population ( $n = 248$ , after removing 3 patients mistakenly categorized with sarcoidosis), the sensitivity and specificity were 0.58 (95% CI, 0.49–0.66) and 0.82 (95% CI, 0.74–0.89) respectively. AUC was 0.70 (95% CI, 0.64–0.75), and

**TABLE 1**  
Patient Characteristics (*n* = 420) and 4 Physician Subsamples

Characteristic	Overall	Observer A	Observer B	Observer C	Observer D
Median age (y)	49 (Q1–Q3, 35–61)	52 (Q1–Q3, 36–67)	52 (Q1–Q3, 37–61)	49 (Q1–Q3, 39–60)	44 (Q1–Q3, 29–55)
Median weight (kg)	75 (Q1–Q3, 63–86)	74 (Q1–Q3, 62–84)	75 (Q1–Q3, 66–85)	72 (Q1–Q3, 62–85)	77 (Q1–Q3, 63–89)
Sex					
Female	179	47	41	45	46
Male	241	62	61	55	64
Diagnosis					
Sarcoidosis	169 (40.2%)	36 (33%)	36 (35.5%)	34 (34%)	63 (57%)
HL	140 (33.3%)	32 (29%)	36 (35.5%)	35 (35%)	37 (34%)
DLBCL	111 (26.5%)	41 (38%)	29 (29%)	31 (31%)	10 (9%)

Q1 and Q3 are interquartile ranges.

accuracy was 0.69 (95% CI, 0.63–0.74). The Cohen  $\kappa$  of 0.40 (95% CI, 0.29–0.51) indicated only fair agreement with the gold standard. When the certainty level was 2, a significantly higher  $\kappa$  of 0.51 (95% CI, 0.41–0.67) was obtained, compared with a  $\kappa$  of 0.20 (95% CI, 0.14–0.39) at level 1 certainty ( $P = 0.003$ ).

Overall and individual observer performance for the diagnosis of HL versus DLBCL for their subsample populations is listed in Table 3. The sensitivity ranged from 0.39 to 0.77 and specificity from 0.77 to 0.85. AUC and accuracy ranged from 0.60 to 0.81 and from 0.59 and 0.82, respectively. Regarding the confidence levels, observers A, B, C, and D selected level 2 in 54%, 46%, 61%, and 45% of cases; level 1 in 38%, 49%, 33%, and 43%; and level 0 in 8%, 5%, 6%, and 12%, respectively. Representative examples of PET studies are shown in Figures 2 and 3.

#### Interobserver Agreement

In the sample of 34 patients, a Fleiss  $\kappa$ -value of 0.66 (95% CI, 0.45–0.87) indicated that the 4 observers were in moderate

agreement with one another in the diagnosis of cancer versus sarcoidosis. Regarding the certainty levels, an intraclass correlation coefficient of 0.353 (95% CI, 0.181–0.547) showed poor agreement among the observers. At the individual level, the agreement with the gold standard was highly variable, as  $\kappa$  ranged from 0.45 to 0.93. The Hotelling  $T^2$  test showed that agreement with the gold standard differed significantly between the 2 extreme values, that is, observers B and D ( $T^2 = 8.70$ ,  $P = 0.006$ ).

For the diagnosis of HL versus DLBCL, in the population of 21 patients diagnosed with cancer evaluated by all 4 observers, the Fleiss  $\kappa$ -value of 0.69 (95% CI, 0.45–0.93) indicated moderate agreement among observers. Regarding certainty levels, an intraclass correlation coefficient of 0.075 (95% CI, 0.076–0.316) showed poor agreement among the observers. At the individual level, only observer A displayed substantial agreement with the gold standard ( $\kappa = 0.70$ ; 95% CI, 0.38–1.01), whereas the other 3 observers showed poor agreement, with  $\kappa$  ranging from 0.07 to 0.27. The Hotelling  $T^2$  test showed that observer A outperformed

**TABLE 2**  
Overall and Individual Performance for Diagnosis of Sarcoidosis Versus Lymphoma

Parameter	Overall	Observer A	Observer B	Observer C	Observer D
Proposed diagnosis: sarcoidosis, cancer	130–290	31–78	21–80	28–72	50–60
Correct classification	375/420: 89.3% (86.3%–92.2%)	100/109: 91.7% (86.6%–96.9%)	86/101: 85.1% (78.2%–92.1%)	92/100: 92% (86.7%–97.3%)	97/110: 88.2% (82.3%–94.2%)
Correct sarcoidosis classification	133/169: 78.7% (72.5%–84.9%)	29/36: 80.6% (67.6%–93.5%)	21/36: 58.3% (42.2%–74.4%)	27/34: 79.4% (65.8%–93%)	56/63: 88.9% (81.1%–96.7%)
Correct cancer classification	248/251: 98.8% (97.5%–100%)	71/73: 97.3% (93.5%–100%)	65/65: 100%	65/66: 98.5% (95.5%–100%)	47/47: 100%
Sensitivity	0.99 (0.97–1.00)	0.97 (0.90–1.00)	1.00 (0.94–1.00)	0.98 (0.92–1.00)	1.00 (0.92–1.00)
Specificity	0.75 (0.68–0.81)	0.81 (0.64–0.92)	0.58 (0.41–0.74)	0.79 (0.62–0.91)	0.79 (0.67–0.89)
PPV	0.86 (0.81–0.89)	0.91 (0.81–0.96)	0.81 (0.71–0.89)	0.90 (0.82–1.00)	0.78 (0.66–0.88)
NPV	0.98 (0.93–1.00)	0.94 (0.79–0.99)	1.00 (0.84–1.00)	0.96 (0.82–1.00)	1.00 (0.93–1.00)
AUC	0.87 (0.84–0.90)	0.89 (0.82–0.96)	0.79 (0.71–0.87)	0.89 (0.82–0.96)	0.90 (0.85–0.95)

Data in parentheses are 95% CIs.

**TABLE 3**  
Overall and Individual Performance for Diagnosis of HL Versus DLBCL Lymphomas

Parameter	Overall	Observer A	Observer B	Observer C	Observer D
Proposed diagnosis: HL, DLBCL	110–180	33–45	22–58	27–45	28–32
Correct HL classification	80/140: 57.1% (49.0%–65.3%)	23/32: 71.9% (56.3%–87.5%)	14/36: 38.9% (23.0%–54.8%)	20/35: 57.1% (40.8%–73.5%)	27/37: 73.0% (58.7%–87.3%)
Correct DLBCL classification	91/111: 82% (74.8%–89.1%)	35/41: 85.4% (74.5%–96.2%)	24/29: 82.8% (69.0%–96.5%)	24/31: 77.4% (62.7%–92.1%)	8/10: 80% (55.2%–100%)
When observer said cancer and gold standard was cancer:					
Correct HL classification	79/137: 57.7% (49.4%–65.9%)	23/30: 76.7% (61.5%–91.8%)	14/36: 38.9% (23.0%–54.8%)	20/34: 58.8% (42.3%–75.4%)	22/37: 59.5% (43.6%–75.3%)
Correct DLBCL classification	91/111: 82% (74.8%–89.1%)	35/41: 85.4% (74.6%–96.2%)	24/29: 82.8% (69.0%–96.5%)	24/31: 77.4% (62.7%–91.1%)	8/10: 80% (55.2%–100%)
Sensitivity	0.58 (0.49–0.66)	0.77 (0.58–0.90)	0.39 (0.23–0.57)	0.59 (0.41–0.75)	0.59 (0.42–0.75)
Specificity	0.82 (0.74–0.89)	0.85 (0.71–0.94)	0.83 (0.64–0.94)	0.77 (0.59–0.90)	0.80 (0.44–0.97)
PPV	0.80 (0.71–0.87)	0.79 (0.60–0.92)	0.74 (0.49–0.91)	0.74 (0.54–0.89)	0.92 (0.73–0.99)
NPV	0.61 (0.53–0.69)	0.83 (0.69–0.93)	0.52 (0.37–0.67)	0.63 (0.46–0.78)	0.35 (0.16–0.57)
Accuracy	170/248: 68.5% (62.7%–74.3%)	58/71: 81.7% (72.7%–90.7%)	38/65: 58.5% (46.5%–70.5%)	44/65: 67.7% (56.3%–79.1%)	30/47: 63.8% (50.1%–77.5%)
AUC	0.70 (0.64–0.75)	0.81 (0.72–0.91)	0.60 (0.50–0.72)	0.68 (0.57–0.79)	0.70 (0.54–0.85)

Data in parentheses are 95% CIs.

the other 3 observers in agreement with the gold standard and that the most significant difference was between observers A and B ( $T^2 = 9.60$ ,  $P = 0.006$ ). There was no significant difference in agreement among observers B, C, and D. Supplemental Tables 1–2 show all the individual  $\kappa$  and Hotelling  $T^2$  values for the inter-observer agreement analysis for the 2 tasks.

#### Performance of Radiomics Models Compared with Gold Standard

In the whole cohort, 2816 VOIs were segmented, including 1,028 (36.5%) for sarcoidosis, 836 (29.7%) for HL, and 952 (33.8%) for DLBCL (mean number of VOIs by patient: 42.1 for sarcoidosis, 44.7 for HL, and 75.8 for DLBCL). One patient with sarcoidosis was excluded from the radiomics analyses ( $n = 419$ ) because of diffuse liver pathologic infiltration that did not allow

delineation of the hepatic background VOI. The results of the best model performance compared with physician performance are summarized in Figures 4 and 5.

An RF classifier, in which features were selected with the embedded RF feature selection using the accuracy decrease as a criterion, yielded the best performance to differentiate cancer from sarcoidosis following a lesion-based approach. This model included 4 TLR radiomics features discretized with a fixed bin width of 0.05 SUV: 2 first-order gray-level statistics features (Stats\_min; Stats\_p10), 1 intensity volume histogram feature (IVH\_AIRV\_90), and 1 textural feature (GLCM\_infoCorr2). This model showed sensitivity of 0.92 (95% CI, 0.89–0.94), specificity of 0.80 (95% CI, 0.75–0.84), PPV of 0.88 (95% CI, 0.86–0.91), and NPV of 0.85 (95% CI, 0.81–0.89). For the test set, performance was excellent, with an AUC and AUCpr of 0.94 (95% CI, 0.93–0.95) and 0.96 (95% CI, 0.95–0.97), respectively, and was significantly better

than the best model with original radiomics (AUC, 0.68; and AUCpr, 0.78). The best patient-based radiomics models included TLR radiomics (intensity volume histogram, shape, and texture features), merged using their minimum values, and age of patients but showed poorer results than for differentiation by lesion, with an AUC and AUCpr of 0.85 (95% CI, 0.82–0.88) and 0.88 (95% CI, 0.84–0.92), respectively. For a decisional threshold of 0.5, sensitivity was 0.84 (95% CI, 0.78–0.90), specificity was 0.67 (95% CI, 0.56–0.76), PPV was 0.79 (95% CI, 0.74–0.84), and NPV was 0.74 (95% CI, 0.67–0.83), respectively. Supplemental Tables 3–6 show the selected features and results of the best original and TLR radiomics models for lesion-based and patient-based analysis.

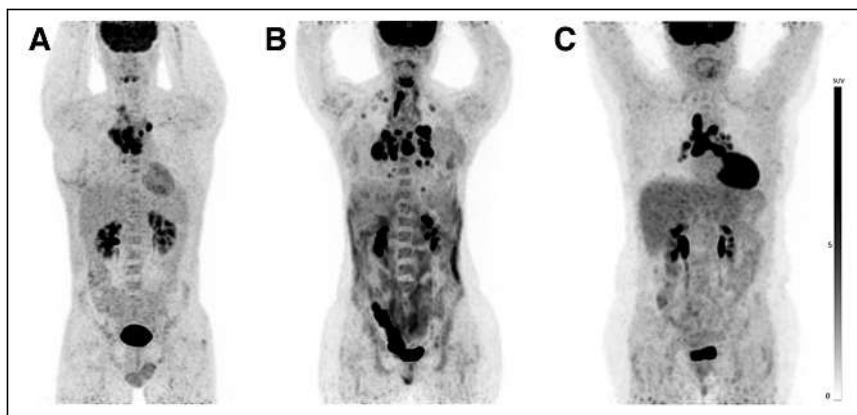


**FIGURE 2.** Representative examples of  $^{18}\text{F}$ -FDG PET/CT studies of diseases localized to thorax: DLBCL (A), HL (B), and sarcoidosis (C).

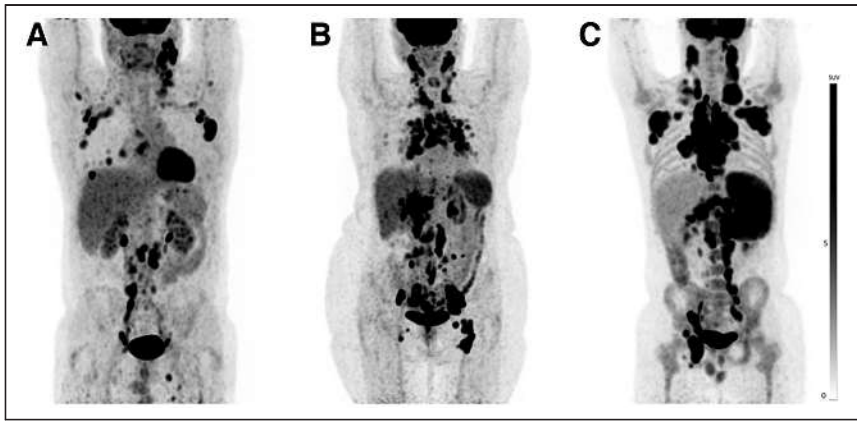


**FIGURE 3.** Representative examples of  $^{18}\text{F}$ -FDG PET/CT studies of diffuse diseases: DLBCL (A), sarcoidosis (B), and HL (C).

To differentiate HL from DLBCL, the lesion-based radiomics model with the best performance used the RF classifier (Gini impurity decrease) and comprised 2 TLR radiomics features discretized with a fixed bin width of 0.05 SUV: 1 first-order gray-level statistics features (Stats\_min) and 1 textural feature (GLCM\_infoCorr2). It showed sensitivity, specificity, PPV, and NPV of 0.89 (95% CI, 0.85–0.92), 0.88 (95% CI, 0.84–0.92), 0.87 (95% CI, 0.83–0.90), and 0.90 (95% CI, 0.87–0.92), respectively. For the test set, performance was excellent, with an AUC and AUCpr of 0.95 (95% CI, 0.93–0.96) and 0.95 (95% CI, 0.92–0.96), respectively, close to those of the validation set (AUC and AUCpr of 0.97, both) and significantly better than the best model with original radiomics (AUC, 0.67; and AUCpr, 0.62). The best patient-based radiomics models used a naive Bayes classifier and a forward MRMR with Pearson correlation for FS. The model included original radiomics features merged with their maximal values and discretized with a fixed bin width of 0.5 SUV (first-order, intensity volume histogram, and textural features: IH-entropy, IVH\_AIRV\_70, GLCM\_infoCorr1, NGLDM\_SM, and NGLDM\_DNN) and patient age. It showed very good performance, with an AUC and AUCpr of 0.86 (95% CI, 0.80–0.91) and 0.87 (95% CI, 0.78–0.91), respectively. For a decisional threshold of 0.5, this model showed sensitivity of 0.79 (95% CI, 0.71–0.86), specificity of 0.85 (95% CI, 0.73–0.86), PPV of 0.87 (95% CI, 0.79–0.89), and NPV of 0.76 (95% CI, 0.70–0.83), respectively.

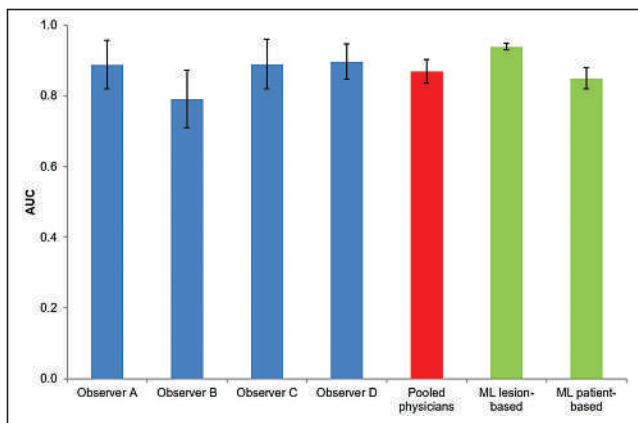


**FIGURE 4.** Chart illustrating performance of physician and ML-radiomics models for diagnosis of sarcoidosis vs. lymphoma. Vertical lines at top of each bar represent CIs.

from sarcoidosis (AUC, 0.85) and HL from DLBCL (AUC, 0.86), which were respectively equivalent and significantly better than human performance. All physicians showed an excellent sensitivity (0.97–1.00) to identify patients with cancer and a good but lower specificity (0.75). Overall, the global performance was good, with an AUC of 0.87. However, there was only moderate agreement among the observers, especially because of the poorer performance of the youngest observer (resident in training with 3 y of experience). Furthermore, the observers greatly varied in their level of certainty when deciding whether a PET/CT scan result was cancer or sarcoidosis. Interestingly enough, this level of certainty correlated significantly with performance; that is, higher confidence was associated with better performance. To differentiate HL from DLBCL, the overall performance of the physicians deteriorated, with an AUC of 0.70, which was related to moderate sensitivity. Again, large variability among observers was observed, with one of them performing significantly better than the others. However, the difference was unrelated to experience level, whereas there was a significant correlation with the degree of certainty. Observer D had a sample of diseases different from the other observers. Yet, the fact that he was not aware of this difference, and the fact that his performance in his subsample and in the interobserver variability analysis was unaffected, were reassuring as to any possible confounding effect on the obtained results.

The findings confirmed that radiomics analysis of the metabolic signal could effectively distinguish not only between inflammatory

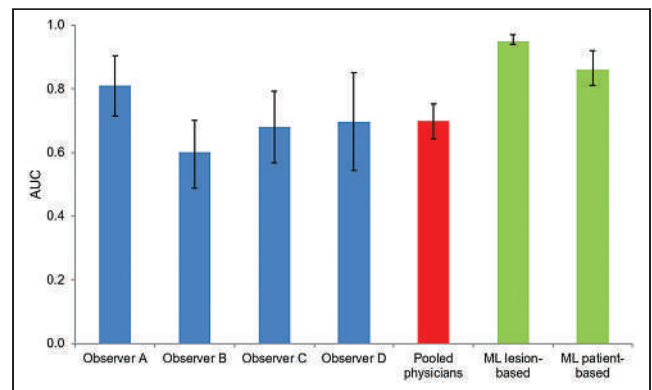


**FIGURE 5.** Chart illustrating performance of physicians and ML-radiomics models for diagnosis of HL vs. DLBCL. Vertical lines at top of each bar represent CIs.

## DISCUSSION

In cancer imaging,  $^{18}\text{F}$ -FDG PET/CT takes advantage of a high sensitivity, but the specificity is intrinsically limited by significant uptake by various inflammatory and infectious lesions. Obviously,  $^{18}\text{F}$ -FDG uptake alone cannot reliably identify the pathology of the tumor. In this study, we developed radiomics signatures to characterize lesions with highly increased  $^{18}\text{F}$ -FDG uptake, as a proof of concept of ML to differentiate inflammation from cancer and to differentiate 2 cancer types. At the lesion level, we found highly accurate signatures, with an AUC of 0.94 for the first task and 0.95 for the second one. At the patient level, we created models with very good performance to differentiate cancer

and neoplastic lesions (20–22) but also among different types of cancer (10,12,23–26). Regarding lymphomas, in a population of 25 patients, Lartizen et al. used  $^{18}\text{F}$ -FDG PET/CT radiomics and a support vector machine classifier to distinguish aggressive lymphoma lesions (B-cell lymphoma and HL) from nonlymphomatous uptake sites (e.g., brown fat, inflammation, infection, and physiologic thymic uptake) with an AUC of 0.91 (27). Lippi et al. reported that ML performed well in discriminating different types of lymphomas from one another, especially HL, but in a small population of patients (11). Recently, de Jesus et al. showed promising results in differentiating follicular lymphoma from DLBCL using radiomics and an ML classifier in a population of 120 patients—findings that might have important clinical use when monitoring for aggressive transformation (14). Their best performing model showed an AUC of 0.86, significantly higher than the performance of the  $\text{SUV}_{\text{max}}$ -based model (AUC, 0.79). In addition to the significant difference in population size and the differences in types of lymphoma, certain methodologic differences should be highlighted with our work, including the type of ML classifier (based on per-lesion only), the segmentation method, the choice of analyzed lesions, the absence of comparison with human performance, and the use of radiomics of PET and CT simultaneously. Beyond the proof of concept, our results may have clinical implications. Indeed, the high sensitivity of the model might avoid an invasive biopsy in patients with sarcoidosis, provided that these excellent results can be confirmed in a large and independent external population.

The performance of ML algorithms depends on several factors, including data size, randomness during learning, and preprocessing steps (28). We therefore tested a different set of models—a set that differs in the feature types, that is, original radiomics or TLR radiomics; the FS strategy and number of features; and the intensity discretization scheme. We have shown in previous studies that using the TLR as a reference organ improves the predictive performance in cervical cancer and the robustness across centers (16). The improvement in model performance might be because a normalizing effect of SUVs on each patient. In the present study, the TLR models systematically outperformed the original radiomics models in the lesion-based approach but not in the patient-based approach. Nevertheless, the performance of the models when using TLR features was close to that when using the original features, showing the high potential of TLR-based features in terms of applicability in different centers.

Even though the present study followed the guidelines of the Imaging Biomarkers Standardization Initiative and scored 56% according to the radiomics quality score (29), it had several limitations, including its retrospective and monocentric design, with the need for external validation within an independent population. It is possible that the performance of physicians in this study was underestimated in comparison to that in clinical routine because of the complete absence of clinical data. Moreover, the fact that the physicians were nuclear medicine specialists without specific training in radiology might potentially influence performance. Conversely, the performance of radiomics and ML might be improved by integrating more clinical data (e.g., sweating and weight loss) and biologic data, the localization of lesions (11), the CT or MRI radiomics (14,24,30), and a deep-learning approach (31). In our study, some VOIs were manually adapted if physiologic activity overflowed into a pathologic VOI. However, such occurrences were rare and were unlikely to result in biased results. Also, we excluded from the study the patients without any VOI generated by the automated segmentation process. Given that these patients represented only a

small part of the population ( $n = 12/448$  patients; 2.5%), it was unlikely that they would have affected the results. Finally, to show the validity, reproducibility, usefulness, and explainability of our results, we add a T.R.U.E. checklist in the supplemental materials.

## CONCLUSION

Characterization of sarcoidosis and lymphoma lesions using ML and radiomics is feasible as seen in their very good to excellent performance, proving to be equivalent to or better than that of physicians, who showed significant interobserver variability in their assessment.

## DISCLOSURE

This project received funding from the European Union's Horizon 2020 research and innovation program under Marie Skłodowska-Curie grant 766276. No other potential conflict of interest relevant to this article was reported.

## ACKNOWLEDGMENTS

We thank Dr. Adeline Deward from the GIGA scientific illustration service for designing the graphical abstract.

## KEY POINTS

**QUESTION:** Are specialists in medical imaging able to differentiate sarcoidosis from lymphoma on the basis of visual analysis of  $^{18}\text{F}$ -FDG PET/CT images, and can ML models using radiomics help them in this task?

**PERTINENT FINDINGS:** Physicians characterized these diseases with variable performance, from moderate to very good. ML and radiomics models achieved similar and better performance, in a more reproducible way.

**IMPLICATIONS FOR PATIENT CARE:** ML and radiomics models can differentiate sarcoidosis from lymphoma, making it possible to consider, after external validation, their use to avoid unnecessary biopsies in patients with high suspicion of sarcoidosis.

## REFERENCES

1. Li YJ, Zhang Y, Gao S, Bai RJ. Cervical and axillary lymph node sarcoidosis misdiagnosed as lymphoma on F-18 FDG PET-CT. *Clin Nucl Med.* 2007;32:262–264.
2. Koo HJ, Kim MY, Shin SY, et al. Evaluation of mediastinal lymph nodes in sarcoidosis, sarcoid reaction, and malignant lymph nodes using CT and FDG-PET/CT. *Medicine (Baltimore).* 2015;94:e1095.
3. Yu C, Xia X, Qin C, Sun X, Zhang Y, Lan X. Is SUVmax helpful in the differential diagnosis of enlarged mediastinal lymph nodes? A pilot study. *Contrast Media Mol Imaging.* 2018;2018:3417190.
4. Brady B, Kamel D, Kiely J, Hennessy B. Dual diagnosis of sarcoidosis and lymphoma. *Ir J Med Sci.* 2013;182:283–286.
5. Sanan P, Lu Y. Multiorgan involvement of chemotherapy-induced sarcoidosis mimicking progression of lymphoma on FDG PET/CT. *Clin Nucl Med.* 2017;42:702–703.
6. Bando-Delaunay A, Luporsi M, Huchet V, Cassou-Mounat T, Jehanno N. A case of sarcoidosis after lymphoma. *Clin Nucl Med.* 2019;44:646–647.
7. Cayci Z, Ozturk K, Ustun C, et al. Sarcoid-like histiocytic proliferations in patients with lymphoma can be FDG-avid concerning for refractory or recurrent disease. *Clin Lymphoma Myeloma Leuk.* 2019;19:e597–e601.
8. Lambin P, Rios-Velazquez E, Leijenaar R, et al. Radiomics: extracting more information from medical images using advanced feature analysis. *Eur J Cancer.* 2012;48:441–446.

9. Gillies RJ, Kinahan PE, Hricak H. Radiomics: images are more than pictures, they are data. *Radiology*. 2016;278:563–577.
10. Kong Z, Jiang C, Zhu R, et al. <sup>18</sup>F-FDG-PET-based radiomics features to distinguish primary central nervous system lymphoma from glioblastoma. *Neuroimage Clin*. 2019;23:101912.
11. Lippi M, Gianotti S, Fama A, et al. Texture analysis and multiple-instance learning for the classification of malignant lymphomas. *Comput Methods Programs Biomed*. 2020;185:105153.
12. Ou X, Zhang J, Wang J, et al. Radiomics based on <sup>18</sup>F-FDG PET/CT could differentiate breast carcinoma from breast lymphoma using machine-learning approach: a preliminary study. *Cancer Med*. 2020;9:496–506.
13. Zhu S, Xu H, Shen C, et al. Differential diagnostic ability of <sup>18</sup>F-FDG PET/CT radiomics features between renal cell carcinoma and renal lymphoma. *Q J Nucl Med Mol Imaging*. 2021;65:72–78.
14. de Jesus FM, Yin Y, Mantzorou-Kyriaki E, et al. Machine learning in the differentiation of follicular lymphoma from diffuse large B-cell lymphoma with radiomic [<sup>18</sup>F]FDG PET/CT features. *Eur J Nucl Med Mol Imaging*. 2022;49:1535–1543.
15. Manabe O, Ohira H, Hirata K, et al. Use of <sup>18</sup>F-FDG PET/CT texture analysis to diagnose cardiac sarcoidosis. *Eur J Nucl Med Mol Imaging*. 2019;46:1240–1247.
16. Ferreira M, Lovinfosse P, Hermesse J, et al. [<sup>18</sup>F]FDG PET radiomics to predict disease-free survival in cervical cancer: a multi-scanner/center study with external validation. *Eur J Nucl Med Mol Imaging*. 2021;48:3432–3443.
17. Buvat I, Orhac F. The T.R.U.E. checklist for identifying impactful artificial intelligence-based findings in nuclear medicine: Is it true? Is it reproducible? Is it useful? Is it explainable? *J Nucl Med*. 2021;62:752–754.
18. Rotondi MA, Donner A. A confidence interval approach to sample size estimation for interobserver agreement studies with multiple raters and outcomes. *J Clin Epidemiol*. 2012;65:778–784.
19. McHugh ML. Interrater reliability: the kappa statistic. *Biochem Med (Zagreb)*. 2012;22:276–282.
20. Du D, Gu J, Chen X, et al. Integration of PET/CT radiomics and semantic features for differentiation between active pulmonary tuberculosis and lung cancer. *Mol Imaging Biol*. 2021;23:287–298.
21. Hu Y, Zhao X, Zhang J, Han J, Dai M. Value of <sup>18</sup>F-FDG PET/CT radiomic features to distinguish solitary lung adenocarcinoma from tuberculosis. *Eur J Nucl Med Mol Imaging*. 2021;48:231–240.
22. Liu Z, Li M, Zuo C, et al. Radiomics model of dual-time 2-<sup>[18</sup>F]FDG PET/CT imaging to distinguish between pancreatic ductal adenocarcinoma and autoimmune pancreatitis. *Eur Radiol*. 2021;31:6983–6991.
23. Kirienko M, Cozzi L, Rossi A, et al. Ability of FDG PET and CT radiomics features to differentiate between primary and metastatic lung lesions. *Eur J Nucl Med Mol Imaging*. 2018;45:1649–1660.
24. Sibille L, Seifert R, Avramovic N, et al. <sup>18</sup>F-FDG PET/CT uptake classification in lymphoma and lung cancer by using deep convolutional neural networks. *Radiology*. 2020;294:445–452.
25. Ren C, Zhang J, Qi M, et al. Machine learning based on clinico-biological features integrated <sup>18</sup>F-FDG PET/CT radiomics for distinguishing squamous cell carcinoma from adenocarcinoma of lung. *Eur J Nucl Med Mol Imaging*. 2021;48:1538–1549.
26. Zhou Y, Ma XL, Zhang T, Wang J, Zhang T, Tian R. Use of radiomics based on <sup>18</sup>F-FDG PET/CT and machine learning methods to aid clinical decision-making in the classification of solitary pulmonary lesions: an innovative approach. *Eur J Nucl Med Mol Imaging*. 2021;48:2904–2913.
27. Lartizien C, Rogez M, Niaf E, Ricard F. Computer-aided staging of lymphoma patients with FDG PET/CT imaging based on textural information. *IEEE J Biomed Health Inform*. 2014;18:946–955.
28. Sarker IH. Machine learning: algorithms, real-world applications and research directions. *SN Comput Sci*. 2021;2:160.
29. Lambin P, Leijenaar RTH, Deist TM, et al. Radiomics: the bridge between medical imaging and personalized medicine. *Nat Rev Clin Oncol*. 2017;14:749–762.
30. Santos FS, Verma N, Marchiori E, et al. MRI-based differentiation between lymphoma and sarcoidosis in mediastinal lymph nodes. *J Bras Pneumol*. 2021;47:e20200055.
31. Aggarwal R, Sounderajah V, Martin G, et al. Diagnostic accuracy of deep learning in medical imaging: a systematic review and meta-analysis. *NPJ Digit Med*. 2021;4:65.

---

---

# Fully Automated, Semantic Segmentation of Whole-Body $^{18}\text{F}$ -FDG PET/CT Images Based on Data-Centric Artificial Intelligence

Lalith Kumar Shiyam Sundar\*<sup>1</sup>, Josef Yu\*<sup>1,2</sup>, Otto Muzik<sup>3</sup>, Oana C. Kulterer<sup>2</sup>, Barbara Fueger<sup>2</sup>, Daria Kifjak<sup>2,4</sup>, Thomas Nakuz<sup>2</sup>, Hyung Min Shin<sup>5</sup>, Annika Katharina Sima<sup>2</sup>, Daniela Kitzmantl<sup>2</sup>, Ramsey D. Badawi<sup>6</sup>, Lorenzo Nardo<sup>6</sup>, Simon R. Cherry<sup>6</sup>, Benjamin A. Spencer<sup>6</sup>, Marcus Hacker<sup>2</sup>, and Thomas Beyer<sup>1</sup>

<sup>1</sup>Quantitative Imaging and Medical Physics Team, Center for Medical Physics and Biomedical Engineering, Medical University of Vienna, Vienna, Austria; <sup>2</sup>Department of Biomedical Imaging and Image-Guided Therapy, Medical University of Vienna, Vienna, Austria; <sup>3</sup>Department of Pediatrics, Wayne State University School of Medicine, Children's Hospital of Michigan, Detroit, Michigan; <sup>4</sup>Department of Radiology, University of Massachusetts Chan Medical School/UMass Memorial Health Care, Worcester, Massachusetts; <sup>5</sup>Division of General Surgery, Department of Surgery, Medical University of Vienna, Vienna, Austria; and <sup>6</sup>Department of Biomedical Engineering and Radiology, University of California–Davis, Davis, California

We introduce multiple-organ objective segmentation (MOOSE) software that generates subject-specific, multiorgan segmentation using data-centric artificial intelligence principles to facilitate high-throughput systemic investigations of the human body via whole-body PET imaging. **Methods:** Image data from 2 PET/CT systems were used in training MOOSE. For noncerebral structures, 50 whole-body CT images were used, 30 of which were acquired from healthy controls (14 men and 16 women), and 20 datasets were acquired from oncology patients (14 men and 6 women). Noncerebral tissues consisted of 13 abdominal organs, 20 bone segments, subcutaneous fat, visceral fat, psoas muscle, and skeletal muscle. An expert panel manually segmented all noncerebral structures except for subcutaneous fat, visceral fat, and skeletal muscle, which were semiautomatically segmented using thresholding. A majority-voting algorithm was used to generate a reference-standard segmentation. From the 50 CT datasets, 40 were used for training and 10 for testing. For cerebral structures, 34  $^{18}\text{F}$ -FDG PET/MRI brain image volumes were used from 10 healthy controls (5 men and 5 women imaged twice) and 14 nonlesional epilepsy patients (7 men and 7 women). Only  $^{18}\text{F}$ -FDG PET images were considered for training: 24 and 10 of 34 volumes were used for training and testing, respectively. The Dice score coefficient (DSC) was used as the primary metric, and the average symmetric surface distance as a secondary metric, to evaluate the automated segmentation performance. **Results:** An excellent overlap between the reference labels and MOOSE-derived organ segmentations was observed: 92% of noncerebral tissues showed DSCs of more than 0.90, whereas a few organs exhibited lower DSCs (e.g., adrenal glands [0.72], pancreas [0.85], and bladder [0.86]). The median DSCs of brain subregions derived from PET images were lower. Only 29% of the brain segments had a median DSC of more than 0.90, whereas segmentation of 60% of regions yielded a median DSC of 0.80–0.89. The results of the average symmetric surface distance analysis demonstrated that the average distance between the reference standard and the automatically segmented tissue surfaces (organs, bones, and brain regions) lies within the size of image voxels (2 mm). **Conclusion:** The proposed segmentation pipeline allows automatic segmentation of 120 unique tissues from whole-body  $^{18}\text{F}$ -FDG PET/CT images with high accuracy.

**Key Words:** multiorgan segmentation; total-body PET; systems medicine; artificial neural networks; automated segmentation

**J Nucl Med 2022; 63:1941–1948**  
DOI: 10.2967/jnumed.122.264063

Living organisms maintain steady internal physiologic conditions through dynamic, self-regulating multiorgan systemic interactions (1), also known as homeostasis. In healthy subjects, any notable deviation from homeostasis is avoided with the aid of systemic feedback loops (2). Chronic pathologies are conceived as sustained disturbances in homeostasis for which systemic communications cannot compensate (3). Molecular imaging modalities, such as PET, can provide essential insights into diverse biologic processes within the human body by using highly specific radiotracers that track molecular function in vivo (4). Assuming that homeostasis is associated with a balanced, albeit variable, glycolytic pattern, PET can help characterize bespoke feedback loops and deviations that lead to pathologies. However, until recently, whole-body PET imaging protocols were typically limited to only a portion of the patient's body (e.g., neck to upper thigh) because of the relatively narrow axial field of view (15–25 cm) of PET systems. This limitation required multiple bed positions to be acquired sequentially to cover the axial field of investigation. Nonetheless, this acquisition mode failed to fully harness the multisystemic physiologic information provided by PET imaging (5).

With the recent advent of PET/CT systems with a large axial field of view (>70 cm) (6–8), the opportunity arose to acquire total-body PET images with only 1–2 bed positions, facilitating multiorgan system analysis. Such systemic analysis might allow the investigation of multiorgan interactions in various pathologies, such as those associated with cancer (9), cachexia (10,11), metabolic syndrome (12), or the more recent severe acute respiratory syndrome coronavirus 2 (13). However, the amount of data generated by this new generation of PET/CT systems is too large to be adequately analyzed without automated processing pipelines.

In response, we developed a multiple-organ objective segmentation (MOOSE) tool, an open-source software framework based on

---

Received Feb. 24, 2022; revision accepted May 16, 2022.  
For correspondence or reprints, contact Otto Muzik (otto@pet.wayne.edu).  
\*Contributed equally to this work.  
Published online Jun. 30, 2022.  
COPYRIGHT © 2022 by the Society of Nuclear Medicine and Molecular Imaging.

**TABLE 1**  
Institutional Review Boards and Approval Numbers for Various Datasets

Dataset	Acquisition system	Institutional review board	Reference number
34 <sup>18</sup> F-FDG PET/MR brain datasets	Biograph mMR; Siemens Healthineers	Medical University of Vienna	EK1960/2014
30 low-dose healthy control CT datasets	uEXPLORER; United Imaging Healthcare	University of California at Davis	I1341792-18
20 low-dose mixed pathologic Siemens CT datasets	Biograph mCT TruePoint TrueV; Siemens Healthineers	Medical University of Vienna	EK1649/2016
Three lymphoma datasets	Gemini GXL16; Philips	Protection des Personnes Sud-Est III, Hôpital Hotel-Dieu, Place de l'Hôpital	Etude REMARC reference no. 2009-006B; Eudract no. 2008-008202-52
Three mesothelioma datasets	Biograph mCT TruePoint TrueV; Siemens Healthineers	Medical University of Vienna	EK1649/2016

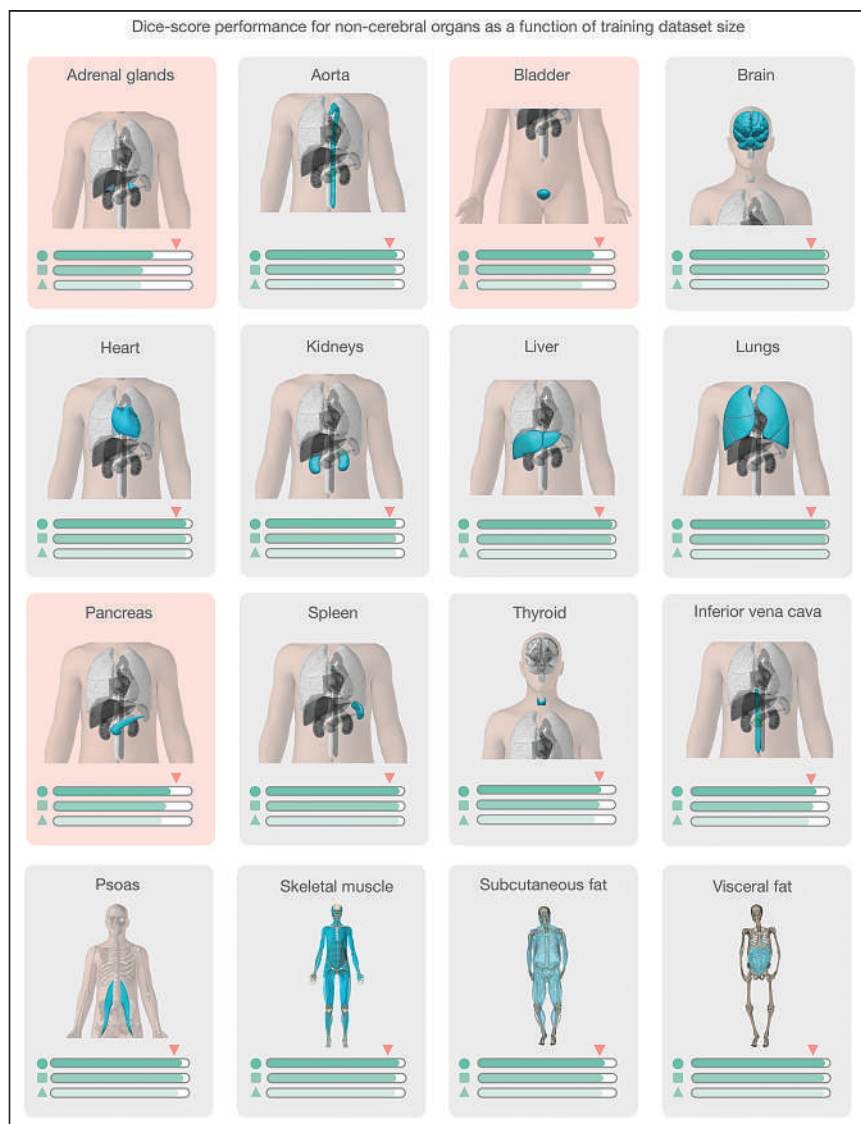


**FIGURE 1.** Median DSCs of abdominal organs (10 test datasets) were obtained from models based on 3 separate training subsets: D40 (circle), D20 (square), and D10 (triangle). Inverted triangle (pink) indicates 0.90 mark. Red background highlights organs characterized by low median DSCs (<0.90) and high SDs (Supplemental Fig. 4).

data-centric artificial intelligence (AI) principles (14) (Supplemental Fig. 1; supplemental materials are available at <http://jnm.snmjournals.org>) to allow fully automated generation of a subject-specific total-body <sup>18</sup>F-FDG PET/CT tissue map consisting of over 100 different tissue types. We named our software pipeline MOOSE120. MOOSE120 is free, open-source software. All codes related to MOOSE120 are available online, and all models for our application are publicly available. A complete description of the processing pipeline is available on our GitHub page (<https://github.com/QIMP-Team/MOOSE>). The development of such a software tool dramatically increases the amount of information that can be efficiently extracted from PET data. Further, such a tool provides a means to observe normal physiology and pathologic conditions globally, permitting systems-level investigations into human physiology. For example, when applied in a clinical setting, this approach will allow physicians to automatically generate a list of SUVs for all organs of interest, which might provide auxiliary information during the diagnostic process. In addition, the automated generation of a complete set of organ-specific SUVs lends itself well to AI-supported diagnostic screening, allowing organ SUV ratios to be compared across subjects and alerting the physician about potential secondary pathologies.

#### MATERIALS AND METHODS

All the data in this study were acquired in accordance with the Declaration of Helsinki. Written informed consent was obtained from all subjects before the examinations. Table 1 details the institutional review boards and approval numbers for the various datasets.

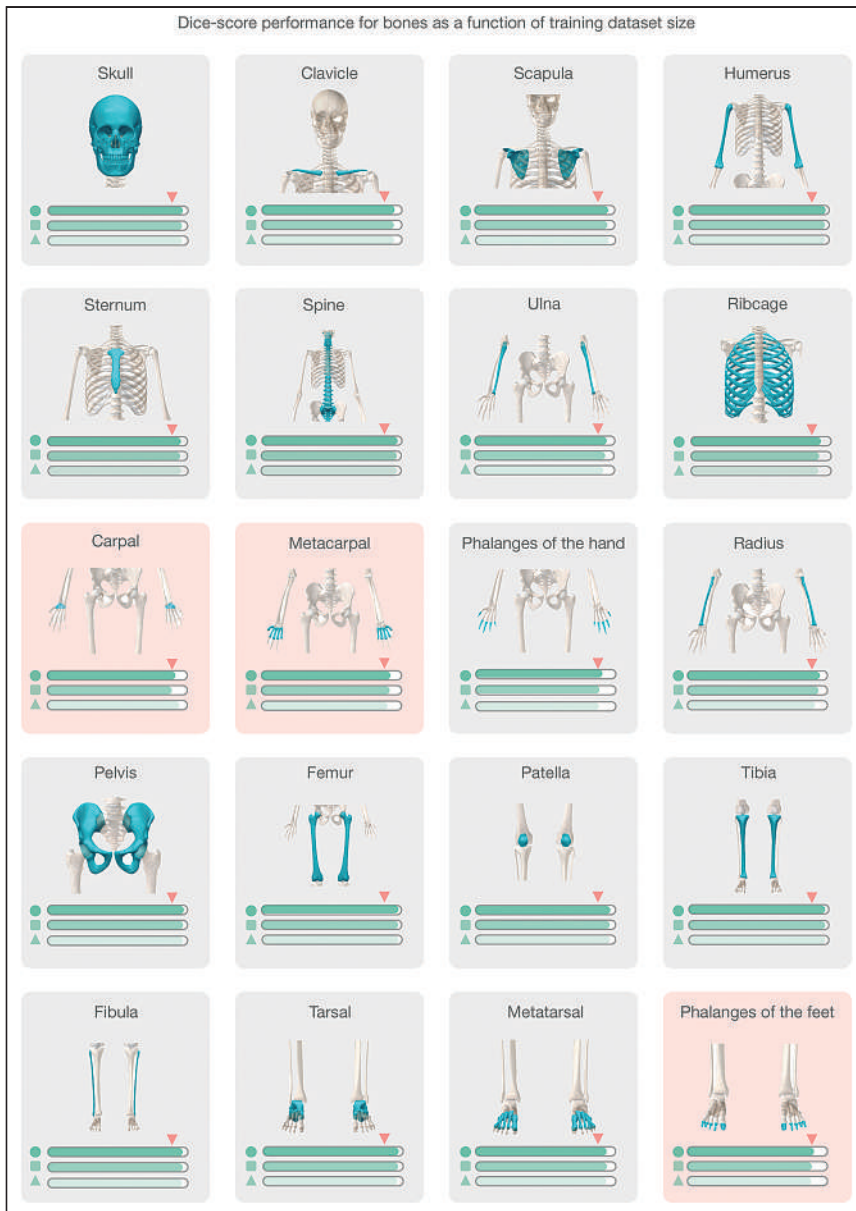


**FIGURE 2.** Median DSCs of bone structures (10 test datasets) as obtained from models based on 3 separate training subsets: D40 (circle), D20 (square), and D10 (triangle). Inverted triangle indicates 0.90 mark. Red background highlights bones characterized by low median DSCs ( $<0.90$ ).

### Overall Segmentation Strategy

Our approach is based on the latest state-of-the-art nnU-Net segmentation framework (15). More importantly, we propose a data-centric approach (14,16) in which the network model is fixed and the data are iteratively augmented to increase the performance of the AI system. As such, the model's performance is continuously monitored. As new data deviating from the training dataset's characteristics enter the processing stream, the model is retrained to enhance performance.

### Data

Two different types of datasets were used for the development of a software tool able to segment both cerebral (83 regions) and noncerebral (37 tissues) structures.

For training and evaluation of noncerebral structures, 50 whole-body low-dose CT datasets were used. Among these 50 datasets, 30 CT images were acquired from healthy volunteers (14 men and 16 women; mean

age  $\pm$  SD,  $47 \pm 13$  y) using the uEXPLORER (United Imaging Healthcare) total-body PET/CT system (17). The remaining 20 datasets belonged to a retrospective patient cohort from a TruePoint TrueView (Siemens Healthineers) PET/CT system (14 men and 6 women; mean age,  $67 \pm 12$  y). The noncerebral tissue atlas consists of 13 abdominal organs, 20 bone segments, subcutaneous fat, visceral fat, psoas muscle, and skeletal muscle (Supplemental Table 1; Supplemental Fig. 2).

An expert segmentation panel comprising 4 physicians and 4 medical students (final year) was responsible for the manual segmentation of all noncerebral structures, except for subcutaneous and visceral fat and skeletal muscle, which were outlined using an established thresholding method (18). The physicians were responsible for segmenting the abdominal organs and psoas muscle, whereas the students generated the bone segments. From the 50 datasets, 40 were used for training, and 10 were used for testing (hold-out dataset).

For training and evaluation of cerebral structures, we used 34  $^{18}\text{F}$ -FDG PET/MRI brain datasets (10 test-retest healthy controls [5 men and 5 women; mean age,  $27 \pm 7$  y] and 14 nonlesional epilepsy patients [7 men and 7 women; mean age,  $29 \pm 9$  y]) (19,20). The cerebral atlas consisted of 83 brain subregions (Supplemental Table 1) automatically created from PET data in combination with T1-weighted MR images and the Hamman-Smith atlas (21). In short, subject-specific T1-weighted MR images were normalized to Montreal Neurological Institute space using SPM 12 (22). The obtained (inverse) transform was then used to spatially transform brain regions of the Hamman-Smith atlas into the individual subject's native space, yielding 83 subject-specific cerebral subregions, which were transferred to coregistered PET image volumes. Of the 34 datasets, 24 and 10 were used for training and testing, respectively.

### Reference Standard Generation

To address intervariability issues in organ segmentation, the simultaneous truth and performance level estimation (STAPLE) algorithm (23) was used to generate reference volumes for further performance assessment. Each reference volume represents a probabilistic estimate of the true segmentation as well as a measure of multioperator segmentation performance (STAPLE variance). The STAPLE method was not used for reference segmentations derived using automatic (brain atlas) or semi-automatic (thresholding) methods.

### U-Net-Based Semantic Segmentation

The nnU-Net implementation of the generic U-Net architecture is a self-configuring method for deep learning-based biomedical image segmentation. This implementation exhibits strong performance by retaining the original U-Netlike architecture while automating the complex process of manual hyperparameter configuration (15).

In our implementation, the nnU-Net was trained separately for the following 4 structure classes: 13 abdominal organs and psoas muscle,

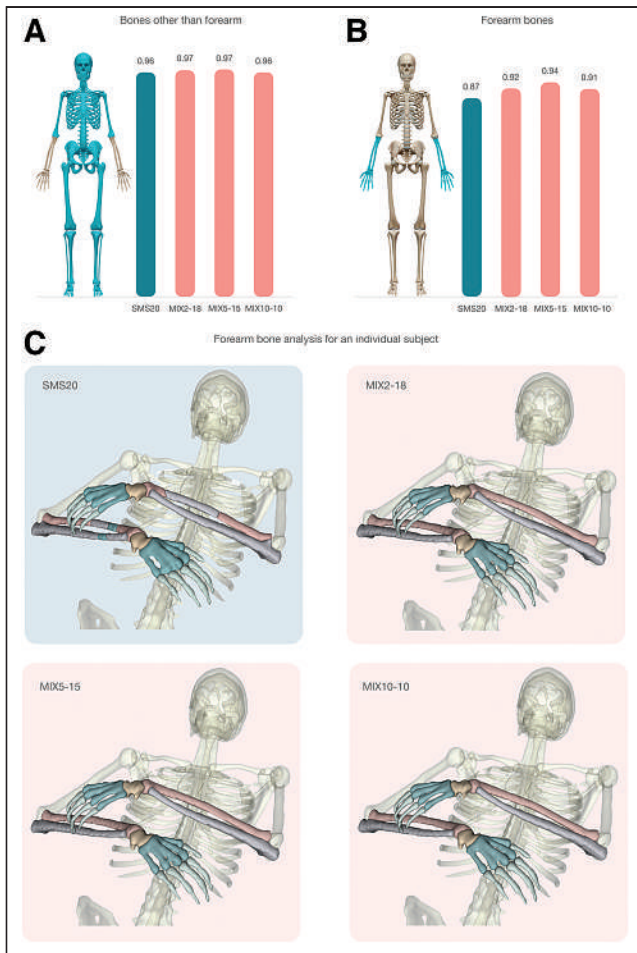


**FIGURE 3.** (A) Bar graph demonstrating similar performance of different models for bone segmentation other than forearm bones. Green bar depicts homogeneous training dataset (SMS-20), whereas mixed training datasets (MIX2-18, MIX5-15, and MIX10-10) are represented by red bars. (B) Bar graph showing segmentation performance of forearm bones. Significant performance improvement is seen in mixed training datasets (red bars) compared with homogeneous training dataset (green bar). (C) Forearm bone analysis of individual subject. Images demonstrate that forearm bones are incorrectly segmented in case of SMS20 (green background) model, whereas all mixed models accurately segmented forearm bones (red background).

20 bone structures, 83 brain regions, and fat (subcutaneous and visceral) and skeletal muscle. Noncerebral tissues were segmented using CT data, whereas cerebral regions were segmented using  $^{18}\text{F}$ -FDG PET images.

#### Assessment of Deviation from Training Dataset Distribution

It is unlikely that any training dataset will be sufficient to fully capture the variability encountered in clinical routine. Accordingly, a data-centric approach is necessary, permitting continuous monitoring of segmentation performance so that data that substantially deviate from the original training data distribution (i.e., out-of-distribution [OOD] data) are detected. Erroneous segmentation results obtained for such data will then require manual correction by a human expert. Once corrected, these data can be appended in suitable quantities to the initial training dataset for retraining purposes.

Since continuous operator-based monitoring of segmentation performance is untenable in clinical routine, we developed an automated error analysis routine that detects OOD datasets on the basis of morphometric analysis of organ shapes (e.g., elongation, volume, area, and maximum

and minimum bounding box diameter), which were determined for each STAPLE-derived segmentation of structures, and a normative morphologic feature database was generated. On segmentation of a new dataset, morphologic features for each segmented structure were calculated and compared with the normative morphology database, yielding a distance ( $z$  score) in similarity space for each structure. The  $z$  score reflects the difference between the shapes of the segmented structure in comparison to its normative value obtained from the training datasets. In our implementation, we chose a  $z$  score of 1.5 as the cutoff for OOD labeling.

#### Algorithm Performance Versus Training Sample Size

A primary performance assessment of the MOOSE automated segmentation was performed for all structures using the Dice score coefficient (DSC) (24). A DSC of 1.0 with respect to STAPLE indicates perfect overlap, and 0 indicates no overlap. In addition, the average symmetric surface distance (ASSD) (25) was used as a secondary metric, representing the average distance (in mm) between surface voxels of the standard and the automated segmentation.

To assess the segmentation performance as a function of training sample size, we calculated for each noncerebral structure the DSC and the ASSD using the segmented volumes derived using 10 (D10), 20 (D20), and 40 (D40) training datasets, respectively. A similar analysis was performed for cerebral regions with 8, 16, and 24 datasets. In both instances, cases were randomly selected from the whole datasets (50 cases for noncerebral structures and 34 cases for cerebral structures). The testing (hold-out) dataset included 10 cases that were not part of the training sets in both instances.

#### Algorithm Performance Versus Training Dataset Variability

To investigate the effect of training dataset variability on segmentation performance, we performed a series of training and test runs using various mixtures of 2 datasets that differed significantly with respect to arm position (either arms down or arms crossed on chest, Supplemental Fig. 3). We created 4 subsets of training datasets, each with a total sample size of 20. The first dataset consisted of 20 low-dose CT images with arms down (SMS20). The other 3 training datasets included mixtures of images: MIX2-18 (18 arms down, 2 crossed), MIX5-15 (15 arms down, 5 crossed), and MIX10-10 (10 arms down, 10 crossed). Networks trained on these 4 training datasets were then used to segment 10 test datasets that included only images with crossed arm positions (X10). The following 4 (training test) scenarios were investigated: SMS20→X10, MIX2-18→X10, MIX5-15→X10, and MIX10-10→X10. Segmentation results were assessed separately for bone structures of the arm (radius, ulna, carpal, metacarpal, and fingers) and for all other bone structures (that did not differ positionally). This analysis provided information on the necessary variability in the training dataset required to segment OOD data accurately.

#### Algorithm Performance for Clinical OOD Datasets

We applied the trained network to 2 small pathologic cohorts that were not part of the initial training set: 3 lymphoma cases and 3 mesothelioma lung cancer cases. The intent was to assess the performance of MOOSE on clinical datasets that differ significantly from the training data distribution. Evaluation of the segmentation quality was based on similarity space analysis ( $z$  scores). OOD datasets with incorrect segmentations were manually corrected, and the corrected segmentations were then appended to the original training datasets for retraining purposes.

#### Statistical Assessment

A paired  $t$  test was applied to determine whether DSCs differed significantly between the various training sample sizes and to investigate the effect of training dataset variability (either fully OOD or mixed) on DSCs. In addition, a correlation analysis (Pearson  $\rho$ ) was performed to investigate the relationship between STAPLE variance and

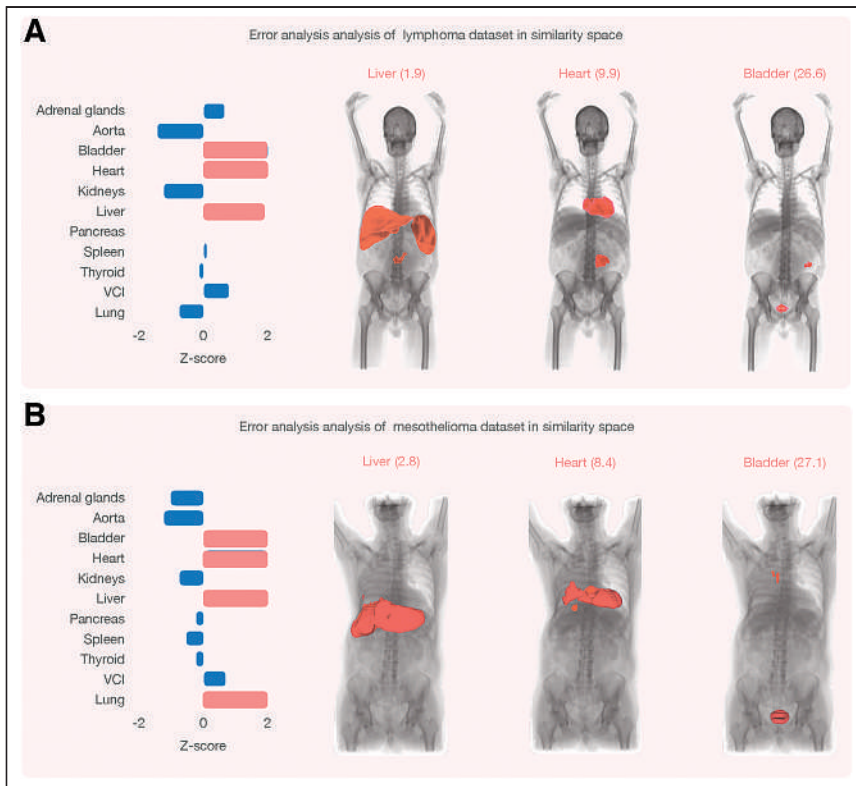


**FIGURE 4.** (A) Error analysis in similarity space for representative lymphoma patient. Horizontal bars depict distance in similarity space, with blue bars characterizing organs with z score of  $<1.5$ . Figure shows z scores of  $>1.5$  for liver, kidneys, and bladder (red bars). Corresponding organ segmentations are displayed to right for liver ( $z = 1.9$ ) and heart ( $z = 9.9$ ), indicating suboptimal segmentation results that require manual correction. (B) Error analysis in similarity space for representative mesothelioma patient with z scores of  $>1.5$  for liver, heart, bladder, and lung. Incorrect organ segmentations are shown to right for liver ( $z = 2.8$ ) and heart ( $z = 8.4$ ). VCI = vena cava inferior.

the DSCs associated with the best (D40) training sample size. A similar analysis was also performed using the ASSD metric.

### Software Tool Implementation

Our processing pipeline is based on the Python and C++ programming languages, with the nnU-Net framework representing the segmentation backbone, built using PyTorch, version 1.6.031 (26). Similarity space was implemented using the morphometric capabilities of SimpleITK, version 2.1.0 (27), and erroneous segmentation results were cleaned manually using 3D Slicer, version 4.11.20210226 (28).

## RESULTS

### Effect of Training Data Size on Segmentation Performance

Most noncerebral tissues (81%) were segmented with high accuracy ( $DSC > 0.90$ ), as seen from Figure 1. DSC analysis generally showed an excellent overlap between STAPLE-derived reference and organ segmentations based on D10, D20, and D40. This excellent overlap was confirmed through ASSD analysis, yielding average distances of  $1.40 \pm 1.29$ ,  $1.05 \pm 1.26$ , and  $0.68 \pm 0.52$  mm for D10, D20, and D40, respectively. However, the performance of the automated segmentation was suboptimal for a small group of organs (Fig. 1), with low median DSCs and high SDs (Supplemental Fig. 4A), such as the adrenal glands ( $DSC, 0.72$ ), pancreas ( $DSC, 0.85$ ), and bladder ( $DSC, 0.86$ ). Subsequent correlation analysis of the STAPLE variance and the DSCs derived from the D40 training set is shown in Supplemental Figure 4B. The graph indicates an overall

highly significant negative correlation ( $\rho = -0.79$ ,  $P = 0.002$ ), with the 3 identified regions showing high STAPLE variance. This significant correlation with the STAPLE variance was also reproduced using the ASSD metric ( $\rho = 0.60$ ,  $P = 0.042$ ; Supplemental Fig. 5), indicating that accurate segmentation of this subset of regions is challenging even for human experts.

The segmentation performance for bone structures was similar to that for the abdominal organs (Fig. 2). Again, one notes an excellent overlap between the reference structure volumes and those obtained using the automated segmentation based on D10, D20, and D40 (ASSDs of  $1.63 \pm 3.01$ ,  $1.61 \pm 3.14$ , and  $0.83 \pm 0.76$  mm, respectively), except for a small number of bone structures with either low mean DSCs or high SDs (Supplemental Fig. 6). These structures were the carpal bones, metacarpal bones, and phalanges of the toes. Removal of these organs resulted in a similar segmentation performance between D20 and D40 ( $P = 0.07$ ), with segmentation based on D10 remaining significantly worse than D20 ( $P = 0.016$ ) and D40 ( $P = 0.010$ ).

Although the median DSCs of brain subregions derived from PET images were relatively low (only 29% of brain segments had median DSCs  $> 0.90$ ; Supplemental Fig. 7), ASSDs showed subvoxel differences between the template regions and the automated segmentation, with similar performance across the D10 ( $0.52 \pm$

$0.35$  mm), D20 ( $0.53 \pm 0.41$  mm), and D40 ( $0.46 \pm 0.27$  mm) datasets.

### Effect of Training Dataset Variability on Segmentation Performance

The results of dataset variability analysis are shown in Figure 3. The figure indicates that segmentation of structures that substantially deviate from the expected position in the training datasets was suboptimal. However, by including at least 2 cases that match the deviant position to the training dataset, performance improved significantly. Specifically, DSCs for bones of the arm were significantly lower for the fully OOD scenario (SMS20 $\rightarrow$ X10) ( $DSC, 0.87 \pm 0.12$ ) than for the 3 scenarios that included 10% (MIX2-18 $\rightarrow$ X10) ( $DSC, 0.92 \pm 0.06$ ;  $P = 0.04$ ), 25% (MIX5-15 $\rightarrow$ X10) ( $DSC, 0.940 \pm 0.003$ ;  $P = 0.01$ ), and 50% (MIX10-10 $\rightarrow$ X10) ( $DSC, 0.91 \pm 0.04$ ;  $P = 0.04$ ) of cases that matched the deviant position. In addition, the coefficient of variation for DSCs derived from the 3 mixed training datasets was significantly lower (6.6% [ $P = 0.01$ ], 3.3% [ $P = 0.03$ ], and 4.3% [ $P = 0.01$ ]) than that for DSCs derived from the fully OOD training dataset (13.5%). In comparison, the performance of all 4 scenarios for bone structures that were matched in position between the training and test datasets was similar, with DSCs of more than 0.95 (Fig. 3).

### Detection of OOD Segmentation Errors

Application of similarity space analysis identified segmentation errors in clinical datasets that included various anatomic pathologies, representing OOD datasets for specific organs. This was clearly

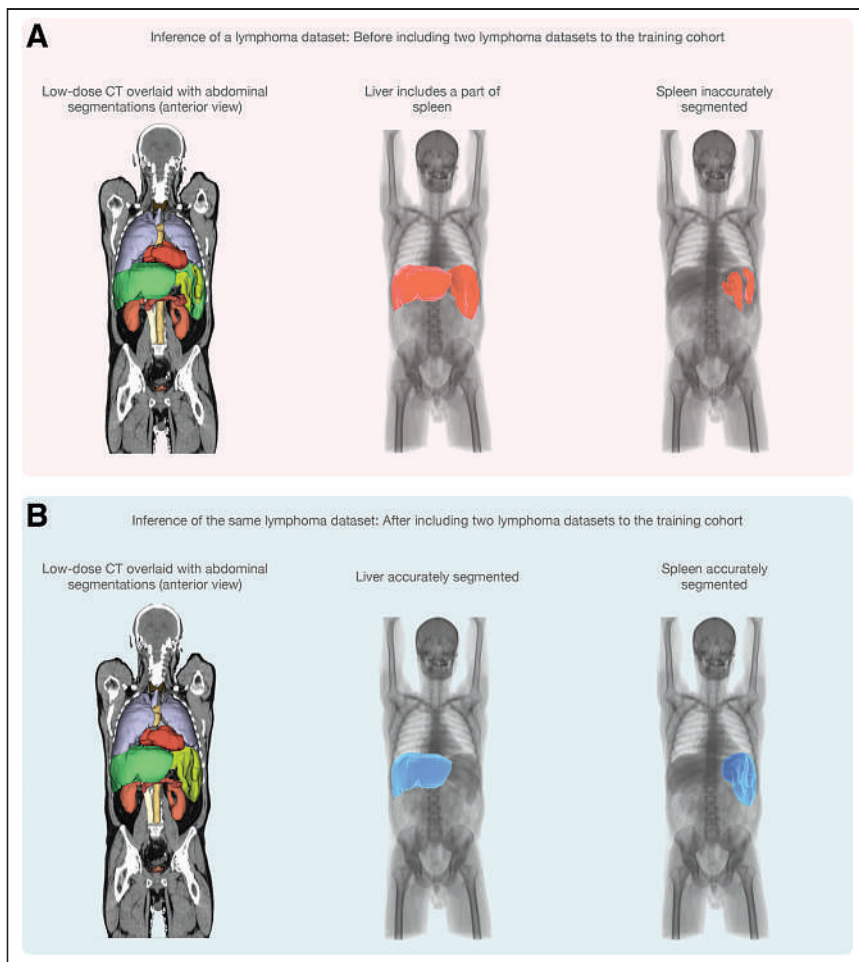


**FIGURE 5.** (A) Organ segmentation of hold-out lymphoma test dataset using training dataset that did not include splenomegaly cases. (B) Organ segmentation of same patient after inclusion of 2 (different) lymphoma datasets and model retraining using expanded training dataset. Updated model was able to recognize new image pattern, resulting in correct segmentation of both liver and spleen.

demonstrated by applying the initially trained neural network to 2 distinct OOD datasets (lymphoma and mesothelioma) that were not part of the initial training set. Specifically, all lymphoma patients presented with splenomegaly, which led to its incorrect classification as a liver and spleen (Fig. 4A). After manual correction (time required, ~3 min per case), we appended 2 corrected datasets to the original training set to retrain the neural network. The retrained neural network correctly segmented the abnormally enlarged spleen in the third lymphoma patient, which was used as a hold-out dataset (Fig. 5).

Similarly, the large tumor mass in the lungs of mesothelioma patients was incorrectly classified as part of the liver, heart, and bladder (Fig. 4B). Again, similarity space analysis identified the incorrect segmentation and labeled the dataset as representing an OOD image pattern (Fig. 6A). After manual correction of 2 of 3 patients, these 2 cases were again appended to the training dataset, and the neural network was retrained using the extended training set. Once again, we determined an improvement in the segmentation performance of the third (uncorrected) dataset (Fig. 6).

## DISCUSSION

Hybrid molecular imaging modalities such as  $^{18}\text{F}$ -FDG PET/CT allow the investigation of multiorgan systemic interactions through

which living organisms maintain homeostasis and allostasis. The resulting images are not mere pictures—they represent a rich pallet of multidimensional data (29). By systemically parcellating these datasets into respective organ and tissue classes, one can, in theory, study system-level interactions in detail between the various homeostatic and allostatic networks, allowing a better understanding of pathologic abnormalities in vivo. Nevertheless, manual segmentation of various tissues in the human body is not tenable, either in research applications or in clinical routine.

To bridge this gap, we developed a fully automated segmentation pipeline, MOOSE, that allows the creation of subject-specific multitissue  $^{18}\text{F}$ -FDG PET/CT atlases (Supplemental Fig. 2). These tissue maps enable the extraction of subject-specific functional information from molecular imaging data with minimal additional effort for further analysis. We based the segmentation pipeline on the latest state-of-the-art nnU-Net architecture (15) and demonstrated that robust training of the convolutional neural network could be achieved with as few as 20 datasets, provided that sufficient variability in the training dataset is present. In addition, our results support the concept of data-centric AI, which focuses primarily on data quality rather than quantity.

In general, MOOSE performed reasonably well in segmenting most of the noncerebral tissues while exhibiting poorer segmentation performance on selected organs such as thyroid, adrenal gland, and bladder. Our correlation analysis revealed a significant negative correlation between the STAPLE variance and the DSCs derived from the D40 training set (Supplemental Fig. 4B). This result suggests that, because of a combination of small organ size, low contrast, and increased noise levels present in low-dose CT images, accurate segmentation of bespoke structures is challenging even for human experts.

## AI, PET Imaging, and Systems Biology

The ultimate objective of the developed multiorgan and tissue segmentation methodology is to promote the concept of whole-person research (30) and systems biomedicine (31) through whole-body  $^{18}\text{F}$ -FDG PET/CT imaging. With the advent of PET/CT systems that have a large axial field of view, most or all organs can be simultaneously imaged, therefore allowing an improved evaluation of interactions between organs in both healthy and diseased states. We envision that through automated extraction of rich physiologic information inherent in PET/CT data (e.g., organ SUVs), disease-specific metabolic fingerprints can be derived that uniquely characterize diverse pathologies affecting system-level organ interaction (Supplemental Fig. 8). Such an analysis might uncover metabolic dependencies among sets of organs and provide novel insights into metabolic pathway dysregulation associated with disease progression. Moreover, given the fact that noncerebral tissues

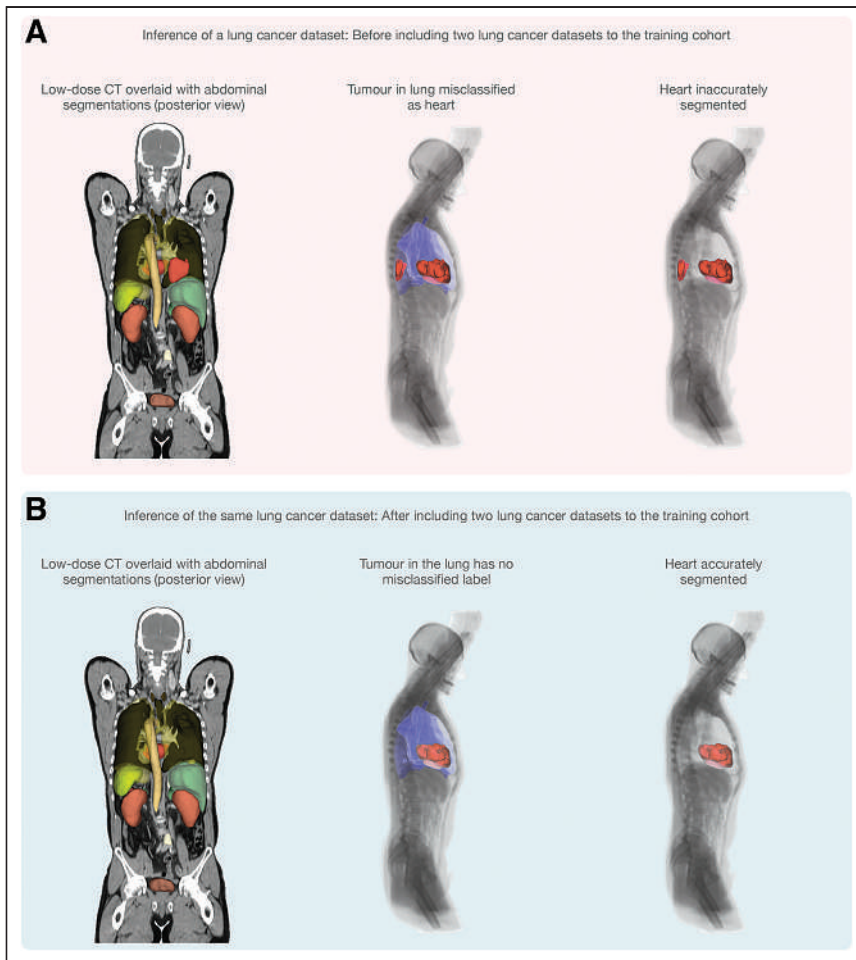


**FIGURE 6.** (A) Organ segmentation of hold-out mesothelioma test dataset using training dataset that did not include mesothelioma cases. (B) Organ segmentation of same patient after inclusion of 2 (different) mesothelioma datasets and model retraining using expanded training dataset. Updated model recognized new image pattern, resulting in correct segmentation of heart.

are segmented directly from CT data, this technique is insensitive to variations in PET tracer uptake patterns, thus allowing the study of diverse system-level functional processes using a multitude of function-specific radiotracers.

#### Training of Neural Networks Using Sparse Datasets

It is commonly assumed that the performance of a neural network increases with the size of the training set. Therefore, most non-health-care image classification applications are trained on vast numbers of training cases (e.g., ImageNet (32)). However, creating large training datasets in the medical field is problematic, as manual curation of medical images is highly time-consuming and heavily dependent on domain-specific human expert knowledge. In this study, 50 medical image datasets were manually segmented (into 120 objects for each dataset) by medical professionals. This process required significant personal effort by each expert and took several months to complete. Such an effort cannot be expected to be repeated numerous times when additional silos of data (possibly with a different distribution) become available.

In recognition of this methodologic constraint, we investigated the effect of both training sample size and training sample variability on segmentation performance. Our results demonstrate that

segmentation performance is dependent primarily on whether the training dataset allows the correct identification of several unique image patterns, each characterized by a mean spatial pattern and the associated variance (Figs. 4–6). This insight also explains why more cases are usually preferred, as it is likely that a greater number of unique image patterns can be captured using a larger dataset. However, the number of images needed per unique pattern is not evident. Our results suggest that accurate segmentation of abnormal image patterns is viable, provided that the training data include a small number (2–4) of cases that establish a distinct image pattern with the associated morphologic variance.

#### A Data-Centric Approach to Segmentation

Over the long run, any clinically viable medical image segmentation method will require a system in which incoming data are constantly used to adjust model parameters to accommodate changing data distributions. To meet this requirement, the implemented data-centric approach executes 2 operations: first, it actively monitors segmentation performance followed by the users' input to correct the erroneous segmentation, and second, it periodically updates model parameters through retraining of the neural network using an updated training set (which includes the manually corrected OOD data).

In particular, segmentation performance is continuously monitored in similarity space, and feedback on segmentation accuracy is provided to the physician in the form of tissue-specific  $z$  scores that signal potential deviations from tissue shape and position in the normative training data distribution. On the basis of this analysis, all tissues that are judged to be OOD ( $z > 1.5$ ) are flagged, and the physician is prompted for corrective action. This approach ensures adequate segmentation of all tissues present in abnormal datasets and provides important curated data for future retraining of the neural network. Moreover, this strategy addresses potential segmentation problems right when they occur in the processing pipeline, when corrective actions can be performed most efficiently and with the least effort.

The presented segmentation framework bears its challenges. First, this methodology mandates a high-performance workstation, which might be cost-prohibitive. Our network training was performed on a dedicated server (Intel Xeon Silver 4216 central processing unit running at 2.10 GHz, 32 central processing unit cores, 256 GB of random-access memory, and a single Nvidia GeForce graphics processing unit), allowing the generation of a single total-body  $^{18}\text{F}$ FDG PET/CT tissue-map from an individual whole-body PET/CT dataset in about 30 min. Moreover, once OOD datasets are collected, the neural network needs to be retrained, which took approximately 2 d to complete using the above server configuration. Finally, there is some unavoidable subjectivity in identifying

OOD datasets, as the cutoff defining OOD data is based on heuristics.

## CONCLUSION

We present here a fully automated, data-centric segmentation pipeline for the creation of a total-body  $^{18}\text{F}$ -FDG PET/CT tissue map. The generated map is modular and consists of 120 tissues and bone structures, enabling the automated extraction of image information for both cerebral and noncerebral regions, potentially providing added information about secondary abnormalities during the diagnostic process.

## DISCLOSURE

This work was supported in part by National Institutes of Health research grant R01CA29422 and the IBM University Cloud Award. No other potential conflict of interest relevant to this article was reported.

## ACKNOWLEDGMENTS

We thank Jakub Gawrylkowicz and Sebastian Gutschmayer for their support in packaging the software, Clemens Spielvogel for helpful discussions throughout the project, Kilian Kluge for organizing the mesothelioma datasets, and Irene Buvat for providing the lymphoma datasets to verify our hypothesis.

## KEY POINTS

**QUESTION:** How can we efficiently extract diagnostic information from whole-body  $^{18}\text{F}$ -FDG PET/CT data?

**PERTINENT FINDINGS:** Our automated approach to multiorgan segmentation of whole-body  $^{18}\text{F}$ -FDG PET data builds on the nnU-Net methodology driven by data-centric principles and supports accurate segmentation of 37 extracerebral and 83 cerebral regions. Over 92% of the noncerebral tissues were segmented with a DSC of more than 0.90, whereas 89% of the cerebral areas had a DSC of more than 0.80.

**IMPLICATIONS FOR PATIENT CARE:** The developed software tool increases the amount of information extracted from standard, whole-body PET/CT datasets and provides a means to perform system-level investigations into human physiology.

## REFERENCES

1. Cannon WB. The wisdom of the body. *Am J Med Sci.* 1932;184:864.
2. Goodman L. Regulation and control in physiological systems: 1960-1980. *Ann Biomed Eng.* 1980;8:281-290.
3. Billman GE. Homeostasis: the underappreciated and far too often ignored central organizing principle of physiology. *Front Physiol.* 2020;11:200.
4. Lammertsma AA. Forward to the past: the case for quantitative PET imaging. *J Nucl Med.* 2017;58:1019-1024.
5. Cherry SR, Badawi RD, Karp JS, Moses WW, Price P, Jones T. Total-body imaging: transforming the role of positron emission tomography. *Sci Transl Med.* 2017;9:eaaf6169.
6. Karp JS, Viswanath V, Geagan MJ, et al. PennPET Explorer: design and preliminary performance of a whole-body imager. *J Nucl Med.* 2020;61:136-143.
7. Spencer BA, Berg E, Schmall JP, et al. Performance evaluation of the uEXPLORER total-body PET/CT scanner based on NEMA NU 2-2018 with additional tests to characterize PET scanners with a long axial field of view. *J Nucl Med.* 2021;62:861-870.
8. Prenosil GA, Sari H, Fürstner M, et al. Performance characteristics of the Biograph Vision Quadra PET/CT system with a long axial field of view using the NEMA NU 2-2018 standard. *J Nucl Med.* 2022;63:476-484.
9. Zhu L, Finkelstein D, Gao C, et al. Multi-organ mapping of cancer risk. *Cell.* 2016;166:1132-1146.e7.
10. Penet M-F, Winnard PT Jr, Jacobs MA, Bhujwala ZM. Understanding cancer-induced cachexia: imaging the flame and its fuel. *Curr Opin Support Palliat Care.* 2011;5:327-333.
11. Argilés JM, Busquets S, Stemmler B, López-Soriano FJ. Cancer cachexia: understanding the molecular basis. *Nat Rev Cancer.* 2014;14:754-762.
12. Priest C, Tontonoz P. Inter-organ cross-talk in metabolic syndrome. *Nat Metab.* 2019;1:1177-1188.
13. Gupta A, Madhavan MV, Sehgal K, et al. Extrapulmonary manifestations of COVID-19. *Nat Med.* 2020;26:1017-1032.
14. Wu A. A chat with Andrew on MLOps: from model-centric to data-centric AI. YouTube website. <https://www.youtube.com/watch?v=06-AZXmwHjo>. Published March 24, 2021. Accessed August 18, 2022.
15. Isensee F, Jaeger PF, Kohl SAA, Petersen J, Maier-Hein KH. nnU-Net: a self-configuring method for deep learning-based biomedical image segmentation. *Nat Methods.* 2021;18:203-211.
16. Motamedi M, Sakharykh N, Kaldewey T. A data-centric approach for training deep neural networks with less data. arXiv website. <https://arxiv.org/abs/2110.03613>. Published October 7, 2021. Revised October 29, 2021. Accessed August 18, 2022.
17. Badawi RD, Shi H, Hu P, et al. First human imaging studies with the EXPLORER total-body PET scanner. *J Nucl Med.* 2019;60:299-303.
18. Weston AD, Korfiatis P, Kline TL, et al. Automated abdominal segmentation of CT scans for body composition analysis using deep learning. *Radiology.* 2019;290:669-679.
19. Traub-Weidinger T, Muzik O, Sundar LKS, et al. Utility of absolute quantification in non-lesional extratemporal lobe epilepsy using FDG PET/MR imaging. *Front Neurol.* 2020;11:54.
20. Shiyam Sundar LK, Muzik O, Rischka L, et al. Promise of fully integrated PET/MRI: noninvasive clinical quantification of cerebral glucose metabolism. *J Nucl Med.* 2020;61:276-284.
21. Hammers A, Allom R, Koeppe MJ, et al. Three-dimensional maximum probability atlas of the human brain, with particular reference to the temporal lobe. *Hum Brain Mapp.* 2003;19:224-247.
22. Ashburner J. SPM: a history. *Neuroimage.* 2012;62:791-800.
23. Warfield SK, Zou KH, Wells WM. Simultaneous truth and performance level estimation (STAPLE): an algorithm for the validation of image segmentation. *IEEE Trans Med Imaging.* 2004;23:903-921.
24. Dice LR. Measures of the amount of ecologic association between species. *Ecology.* 1945;26:297-302.
25. Yeghiazaryan V, Voiculescu I. Family of boundary overlap metrics for the evaluation of medical image segmentation. *J Med Imaging (Bellingham).* 2018;5:015006.
26. Paszke A, Gross S, Massa F, et al. PyTorch: an imperative style, high-performance deep learning library. arXiv website. <https://arxiv.org/abs/1912.01703>. Published December 3, 2019. Accessed August 18, 2022.
27. Lowekamp BC, Chen DT, Ibáñez L, Blezek D. The design of SimpleITK. *Front Neuroinform.* 2013;7:45.
28. Fedorov A, Beichel R, Kalpathy-Cramer J, et al. 3D Slicer as an image computing platform for the Quantitative Imaging Network. *Magn Reson Imaging.* 2012;30:1323-1341.
29. Gillies RJ, Kinahan PE, Hricak H. Radiomics: images are more than pictures, they are data. *Radiology.* 2016;278:563-577.
30. NCCIH strategic plan FY 2021-2025. NCCIH website. <https://www.nccih.nih.gov/about/nccih-strategic-plan-2021-2025>. Accessed August 18, 2022.
31. Hacker M, Hicks RJ, Beyer T. Applied systems biology: embracing molecular imaging for systemic medicine. *Eur J Nucl Med Mol Imaging.* 2020;47:2721-2725.
32. Deng J, Dong W, Socher R, Li L-J, Li K, Fei-Fei L. ImageNet: a large-scale hierarchical image database. In: *2009 IEEE Conference on Computer Vision and Pattern Recognition.* IEEE; 2009:248-255.

---

---

# Development of Fluorinated NP-59: A Revival of Cholesterol Use Imaging with PET

Allen F. Brooks<sup>1</sup>, Wade P. Winton<sup>1</sup>, Jenelle Stauff<sup>1</sup>, Janna Arteaga<sup>1</sup>, Bradford Henderson<sup>1</sup>, Jeremy Niedbala<sup>1</sup>, Peter J.H. Scott<sup>1,2</sup>, and Benjamin L. Viglianti<sup>1</sup>

<sup>1</sup>*Division of Nuclear Medicine, Department of Radiology, The University of Michigan Medical School, Ann Arbor, Michigan; and*

<sup>2</sup>*The Interdepartmental Program in Medicinal Chemistry, The University of Michigan, Ann Arbor, Michigan*

---

Imaging of cholesterol use is possible with the <sup>131</sup>I scintiscanning/SPECT agent NP-59. This agent provided a noninvasive measure of adrenal function and steroid synthesis. However, iodine isotopes resulted in poor resolution, manufacturing challenges, and high radiation dosimetry to patients that have limited their use and clinical impact. A <sup>18</sup>F analog would address these shortcomings while retaining the ability to image cholesterol use. The goal of this study was to prepare and evaluate a <sup>18</sup>F analog of NP-59 to serve as a PET imaging agent for functional imaging of the adrenal glands based on cholesterol use. Previous attempts to prepare such an analog of NP-59 have proven elusive. Preclinical and clinical evaluation could be performed once the new fluorine analog of NP-59 production was established. **Methods:** The recent development of a new reagent for fluorination along with an improved route to the NP-59 precursor allowed for the preparation of a fluorine analog of NP-59, FNP-59. The radiochemistry for the <sup>18</sup>F-radiolabeled <sup>18</sup>F-FNP-59 is described, and rodent radiation dosimetry studies and in vivo imaging in New Zealand rabbits was performed. After in vivo toxicity studies, an investigational new drug approval was obtained, and the first-in-humans images with dosimetry using the agent were acquired. **Results:** In vivo toxicity studies demonstrated that FNP-59 is safe for use at the intended dose. Biodistribution studies with <sup>18</sup>F-FNP-59 demonstrated a pharmacokinetic profile similar to that of NP-59 but with decreased radiation exposure. In vivo animal images demonstrated expected uptake in tissues that use cholesterol: gallbladder, liver, and adrenal glands. In this first-in-humans study, subjects had no adverse events and images demonstrated accumulation in target tissues (liver and adrenal glands). Manipulation of uptake was also demonstrated with patients who received cosyntropin, resulting in improved uptake. **Conclusion:** <sup>18</sup>F-FNP-59 provided higher resolution images, with lower radiation dose to the subjects. It has the potential to provide a noninvasive test for patients with adrenocortical diseases.

**Key Words:** endocrine; radiobiology/dosimetry; radiochemistry; NP-59; adrenal gland; aldosterone; cholesterol

**J Nucl Med 2022; 63:1949–1955**

DOI: 10.2967/jnumed.122.263864

Cholesterol is essential in numerous biologic processes. Changes in the trafficking of cholesterol are an important feature of many diseases such as Cushing's syndrome, primary aldosteronism, hyperandrogenism, adrenocortical carcinoma, and most importantly, based on number of patients affected, atherosclerosis. Given the importance of cholesterol, efforts to image its distribution and specifically its involvement in the adrenal glands was an area of focus. In the 1970s cholesterol analogs radiolabeled with <sup>131</sup>I were developed as scintiscanning agents, beginning with 19-iodocholesterol (1). It was then discovered that a modification of the steroid scaffold via a thermal rearrangement gave NP-59 a remarkably improved tracer with superior adrenal uptake (2). NP-59 was subsequently developed for the use of diagnosing primary aldosteronism and other related diseases of the adrenal cortex related to the increased use of cholesterol.

The precursor for aldosterone is cholesterol, and an excessive accumulation of cholesterol esters is present in primary aldosteronism which was exploited with imaging of NP-59 to differentiate bilateral adrenal hyperplasia versus a unilateral solitary adenoma when blood work indicated a hormone imbalance (3–14). It has also been used to identify primary Cushing's disease and classify an adrenal lesion as adrenal cortical carcinoma when there is a lack of uptake (2). NP-59 provided a noninvasive alternative to the gold standard for localizing abnormal cortical steroid production the invasive adrenal vein sampling procedure. However, NP-59 never saw wide adoption as a diagnostic agent given the limitations of <sup>131</sup>I: difficult synthesis, requirement of a multiday imaging protocol allowing background tissue clearance, free <sup>131</sup>I accumulation in the thyroid, poor image quality due to high-energy photons emitted by <sup>131</sup>I, and, consequently, poor radiation dosimetry excluding its routine screening use. Although still used in Asia and Europe in select cases, production was discontinued at our institution (the sole source in the United States) given NP-59's limitations and subsequent improvements in CT/MRI. However, CT/MRI alone is unable to reliably differentiate bilateral adrenal gland hyperplasia versus a unilateral solitary adenoma in up to 50% of patients (15,16). In the absence of NP-59, invasive adrenal vein sampling is the only method of determining lateralization of primary aldosteronism.

Given the limitations of NP-59, many efforts to image the cause of primary aldosteronism have been investigated that do not rely on cholesterol accumulation. These include metomidate labeled with <sup>11</sup>C or <sup>18</sup>F that relies on the detection of extracortical adrenal tissue (17,18); fluorine-labeled ligands for CYP11B2, an enzyme involved with aldosterone production, which is overexpressed in functional adenomas (18,19); and most recently CXCR-4 ligand analogs (notably <sup>68</sup>Ga-pentixafor), imaging overexpression of the receptor in adrenal adenomas (20–22). Imaging agents for these

---

Received Jan. 23, 2022; revision accepted Mar. 29, 2022.

For correspondence or reprints, contact Benjamin L. Viglianti (bviglia@med.umich.edu) and Allen F. Brooks (afb@umich.edu).

Published online Apr. 28, 2022.

Immediate Open Access: Creative Commons Attribution 4.0 International License (CC BY) allows users to share and adapt with attribution, excluding materials credited to previous publications. License: <https://creativecommons.org/licenses/by/4.0/>. Details: <http://jnm.snmjournals.org/site/misc/permission.xhtml>.

COPYRIGHT © 2022 by the Society of Nuclear Medicine and Molecular Imaging.

targets (CXCR-4 and CYP11B2) have the advantage of identifying adrenal adenomas based on the expression/overexpression of targets not generally seen in normal adrenal tissue, and likely have clinical utility for primary aldosteronism detection. However, as ligands they have the limitation of not being a functional imaging agent. The signal observed from their imaging does not represent the production of aldosterone or the other steroid hormones produced by the adrenal gland. Consequently, imaging agents based on the precursor (cholesterol) of aldosterone (or other cortical steroid hormones) are able to represent their production by their uptake, similar to FDG as a surrogate of glycolysis. This allows cholesterol imaging to be used for primary aldosteronism, as well as excessive cortisol production and other pathologies that rely on cholesterol.

In the years that followed the introduction of NP-59 and its study as an imaging agent for behavior as a labeled cholesterol, numerous efforts were undertaken to improve the molecule using various radionuclides and structural modifications, shown in Figure 1 (1,2,23–26). Prominent among these efforts was the preparation of a  $^{18}\text{F}$  analog to yield an improved PET imaging agent. However, those efforts over 3 decades failed to generate the fluorinated analog (23,24). Advances in fluorine chemistry and  $^{18}\text{F}$  radiochemistry now make the radiolabeling of a fluorinated cholesterol analog (FNP-59) possible (with results demonstrated herein). Access to  $^{18}\text{F}$ -FNP-59 will provide higher resolution images with lower radioactive dose to the subject, and potentially offer a noninvasive alternative to adrenal vein sampling.

## MATERIALS AND METHODS

All animal work was done under the approval by the Institutional Animal Care and Use Committee at the University of Michigan. All

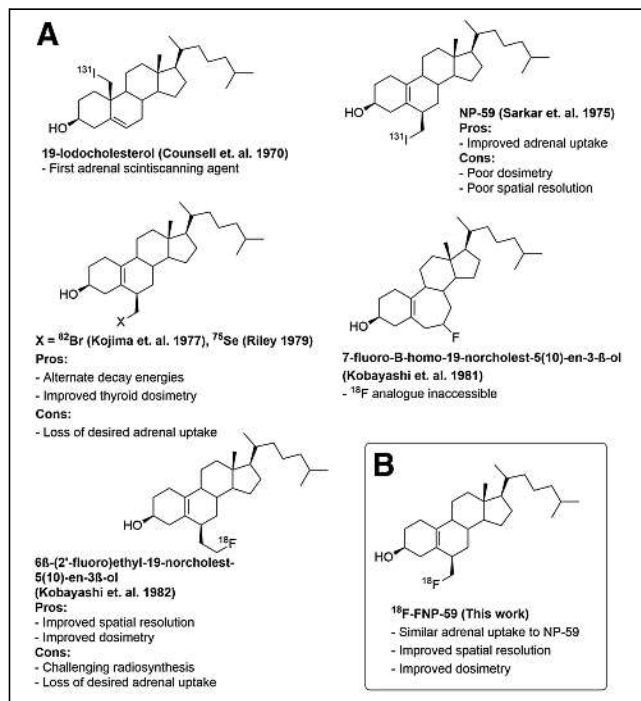


**FIGURE 1.** (A) Examples of previous efforts to prepare cholesterol-based adrenal imaging agents and their limitations. (B) Improved adrenal imaging agent  $^{18}\text{F}$ -FNP-59 and its advantages.

human studies were performed under an Food and Drug Administration (FDA) investigational new drug (IND), registered at clinicaltrials.gov (NCT04532489 and NCT04546126), and local approval by the University of Michigan institutional review board with written informed consent obtained.

## Synthesis of FNP-59 Reference Standard and $^{18}\text{F}$ -FNP-59

The generation of a fluorinated analog of NP-59 has been attempted for more than 40 y (24). Several advances in radiochemistry techniques have been developed by our laboratory that have allowed the development of FNP-59 (27,28). Before the synthesis of the radioactive version, a reference standard needed to be produced with nonradioactive fluoride. This reference standard would allow quality control to confirm the preparation of radioactive FNP-59 ( $^{18}\text{F}$ -FNP-59) and to perform toxicity studies for evaluation and IND approval of the agent for human study.

Preparation of the reference standard for FNP-59 was achieved and published by our group (27). Once the nonradioactive FNP-59 standard was prepared, we turned our attention to  $^{18}\text{F}$ -FNP-59. We were able to achieve the synthesis using the radiofluorination chemistry techniques pioneered at our facility over the past 5 y. Starting from cholesterol (Supplemental Fig. 1; supplemental materials are available at <http://jnm.snmjournals.org>), this synthesis requires fewer steps and used safer chemistry techniques than the synthesis of NP-59 (2). Specifically, the radiosynthesis uses only class 3 solvents (International Conference on Harmonisation guideline for residual solvents based on solvent toxicity) and is conducted according to current good manufacturing practices (GMPs), with the resulting dose formulated at a higher specific activity than NP-59 (28,29).

Detailed synthesis procedures including quality control/high-performance liquid chromatography data for the agent and intermediate precursors are provided in the supplemental materials, or can be obtained on request from the authors.

## Preclinical Studies of $^{18}\text{F}$ -FNP-59

**Radiation Dosimetry.** The  $^{18}\text{F}$ -FNP-59 uptake and dosimetry studies were performed in Sprague–Dawley rats ( $n = 4$ , 2 males/2 females) at 10, 30, 60, 120, and 360 min. Rats were anesthetized with isoflurane, and  $^{18}\text{F}$ -FNP-59 ( $3,349 \pm 827$  kBq for 10 min;  $3,709 \pm 255$  kBq for 30 min;  $3,312 \pm 608$  kBq for 60 min;  $3,645 \pm 71$  kBq for 120 min;  $8,297 \pm 237$  kBq) was administered via tail vein injection. At the appropriate time points, animals were euthanized and their tissues procured for measuring radioactivity. Radioactivity was measured in a well counter and expressed as decay-corrected percentage injected dose per gram of tissue. These data were then compared with historical  $^{131}\text{I}$ -NP-59 data as mean  $\pm$  SD. Radiation dosimetry was calculated from the distribution data and was used to determine estimates of human dosimetry with OLINDA/EXM 2.0 software (29).

**Toxicology Study.** A single-dose acute toxicity study for FNP-59 was performed at the Michigan State In Vivo Facility. In this study, male and female Sprague–Dawley rats ( $n = 20$ , 10 males/10 females) were administered FNP-59 (416  $\mu\text{g}/\text{kg}$ ) intravenously at 1,000 times the expected human equivalent dose in the formulation to be used for PET imaging studies;  $^{18}\text{F}$ -FNP-59 was administered intravenously. Body weights were recorded; blood was collected at intervals for clinical chemistry and complete blood count; clinical observations were recorded daily; and food consumption was monitored. Two points (day 4 and day 15) were used for necropsies, with half of the males and females analyzed at each time point. Organs were inspected and weighed, and slides were prepared for pathology.

## In Vivo Imaging

A pilot study was performed with New Zealand rabbits. Rabbits ( $n = 2$ ) were anesthetized with isoflurane and were dosed via intravenous

**TABLE 1**  
Human Dosimetry for <sup>18</sup>F-FNP-59 (*n* = 4; 2 Men, 2 Women), Compared with Rodent-Derived Human Estimated <sup>18</sup>F-FNP-59, Human <sup>131</sup>I-NP-59, and Human <sup>18</sup>F-FDG

Target organ	Human sex average dose		Rodent sex average dose (mSv/MBq)	Human <sup>131</sup> I-NP59* average dose (mSv/MBq)	<sup>18</sup> F-FDG <sup>†</sup> average dose (mSv/MBq)
	mSv/MBq	±95% error, mSv/MBq			
Adrenals	2.72E-02	6.82E-03	6.82E-02	4.0E+00	1.3E-02
Brain	7.92E-03	1.41E-03	3.70E-03		1.9E-02
Breasts	8.43E-03	1.12E-02	1.17E-02	4.0E-01	9.2E-03
Esophagus	1.43E-02	1.90E-03	1.43E-02		
Eyes	7.94E-03	1.42E-03	5.22E-03		
Gallbladder wall	3.09E-01	3.73E-01	2.11E-02		1.3E-02
Left colon	1.40E-02	3.91E-03	2.85E-02		
Small intestine	1.34E-02	3.71E-03	5.14E-02	4.1E-01	1.3E-02
Stomach wall	1.48E-02	3.18E-03	1.57E-02	4.0E-01	1.3E-02
Right colon	1.88E-02	9.58E-03	5.76E-02		
Rectum	1.07E-02	2.09E-03	1.65E-02		
Heart wall	1.10E-02	3.02E-03	1.60E-02		5.9E-02
Kidneys	1.91E-02	9.46E-03	1.51E-02	4.1E-01	2.0E-02
Liver	7.29E-02	7.70E-03	3.45E-02	1.2E+00	1.6E-02
Lungs	2.19E-02	8.57E-03	2.44E-02		1.7E-02
Ovaries	1.06E-02	1.72E-02	3.11E-02	3.8E-01	1.4E-02
Pancreas	1.91E-02	1.01E-02	1.68E-02	4.3E-01	2.6E-02
Prostate	1.69E-02	1.08E-02	1.32E-02		
Salivary glands	8.90E-03	1.95E-03	1.10E-02		
Red marrow	1.07E-02	2.14E-03	1.22E-02	3.9E-01	1.3E-02
Osteogenic cells	1.66E-02	5.59E-03	1.04E-02	3.7E-01	
Spleen	5.75E-02	7.92E-02	3.36E-02	3.9E-01	3.8E-02
Testes	9.99E-03	2.94E-02	6.02E-03	3.6E-01	1.1E-02
Thymus	1.16E-02	2.16E-03	1.40E-02		1.2E-02
Thyroid	1.01E-02	2.38E-03	1.25E-02	3.0E+01	1.1E-02
Urinary bladder wall	1.11E-02	5.23E-03	1.32E-02	3.9E-01	8.6E-02
Uterus	1.03E-02	1.63E-02	1.54E-02	4.0E-01	1.7E-02
Total body	1.20E-02	2.08E-03	1.36E-02		
Effective dose	1.75E-02	5.33E-03	1.92E-02	5.6E+01	

\*ICRP 53 (44).

†FDA product insert (45).

Significant decreased dose, 2 orders of magnitude, is seen with <sup>18</sup>F-FNP-59 compared with <sup>131</sup>I-NP-59.

administration of <sup>18</sup>F-FNP-59 (83.62 ± 3.33 MBq [2.26 ± 0.09 mCi]). Imaging of the rabbits with PET (Concorde microPET) occurred at 2 and 3 h. At 4 h, the rabbits were sacrificed and imaged on a clinical PET/CT scanner (Biograph True Point; Siemens) within in 20 min of euthanasia.

#### Human Imaging

With the data from the preclinical studies of <sup>18</sup>F-FNP-59, the FDA approved a physician-sponsored IND (#150397; principal investigator, Benjamin L. Viglianti) in June 2020 to begin testing <sup>18</sup>F-FNP-59 in human subjects. A University of Michigan Institutional Review Board (IRB) protocol (#HUM00179097) was also approved. After informed consent was obtained, 4 subjects (> 18 y, no known adrenal pathology,

nonpregnant females) were chosen; 2 men and 2 women were imaged dynamically for 30 min after 222 MBq (6 mCi) of <sup>18</sup>F-FNP-59 were injected into the antecubital fossa. Static imaging at a 3-h time point (*n* = 4) along with a 1- and 6-h time point were also obtained (*n* = 2 for each).

An additional 3 patients without adrenal pathology were imaged under adrenal stimulation to test if we could artificially increase <sup>18</sup>F-FNP-59 uptake. These patients were given 250 μg of cosyntropin intravenously over approximately 2 min. Five minutes after cosyntropin administration, 222 MBq (6 mCi) of <sup>18</sup>F-FNP-59 were injected into the antecubital fossa. Dynamic imaging over the abdomen occurred for 30 min followed by a 1- and 3-h whole-body acquisition.

## Human Radiation Dosimetry and Image Analysis

Organs (liver, kidney, spleen, gallbladder, pancreas, kidneys, lungs, bones, heart, male gonads, and bladder) were segmented on MIM encore software, and SUVs, absolute, and decay-corrected/attenuated counts were generated. Given that the adrenal glands were nonenlarged, segmentation was not practical. Consequently a 2-cm sphere centered over the left adrenal gland was used for adrenal uptake measurement. The right adrenal gland was not directly measured to avoid partial-volume effect from the liver. All counts measured from the left adrenal gland were doubled to account for this.

For each patient, measured uptake data were expressed as a percentage injected dose in each organ. Time-activity curves were generated, and the resulting fractions and half-times or results of manual integrations were input into the OLINDA/EXM 2.0 software (29,30). Radiation dose to each organ or tissue was then calculated using either the ICRP Adult Male or the ICRP Adult Female models. All patients' results were then averaged and a 95% CI for each organ was generated.

The segmentation used for radiation dosimetry was also used to report SUV versus time data. Results were reported as mean for the region of interest with a 95% confidence range.

## RESULTS

### Synthesis of FNP-59 Reference Standard and $^{18}\text{F}$ -FNP-59

We have developed and demonstrated the synthesis of  $^{18}\text{F}$ -FNP-59 starting from cholesterol. Final products and intermediates have been confirmed via nuclear magnetic resonance spectroscopy analysis and mass spectrometry. Precursor and reference standard purity (>90%) were additionally confirmed via reversed-phase high-performance liquid chromatograph using ultraviolet detection at 212 nm; the supplemental data provides detailed data for the synthesis and characterization for standard, precursor, and intermediates. The radiosynthesis used only class 3 solvents and was conducted according to current GMPs, with the resulting dose formulated at a specific higher activity than those achieved for NP-59 (31,32).

**Rodent Dosimetry.** Biodistribution data in rats demonstrated increasing  $^{18}\text{F}$ -FNP-59 adrenal and ovary uptake over time (Supplemental Fig. 2A), as has been demonstrated to occur with  $^{131}\text{I}$ -NP-59 (2), and are consistent with the expected trafficking of cholesterol. Importantly, the adrenal-to-liver ratio is greater than 5 to 1. This result overcomes one of the main limitations of  $^{131}\text{I}$ -NP-59 imaging, the requirement of a multiday imaging protocol to allow background uptake to dissipate to resolve the image. Additionally, the data demonstrated that imaging is possible within the decay time of  $^{18}\text{F}$  (Supplemental Fig. 2C).

Radiation dosimetry estimates were calculated with OLINDA/EXM 2.0 software, using both rodent and human biodistribution data (Table 1). The results demonstrate a significantly decreased radiation dose in target organs (gonads/liver/adrenal/thyroid), compared with  $^{131}\text{I}$ -NP-59 historic data as well as an overall effective dose that is nearly 2 orders of magnitude less than  $^{131}\text{I}$ -NP-59 (29).

### In Vivo Imaging Results

A pilot study in New Zealand rabbits was performed with PET images obtained at 1 and 4 h. Subsequent PET/CT images were taken immediately after euthanasia

(Supplemental Fig. 3). The results demonstrate expected  $^{18}\text{F}$ -FNP-59 accumulation in the liver and the gallbladder. Gallbladder uptake was not seen in rats, as they lack a gallbladder anatomically. However, gallbladder uptake was seen in the historic NP-59 patients. More importantly, the rabbits demonstrated adrenal gland uptake in a temporal relationship similar to that in rat experiments but to a lesser degree; adrenal-to-liver ratio was approximately 2:1.

### Human Imaging Results

Four humans (2 men/2 women) were imaged with  $^{18}\text{F}$ -FNP-59. Supplemental Figure 4 and Figure 2 show examples of a 20-y-old woman and a 21-y-old woman imaged without and after an injection of cosyntropin (250 mcg), respectively. Both women had no known history of medical or endocrine disease and both were imaged at 3 h after injection of 222 MBq (6 mCi) of  $^{18}\text{F}$ -FNP-59. In all subjects, there was intense tracer uptake in the liver and gallbladder, similar to that in the rabbit experiments (Fig. 3). This uptake in the liver decreased with time as bile production occurred. Adrenal gland uptake was also seen, but was less than expected compared with the rat experiments. The adrenal to liver ratio was approximately 0.25:1 at 1 h, approximately 0.5:1 at 3 h, and about 1:1 at 6 h for an unstimulated subject (Fig. 3C), compared with animal data that suggested a 5:1 ratio at 6 h (Supplemental Fig. 2). However, this adrenal-to-liver ratio did increase over time, following kinetics similar to those in the rat experiments. Similarly, gonadal uptake (not shown) was less than the animal data had suggested it would have been.

Three subjects were pretreated with cosyntropin before  $^{18}\text{F}$ -FNP-59 administration to stimulate adrenal gland cholesterol uptake through increased hormone synthesis (Fig. 2). This pretreatment resulted in more than doubling of  $^{18}\text{F}$ -FNP-59 uptake at 1 and 3 h (Figs. 3B and 3C) along with increased uptake during dynamic phase imaging.

Overall, after injection of  $40 \pm 4 \mu\text{g}$  of  $^{18}\text{F}$ -FNP-59, no adverse events were observed after injection or within the following days.

## DISCUSSION

NP-59 has had a long and useful clinical history of identifying cholesterol use, accumulating in pathology where excessive production

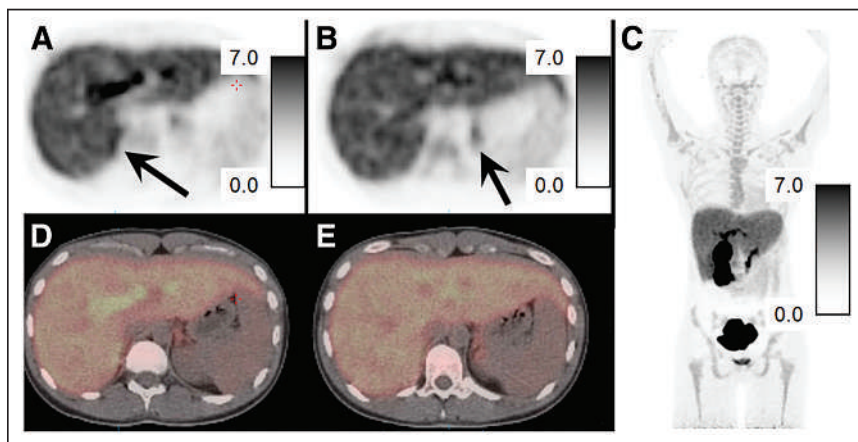


**FIGURE 2.** PET/CT images of  $^{18}\text{F}$ -FNP-59 in a 21-y-old woman without adrenal pathology and pretreated with cosyntropin given before 222 MBq (6 mCi) of  $^{18}\text{F}$ -FNP-59. (A and B) Axial PET images obtained at 3 h after injection of in upper abdomen, with adrenal glands (black arrows) identified on right (A) and left (B). Scale bars are 0–7 SUV. Adrenal-to-liver ratio at approximately 1.3:1 on right and 1:1.1 on left at 3 h. (C–E) Fused PET/CT images of adrenal glands are also shown (D and E) along with maximum-intensity-pixel image (C) that demonstrates expected gallbladder/biliary/bowel uptake given bile secretion.

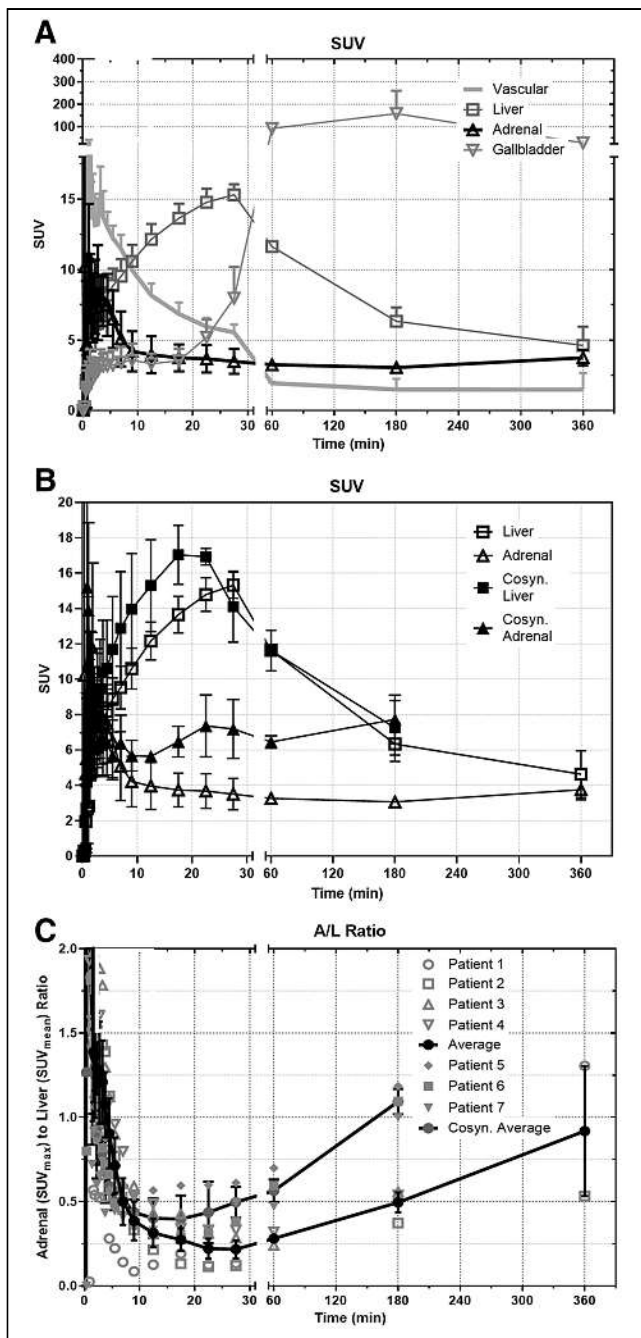


**FIGURE 3.** (A) SUV  $^{18}\text{F}$ -FNP-59 uptake in selected organ versus time in nonstimulated patients ( $n = 4$ ; 2 men/2 women, at 180 min;  $n = 2$  at 60 and 360 min). Over time, after first pass, liver uptake slowly clears as  $^{18}\text{F}$ -FNP-59 is excreted into bile and sent back out into enterohepatic circulation. (B) Uptake comparison in liver and adrenal gland of 3 patients stimulated with cosyntropin showing significant increased uptake in adrenal gland. Overtime, left adrenal uptake slowly increases. (C) Adrenal-to-liver (A/L) ratio is also shown, demonstrating increasing ratio over time after first pass vascular uptake (time < 30 min) is cleared. Additionally, A/L ratio of 3 female patients (5–7) given cosyntropin is shown. This cosyntropin stimulation resulted in significant increased uptake ratio compared with unstimulated patients. Error bars are SEM.  $n = 4$  for dynamic imaging and at 180 min;  $n = 2$  at 60 and 360 min for patients 1–4.

of hormones that use cholesterol as its backbone are produced. The most common use is for characterizing primary aldosteronism. Although its clinical utility has been established for approximately the

past 40 y, limitations of the  $^{131}\text{I}$  label, for example, adverse dosimetry due to  $^{131}\text{I}$ , allow it to be used only in select clinical cases rather than in broader screening applications. It had been suggested that the tracer could be improved by replacing  $^{131}\text{I}$  with  $^{18}\text{F}$  ( $^{18}\text{F}$ -FNP-59), but the prior chemistry techniques attempted and described in the literature were unsuccessful (23,24).

We have demonstrated an improved concise route to synthesize the FNP-59 reference standard and radiolabeling precursor. A GMP-compliant process has been developed for the production of  $^{18}\text{F}$ -FNP-59 using only class 3 solvents in accordance with green radiochemistry principles (33,34). In addition, radiation dosimetry calculations and single acute toxicity dosing studies have been conducted and showed the agent was safe and appropriate for the filing of an IND application with the FDA. The preliminary evaluation demonstrated that  $^{18}\text{F}$ -FNP-59 behaved in a manner nearly identical to historic  $^{131}\text{I}$ -NP-59 data, with a greatly improved safety profile given the 2 orders of magnitude reduction in radioactive dose to target organs, and that the required target-to-background ratios can be achieved within the physical half-life limitations of  $^{18}\text{F}$ .

In vivo imaging was performed in New Zealand rabbits. This animal model demonstrated  $^{18}\text{F}$ -FNP-59 uptake in expected tissues (adrenal glands and liver). Notably, uptake was also seen in the gallbladder of New Zealand rabbits, which was expected, and not seen in rats given their anatomic absence of a gallbladder.

First-in-humans imaging for radiation dosimetry measurements was performed in 4 individuals. There were no serious adverse events or uptake in target organs observed, and the calculated radiation dose was nearly 2 orders of magnitude less than the historic  $^{131}\text{I}$ -NP-59 radiation dose. Most important, uptake was observed in the adrenal glands, via functional imaging of cholesterol uptake. However, the adrenal-to-liver ratio was less than the animal biodistribution data would have suggested, at approximately 1:1 (Fig. 3C) rather than 5:1 (Supplemental Fig. 2A) at 6 h. Given the animal data, this ratio would likely continue to improve at later time points past 6 h. However, the physical half-life of  $^{18}\text{F}$  (109.8 min) and the sensitivity of our current equipment coupled to partial-volume effects that occur when imaging the small anatomy of a normal adrenal gland limit the ability of measuring the uptake past 6 h.

At later time points, >6 h, there would be more time available for the  $^{18}\text{F}$ -FNP-59 (acting as free cholesterol) to be incorporated into lipoproteins (primarily high-density lipoprotein) (35–37) and then accumulate in the adrenal glands through scavenger receptors while the liver and gallbladder are cleared via excretion (38). This process of cholesterol incorporation into lipoproteins and subsequent redistribution occurs much more quickly in rodents than in humans (39) and is the result of an improved adrenal-to-liver ratio seen in preclinical animal studies (Fig. 3A). This difference between rodent and humans' redistribution was the reason that the original  $^{131}\text{I}$ -NP-59 agent was imaged 3 d after administration, which was possible given  $^{131}\text{I}$  half-life.

Although  $^{18}\text{F}$ -FNP-59 uptake in human adrenal glands was less than that observed in rodents, the data here suggest that there may be enough activity to allow imaging at time points later than the 6 h that was demonstrated. One of the proposed advantages of total-body PET/CT scanners coming online is that they offer greater sensitivity as more disintegrations are observed compared with standard equipment (40,41). However, these advantages have yet to be demonstrated—a future goal we are working toward.

Although delayed imaging may demonstrate improved adrenal uptake given the rates of biologic redistribution of cholesterol, the need for delayed imaging may not be necessary when evaluating patients with pathology. Gross et al. showed that approximately 50% of normal  $^{131}\text{I}$ -NP-59 uptake in dogs (which are more similar to humans than rats in terms of how they handle cholesterol) was based on cosyntropin-stimulated cortisol production, and 10%–15% was aldosterone production (42). In a situation in which native/normal cortisol production is suppressed with dexamethasone, and a patient has pathologic primary aldosteronism,  $^{18}\text{F}$ -FNP-59 uptake may be high enough to determine laterality of abnormal production. This manipulation maneuver—dexamethasone suppression of normal cortisol production—is needed with  $^{131}\text{I}$ -NP-59 imaging to suppress normal cortisol production. When this process is performed, very minimal adrenal uptake of  $^{131}\text{I}$ -NP-59 is seen in a normal gland. A recent examination of  $^{131}\text{I}$ -NP-59 uptake in primary adrenal aldosteronism from adenoma by Lu et al. describes the adrenal-to-liver ratio of  $^{131}\text{I}$ -NP-59 as 2–2.8 after dexamethasone suppression depending on the genetic profile (43). Similarly, there was a 40%–75% increased uptake of  $^{131}\text{I}$ -NP-59 in the pathologic adrenal gland versus the normal gland. Consequently, when the data on uptake ratios and rearrangement from Lu et al. are used, the average adrenal-to-liver ratio in a normal adrenal gland for  $^{131}\text{I}$ -NP-59 would range from 1.1 to 1.6.

Stimulation with cosyntropin of 3 normal subjects demonstrated an adrenal-to-liver ratio of at least 1.2:1 at 3 h, >2 times the uptake in unstimulated subjects. If the uptake kinetics hold, the adrenal-to-liver ratio at 6 h would have been approximately 1.5–2:1. This degree of uptake is in the range of Lu et al. However, these data need to be replicated with other normal subjects stimulated with cosyntropin and imaged at later time points. More important, testing in patients who have pathology with and without dexamethasone suppression needs to be performed.

Consequently, we are currently planning to image more patients at later time points, optimizing the imaging protocol along with imaging patients with and without dexamethasone and cosyntropin stimulation. This will give us the normal expected dynamic range of uptake that can be seen with this agent. Finally, we plan to study patients who have been diagnosed with primary aldosteronism and will receive adrenal vein sampling to determine whether imaging by PET/CT using  $^{18}\text{F}$ -FNP-59 can lateralize disease.

## CONCLUSION

Overall this work demonstrates the initial feasibility of  $^{18}\text{F}$ -FNP-59 to image cholesterol trafficking and specifically uptake in human cortical adrenal tissue. Future studies will explore whether  $^{18}\text{F}$ -FNP-59 can serve as a noninvasive method to image lateral versus bilateral cause of primary aldosteronism.

## DISCLOSURE

Funding for this work is the result University of Michigan Department of Radiology, Fast Forward Medical Innovation (principal investigator, Benjamin L. Viglianti), Michigan Memorial Phoenix Project (principal investigator, Benjamin L. Viglianti), Michigan Drug Discovery (principal investigators, Allen F. Brooks and Benjamin L. Viglianti), and R01EB021155 (principal investigator, Peter J. H. Scott). No other potential conflict of interest relevant to this article was reported.

## KEY POINTS

**QUESTION:** Can a fluorinated NP-59 be made and successfully accumulate in the adrenal glands?

**PERTINENT FINDINGS:** Fluorinated NP-59 was made, demonstrated improved radiation dosimetry, and accumulated in the adrenal glands. This accumulation appears dependent on a adrenal gland hormone synthesis similar to that of the prior iodine agent for which overproduction/stimulation resulted in increased accumulation.

**IMPLICATIONS FOR PATIENT CARE:** With the development of FNP-59, we were able to explore whether this agent could identify the cause of primary aldosteronism (adenoma vs. bilateral hyperplasia), potentially limiting the need for adrenal vein sampling before definitive therapy.

## REFERENCES

- Counsell RE, Ranade VV, Blair RJ, Beierwaltes WH, Weinhold PA. Tumor localizing agents. IX. Radioiodinated cholesterol. *Steroids*. 1970;16:317–328.
- Sarkar SD, Beierwaltes H, Ice RD, et al. A new and superior adrenal scanning agent, NP-59. *J Nucl Med*. 1975;16:1038–1042.
- Chen YC, Wei CK, Chen PF, Tzeng JE, Chuang TL, Wang Y-F. Seeking the invisible: I-131 NP-59 SPECT/CT for primary hyperaldosteronism. *Kidney Int*. 2009;75:663.
- Chen Y-C, Chiu J-S, Wang Y-F. NP-59 SPECT/CT imaging in stage 1 hypertensive and atypical primary aldosteronism: a 5-year retrospective analysis of clinicolaboratory and imaging features. *ScientificWorldJournal*. 2013;2013:317934.
- Chen Y-C, Su Y-C, Wei C-K, et al. Diagnostic value of I-131 NP-59 SPECT/CT scintigraphy in patients with subclinical or atypical features of primary aldosteronism. *J Biomed Biotechnol*. 2011;2011:209787.
- Kazerouni EA, Sisson JC, Shapiro B, et al. Diagnostic accuracy and pitfalls of [iodine-131]6-beta-iodomethyl-19-norcholesterol (NP-59) imaging. *J Nucl Med*. 1990;31:526–534.
- Papierska L, Ćwikła J, Rabijewski M, Glinicki P, Otto M, Kasperlik-Zaluska A. Adrenal  $^{131}\text{I}$ -6-beta-iodomethyl-19-norcholesterol scintigraphy in choosing the side for adrenalectomy in bilateral adrenal tumors with subclinical hypercortisolemia. *Abdom Imaging*. 2015;40:2453–2460.
- White ML, Gauger PG, Doherty GM, et al. The role of radiologic studies in the evaluation and management of primary hyperaldosteronism. *Surgery*. 2008;144:926–933, discussion 33.
- Wong KK, Komissarova M, Avram AM, Fig LM, Gross MD. Adrenal cortical imaging with I-131 NP-59 SPECT-CT. *Clin Nucl Med*. 2010;35:865–869.
- Yen R-F, Wu V-C, Liu K-L, et al.  $^{131}\text{I}$ -6beta-iodomethyl-19-norcholesterol SPECT/CT for primary aldosteronism patients with inconclusive adrenal venous sampling and CT results. *J Nucl Med*. 2009;50:1631–1637.
- Wong KK, Gandhi A, Viglianti BL, Fig LM, Rubello D, Gross MD. Endocrine radionuclide scintigraphy with fusion single photon emission computed tomography/computed tomography. *World J Radiol*. 2016;8:635–655.
- Wale DJ, Wong KK, Viglianti BL, Rubello D, Gross MD. Contemporary imaging of incidentally discovered adrenal masses. *Biomed Pharmacother*. 2017;87:256–262.
- Wu MH, Liu FH, Lin KJ, Sun JH, Chen ST. Diagnostic value of adrenal iodine-131 6-beta-iodomethyl-19-norcholesterol scintigraphy for primary aldosteronism: a retrospective study at a medical center in North Taiwan. *Nucl Med Commun*. 2019;40:568–575.
- Wu VC, Hu YH, Er LK, et al. Case detection and diagnosis of primary aldosteronism: the consensus of Taiwan Society of Aldosteronism. *J Formos Med Assoc*. 2017;116:993–1005.
- Nanba AT, Nanba K, Byrd JB, et al. Discordance between imaging and immunohistochemistry in unilateral primary aldosteronism. *Clin Endocrinol (Oxf)*. 2017;87:665–672.
- Sam D, Kline GA, So B, Leung AA. Discordance between imaging and adrenal vein sampling in primary aldosteronism irrespective of interpretation criteria. *J Clin Endocrinol Metab*. 2019;104:1900–1906.
- Burton TJ, Mackenzie IS, Balan K, et al. Evaluation of the sensitivity and specificity of  $^{11}\text{C}$ -metomidate positron emission tomography (PET)-CT for lateralizing aldosterone secretion by Conn's adenomas. *J Clin Endocrinol Metab*. 2012;97:100–109.

18. Abe T, Naruse M, Young WF Jr, et al. A novel CYP11B2-specific imaging agent for detection of unilateral subtypes of primary aldosteronism. *J Clin Endocrinol Metab.* 2016;101:1008–1015.
19. Bongarzone S, Basagni F, Sementa T, et al. Development of [<sup>18</sup>F]FAMTO: a novel fluorine-18 labelled positron emission tomography (PET) radiotracer for imaging CYP11B1 and CYP11B2 enzymes in adrenal glands. *Nucl Med Biol.* 2019;68–69: 14–21.
20. Ding J, Zhang Y, Wen J, et al. Imaging CXCR4 expression in patients with suspected primary hyperaldosteronism. *Eur J Nucl Med Mol Imaging.* 2020;47:2656–2665.
21. Ding L, Li J, Wu C, Yan F, Li X, Zhang S. A self-assembled RNA-triple helix hydrogel drug delivery system targeting triple-negative breast cancer. *J Mater Chem B.* 2020;8:3527–3533.
22. Heinze B, Fuss CT, Mulatero P, et al. Targeting CXCR4 (CXC chemokine receptor type 4) for molecular imaging of aldosterone-producing adenoma. *Hypertension.* 2018;71:317–325.
23. Kobayashi T, Maeda M, Haradahira T, Kojima M. Fluoro norcholesterol analogues. Synthesis of 6 beta-(2-fluoro) ethyl-19-norcholest-5(10)-en-3 beta-ol. *Steroids.* 1982;39:585–593.
24. Kobayashi T, Maeda M, Komatsu H, Kojima M. Synthesis of 7-fluoro-B-homo-19-norcholest-5(10)-En-3-beta-ol acetate. *Chem Pharm Bull (Tokyo).* 1982;30: 3082–3087.
25. Kojima M, Maeda M, Komatsu H, et al. Radio-bromine labeled nor-cholesterol analogs: synthesis and tissue distribution study in rats of Br-82 labeled 6beta-bromomethyl-19-norcholest-5(10)-En-3beta-ol. *Steroids.* 1977;29:443–451.
26. Riley A. The development of selenium-75 cholesterol analogues. *J Labelled Compd.* 1965;207:1134–1135.
27. Winton WP, Brooks AF, Wong KK, Scott PJH, Viglianti BL. Synthesis of 6-(fluoromethyl)-19-norcholest-5(10)-en-3-ol, a fluorinated analogue of NP-59, using the mild fluorinating reagent, TBAF(Pinacol)(2). *Synopen.* 2019;3:55–58.
28. Winton WP, Viglianti BL, Wong KK, Scott PJ, Brooks AF. Improved synthesis and preclinical evaluation of [<sup>18</sup>F]FNP-59: a radiotracer for imaging cholesterol trafficking [abstract]. *J Nucl Med.* 2020;61(suppl 1):976.
29. Stabin MG, Sparks RB, Crowe E. OLINDA/EXM: the second-generation personal computer software for internal dose assessment in nuclear medicine. *J Nucl Med.* 2005;46:1023–1027.
30. Stabin MG, Siegel JA. Physical models and dose factors for use in internal dose assessment. *Health Phys.* 2003;85:294–310.
31. Branch SK. Guidelines from the International Conference on Harmonisation (ICH). *J Pharm Biomed Anal.* 2005;38:798–805.
32. Wang T, Jacobson-Kram D, Pilaro AM, et al. ICH guidelines: inception, revision, and implications for drug development. *Toxicol Sci.* 2010;118:356–367.
33. Shao X, Fawaz MV, Jang K, Scott PJ. Ethanolic carbon-11 chemistry: the introduction of green radiochemistry. *Appl Radiat Isot.* 2014;89:125–129.
34. Stewart MN, Hockley BG, Scott PJ. Green approaches to late-stage fluorination: radiosyntheses of (18F)-labelled radiopharmaceuticals in ethanol and water. *Chem Commun (Camb).* 2015;51:14805–14808.
35. Schwartz CC, Berman M, Vlahcevic ZR, Halloran LG, Gregory DH, Swell L. Multicompartmental analysis of cholesterol metabolism in man. Characterization of the hepatic bile acid and biliary cholesterol precursor sites. *J Clin Invest.* 1978; 61:408–423.
36. Schwartz CC, Berman M, Vlahcevic ZR, Swell L. Multicompartmental analysis of cholesterol metabolism in man. Quantitative kinetic evaluation of precursor sources and turnover of high density lipoprotein cholesterol esters. *J Clin Invest.* 1982;70: 863–876.
37. Schwartz CC, Vlahcevic ZR, Berman M, Meadows JG, Nisman RM, Swell L. Central role of high density lipoprotein in plasma free cholesterol metabolism. *J Clin Invest.* 1982;70:105–116.
38. Kraemer FB. Adrenal cholesterol utilization. *Mol Cell Endocrinol.* 2007;265–266: 42–45.
39. Bravo E, Botham KM, Mindham MA, Mayes PA, Marinelli T, Cantafora A. Evaluation in vivo of the differential uptake and processing of high-density lipoprotein unesterified cholesterol and cholesteryl ester in the rat. *Biochim Biophys Acta.* 1994;1215:93–102.
40. Vandenberghe S, Moskal P, Karp JS. State of the art in total body PET. *EJNMMI Phys.* 2020;7:35.
41. Badawi RD, Shi H, Hu P, et al. First Human Imaging Studies with the EXPLORER Total-Body PET Scanner. *J Nucl Med.* 2019;60:299–303.
42. Gross MD, Grekin RJ, Brown LE, Marsh DD, Beierwaltes WH. The relationship of adrenal iodocholesterol uptake to adrenal zona glomerulosa function. *J Clin Endocrinol Metab.* 1981;52:612–615.
43. Lu CC, Yen RF, Peng KY, et al. NP-59 Adrenal Scintigraphy as an Imaging Biomarker to Predict KCNJ5 Mutation in Primary Aldosteronism Patients. *Front Endocrinol (Lausanne).* 2021;12:644927.
44. International Commission on Radiological Protection (ICRP). Radiation dose to patients from radiopharmaceuticals. ICRP publication 53. *Ann ICRP.* 1988;18:1–4.
45. Fludeoxyglucose F18 injection [package insert]. U.S. Food and Drug Administration website. [https://www.accessdata.fda.gov/drugsatfda\\_docs/label/2010/021870s0041b1.pdf](https://www.accessdata.fda.gov/drugsatfda_docs/label/2010/021870s0041b1.pdf). Revised July 2010. Accessed September 13, 2022.

---

---

# Staging Liver Fibrosis by Fibroblast Activation Protein Inhibitor PET in a Human-Sized Swine Model

Ali Pirasteh<sup>1</sup>, Sarvesh Periyasamy<sup>2</sup>, Jennifer Jean Meudt<sup>3</sup>, Yongjun Liu<sup>4</sup>, Laura M. Lee<sup>5</sup>, Kyle M. Schachtschneider<sup>6,7</sup>, Lawrence B. Schook<sup>8,9</sup>, Ron C. Gaba<sup>9</sup>, Lu Mao<sup>10</sup>, Adnan Said<sup>11,12</sup>, Alan Blair McMillan<sup>1</sup>, Paul F. Laeseke<sup>2</sup>, and Dhanansayan Shanmuganayagam<sup>3,13,14</sup>

<sup>1</sup>Radiology and Medical Physics, University of Wisconsin–Madison, Madison, Wisconsin; <sup>2</sup>Radiology and Biomedical Engineering, University of Wisconsin–Madison, Madison, Wisconsin; <sup>3</sup>Animal and Dairy Sciences, University of Wisconsin–Madison, Madison, Wisconsin; <sup>4</sup>Pathology and Laboratory Medicine, University of Wisconsin–Madison, Madison, Wisconsin; <sup>5</sup>Research Animal Resources and Compliance, University of Wisconsin–Madison, Madison, Wisconsin; <sup>6</sup>Radiology and Biochemistry and Molecular Genetics, University of Illinois at Chicago, Chicago, Illinois; <sup>7</sup>National Center for Supercomputing Applications, University of Illinois at Urbana–Champaign, Champaign, Illinois; <sup>8</sup>Animal Sciences, University of Illinois at Chicago, Chicago, Illinois; <sup>9</sup>Radiology/Interventional Radiology, University of Illinois at Chicago, Chicago, Illinois; <sup>10</sup>Biostatistics and Medical Informatics, University of Wisconsin–Madison, Madison, Wisconsin; <sup>11</sup>Medicine, Gastroenterology, and Hepatology, University of Wisconsin–Madison, Madison, Wisconsin; <sup>12</sup>William S. Middleton VA Medical Center, Madison, Wisconsin; <sup>13</sup>Surgery, University of Wisconsin–Madison, Madison, Wisconsin; and <sup>14</sup>Center for Biomedical Swine Research and Innovation, University of Wisconsin–Madison, Madison, Wisconsin

Current methods of staging liver fibrosis have notable limitations. We investigated the utility of PET in staging liver fibrosis by correlating liver uptake of <sup>68</sup>Ga-labeled fibroblast activation protein inhibitor (FAPI) with histology in a human-sized swine model. **Methods:** Five pigs underwent baseline <sup>68</sup>Ga-FAPI-46 (<sup>68</sup>Ga-FAPI) PET/MRI and liver biopsy, followed by liver parenchymal embolization, 8 wk of oral alcohol intake, endpoint <sup>68</sup>Ga-FAPI PET/MRI, and necropsy. Regions of interest were drawn on baseline and endpoint PET images, and SUV<sub>mean</sub> was recorded. At the endpoint, liver sections corresponding to regions of interest were identified and cut out. Fibrosis was histologically evaluated using a modified METAVIR score for swine liver and quantitatively using collagen proportionate area (CPA). Box-and-whisker plots and linear regression were used to correlate SUV<sub>mean</sub> with METAVIR score and CPA, respectively. **Results:** Liver <sup>68</sup>Ga-FAPI uptake strongly correlated with CPA ( $r = 0.89$ ,  $P < 0.001$ ). <sup>68</sup>Ga-FAPI uptake was significantly and progressively higher across F2 and F3/F4 fibrosis stages, with a respective median SUV<sub>mean</sub> of 2.9 (interquartile range [IQR], 2.7–3.8) and 7.6 (IQR, 6.7–10.2) ( $P < 0.001$ ). There was no significant difference between <sup>68</sup>Ga-FAPI uptake of baseline liver and endpoint liver sections staged as F0/F1, with a respective median SUV<sub>mean</sub> of 1.7 (IQR, 1.3–2.0) and 1.7 (IQR, 1.5–1.8) ( $P = 0.338$ ). **Conclusion:** The strong correlation between liver <sup>68</sup>Ga-FAPI uptake and the histologic stage of liver fibrosis suggests that <sup>68</sup>Ga-FAPI PET can play an impactful role in noninvasive staging of liver fibrosis, pending validation in patients.

**Key Words:** fibroblast activation protein inhibitor; liver fibrosis; PET; MRI; swine

**J Nucl Med 2022; 63:1956–1961**  
DOI: 10.2967/jnumed.121.263736

Liver fibrosis is the consequence of chronic liver injury of any etiology that affects 1.5 billion people worldwide (1,2). End-stage liver fibrosis (i.e., cirrhosis) is the global leading cause of liver-disease–related deaths and the most important risk factor for developing liver cancer (1). Fibrosis is the only histologic feature that predicts long-term outcomes, and serial assessments of fibrosis are of key prognostic importance in patient outcomes and assessing treatment response (3). Although liver transplant remains the only available cure for decompensated end-stage liver fibrosis, earlier stages of liver injury and fibrosis are treatable and reversible (4,5).

Current methods of assessing liver fibrosis have notable limitations. Laboratory markers are unreliable (6,7), and liver biopsy (the current gold standard) carries morbidity and mortality risks and is prone to undersampling and variability in sampling and interpretation (8–13). MR elastography is the best validated noninvasive tool and estimates liver stiffness as a surrogate for the histologic fibrosis stage (14–18). MR elastography has lower sensitivity for detection of lower stages of fibrosis, can be nondiagnostic because of liver iron overload or operator error, and cannot differentiate fibrosis from concurrent liver inflammation, as both processes increase liver stiffness (18–20). Hence, there remains a clear unmet need for a noninvasive, quantitative, and accurate tool for staging liver fibrosis.

Fibroblast activation protein (FAP) is a cell surface peptidase expressed in disease processes with matrix remodeling, such as by the fibrogenic liver stellate cells (21,22). Radiolabeled FAP inhibitors (FAPIs) have been used with PET to target FAP in vivo as an imaging tool (23,24). Advantages of PET include quantitative evaluation of radiotracer uptake by SUV and relatively operator-independent, simple whole-liver imaging. Hence, the goal of this study was to prospectively investigate the correlation between liver <sup>68</sup>Ga-FAPI-46 (<sup>68</sup>Ga-FAPI) uptake on PET and the gold standard histologic stage of liver fibrosis in a human-sized swine model of alcohol-induced liver fibrosis.

## MATERIALS AND METHODS

This study was conducted under protocols approved by the local Institutional Animal Care and Use Committee in accordance with

---

Received Dec. 23, 2021; revision accepted Apr. 7, 2022.  
For correspondence or reprints, contact Ali Pirasteh (pirasteh@wisc.edu).  
Published online Apr. 21, 2022.  
COPYRIGHT © 2022 by the Society of Nuclear Medicine and Molecular Imaging.

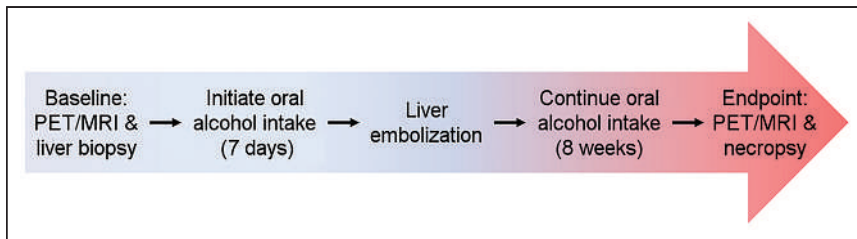


**FIGURE 1.** Study overview: after baseline PET/MRI, animals underwent period of gradual increase in oral alcohol intake, followed by liver parenchymal transarterial embolization. After 8 wk of oral alcohol intake, they underwent endpoint imaging followed by necropsy and tissue analysis.

published guidelines of the National Institutes of Health and U.S. Department of Agriculture. Figure 1 summarizes the study design. The swine model used in this study has been demonstrated to successfully achieve liver fibrosis (25,26) and is detailed in the supplemental materials (available at <http://jnm.snmjournals.org>). Five human-sized, age-matched male Wisconsin Miniature Swine™ underwent same-day PET/MRI and core-needle liver biopsy to establish baseline histologic and imaging characteristics of the liver. Increasing volumes of ethanol were then added to their daily diets over a 7-d period, followed by transarterial liver embolization with an emulsion of ethanol and ethiodized oil. The animals continued oral alcohol intake for 8 more weeks, after which they underwent endpoint PET/MRI and necropsy.

### Imaging

Images were acquired under general anesthesia in the supine position on a whole-body PET/MRI scanner (Signa PET/MR; GE Healthcare). Continuous dynamic PET data of the liver were acquired for 92 min; <sup>68</sup>Ga-FAPI was administered intravenously 1 min after the initiation of data acquisitions. The average dose was 4.3 MBq (range, 3.5–4.6 MBq) per kilogram of body weight. Attenuation-corrected dynamic PET images were reconstructed with 15 s/frame for the first 5 min and 3 min/frame for the rest of the acquisition. An additional static image was generated at 60 min after radiotracer injection (using PET data at 60–69 min). Images were reviewed and analyzed by a dual board-certified nuclear medicine physician/radiologist with fellowship training in abdominal imaging and nuclear medicine, using MIM Encore (R), version 7.1.2 (MIM Software Inc.). Image analysis was performed before histologic tissue assessment to minimize bias.

### Baseline Image Analysis

Circular regions of interest (ROIs) were placed on the liver parenchyma on MRI, avoiding major vessels: 1 in the right lobe and 1 in the left lobe, with a minimum diameter of 1.5 cm. Each ROI was propagated across 1 slice cranially and 1 slice caudally, yielding a cylindrical ROI with a minimum volume of 4 cm<sup>3</sup>. To minimize bias, ROIs were propagated directly by the software into both dynamic and static PET images. The SUV<sub>mean</sub> for each ROI was recorded, yielding 10 data points at baseline (2 per animal).

### Endpoint Image Analysis

Because of the heterogeneous nature of the fibrosis achieved by this model (dictated by preferential liver arterial flow carrying different volumes of embolic emulsion to different liver regions), 4 ROIs for each animal were placed on the static PET images. To achieve

adequate assessment across the uptake spectrum, 2 of the ROIs were placed on the most avid areas and 2 on relatively less avid areas. Second, ROIs were placed in areas that could be localized on harvested livers using anatomic landmarks (e.g., gallbladder fossa and major vessels). This approach yielded 20 data points at the endpoint (4 per animal).

### Tissue Procurement and Histology

Baseline core samples were obtained from each liver lobe. Livers were harvested at the endpoint, and lobar surfaces were marked with ink to preserve the landmarks needed for imaging–histology colocalization. Livers were sectioned using a bread-loafing technique in the axial plane to resemble the slices on PET/MRI, and all slices were fixed in formalin. Using anatomic landmarks, liver areas corresponding to the ROIs on endpoint images were identified, and wedge sections from these regions were cut out.

All tissue samples were processed with Masson trichrome stain, picrosirius red stain, and anti-FAP immunohistochemistry. Histologic review and analysis were performed by a board-certified fellowship-trained hepatobiliary pathologist, unaware of the imaging results and the time points of tissue procurement. Two histologic standards were used as references: METAVIR fibrosis score (27,28) and collagen proportionate area (CPA) (29–35). The METAVIR score is an ordinal 5-point scale (F0–F4); in humans, F0 is absence of fibrosis and F4 is end-stage fibrosis/cirrhosis. Given that normal swine liver has thin, organized bands of fibrosis, for the purposes of this study F0 and F1 were grouped into 1 category (F0/F1) and assigned to normal swine liver (Fig. 2). CPA is the proportion of collagen deposition area relative to the total tissue area (reported in %) on picrosirius red–stained slides. CPA analysis was performed only for endpoint wedge sections and not for baseline tissues, because of the relatively small amount of tissue procured through core needle biopsy at baseline.

### Statistical Analysis

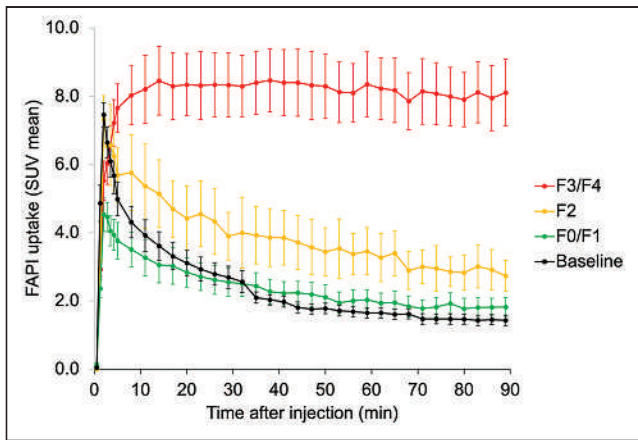
Liver FAPI uptake time–activity curves were generated by plotting the pooled ROI SUV<sub>mean</sub> against time for different stages of fibrosis. Box-and-whisker plots were generated to compare liver <sup>68</sup>Ga-FAPI uptake and CPA across different histologic stages of liver fibrosis,

Human Liver: METAVIR fibrosis score	Swine Liver: modified METAVIR fibrosis score
F0: No fibrosis	F0/F1: Expected thin bands of fibrosis seen in normal swine liver
F1: Portal fibrosis without septa	
F2: Portal fibrosis with rare septa	F2: Thickened bands of fibrosis and/or rare septa
F3: Numerous septa without cirrhosis	F3: Thickened bands of fibrosis with numerous septa without cirrhosis
F4: Cirrhosis	F4: Cirrhosis

F0/F1 (normal swine liver)	F2	F3	F4

**FIGURE 2.** Modified METAVIR score to stage swine liver fibrosis: because of presence of thin bands of fibrosis in normal swine liver and absence of this finding in normal human liver, METAVIR score used for staging human liver fibrosis was modified, such that a new stage (F0/F1) corresponds to normal swine liver with expected thin bands of fibrosis. Representative Masson trichrome–stained histologic slides of swine liver demonstrate extent of fibrosis at each stage.



**FIGURE 3.** Pooled-data time-activity curves demonstrate similar pattern of  $^{68}\text{Ga}$ -FAPI uptake by both normal liver at baseline and F0/F1 sections at endpoint. Conversely, there is incremental increase in delayed  $^{68}\text{Ga}$ -FAPI uptake by liver sections histologically staged as F2 and as F3/F4 ( $P < 0.001$ ).

using the Kruskal–Wallis rank sum test. Linear regression was used to correlate liver  $^{68}\text{Ga}$ -FAPI uptake with CPA, applying the Pearson correlation coefficient. To account for the correlation among repeated measurements and their nonmonotone change over time, a linear mixed-effects model was used with pig- and ROI-specific random effects and a piecewise linear time trend. Time-activity curves were compared using an  $F$  test on longitudinal measurements assuming normally distributed errors.  $P$  values of less than 0.05 were considered statistically significant. A post hoc power analysis for testing F2 versus F0/F1, and F3/F4 versus F0/F1, under the current sample size was performed.

## RESULTS

All animals completed the study procedures. Baseline PET imaging of animal 2 was terminated at 69 min after injection, when the animal had to be removed from the scanner to reestablish the airway and ensure animal safety. For animal 3, PET data at 37–42 min were discarded because of a shift in the animal's position inside the scanner during that period, but imaging was completed successfully. Time-activity curves demonstrated incrementally higher delayed  $^{68}\text{Ga}$ -FAPI uptake in stage F2 and F3/F4 sections ( $P < 0.001$ , Fig. 3). Uptake was stabilized at 60 min, the time point at which the static images were generated for purposes of quantitative analysis and imaging-histology correlation.

Figure 4 is an example of imaging-histology correlation in the same animal at baseline and at the endpoint; the embolized region of the liver demonstrated fibrosis with avid  $^{68}\text{Ga}$ -FAPI uptake. Table 1 summarizes the  $^{68}\text{Ga}$ -FAPI uptake and the corresponding METAVIR score and CPA for all liver sections. All baseline liver samples were normal (stage F0/F1). At the endpoint, of the total 20 liver sections, 9 were staged as F0/F1, 3 as F2, 1 as F3, and 7 as F4. Given that only 1 specimen was staged as

F3, it was grouped with the F4 specimens (i.e., group F3/F4) to provide for a meaningful quantitative analysis.

There was a strong linear correlation between liver  $^{68}\text{Ga}$ -FAPI uptake and histologic CPA ( $r = 0.89$ ,  $P < 0.001$ , Fig. 5A). There was no significant difference between the uptake of baseline liver and endpoint liver sections staged as F0/F1, with a respective median  $\text{SUV}_{\text{mean}}$  of 1.7 (interquartile range [IQR], 1.3–2.0) and 1.7 (IQR, 1.5–1.8) ( $P = 0.338$ ). Conversely,  $^{68}\text{Ga}$ -FAPI uptake was significantly higher across the F2 and F3/F4 stages and directly correlated with the histologic fibrosis stage, with a respective median  $\text{SUV}_{\text{mean}}$  of 2.9 (IQR, 2.7–3.8) and 7.6 (IQR, 6.7–10.2) ( $P < 0.001$ , Fig. 5B). There was also a significant increase in CPA across fibrosis stages, with a median CPA of 14% (IQR, 13%–16%) for F0/F1, 33% (IQR, 31%–36%) for F2, and 49% (IQR, 47%–61%) for F3/F4 (all  $P < 0.001$ , Fig. 5C). The post hoc power of testing F2 versus F0/F1, and F3/F4 versus F0/F1, under the current sample size was calculated as, respectively, 44% and 99.99%.

## DISCUSSION

We demonstrated that liver  $^{68}\text{Ga}$ -FAPI uptake strongly correlates with 2 accepted histologic metrics of liver fibrosis across the observed fibrosis stages in a human-sized swine model. Other molecular imaging agents have also been investigated for this purpose. Increased liver uptake of  $^{18}\text{F}$ -alfatide in more advanced stages of fibrosis in a mouse model has been reported (36). However, normal liver uptake of  $^{18}\text{F}$ -alfatide appears to be substantial enough to render this agent suboptimal for discerning lower stages of fibrosis (36,37). A study of  $^{11}\text{C}$ -aminoglycerol PET in a rat model demonstrated an inverse correlation between liver radiotracer uptake and fibrosis stage. Key limitations of this approach include a very short radiotracer half-life and overlap of uptake intensity between fibrosis stages (38). Last,  $^{18}\text{F}$ -FDG PET plays only a limited role in evaluation of liver fibrosis, mainly due to altered liver glucose metabolism in the setting of chronic liver disease (39).

$^{68}\text{Ga}$ -FAPI PET can offer several key potential advantages for evaluation of liver fibrosis. In our human-sized swine model,  $^{68}\text{Ga}$ -FAPI differentiated between various stages of disease.

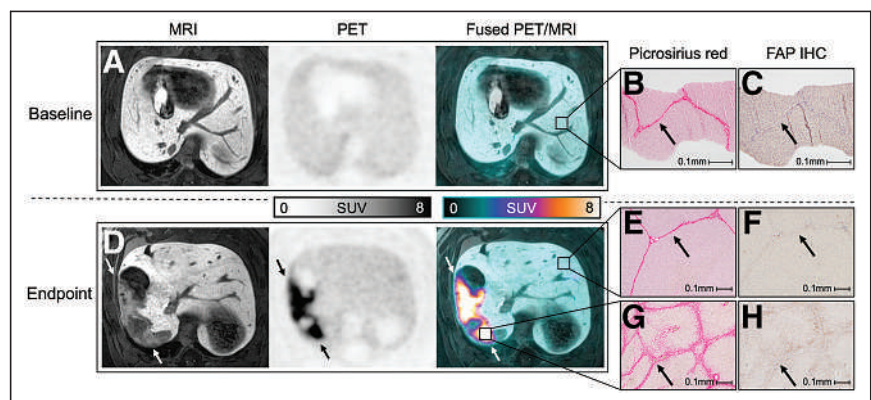


**FIGURE 4.** Imaging-histology correlation at baseline and endpoint. (A) Baseline axial PET/MRI images of animal 5 demonstrate homogeneous liver parenchyma and mild  $^{68}\text{Ga}$ -FAPI uptake. (B and C) Core biopsy of left liver lobe (at  $\times 100$  magnification) demonstrates expected thin bands of fibrosis (B, arrow), with very faint staining on FAP immunohistochemistry (C, arrow). (D) At endpoint, geographic region in right lobe demonstrates hypoenhancement on MRI and increased  $^{68}\text{Ga}$ -FAPI uptake (arrows). (E–H) Liver sections obtained from avid (abnormal) and nonavid (normal/spared) regions (at  $\times 40$  magnification) demonstrate expected thin bands of fibrosis in normal/spared region (E, arrow), with minimal staining on FAP immunohistochemistry (F, arrow), and, conversely, thickened bridging bands of fibrosis in abnormal region (G, arrow), with positive staining on FAP immunohistochemistry (H, arrow). IHC = immunohistochemistry.

**TABLE 1**  
Summary of Liver <sup>68</sup>Ga-FAPI Uptake on PET and Histologic Analysis of Liver Tissue Core Biopsy and Wedge Sections in All Subjects at Baseline and at Endpoint

Animal no.	Liver tissue	<sup>68</sup> Ga-FAPI SUV <sub>mean</sub>	METAVIR score	CPA* (%)
1	Baseline core (left lobe)	1.8	F0/F1	—
	Baseline core (right lobe)	1.6	F0/F1	—
	Endpoint section 1	7.0	F4	50
	Endpoint section 2	1.5	F0/F1	15
	Endpoint section 3	5.8	F4	49
2	Endpoint section 4	1.5	F0/F1	14
	Baseline core (left lobe)	2.4	F0/F1	—
	Baseline core (right lobe)	2.0	F0/F1	—
	Endpoint section 1	2.5	F2	39
	Endpoint section 2	2.9	F2	33
3	Endpoint section 3	1.7	F0/F1	9
	Endpoint section 4	1.5	F0/F1	12
	Baseline core (left lobe)	2.2	F0/F1	—
	Baseline core (right lobe)	1.9	F0/F1	—
	Endpoint section 1	6.9	F4	40
4	Endpoint section 2	2.1	F0/F1	22
	Endpoint section 3	1.8	F0/F1	13
	Endpoint section 4	4.9	F3	49
	Baseline core (left lobe)	0.8	F0/F1	—
	Baseline core (right lobe)	1.2	F0/F1	—
5	Endpoint section 1	4.7	F2	29
	Endpoint section 2	10.6	F4	77
	Endpoint section 3	4.5	F0/F1	16
	Endpoint section 4	12.6	F4	67
	Baseline core (left lobe)	1.3	F0/F1	—
5	Baseline core (right lobe)	1.3	F0/F1	—
	Endpoint section 1	8.3	F4	59
	Endpoint section 2	10.1	F4	44
	Endpoint section 3	1.6	F0/F1	13
	Endpoint section 4	1.7	F0/F1	18

\*CPA was not calculated at baseline because only core biopsies were obtained.

Furthermore, considering minimal uptake in normal human liver (40,41), <sup>68</sup>Ga-FAPI may detect early changes of fibrosis, which would be advantageous over elastography. Additional advantages of <sup>68</sup>Ga-FAPI PET over elastography would be whole-liver evaluation, minimal opportunity for operator error, and robustness against factors that contribute to or confound liver stiffness measurement, most notably concurrent liver inflammation (16). Although a more novel 3-dimensional MR elastography technique has demonstrated potential to address this limitation (42), this concept has not been validated in clinical practice. However, considering the ability of MRI to accurately assess several key aspects of diffuse liver disease, such as fat, iron, and stiffness (43,44), it is likely that combined <sup>68</sup>Ga-FAPI PET and MRI/MR elastography may provide complementary information to paint a more complete picture of the state of liver disease. Potential disadvantages of <sup>68</sup>Ga-FAPI PET include radiation exposure

and radiotracer availability. However, human dosimetry of <sup>68</sup>Ga-FAPI has demonstrated a whole-body exposure that is similar to that of <sup>18</sup>F-FDG (41,45). There remain challenges and unknowns that should be addressed as part of further validation of the utility of <sup>68</sup>Ga-FAPI PET in assessment of liver fibrosis. Although <sup>68</sup>Ga-FAPI uptake directly correlated with the stage of fibrosis in the presented model, this correlation was observed in the setting of active fibrosis in which the animals continued alcohol intake daily. Whether this observation is reproducible in other chronic disease processes, such as in viral hepatitis and nonalcoholic steatohepatitis, is of significant scientific and clinical relevance and requires further validation.

This study had some limitations. Although the sample size was small, a post hoc power analysis demonstrated its adequacy, which was also on a par with a previous report (46). Furthermore, this model generated patchy or geographic areas of fibrotic and normal

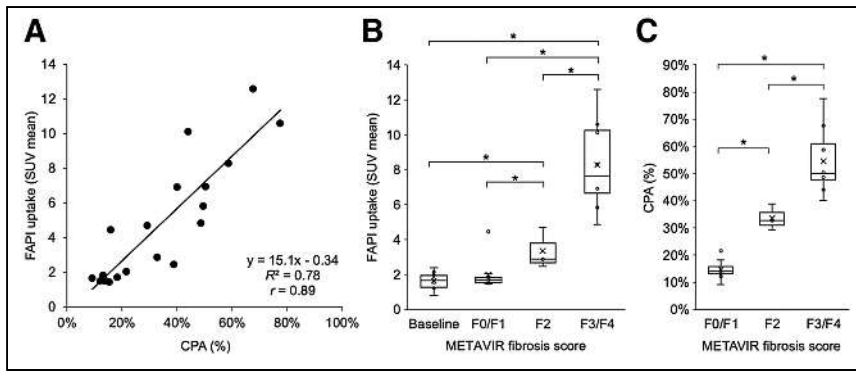


**FIGURE 5.** (A) Linear regression demonstrates strong correlation between liver  $^{68}\text{Ga}$ -FAPI uptake and histologic CPA ( $r = 0.89$ ). (B) Box-and-whisker plot of liver  $^{68}\text{Ga}$ -FAPI uptake for METAVIR fibrosis stage groups demonstrates no significant difference between baseline liver uptake and endpoint uptake in liver sections staged as F0/F1 ( $P = 0.338$ ); however, there is significant and incrementally higher  $^{68}\text{Ga}$ -FAPI uptake across F2 and F3/F4 stages, with minimal overlap between different stages ( $P < 0.001$ ). (C) Box-and-whisker plot of histologic CPA for each METAVIR fibrosis stage group at endpoint, demonstrating significant and incrementally increased CPA with increasing fibrosis stage ( $P < 0.001$ ). CPA was not performed for baseline tissues because relatively small amount of tissue was procured through core needle biopsy at baseline. \*Statistical significance.

liver, a pattern that is different from the pattern of disease in humans. However, this feature allowed for an internal negative control. Another limitation of a swine model is the presence of thin fibrotic bands in normal liver, explaining  $^{68}\text{Ga}$ -FAPI uptake by normal liver. Hence, the potential of  $^{68}\text{Ga}$ -FAPI PET to differentiate between F0 and F1 stages of disease would have to be investigated in human subjects. Our data yielded only 1 specimen with F3 liver fibrosis; hence, we were unable to evaluate the ability of  $^{68}\text{Ga}$ -FAPI PET to discern between F3 and F4 stages. Although worth investigating, the significance of this limitation is unknown, as often in clinical practice or in the research setting, F0 and F1 stages as well as F3 and F4 stages are grouped for treatment or prognostic purposes. Last, despite the careful approach to achieve accurate and unbiased imaging–histology correlation through masking and using only anatomic landmarks to obtain tissue samples that correspond to ROIs, sampling error or variability cannot be completely eliminated. This variability and limitation are not unique to this study and are also present in current clinical practice, as well as in nearly all studies that have evaluated liver fibrosis. We anticipate that once  $^{68}\text{Ga}$ -FAPI PET for assessment of liver fibrosis is further investigated and potentially validated in humans, it will largely overcome the aforementioned limitations of the current techniques and enhance our ability to understand disease progression and evolution among those with chronic liver disease.

## CONCLUSION

The strong correlation between liver  $^{68}\text{Ga}$ -FAPI uptake and the histologic stage of liver fibrosis suggests that  $^{68}\text{Ga}$ -FAPI PET can play an impactful role in noninvasive staging of liver fibrosis, pending validation in patients. This technique can be used not only in the clinical setting but also for clinical trials (e.g., drug development) or for validation of other novel techniques for assessment of diffuse liver disease.

## DISCLOSURE

This work was supported in part by the Biomedical and Genomic Research Group Discretionary Fund (University of Wisconsin–Madison). Sarvesh Periyasamy is supported by the National Cancer Institute (F30CA250408) and the National Institute of General Medical Sciences (T32GM140935). Ali Pirasteh is

supported by GE Healthcare (departmental research support), TheraCea, and Sanofi Genzyme (consultant). Sarvesh Periyasamy is supported by Johnson & Johnson, HEPTA Medical, and Vector Surgical (consultant). Kyle Schachtschneider is supported by Guerbet, Janssen Research & Development, NeoTherma Oncology, TriSalus Life Sciences (research support), and Sus Clinicals, Inc. (consultant). Lawrence Schook is supported by Guerbet, Janssen Research & Development, NeoTherma Oncology, TriSalus Life Sciences (research support), and Sus Clinicals, Inc. (chief scientific officer). Ron Gaba is supported by Guerbet, Janssen Research & Development, NeoTherma Oncology, TriSalus Life Sciences (research support), and Sus Clinicals, Inc. (consultant). Adnan Said is supported by Intercept Pharmaceuticals and Exact Sciences (research support). Paul Laeseke is supported by Johnson & Johnson/Ethicon/

NeuWave (consultant), HistoSonics (consultant, shareholder, and research agreement), Elucent (consultant and shareholder), Siemens (research agreement), and McGinley Orthopedic Innovations (shareholder). Dhanansayan Shanmuganayagam is supported by Wisconsin Miniature Swine (Coinventor). No other potential conflict of interest relevant to this article was reported.

## KEY POINTS

**QUESTION:** Is there potential for  $^{68}\text{Ga}$ -FAPI PET in staging liver fibrosis?

**PERTINENT FINDINGS:** This animal study demonstrated a direct correlation between quantitative liver  $^{68}\text{Ga}$ -FAPI uptake on PET and both histologic measures of liver fibrosis, that is, the ordinal METAVIR score and the quantitative CPA.

**IMPLICATIONS FOR PATIENT CARE:** Pending further validation in patients,  $^{68}\text{Ga}$ -FAPI PET is a promising tool for noninvasive liver fibrosis staging.

## REFERENCES

- GBD 2017 Cirrhosis Collaborators. The global, regional, and national burden of cirrhosis by cause in 195 countries and territories, 1990–2017: a systematic analysis for the Global Burden of Disease Study 2017. *Lancet Gastroenterol Hepatol.* 2020;5:245–266.
- Ge PS, Runyon BA. Treatment of patients with cirrhosis. *N Engl J Med.* 2016;375:767–777.
- Angulo P, Kleiner DE, Dam-Larsen S, et al. Liver fibrosis, but no other histologic features, is associated with long-term outcomes of patients with nonalcoholic fatty liver disease. *Gastroenterology.* 2015;149:389–397.e10.
- D'Ambrosio R, Aghemo A, Rumi MG, et al. A morphometric and immunohistochemical study to assess the benefit of a sustained virological response in hepatitis C virus patients with cirrhosis. *Hepatology.* 2012;56:532–543.
- Marcellin P, Gane E, Buti M, et al. Regression of cirrhosis during treatment with tenofovir disoproxil fumarate for chronic hepatitis B: a 5-year open-label follow-up study. *Lancet.* 2013;381:468–475.
- Alberti A, Noventa F, Benvegno L, Boccato S, Gatta A. Prevalence of liver disease in a population of asymptomatic persons with hepatitis C virus infection. *Ann Intern Med.* 2002;137:961–964.
- Harris R, Harman DJ, Card TR, Aithal GP, Guha IN. Prevalence of clinically significant liver disease within the general population, as defined by non-invasive

- markers of liver fibrosis: a systematic review. *Lancet Gastroenterol Hepatol*. 2017; 2:288–297.
8. Sumida Y. Limitations of liver biopsy and non-invasive diagnostic tests for the diagnosis of nonalcoholic fatty liver disease/nonalcoholic steatohepatitis. *World J Gastroenterol*. 2014;20:475–485.
  9. Rousset M-C, Michalak S, Dupré F, et al. Sources of variability in histological scoring of chronic viral hepatitis. *Hepatology*. 2005;41:257–264.
  10. Goldin RD, Goldin JG, Burt AD, et al. Intra-observer variation in the histopathological assessment of chronic viral hepatitis. *J Hepatol*. 1996;25:649–654.
  11. Maharaj B, Maharaj RJ, Leary WP, et al. Sampling variability and its influence on the diagnostic yield of percutaneous needle biopsy of the liver. *Lancet*. 1986;1: 523–525.
  12. Regev A, Berho M, Jeffers LJ, et al. Sampling error and intraobserver variation in liver biopsy in patients with chronic HCV infection. *Am J Gastroenterol*. 2002;97: 2614–2618.
  13. Bravo AA, Sheth SG, Chopra S. Liver biopsy. *N Engl J Med*. 2001;344:495–500.
  14. Singh S, Venkatesh SK, Wang Z, et al. Diagnostic performance of magnetic resonance elastography in staging liver fibrosis: a systematic review and meta-analysis of individual participant data. *Clin Gastroenterol Hepatol*. 2015;13:440–451.e6.
  15. Yin M, Woollard J, Wang X, et al. Quantitative assessment of hepatic fibrosis in an animal model with magnetic resonance elastography. *Magn Reson Med*. 2007; 58:346–353.
  16. Tang A, Cloutier G, Szevenyi NM, Sirlin CB. Ultrasound elastography and MR elastography for assessing liver fibrosis: part 2, diagnostic performance, confounders, and future directions. *AJR*. 2015;205:33–40.
  17. Wang QB, Zhu H, Liu HL, Zhang B. Performance of magnetic resonance elastography and diffusion-weighted imaging for the staging of hepatic fibrosis: a meta-analysis. *Hepatology*. 2012;56:239–247.
  18. Yin M, Glaser KJ, Talwalkar JA, Chen J, Manduca A, Ehman RL. Hepatic MR elastography: clinical performance in a series of 1377 consecutive examinations. *Radiology*. 2016;278:114–124.
  19. Chen J, Talwalkar JA, Yin M, Glaser KJ, Sanderson SO, Ehman RL. Early detection of nonalcoholic steatohepatitis in patients with nonalcoholic fatty liver disease by using MR elastography. *Radiology*. 2011;259:749–756.
  20. Salameh N, Larrat B, Abarca-Quinones J, et al. Early detection of steatohepatitis in fatty rat liver by using MR elastography. *Radiology*. 2009;253:90–97.
  21. Levy MT, McCaughan GW, Abbott CA, et al. Fibroblast activation protein: a cell surface dipeptidyl peptidase and gelatinase expressed by stellate cells at the tissue remodelling interface in human cirrhosis. *Hepatology*. 1999;29:1768–1778.
  22. Uitte de Willige S, Malfliet JJMC, Janssen HLA, Leebeek FWG, Rijken DC. Increased N-terminal cleavage of alpha-2-antiplasmin in patients with liver cirrhosis. *J Thromb Haemost*. 2013;11:2029–2036.
  23. Shi X, Xing H, Yang X, et al. Fibroblast imaging of hepatic carcinoma with <sup>68</sup>Ga-FAPI-04 PET/CT: a pilot study in patients with suspected hepatic nodules. *Eur J Nucl Med Mol Imaging*. 2021;48:196–203.
  24. Loktev A, Lindner T, Mier W, et al. A tumor-imaging method targeting cancer-associated fibroblasts. *J Nucl Med*. 2018;59:1423–1429.
  25. Gaba RC, Mendoza-Elias N, Regan DP, et al. Characterization of an inducible alcoholic liver fibrosis model for hepatocellular carcinoma investigation in a transgenic porcine tumorigenic platform. *J Vasc Interv Radiol*. 2018;29:1194–1202.e1.
  26. Avritscher R, Wright KC, Javadi S, et al. Development of a large animal model of cirrhosis and portal hypertension using hepatic transarterial embolization: a study in swine. *J Vasc Interv Radiol*. 2011;22:1329–1334.
  27. The French METAVIR Cooperative Study Group. Intraobserver and interobserver variations in liver biopsy interpretation in patients with chronic hepatitis C. *Hepatology*. 1994;20:15–20.
  28. Bedossa P, Poinard T. An algorithm for the grading of activity in chronic hepatitis C. *Hepatology*. 1996;24:289–293.
  29. Buzzetti E, Hall A, Ekstedt M, et al. Collagen proportionate area is an independent predictor of long-term outcome in patients with non-alcoholic fatty liver disease. *Aliment Pharmacol Ther*. 2019;49:1214–1222.
  30. Tsochatzis E, Bruno S, Isgro G, et al. Collagen proportionate area is superior to other histological methods for sub-classifying cirrhosis and determining prognosis. *J Hepatol*. 2014;60:948–954.
  31. Calvaruso V, Dhillon AP, Tsochatzis E, et al. Liver collagen proportionate area predicts decompensation in patients with recurrent hepatitis C virus cirrhosis after liver transplantation. *J Gastroenterol Hepatol*. 2012;27:1227–1232.
  32. Manousou P, Burroughs AK, Tsochatzis E, et al. Digital image analysis of collagen assessment of progression of fibrosis in recurrent HCV after liver transplantation. *J Hepatol*. 2013;58:962–968.
  33. Calvaruso V, Burroughs AK, Standish R, et al. Computer-assisted image analysis of liver collagen: relationship to Ishak scoring and hepatic venous pressure gradient. *Hepatology*. 2009;49:1236–1244.
  34. Xie SB, Ma C, Lin CS, Zhang Y, Zhu JY, Ke WM. Collagen proportionate area of liver tissue determined by digital image analysis in patients with HBV-related decompensated cirrhosis. *Hepatobiliary Pancreat Dis Int*. 2011;10:497–501.
  35. Isgro G, Calvaruso V, Andreana L, et al. The relationship between transient elastography and histological collagen proportionate area for assessing fibrosis in chronic viral hepatitis. *J Gastroenterol*. 2013;48:921–929.
  36. Shao T, Chen Z, Belov V, et al. [<sup>18</sup>F]-Alfatide PET imaging of integrin  $\alpha\beta 3$  for the non-invasive quantification of liver fibrosis. *J Hepatol*. 2020;73:161–169.
  37. Wu J, Wang S, Zhang X, et al. <sup>18</sup>F-Alfatide II PET/CT for identification of breast cancer: a preliminary clinical study. *J Nucl Med*. 2018;59:1809–1816.
  38. Chen X, Zhang X, Du M, et al. In vivo preclinical PET/CT imaging of carbon-11-labeled aminoglycerol probe for the diagnosis of liver fibrosis. *Ann Nucl Med*. 2019;33:806–812.
  39. Verloh N, Einspieler I, Utpatel K, et al. In vivo confirmation of altered hepatic glucose metabolism in patients with liver fibrosis/cirrhosis by <sup>18</sup>F-FDG PET/CT. *EJNMMI Res*. 2018;8:98.
  40. Kratochwil C, Flechsig P, Lindner T, et al. <sup>68</sup>Ga-FAPI PET/CT: tracer uptake in 28 different kinds of cancer. *J Nucl Med*. 2019;60:801–805.
  41. Giesel FL, Kratochwil C, Lindner T, et al. <sup>68</sup>Ga-FAPI PET/CT: biodistribution and preliminary dosimetry estimate of 2 DOTA-containing FAP-targeting agents in patients with various cancers. *J Nucl Med*. 2019;60:386–392.
  42. Shi Y, Qi YF, Lan GY, et al. Three-dimensional MR elastography depicts liver inflammation, fibrosis, and portal hypertension in chronic hepatitis B or C. *Radiology*. 2021;301:154–162.
  43. Yokoo T, Serai SD, Pirasteh A, et al. Linearity, bias, and precision of hepatic proton density fat fraction measurements by using MR imaging: a meta-analysis. *Radiology*. 2018;286:486–498.
  44. Wood JC, Enriquez C, Ghugre N, et al. MRI R2 and R2\* mapping accurately estimates hepatic iron concentration in transfusion-dependent thalassemia and sickle cell disease patients. *Blood*. 2005;106:1460–1465.
  45. Johansson L, Mattsson S, Nosslin B, Leide-Svegborn S. Effective dose from radiopharmaceuticals. *Eur J Nucl Med*. 1992;19:933–938.
  46. Yin M, Glaser KJ, Manduca A, et al. Distinguishing between hepatic inflammation and fibrosis with MR elastography. *Radiology*. 2017;284:694–705.

# A Long Axial Field of View Enables PET/CT in Toddler Without Sedation

Michala Reichkendler<sup>1</sup>, Flemming L. Andersen<sup>1</sup>, Lise Borgwardt<sup>1</sup>, Ulrikka Nygaard<sup>2</sup>, Elisabeth Albrecht-Beste<sup>1</sup>, Kim F. Andersen<sup>1</sup>, Anna Ljunggren<sup>1</sup>, Nynne Abrahamsen<sup>1</sup>, Annika Loft<sup>1</sup>, Liselotte Højgaard<sup>1,3</sup>, and Barbara M. Fischer<sup>1,3</sup>

<sup>1</sup>Department of Clinical Physiology and Nuclear Medicine, Rigshospitalet, Copenhagen, Denmark; <sup>2</sup>Department of Pediatrics and Adolescent Medicine, Rigshospitalet, Copenhagen, Denmark; and <sup>3</sup>Department of Clinical Medicine, University of Copenhagen, Copenhagen, Denmark

**T**otal-body PET and long-axial-field-of-view (LAFOV) PET are game-changing innovations at the threshold of clinical implementation. Early experience has demonstrated high sensitivity (84 cps/kBq), a time-of-flight resolution of 214 ps, and improved image quality enabling ultrafast or low-dose scanning (1). An LAFOV PET/CT scanner (Siemens Biograph Vision Quadra) was installed at Rigshospitalet in September 2021. This post illustrates how this 10-fold increase in sensitivity can enable avoidance of general anesthesia by fast and flexible PET acquisition. The departmental review board approved this study, and the parents gave written informed consent.

An LAFOV <sup>18</sup>F-FDG PET/CT scan was performed on a 17-mo-old girl suspected of having incomplete Kawasaki disease after 12 d of fever despite broad-spectrum antibiotics. Previously, she had undergone left heminephrectomy due to a duplex kidney and repeated urinary tract infections. She had high C-reactive protein, anemia, hypoalbuminemia, and thrombocytosis, as well as relapse of fever despite immunoglobulin therapy and high-dose acetylsalicylic acid. PET/CT was performed to rule out malignancy or focal infection.

The patient was positioned in a vacuum fix pillow supplemented with light fixation across the body using a hook-and-loop belt with arms free. The mother was present during the scan, keeping the toddler calm by singing. The scan was acquired 74 min after injection of 35 MBq of <sup>18</sup>F-FDG (3 MBq/kg); low-dose CT was followed by a 5-min PET acquisition in list mode while the patient was observed for movement. An image frame of 120 s with minimal movement was reconstructed using a standard protocol of 4 iterations and 5 subsets, 1.65 × 1.65 mm voxels, and a gaussian postprocessing filter of 2.0 mm in full width at half maximum. The reconstruction method was ordinary Poisson using point-spread modeling and time of flight with a maximum ring distance of 85. The images

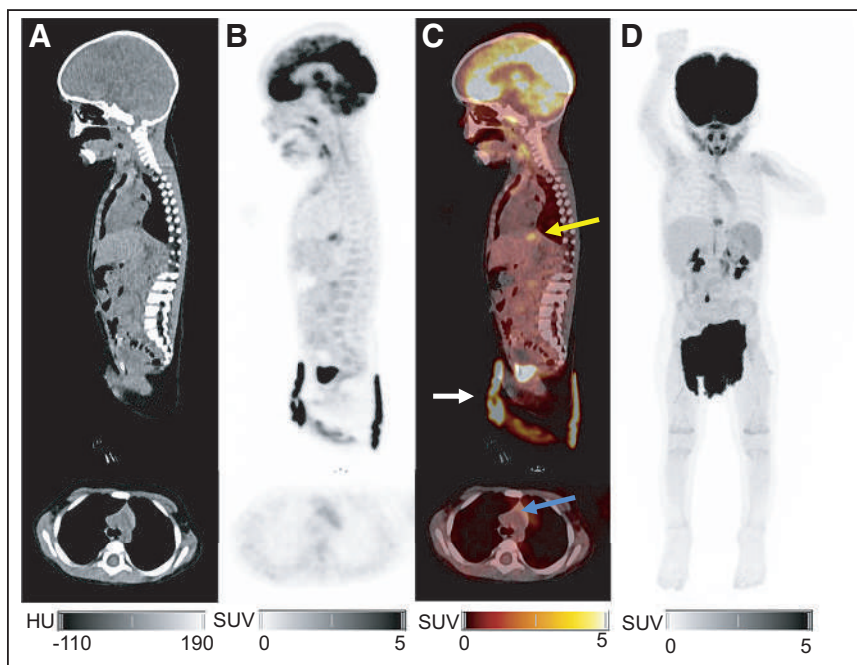


**FIGURE 1.** Sagittal (top) and axial (bottom) CT (A), PET (B), and PET/CT (C) images and maximum-intensity-projection reconstruction (D) after 120-s PET acquisition. No pathologic uptake is seen, but there is reactive accumulation in distal part of esophagus (yellow arrow), physiologic thymic uptake (blue arrow), and accumulated urinary activity in diaper (white arrow).

were of good quality for interpretation despite slight misalignment over the extremities.

PET/CT demonstrated no signs of infection or malignancy (Fig. 1). Thus, the patient was discharged. All parameters had normalized at follow-up a week later. This case illustrates how LAFOV PET enables whole-body PET imaging in children without the risks and logistical challenges associated with sedation.

## DISCLOSURE

No potential conflict of interest relevant to this article was reported.

## REFERENCE

1. Alberts I, Hünermund J, Prenosil G, et al. Clinical performance of long axial field of view PET/CT. *Eur J Nucl Med Mol Imaging*. 2021;48:2395–2404.

Received Dec. 7, 2021; revision accepted Jun. 11, 2022.  
For correspondence or reprints, contact Barbara M. Fischer (malene.fischer@regionh.dk).  
Published online Jun. 16, 2022.  
COPYRIGHT © 2022 by the Society of Nuclear Medicine and Molecular Imaging.  
DOI: 10.2967/jnumed.121.263626



June 24-27  
2023  
SNMMI ANNUAL MEETING

Chicago, Illinois, USA

# CALL FOR ABSTRACTS

Attention physicians, scientists, technologists, lab professionals, residents, students, or educator/course directors in the field of nuclear medicine and molecular imaging! Submitting an abstract for **SNMMI's 2023 Annual Meeting** provides you the ideal platform to present your research to a global audience of your peers, while increasing your professional recognition.

**Original abstracts will be accepted on the following scientific tracks:**

- ▶ Cardiovascular
- ▶ Educational Exhibits
- ▶ General Clinical Specialties
- ▶ Molecular Targeting Probes
- ▶ Neurosciences
- ▶ Oncology – Basic
- ▶ Oncology – Clinical Diagnosis and Therapy
- ▶ Physics, Instrumentation and Data Sciences
- ▶ Technologist/Technologist Student

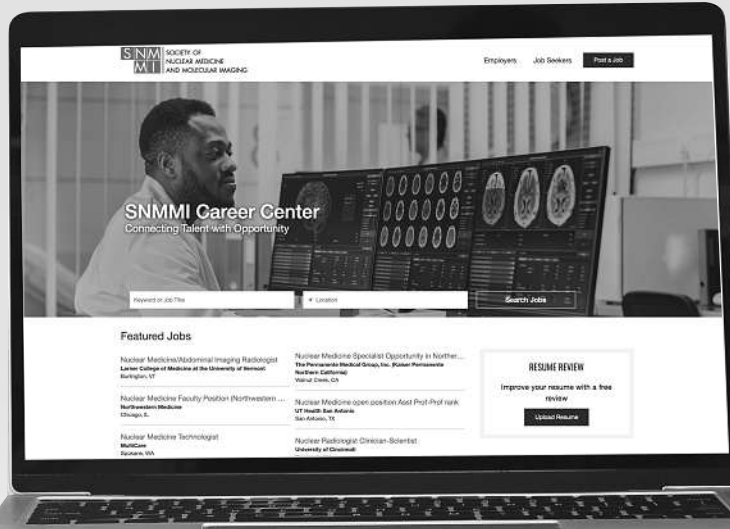
**ABSTRACT SUBMISSION DEADLINE:  
TUESDAY  
JANUARY 11, 2023**

[WWW.SNMMI.ORG/AM2023](http://WWW.SNMMI.ORG/AM2023)



# Explore SNMMI's Online Career Center!

Explore the benefits of SNMMI's online career center by logging in or creating a new account today.



[careercenter.snmmi.org](http://careercenter.snmmi.org)

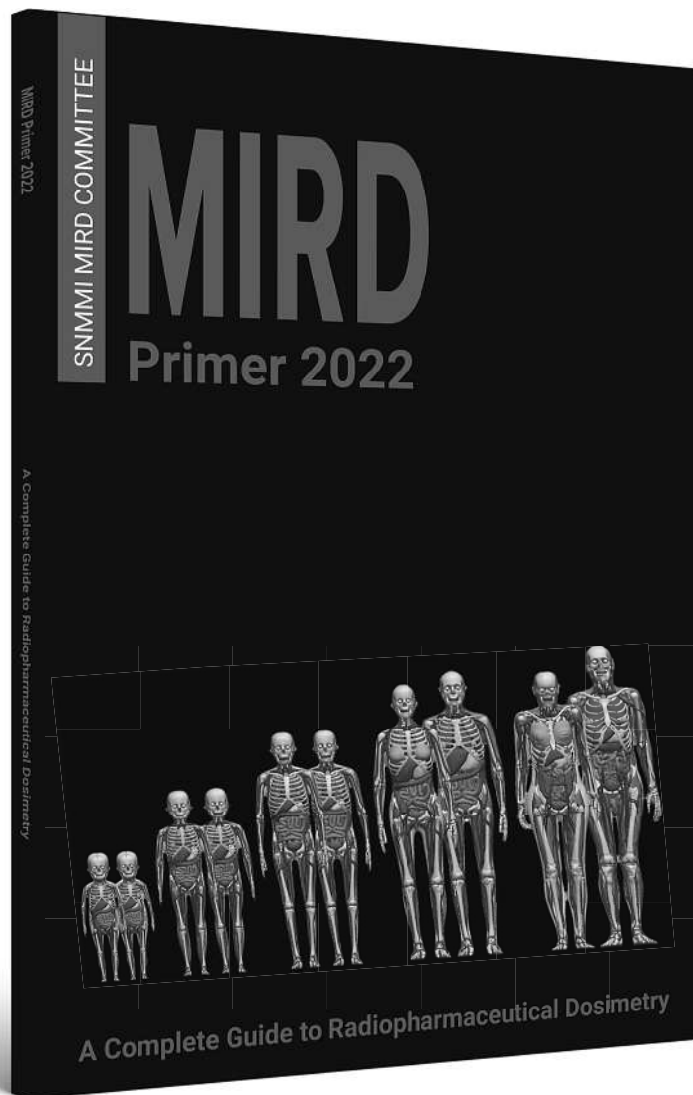
\*Note: Single sign-on has been enabled for this platform and you can use your member login credentials to access the Career Center. If you are unsure of your password, to go to the SNMMI password reset link to create a new password.



## UNITED STATES POSTAL SERVICE® (All Periodicals Publications Except Requester Publications)

1. Publication Title JOURNAL OF NUCLEAR MEDICINE		2. Publication Number 281 - 560		3. Filing Date 10/1/2022	
4. Issue Frequency MONTHLY		5. Number of Issues Published Annually 12		6. Annual Subscription Price \$603 US/Can; \$648 Intl	
7. Complete Mailing Address of Known Office of Publication (Not printer) (Street, city, county, state, and ZIP+4®) 1850 Samuel Morse Dr., Reston, VA 20190					
8. Complete Mailing Address of Headquarters or General Business Office of Publisher (Not printer) 1850 Samuel Morse Dr., Reston, VA 20190					
9. Full Names and Complete Mailing Addresses of Publisher, Editor, and Managing Editor (Do not leave blank) Publisher (Name and complete mailing address) Society of Nuclear Medicine and Molecular Imaging, 1850 Samuel Morse Dr., Reston, VA 20190 Editor (Name and complete mailing address) Johannes Czernin, MD, 1850 Samuel Morse Dr., Reston, VA 20190 Managing Editor (Name and complete mailing address) Rebecca Maxey, 1850 Samuel Morse Dr., Reston, VA 20190					
10. Owner (Do not leave blank. If the publication is owned by a corporation, give the name and address of the corporation immediately followed by the names and addresses of all stockholders owning or holding 1 percent or more of the total amount of stock. If not owned by a corporation, give the names and addresses of the individual owners. If owned by a partnership or other unincorporated firm, give its name and address as well as those of each individual owner. If the publication is published by a nonprofit organization, give its name and address.)					
Full Name		Complete Mailing Address			
Society of Nuclear Medicine and Molecular Imaging		1850 Samuel Morse Dr., Reston, VA 20190			
11. Known Bondholders, Mortgagees, and Other Security Holders Owning or Holding 1 Percent or More of Total Amount of Bonds, Mortgages, or Other Securities. If none, check box <input checked="" type="checkbox"/> None					
Full Name		Complete Mailing Address			
12. Tax Status (For completion by nonprofit organizations authorized to mail at nonprofit rates) (Check one) The purpose, function, and nonprofit status of this organization and the exempt status for federal income tax purposes: <input checked="" type="checkbox"/> Has Not Changed During Preceding 12 Months <input type="checkbox"/> Has Changed During Preceding 12 Months (Publisher must submit explanation of change with this statement)					

13. Publication Title JOURNAL OF NUCLEAR MEDICINE		14. Issue Date for Circulation Data Below September 2022	
15. Extent and Nature of Circulation			
		Average No. Copies Each Issue During Preceding 12 Months	No. Copies of Single Issue Published Nearest to Filing Date
a. Total Number of Copies (Net press run)		2660	2867
b. Paid Circulation (By Mail and Outside the Mail)	(1) Mailed Outside-County Paid Subscriptions Stated on PS Form 3541 (Include paid distribution above nominal rate, advertiser's proof copies, and exchange copies)	2091	2242
	(2) Mailed In-County Paid Subscriptions Stated on PS Form 3541 (Include paid distribution above nominal rate, advertiser's proof copies, and exchange copies)	0	0
	(3) Paid Distribution Outside the Mails Including Sales Through Dealers and Carriers, Street Vendors, Counter Sales, and Other Paid Distribution Outside USPS®	343	441
	(4) Paid Distribution by Other Classes of Mail Through the USPS (e.g., First-Class Mail®)	0	0
c. Total Paid Distribution (Sum of 15b (1), (2), (3), and (4))		2434	2683
d. Free or Nominal Rate Distribution (By Mail and Outside the Mail)	(1) Free or Nominal Rate Outside-County Copies included on PS Form 3541	0	0
	(2) Free or Nominal Rate In-County Copies included on PS Form 3541	0	0
	(3) Free or Nominal Rate Copies Mailed at Other Classes Through the USPS (e.g., First-Class Mail)	0	0
	(4) Free or Nominal Rate Distribution Outside the Mail (Carriers or other means)	32	33
e. Total Free or Nominal Rate Distribution (Sum of 15d (1), (2), (3), and (4))		32	33
f. Total Distribution (Sum of 15c and 15e)		2465	2716
g. Copies not Distributed (See Instructions to Publishers #4 (page #3))		195	151
h. Total (Sum of 15f and g)		2660	2867
i. Percent Paid (15c divided by 15f times 100)		98.71%	98.78%
* If you are claiming electronic copies, go to line 16 on page 3. If you are not claiming electronic copies, skip to line 17 on page 3.			
16. Electronic Copy Circulation		Average No. Copies Each Issue During Preceding 12 Months	No. Copies of Single Issue Published Nearest to Filing Date
a. Paid Electronic Copies			
b. Total Paid Print Copies (Line 15c) + Paid Electronic Copies (Line 16a)			
c. Total Print Distribution (Line 15f) + Paid Electronic Copies (Line 16a)			
d. Percent Paid (Both Print & Electronic Copies) (16b divided by 16c x 100)			
<input checked="" type="checkbox"/> I certify that 50% of all my distributed copies (electronic and print) are paid above a nominal price.			
17. Publication of Statement of Ownership			
<input checked="" type="checkbox"/> If the publication is a general publication, publication of this statement is required. Will be printed in the <u>December 2022</u> issue of this publication. <input type="checkbox"/> Publication not required.			
18. Signature and Title of Editor, Publisher, Business Manager, or Owner <i>Rebecca Maxey</i>			Date 10/1/2022



## MIRD Primer 2022

### A Complete Guide to Radiopharmaceutical Dosimetry

Richly illustrated and thoroughly referenced, the **MIRD Primer 2022** is a comprehensive, state-of-the-art guide to radiopharmaceutical dosimetry that reflects the dramatic evolution of the field of nuclear medicine, including molecular imaging and, increasingly, radiopharmaceutical therapy.

The MIRD Primer 2022 serves as

- a foundation for nuclear medicine and other medical professionals who require a working knowledge of internal radionuclide dosimetry and its radiobiological implications—without having to delve too deeply into the underlying mathematics.
- an authoritative reference on the latest, complete mathematical formulation of the MIRD schema for those seeking a more rigorous understanding of internal dosimetry.
- an invaluable teaching tool, with a large number and wide variety of clinically relevant calculational examples.

Order your copy today!  
**[WWW.SNMMI.ORG/MIRD2022](http://WWW.SNMMI.ORG/MIRD2022)**

# SNMMI Ones to Watch for 2023

## The Search Is Underway!

SNMMI is now accepting nominations for our **2023 Ones to Watch** selections. As the field continues to expand, a new wave of talent is at the forefront of this cutting-edge specialty. We hope you'll help us identify those early career professionals working to shape the future of nuclear medicine and molecular imaging.

Members can nominate someone they know—currently in training or who have completed their training within the last 5 years—whose actions, work, or studies have set them apart as a future thought leader in the field.

Nominations Must Include:

- Name and credentials
- Years in nuclear medicine/molecular imaging/radiology profession
- Occupation and employer \*Substitute program name if still in training\*
- 250 (maximum) words about their achievements or demonstrated potential in the field of nuclear medicine or molecular imaging
- A headshot of the nominee

Submit your **Ones to Watch** nomination by **December 31, 2022** for consideration.



# MY SNMMI

## Get Ready for 2023 by Updating Your Member Profile

Your “My SNMMI” dashboard is an easy way to navigate the many member benefits available to you. Take 5 minutes to customize your member experience through SNMMI profile options.

-  Access the SNMMI Member Directory to begin expanding your professional network
-  Manage your credit history, see your transcript, and access the SNMMI Learning Center
-  Manage your email and publication preferences to ensure you get the latest news from SNMMI
-  Review and update new demographic questions and professional certifications
-  Choose your journal preferences for both JNM and JNMT online or print issues
-  Stay up-to-date by updating your email and mailing address as needed

[www.snmmi.org/MySNMMI](http://www.snmmi.org/MySNMMI)

*We encourage you to bookmark this page for future use*

**SNMMI** Value Initiative  
SOCIETY OF NUCLEAR MEDICINE & MOLECULAR IMAGING

 **ALZHEIMER'S<sup>®</sup>  
ASSOCIATION**

**AAIC>23**

**PRESENT  
YOUR  
DISCOVERIES.**



Submit an abstract or session proposal for the Alzheimer's Association International Conference<sup>®</sup> 2023 (AAIC<sup>®</sup>), the world's largest and most influential dementia research conference.

**Submission deadline: January 23, 2023 by 11:59 p.m. EST**

**AAIC 2023: JULY 16-20**

**Amsterdam, Netherlands and Online**

Educational Workshops and Preconferences: July 14-15

Exhibits: July 16-19

**[alz.org/AAIC-JNM](https://alz.org/AAIC-JNM)**

# 2 | **The Journal of Muscular Medicine** • December 2022 • Vol. 63 • Pages 1783-1962